The Oceanographic Influence of Sedimentation on the Continental Shelf: A Numerical Comparison Between Tropical and Antarctic Environments.

by

Mark A. Hemer, BSc(Hons I)

Flinders University of South Australia

Submitted in fulfilment of the requirements

for the Degree of

Doctor of Philosophy

University of Tasmania

August, 2003

Declaration

This thesis contains no material which has been accepted for a degree or diploma by the University or any other institution. To the best of my knowledge and belief this thesis contains no material previously published or written by another person except where due acknowledgement is made in the text.

Mark A. Hemer

Authority of access

This thesis may be made available for loan and limited copying in accordance with the *Copyright Act 1968*.

Mark A. Hemer

University of Tasmania

August 2003

Abstract

Sedimentation of two contrasting continental shelf environments have been investigated. Numerical ocean models were used to assess the oceanic processes which dominate Torres Strait and the Gulf of Papua, Northern Australia, and then the ocean cavity beneath the Amery Ice Shelf, East Antarctica.

A three-dimensional, numerical ocean model (MECO) was applied to the Torres Strait/Gulf of Papua region at 0.05° resolution. Validation of the model was carried out against current meter and sea-level observational data. Dispersal pathways of sediments, derived from the Fly River, Papua New Guinea, and from a resuspension event on the Northern Great Barrier Reef, into Torres Strait were investigated via the introduction of passive tracers into the model. Sediment input into Torres Strait is found to be greater during the Trade season by approximately 10%. Wave data was also obtained, and together with hydrodynamic model output, sediment mobility due to currents, waves and wave-current interactions was considered for both the Trade and Monsoon seasons. Sediment mobility in the Gulf of Papua is dominated by wave motion, whereas Torres Strait is a mixed environment of waves and tidal currents.

Two numerical ocean models were applied to the Amery Ice Shelf/Prydz Bay region to determine the oceanic processes responsible for the distribution of marine sediments beneath the ice shelf. The MECO model was used to determine the sub-ice-shelf tidal environment. A modified version of the Princeton Ocean Model was applied to determine the baroclinic circulation beneath the ice shelf. Validation of the tides within each model was carried out against available current meter data and sea-level records. Spring tidal currents (up to 10-15 cms^{-1}) are approximately two to three times the magnitude of the maximum density-driven flows (5-6 cms^{-1}). However, the influence of tides on the mean sub-ice-shelf melt-rates, and the mean density-driven currents, was shown to be insignificant. Thermohaline flows dominate the predicted mean sub-ice-shelf circulation and indicate a depth-integrated mass transport of 0.2 Sv, of the same order of magnitude as the overturning circulation. Combined tidal and density-driven maximum bottom currents are too small (up to 16 cms^{-1}) to remobilise sediments.

Sediments were collected from beneath, and directly in front of, the Amery Ice Shelf. The observed sub-ice-shelf surface sediment distribution supports the dispersal pathways of diatoms beneath the ice shelf, predicted using the baroclinic model. The sediment core collected from beneath the eastern side of the Amery Ice Shelf in a region of predicted inflow (site AM02) contains a Holocene-age, siliceous mud and ooze layer, providing evidence that landward transport

of hemipelagic sediments occurs beneath the Amery Ice Shelf. An imposed increase in the ocean temperature in the baroclinic model predicts increased melt rates at the ice-ocean interface, and a strengthened sub-ice-shelf circulation. An increase in sea-ice associated diatom deposition during the mid-Holocene is interpreted from AM02 down-core changes in the diatom assemblage. Results of the hydrodynamic model suggest the diatom signal may be a response to increased temperatures which may have occurred during the mid-Holocene climatic optimum.

The dominant processes acting in the two continental shelf environments are able to be distinguished from each other allowing separate classification; the Torres Strait/Gulf of Papua environment is classified as a wave- and tide-dominated shelf, and the Prydz Bay/sub-Amery Ice Shelf environment is classified as a density-driven current-dominated continental shelf, and is probably typical of Antarctic shelf environments.

Acknowledgements

A PhD is not an achievable task without the assistance of others. There are many people whom I would like to thank for their many and varied contributions.

Firstly, I would like to express my greatest appreciation to my supervisors, Peter Harris, John Hunter, Richard Coleman, and Bill Budd. I have enjoyed working with each of you immensely. I am very grateful for the oppurtunities, guidance and encouragement that you have each given me, it has far exceeded anything I had expected before I began. I feel very fortunate to have gained so much experience from working with each of you in your respective fields, and look forward to continuing this in the future.

The thesis was carried out under an Australian Postgraduate Award PhD scholarship, with extra resources provided by the Antarctic Co-operative Research Centre. I would like to take this opportunity to acknowledge this support.

Thankyou to the people who supplied data that enabled this research to be carried out. These include: Stephen Walker (formerly CSIRO Marine Research), Peter Craig and Jason Waring (CSIRO Marine Research) for providing the code for the MECO numerical model; John Hunter (Antarctic CRC) for supplying code and continual support for the *OzPOM* numerical ocean model; Mike Davis and Paul Davill (National Tidal Facility) for supplying Torres Strait, and Prydz Bay, sea-level tidal data; Matt King (Formerly University of Tasmania) and Richard Coleman (University of Tasmania) for GPS sea-level data from the Amery Ice Shelf; Peter Harris (Geoscience Australia) for Torres Strait current meter data; Rick Porter-Smith (Geoscience Australia) for Torres Strait bathymetry; Jeff Dunn (CSIRO Marine Research) for CARS ocean climatology data; Andrew Ruddell (formerly Australian Antarctic Division) for ice draft and bed elevation data from beneath the Amery Ice Shelf; Phil O'Brien (Geoscience Australia) for bathymetric soundings in Prydz Bay; David Connell (Australian Antarctic Division) for re-discovering the 1985 Prydz Bay current meter mooring data for me, and Bernadette Heaney (CSIRO Marine Research) for helping me to read the 'ancient' data tapes; Nathan Bindoff and Mark Rosenberg (Antarctic CRC) for CTD and ADCP data from adjacent to the Amery Ice Shelf front, and; Heidi Leffanue (Flinders University of South Australia) for tidal current data from adjacent to the Amery Ice Shelf front.

To date, two publications have come from this work, co-authored by my supervisors. The first of these, Hemer et al. (2003), presents results from Part I of the thesis, and the second of these, Hemer and Harris (2003), presents results from Chapter 7. I would like to thank the anonymous reviewers for their constructive comments of these two papers, which also provided help for

presenting and interpreting results in this thesis.

Thankyou to colleagues at the Antarctic CRC who have provided some useful discussions and technical assistance, especially during my sojourn into the chemistry labs. In particular, I would like to thank Lisette Robertson and Suenor Woon for technical support in the labs, and Leanne Armand for introducing me to the world of diatoms. Four years ago, I had never expected to have spent time in the lab , or looking down the barrel of a microscope, during my PhD studies. Thankyou for giving me the opportunity to follow my inquisitiveness.

The field component of the study requires many acknowledgements. To the AMISOR hot water drill team from the 2000/2001 summer; Mike 'duk' Craven, Russell Brand, Allen Elchiekh, Nick Jones, and Ruth Baldwin, thankyou for a fantastic experience. To have spent a balmy Antarctic summer with you was an extremely memorable part of my life. Thanks also to the 2001/2002 drill team for heading back and getting a little more sediment for me. Similarly, thanks to Nathan Bindoff, John Hunter, and Mark Rosenberg, for taking time out from the AMISOR oceanographic science ship-time to collect sediment from adjacent to the ice shelf front for this study. I would also like to thank the scientific and ship crew aboard the RV Franklin during voyage FR01/02 in the Torres Strait for assistance deploying, and retrieving, the BRUCE mooring. In particular, thanks to Mike Hughes, Andrew Heap, Bernadette Heaney, and John Stratton, who made the night shift a pleasure.

On a personal level, thankyou to the many people who have shared a quiet ale, a noisy ale, or time in the Tasmanian wilderness, with me over the past four years. I will leave Tassie with some amazing memories because of the company I have shared my time with. I am sure you all know how much you have helped in making this thesis a reality.

To my family, thankyou for your continual support from as long ago as I can remember. You have always allowed me to pursue my dreams, and shown me that with a bit of work, they are not always beyond reach.

Finally, to Jennifer. Thankyou for being such a wonderful friend. Your patience, care, and love, especially over these last few months, has been more than I could ever wish for. Thankyou for feeding me, thankyou for staying up at night until I got home for a chat, and thankyou for bringing my kayak to work and making me go for a paddle. I look forward to spending so many extra hours with you, and enjoying our new married life together in Ireland, with you as my wife!

Contents

List of Tables

List of Figures

Chapter 1

Introduction

In the present high sea-level condition of the earth, continental shelves fringe every continental landmass and constitute approximately five percent of the earth's surface (Knight and McLean, 1986). The continents are the largest source of particulate material entering the world's oceans, and the fraction of material that is carried to the deep ocean beyond the continental shelf is dependent on the oceanic processes that transport particles across the shelves (Nittrouer and Wright, 1994). Particle transport is driven almost entirely by water motions. Consequently, this study is concerned with the oceanic processes which occur on the continental shelf, and the manner in which these flows entrain and move sediment. An understanding of these processes is essential to solve a wide variety of environmental and engineering problems. Typical applications include: determining rates of sediment bed erosion, the fate of contaminated sediments, and the selection of suitable disposal sites for dredged material and sewage sludge. Other uses, important to the Antarctic continental shelf which is a focus of this thesis, include determining the distribution of sediment facies which occur on the continental shelf, and the consequent formation of shelf stratigraphy, allowing insight into the shelf sedimentary sequences in the geological record.

Four key ocean current mechanisms exist on continental shelves. These include (Fig. 1.1; Swift et al., 1971): (i) Intruding ocean currents; (ii) Tidal currents; (iii) Meteorological (storm) currents; and (iv) Density currents. This distinction lead Swift and Niedoroda (1985) to suggest that continental shelves could be classified on the basis of the mechanisms which dominate reworking and transport of the sediments, dividing them into three main types: (i) Tide dominated, accounting for 17% of the world's continental shelves, including the North Sea; (ii) Storm-dominated, which account for 80% of modern shelves, including the Atlantic Shelf of North America; and (iii) Shelves dominated by intruding ocean

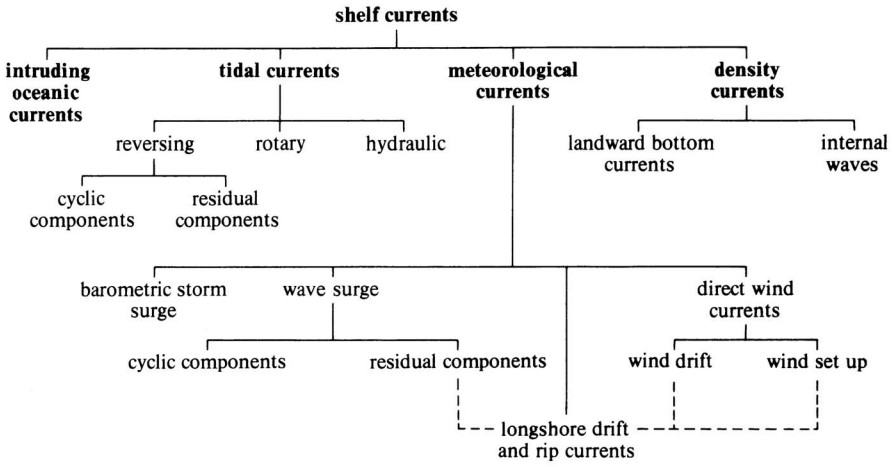

Figure 1.1: Diagram showing types of currents that influence sediment mobility on the continental shelf. From Swift et al. (1971)

currents, which account for 3% of the world's continental shelves, including the Southwest African Shelf which is in contact with the Agulhas Current. One of the aims of this thesis is to answer the question:

- How are the continental shelves of Antarctica, particularly the sub-ice-shelf environments, classified under the scheme proposed by Swift and Niedoroda (1985)?

and consequently demonstrate the uniqueness of the Antarctic continental shelf through comparison against a contrasting shelf environment.

Numerous factors distinguish particulate transport on the continental shelf. Some of these result from the combination of physical processes operating for a particular region. Other factors are more general characteristics of continental shelves. Nittrouer and Wright (1994) identified the latitudinal location of a site as a factor important to the across-shelf transport of particulate material. This study presents examples from the extremes: polar and tropical settings, to identify these latitudinal variations. The two regions studied are the tropical Torres Strait/Gulf of Papua environment in Northern Australia, and the polar setting of Prydz Bay and the ocean cavity beneath the Amery Ice Shelf, East Antarctica.

Numerical ocean models provide a useful tool to improve knowledge of basic ocean processes and their interconnectedness, and help to interpret sparse observations. The approach taken in this thesis uses numerical ocean models, validated using available field data, to provide useful insights into the dominant ocean processes responsible for sediment mobilisation from the sea-bed, and to determine the dispersal pathways of suspended sediments, derived from major sources of sediment supply, across the continental shelf, for each of the two contrasting environments.

Particulate transport is dependent on the time scale of interest (Nittrouer and Wright, 1994). Tidal processes are capable of changing the speed and direction of particulate transport on a time scale of a few hours, or on a spring-neap cycle, the net effect of tidal currents is altered on fortnightly scales. In both the Torres Strait environment, where tidal currents reach up to 2.5 ms^{-1} (Harris, 1988), and in the sub-ice-shelf environment beneath the Amery Ice Shelf, where constriction of the water column thickness due to the imposing ice shelf can accelerate tidal currents (Holdsworth, 1977), tides are suggested to be an important process. This thesis aims to discuss the effects of the tides on particulate transport in each environment, and investigate which processes at other time scales may also be important. At shorter time scales, surface gravity waves may be of importance. As a result of their short periods of oscillation, they are an important mechanism for the resuspension of sediments from the sea-bed (Grant and Madsen, 1986), and are capable of reversing transport direction over a single wave period. The net transport from surface gravity waves may reverse between fair weather and storm conditions (Swift et al., 1986). At time scales of greater length than the tides, synoptic scale storms, seasonal winds (monsoon and trade seasons in the tropics) and seasonal river discharge may alter the sediment transport on the continental shelf. On the Antarctic continental shelf, increased melting of icebergs and sea-ice and increased biological production in the spring and summer months alter sediment supply and transport on a seasonal time scale. On the long-term extreme, sea-level fluctuations over millenia influence particulate transport on the continental shelf. Most particulate transport occurs over short time periods when shear stress is sufficient for erosion and transport. These are separated by longer quiet periods when particles rest on the bottom. During the quiet periods, particles may be buried or mixed downward by bioturbation and thus removed from the transport system.

Observational data are required to support the predictions made using numerical models. To investigate the influence of shorter time scale processes, i.e., waves and tides, instrumented systems such as current meter moorings and tide gauges are used. Over time scales longer than typical observation periods of such moorings, the characteristics of sedimentary deposits, i.e., shelf morphology, sediment composition, and accumulation rates, provide evidence of across-shelf transport of particulate material and allow net effects to be determined (Nittrouer and Wright, 1994). Comparison of the sedimentary characteristics with short term observations and predictions may provide additional information on the importance of various processes.

The two shelf locations focussed on in this project, the Torres Strait and sub-Amery

Ice Shelf regions, were chosen as they display similarities under which they could possibly be classified together. In each environment, a major outlet stream exists to carry terrigenous sediments from the continental land mass to the continental shelf. In the Torres Strait/Gulf of Papua region, high rainfall and erosion in the Papua New Guinea highlands contributes to one of the world's largest rivers in terms of annual sediment load, the Fly River, which transports 125×10^6 tonnes of sediment per year to the river delta (Harris et al., 1993). The Prydz Bay/Amery Ice Shelf region encompasses the drainage basin of arguably the world's largest glacier, the Lambert Glacier (Allison, 1979). The Amery Ice Shelf receives drainage from a catchment area of 1.3×10^6 km^2, or 14% of the East Antarctic ice sheet (Allison, 1979). The glacial ice carries terrigenous material which is deposited on the glacier surface (e.g., scree fall or aeolian transport) and overlain with seasonal snow accumulation , or collected from underlying bedrock, and consequently transported in the ice, until melting of the ice by the relatively warm ocean results in deposition of the material on the continental shelf.

Similarly, each region contains deposits, distant from the major outlet streams, of material produced by marine organisms. The source of these sediments (biological production) is distributed across the continental shelf. The sediments in Torres Strait, distal to the terrigenous input of the Fly River, display a high carbonate content. They are derived from benthic foraminifers and the physical breakdown by wave and current action of bryozoans, molluscs, alga *Halimede*, and some coral (Harris, 1988). The sediments in Prydz Bay are characterised by high levels of biogenic silica, supplied by deposition of marine diatoms, either directly or via faecal pellets, to the sea-bed (Taylor et al., 1997). Calcareous sediments are also found on the outer shelf, consisting of mainly bivalves, echinoderms and foraminifera (Franklin, 1997).

However, this study is directed towards outlining the different marine processes responsible for the transport of the sediments across the continental shelf in each region. There are many mechanisms by which the two environments may differ. Torres Strait is an ocean region of considerable economic importance to both Australia and Papua New Guinea. Consequently many field programs have been carried out in the area, contributing to significant knowledge of the oceanography (water properties, and tidal, wind, and density-driven currents), geomorphology, sediments and bedforms, and seagrass communities (Harris, 1988, 1994b; Wolanski, 1986; Wolanski et al., 1988; Long et al., 1997). Strong tidal currents, and an almost continual source of energy from the Trade winds, for production of surface gravity waves and currents, in a shallow complex topography suggest that this region displays shelf

environments typical of the tide and storm-dominated variety, which contribute to 97% of the world's continental shelves, discussed by Swift and Niedoroda (1985). The primary characteristics of the Antarctic continental shelf are the great average depth of $\sim$ 500 m, and rugged topography, resulting from glacial erosion and isostatic depression by the grounded ice sheet (Jacobs, 1989). The consequent lack of a wave-dominated coastal zone suggest marine currents and mass flow processes are likely to be key sedimentary agents on the Antarctic shelf (Dunbar et al., 1985). On the outer Antarctic continental shelf, seasonal growth and melt of sea-ice, prevailing winds off the ice sheet, the intruding circumpolar current, and large lateral property gradients combined with upwelling and sinking over the continental slope dominate the ocean circulation (Dunbar et al., 1985). Intrusions of upwelled deepwater onto the inner continental shelf influence melting at the base of ice tongues and ice shelves (Jacobs, 1989). Melting, freezing and tidal currents beneath ice shelves influence both the fate of basal debris in the ice sheet, and the large scale circulation (Jacobs, 1989). Jacobs (1989) further suggested that the changes in circulation near the front of floating ice shelves, along with the variability of the position of the ice front, may account for several features of the sediment record. An aim of this thesis is to identify these features in the environs of the Amery Ice Shelf, East Antarctica.

Knowledge of the ocean processes controlling sedimentation on the continental shelf in the Torres Strait/Gulf of Papua region from previous field campaigns is useful for validation of numerical models. The thesis aims to establish confidence in the use of a numerical model to determine the oceanographic influence on sedimentation on the continental shelf, using model to observation comparisons in Torres Strait. The focus of the thesis then shifts to the Antarctic shelf and to the ocean cavity beneath the Amery Ice Shelf. Oceanographic observations in this setting are much more sparsely distributed, and numerical models provide the primary approach for determining ocean circulation, and therefore, those marine processes which dominate sedimentation in that environment.

Following this brief introduction to the study, the thesis is presented in three sections. The Torres Strait component of the project is presented in Part I, followed by the sub-Amery Ice Shelf component of the study presented in Part II. Each of Part I and Part II of the thesis are able to stand alone, aiming to identify the oceanographic processes important to sedimentation in each respective region. A discussion to compare and contrast the results from each environment, and some general conclusions, are presented in Part III.

Part I

TORRES STRAIT

How calm, how beautiful comes on
The stilly hour, when storms are gone!
When warring winds have died away,
And clouds, beneath the glancing ray,
Melt off, and leave the land and sea
Sleeping in bright tranquillity.

Thomas Moore - Lalla Rookh, 1867

Chapter 2

Introduction and Background

2.1 Introduction

Torres Strait (hereafter referred to as the Strait) is located at the northern end of the Great Barrier Reef in the northeast of Australia. It forms an oceanographic boundary between two quite separate ocean basins (the Coral Sea/ Gulf of Papua and the Gulf of Carpentaria/ Arafura Sea). It also defines a biological barrier correlating with the northern limit of the Great Barrier Reef, a political boundary between Australia, Papua New Guinea and Irian Jaya, and a geological mixing zone of terrigenous and calcareous sediments (Harris, 1999). The Strait is an important national, and international, shipping channel, contains valuable fisheries for prawns and crayfish, and a known habitat of the dugong *Dugong dugon*. Thus, the Strait is an ocean region of considerable economic, social and environmental importance to both Australia and Papua New Guinea. The natural environment however is being impacted upon by mining activities in the New Guinea highlands which input mine tailings into rivers that discharge into the coastal zone. The approval of a gas pipeline to be laid across the Strait also has possible implications for the Torres Strait environment.

The above reasons indicate that knowledge of the Strait's physical and environmental processes is vital to the regions successful management. Harris (1994b) states that sediment transport pathways are of crucial importance to predict impacts which may arise due to increased sediment input to the marine environment from increased mining and logging operations on the New Guinea landmass. This increased sediment load is capable of smothering corals, or restricting seagrass growth due to sunlight blockage. The transport pathways of sediments are also relevant to the fate of many environmentally harmful substances, such as heavy metals, commonly associated with fine sediments.

Harris (1999) identified two key marine geological questions important to the management of the marine environment of the Strait.

- What are the main dispersal pathways and deposition sites for sediment derived from the Fly River in Torres Strait? and ;
- What are the main physical processes controlling sediment erosion, transport and deposition in Torres Strait?

and addressed these questions from available current meter, surficial sediment distributions, seismic survey and coring data on terrigenous sediment input and dispersal in Torres Strait. The aims of this part of the thesis are to address these questions with the use of a three-dimensional hydrodynamic model, with wave, current and sediment transport modules, and to investigate seasonally dominant sediment transport mechanisms in the region.

The following sections of this chapter provide background material of previous work done in the region. It details the climatology, oceanography and physical sedimentology of the region.

Chapter 3 provides a detailed description of the hydrodynamic model used for the study, and the verification of the model with available tidal elevation and current meter data. It also details the deployment of a newly constructed benthic frame for collection of current and sediment data in the region.

Chapter 4 outlines the results of the model applied to the study of sediment dispersal and the identification of dominant processes controlling sediment mobilisation on the continental shelf in the area.

Chapter 5 draws together Part I of the thesis, outlining the main results and conclusions of the study.

2.2 Background

2.2.1 Topography

The area studied, shown in Figure 2.1, includes the waters of the northern Great Barrier Reef (GBR) continental shelf and the Gulf of Papua along with the north-eastern section of the Gulf of Carpentaria. Numerous islands, coral reefs and shoals scatter the shelf forming a complex bathymetry. The shelf is separated from the Coral Sea by a string of reefs forming the outer GBR. The GBR continental shelf is then open to the Gulf of Papua

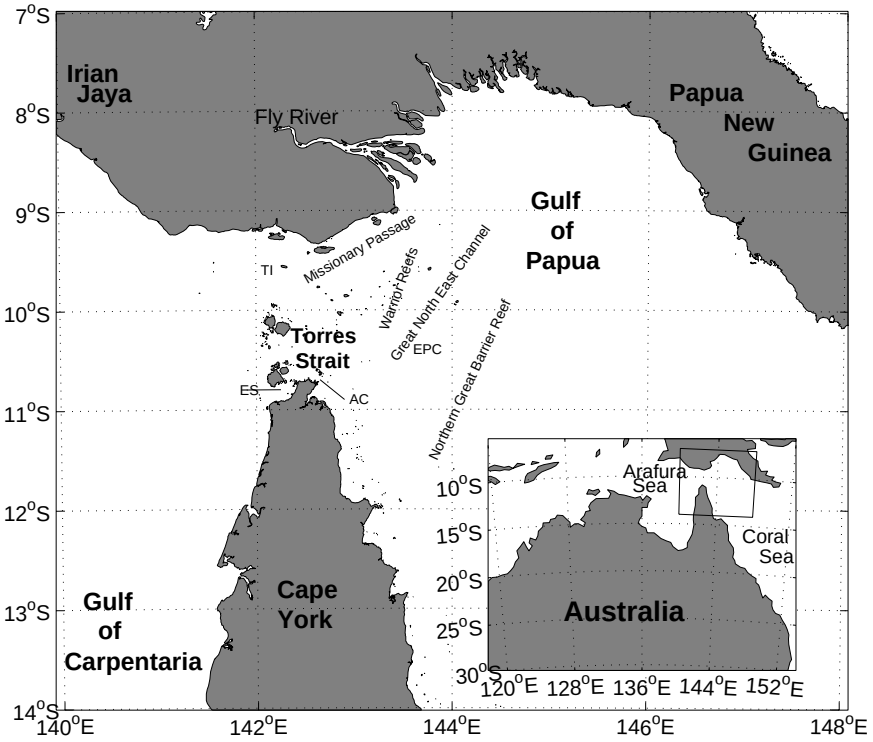

Figure 2.1: Torres Strait and Gulf of Papua location. The Adolphus Channel (AC), Endeavour Strait (ES), and the Eastern Patch Reefs (EPR) are also marked.

by the Great North East Channel, and the Gulf of Carpentaria by Torres Strait. The Strait is approximately $100km$ long in the north-south and $20-60km$ wide east-west. The bathymetry of the main shipping channels within the Strait itself have been well charted and indicate a shallow sea-bed, with depths generally in the range of $6-9m$, with channels up to $12m$ depth (Harris, 1994a). However, there remain large un-navigable regions of the Strait where bathymetric data are sparse. The 'Torres Strait Islands' extend north-north-westwards from Cape York, where fringing coral reefs with an East-West elongation have grown around the islands. The waters west of the Strait are shallow, gradually deepening westward, with the $20m$ isobath $75km$ to the west in the Gulf of Carpentaria. The Great North East Channel is $20-30m$ deep and approximately 50km wide. It is confined to the west by the Warrior Reefs, a complex of platform reefs divided by passages scoured by tidal currents, and to the east by the tightly packed matrix of reefs on the shelf edge.

To the north of the Great North East Channel, positioned on the south coast of Papua New Guinea, the Fly River Delta is a funnel shaped, highly dynamic, macro-tidal deltaic system (Harris et al., 1993).

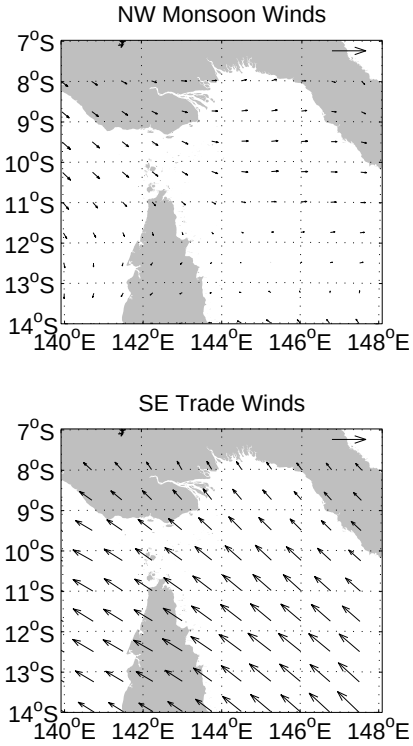

Figure 2.2: Averaged 10 m elevation winds over the NCEP-NCAR Reanalysis Period from 1958-1998, for each season. The NW Monsoon season (top) is averaged for the months December through to March inclusive, and the SE Trades season (bottom) averages from April through to November inclusive. In the north-east of each subplot, a 10 knot (5.15 ms^{-1}) scale vector is shown.

2.2.2 Winds

Seasonal variations in the annual wind field with an almost complete reversal of direction are well known in the region. During the southern hemisphere winter (Apr-Nov), the south-easterly (SE) trade winds dominate, and in the summer (Dec-Mar), the north-westerly (NW) monsoon takes over. Wolanski and Thomson (1984) found the monsoon and trades seasons to have currents through Torres Strait with alternating easterly and westerly components respectively, in the region. Typical wind speeds in the area are of order $1 - 2ms^{-1}$ during the monsoon season, and $\sim 5ms^{-1}$ during the trade season.

Figure 2.2 shows NCEP 10m elevation wind vectors for the region, encompassing the model domain, averaged over Monsoon and Trade season periods, over all years of the NCEP-NCAR Reanalysis project (Kalnay et al., 1996) from 1958-1998.

2.2.3 Waves

During the SE trades, Torres Strait is generally protected from surface waves generated in the Coral Sea by the northern most extension of the GBR, serving to block long period

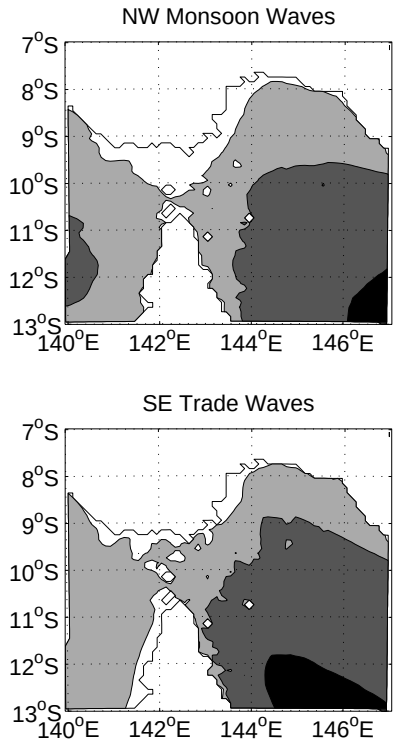

Figure 2.3: Seasonally averaged significant wave heights, for a given year (1998) of Bureau of Meteorology WAM results. The NW Monsoon season (top) is averaged for the months December through to March inclusive, and the SE Trades season (bottom) averages from April through to November inclusive. Contours are at 0.5 m intervals. Black indicating significant wave heights in excess of 2 m.

swell. As a result, only locally generated waves are found on the GBR shelf. In contrast however, the Fly River Delta remains exposed to Coral Sea generated swell. During the NW Monsoon, offshore winds result in little or no long period swell propagating towards the south coast of Papua New Guinea. Satellite altimeter data from past missions (Geosat) indicates that significant wave height (H_S) rarely if ever exceeds $3.5m$ in Torres Strait and during the NW monsoon, are nearly always less than $1.5m$ (Harris, 1994b). Figure 2.3 shows significant wave heights averaged seasonally for a year using data from the Bureau of Meteorology (WAM) WAve Model (WAMDI Group, 1988).

2.2.4 Physical Oceanography

Tides and wind driven currents control the sediment transport pathways and distribution patterns in Torres Strait. Despite Torres Strait joining two large oceanic water bodies, the large volume E-W transport between the Gulf of Carpentaria and the Coral Sea has been shown to be insignificant (Wolanski et al., 1988).

Wyrtki (1960) suggested that a strong seasonal current through the Strait existed, bringing fresher water from the Gulf of Carpentaria and the Arafura Sea eastward into the Coral Sea during the NW monsoon. It was later shown (Wolanski and Ruddick, 1981) that the freshwater is more likely to originate from the large discharge of the New Guinea rivers, the Fly, Kikori and Purari rivers, into the Gulf of Papua.

Tides

Tides within Torres Strait are characterised by strong tidal currents and rapid spatial changes in tidal elevations. Tidal ranges are of the order of $3m$ (Amin, 1978). Torres Strait forms the intersection of two separate and dissimilar tidal regimes of the Gulf of Papua/ Coral Sea and the Gulf of Carpentaria/ Arafura Sea[1], both dominated by the M_2 constituent (Amin, 1978). The two domains are out of phase with each other (Variations in phase of the M_2 constituent of $\sim 180°$ through the Strait proper are observed) and show little correlation in the tidal records either side of the Strait (Bode and Mason, 1994). As a result of the tides being incoherent on either side of the Strait, large pressure gradients are experienced through the Strait which drive strong tidal currents magnified by flow channelisation in passages amongst dense coral reefs through the Strait. The incoherency also indicates that the tidal waves are unable to propagate significantly across the Strait with only about 30% of the tidal wave transmitted from basin to basin, the rest being dissipated through friction (Wolanski et al., 1988). This large tidal energy expenditure leads to tidal current scour and sediment reworking (Harris and Baker, 1991). Dense coral reefs further complicate the tidal dynamics. Previous modelling work (Bode and Mason, 1994) indicates that north of Cape York, M_2 tidal elevations are at a minimum and currents at a maximum, equivalent to the setup of a standing wave.

Tides in the Gulf of Papua and the northern GBR shelf are typical of those found in the Coral Sea. The higher frequency semi-diurnal tidal waves are considered to shoal to a greater extent than the lower frequency diurnal waves, resulting in an increase in the ratio of semi-diurnal to diurnal components with progression towards the shore.

Non-Tidal Sea-Level Oscillations

A number of non-tidal sea-level oscillations exist within the area. These include: (i) 50 cm amplitude sea-level oscillations in the Gulf of Carpentaria driven by cyclones in the Arafura Sea (Melville and Buchwald, 1976); (ii) surges generated on either side of the Strait (Amin,

[1]The Gulf of Carpentaria is strongly diurnal, however this is restricted to the gulf itself (Church and Forbes, 1981)

1978); (iii) large low-frequency sea-level oscillations on the Northern GBR shelf (highly coherent on the shelf) that are about 30 cm peak to trough (Wolanski and Thomson, 1984); and (iv) monthly mean sea-levels (Wolanski, 1986). All of these have been concluded to be incoherent on either side of the Strait, so it is expected that at all time scales, there is little propagation through Torres Strait.

Non-Tidal Currents

Within the Strait, the low-frequency (mainly wind-driven) component of the current is significantly weaker than the tidal component. Over a sampling period of 2 months, the low frequency currents were observed to reverse direction several times with mean speeds always less than $0.1 ms^{-1}$ indicating that the net flow through the Strait is minimal (Wolanski et al., 1988). Wind driven currents are observed to reverse in sign seasonally, with flow being generally westwards during the SE trades season (Apr - Nov) and eastwards during the NW monsoon (Dec-Mar) (Harris, 1994a). These seasonally reversing current vectors are capable of enhancing or diminishing the maximum tidal flow, but due to the shallow depths and low current speeds, are negligible for oceanic budget calculations (Wolanski et al., 1988). Wolanski et al. (1988) found that baroclinic motions within the Strait are negligible due to the high energy shallow waters of the region.

In the Gulf of Papua, a branch of the South Equatorial Current forms a clockwise rotating gyre in the Coral Sea. This gyre gives rise to a northward-flowing oceanic current at the Gulf of Papua shelf break, known as the 'Coral Sea Coastal Current' (Andrews and Clegg, 1989). Surface speeds of 50 cms^{-1} on the outer part of the shelf have been attributed to this current, however surface speeds reduce to less than 5 cms^{-1} in the inner shelf zone (Wolanski et al., 1990).

Water Properties

Vertical distribution of properties There are three basic vertical structures (Wolanski et al., 1984) of water properties in the region of interest (Fig. 2.4). The first one (Type 1) is found within the Strait and the northern GBR shelf where tidal mixing is large and the water has well mixed properties of temperature and salinity. The second type (Type 2) are of estuarine character and are found in the inshore waters of the Gulf of Papua and characterised by stepped salinity and temperature profiles resulting from river runoff. The third type (Type 3) is found in the Coral Sea and is characterised by a stepped temperature profile and a fairly uniform vertical profile of salinity.

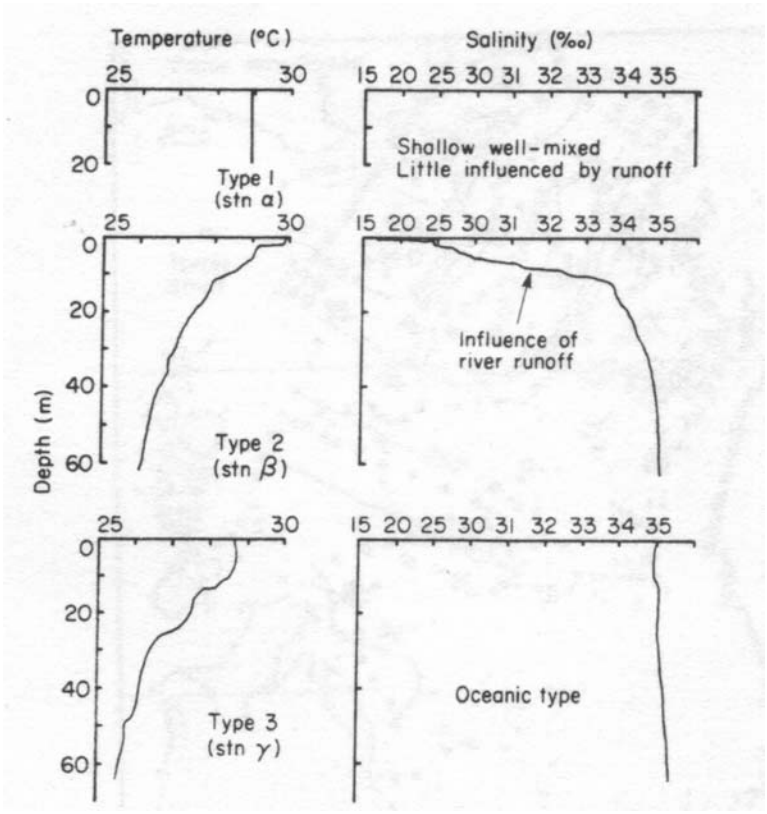

Figure 2.4: Torres Strait/Gulf of Papua Temperature and Salinity profiles. From Wolanski et al. (1984)

Horizontal distribution of properties The annual average horizontal distributions of surface salinity and temperature, taken from the Climatology of Australian Regional Seas (CARS) database (Ridgway et al., 2001), are shown in Figure 2.5. Figure 2.5 also displays the seasonal variability of salinity and temperature, with monsoon, and trade season averages also being shown. These data correspond with the horizontal distribution as given by Wolanski et al. (1984) for cruises during both seasons. Isohalines run generally north-east to south-west with low salinities on the north-west side, and the lowest values at the north end close to the Gulf of Papua coast. Very little seasonal difference in salinity is observed between the trade and monsoon seasons. Temperature distribution is not as systematic as the salinity. Temperature distributions show differences of $1 - 2°C$ between trade and monsoon throughout most of the study region.

The CARS database is a set of seasonal maps of temperature, salinity, dissolved oxygen, nitrate, silicate and phosphate mapped onto a 1/2 degree grid in the region 100 $°E$ - 200 $°E$, 50 $°S$ - Equator on 56 standard depths. Quadratics are fitted in horizontal and vertical coordinates, with bathymetry influenced weighting. For temperature and salinity, which have been used in this thesis, semi-annual and annual harmonics have been simulta-

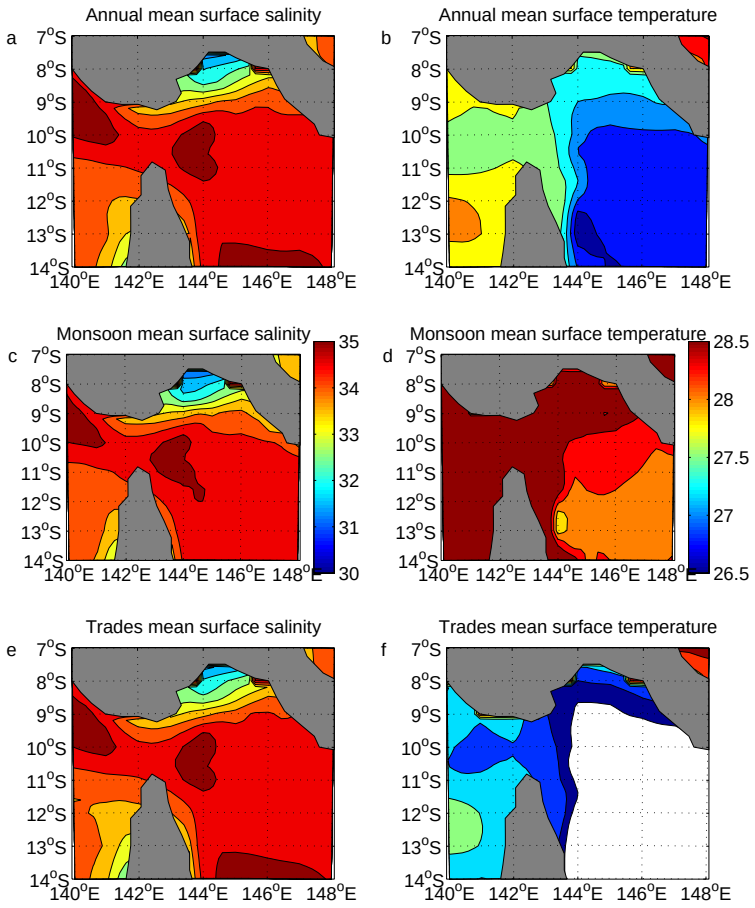

Figure 2.5: Surface Salinity distributions a) Annual Mean, c) Monsoon (Dec-Mar) mean, and e) Trades (Apr-Nov) mean. Surface Temperature distributions b) Annual mean, d) Monsoon mean, and f) Trades mean. The colorbar for c) applies for a) and e) also, and the colorbar for d) applies for b) and f) also.

neously fitted down to 1000 m (Ridgway et al., 2001), from which an annual time series may be obtained at each latitude, longitude, and depth. Distribution of CARS data in the study region is sparse, and could lead to error (Ridgway et al., 2001).

2.2.5 Sediments

Surficial sediments

The nature of the surficial sediments varies as a function of both the vicinity of river sediment sources (i.e., the Fly River) and of the tidal current regime (Harris, 1999).

Grain size distribution and percentage content of calcium carbonate are the two most useful descriptors of surficial sediment.

A high carbonate content indicates sediment derived from benthic foraminifers, supplied by bryozoans, molluscs, alga *Halimede* and small amounts of coral (Harris, 1988). The Fly River Delta is characterised by sediments of low carbonate content (terrigenous sedi-

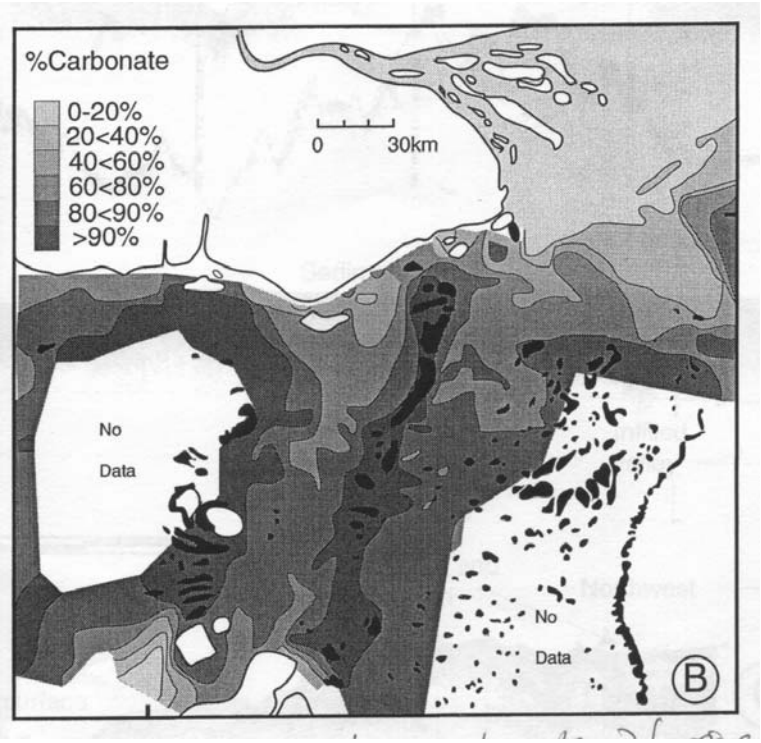

Figure 2.6: Carbonate distribution in Torres Strait surficial sediments.

ments; Fig. 2.6), whereas the sediments within Torres Strait generally have a high carbonate content in excess of 80% (Harris, 1988).

An effective measure of grain size distribution is mud content, defined as the percentage by dry weight of grains less than 63 μm (Harris, 1999), and relates relative current energy to the relative position of the sediment along the transport path, from source to depositional environments. Harris (1988) mapped the surficial sediments of Torres Strait displaying mud content (Fig. 2.7). This shows two regions of high mud content, one forms a belt of $> 80\%$ mud across the front of the Fly River Delta, the other ($> 60\%$ mud) in the eastern section of Torres Strait between the numerous reefs. Both of these regions are low energy depositional areas (Harris, 1999). Regions of low mud content represent regions of mainly sand and gravel. These more winnowed areas, where mud content is less than 10%, are associated with bedforms.

Sediment Transport

Bedload Tidally influenced bedload is characterised by bedload partings (BLPs), where tidally averaged bedload transport vectors diverge from zones of maximum bottom stress (Stride, 1982). Such areas are characterised by surficial sediments that have been scoured clear of unconsolidated sediments leaving behind a lag gravel (armoured beds), or in extreme

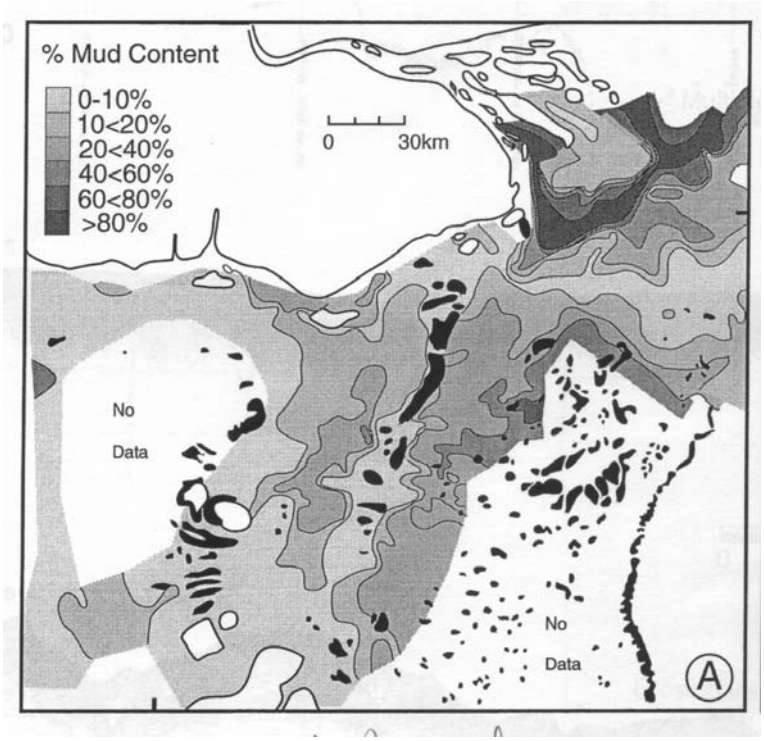

Figure 2.7: Mud distribution in Torres Strait surficial sediments.

cases, a limestone pavement (exposed bedrock). With increased distance from the BLP, the process changes from erosion to transport, forming mobile sand deposits (dunes and ribbons; Johnson et al. (1982)). Between these 2 zones of scour and deposition, regions of areally extensive bedforms occur. Bedforms indicate that in these regions, the bed sediments are regularly mobilised, and that the associated surficial sediments comprise well sorted sands and gravels (Harris, 1999). Sandwaves (subtidal dunes) of 4-5 m height are observed to reverse asymmetry and migration direction with the seasonal changes in wind-driven current direction (Harris, 1989).

Sand and mud distributions are affected by the combined action of tidal and wind driven currents, producing areas of migrating bedforms, in which soft, sand size carbonate grains are reworked and broken down into silt size particles for removal, in suspension, away from tidal scour zones to high carbonate sediment depocentres located in eastern and central Torres Strait (Harris, 1994b).

Suspended load Harris (1999) indicates that the highest concentrations of suspended sediment occur in constricted passages between reefs. Measurements during the trade wind season (September) showed higher suspended sediment concentration (SSC) associated with the Fly Delta and the southern coast of Papua New Guinea. Similar concentrations are

observed elsewhere in the region with the mean surface SSC of 9.14 mg/l in the NW Monsoon, and a mean SSC of 5.4 mg/l during the SE trades at all stations (excluding the Fly Delta stations).

The direction of residual (tidally-averaged) flow determines the predominate path of a suspended sediment particle in Torres Strait (Harris, 1999). Turbidity measurements from Missionary Passage indicate that during spring tides, SSC are higher ($20-30$ mg/l) than on neaps (< 10 mg/l). For both spring and neap tides, high SSC coincide with periods of high current speed. The passage north of Saibai Island displayed similar features. Harris (1999) found that for both of these regions the net suspended sediment transport was towards the west (flood-dominated). Hence it may be concluded that the westward flowing wind-driven residual current, which dominates Torres Strait during the SE Trades, controls the local westward transport of suspended sediments along the southern coast of Papua New Guinea between Daru and Saibai Island. Tidal currents in combination with wind generated waves give rise to a turbidity maximum in central Torres Strait (Harris and Baker, 1991). This persistent zone of high turbidity water is made up of mainly carbonate sediments, distinct from the suspended Fly River plume made up mostly of terrigenous sediments.

At the Fly River Delta front, surface waves generated by the SE trades rework muds and sands to winnow out the fine grained sediments. During the NW monsoon, minimal surface wave activity results in the deposition of a mud drape, resulting in seasonal sand-mud interbeds (varves; Harris et al., 1993).

The Fly is one of the largest rivers in terms of annual sediment load ($125 \times 10^6 tonnes/a$) (Harris et al., 1993) and has a tidal range greater than 3m indicating a tidally dominated delta (in contrast to deltas which may also be dominated by surface waves or river input). Approximately $238 km^3 a^{-1}$ of water is discharged from the Fly (Alongi et al., 1992), with most of the sediment load provided from mountain areas as a result of land slides triggered by tectonic events. Deforestation and mining in the catchment have further increased the sediment load. 'Fluid muds', with SSC of up to 40 g/l, have been observed in the delta as a result of the high wave and tidal current energy (Wolanski and Eagle, 1991).

Harris et al. (1993) estimated a sediment budget based on the sediment load prior to to the opening of the Ok Tedi gold and copper mine (Fig. 2.8). Before the mine opened, $85 \times 10^6 tonnes$ of sediment (90% suspended load, 10% bedload) was discharged from the Fly annually. 47×10^6 tonnes of this is estimated to be deposited within the Fly delta. Sands are deposited in the upper estuary, and muds deposited further offshore in the pro-deltaic environment. The remaining sediments are dispersed over the shelf regions. Harris et al.

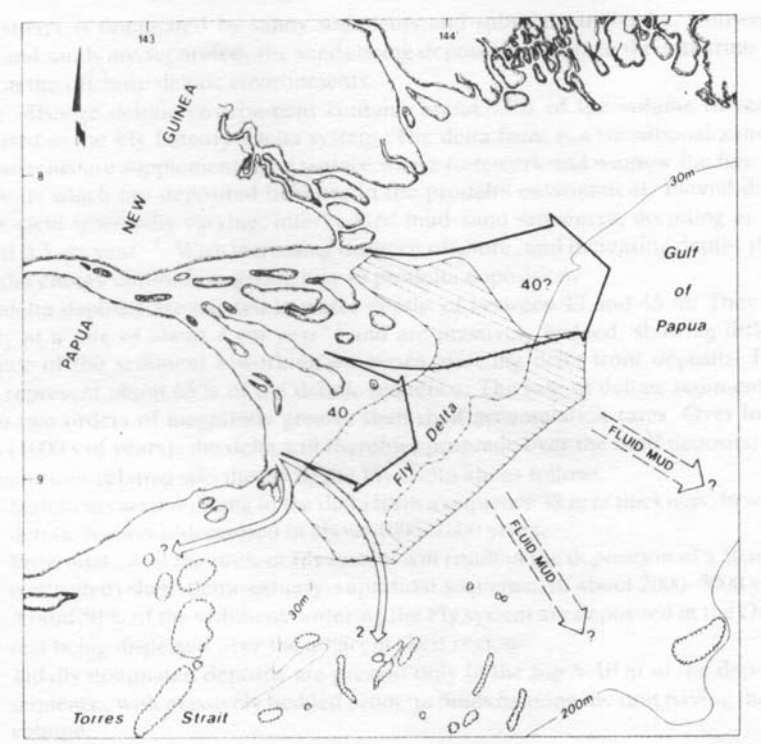

Figure 2.8: Sediment transport pathways for the dispersal of Fly River sediment. From Harris et al. (1993)

(1993) postulated that density-driven currents could transport 'fluid muds' eastwards onto the shelf across isobaths and into the Coral Sea basin, possibly following submarine drainage channels. Wind driven currents are thought to transport 40% of the annual Fly discharge in suspension north-eastwards into the Gulf of Papua, and a further 5% westwards along the south coast of Papua New Guinea. Less that 2% of the Fly sediments are thought to be deposited in Torres Strait to the south (Harris et al., 1993).

The amount of sediment not accounted for in the budget may follow a number of paths.

- Sediment retained and deposited in the estuary.
- Transported offshore for deposition in the Gulf of Papua.
- Transported westwards along the south coast of Papua New Guinea
- Transported southwards into Torres Strait
- Some combination of the above - the more likely result.

An aim of this study is to identify which of these paths are a more likely combination.

Chapter 3

Numerical Modelling of the Torres Strait circulation and its Verification

The Model for Estuaries and Coastal Oceans (MECO) model used for this study is a three dimensional, non-linear, variable density, hydrodynamic model, developed at CSIRO Marine Research (Walker and Waring, 1998). It provides three dimensional distributions of salinity, temperature, velocity and concentrations of passive tracers, given input fluxes of water, salt, heat and passive tracers, and forcing by winds, atmospheric pressure gradients and sea levels. MECO is based on the equations described by Blumberg and Herring (1987) using a z-grid in the vertical and an Arakawa C-grid in the horizontal. The model is described in detail by Walker and Waring (1998) and Walker and Fandry (1993) and has been validated in field studies (Walker and Fandry, 1993; Walker, 1996, 1999; Andrewartha and Walker, 1997, 1999). A brief description is provided here for completeness.

MECO, being a z-layer model, has implemented a scheme of variable bottom layer thickness so that the bathymetry may be better resolved, removing the step-like features at the bottom which appear in other z-layer models.

3.1 Equations

The equations which form the basis of the circulation model are well established in general orthogonal coordinates. They describe the velocity and surface elevation fields, and the salinity and temperature fields. The assumptions on which the following equations are based are:

- The hydrostatic assumption, i.e., it is assumed that the weight of the fluid identically

balances the pressure, and;

- The Boussinesq approximation, i.e., that density differences are neglected unless the differences are multiplied by gravity (Blumberg and Mellor, 1987).

In a system of orthogonal cartesian coordinates, where x increases eastwards, y increases northwards, and z increases vertically upwards, the free surface is located at $z = \eta(x, y, t)$, and the bottom is located at $z = -H(x, y)$. If the horizontal velocity vector has components (U, V), the continuity equation may be used to solve for the vertical velocity, W:

$$\frac{\partial U}{\partial x} + \frac{\partial V}{\partial y} + \frac{\partial W}{\partial z} = 0 \tag{3.1}$$

The Reynolds momentum equations, describing the time evolution of the velocities U and V are:

$$\frac{\partial U}{\partial t} + \frac{\partial U^2}{\partial x} + \frac{\partial UV}{\partial y} + \frac{\partial UW}{\partial z} - fV = -\frac{1}{\rho_o}\frac{\partial P}{\partial x} + \frac{\partial}{\partial z}\left(K_M \frac{\partial U}{\partial z}\right) + F_x \tag{3.2}$$

$$\frac{\partial V}{\partial t} + \frac{\partial UV}{\partial x} + \frac{\partial V^2}{\partial y} + \frac{\partial VW}{\partial z} + fU = -\frac{1}{\rho_o}\frac{\partial P}{\partial y} + \frac{\partial}{\partial z}\left(K_M \frac{\partial V}{\partial z}\right) + F_y \tag{3.3}$$

and

$$\rho g = -\frac{\partial P}{\partial z} \tag{3.4}$$

where ρ_o is the reference density, ρ is the in situ density, g the gravitational acceleration, P the pressure, K_M the vertical eddy diffusivity of turbulent momentum mixing, and f is the Coriolis parameter, where any latitudinal variation is introduced by use of the β plane approximation.

The vertical component of the equation of motion, equation 3.4, can be vertically integrated from z to the free surface η, to give the pressure at depth z:

$$P(x, y, z, t) = P_{atm} + g\int_z^\eta \rho(x, y, z', t)dz' \tag{3.5}$$

where P_{atm} is the atmospheric pressure at the water surface.

The conservation equations for a tracer with concentration T in MECO (for example, temperature, salinity or some contaminant) may be written:

$$\frac{\partial T}{\partial t} + \vec{V} \cdot \bigtriangledown T + W\frac{\partial T}{\partial z} = \frac{\partial}{\partial z}\left(K_H \frac{\partial T}{\partial z}\right) + F_T \tag{3.6}$$

where K_H denotes the vertical diffusivity for turbulent mixing of the tracer.

Temperature and salinity are used to compute the density according to an equation of state of the form (Fofonff and Millard, 1983):

$$\rho=\rho(T,S)$$

Subgrid-scale processes are parameterised in terms of horizontal mixing processes. The terms F_x, F_y and F_T found in the above equations represent these small-scale processes, and along with the molecular diffusion are written as:

$$F_x = \frac{\partial}{\partial x}\left[2A_M\frac{\partial U}{\partial x}\right] + \frac{\partial}{\partial y}\left[A_M\left(\frac{\partial U}{\partial y}+\frac{\partial V}{\partial x}\right)\right] \tag{3.7}$$

$$F_y = \frac{\partial}{\partial y}\left[2A_M\frac{\partial V}{\partial y}\right] + \frac{\partial}{\partial x}\left[A_M\left(\frac{\partial U}{\partial y}+\frac{\partial V}{\partial x}\right)\right] \tag{3.8}$$

and

$$F_T = \frac{\partial}{\partial x}A_H\frac{\partial T}{\partial x} + \frac{\partial}{\partial y}A_H\frac{\partial T}{\partial y} \tag{3.9}$$

where A_M is the horizontal kinematic viscosity and A_H is the horizontal heat diffusivity.

MECO, however, is based on the conversion of these equations of motion to an orthogonal curvilinear coordinate system as carried out by (Blumberg and Herring, 1987). Considering such a coordinate system with horizontal coordinates (ξ_1, ξ_2) and vertical coordinate (z). The metric coefficients h_1 and h_2 are defined such that a distance increment ds satisfies:

$$ds^2 = h_1^2 d\xi_1^2 + h_2^2 d\xi_2^2$$

If the three-dimensional velocity vector has components u_1 in the ξ_1 direction, u_2 in the ξ_2 direction and w in the z direction, then:

$$u_1 = h_1\frac{\partial \xi_1}{\partial t}$$

$$u_2 = h_2\frac{\partial \xi_2}{\partial t}$$

$$w = \frac{\partial z}{\partial t}$$

The horizontal momentum equations can be written (Blumberg and Herring, 1987) as:

$$\begin{aligned}\frac{\partial u_1}{\partial t} &+ \frac{1}{h_1^2 h_2}\left[\frac{\partial}{\partial \xi_1}\left(u_1^2 h_1 h_2\right) + \frac{\partial}{\partial \xi_2}\left(u_1 u_2 h_1^2\right)\right] + \frac{\partial}{\partial z}\left(w u_1\right) \\ &- \frac{u_1^2}{h_1^2}\frac{\partial h_1}{\partial \xi_1} - \frac{u_2^2}{h_1 h_2}\frac{\partial h_2}{\partial \xi_1} - f u_2 = -\frac{1}{h_1 \rho_o}\frac{\partial P}{\partial \xi_1} + \frac{\partial}{\partial z}\left[K_M \frac{\partial u_1}{\partial z}\right] + D_1 \end{aligned} \tag{3.10}$$

$$\begin{aligned}\frac{\partial u_2}{\partial t} &+ \frac{1}{h_1 h_2^2}\left[\frac{\partial}{\partial \xi_1}\left(u_1 u_2 h_2^2\right) + \frac{\partial}{\partial \xi_2}\left(u_2^2 h_1 h_2\right)\right] + \frac{\partial}{\partial z}\left(w u_2\right) \\ &- \frac{u_1^2}{h_1 h_2}\frac{\partial h_1}{\partial \xi_2} - \frac{u_2^2}{h_2^2}\frac{\partial h_2}{\partial \xi_2} + f u_1 = -\frac{1}{h_2 \rho_o}\frac{\partial P}{\partial \xi_2} + \frac{\partial}{\partial z}\left[K_M \frac{\partial u_2}{\partial z}\right] + D_2 \end{aligned} \tag{3.11}$$

D_1 and D_2 are an approximate transformed form of F_x and F_y terms above as used in MECO, and are written:

$$D_1 = A_M\left[\frac{1}{h_1^2}\frac{\partial^2 u_1}{\partial {\xi_1^2}^2} + \frac{1}{h_2^2}\frac{\partial^2 u_1}{\partial {\xi_2^2}^2}\right],$$

$$D_2 = A_M\left[\frac{1}{h_1^2}\frac{\partial^2 u_2}{\partial {\xi_1^2}^2} + \frac{1}{h_2^2}\frac{\partial^2 u_2}{\partial {\xi_2^2}^2}\right].$$

This approximation is only formally correct for uniform rectangular grids and a constant horizontal diffusion coefficient, A_M, and ignores the shear diffusion term.

The vertical momentum equation with the hydrostatic assumption, equation 3.4, remains unchanged, as does its vertical integral detailing the pressure, P at depth z, equation 3.5.

This form of the momentum equations is quite similar to that in the cartesian coordinate system, except for the additional terms which account for the curvature of the coordinate system itself, the 5th and 6th terms on the left hand side of equations 3.10 and 3.11. The cartesian system equations are recovered by the transformation $h_1 d\xi_1 \rightarrow dx$ and $h_2 d\xi_2 \rightarrow dy$.

The continuity equation (equation 3.1) is written in orthogonal curvilinear coordinates as:

$$\frac{1}{h_1 h_2}\left[\frac{\partial (h_2 u_1)}{\partial \xi_1} + \frac{\partial (h_1 u_2)}{\partial \xi_2}\right] + \frac{\partial w}{\partial z} = 0 \tag{3.12}$$

The tracer conservation equation, equation 3.6, is written in the orthogonal curvilinear coordinate system as:

$$\begin{aligned}\frac{\partial T}{\partial t} &+ \frac{1}{h_1 h_2}\left[\frac{\partial}{\partial \xi_1}(h_2 u_1 T) + \frac{\partial}{\partial \xi_2}(h_1 u_2 T)\right] + \frac{\partial (w+s)T}{\partial z} \\ &= \frac{1}{h_1 h_2}\left[\frac{\partial}{\partial \xi_1}\left(\frac{h_2}{h_1} A_H \frac{\partial T}{\partial \xi_1}\right) + \frac{\partial}{\partial \xi_2}\left(\frac{h_1}{h_2} A_H \frac{\partial T}{\partial \xi_2}\right)\right] + \frac{\partial}{\partial z}\left[K_H \frac{\partial T}{\partial z}\right] \qquad (3.13)\end{aligned}$$

where the extra term s added to the vertical velocity, represents a vertical settling velocity. This is set to zero for temperature and dissolved substances. Horizontal mixing of tracers is not currently implemented in MECO. In almost all applications, the numerical diffusion associated with a particular grid and the MECO advection scheme is larger than the real-world horizontal diffusion. Thus no additional diffusion term is included, i.e., $F_T = 0$.

Vertical turbulent mixing is modelled through the use of the vertical momentum diffusion coefficient K_M and vertical tracer diffusion coefficient K_H. These are calculated in MECO using a formulation based on that of Csanady (1982), with modifications to allow for stratification as described by Bowden and Hamilton (1975):

$$K_M = K_{M0} + K_{M1} H \left|\vec{V}\right| (1 + 7R_i)^{-1/4},$$

$$K_H = K_{H0} + K_{H1} H \left|\vec{V}\right| (1 + R_i)^{-7/4},$$

where $\vec{V}$ is the depth-averaged velocity, K_{M0}, K_{H0}, K_{M1} and K_{H1} are constants, and R_i is a Richardson number, dependent on the vertical stratification and vertical velocity shear. If the water column is well mixed, then the Richardson number is always zero and the equations of K_M and K_H reduce to:

$$K_M = K_{M0} + K_{M1} H \left|\vec{V}\right|,$$

$$K_H = K_{H0} + K_{H1} H \left|\vec{V}\right|.$$

For computational efficiency, the external mode (barotropic mode) is separated from the internal mode (baroclinic mode) using a mode-splitting technique, where the external mode is computed using a smaller time step than the internal mode. The velocity components are written as the sum of a depth average and depth varying part:

$$u_1 = \overline{u}_1 + u_1'$$

$$u_2 = \overline{u}_2 + u_2'$$

where the overbar denotes taking a depth average, for example for variable x:

$$\overline{x} = \frac{1}{H+\eta}\int_{-H}^{\eta} x dz$$

An external mode, derived by vertically integrating equations 3.12, 3.10 and 3.11 from $z = -H$ to $z = \eta$, is written (Blumberg and Herring, 1987):

$$\frac{\partial \eta}{\partial t} + \frac{1}{h_1 h_2}\left[\frac{\partial}{\partial \xi_1}(\overline{u_1} D h_2) + \frac{\partial}{\partial \xi_2}(\overline{u_2} D h_1)\right] = 0 \tag{3.14}$$

where $D = H + \eta$ is the perturbed water depth. The depth averaged momentum equations are written:

$$\frac{\partial \overline{u}_1 D}{\partial t} + \frac{gD}{h_1}\frac{\partial \eta}{\partial \xi_1} - f\overline{u}_2 D = \Lambda_1 \tag{3.15}$$

$$\frac{\partial \overline{u}_2 D}{\partial t} + \frac{gD}{h_2}\frac{\partial \eta}{\partial \xi_2} + f\overline{u}_1 D = \Lambda_2 \tag{3.16}$$

where Λ_1 and Λ_2 contain vertical integrals of the density gradient, advective and diffusive terms, and surface and bottom stress component terms. The complete expressions for Λ_1 and Λ_2 can be found in Blumberg and Herring (1987) or Walker and Waring (1998).

The computational strategy is to solve equations for the external mode with a short time step to resolve high frequency motions. The terms on the right hand side of equations 3.15 and 3.16 are supplied from the internal mode and are held constant in time over the external mode integration period. The external mode then provides $\partial\eta/\partial\xi_1$ and $\partial\eta/\partial\xi_2$ to the internal mode which is then solved with a much longer time step. Once the vertical structure has been determined, the terms on the right hand side of equations 3.15 and 3.16 are updated, and another external mode solution begins.

3.2 Finite difference formulation

The equations presented in the previous section may be solved numerically using finite difference techniques.

MECO uses the staggered "Arakawa-C" grid on each z-level to distribute surface elevation, velocity and tracer points. The arrangement of points, displayed in Figure 3.1, has u_1 at points $\pm\Delta\xi_2/2$ away from the point where H and η are defined, and u_2 at points $\pm\Delta\xi_2/2$ away from the H and η points. Metrics h_1 and h_2 are defined at u_2 and u_1

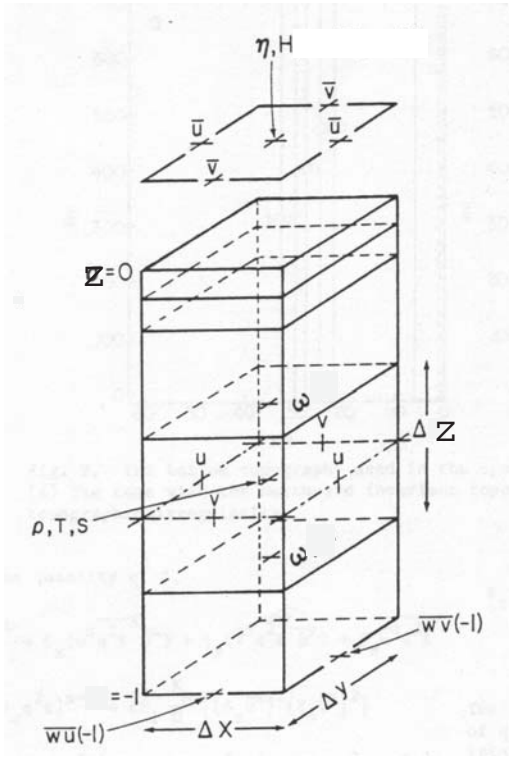

Figure 3.1: The locations of the variables on the model finite difference grid. Altered from Blumberg and Mellor (1987)

respectively. The vertical grid points are also staggered, with horizontal velocities and tracers defined at the centres of vertical boxes, and the vertical velocities defined at the interfaces between boxes.

The time stepping scheme is explicit, apart from the vertical mixing of momentum and tracers which is treated implicitly (to allow large mixing coefficients to provide a way of dealing with convectively unstable situations). Differences are forward in time, and centred in space, apart from the advection of momentum and tracers (the non-linear momentum terms), which are treated in an upstream manner (Roache, 1976)

3.3 Boundary conditions

3.3.1 Vertical boundary conditions

The boundary conditions on the scalar conservation equations are (Walker and Waring, 1998):

$$K_H \frac{\partial T}{\partial z} = -(< w\theta(0) >), z = \eta$$

$$K_H \frac{\partial T}{\partial z} = 0, z = -H$$

indicating that no heat or salt is permitted across the sea-bed, and at the surface, an input flux $< w\theta(0) >$ may be defined.

At the water surface, the boundary conditions are (Walker and Waring, 1998):

$$K_M \frac{\partial \vec{V}}{\partial z} = \frac{\vec{\tau}_{top}}{\rho}$$

and

$$w = \frac{\partial \eta}{\partial t} + \frac{u_1}{h_1}\frac{\partial \eta}{\partial \xi_1} + \frac{u_2}{h_2}\frac{\partial \eta}{\partial \xi_2},$$

where $\vec{V} = (u_1, u_2)$ and $\vec{\tau}_{top}$ is the surface wind stress vector.

At the bottom of the water column (where H is the water depth, so that $z = -H$), the boundary conditions are (Walker and Waring, 1998):

$$K_M \frac{\partial \vec{V}}{\partial z} = \frac{\vec{\tau}_{bot}}{\rho}$$

and

$$w = -\frac{u_{1bot}}{h_1}\frac{\partial H}{\partial \xi_1} - \frac{u_{2bot}}{h_2}\frac{\partial H}{\partial \xi_2}.$$

The bottom stress vector, $\vec{\tau}_{bot}$, is given by the quadratic friction law:

$$\vec{\tau}_{bot} = \rho C_d \left|\vec{V}\right| \vec{V},$$

where the drag coefficient, C_d, is calculated using (Walker and Waring, 1998):

$$C_d = max\left(\left[\frac{1}{\kappa}\ln\left(\frac{H + z_b}{z_0}\right)\right]^{-2}, C_{dmin}\right).$$

In this formulation for C_d, κ is the von Karman constant (0.4), z_b is the height of the velocity point above the sea bed and z_0 is the bottom roughness length scale. C_{dmin} is a parameter, typically between 0.002 and 0.003, which places a lower limit on the value of C_d in deep water.

MECO can implement a Grant-Madsen style bottom boundary layer (Grant and Madsen, 1986; Madsen, 1994). This formulation results in a time and space varying apparent bottom roughness, calculated according to specified wave input data. z_0 becomes the bottom roughness in the absence of waves.

Wave-Current Bottom Boundary Layer Flows

In the presence of waves, the shear stress within the immediate vicinity of the sea-bed is due to the combined effect of waves and currents (Grant and Madsen, 1979). Boundary layer theory states that the thickness of the boundary layer scales as $u*/f$, where $1/f$ is the time scale over which the boundary layer can develop, and $u*$ is a friction velocity. Typically, f is the tidal or inertial frequency, and hence the time scale for currents is of the order of $10^5 s$, or 10 hours. Typical shear velocities are of order $0.01 ms^{-1}$, and so boundary layers due to currents are typically of the order of 100 m thick and occupy the entire water column. In contrast however, wave frequencies are much higher, with a time scale of only 10 s. This suggests that wave boundary layers are only a few cm thick.

Prandtl (1945) mixing length theory introduces the concept of the eddy viscosity varying linearly with distance from the shear boundary:

$$K = \kappa u* z$$

where $u*$ is a characteristic shear velocity representing the turbulence level in the flow, $u* = (\tau/\rho)^{(1/2)}$, κ is Von Karman's constant, and z is the distance from the boundary. The logarithmic velocity profile in the region close to the shear boundary (law of the wall) follows from this assumption.

Wave-current bottom boundary layer flows suggest that close to the boundary, within the wave boundary layer, the eddy viscosity is scaled with the combined wave-current shear velocity $u*_{cw} = (\tau_{cw}/\rho)^{1/2}$, and above the wave boundary layer, but still within the near constant stress layer of the current, the eddy viscosity is scaled by the current shear velocity $u*_c = (\tau_c/\rho)^{1/2}$ (Grant and Madsen, 1979, 1986; Madsen, 1994).

$$K = \begin{cases} \kappa u*_{cw} z & if\ z < \delta_{WBL} \\ \kappa u*_c z & if\ z > \delta_{WBL} \end{cases}$$

where δ_{WBL} is the thickness of the wave boundary layer, given by (Madsen, 1994)

$$\delta_{WBL} = \alpha \frac{\kappa u*_w}{\omega_r}$$

where α is has been determined by Grant and Madsen (1986) to have values in the range $1 - 2$, ω_r is the angular wave frequency, and $u*_w = (\tau_w/\rho)^{1/2}$ is the wave induced shear velocity.

The maximum bottom stress experienced due to waves, τ_w, is expressed in terms of a quadratic friction or drag law (Jonsson, 1966)

$$\tau_w = \rho C_f \, u_{b,max} \, |u_{b,max}|$$

where $u_{b,max}$ is the maximum, near-bottom wave orbital velocity just outside the wave boundary layer, and C_f is a wave friction coefficient.

Grant and Madsen (1979, 1986) and Madsen (1994) assume that the wave and current stresses can be summed linearly in a vector fashion, so that waves and currents combine at some angle $\phi_{cw} = \phi_c - \phi_w$, and the combined wave-current shear stress is expressed

$$\tau_{cw}^2 = (\tau_w + \tau_c cos\phi_{cw})^2 + (\tau_c sin\phi_{cw})^2$$

This yields

$$u*_{cw}^2 = C_\mu u*_w^2$$

where

$$C_\mu = \left(1 + 2\left(\frac{u*_c}{u*_w}\right)^2 cos\phi_{cw} + \left(\frac{u*_c}{u*_w}\right)^4\right)^{1/2}$$

A generalised friction coefficient follows $C_\mu C_f$, so that the wave-current induced shear velocity is expressed as a function of the maximum near bottom wave orbital velocity

$$u*_{cw}^2 = C_\mu u*_w^2 = C_\mu C_f \, u_{b,max}^2$$

These models have shown that the wave friction coefficient of the drag law model is not a constant as is often assumed, but is a function of the Reynolds number, and the ratio of bottom roughness to the semi-excursion of the wave orbital displacement. Determination of the bottom roughness is not straightforward given that it is a function of both the geometrical properties at the sea-bed (grainsize, ripple height and wavelength etc), and the flow properties. Madsen (1994) derived an expression for the wave friction coefficient for wave-current bottom boundary layer flows

$$C_f = \frac{1}{2}\begin{cases} C_\mu exp\left[7.02\left(\frac{C_\mu u_{b,max}}{k_N \omega_r}\right)^{-0.078} - 8.82\right] & for\ 0.2 < \frac{C_\mu u_{b,max}}{k_N \omega_r} < 10^2 \\ C_\mu exp\left[5.61\left(\frac{C_\mu u_{b,max}}{k_N \omega_r}\right)^{-0.109} - 7.30\right] & for\ 10^2 < \frac{C_\mu u_{b,max}}{k_N \omega_r} < 10^4 \end{cases}$$

where $k_N = 30 z_o$ is the bottom roughness, z_o being the roughness length.

Near bottom current profiles are solved subject to the no-slip boundary conditions at $z = z_o$ for $z < \delta_{WBL}$ and $z = z_{oa}$ for $z > \delta_{WBL}$, where z_{oa} is the 'apparent bottom roughness' experienced by the current in the presence of waves, i.e., the roughness determined from a log-profile analysis of current observations outside the wave boundary layer.

The apparent bottom roughness, z_{oa} is obtained, matching the current from each boundary layer at the top of the wave boundary layer, $z = \delta_{WBL}$, such that

$$\frac{u*_c}{\kappa} ln \left(\frac{\delta_{WBL}}{z_{oa}} \right) = \frac{u*_c^2}{\kappa u*_{cw}} ln \left(\frac{\delta_{WBL}}{z_o} \right)$$

where the right-hand side of the equation represents the current at the top of the wave boundary layer, as a result of the combined wave-current interactions, and the left hand side represents the current at the top of the wave boundary layer as a result of the near constant stress layer of the current above the wave boundary layer, and leads to an expression for z_{oa}. It is this value of z_{oa} that is updated in the MECO model. MECO also provides output of the wave-current induced shear velocity.

3.3.2 Coastlines

MECO has the option of a full slip condition at closed lateral boundaries, being:

$$\frac{\partial u}{\partial n} = 0$$

where n is a unit vector normal to the closed boundary, a no slip condition such that:

$$u_T = 0$$

where u_T represents the tangential velocity at the coast, or a half slip condition which lies halfway between. The full slip condition is used for this study as it is expected that friction near the closed boundaries will be dominated by bottom friction in the shallow waters, without adding extra lateral friction at these boundaries.

3.3.3 Open boundaries

MECO is capable of implementing two fundamentally different types of open boundary conditions. First, a mass, or conservation, boundary condition, requires specification of sea surface elevation, which may include tidal and non-tidal components, along with tracer concentrations, such as temperature and salinity, at the open boundary. Velocity is then

calculated by the model from pressure gradients. This type of boundary condition was used for the marine open boundaries (the east and west boundaries) of the model domain and are discussed below. The second 'flux' boundary condition requires specification of fluxes of water and tracers at the open boundary. This requires knowledge of velocity and tracers at the open boundary, and it was this type of open boundary condition that was implemented for the Fly River outflow, also discussed below.

The mass or conservation boundary condition is susceptible to the reflection of waves generated in the interior of the model domain (Chapman, 1985). This behaviour can lead to an increase of energy in the domain, and eventual instability. To overcome this problem, MECO incorporates a sponge layer immediately adjacent to the open boundary. The first four grid points inside the open boundary are assigned a horizontal viscosity increased by a factor of 4, providing energy loss and damping of oscillations near the boundary.

Further model details will be discussed in the following section on model inputs and forcing.

3.4 Model Input

This section of the project is aimed at modelling the flow dynamics of the Torres Strait region using the MECO three-dimensional hydrodynamic model. Both tidally induced flow, and that flow produced by wind and pressure regimes are considered.

All available data within Torres Strait have been used to assess the ability to model the flow dynamics.

With the flow dynamics represented, ultimately the dynamics of the continental shelf boundary layer will be modelled to further the understanding of sediment transport, both bedload and suspended load, under present climatic conditions.

3.4.1 Model grids

2-D Grid (0.05° horizontal resolution)

It was required that the model domain encompass all of Torres Strait and the Fly River Delta - plus most of the Gulf of Papua and a region of the Gulf of Carpentaria - to allow good representation of flow through Torres Strait. It was preferred that the open boundaries were bounded by existing ports in order that tide, sea-level and meteorological data would be readily available at these points. As a result, the main grid (Fig. 3.2) was chosen such that the western boundary was defined by Merauke, Irian Jaya, ($8^\circ 31.8S, 140^\circ 20E$) in the north,

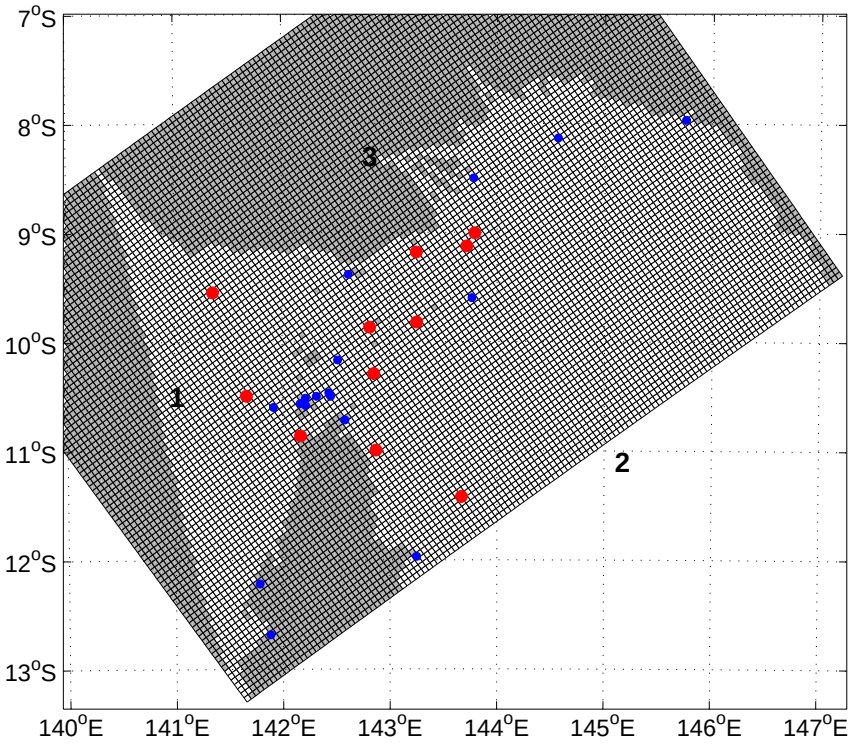

Figure 3.2: The Torres Strait - Gulf of Papua model grid. Darker cells indicate the cell is outside of the computation domain, i.e., either land or designated outside the grid. Open boundaries are numbered 1 to 3. The position of tide gauges (blue dots) and current meters (red dots) used for model comparison are also shown.

and Archer River, Qld, Australia ($13°20S, 141°39E$), in the south. The eastern boundary was defined by Piper Island ($12°15'S, 143°15'E$), Raine Island ($11°36'S, 144°3'E$) and Port Moresby, Papua New Guinea ($8°30'S, 148°47'E$). The grid was aligned at an azimuth of approximately 40 degrees.

The grid geometry is 'rectangular' but based on geographic coordinates so that cell dimensions vary slightly across the grid. The grid origin (i.e. bottom left corner) was located at $13°20'S, 141°39'E$. Model run time and memory requirements were the primary determining factors for 'standard' model runs, the grid was chosen to contain 138 cells in the i-direction (SW-NE), and 96 cells in the j-direction (SE-NW). Each cell has a dimension of $0.05 \times 0.05°$ ($\sim 4.5km$ square). For spatial variation of cell size to be kept to a minimum, the grid was positioned on a 'false earth' such that the 'false equator' runs through the centre of the grid in the i-direction. This resulted in the 'false north pole' being positioned at $55°S, 50°E$ on the real earth.

Having defined the grid as above, a land mask (section 3.4.2) was applied and manually edited to best represent the coastline with the given grid resolution. Cells to the west of the western boundary defined by a straight line between Merauke and Archer River were

Table 3.1: Grid parameters for the fine resolution Torres Strait Model Grid.

Parameter	Value
Origin Longitude	$141.65°E$
Origin Latitude	$13.33°S$
X cell width	$0.05°$
Y cell width	$0.05°$
False Pole Longitude	$50°$
False Pole Latitude	$55°$
No. x cells	138
No. y cells	96
Total No. cells	13248
No. Wet Grid Points	6756

designated out of the grid. The final grid contains 3 open boundaries designated 1-3. These, along with the land/water mask, are shown in Figure 3.2.

The model was generally run for a period of 90 days. This allowed harmonic analysis to obtain reliable estimates of the main 5 tidal constituents (M_2, S_2, K_1, O_1 and N_2).

A complete set of grid parameters is given in Table 3.1.

3-D Grid (0.05° horizontal resolution)

The 3-D grid was obtained from the 0.05° 2-D grid by assigning 22 z-layer interfaces in the vertical direction to accommodate uniform 3m spacing from the surface to the 30m isobath (covering the dominant portion of Torres Strait) and then parabolic spacing up to the 3000m maximum depth. The depths of the base of each layer are shown in Table 3.2.

For the 0.05° grids, the 2-D time step was set at 10 seconds to satisfy the Courant-Friedrich-Levy (CFL) criterion. The maximum value obtainable for the 3-D time step whilst maintaining model stability was 100 seconds.

2-D grid (0.1 deg resolution)

A coarse resolution model grid was trialled for sensitivity, and to increase the rate of computation. This grid was obtained from the 0.05° grid by simply halving the number of cells in each direction. This resulted in a grid with 69 cells in the i-direction (SW-NE) and 48 cells in the j-direction (SE-NW) with a resolution of $0.1 \times 0.1°$ ($\sim 9.5km$) Some subsequent editing of the land mask and bathymetry was required to better represent the bottom topography. Grid parameters are given in Table 3.3.

Table 3.2: Depths of base of each z-layer for the Torres Strait model grid.

Layer No.	Depth (m)
top 1	3
2	6
3	9
4	12
5	15
6	18
7	21
8	24
9	27
10	30
11	33
12	51
13	75
14	99
15	150
16	300.7
17	550
18	855.2
19	1250
20	1815.3
21	2400
22	3000

Table 3.3: Grid parameters for the coarse resolution Torres Strait model grid.

Parameter	Value
Origin Longitude	$141.65°E$
Origin Latitude	$13.33°S$
X cell width	$0.1°$
Y cell width	$0.1°$
False Pole Longitude	$50°$
False Pole Latitude	$55°$
No. x cells	69
No. y cells	48
Total No. cells	3112
No. Wet Grid Points	1587

3-D grid (0.1 deg resolution)

The 0.1° 3-D grid was obtained from the 0.1° 2-D grid and assigning the same 22 z-layer interfaces in the vertical direction as were defined in the 0.05° 3-D grid.

For the 0.1° grids, the 2-D time step was set at 20 seconds to satisfy the CFL criterion and after trying longer time steps, a maximum 3-D time step of 200 seconds was prescribed to maintain model stability.

3.4.2 Topographic Data

Coastlines

Digital coastline data were obtained from the Global Self-consistent Hierarchial High-resolution Shoreline (GSHHS) database as described by Wessel and Smith (1996). This database provides coastline data for the entire world at 5 different resolutions ranging from 25km to a few hundred metres. The tolerance of the GSHHS_h database used in this project is 200 m.

Bathymetry

Digital bathymetry data were obtained from the AGSO bathymetric 30 second grid of the Australian region (Porter-Smith, 2000). North of $8.5°S$, bathymetry is provided by the ETOPO5 5 minute lat-lon grid (National Geophysical Data Center, 1988), referenced to mean sea-level. Smoothing has been applied over the discontinuities observed between the bathymetry model grids. The bathymetry model contains water depths relative to mean sea level on an approximate 1 km grid surrounding all of Australia.

Water depths were assigned to each water cell using the bathymetric data described above, interpolated onto the model grid. For cells containing 1 or more data points, those data were averaged to determine the cell depths. Unfortunately this created many cells with very large false depths near the coast where 'wet' data points were averaged with 'dry' data points. As all of these points were found next to the coast, these cells were manually edited to match the minimum depth of 7m. For the few cells for which no data were available, depths z were calculated from nearby cells using a nearest-neighbour interpolation with a 1/r weighting:

$$z'_{ij} = \frac{\sum r_k^{-1} z_k}{\sum r_k^{-1}} \tag{3.17}$$

over the nearest point from each quadrant. z_k are depths from bathymetric data, z' are depths interpolated onto the model grid, and r_k is the distance between the model grid point and the position of the known bathymetric data point. Depths were truncated to lie

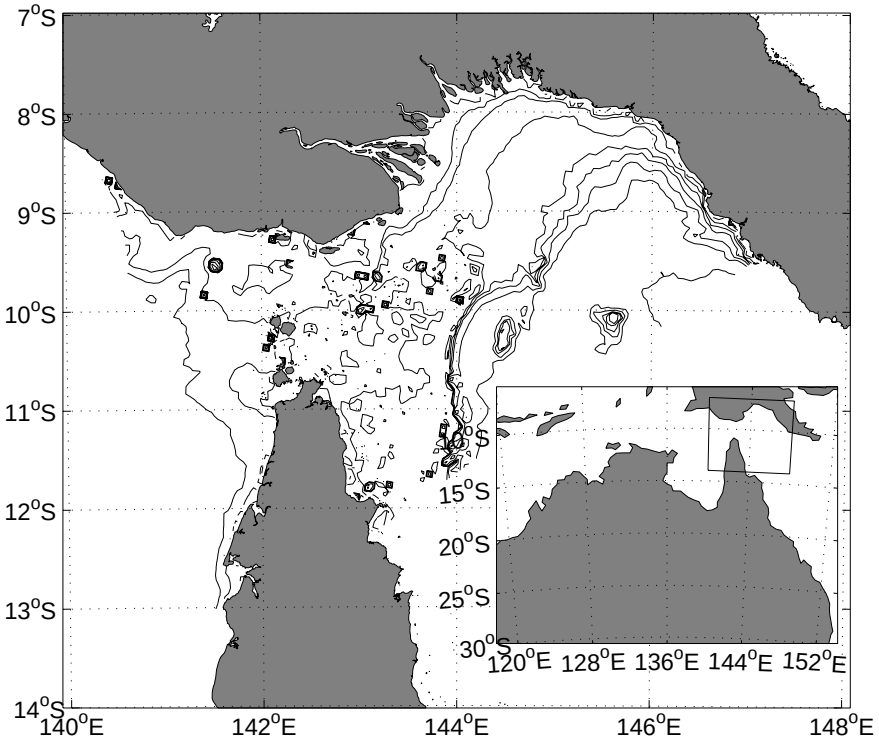

Figure 3.3: Torres Strait and Gulf of Papua model bathymetry. Contours are at depths of 0, 10, 20, 50, 100, 200, 500, 1000, and 2000 m depth

between a minimum of 7 m and a maximum of 3000 m to avoid problems with wetting and drying of coastal zones given large tidal ranges.

Some other manual smoothing of bathymetry in cells was required in 3 other regions to alleviate instabilities which occurred during some model runs. These areas included: 1 - the steep shelf off the coastline of Papua New Guinea, nearby Port Moresby, 2 - the steep shelf to the north of Raine Island, and 3 - the shallow waters between the western boundary and the eastern coast of the Gulf of Carpentaria. A contour plot of the final model bathymetry is shown in Figure 3.3.

3.4.3 Atmospheric Forcing

Forcing data to simulate the effect of surface wind and pressure on the sea surface was obtained from the NCEP-NCAR 40-Year Reanalysis Project (Kalnay et al., 1996). Wind and pressure are produced from a global assimilation model incorporating all available observations with wind and pressure as class A and B variables, respectively. This indicates that wind and pressure are amongst the more reliable of the variables produced for the NCEP database because of strong model dependence on observations, with class A being more strongly dependent than class B. The third class, C, denotes variables that are calculated

from the model output and have no direct observations (Kalnay et al., 1996).

Atmospheric mean sea-level pressure and surface wind data were obtained from the NCEP-NCAR reanalysis project database (Kalnay et al., 1996). Data were provided at 6 hourly intervals on a 2.5 degree grid spanning the Australian region for the years 1958 to 1999. Data were then interpolated onto the model grid using the same 1/r nearest neighbour method as given in equation 3.17. Atmospheric pressure is capable of altering sea level through the 'inverse barometer effect', where a decrease in atmospheric pressure will result in a rise in sea level. The friction at the air-sea interface transfers momentum from the wind to the ocean currents. The model calculates this frictional term with the commonly used formula of Large and Pond (1981) at each model time step. The surface stress, $\vec{\tau_{top}}$, is given by:

$$\vec{\tau_{top}} = \rho_{air}\, C_d\, \vec{V} \left|\vec{V}\right|$$

where ρ_{air} is the air density, $\vec{V}$ is the wind velocity vector (ms^{-1}) and C_d is the surface drag coefficient given by:

$$C_d = \begin{cases} C_{d0} & V \leq V_0 \\ C_{d0} + (C_{d1} - C_{d0})\,\frac{(V - V_0)}{(V_1 - V_0)} & V_0 < V < V_1 \\ C_{d1} & V \geq V_1 \end{cases}$$

where V is the wind speed, and C_{d0}, C_{d1}, V_0 and V_1 are parameters with specified values of 0.00114, 0.00218, 10.0, and 26.0 respectively (Large and Pond, 1981). V_0 and V_1 have units of ms^{-1}.

3.4.4 Density

The model is capable of simulating effects due to the three dimensional variation in water density, calculated from temperature and salinity values using the equation of state (Gill, 1982).

Many model runs were carried out for the assumption of a well mixed water-body (as Torres Strait itself is) i.e., density variations were neglected and a constant value of $1025 kgm^{-3}$ was specified throughout the domain. In this unstratified case the vertical mixing of momentum (and sediments) is likely to be higher than the case where stratification is considered.

The Gulf of Papua however is a stratified water body, as a result of the large freshwater input of the Fly River. Therefore a density distribution is required to represent the mean

currents in the region.

Temperature and salinity needed to be specified in the model in three ways. A thermohaline field was required to initialise the model, temperature and salinity must be specified at the open boundaries, and since relaxation of the thermohaline field was used in this project, a relaxation field was also required.

The temperature and salinity fields were specified by a temporally uniform mean density field designated from the Climatology of Australian Regional Seas (CARS; Ridgeway et al. 2000). This climatology consists of a harmonic fit with mean, annual and semi-annual constituents for temperature and salinity on a 0.5 degree grid encompassing a region enclosing Australia, including the Torres Strait/ Gulf of Papua region. The climatology field is derived mainly from CTD casts (Ridgway et al., 2001) and may represent a source of error as there are a low density of hydrographic data available for Torres Strait particularly.

Salinity and temperature were required on the open boundaries. These tracers were set by values obtained from the mean CARS climatology. This parameterisation ignores the seasonal variation of salinity and temperature in the model domain. Although seasonal salinity variations are small, temperature varies by up to 2-3°. At high tropical temperatures, such a variation in temperature leads to a variation in water density of approximately 0.5 kgm^{-3}.

Temperature and salinity are influenced by advective and diffusive processes in the model. The adopted model configuration has no surface heat input, significant lack of freshwater inflows into the Gulf of Papua, and no evaporation. Without such forcing, the thermohaline field will become unrealistic. This is overcome by 'relaxing' the field towards climatological values. The relaxation follows an exponential decay at a rate specified by a time constant set at 20 days and is calculated every 5 hours. In each model run, the relaxation was towards a temporally uniform 3-D field sourced from CARS which varied spatially. MECO requires that the CARS harmonic values be converted to an annual time series.

3.4.5 Open Boundaries

Tidal Data

The western and eastern boundaries of the model were tidally forced. Surface elevations were calculated using Harmonic constants for nine tidal constituents (M_2, S_2, K_1, O_1, N_2, Q_1, Sa, Ssa, Msf) obtained from the Admiralty data set (Flater, 1999). The Admiralty dataset was updated to take constituents from the 1999 Australian National tide tables

(Australian Hydrographic Office, 1999).

Points on the western boundary were forced by interpolating elevation time series calculated at Archer River and Merauke using a linear $1/r$ nearest neighbour interpolation. Points on the Eastern open boundary between the Australian mainland and Raine Island (in the Coral Sea) were forced by interpolating elevations calculated at Piper Island and Raine Island. The remaining boundary, northeast of Raine Island was forced by interpolating data between Raine Island and Port Moresby.

Low Frequency Sea Level Data

To provide a long term pressure gradient, low frequency sea level information is specified for each of the open boundaries. This was specified in the form of dynamic height calculated from the CARS temperature and salinity climatology described above. A reference level of no motion at 500 m was assumed, believed to be below the base of most density flows in the Gulf of Papua, which are dominated by fresh water input at the surface. The dynamic height is determined from integrating the specific volume anomaly through the water column (Gill, 1982) and the resulting sea surface elevation contains the baroclinic component (that component driven by density variations) of sea surface elevation. The resulting signal varies over an annual time series, corresponding with seasonal changes in density. No variation on a synoptic time scale is considered at the boundaries.

Fly River Outflow

The outflow of the Fly River was specified by an open boundary of one cell width with a velocity providing an addition of momentum to the model. The velocity input data was estimated given the cell width ($\sim 4.5km$) and a depth of 7 m. The outflow of the Fly is estimated at $238km^3/a$ (Alongi et al., 1992), and this results in a depth averaged flow velocity of approximately 0.2 m/s. The 0.1° grid, resulted in an input flow of 0.1 m/s. The inflow was specified to be a 'freshwater' input, with a forcing salinity of 12 specified.

3.4.6 Waves

Twelve months of predicted swell data has been obtained from the Bureau of Meteorology WAM runs (Greenslade, 2001). These data are provided on a 0.5°grid at 6 hourly intervals, and include significant wave height (H_s), mean wave period (T_m) and mean wave direction (ϕ_m). From these parameters, maximum bottom wave orbital velocities can be determined.

3.4.7 Friction

Bottom friction calculations within the model are determined using the quadratic law described in Walker and Fandry (1993). This involves the choice of a typical bottom roughness length scale $z_0 = 0.002m$, and a minimum drag coefficient, $C_{dmin} = 0.0033$. These values are typical of those taken from the literature, e.g., Jonsson (1966). Many model runs showed that the model results are insensitive to the choice of the friction parameters. The same result was also observed by Andrewartha and Walker (1999). The use of wave-enhanced bottom friction calculations (Section 3.3.1) were included on separate runs to better represent the enhanced bottom friction in the near-shore zone, with little influence on the predicted currents.

3.4.8 Vertical Mixing

Momentum is transferred vertically within the water column by turbulent mixing, represented in the model using an eddy viscosity parameterisation as described by Bowden and Hamilton (1975) (Section 3.1). Here, the vertical mixing is dependent upon current velocities, water depth and stratification (stratification ultimately reducing vertical mixing).

The background mixing constants K_{M0} and K_{H0} were set to the values of $0.0005m^2s^{-1}$ and $0.00025m^2s^{-1}$ respectively, with these values taken from Bowden and Hamilton (1975). Values for K_{M_1} and K_{H_1} were set at 0.0625 and 0.03 respectively, taken from Csanady (1982). These values were found to significantly alter currents and sea surface levels throughout the model domain, and were tuned to match the comparing data. Sensitivity studies specifying uniform, constant vertical diffusivity for momentum and mass of $0.001m^2s^{-1}$ were carried out. The mixing formulation of Csanady (1982) improved results markedly.

3.4.9 Other Effects

Horizontal diffusion of momentum with a diffusivity of $10.0m^2s^{-1}$ was added to ensure model stability. This value, the minimum value used to achieve stability, is small in comparison to previous applications of MECO ($10.0m^2s^{-1}$, Andrewartha and Walker, 1999). Small values of diffusivity may be defined in MECO to retain stability given the large numerical diffusion resulting from the advection scheme used in the model.

Terms involving surface elevation were treated as non-linear due to shallow water and the large tidal range in the model region. The model was trialled to both include and exclude the non-linear advective terms in the momentum equations. The non-linear runs show better agreement with comparison data within the domain (See section 3.6.1).

3.5 Data available for Model Verification

3.5.1 Tidal Elevations

Sea level data from seventeen additional points within the model domain were used for comparison with modelled tides. These points were:

- Albany Island (AI; $10°41.4'S$, $142°38.4'E$)
- Booby Island (BI; $10°36.0'S$, $141°55.2'E$)
- Cape Grenville (CG; $11°58.2'S$, $143°16.2'E$)
- Darnley Island (DI; $9°36.0'S$, $143°41.4'E$)
- East Strait Island (ES; $10°30.0'S$, $142°27.0'E$)
- Goods Island (GI; $10°34.2'S$, $142°10.2'E$)
- Ince Point (IP; $10°30.0'S$, $142°19.2'E$)
- Kerema (K; $7°58.2'S$, $145°45.0'E$)
- Kumul Trk Mar (KTM; $8°7.8'S$, $144°34.2'E$)
- Pennefather River (PR; $12°12.6'S$, $141°43.2'E$)
- Saibai Island (SI; $10°22.8'S$, $142°37.2'E$)
- Suarji Island (Su; $10°10.2'S$, $142°31.2'E$)
- Turtle Head (TH; $10°31.2'S$, $142°13.2'E$)
- Twin Island (TI; $10°28.2'S$, $142°25.8'E$)
- Thursday Island (ThI; $10°34.8'S$, $142°13.2'E$)
- Umuda Island (UI; $8°33.0'S$, $143°51.0'E$)
- Weipa Island (W; $12°40.8'S$, $141°49.8'E$)

The sources of these data include the Admiralty data set (Flater, 1999), National Tidal Facility (NTF; National Tidal Facility (2000)) and the Australian National Tide Tables (ANTT; Australian Hydrographic Office (1999)). The location of these sites is given in Figure 3.2.

3.5.2 Previously Collected Current Meter Data

Measured current meter data within the model domain, with records in excess of 30 days have been obtained for 2 scenarios. These are :-

- 3 sites (stations 5,6,7) during the period of Feb-April, 1990. (Harris, 1994b)
- 7 sites (stations 12,13,14,16,17,19,20) during the period of Jan-Mar, 1993. (Harris, 1994b).

Further details of the deployment and recovery of these current meters is available from Harris (1993). The sites of these moorings are shown in Figure 3.2.

Each of these current meters were Anderaa current meters. Harris (1993) states that on recovery, many of the current meters had observed problems of biofouling. Only records from current meters not severely affected were used in this study.

3.5.3 New Current Meter Data, and Observed Processes

Introduction Here, details of data obtained from Torres Strait in January-February 2002 using a newly constructed benthic frame designed for deployment in shelf water depths of up to 300 m are presented. The Benthic Research for Underwater sediment ConcEntrations probe (BRUCE), designed by Geoscience Australia, comprised a Sequoia Laser In-Situ Scattering and Transmissiometry (LISST) - 100 transmissometer laser particle sizer and Seabird CTD located at 27 cm above the base of the benthic frame, and a Nortek vector acoustic current meter and Benthos optical backscatter sensor (OBS) located at 100 cm above the frame base (Fig. 3.4). The aims of the deployment were to verify and quantify modelling results predicting the occurrence of a potential sediment transport path from the Fly River Delta into Torres Strait.

Instruments and Data BRUCE was deployed at location $9°7.364'S, 143°43.113'E$ in 31.5 m of water from the Research Vessel *Franklin*, Geoscience Australia cruise 234 (Fig. 3.2). Data began recording at 2321 21-Jan-2002 GMT, however the mooring was not complete until 0721 22-Jan-2002 GMT. The mooring was recovered at 1200 6-Feb-2002 GMT with some hairy growth, however not sufficient to affect data. The Nortek vector acoustic current meter (ADV $\#N4103$) was positioned to sample at 100 cm above the base of the benthic frame. The ADV was programmed to burst sample every 20 minutes for 90 s at 8 Hz to record at turbulent time scales. Vector components of velocity (east, north and up) and temperature were logged internally and downloaded on recovery. Data were checked for

Figure 3.4: The Benthic Research for Underwater sediment ConcEntrations (BRUCE) probe. The central three pronged probe is a Nortek vector acoustic current meter, The Sequoia LISST-100 and Seabird CTD lie horizontally at $\sim$ 27 cm above the base, and the Benthos OBS faces inwards from a vertical support bar at 100 cm above the base.

consistency and, when necessary, edited to remove clearly erroneous measurements. The Benthos optical backscatter sensor (OBS #897) was positioned at 100 cm above the base of the benthic frame, facing inwards from one vertical support bar. The OBS was powered by, sampled at the same rate as, and logged to, the ADV. OBS output is recorded in counts as an analog input to the ADV. This is converted to volts (5 V = 65535 counts) and subsequently converted to turbidity (ftu).

Turbidity (ftu)= $356.7 \times (x + 0.002)$

where x is the output in Volts. Turbidity at 1 m above the sea-bed was below the measurement threshold of the OBS of 7 ftu for most of the deployment, however meaningful data were recorded in the final 36 hours of deployment. The Sequoia LISST-100 transmissometer laser particle sizer (LISST #104579) was placed 27 cm above the base of the benthic frame. The LISST was programmed to burst sample every 20 minutes for 90 s at 2 Hz. The LISST logged internally until the 2MB memory card was full (13 days, or 2

days short of the total deployment period). Data were downloaded on recovery in day long segments. Transmissivity, battery voltage and volume concentration for 32 size bins were recorded. The Seabird CTD (CTD #1620) was also placed at 27cm above the base of the frame. The CTD was programmed to sample at the same rate as the LISST. Temperature and conductivity were logged to the LISST internal memory. Two 20 cm lengths of 9 cm diameter plastic pipe were placed in the frame at 30 cm and 100 cm height above the base of the frame, to serve as sediment traps for the deployment. Sediment trap results are detailed in Harris et al. (2002).

Observations

Sea-Level The burst-averaged CTD pressure record indicates that sea-level is dominated by the semi-diurnal tides (Fig. 3.5a). The mooring began (Day 21) during neap tide, with a tidal range of approximately 1 m. Spring tides were experienced on day 28, with a maximum tidal range of 3.57m. A 40 hr low pass filter of the pressure record has a maximum deviation from the mean of $\sim 5cm$. The sea-level record shows a return to neap tides on day 34, before the mooring was completed on day 36.

Winds Winds were measured aboard the RV *Franklin*. The Ship was up to 80 km distance from the BRUCE deployment at times, however they are assumed representative of winds at the BRUCE site for the period of deployment. Winds were generally characterised by weak north-westerlies. A diurnal pattern is evident in the wind record, with very weak variable winds (1-2 knots) occurring each afternoon, and 10 kt north-westerly winds occurring each night and early morning (Fig. 3.5b-c).

BRUCE was deployed during a period of abating 10 kt south-easterly winds which lasted for approximately two days before the lighter north-westerly winds commenced. A period of stronger winds from the north-west was observed between days 31-33, when the mean exceeded 20 kts. Mean winds were directed from $303°T$ at ~ 6 knots during the period of north-westerlies, occurring during most of the deployment.

Currents The burst-averaged ADV current record is dominated by the semi-diurnal tides (Fig. 3.6). Maximum bottom currents of speeds $\sim 50cms^{-1}$ directed towards the south-west occur during spring tides at day 28. Rising tides are associated with a current towards the west-south-west (260°), falling tides with a current towards the east-north-east (80°), with an anti-clockwise rotation. Low frequency (sub-tidal) currents were estimated

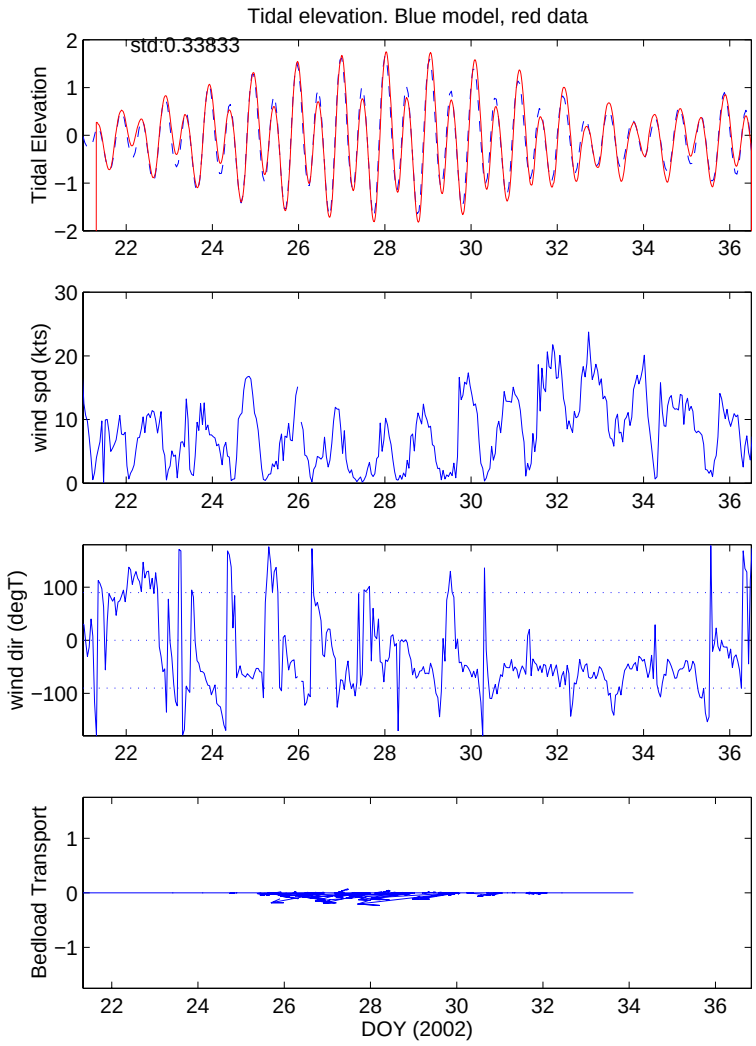

Figure 3.5: (a) Sea Surface Elevation (m) as observed by BRUCE probe (blue line) and predicted (red line) using MECO model. (b) Wind Speed (knots) measured aboard the RV *Franklin*, (c) Wind Direction ($^{\circ}T$) measured aboard the RV *Franklin*, and (d) Bedload Transport Vectors (g/cm/s) for the period of the BRUCE deployment.

by applying a frequency domain 40 hr low pass filter to the ADV data. Low pass filtered currents are relatively weak ($\sim 5cms^{-1}$). During the first 2 days of south-easterly winds, weak ($< 2cms^{-1}$) non-tidal bottom currents are directed to the north-east. North-westerly winds direct the current to the west. Periods of increased north-westerly winds at days 31-33 increase the non-tidal currents to $\sim 8cms^{-1}$, directing them to the south-south-west (190°). During the period of deployment, mean currents were heading towards the west-south-west (bearing $260^{\circ}T$) at $2.5cm/s$ (Table 3.9).

Waves Each burst file was used to determine a wave spectrum from the pressure record (Energy levels at wave frequencies in the u and v components of velocity were too low (amongst noise levels) to compute a directional wave spectrum). The pressure power

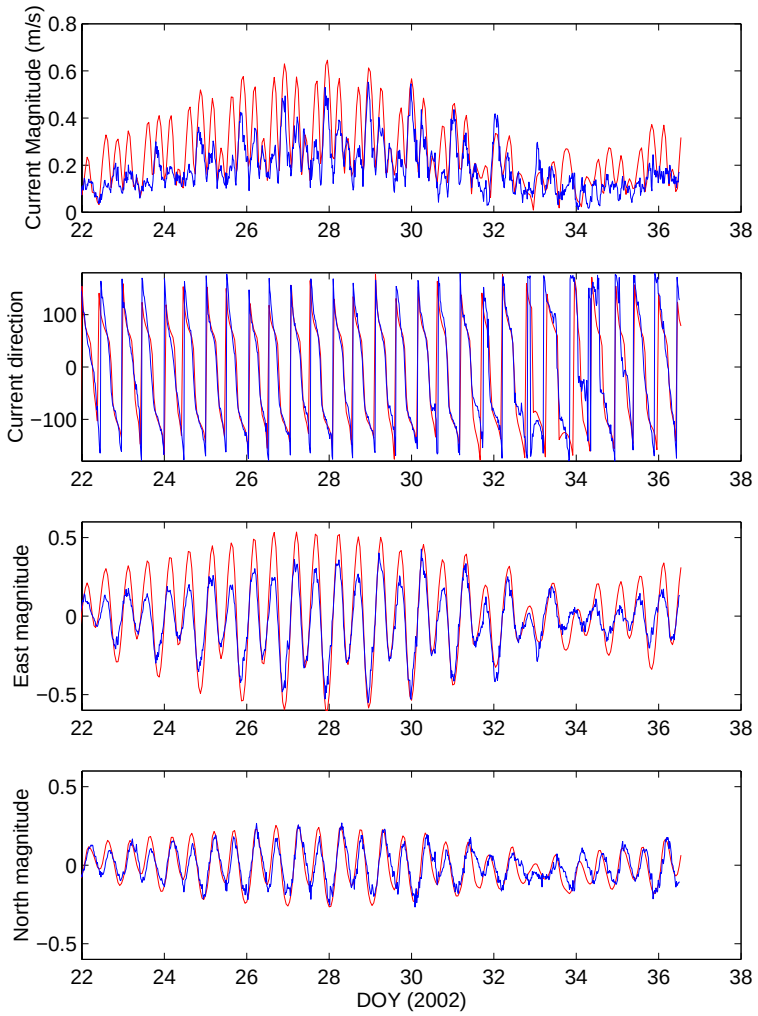

Figure 3.6: Time series comparisons of currents measured by the BRUCE probe (blue line) and predicted by the Model (red line). (a) Current speed (m/s). (b) Current Direction (°). (c) Eastwards current (m/s), and (d) Northwards current (m/s)

spectrum, C_{pp} was converted to the surface elevation spectrum, $F(\omega)$, using the relationship (Philips, 1977):

$$F(\omega) = \left[\frac{cosh(kh)}{cosh(k(h+z))}\right]^2 \frac{C_{pp}}{\rho^2 g^2}$$

where k is the wavenumber, h is the mean water level with respect to the seabed, z is the vertical distance with respect to the mean water level (positive up), ρ is water density, and g is gravity.

For each burst spectrum, the significant wave height was determined from the relation (Philips, 1977):

$$H_s = 4\sqrt{\int F(\omega)d\omega}$$

where $F(\omega)$ is the wave energy spectrum, and ω is the wave frequency. Maximum wave energy is observed at day 24 with a Significant wave height of $\sim 1m$, and a significant wave period of $\sim 8s$. The significant wave period is greatest during day 28 at 11 s. During periods of greatest recorded winds, on days 31-33, the wave energy is least ($H_s \sim 60cm$) suggesting one of three things: 1. The wind direction whilst the winds were strong was such that the fetch was too short for any large waves to be generated; 2. The wind record taken from the Ship's log is not a good indicator of winds at the BRUCE deployment site for the given period, or 3, the most likely scenario, the 30 m depth is beneath the wave base of the short wave-length, locally generated waves, and thus not resolved by the ADV at all. Greater significant wave heights during the early deployment may be left over from the south-easterly winds experienced prior to, and during, the early deployment period, and thus have a greater fetch, a longer wavelength, and a deeper wave base.

Salinity The salinity record obtained from the CTD has a semi-diurnal signature associated with the tide (Fig. 3.7a). Low salinities are correlated with periods of high tide, and high salinities are observed during low tide. Tidal variation of salinity is of the order of 0.2 psu. Over the period of deployment, salinities fall from ~ 34.3 to ~ 33.7.

Approximately 1 day after deployment of the BRUCE probe, visual observations from the deck of the RV *Franklin* recorded a sharp boundary oceanic front, of less dense fresh water intruding over the more dense, more saline water in the study area. The Ship's log of surface salinity shows a drop from $\sim$ 32.5 to $\sim$ 31 associated with this front (Harris et al., 2002). The recorded bottom salinity from BRUCE during this period does not show a salinity drop associated with this front indicating that the water profile was quite stratified with a 3 psu variation in salinity through the water column. Less tidal variation of salinity is observed during this period.

Temperature The temperature record indicates similar trends to the salinity record. Higher temperatures are observed at periods of low tide, and lower temperatures are observed at high tide. Semi-diurnal variation of temperature, of up to $1°C$, during periods of spring tide (Day 28) are observed. Over the duration of the deployment, a decrease of $\sim 1°C$ in mean temperature is observed.

Suspended Material (Transmissivity/ Turbidity) The LISST transmissometer recorded transmissivity (Fig. 3.7b) for the entire period that the LISST was recording (Days 21-34). The water is initially quite clear (Transmissivity 0.85). Transmissivity displays

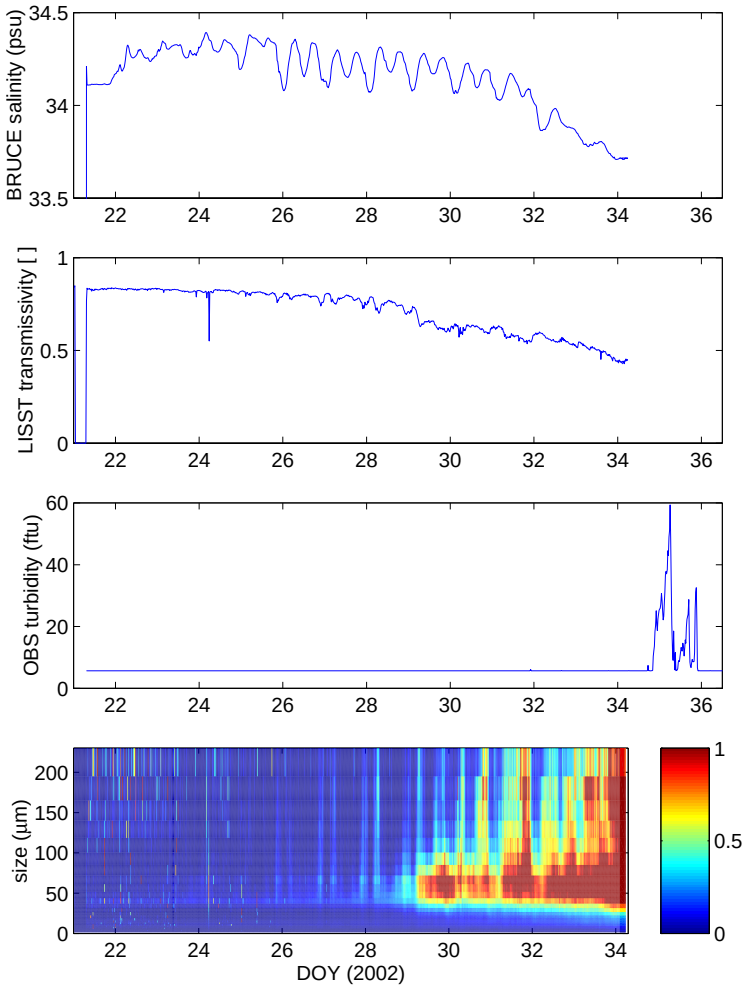

Figure 3.7: Time series of BRUCE measurements. (a) Salinity (psu), (b) LISST Transmissivity [ ]. The LISST memory card filled to capacity on day 34. No measurements from the LISST or Seabird are available for the final 2 days of deployment. (c) OBS turbidity (ftu). Turbidity levels were below the OBS measurement threshold for much of the deployment, and (d) Grain size spectrum as a concentration volume ($\mu l/l$). The y-axis is grain size in μm.

some small semi-diurnal variation (0.05) during the period of spring tides. Transmissivity follows the same gradual trend as salinity and temperature, decreasing to ~ 0.50 by the end of recording. Having shown a similar trend as S and T, this suggests a real event, rather than an optical effect of biofouling. OBS-measured turbidity (Fig. 3.7c) is below noise levels for the majority of the time of deployment. On day 25, after the LISST stopped recording, turbidity was great enough to be resolved (up to 60 ftu). Semi-diurnal variability seems to be observed in the turbidity record, however only one day of record exists. The OBS record does confirm that the water column had more suspended material at the end of deployment than at the start. No overlap in OBS turbidity and LISST transmissivity record means that no relationship between the two quantities could be developed.

Grain Size The grain size distribution spectrum (Fig. 3.7d) is noisy for the first 3 days of the record, associated with the low number of reflectors in the water column for aiding measurements. Through days 26-29, low volume concentrations over all grain-sizes are observed. The grain-size distribution spectra were used to compute time series of grain size statistics: Mean, Sorting, Skewness and Kurtosis. Mean grain size is approximately $50\mu m$. Mean grain size and volume concentration over all size bins is observed to increase after day 28, as spring tides begin to wane. A semi-diurnal tidal variation of mean grain size is evident. Separating the fine and coarse fractions at $63\mu m$, the volume concentrations of the two size fractions suggest differing origins (Fig. 3.8). Both fractions indicate increasing concentrations associated with decreasing transmissivity, salinity and temperature, and the south-westwards current as observed by other sensors. However, the semi-diurnal tidal variability is more strongly apparent in the coarse fraction than the fine. Rising tides, with increased currents towards the west-south-west are correlated with periods of decreased coarse fraction volume concentrations. Falling tides, with increased currents to the east-north-east are correlated with periods of greater coarse fraction volume concentrations. Currents are generally greater on the rising tide.

Computation of the sediment flux over the period of BRUCE deployment displays little variation between the two size fractions. The mean sediment flux of the fine fraction is 0.112 $\mu l/lms^{-1}$ directed towards $242.2°T$. The respective flux of the coarse fraction is 0.045 $\mu l/lms^{-1}$ towards $201°T$.

Bed Shear Stress The ADV resolves currents in the E, N and up directions. Resolving the vertical component of velocity allows the computation of bed shear stress due to turbulence in the water column, without the assumption of the quadratic stress 'drag' law, i.e., (Gill, 1982):

$$\tau = \rho \left| u_b' w' \right| \tag{3.18}$$

can be used without the assumption of any drag coefficient C_D in

$$\tau = \rho C_D \overline{u_b}^2 \tag{3.19}$$

where $u_b = \overline{u_b} + u_b'$ is the current velocity at the sea bed, made up of a mean component from each burst $\overline{u_b}$, and a perturbed component u_b', and w' is a perturbed component from the mean vertical velocity near the sea-bed. Figure 3.9a shows the bed shear stress from equation 3.18, and Figure 3.9b shows the bed shear stress using the assumed drag law.

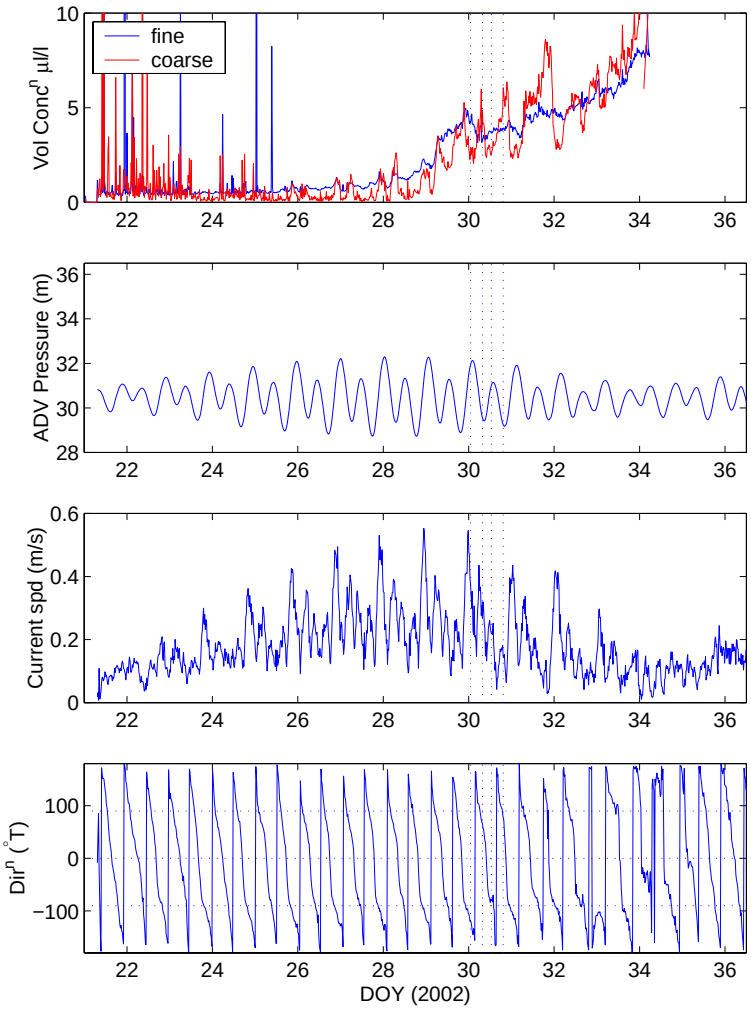

Figure 3.8: Separation of the grain size spectra into fines ($< 63\mu m$) and coarse fraction ($> 63\mu m$) for the BRUCE deployment period, and the relationship to tides. (a) Volume concentration of the two size fractions. (b) The Pressure measured by the ADV, representing sea surface elevation. (c) The current speed, and (d) the current direction. The four vertical dotted lines are placed at 6 hour intervals to represent periods of maximum velocities associated with rising and falling tides respectively.

The drag law bed shear stress indicates maximum bed shear stresses are experienced during the period of strong spring tide currents, at a maximum of $\sim 1 Nm^{-2}$. The 'turbulent' bed shear stress, the better measure of shear stress experienced at the sea-bed, indicates that maximum bed shear stress, of magnitude $\sim 4 Nm^{-2}$ is experienced on approximately day 32. Increased winds ($\sim$ 25 knots) were experienced throughout days 31-33, suggesting that the increased turbulence derives from the transfer of momentum through the water column from the surface momentum flux, rather than tidal current friction in the bottom boundary layer.

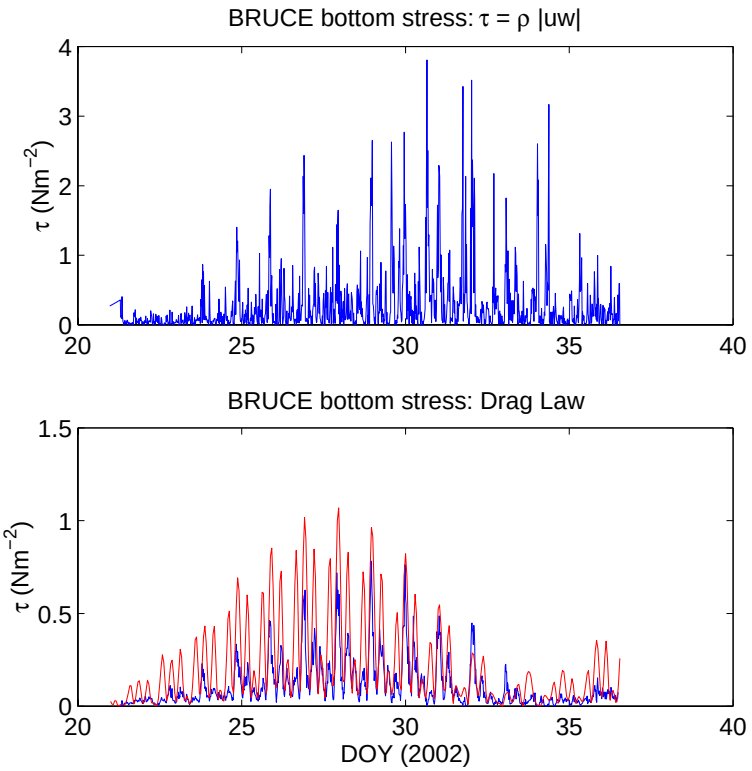

Figure 3.9: Bed Shear Stress computed for the BRUCE deployment period. (a) The bed shear stress computed using eqn. 3.18. (b) The bed shear stress computed using the assumed drag law using observed (blue line) and Modelled (red line) bottom currents.

Bedload Transport The Bagnold (1966) bedload equation evolves from the equation

$$q = k(\tau - \tau_{cr})u_{100}$$

where τ_{cr} is the critical shear stress required to initiate motion, τ is the shear stress at the site, U_{100} is the transporting current velocity measured 100 cm above the bed, as measured by the ADV, and k is an empirical constant dependent upon grain size. Hardisty (1983) reduced this equation, under the assumption of a quadratic stress 'drag' law to the form:

$$q = k_1(U_{100} - U_{100cr})^2 U_{100}$$

where U_{100cr} is the threshold speed at which bedload transport commences, and k_1 is an empirically derived coefficient, dependent only upon grain size:

$$k_1 = (6.6 \times D_{mm}^{1.23})^{-1} \times 10^{-5} g cm^{-4} s^2$$

in which D_{mm} is the sediment grain size in millimetres. k_1 and k are related by $k_1 = k\rho C_D$ under the drag law assumption. The threshold speed U_{100cr} was selected as $30cms^{-1}$ for inter-comparison to previous studies (Harris, 1993).

Bedload transport rates can be calculated with or without the drag law assumption. Bedload transport rates are estimated for the period that the LISST was recording. The bedload transport time series plot (Fig. 3.5d) indicates that the threshold speed of $30cms^{-1}$, corresponding to a 0.1 mm mean grain size, was generally exceeded only during the period of spring tides. Grain size statistics for the sediment grab taken from the sea-bed at the BRUCE deployment site were not available at the time of analysis, else a threshold speed based on the mean grain size of the grab would be quantitatively more useful.

Bedload transport estimates for the period of deployment are 0.015 g/cm/s at a bearing of $260.6°T$ (towards the SW). The influence of the wind driven event on the bed shear stress (Fig. 3.9) is minimal. The bedload transport estimate, assuming a drag law, for the period of deployment is 0.014 g/cm/s at a bearing of $259.6°T$. Harris (1993) made estimates of the bedload transport from the current meter data used for model comparison in Section 3.6.3. At the site closest to the BRUCE deployment, station 14 (referred to as Station 4 in Harris (1993)), the bedload transport, assuming a threshold speed of 30 cms^{-1}, is estimated to be 0.036 g/cm/s at a bearing of $276°T$.

Discussion The BRUCE current meter mooring shows a semi-diurnal, tide-dominated system. Bedload transport of sediments occurs only during the period of maximum tides, and always towards the south-west (on a rising tide).

A minor wind-driven effect is observed during the period of deployment. North-westerly monsoon winds appear to push cooler, fresher water of increased suspended sediment load, presumably from the Fly River Delta, toward and past the BRUCE deployment site. Cooler fresher waters are observed during periods of increased north-westerly winds, south-westwards currents, and increased turbidity/decreased transmissivity. Counteracting this effect however, falling tidal currents directed to the north-east appear to transport increased loads of coarser sediments past the probe.

The calculated turbulent bed shear stress indicates that the increase in wind strength on days 31-33 had a marked effect at the site, increasing the shear stress from $\sim 1Nm^{-2}$ due to tidal currents, to $\sim 4Nm^{-2}$. However, despite this increase in shear stress, the turbidity, transmissivity and grain-size distribution shows little evidence of local resuspension. Increase in turbidity is associated with a decrease in salinity and temperature, suggesting advection

Table 3.4: Model parameters for the Torres Strait sensitivity runs.

Run	*Resolution*	*Dimensions*	*QBFC*	V_{z0}	V_{z1}
R1	0.05	3	0.0033	0.0005	0.0625
R2	0.1	3	0.0033	0.0005	0.0625
R3	0.05	2	0.0033	0.0005	0.0625
R4	0.05	3	0.0015	0.0005	0.0625
R5	0.05	3	No Friction	0.0005	0.0625
R6	0.05	3	0.0033	0.001	NA
R7	0.05	3	0.0033	0.00001	0.0625
R8	As for R1, but forced with M_2 tide only				
R9	As for R1, but forced with 22 tide constituents				
R10	As for R1, but no non-linear tidal interactions				
R11	As for R1, but uses constant depth of 50 m.				
R12	As for R1, but forced at the eastern boundary only				

of a Fly River Delta water plume past the BRUCE deployment site near the end of the record as a delayed response to the wind event.

3.6 Model Verification

3.6.1 Model Sensitivity

A number of model runs with purely tidal forcing were carried out to investigate model sensitivity to various parameters - namely:

- Model Resolution (R1 & R2),
- 3rd Dimension (R1 & R3),
- Choice of friction parameter (R1, R4 & R5),
- Choice of mixing parameters (R1, R6 & R7),
- Number of forcing tidal constituents (R1, R8 & R9),
- Choice of non-linear momentum terms (R1 & R10),
- Bathymetry Effects (R1 & R11), and
- Investigation of the transmission of a tidal wave through Torres Strait (R1 & R12).

For this purpose, runs covered a 90 day period from 0000h on 01 January 1993 (corresponding to the 1993 field measurement period). The combinations of parameters are outlined in Table 3.4.

Tidal Elevations

Tidal Harmonic Constituent Comparisons Harmonic constants from the 17 sites listed in section 3.5.1 for which sea-level data were available, were compared with those obtained from a harmonic analysis of hourly time-series of surface elevation produced by the model for the model cells nearest to the respective observational sites.

Appendix A lists results from the harmonic analysis of the modelled tidal elevation at these 17 points, and the observed harmonic constants (taken from the Australian Hydrographic Office (1999)) for the 4 main constituents (M_2, S_2, K_1, O_1).

Values in Appendix A generally indicate a good agreement between modelled and observed tidal constituents on the eastern side of Torres Strait within the Gulf of Papua and on the Northern Great Barrier Reef. Within the Strait, agreement is not as good with Goods Island showing largest errors with a 56% overestimation of the M_2 tidal amplitude and a 60° difference in phase. Given that amplitude and phase of the M_2 tide differ by 25 cm. and 120° respectively through the $\sim$ 60 km of the Strait between Booby Island and East Strait Island, a large model error in this region is not entirely unexpected.

The general behaviour of the model is not sensitive to the choice of friction parameter or mixing coefficients - provided the Csanady mixing scheme is used in the model. Modelled tidal constituent values are generally insensitive to the inclusion of the non-linear momentum terms. However, their inclusion slightly alters the magnitude of the modelled M_2 constituent. Bathymetry and resolution effects are observed to be the dominant influence on model constituents. An interesting outcome results from R12, where forcing was applied at the eastern boundary only, where on the eastern side of the Strait, model to observation comparisons are similar to the results of R1. This strengthens the observations of Wolanski et al. (1988) that very little of the tidal wave energy propagates through Torres Strait from either side.

Time-Series Comparisons Time-series of model-computed tidal elevation for 90 days at the 17 ports were compared with the estimated values generated from their respective 9 constituents. The standard deviation between the 2 time series was determined for the period minus the first 3 days 'runup' period. Table 3.5 lists the standard deviation between modelled and 'observed' sea surface elevation for each run at each location.

Table 3.5 indicates similar agreements between modelled and observed sea surface elevations as observed in the comparisons of harmonic constituents (Appendix A). Standard deviation values are small in the Gulf of Papua and on the eastern side of Torres Strait. In

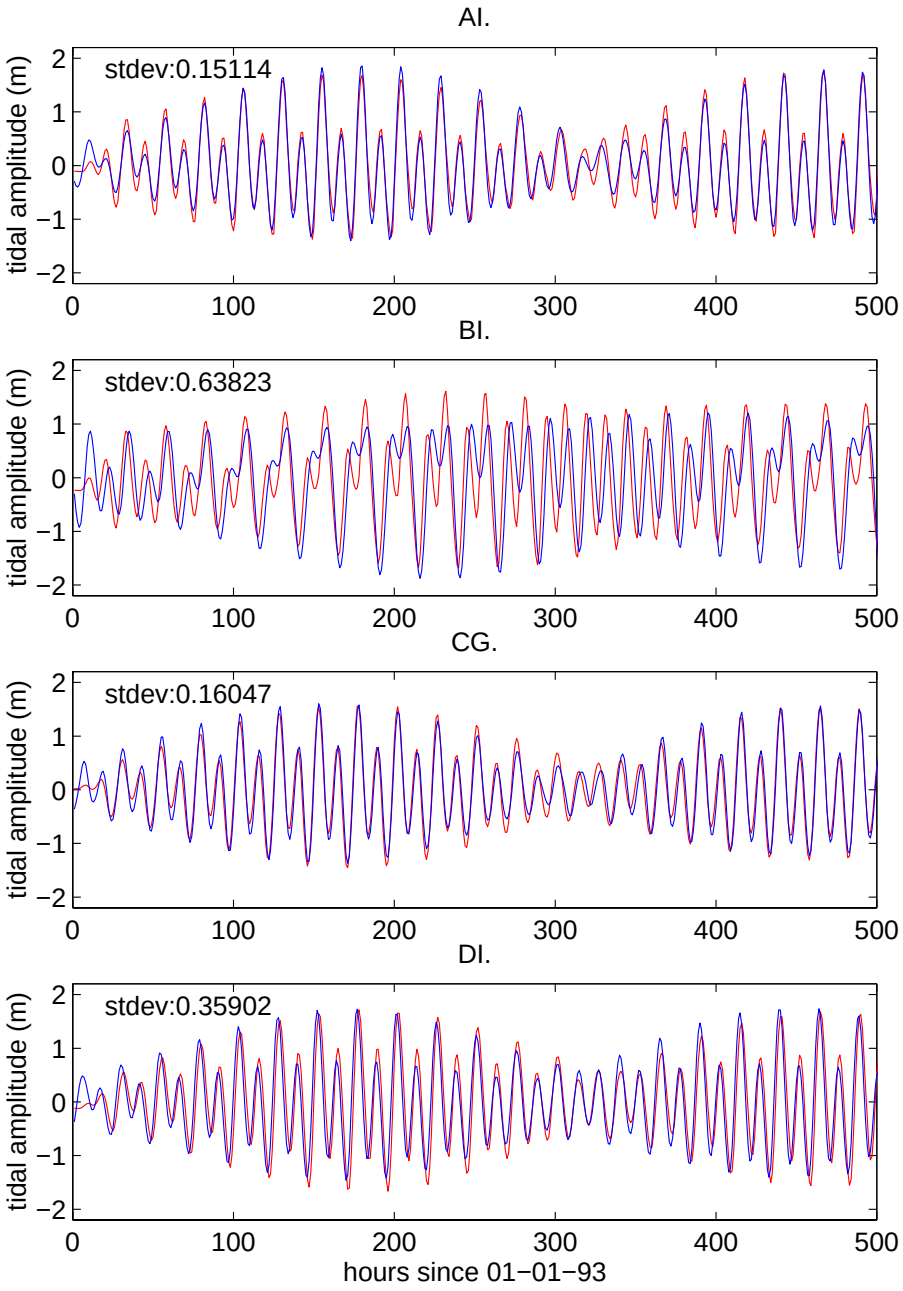

Figure 3.10: Time series comparisons of observed (blue line) and predicted (red line) tidal elevations at tidal stations in Torres Strait. Albany Island (AI), Booby Island (BI), Cape Grenville (CG), and Darnley Island (DI).

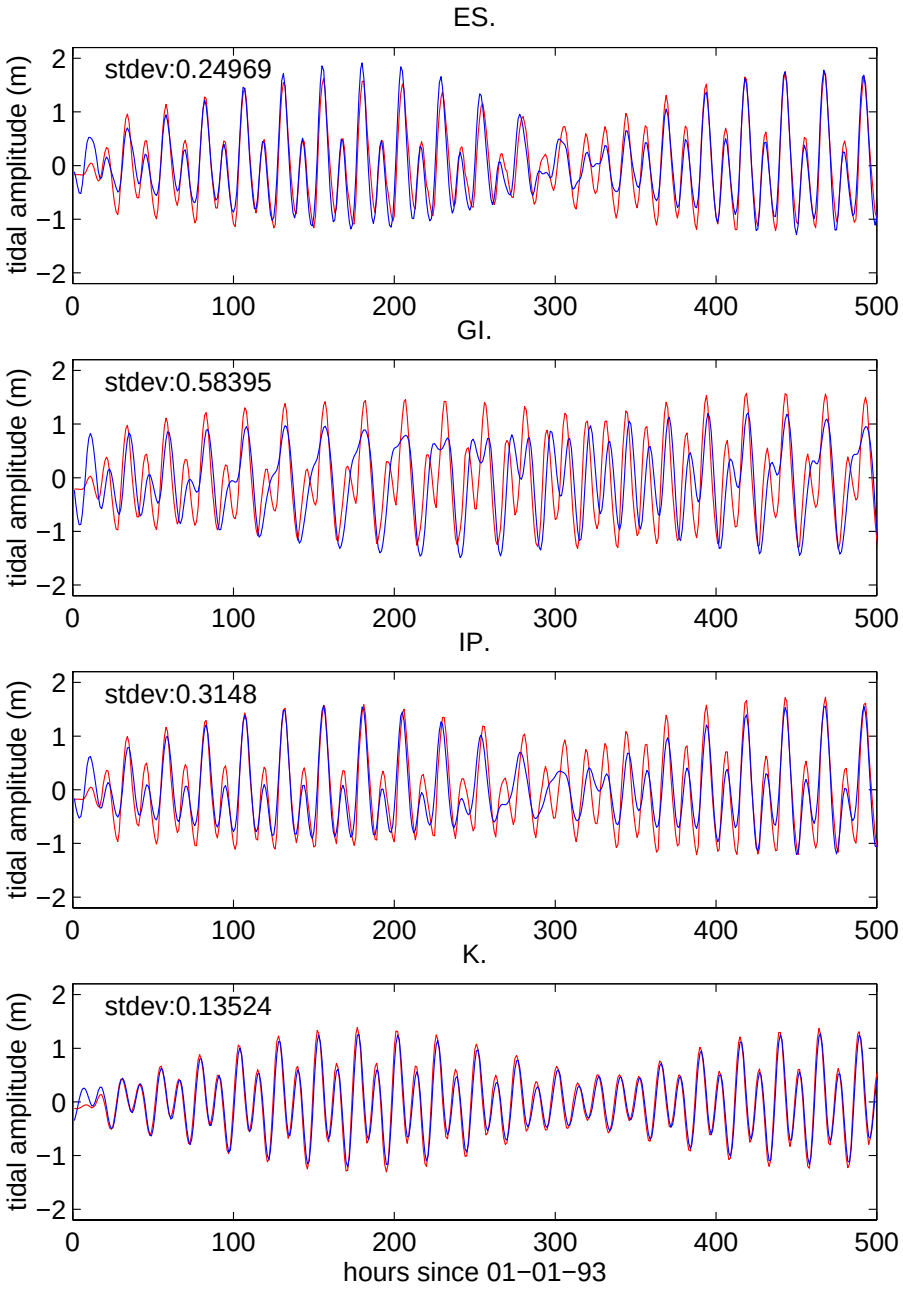

Figure 3.11: Time series comparisons of observed (blue line) and predicted (red line) tidal elevations at tidal stations in Torres Strait. East Strait Island (ES), Goods Island (GI), Ince Point (IP), and Kerema (K).

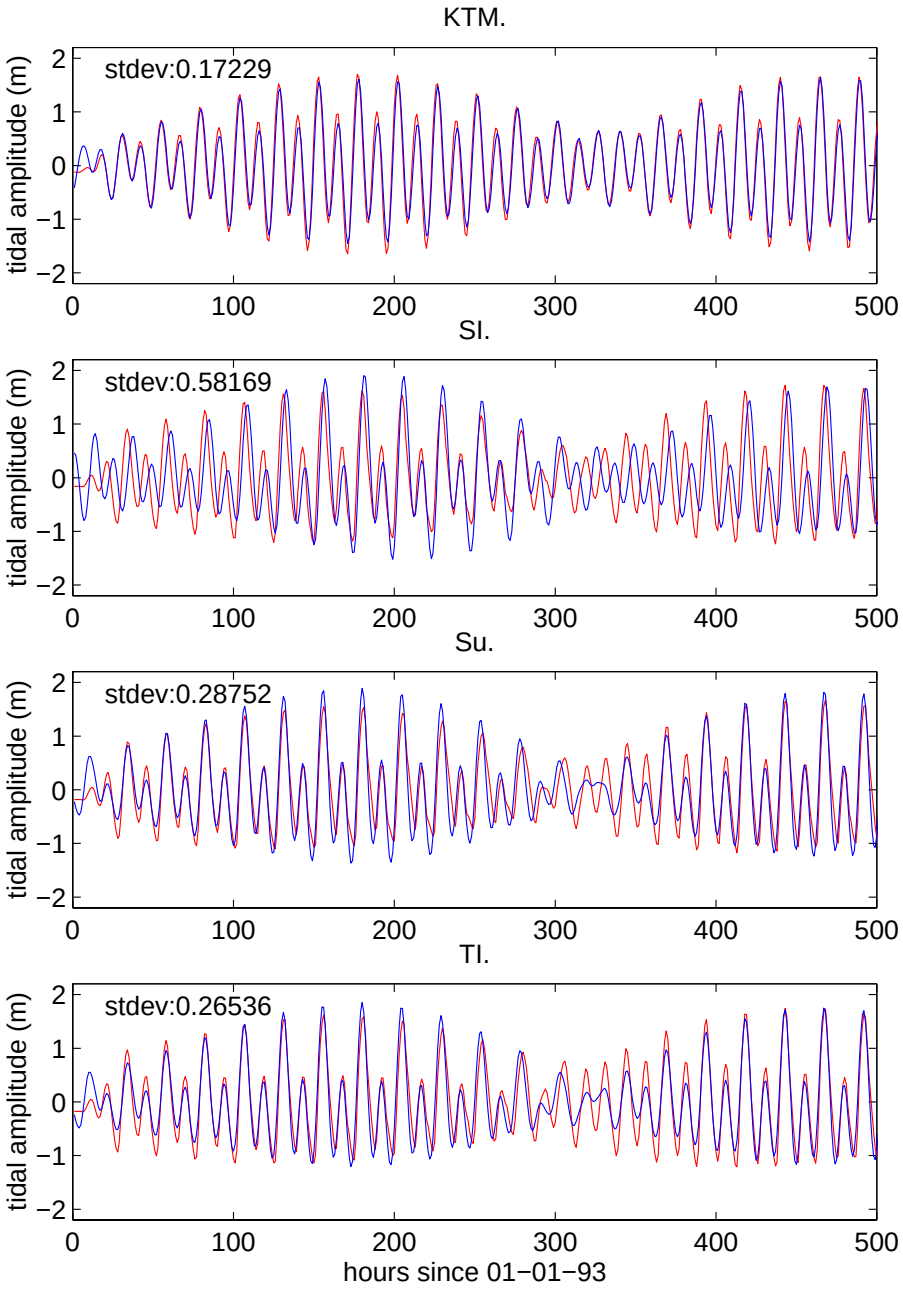

Figure 3.12: Time series comparisons of observed (blue line) and predicted (red line) tidal elevations at tidal stations in Torres Strait. Kumul Trk Mar (KTM), Saibai Island (SI), Suarji Island (Su), and Twin Island (TI).

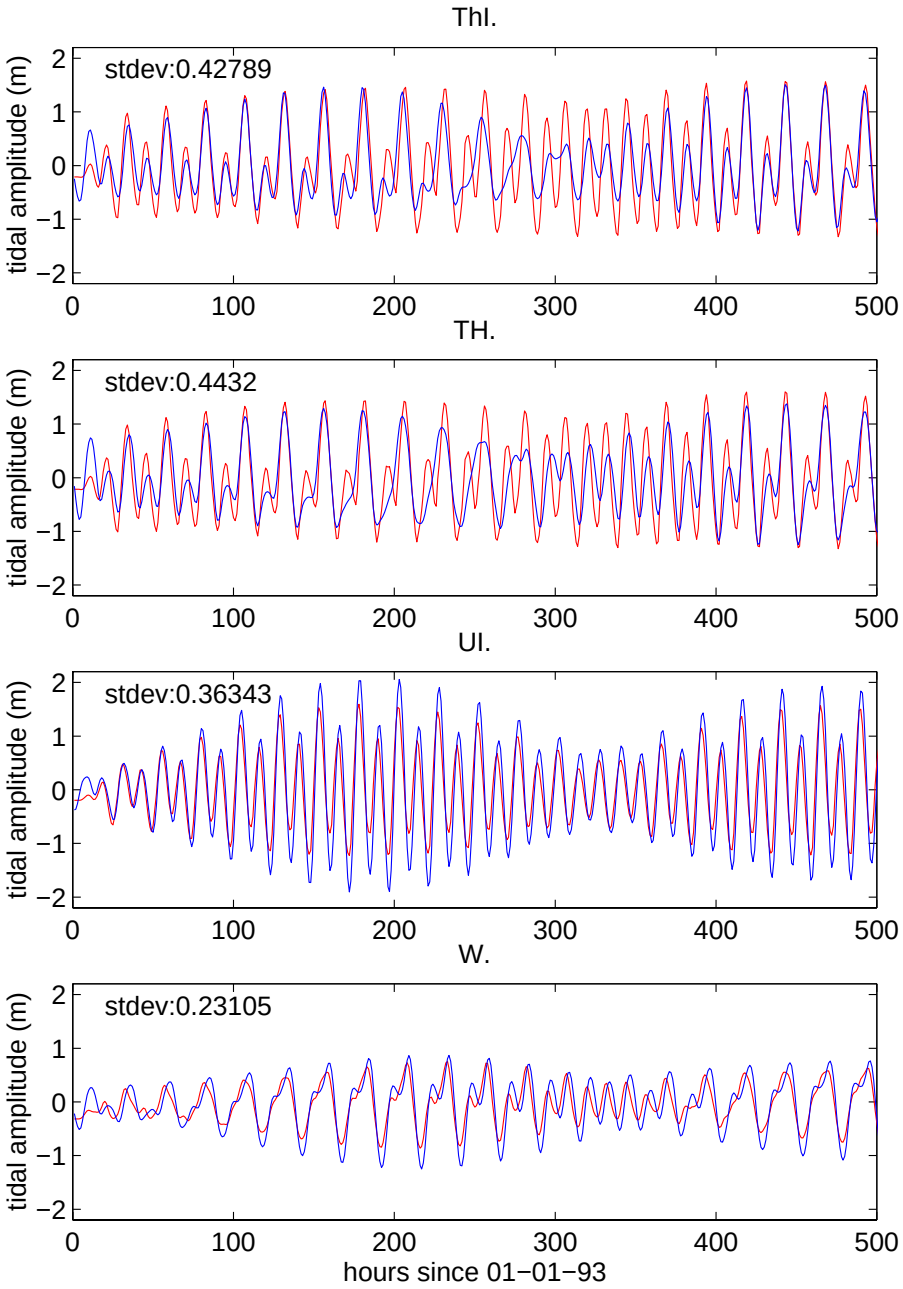

Figure 3.13: Time series comparisons of observed (blue line) and predicted (red line) tidal elevations at tidal stations in Torres Strait. Thursday Island (ThI), Turtle Head (TH), Umuda Island (UI), and Weipa (W).

Table 3.5: Standard deviation (m) between observed and modelled tidal sea surface elevations for tidal stations in Torres Strait, for each sensitivity model run. Details of each model run are listed in Table 3.4.

Stn.	R1	R2	R3	R4	R5	R7	R8	R10	R11	R12
AI.	0.151	0.238	0.175	0.151	0.303	0.151	0.531	0.158	0.486	0.211
BI.	0.638	0.694	0.586	0.639	0.793	0.641	0.730	0.648	0.949	0.789
CG.	0.161	0.250	0.146	0.161	0.187	0.161	0.452	0.156	0.158	0.159
DI.	0.359	0.442	0.361	0.357	0.354	0.359	0.498	0.353	1.320	0.364
ES.	0.250	0.277	0.267	0.249	0.298	0.250	0.578	0.266	0.562	0.302
GI.	0.584	0.645	0.531	0.585	0.730	0.586	0.690	0.600	0.906	0.750
IP.	0.315	0.344	0.289	0.315	0.398	0.317	0.561	0.329	0.580	0.402
K.	0.135	0.135	0.135	0.136	0.147	0.136	0.364	0.135	1.295	0.135
KTM.	0.172	0.183	0.166	0.177	0.202	0.172	0.431	0.175	1.707	0.169
PR.	0.330	0.330	0.328	0.331	0.336	0.330	0.478	0.330	0.352	0.508
SI.	0.582	0.661	0.537	0.583	0.783	0.583	0.737	0.571	0.808	0.627
Su.	0.288	0.250	0.315	0.286	0.389	0.287	0.582	0.294	0.610	0.284
TH.	0.443	0.463	0.398	0.443	0.537	0.445	0.624	0.467	0.732	0.553
TI.	0.265	0.275	0.278	0.264	0.331	0.266	0.559	0.276	0.552	0.285
ThI.	0.428	0.448	0.391	0.427	0.465	0.429	0.616	0.455	0.609	0.413
UI.	0.363	0.263	0.360	0.367	0.360	0.364	0.598	0.366	1.561	0.360
W.	0.231	0.214	0.232	0.231	0.243	0.231	0.426	0.228	0.255	0.469

the central part of the Strait, and on the western side, model to observation comparisons are poor. The largest standard deviation values are observed at Booby Island (SD = 0.6382 m), Goods Island (SD = 0.5840 m) and Saibai Island (SD = 0.5817 m). Standard Deviation values for the 2-D run (R3) at these three positions are slightly less - 0.5859, 0.5310 and 0.5373 m respectively. However, R3 has increased standard deviation values at various other positions. For tides, little difference in accuracy is expected between the 2-D and 3-D model runs, supported by these results.

Albany Island (AI) and Cape Grenville (CG) are observed to be the two most accurate stations. Standard deviation values at these points are 0.1511 and 0.1605 m respectively.

As per the harmonic constituent comparisons, bathymetry and resolution effects are clearly indicated to have the most dominant influence on model behaviour with effects due to mixing, friction and non-linearity having little effect.

Figures 3.10 - 3.13 overlay modelled (R1) sea-levels with generated observational data for 16 of the sites within the model domain. Differences between model and observations discussed at Goods Island, Booby Island and Saibai Island are clearly observed. Remaining station comparisons are quite good with an average standard deviation of approximately 0.25 m.

Scatter Plot Comparisons Scatter and regression analyses were carried out using the modelled sea-levels (R1) against the 'observed' data for the same tide gauge locations listed above (Figs. 3.14- 3.17). These plots give an overall indication of model performance with respect to predicting the total sea-level due to tides alone. A mis-match in amplitude is

Table 3.6: Slope (m) and Correlation Coefficient (R^2) of Observed vs. Modelled Tidal Sea Surface Elevations for Torres Strait points for each sensitivity model run. The details of each model run are given in Table 3.4.

	Slope, m									
Location	R1	R2	R3	R4	R5	R7	R8	R10	R11	R12
AI.	0.980	0.830	1.079	0.978	0.756	0.976	0.940	0.989	0.717	0.921
BI.	0.657	0.599	0.753	0.656	0.481	0.653	0.571	0.641	0.262	0.280
CG.	0.958	0.922	0.991	0.957	0.932	0.957	0.930	0.966	1.082	0.957
DI.	0.822	0.798	0.851	0.821	0.799	0.821	0.831	0.818	-0.273	0.825
ES.	0.920	0.804	1.034	0.918	0.749	0.916	0.797	0.894	0.591	0.906
GI.	0.615	0.544	0.714	0.614	0.453	0.612	0.478	0.591	0.237	0.179
IP.	0.769	0.711	0.877	0.768	0.629	0.765	0.587	0.746	0.509	0.751
K.	0.900	0.900	0.906	0.899	0.891	0.900	0.895	0.899	-0.222	0.901
KTM.	0.909	0.900	0.928	0.906	0.862	0.909	0.929	0.908	-0.205	0.913
PR.	0.919	0.919	0.927	0.918	0.900	0.919	0.670	0.916	0.864	1.163
SI.	0.698	0.559	0.829	0.694	0.419	0.694	0.383	0.707	0.387	0.626
Su.	0.993	0.884	1.115	0.992	0.729	0.988	1.049	0.973	0.565	0.997
TH.	0.661	0.632	0.752	0.661	0.547	0.658	0.442	0.631	0.372	0.650
TI.	0.897	0.795	1.008	0.896	0.721	0.893	0.830	0.876	0.589	0.912
ThI.	0.635	0.606	0.704	0.635	0.572	0.632	0.411	0.606	0.466	0.998
UI.	1.217	1.151	1.219	1.211	0.989	1.216	1.173	1.144	-0.010	1.228
W.	1.141	1.412	1.137	1.141	1.127	1.140	0.926	1.134	1.163	0.713
	Correlation Coefficient, R^2									
Location	R1	R2	R3	R4	R5	R7	R8	R10	R11	R12
AI.	0.951	0.919	0.939	0.951	0.894	0.951	0.392	0.946	0.581	0.911
BI.	0.438	0.388	0.477	0.437	0.315	0.436	0.248	0.434	0.073	0.007
CG.	0.935	0.849	0.945	0.935	0.914	0.935	0.475	0.938	0.941	0.936
DI.	0.761	0.643	0.745	0.765	0.782	0.761	0.491	0.773	0.131	0.751
ES.	0.863	0.881	0.837	0.864	0.896	0.863	0.245	0.849	0.524	0.798
GI.	0.431	0.387	0.465	0.430	0.336	0.430	0.150	0.423	0.083	0.011
IP.	0.787	0.797	0.776	0.787	0.838	0.787	0.190	0.780	0.506	0.603
K.	0.945	0.945	0.944	0.944	0.935	0.945	0.522	0.945	0.175	0.945
KTM.	0.944	0.941	0.945	0.941	0.935	0.944	0.598	0.943	0.160	0.946
PR.	0.582	0.582	0.588	0.580	0.570	0.582	0.151	0.582	0.534	0.001
SI.	0.408	0.370	0.449	0.406	0.228	0.407	0.046	0.430	0.191	0.346
Su.	0.825	0.886	0.799	0.827	0.788	0.826	0.282	0.817	0.515	0.830
TH.	0.614	0.623	0.628	0.614	0.625	0.614	0.145	0.595	0.266	0.208
TI.	0.845	0.885	0.818	0.846	0.871	0.845	0.273	0.837	0.547	0.815
ThI.	0.653	0.682	0.643	0.654	0.761	0.653	0.157	0.631	0.455	0.474
UI.	0.843	0.925	0.847	0.838	0.820	0.842	0.513	0.827	0.000	0.848
W.	0.769	0.871	0.768	0.769	0.742	0.769	0.178	0.775	0.719	0.000

given by a best-fit slope differing from 1. A slope greater than 1 indicates that the model underestimates the tidal elevation, whereas a slope less than 1 indicates an overestimation in sea surface elevation by the model. A mis-match in phase is given by a large spread of points about the best fit line and hence a reduced correlation coefficient (R^2).

Table 3.6 gives the slope (m) and correlation coefficient (R^2) for each run at each location.

Similar deductions of model performance may be derived from the scatter plot comparisons as for the time-series comparisons. Booby Island, Goods Island and Saibai Island show a large spread of points indicating differing phases between model and predictions. These 3 points have the lowest correlation coefficients (R^2) of 0.438, 0.431 and 0.408 respectively.

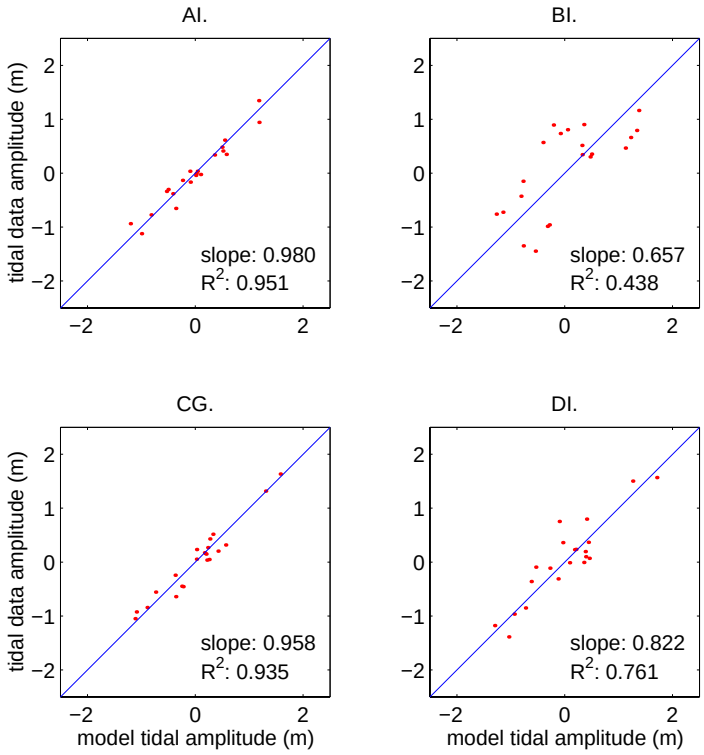

Figure 3.14: Scatter plot comparing modelled and observed tidal elevations at tidal stations in Torres Strait. Albany Island (AI), Booby Island (BI), Cape Grenville (CG), and Darnley Island (DI).

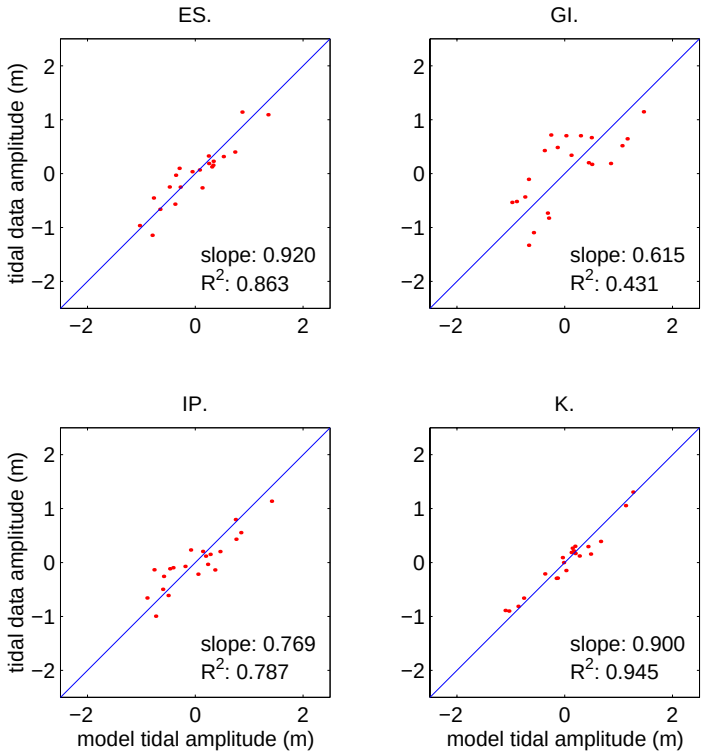

Figure 3.15: Scatter plot comparing modelled and observed tidal elevations at tidal stations in Torres Strait. East Strait Island (ES), Goods Island (GI), Ince Point (IP), and Kerema (K).

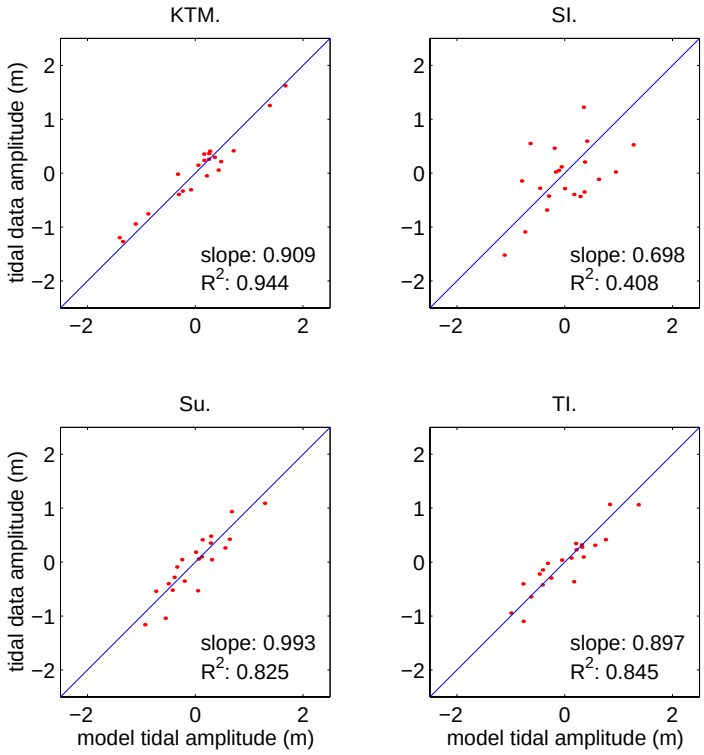

Figure 3.16: Scatter plot comparing modelled and observed tidal elevations at tidal stations in Torres Strait. Kumul Trk Mar (KTM), Saibai Island (SI), Suarji Island (Su), and Twin Island (TI).

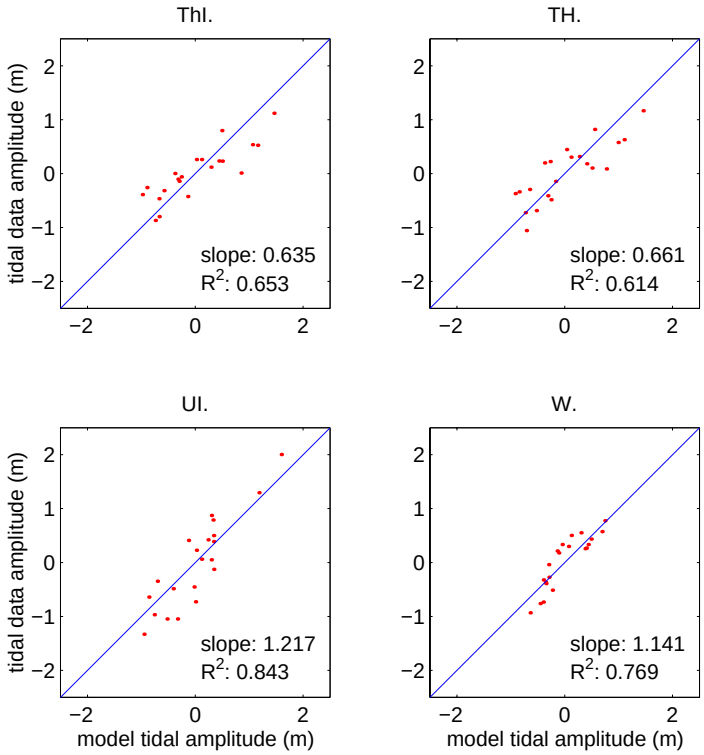

Figure 3.17: Scatter plot comparing modelled and observed tidal elevations at tidal stations in Torres Strait. Thursday Island (ThI), Turtle Head (TH), Umuda Island (UI), and Weipa (W).

Scatter plots generally show good agreement between model and observations, although a slight over-estimation by the model is observed. On each plot, a line of unity slope is drawn through the origin for reference, and each plot shows a general trend about this line. Calculated 'best fit' slopes indicate otherwise, with slopes ranging from 0.61526 at Goods Island to 1.2171 at Umuda Island. Generally slopes are less than 1, suggesting an overestimation of the Sea Surface Elevation by the model. Exceptions to this are Weipa (slope = 1.1408), just inside the western boundary and Umuda Island on the eastern side of Torres Strait. Andrewartha and Walker (1999) used MECO to model the Australian North-West Shelf. R^2 values range from 0.899 to 1, and slope from 0.939 to 1.2 in their study, however the bathymetry of the North-West Shelf is not nearly as complex as the Torres Strait environment. Bode and Mason (1994) display *rms* errors between modelled and observed tidal elevations of between 0.04 and 0.5 m in their model of the Torres Strait tides.

3.6.2 Forcing Analysis

This section describes the results of nine model runs carried out to determine the relative importance of the various forcing variables. A reference model run was set up with all forcing - tidal sea surface elevations at the open boundary, wind and pressure forcing at the surface, and a density distribution throughout the 3-D model domain. Subsequent model runs were performed which were forced with combinations of each of the four variables, and are outlined here : -

- F1 : Tidal, Wind, Atmospheric Pressure and Density forcing
- F2 : Tidal, Wind and Atmospheric Pressure forcing
- F3 : Tidal forcing only
- F4 : Wind forcing only
- F5 : Atmospheric Pressure forcing only
- F6 : Atmospheric forcing (Wind + Pressure)
- F7 : Density forcing only

To give some representation of the relative current magnitudes given from each forcing constituent, the maximum current velocities given by the 1993 current meters (Section

Table 3.7: Maximum currents (speed and direction) for model runs with different forcing mechanisms, as outlined in the text.

Maximum Current Speed (cms^{-1})								
Station	Measured	F1	F2	F3	F4	F5	F6	F7
12	59.04	54.61	51.14	47.35	31.28	5.42	31.72	23.61
13	42.07	50.41	44.45	40.36	27.44	7.77	26.70	11.21
14	47.01	33.06	87.46	33.42	24.34	9.33	24.72	31.54
16	44.20	62.09	58.52	56.25	36.56	10.83	35.97	28.84
17	73.48	110.15	109.99	82.15	35.83	18.80	32.34	18.08
19	58.32	60.96	91.46	91.97	28.62	10.17	30.49	19.28
20	86.20	67.64	98.43	97.50	78.14	20.90	78.90	43.63
Direction of Maximum Current ($^{\circ}T$)								
Station	Measured	F1	F2	F3	F4	F5	F6	F7
12	298	349	231	224	28	295	28	127
13	323	242	269	99	95	97	95	211
14	280	345	64	16	57	342	55	139
16	60	342	201	19	5	293	5	150
17	35	163	31	192	9	279	360	137
19	71	143	193	193	332	286	329	169
20	261	149	16	17	17	9	16	69

3.6.3), and for each forcing test have been tabulated (Table 3.7). Note that only the maximum current speeds are shown, and they do not necessarily correspond in time.

From this analysis, it is clear that tides provide the main forcing for maximum tidal currents in the model domain. Following tides, wind forcing is the next dominant mechanism for generating maximum currents in the region. Currents generated by spatial and temporal variations in atmospheric pressure are minimal.

Model runs carried out with a spatial and temporally variable density field, sourced from CARS, suffered instabilities after approximately 40 days. These instabilities all occurred at 1 of 2 places, either at the submarine channels to the east of Port Moresby on the shelf edge, or the steep shelf edge located offshore from the Warrior Reefs. No reasonable alterations of bathymetry could overcome these instabilities, and as a result a temporally uniform density field representing dominant density driven flows was used. Currents driven by spatial variations of density in the model domain are approximately 50% of the magnitude of the wind generated currents. Given that the spatial variation of density has a relatively small impact on the currents, it was considered that temporal variations of density could safely be ignored for the purpose of identifying dominant sediment transport mechanisms in the region.

At each station, tidal forcing counts for greater than 75% of the maximum currents. Wind forcing counts for another large portion of the maximum current. Given that the wind

forcing changes direction seasonally, the wind-generated residual currents are likely to be a major force in sediment transport pathways and their variability.

It is little wonder that the flows are not linear, i.e., the separate flow vectors due to tides, wind, atmospheric pressure and density sum to a greater current velocity than the model flow with all four forcing mechanisms considered.

No single dominant forcing mechanism of current direction can be deduced from the model results.

3.6.3 Comparison of Model with Observations

Previously Collected Current Meter Data

Model performance was assessed against observed currents by four methods. (1.) A direct time series comparison of modelled and measured currents; (2.) Both modelled and measured currents were passed through a 40hr low pass frequency filter, and time series of low frequency modelled and measured currents were compared; (3.) A spectral analysis of modelled and measured currents (Emery and Thomson, 1998, pages 427–432)) was carried out, comparing the two-sided power spectral densities, the coherence, the gain and the phase; and (4.) Tidal ellipses were determined for the four main constituents for both modelled and measured currents for comparison. Figures B.1- B.10 display the overlain time series of modelled and measured currents. In all time series plots, directions are those to which the current is heading, in degrees from geographical North.

Mean currents were subtracted from each dataset before carrying out the spectral analysis. These are tabulated in Table 3.9.

Regression statistics for modelled v. observed currents at all current meter stations are listed in Table 3.8. The predicted currents are generally analogous to those observed at stations 5, 13, 14, 16, 19 and 20 with R^2 values ranging from $0.3 - 0.7$, and slopes ranging from $0.3 - 1.8$.

Hydrodynamic model performance for currents in stations 6, 7, 12 and 17 is poorer, with R^2 values ranging from near zero to 0.2. It is evident that some processes within the Strait are poorly represented in the model, and the most likely candidates are rapid changes in tidal constituents across the Strait that are due to complex topography not being represented in the bathymetric model. Previous modelling of the tidal current regime of the region (Bode and Mason, 1994) consisted of an involved sub-grid scale parameterisation of reef porosities.

Possible errors may exist in the current meter data. Many of the current meters had

Table 3.8: Linear regression slope and R^2 values for modelled v. observed low pass filtered currents. Values quoted for east component and north component (in brackets). CM is Current Meter, and ** indicates that a mismatch in model depth and real depth exists.

Site	Water Depth (m)	CM Height (m)	n	slope	R^2
Stn 5	7	31**	6802	1.60 (0.14)	0.64 (0.44)
Stn 6	25	4	4153	1.15 (0.60)	0.09 (0.07)
Stn 7	26	7	5659	0.03 (0.23)	0.17 (0.05)
Stn 12	31	10	5174	0.29 (1.21)	0.18 (0.48)
Stn 13	27	5	5173	0.79 (1.80)	0.66 (0.24)
Stn 14	24	4	5013	0.15 (1.58)	0.44 (0.45)
Stn 16	31	6	5000	0.46 (1.60)	0.49 (0.56)
Stn 17	19	4	4790	0.37 (0.067)	0.012 (0.09)
Stn 19	23	6	4790	0.24 (0.84)	0.50 (0.37)
Stn 20	16	5	4871	0.08 (1.72)	0.24 (0.66)
BRUCE	30	1	1122	0.63 (0.63)	0.89 (0.56)

problems of marine fouling (Harris, 1993), and hence are capable of reducing the observed current signal.

A description of the comparison for each current meter is given in Appendix B.

New Current Meter Data

A comparison model run was set up for validation of the model against the BRUCE dataset. The model was run for 90 days beginning on the 01-Jan-2002. Inputs were generally similar to the model runs discussed above, however some alterations were required.

The effects of atmospheric pressure have been ignored for comparison to the BRUCE dataset. Section 3.6.2 has shown that currents generated by variations in atmospheric pressure are small in comparison to those generated by the wind and tides.

Wind speed and direction were available from the Ships log only for the period of observation. The model run has assumed a spatially uniform, temporally varying wind field matching that recorded from the RV *Franklin* Ship log. The voyage began in Brisbane, thus the first 7 days of Ship log winds are not representative of Torres Strait conditions, although they are still used for model forcing.

The same annual mean density (Temperature and Salinity) fields have been assigned as for the previous runs.

Open boundary forcing was designated in the same manner described above, calculating tidal sea levels for the period 010102 - 310302. Comparisons to the BRUCE dataset are given below.

Table 3.9: Measured and Modelled mean East and North current components, mean magnitude and direction for each station

Station		E (m/s)	N (m/s)	magnitude (m/s)	direction ($^\circ N$)
Stn 5	Measured	0.020	-0.237	0.238	175
	Modelled	0.252	-0.223	0.337	132
Stn 6	Measured	0.187	-0.239	0.303	142
	Modelled	0.216	-0.338	0.401	147
Stn 7	Measured	-0.077	-0.221	0.234	199
	Modelled	-0.012	-0.240	0.241	183
Stn 12	Measured	-0.107	-0.0033	0.107	182
	Modelled	-0.095	0.053	0.109	151
Stn 13	Measured	-0.068	-0.108	0.128	212
	Modelled	0.0079	-0.095	0.096	175
Stn 14	Measured	-0.028	-0.106	0.109	195
	Modelled	-0.079	0.020	0.082	285
Stn 16	Measured	-0.128	0.007	0.129	273
	Modelled	-0.093	0.076	0.120	309
Stn 17	Measured	-0.191	-0.097	0.214	243
	Modelled	-0.312	0.031	0.313	276
Stn 19	Measured	-0.162	0.079	0.180	297
	Modelled	-0.339	0.152	0.371	295
Stn 20	Measured	-0.228	0.077	0.240	289
	Modelled	-0.227	0.268	0.352	320
BRUCE	Measured	-0.0247	-0.0043	0.0251	260
	Modelled	-0.0138	-0.008	0.0157	239

Sea-Level Figure 3.5a overlays time series plots of model sea surface elevation and the BRUCE CTD pressure record (referenced about the mean) at the site. The 14 day record is not sufficient to suitably compare tide constituents from the mooring, however a standard deviation between the two time series of 0.3383m indicates comparison in line with the other stations in the model domain. A scatter plot and regression analysis was also carried out, comparing model output with the observed sea level. The correlation coefficient value (R^2) of 0.90 suggests relatively good comparison. The slope of 0.93 suggests that the model slightly over-estimates the tidal range in the sea-surface elevation record. The model appears capable of predicting tidal elevations at the BRUCE site to a good level of accuracy.

Currents Figure 3.6 overlays time series of the BRUCE data currents and the model derived currents from the BRUCE site.

There is good agreement between model and observations. The model slightly over-estimates current speeds, however comparison of phase and direction are very good.

Correlation between the N-S component of model and data ($R^2 = 0.561$) is not as good as the correlation between the E-W components ($R^2 = 0.889$). The model overestimates velocities in both the N-S and E-W directions, with the regression line slopes of 0.627 and

0.626 respectively. The anticlockwise rotation of the main tidal constituents is reproduced.

The sub-tidal currents are also well reproduced by the model (Table 3.9). The assumption of ship log winds as representative of the entire model domain gives wind driven currents comparable to those measured in the field. The mean current to the south-west during deployment is slightly underestimated, however the mean direction is well represented.

The increase in north-westerly winds on days 31-33, results in the advection of the Fly River plume past the BRUCE site in the model results (c.f. Tracer studies, section 4.2) increasing tracer concentrations, analagous to the increase in volume concentration observed from the LISST. Model tracer concentrations increase by a factor of ~ 10, LISST volume concentrations increase by a factor of ~ 15, during the period. This appears to reflect the underestimated value of the south-west mean current by the model.

Bed shear stress comparisons between the model and observations (Fig. 3.9) show a similar response to the tidal currents. Maximum low frequency currents of $\sim 8 cms^{-1}$, are negligible opposed to maximum tidal currents of $\sim 65 cms^{-1}$.

3.7 Summary

The three-dimensional, hydrodynamic, numerical ocean model, MECO, has been applied to the Torres Strait and Gulf of Papua region and forced with tidal, meteorological, and mean density, data within the model domain. Comparisons between the MECO model results to sea-level and current meter observations indicate good agreement. To precisely predict sea-level and currents in the region, some changes to the model may be required. For example, complex bathymetry in the model domain is poorly resolved by the model grid. More accurate bathymetry used in the model is likely to significantly improve model predictions. Errors in the atmospheric NCEP wind and pressure data may also be a source of error in the model. Trial of other atmospheric forcing data-sets, such as COADS (Woodruff et al., 1993) or ECMWF, may provide more accurate model estimates in the future. Another source of possible error in the model is the interpolation of sea-level along the open boundaries. Satellite altimetry provides more regular spatial estimates of sea-level near the open boundary. However, the accuracy of satellite altimetry derived sea-level in a shallow water region such as Torres Strait is not good. Similarly, global tide models have large errors in these shallow areas. Additional tide gauges along the open boundaries of the model grid seems to be the best method for determining better estimates of sea-level on the model boundaries.

However, the aim of the modelling work presented in this Chapter is not to accurately

predict currents, or sea-level, in the Torres Strait and Gulf of Papua region, but to identify the ocean processes which dominate sedimentation on the continental shelf there. The model predicts currents and sea-levels which coincide in magnitude and direction with those observed, and therefore the model is a useful tool for recognising the important oceanic influences in the region. These are addressed in the next chapter.

Chapter 4

Torres Strait Sedimentation Studies

The application of sedimentary research lies in predicting the dispersal of contaminants and their effect on water quality and the biological communities, on siltation of harbours and navigational channels, on coastal construction (e.g., of tidal barrages), and on coast protection (Dyer, 1989). The Fly Delta has significant impact on the continental shelf and oceanic waters as a result of the exchange of water, and sediment between the delta and the coastal sea (Harris et al., 1993). The aim of this chapter is to investigate sediment transport pathways from regions of increased sediment load through the use of the hydrodynamic model, and to assess the influence of seasonal wind variability on both the sediment dispersal, and the relative influence of dominant processes, including tidal and wind-driven currents and surface gravity waves.

4.1 Steady Current Induced Bed Shear Stresses and Bedload Transport Pathways

Bottom currents were output from the MECO model, taken as the currents at mid-depth of the bottom layer of the model. A current-induced, bed shear stress τ_{bc} was computed from the friction velocity, determined using the Von Karman - Prandtl equation:

$$\frac{u_c}{u*_c} = \frac{1}{\kappa} ln(\frac{z}{z_0})$$

where u_c is the current speed at depth z above the sea-bed, $u*_c$ is the current induced friction velocity, κ is Von Karman's constant ($\kappa = 0.41$), z_0 is the roughness length, $z_0 = k_{bc}/30$, where k_{bc} is the sand grain roughness or grain size. The current-induced bed shear stress

can then be determined as $\tau_{bc} = \rho u*_c^2$.

However, the mid-layer depth of the bottom layer of the model, z, in some cases, was up to $300m$ above the sea-bed, suggesting a large boundary layer, and in other grid cells was just $1\frac{1}{2}m$ thick. This led to variable bed shear stresses, and as a result, the level z, was assigned uniform $3.5m$ throughout the model domain..

Maximum current induced bed shear stress vectors were computed from the maximum current from each grid point during each model run, and averaged for each season from the 90 day model runs. NW Monsoon seasonal averages were taken from five 90 day model runs, each beginning on the 1st January for years 1990-1994 inclusive, and the SE Trades seasonal averages from five 90 day model runs, beginning on the 1st April for years 1990-1994 inclusive. Maps of seasonally averaged maximum current-induced bed shear stress vectors are displayed in Figure 4.1. The seasonal winds of the region are known for their regularity. This led to only small variation between the 5 model runs for each season, and therefore, the 5 year average was considered sufficient to capture the seasonality.

During the NW monsoon, Figure 4.1, regions of maximum bed shear stress coincide closely with those predicted by Harris (1994b) from the facies model in areas between the Warrior Reefs, and in passages amongst the Torres Strait Islands. An additional region of high bed shear stress is found along the northern extent of the Great Barrier Reef where bed stress magnitudes are as large as $3Nm^{-2}$. The maximum bed stress vectors indicate regions of bedload parting (BLP) diverging from a region of maximum bed shear stress (in western Torres Strait, and between the Torres Strait Islands and Warrior Reefs). However the Northern Great Barrier Reef region appears to be a region of converging bed stresses suggesting this may be an area of high deposition. A westward trend is observed throughout the region.

The maximum bed shear stress during the trades (Fig. 4.1) indicates a similar situation to the monsoon. One zone observed to have changed direction seasonally is the Adolphus Channel at the northern tip of Cape York. This seasonal reversal has been previously observed from reversing bedform direction (Harris, 1989). The other main area is in the shallow waters to the west of Cape York. The greatest seasonal variation is observed at the far east of the model domain, adjacent to Port Moresby. These large vectors are likely to be a result of direct boundary forcing, magnified due to the narrow shelf in the area. However, the seasonal dependence is probable. The strong persistent westward bed stress vectors to the northwest of the Strait reflect the large sandwaves observed in this area by Harris (1991). Areas of decreasing bed stress magnitude suggest sediment depocentres, and

the location of these correspond to those listed by Harris (1988) as: (1) the Endeavour Strait tidal delta; (2) the Turnagain Island region; and (3) a small area in the Eastern Patch Reefs is suggested.

Maximum stress magnitudes and directions differ only slightly between the trade and monsoon seasons. Shelf bottom stress magnitudes of approximately $2Nm^{-2}$ are observed during each season. The similarities between seasons suggest that maximum bottom stress vectors are a result of tidal forcing, and not the prevailing wind conditions.

4.2 Tracer studies of Sediment Dispersal

Ocean currents and sediment dispersal were simulated for 90 days from the 1st of January (representing the Monsoon), and for 90 days from the 1st of April (representing the Trades) for years 1990-1994 and averaged. The model parameters chosen for these simulations were the same as for the model-observation runs described above. These runs allow for comparisons of sediment transport pathways on a seasonal basis. Sediment was input in two areas, one to represent the Northern Great Barrier Reef (NGBR) and one to represent the Fly River. The model allows sediment to leave the grid by settling and/or lateral transport, however no resuspension mechanism is included in the model.

4.2.1 Northern Great Barrier Reef Resuspension Event

The regions of maximum current-induced shear stress along the Northern Great Barrier Reef suggest that this may be a region of high sediment resuspension. Model runs were performed to simulate the dispersal pathways of the suspended calcareous muds derived from the breakdown of clastic carbonates along the Northern Great Barrier Reef and the accumulation/deposition zones resulting from a resuspension event in the region.

Sediment was introduced into the model as a passive tracer at position $9°30'S, 144°15'E$ at a depth of $1m$ above the seafloor to represent suspended sediment. The sediment was introduced 2 days after the start of the run to avoid model starting transients, and was continuous thereafter. The sediment for this application, to avoid immediate fallout, was assumed to have a settling velocity, s, of $-5 \times 10^{-4} ms^{-1}$ representing a medium silt (Dyer, 1986).

Sediment was added at a constant rate of $1m^3s^{-1}$, equivalent to an erosion rate of 1 mm/day, at a concentration of $0.1g/l$ representing a source of suspended calcareous sediment mobilised on the northern Great Barrier Reef shelf.

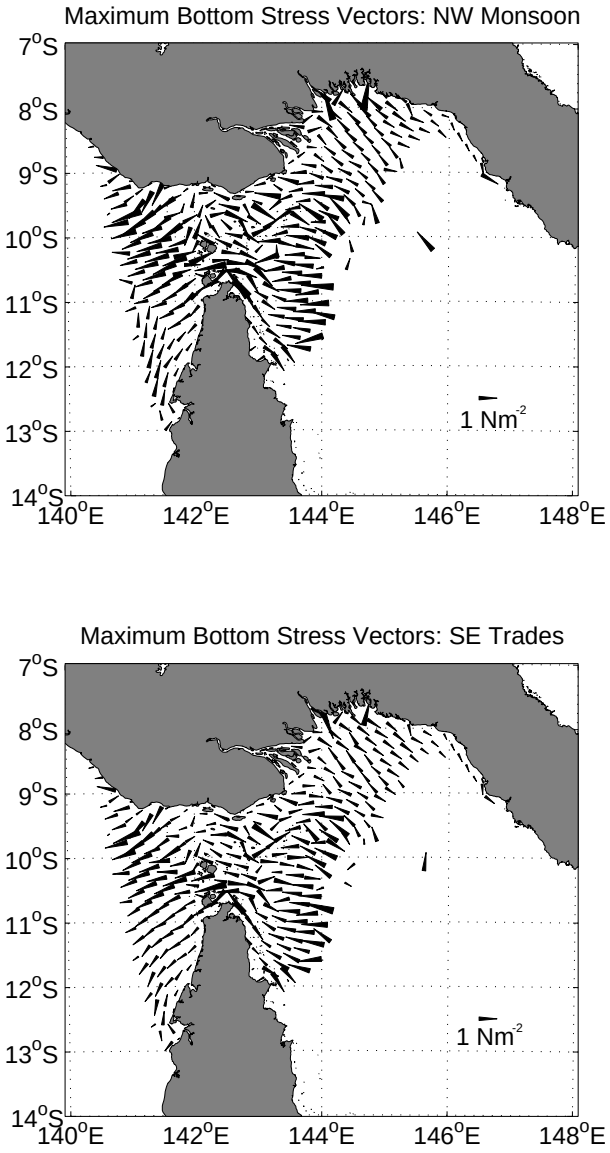

Figure 4.1: Predicted maximum current-induced bed stress vectors in Torres Strait and the Gulf of Papua during (a) the north-westerly Monsoon, and (b) the south-easterly Trades

The modelled, depth-integrated, suspended sediment concentrations for periods of 90 days after the sediment was initially introduced at the Northern Great Barrier Reef, averaged over the years 1990-1994, are shown in Figure 4.2. The mean depth averaged currents are also shown. The path of the suspended calcareous muds is highly dependent on residual currents, both tidal and wind driven.

The Northern Great Barrier Reef sediment plume indicates a reverse in direction seasonally as found by Wolanski et al. (1988) and suggested from bedforms (Harris, 1989). Monsoon conditions lead to a large component of sediment moving north-eastwards, along the south coast of Papua New Guinea. The suspended sediment plume is also observed to travel southwards past the eastern edge of Cape York, inside the Northern Great Barrier Reef. SE Trade conditions lead to a greater component of the plume moving directly offshore to be deposited in the Coral Sea, and extending into and through Torres Strait to the west.

4.2.2 The Fly River Sediment Outflow Plume

To simulate the dispersal of suspended terrigenous sediments derived from the Fly River, suspended sediments were introduced into the model at 2 locations at the front of the Fly River Delta. One in the southern channel, at position $8°45'S, 143°30'E$, and the other in the northern channel, at $8°15'S, 143°30'E$, at a height of 1 m above the seafloor (Fig. 4.2. The sediment was introduced to the model 2 days after the start of each run to avoid model starting transients, and was continuous thereafter. The sediment was assumed to be a coarse silt, with settling velocity, s, equal to $-0.00081 ms^{-1}$ (Dyer, 1986). Sediment was added at a rate of $1000 m^3 s^{-1}$ at a concentration of 0.5 g/l representing a source of suspended sediment of typical suspended sediment concentrations from the Fly River Delta(Alongi et al., 1992).

Contour plots of the modelled depth-integrated suspended sediment concentrations for periods of 90 days after the sediment was initially introduced for the Fly River plume, averaged over the years 1990-1994, along with the mean depth averaged currents, are shown in Figure 4.2. The direction of travel and shape of the suspended sediment dispersal pathway are determined by the wind-driven currents, with tidal currents having little net effect.

During the NW Monsoon (Jan-Mar), the sediment plume from the Fly River shows a generally eastward flow (Fig. 4.2). Very little of the sediment moves westwards along the south coast of New Guinea or south-westwards through Torres Strait. Some sediment diffuses into these regions, however concentrations are low. The upwind advective scheme implemented in MECO has a numerical diffusion rate of $\frac{1}{2}udx$. In the high speed currents modelled in Torres Strait, this numerical diffusion may sum to be a considerable input to

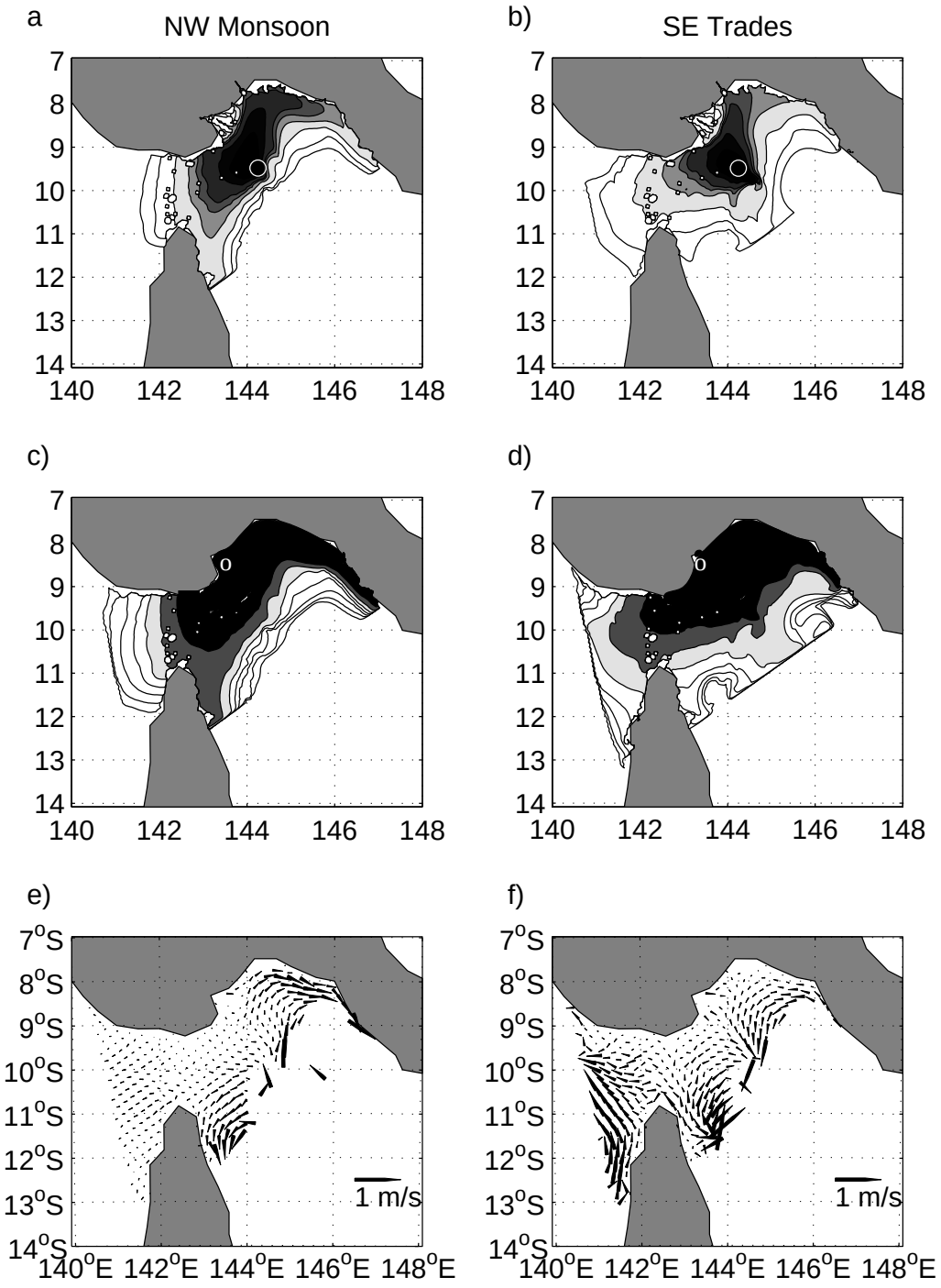

Figure 4.2: Modelled plumes, with mean depth integrated currents after 90 days, averaged from 1990-1994. a & b) Resultant plume from resuspension event on the Northern Great Barrier Reef during the a) Monsoon season, and b) Trades season; c & d) Resultant plume from Fly River suspended sediment during the c) Monsoon season, and d) Trades season; e & f) Mean depth-integrated currents during the e) Monsoon season, and f) Trades season. (o - marks position of introduced tracer. Monsoon tracers introduced on 1st January each year. Trades tracers introduced on the 1st April each model year). Contours in the plume plots are fractions of the initial concentration on a log_{10} scale, i.e., 1, 0.01, 0.001 and decrease in order of magnitude onwards.

tracer concentrations and may account for a large portion of the observed higher tracer concentrations to the east and south of the sediment source. The sediment plume from the Fly River moves in two dominant directions following the mean flow (Fig. 4.2e). Under the assumption that $\sim 50\%$ of the Fly River sediment is deposited directly offshore from the delta (Harris et al., 1993), 34% of the plume moves north-eastwards along the south coast of Papua New Guinea, and then southwards past Port Moresby (Fig. 4.2c). Another significant portion of the plume (10%) moves southwards to the east of Cape York, inside the Northern Great Barrier Reef. 3% of the plume heads westwards through Torres Strait, and the remaining 3% offshore to be deposited in the Coral Sea. The component of flow was computed as a mass fraction intercepting the given sector, equidistant from the sediment source.

During the SE Trades (Apr-Jun), the Fly River plume alters its path such that 24% of the sediment is distributed to the north-east along the south coast of Papua New Guinea, 13% directly offshore to the Coral Sea, and 11% westwards into, and through Torres Strait. The remaining 2% travels southwards on the eastern side of Cape York (Fig. 4.2d). Wolanski et al. (1984) analysed LANDSAT and Coastal Zone Colour Scanner imagery, and their modelled Trades plume indicate similar characteristics. The predicted sediment budget from this modelling study agrees qualitatively with the preliminary budget proposed by Harris et al. (1993), described in Section 2.2.5. However, a strong seasonal dependence is evident which was not apparent from the sediment facies models.

The period over which the trades dominate (Apr-Nov), is greater than the period over which the monsoon dominates (Dec-Mar). A greater component of the Fly River plume is predicted to head westwards through Torres Strait under trade wind conditions in the model. As to where this terrigenous sediment may be deposited is unknown, as the high carbonate content in Torres Strait (Harris, 1994b) suggests that Fly River sediments are not represented in the surficial sediments found in the Strait. The terrigenous muds may be transported through the Strait to the Gulf of Carpentaria before being deposited. Additional field data in the Gulf of Carpentaria is required to confirm this.

4.3 The Influence of Waves on Sediment Movement in Torres Strait

Considerable research has been carried out on the dynamics of marine bottom boundary layers due to the currents alone and waves alone. In more recent years, the interactions of

currents and waves have been considered (Smith, 1977; Grant and Madsen, 1979; Wiberg and Smith, 1993; Christofferson and Jonsson, 1985; Grant and Madsen, 1986; Mathisen and Madsen, 1993; Madsen, 1994; Lou and Ridd, 1996). The combined wave-current bottom boundary layer flow (refer Section 3.3.1) is discussed in this chapter.

The seasonal variation of wave activity in Torres Strait and the Gulf of Papua is a process of interest. In addition to the current movements discussed in Section 4.2, wave activity alone, and wave-current interactions, contribute significantly to the movement of sediment, particularly in the Gulf of Papua during the SE trade season as the long period swell generated in the Coral Sea travels into the Gulf and resuspends a large quantity of sediment. This seasonal variation due to waves has been identified by Harris et al. (1993) where seasonal sand-mud interbeds are observed in sediment cores. High wave activity during the trades suggests a winnowing out of the fine grained sediment, and minimal wave activity during the monsoon results in the deposition of a mud drape.

For sediment to be resuspended from the sea-bed, the bed shear stress must exceed some critical shear stress τ_{cr}, which is a function of grain size, density and shape, water density and viscosity and whether the sediment grains are cohesive or cemented. Here, τ_c is determined using the method outlined in Madsen and Grant (1976). Expressing the critical value of the Shield's parameter (a function of the Reynolds number) as:

$$\psi_{cr} = \frac{\tau_{cr}}{(s-1)\rho g D} = \frac{u*_{cr}^2}{(s-1)gD} = f(Re_*)$$

where $s = \rho_s/\rho$, to obtain the sediment-fluid parameter $S*$,

$$S* = \frac{D}{4\nu}\sqrt{(s-1)gD}$$

Then

$$\psi_{cr} = \begin{cases} 0.1S*^{-2/7} & S* < 0.8 \\ 0.06 & S* > 300 \end{cases}$$

For $0.8 < S* < 300$, ψ_{cr} is obtained from Figure 4.3. $u*_{cr}$ can then be solved given ψ_{cr}, allowing the critical shear stress τ_{cr} to be computed.

The model has been run for τ_{cr} values of 0.05, 0.27, and $1.25 Nm^{-2}$, the lower value indicative of very fine (0.01 mm) non-cohesive sediments, and the upper value indicative of coarser (2 mm) non-cohesive sediment, or fine cohesive sediments with a medium to

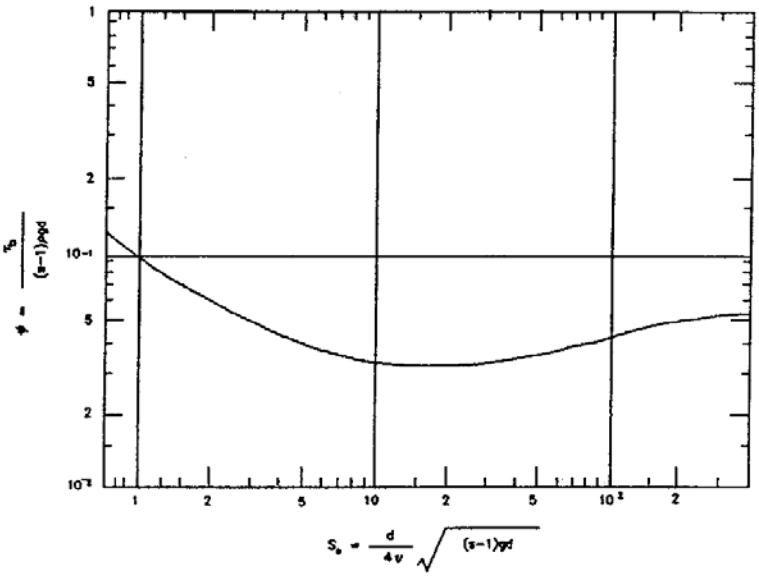

Figure 4.3: Modified Shields Diagram (from Madsen and Grant (1976))

large bulk density (Madsen and Grant, 1976; Mitchener and Torfs, 1996). However, it is easiest to consider the increase in critical shear stress as representative of an increase in the size of cohesionless grains. The shear stress as a result of currents, waves, and combined wave-current flows was then determined.

The determination of current induced shear stress has already been discussed in the previous section. τ_c was determined from the Monsoon series of runs, and the Trades series of runs for the entire period at each 3 hourly output time step.

Significant wave height, H_s, mean wave period, T_m and mean wave direction, ϕ_w were obtained from the Bureau of Meteorology WAM runs for a 12 month period at 6 hourly intervals. Using linear wave theory, maximum bottom wave orbital velocities $u_{b,max}$, due to the swell were estimated using the equation (LeBlond and Mysak, 1978):

$$u_{b,max} = \frac{\pi H_s}{T_m sinh(kh)}$$

in which h is water depth, and k is the wavenumber of the swell, which may be estimated from the approximate formula (Fenton, 1990)

$$k \approx \frac{4\pi^2}{gT_m^2}(coth(\frac{2\pi}{T_m}\sqrt{\frac{h}{g}})^{\frac{3}{2}})^{\frac{2}{3}}$$

in which g is the acceleration due to gravity.

Wave-induced bottom shear stress is calculated using equations of Jonsson (1966) of:

$$\tau_w = \rho C_{Dw} u_{b,max}^2$$

τ_w was determined at 6 hourly intervals for the period of January-June of the available wave data. Jonsson (1966) uses a value of the wave friction coefficient, C_{Dw}, of 0.0033.

Wave current interactions have also been considered. Wave data was interpolated onto the model grid using a 1/r nearest neighbour interpolation. The iterative procedure of Madsen (1994) to determine $u*_{wc}$ was used.

τ_{wc} was determined at 6 hourly intervals from output bottom currents and available wave data (same for each year) for the 3 month monsoon period (Jan-March) for each of the five Monsoon runs, and the 3 month trades period (Apr-Jun) for each of the five Trade runs.

For each of τ_c, τ_w and τ_{cw}, the number of times the critical shear stress for a given grain size was exceeded at each bathymetric grid point was summed to derive a threshold exceedance map of the Torres Strait and Gulf of Papua region. Threshold exceedances were computed from each individual run. A Monsoon average threshold exceedance was then determined from the Monsoon series of runs, and similarly for the average Trades threshold exceedances.

Spatial maps of the threshold exceedance due to currents, waves and wave-current flows of sediments with a critical shear stress, $\tau_c = 0.27\ Nm^{-2}$ (0.5 mm diameter non-cohesive sediments), are shown in Figures 4.5 - 4.10. Similar threshold exceedance maps for the two other defined critical shear stresses ($\tau_c = 0.05$ and $1.25\ Nm^{-2}$) are presented in Appendix C. Some boundary effects are apparent in these images and should be taken into account in the interpretation. Notable examples include the coast along the Papua New Guinea coast near Port Moresby, and the eastern side of Cape York, south of Cape Grenville.

Figures displaying surface areas of the shelf (defined as $< 300m$) where the relative bottom stress exceeds the critical shear stress for the 3 defined values are displayed in Figure 4.4. Note that the estimated areas are for assumed grain sizes and show only the possibility of mobilising a certain grain size if it were present at a given location on the shelf.

A review of these Figures is given here.

4.3.1 Current Induced Threshold Exceedances

The maps of threshold exceedance due to tidal and wind generated currents (Figs. 4.5 and 4.6) indicate that throughout almost the entire model domain, bottom currents are strong enough to shift cohesionless quartz sediment of grain size 0.5 mm during both Monsoon and Trade conditions.

There are notable regions of high threshold exceedances. These include large patches throughout Torres Strait, in particular a band through the Warrior Reefs and a large area north of the Torres Strait Islands.

By considering uniform sediment size throughout the region, sediments with a larger critical shear stress show regions of high bed shear stress more clearly. The sediment with $\tau_{cr} = 0.27 Nm^{-2}$ indicate a band through the Warrior Reefs, patches amongst the Torres Strait islands, a large area northwest of the islands, a band along the Northern Great Barrier Reef and a patch in the Fly and Kikori River deltas which indicate sediment movement approximately $50 - 60\%$ of the time while the remainder of the shelf is only moving approximately 20% of the time.

Figure 4.4 indicates that tidal currents are capable of moving 0.01mm diameter sediment over almost the entire shelf. These plots indicate that not all of the shelf will be resuspended at some point in time, and no part of the shelf will be resuspended the entire time. However it is apparent that large portions of the shelf are moving due to currents alone. Larger sediments ($\tau_{cr} = 1.25 Nm^{-2}$; 2 mm diameter non-cohesive sediments) are not mobilised nearly as often, only 35% of the shelf area moves at all. Only a small portion of the shelf ($< 2\%$) is moving for 80% of the time.

The similarity between the Monsoon and Trade threshold exceedance maps support the suggestion that tidal currents dominate over wind-generated currents in the mobilisation of sediments in the region.

4.3.2 Wave Induced Threshold Exceedances

Maps of threshold exceedance due to waves during the Monsoon and Trades for a sediment surfaces with a critical shear stress of 0.27 Nm^{-2}, are shown in Figures 4.7 and 4.8.

During the NW Monsoon (Jan-Mar), wave heights are generally less than during the SE trades, particularly throughout the Gulf of Papua. The western side of Torres Strait has larger wave heights during the monsoon. To the west of Torres Strait, the fetch is larger during periods of north-westerly monsoon winds, than during periods of south-easterly trade winds, where Cape York and the Great Barrier Reef provide shelter from the winds.

Comparatively, the 0.5 mm cohesionless sediment is resuspended more in the Gulf of Papua during the trades than the monsoon. Unexpected is the large percent time threshold exceedance inside the Great Barrier Reef due to waves, despite waves being less than 1.5m (Fig. 2.3). Regions of high wave-induced bed stress remain in similar areas to that due to tidal currents. A large ill defined band of high percent time threshold exceedance extends from the tip of Cape York, through the Warrior Reefs to Daru Island. Similar high threshold exceedance patches are observed from the northern most of the Torres Strait Islands to the northwest to the western side of Torres Strait, the shelf to the east of the Strait, and the coast band in the Gulf of Papua on the south coast of Papua New Guinea. This stretch of coast in the Gulf of Papua has the largest wave-induced percent time threshold exceedances during both the Monsoon and the Trades. The similarity between regions of high percent time threshold exceedance as a result of waves and currents indicates that bathymetry is the dominant influence.

A large seasonal variation in threshold exceedances due to waves in the model domain is predicted (Fig. 4.4) as a result of the increased wave activity in the Gulf of Papua during the SE Trades season. During the Monsoon it is notable that almost 100% of the 0.01mm cohesionless sediment on the shelf is resuspended at some point in time. However, during the trades a large portion is not moved at all, with only approximately 80% of the shelf area being resuspended at some point in time. During the Monsoon, only a small area ($< 5\%$) of the 0.01 mm diameter cohesionless sediment on the shelf is mobilised for the whole time. However during the Trades, a much larger portion ($\sim 15\%$) of the shelf moves the entire time. This pattern showing a seasonal crossover is repeated for each grain size distribution, clearly indicating the influence of the Northern Great Barrier Reef in sheltering the south-east Trades wave activity from a large portion of the model domain. Hence during the Trades, waves are capable of resuspending sediments in the Gulf of Papua only, but they tend to keep these sediments mobilised for a larger portion of time than observed during the Monsoon (refer Fig. 2.3 for seasonal wave activity).

4.3.3 Wave-Current Induced Threshold Exceedances

Percent time threshold exceedances due to the combined wave-current induced bed shear stress are the most realistic case. Spatial maps of the percent time threshold exceedance are shown in Figures 4.9 and 4.10. During the Monsoon period, a narrow ribbon along the coast in the Gulf of Papua is mobilised for the entire time, and also a small area in the north-west of Torres Strait. This region in the north-west of the Strait corresponds to

a zone of large seasonally-reversing bedforms (Harris, 1999). The increase in wave energy during the Trades has a marked effect, with these two regions of high threshold exceedance growing in area.

This is well represented by Figure 4.4. For the 0.01 mm cohesionless sediments on the shelf during the SE trades, $\sim$ 70% move at some stage during the 90 day model run, and $\sim$ 55% of the shelf study area is resuspended for the entire period. These numbers both reduce to $\sim$ 20% for the 2 mm (or cohesive) sediment. This would suggest, shown by the near horizontal lines in Figure 4.4f, that sediment moves either the entire time, or not at all, and hence, wave-current induced bed stresses are more energetic than the oscillations in magnitudes of currents or waves alone. During the Monsoon, similar areas are mobilised for some period, however, significantly less (25% and 5% for 0.01mm and 2mm (or cohesive) sediments respectively) are mobilised for the entire Monsoon period. More sediment is mobilised during the Trades than the Monsoon when wave-current interactions are considered due to increased wave activity during the Trades, and mobilisation increases markedly when wave-current interactions are considered compared to waves only, and currents only. Seasonal variation of the percent time threshold exceedances as a result of the combined wave-current induced bed shear stress is observed for both fine and coarse grained sediment.

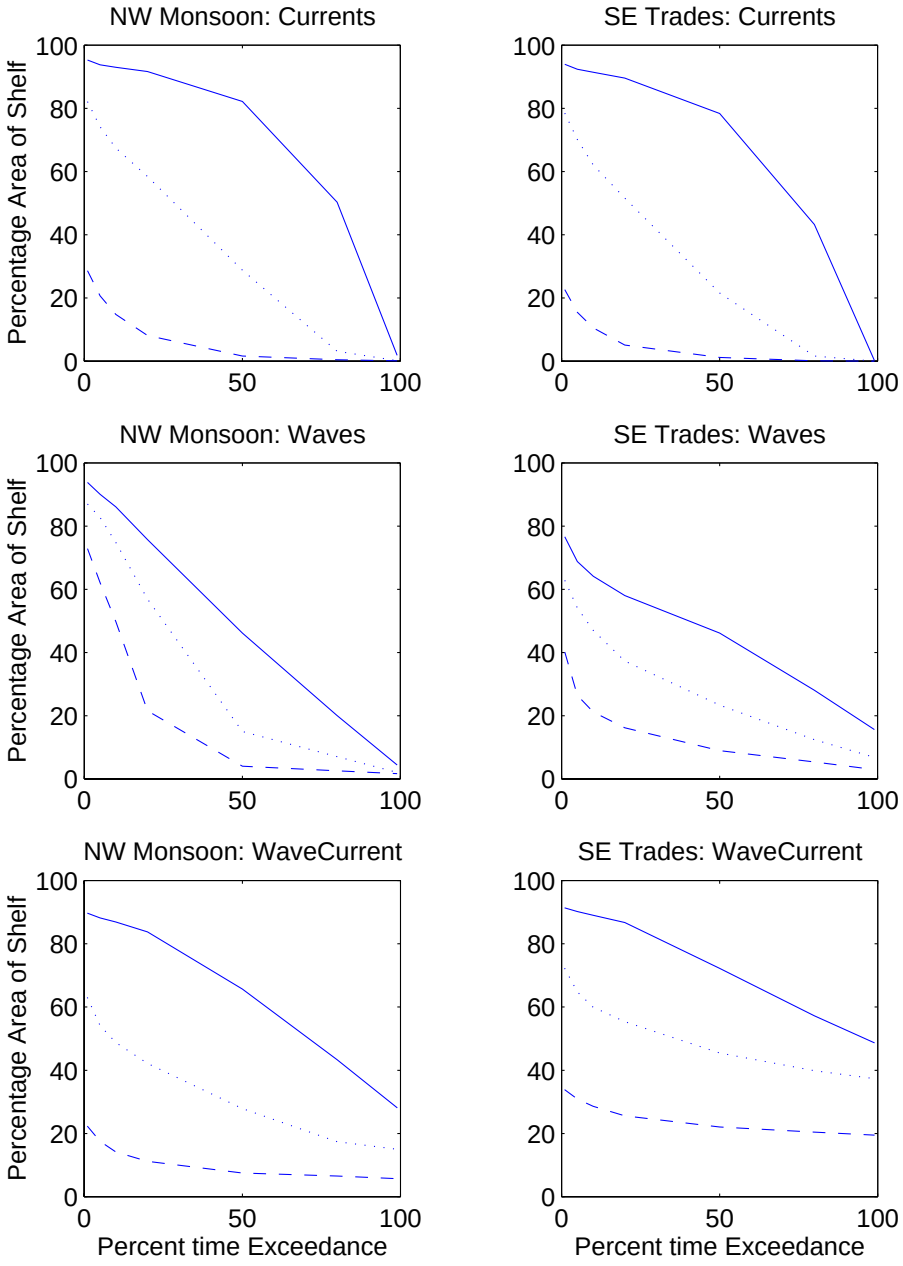

Figure 4.4: Percentage time threshold exceedance over the continental shelf ($< 300m$) for 3 defined critical shear stress τ_{cr} values (Solid line) 0.05, (dotted line) 0.27 and (dashed line) $1.25 Nm^{-2}$ due to currents alone (a,b), waves alone (c,d), and combined wave-current flow (e,f) during the Monsoon (a,c,e) and Trades (b,d,f).

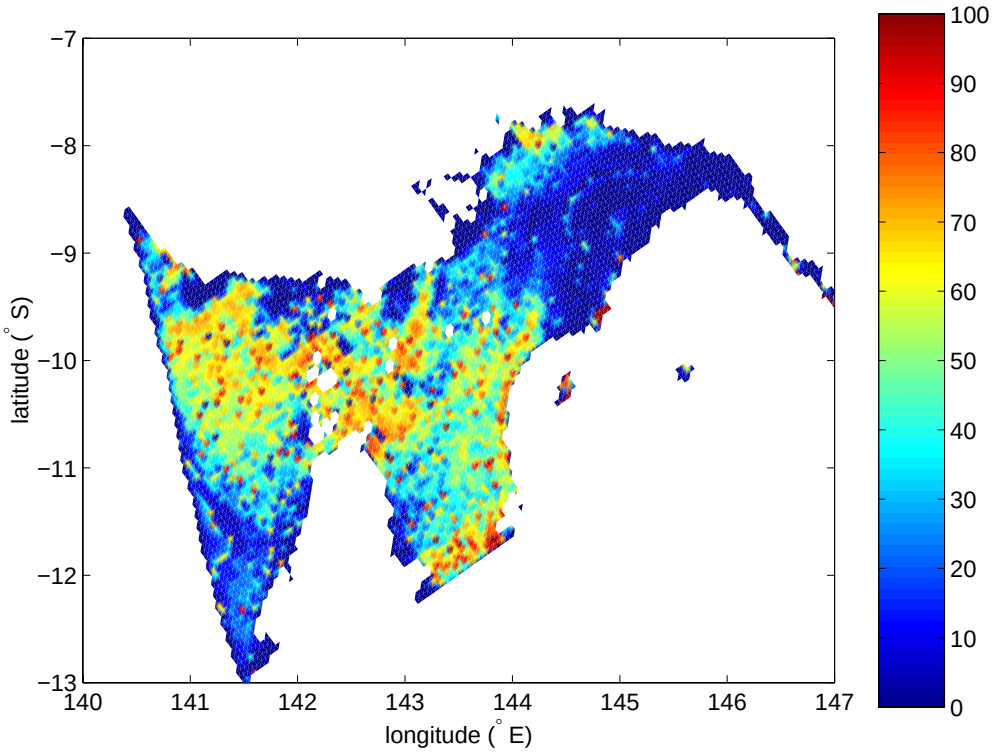

Figure 4.5: Percentage time threshold exceedance due to currents during the NW Monsoon. $\tau_{cr} = 0.27 Nm^{-2}$, i.e., 0.5 mm diameter cohesionless sediment

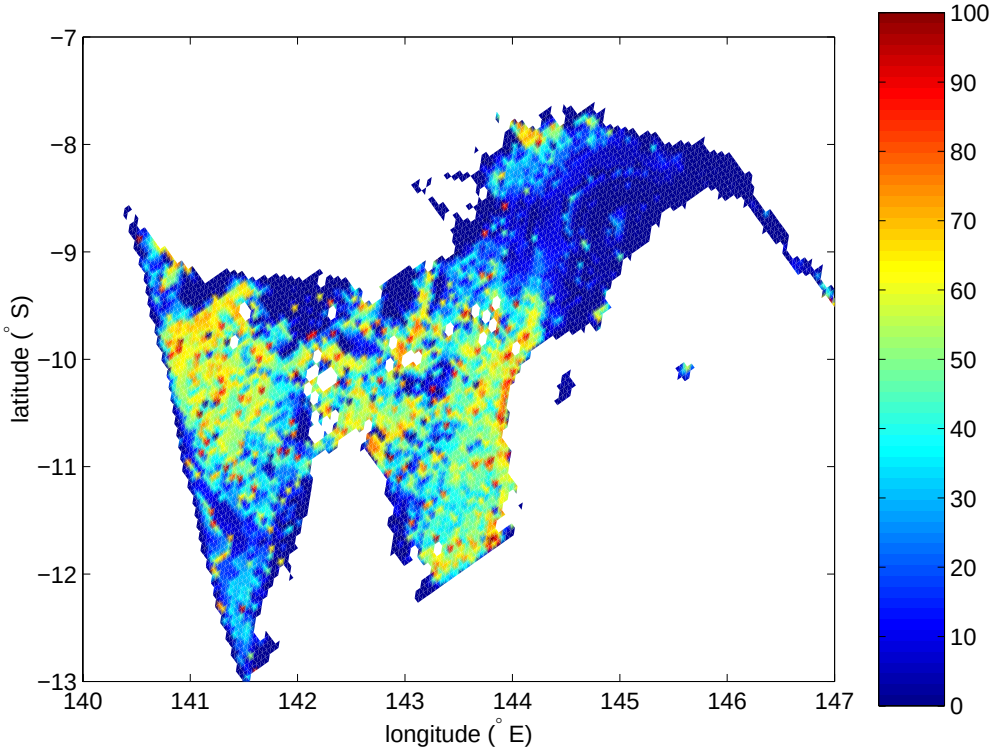

Figure 4.6: Percentage time threshold exceedance due to currents during the SE Trades. $\tau_{cr} = 0.27 Nm^{-2}$, i.e., 0.5 mm diameter cohesionless sediment

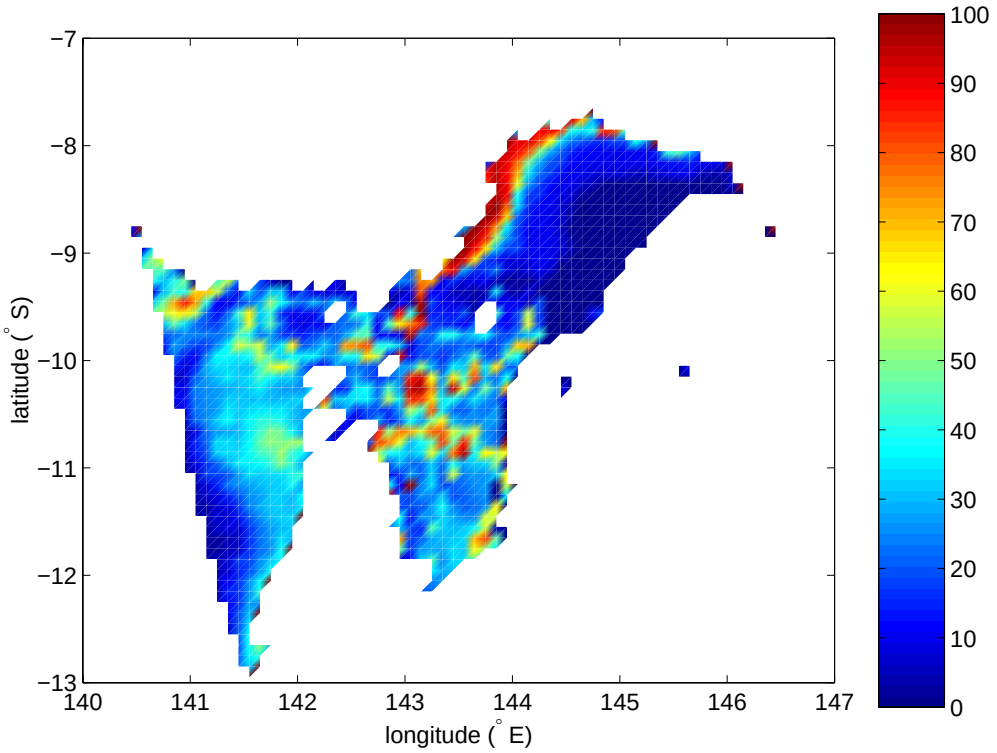

Figure 4.7: Percentage time threshold exceedance due to waves during the NW Monsoon. $\tau_{cr} = 0.27 N m^{-2}$, i.e., 0.5 mm diameter cohesionless sediment

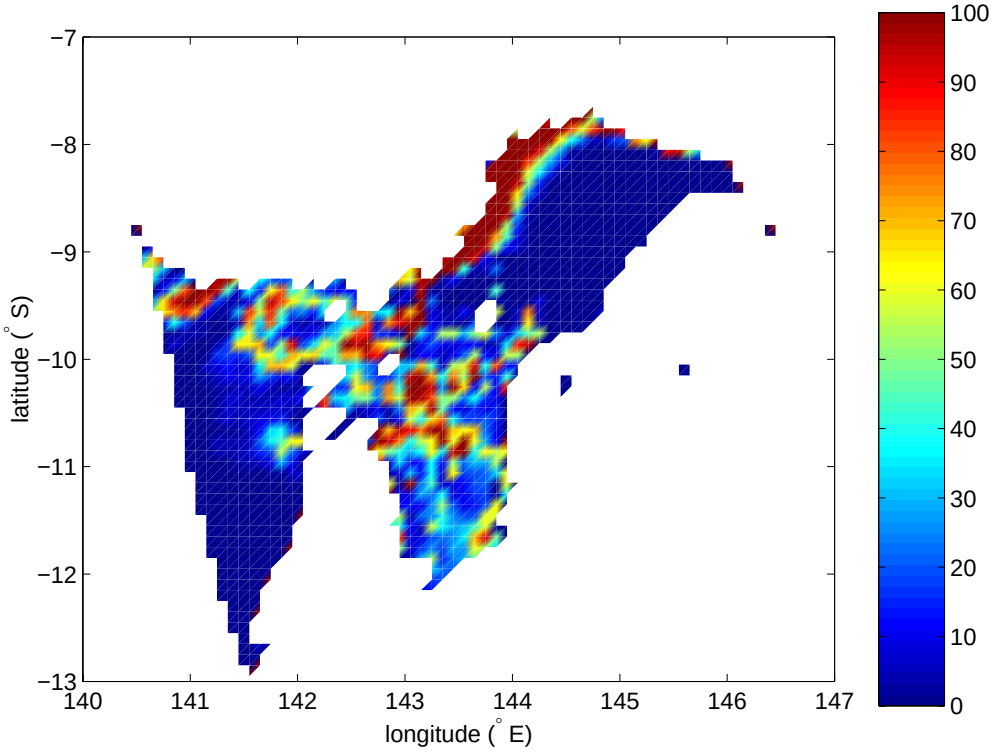

Figure 4.8: Percentage time threshold exceedance due to waves during the SE Trades. $\tau_{cr} = 0.27 N m^{-2}$, i.e., 0.5 mm diameter cohesionless sediment

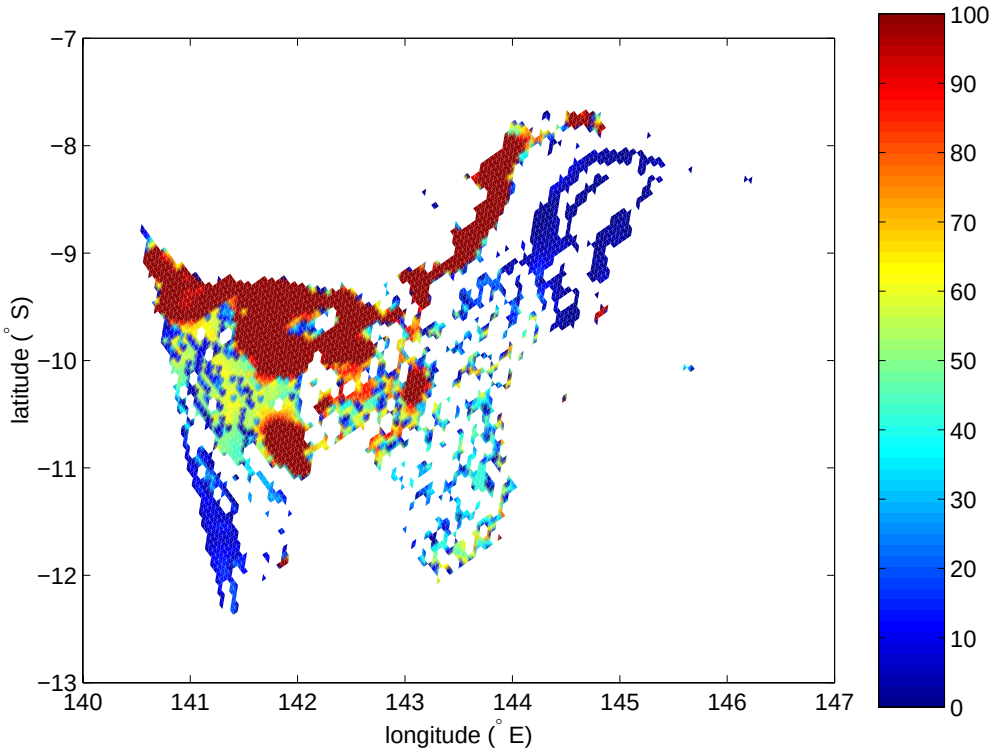

Figure 4.9: Percentage time threshold exceedance due to wave-current flow during the NW Monsoon. $\tau_{cr} = 0.27 Nm^{-2}$, i.e., 0.5 mm diameter cohesionless sediment

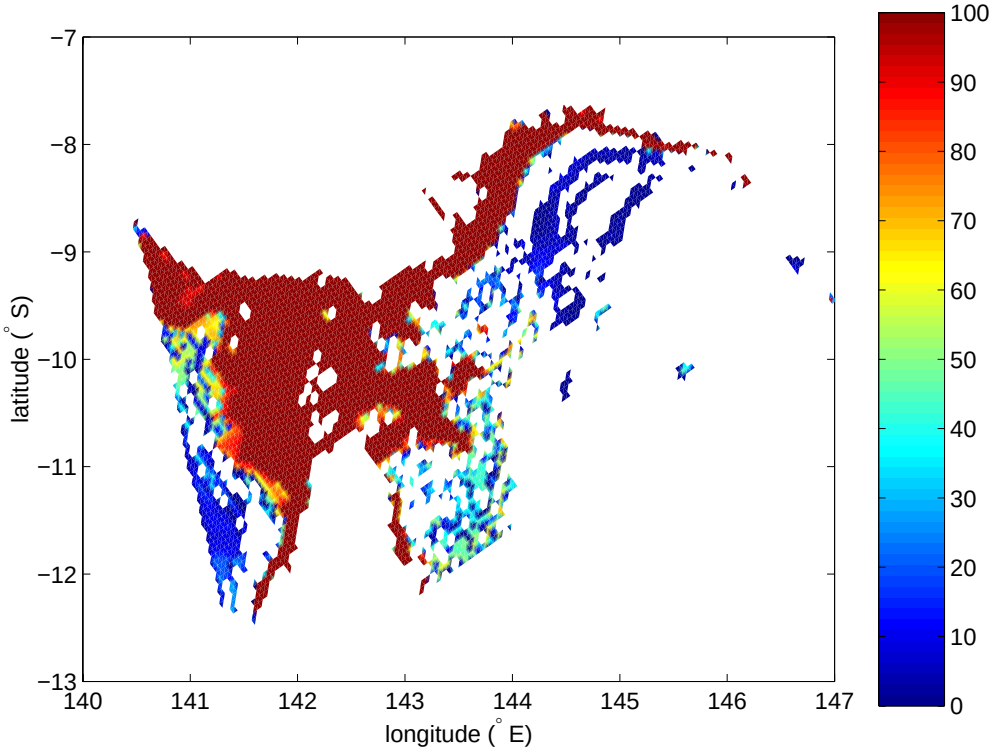

Figure 4.10: Percentage time threshold exceedance due to wave-current flow during the SE Trades. $\tau_{cr} = 0.27 Nm^{-2}$, i.e., 0.5 mm diameter cohesionless sediment

Table 4.1: The percentage area of the continental shelf where the sediment mobility is potentially dominated by waves, currents, or where waves and currents are equally responsible, for sediments requiring different shear stresses for mobilisation. $\tau_{cr} = 0.05(0.27)[1.25]Nm^{-2}$ represents 0.01 (0.5) [2.0] mm diameter non-cohesive sediments.

Season	Category	τ_{cr} (Nm^{-2})		
		0.05	**0.27**	**1.25**
MONSOON	Wave-dominated	4.4502	7.9509	63.0340
	Current-dominated	28.8172	39.8339	5.9731
	Mixed Region	65.9415	50.5934	15.9019
TRADES	Wave-dominated	5.6962	9.4739	43.0182
	Current-dominated	40.9810	54.3710	15.1305
	Mixed Region	52.1163	33.7223	7.7136

4.3.4 Classification of dominant processes

The large portions of shelf moved due to wave-current interaction poses the question as to whether the area is wave dominated, tidally dominated, or whether it is a truly mixed region.

Harris et al. (2001b) presents a classification scheme based on percent exceedances where:

$\frac{t}{w} < \frac{1}{3} \Rightarrow$ waves dominate

$\frac{t}{w} > 3 \Rightarrow$ tides dominate

$\frac{1}{3} < \frac{t}{w} < 3 \Rightarrow$ Mixed Area

where w is the % time of wave threshold exceedance and t is the % time of tidal current threshold exceedance. Three sets of maps of $\frac{t}{w}$ for the NW monsoon and SE trades for sediments with defined critical shear stress values of 0.05, 0.27, and 1.25 Nm^{-2} are shown in Figures 4.11 - 4.16.

Table 4.1 presents the shelf area, by percentage of the total shelf area within the model domain, which are categorised as wave or tide dominated, or equally influenced by wave and tidal processes, for each season. Wave processes are more influential mobilising coarse, or cohesive, sediments during both the Trade and Monsoon seasons. Consequently, the percentage area of the shelf dominated by waves increase, and dominated by currents decrease, with an increase in the critical shear stress of the sediment.

During the NW monsoon, fine sediment is largely tidally dominated amongst the Torres Strait islands. A narrow band along the coast of Papua New Guinea in the Gulf of Papua is wave dominated, and the remaining large area indicates a mixed environment. As the critical shear stress increases, the areas which are tidally dominated diminish to near zero for coarse (or cohesive) sediment, where some small patches amongst the Torres

Strait Islands are tidally dominated, and the shelf becomes predominantly wave dominated. The wave motion during the monsoon, although small, is the dominant mechanism for resuspending larger sediments.

During the Trades, the map of $\frac{t}{w}$ is very similar as for the Monsoon for fine sediment. A larger area to the west of Torres Strait is tidally dominated as a result of the decreased wave activity in this region during the Trades due to the shelter of the Northern Great Barrier Reef and Cape York. As sediment size increases, mixed areas and those dominated by the tide decrease in size, and the wave dominated areas increase in size, as with the Monsoon case. The Trades show less variation with sediment size than the Monsoon. For larger sediments (D = 2mm) during the Trades, a large area of Torres Strait, west of Torres Strait and just inside the Great Barrier Reef, remains dominated by tides, and much less mixed or wave dominated as during the Monsoon. This result is an indicator of the shelter of wave activity provided by the Northern Great Barrier Reef, where offshore winds during the Monsoon may create more wave activity in Torres Strait and inside the reef than swell generated during the trades in the Coral Sea. The size of the wave dominated area in the Gulf of Papua is similar for each season, although is slightly larger during the Monsoon (Table 4.1).

Harris (1995), using available sedimentological data, initially classified the Torres Strait region as one where sediment mobilisation is caused mainly by tidal currents. Harris et al. (2001b) use a modelling approach to classify the entire Australian continental shelf based on annual means of tidal currents and wave activities, i.e., no seasonal variation was considered. They also found the stretch of coast along the south coast of Papua New Guinea in the Gulf of Papua to be wave dominated. The shelf area within the Torres Strait shows more variation, generally a mixed environment, with variable grain sizes. Small areas within Torres Strait were classified as tides only. The higher resolution regional study presented here suggests wave-induced bed shear stress is also important throughout Torres Strait.

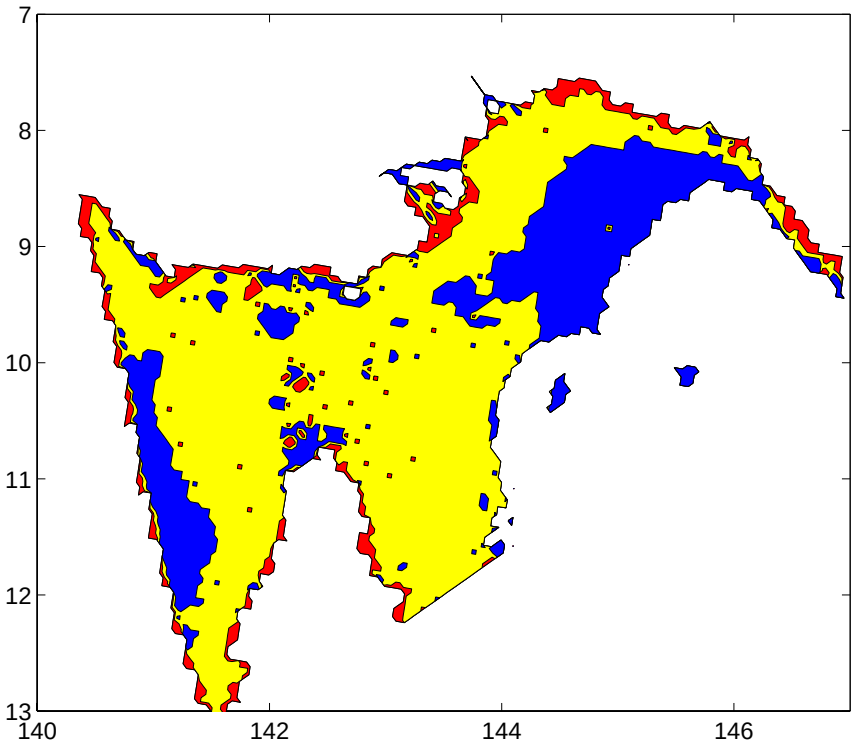

Figure 4.11: Classification of shelf as tide dominated (blue), wave dominated (red), or a mixed wave-current environment (yellow) during the NW Monsoon for $\tau_{cr} = 0.05 Nm^{-2}$, i.e., 0.01 mm diameter cohesionless sediment

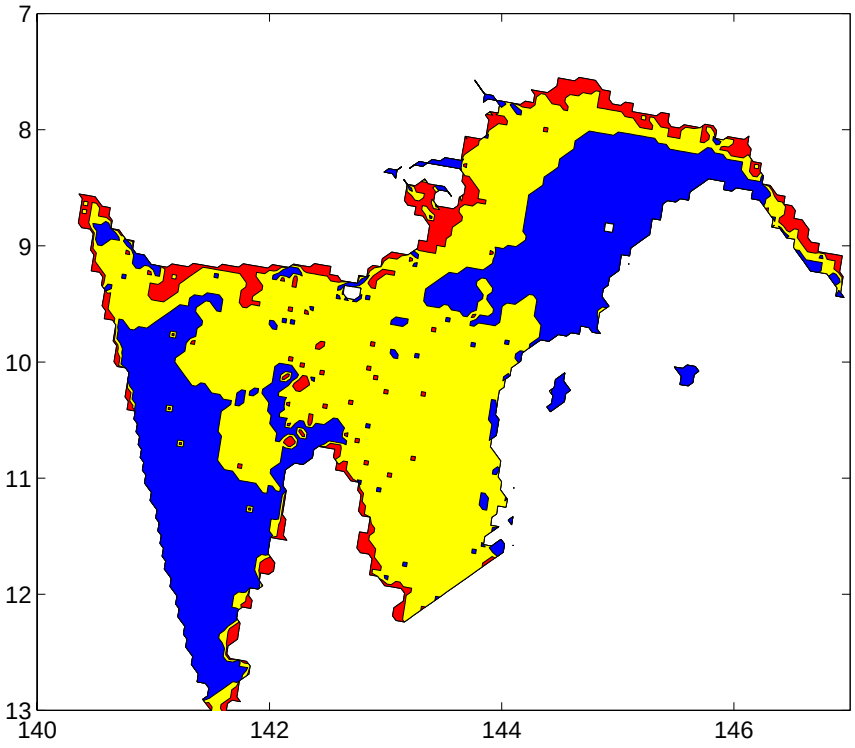

Figure 4.12: Classification of shelf as tidally dominated (blue), wave dominated (red), or a mixed wave-current environment (yellow) during the SE Trades for $\tau_{cr} = 0.05 Nm^{-2}$, i.e., 0.01 mm diameter cohesionless sediment

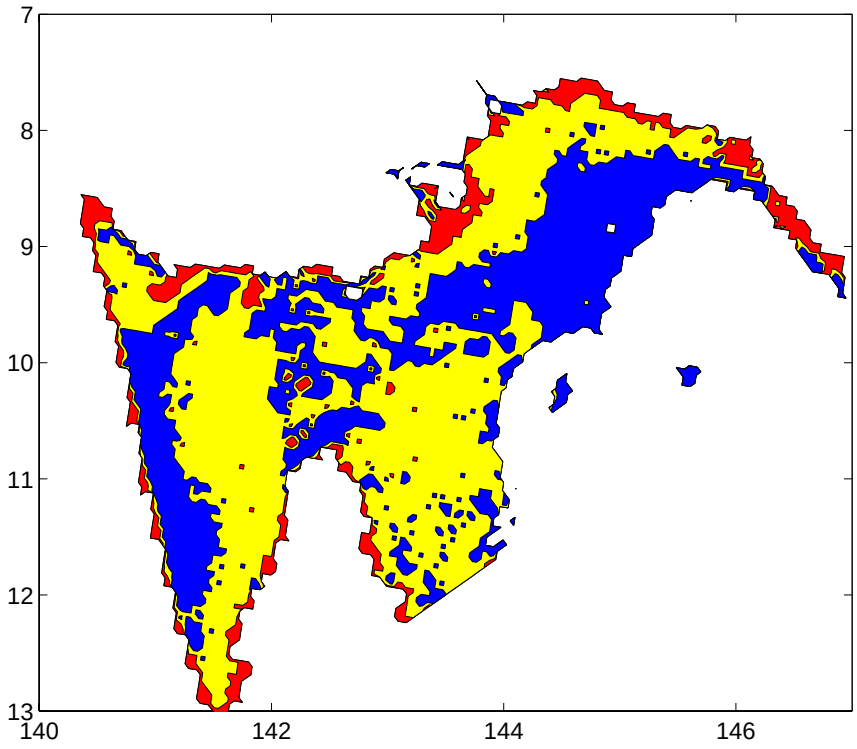

Figure 4.13: Classification of shelf as tidally dominated (blue), wave dominated (red), or a mixed wave-current environment (yellow) during the NW Monsoon for $\tau_{cr} = 0.27 N m^{-2}$, i.e., 0.5 mm diameter cohesionless sediment

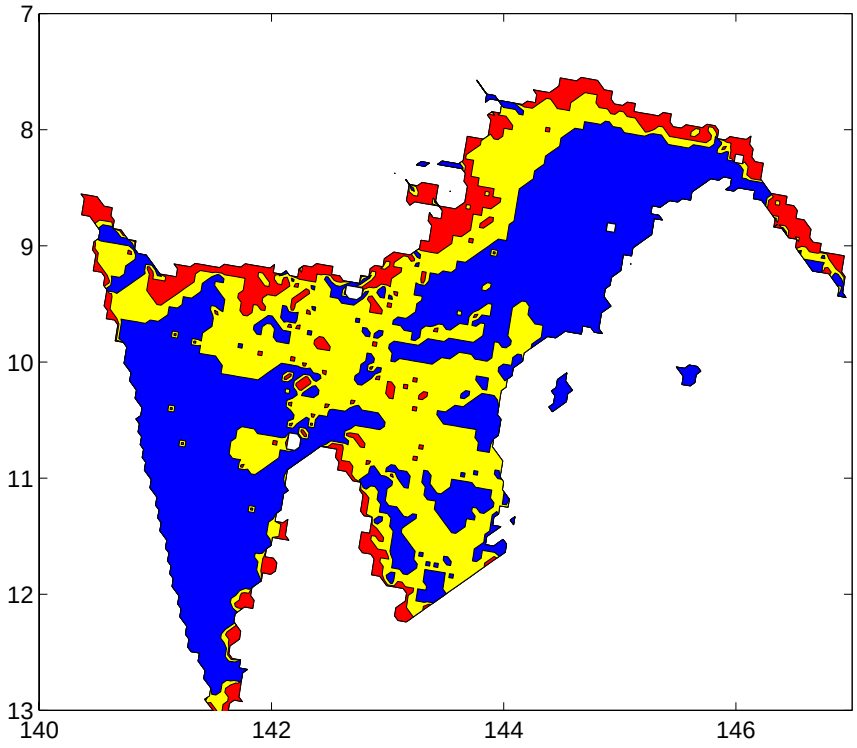

Figure 4.14: Classification of shelf as tidally dominated (blue), wave dominated (red), or a mixed wave-current environment (yellow) during the SE Trades for $\tau_{cr} = 0.27 N m^{-2}$, i.e., 0.5 mm diameter cohesionless sediment

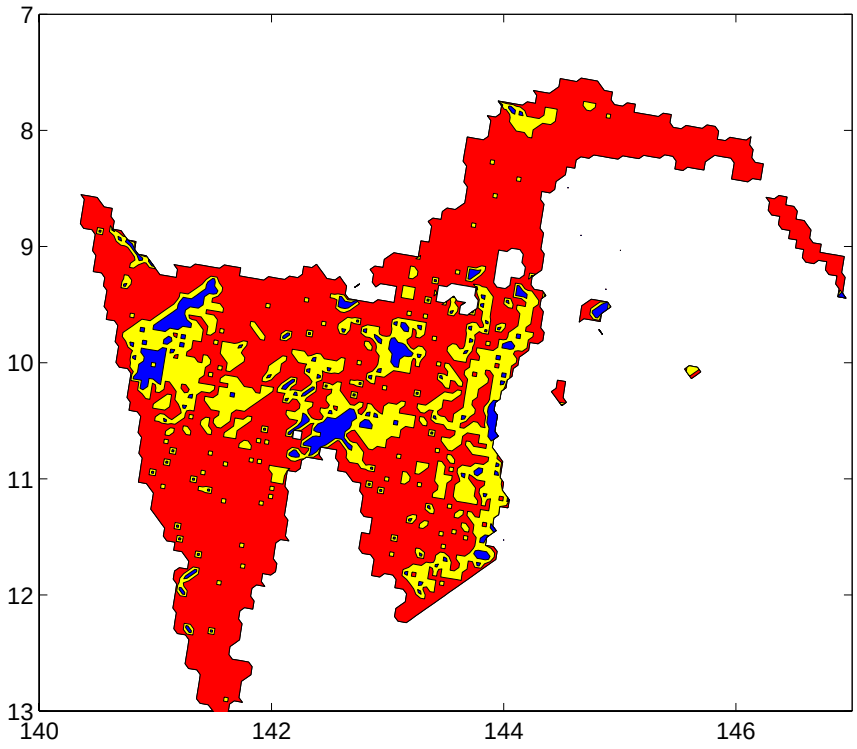

Figure 4.15: Classification of shelf as tidally dominated (blue), wave dominated (red), or a mixed wave-current environment (yellow) during the NW Monsoon for $\tau_{cr} = 1.25 N m^{-2}$, i.e., 2 mm diameter cohesionless sediment

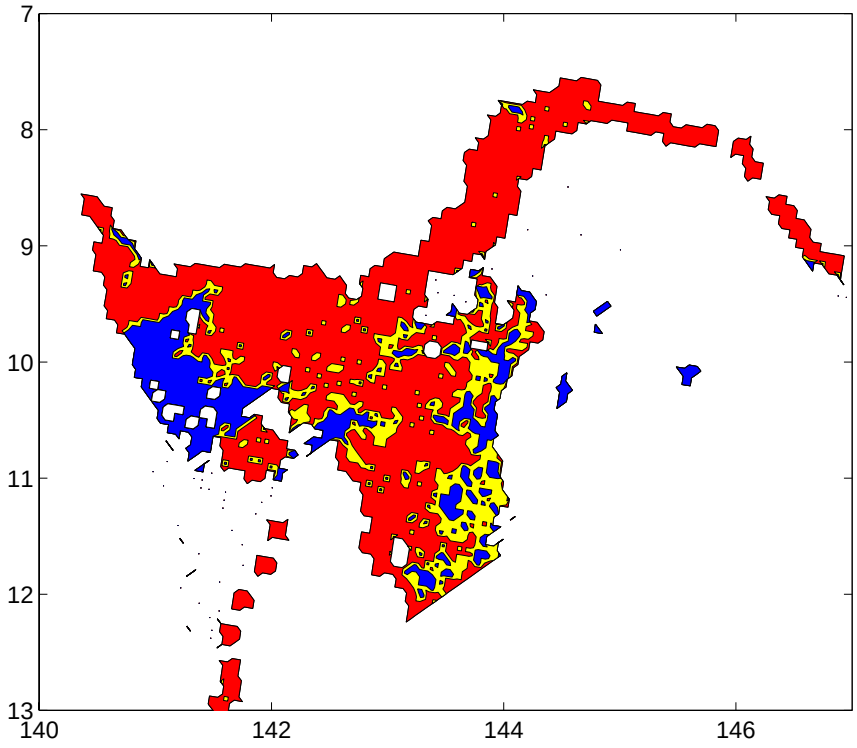

Figure 4.16: Classification of shelf as tidally dominated (blue), wave dominated (red), or a mixed wave-current environment (yellow) during the SE Trades for $\tau_{cr} = 1.25 N m^{-2}$, i.e., 2 mm diameter cohesionless sediment

Chapter 5

Summary, Discussion and Outlook

The aim of the research presented in this part of the thesis was to apply a non-linear, three-dimensional hydrodynamic model to identify the main dispersal pathways for sediments derived from the Fly River, Papua New Guinea, and to determine the main physical processes controlling sediment mobilisation in the Torres Strait - Gulf of Papua region.

The three steps required to achieve these aims have been detailed: The implementation of the numerical model; an assessment of model sensitivity and performance; and, the application of the model for the outlined purposes.

The model was forced with realistic fields of temporally and spatially varying atmospheric inputs (wind and atmospheric pressure), and spatially varying density. Tidal elevations derived from 9 main tidal constituents were used to force the model on the open boundaries.

Despite the complex bathymetry of the study region, the model provided currents qualitatively consistent to those measured in the field. The hydrodynamic model results are suitable for the purpose of investigating seasonal variation of the oceanic currents, capable of reproducing observed trends in the area. However, quantitatively, the model could be improved. An approach similar to that taken by Bode and Mason (1994) of a sub-grid-scale parameterisation of reef porosity may be valuable for improving quantitative comparisons in the future in such a reef dominated region.

Errors in the bathymetry are expected to account for a large portion of the model error. Large areas of the model domain are not suitable for ship navigation, thus detailed bathymetry is not available. Portions of the model domain are highly mobile, such as the 5 m amplitude mobile sand waves in north-west Torres Strait (Harris, 1999) which change direction seasonally. Such morphological changes are not accounted for in the model

bathymetry grid. The smoothed offset between the AGSO 30' bathymetry grid and the ETOPO5 bathymetry grid at 8.5 deg S may account for a small portion of the error, however tidal elevation comparisons at Kerema (K) and Kumul Trk Mar (KTM), in this region, are quite good (Section 3.6.1).

The nature of the tidal system within the domain, with 180° changes in phase of the dominant tidal constituent, M_2, across a distance of approximately 30 km amongst the Torres Strait Islands, makes it a difficult system to simulate given the model's spatial extent, and resultant resolution. Such rapid changes in phase correspond with a change in phase of 24° per grid cell at the given $\sim$ 4 km resolution. The inclusion of nested, higher resolution, grids in such regions is suggested in the future to better resolve these rapid spatially varying changes. A spatial resolution of 500 m would decrease the phase difference between adjacent cells to approximately 3°. Resolution of this order would be likely to improve model to observation comparisons in this region markedly.

The implementation of a model with a z-layer grid in the vertical may not be ideal for the study of processes in the bottom boundary layer. A terrain following sigma-coordinate model is capable of resolving the bottom boundary layer more accurately. However, in a bathymetrically complex model domain as covered in this study, it was considered that the numerical error in the pressure gradient calculation over steep topography (Haney, 1991; Beckmann and Haidvogel, 1993; Mellor et al., 1994, 1998) i.e., the rapid changes in the depth associated with the coral reefs and steep continental slopes in the model domain, may be large enough to be a problem in reproducing realistic flow fields.

The BRUCE probe was deployed for validation of the model, with good results. The deployment was the first time such a suite of instruments had been deployed in Torres Strait, allowing for insight into the synoptic scale wind effects on the dispersal pathway of the Fly River plume, and verification of the bed shear stress values in the model. Comparisons of the tidal current-induced bottom shear stress are good at the BRUCE site.

Validation of the model against current meter data indicates better model agreement of sea surface elevation and tidal currents for the BRUCE mooring than for the previously recorded current meter moorings from 1990 and 1993. There are a number of possible reasons for this. Firstly, the BRUCE site was chosen for the purpose of model validation. The site was therefore chosen in a region of spatially uniform depth, minimising any local bathymetry effect which may alter currents given the constraint of poor model bathymetry and resolution. Secondly, the quality of the BRUCE dataset is considered superior to the previous moorings. Biofouling causes havoc on scientific equipment in the highly productive

waters of Torres Strait. Anderaa current meters deployed previously are subject to the effect of drag on rotors, and organisms and weeds jamming the rotors completely. Zero current output is observed through many of the current meter records, giving evidence of this occurring. For validation of the model, only current meter records with greater than 30 days of data were chosen, to allow for tidal analysis of the currents. However, data records of this length may be subject to a greater influence of biofouling. The acoustic doppler current meter used in the BRUCE mooring removes errors associated with this. Thirdly, the BRUCE site was chosen to be a sufficient distance away from the region of rapidly changing tidal phase where the model elevation comparisons indicate large phase errors.

The maximum current induced bed shear stress values hindcast by the model suggest only small regions are influenced by the seasonal prevailing winds, and that the dominant influence on the associated bedload transport throughout most of the model domain is the tidal currents. New data collected from the BRUCE (Benthic Research of Underwater sediment ConcEntrations) frame during February 2002 (Monsoon) season suggest that the effect of tidal currents was exceeded during a local wind event, with vertical transfer of momentum from the surface influencing the turbulent bed shear stress. The net effect of this is not large. The net bedload transport was directed, along with maximum bed stress vectors obtained from tidal currents, towards the south-west.

Tracers were input into the model to establish a sediment budget of the Fly River sediment plume. The predicted budget, during the Monsoon, is consistent with the preliminary form proposed by Harris et al. (1993) based upon the sedimentology and morphology of the area. However, it is found that there is a strong seasonal dependence on the Fly River sediment budget. Increased sediment load is directed towards Torres Strait during the Trade season. The BRUCE deployment appears to indicate that although tidal currents dominate the bed shear stress influence, lower frequency currents associated with the prevailing winds dominate the seasonality of the dispersal pathway of the Fly River plume. The density driven Coral Sea Coastal Current remains constant in the model, and thus no seasonal change is accounted for. This current accounts for only 6% of the flow on the continental shelf. The relative magnitude of the Coral Sea Coastal Current is expected to be larger in deeper water and on the continental slope.

The seasonal variation of the dispersal pathways outlines various oceanic processes. During the Trades, onshore winds drive water against the Gulf of Papua coast in the Fly Delta region. Wright (1989) describes the predominantly along-shore north-eastward geostrophic current which is generated as a result of the sloping water surface. Similarly,

during the Monsoon, north-westerly offshore winds drive water away from the coast which sets up a small south-westward barotropic current. However, the model predicts a greater westward transport of the Fly River plume to occur during the Trades than during the monsoon, suggesting that the Ekman transport, veered to the left of the wind stress in the southern hemisphere as a result of the coriolis force, and therefore directed in the opposite direction to the geostrophic current, is of the same order of magnitude as the flow setup by the sloping sea surface. Thus, during the period of south-easterly Trades, a greater component of the Fly River derived sediment budget is directed to the west into Torres Strait.

No effort has been made to show any seasonal changes to sediment input. Terrigenous sediments are sourced from erosion in the Papua New Guinea highlands as a result of high rainfall in the region. Rainfall in highlands of Papua New Guinea is roughly uniform throughout the year, and consequently, there is only small temporal variability, on a seasonal scale, of the terrigenous sediment input, and can safely be ignored. Biogenic sediment supply, however, varies depending on the energy available to both break up and then resuspend organisms (sediments) on the continental shelf. Without having parameterised resuspension in the model physics, the seasonality in biogenic sediment input is not easily quantified, and is a limitation of the approach used here. During periods of increased energy at the seabed (i.e., the trade season), an increased abundance of biogenic sediments is expected, and such seasonal variability is observed in sediment cores collected from the Fly River delta front (Harris et al., 1993).

Differences between the preliminary sediment budget derived from the surficial sediment distribution, seismic survey and coring data (Harris et al., 1993) and the model budget must be addressed. The field derived sediment budget accounts for a large proportion (40%) of the Fly discharge in suspension to be transported by wind and density (Coral Sea Coastal Current) currents north-eastward into the Gulf of Papua along the south coast of Papua New Guinea. The model derived budget suggests 34% during the Monsoon and 24% during the Trades of the Fly discharge is transported north-eastwards. The model has isolated the influence of sediment derived from the Fly River, ignoring the sediment input of the Kikori and Purari rivers which enter the Gulf of Papua further to the east. Although there are uncertainties in the model results, the influence of the Kikori and Purari rivers on the sediment distribution in the Gulf of Papua may overestimate the component of the Fly River sediments being transported north-eastwards along the south coast of Papua New Guinea. However, the model predicts an increased sediment load being transported into Torres Strait.

High carbonate content, and low suspended sediment concentrations in Torres Strait, indicates very little deposition of terrigenous sediments. Whether these sediments remain in suspension while being transported through Torres Strait to the Gulf of Carpentaria before being deposited cannot be resolved by presently available datasets. This study calls for the collection of additional field data west of the model domain to observe the extent of Fly River derived terrigenous sediment into the Gulf of Carpentaria.

Harris et al. (1993) collected sediment cores from the Fly Delta which indicate seasonal sand-mud interbeds. In support of these results, predictions of sediment mobility due to wave-current interactions were found to alter significantly between the Trades and Monsoon seasons. Sediment was found to be mobilised over a larger portion of the shelf in the Gulf of Papua during the Trade season.

Although the interactions of waves and currents has been considered, several factors complicating the modelling of where mobilisation occurs have been ignored. Real shelf sediments are rarely cohesionless quartz spheroids, but a mixture of poorly sorted gravel, sand and mud, and are often transported across continental shelves to locations where they are in hydrodynamic equilibium (Nittrouer and Wright, 1994). By assuming a constant grain size, areas of continuous mobilisation (100% exceedance) are most likely an overestimate.

The estimate of current induced shear stress ignores the frictional drag of bedforms (Davies, 1985). Large bedforms are found in Torres Strait (Harris, 1988), and where these occur, threshold exceedances will be overestimated. The estimate of wave, and wave-current, induced bed shear stress will likewise be hindered by the presence of bed ripples.

The wave data obtained from the Bureau of Meteorology is modelled using the WAM wave model. Although this model performs well in open water, the scale of the wave calculations and the physics of the model cannot account for the bathymetrically complex areas such as Torres Strait and the northern Great Barrier Reef, where wave sheltering, refraction and reflection occur. Hence the wave induced, and the influence on the wave-current induced, 100% threshold exceedances within the domain are most likely overestimated. The spatial resolution of the modelled wave data is much coarser than the modelled currents. Therefore, smaller scale bathymetry effects resolved by the hydrodynamic model may not be resolved by the modelled wave data.

Resuspension of settled sediment is not included in the tracer model carried out in this study. Resuspension of material from the seabed would result in plumes of higher suspended sediment concentrations. As a result, the modeled sediment budget may be an underestimate in regions of greater mobility. Flocculation processes are also not included in

the model. Flocculation will increase settling velocities such that the distance that modeled plumes extend, may be overestimated in areas where flocculation is important.

Given the above mentioned model constraints, the main transport paths of mining waste derived from the Fly River, which pose a possible threat to the Torres Strait marine environment, have been identified. The model predicts a zone of possible increased bed shear stress on the Northern Great Barrier Reef, which has implications for the proposed emplacement of the Torres Strait 'Chevron' gas pipeline, through increased scour along the line with the potential for environmental impact on the nearby coral reefs. Available data are unable to resolve many of the model predictions from this study, highlighting that the region requires continuing investigation.

Part II

AMERY ICE SHELF

And now there came both mist and snow,

And it grew wondrous cold:

And ice, mast-high, came floating by,

As green as emerald.

Samuel Taylor Coleridge - The Ancient Mariner, 1798

Chapter 6

Introduction and Background

6.1 Introduction

The Antarctic continental shelf is unique in its comparative great depth (mean $\sim 500m$ (Vanney and Johnson, 1985)), rugged bathymetry, deepening in onshore direction and almost total glacier ice cover at its rim. These characteristics are the result of isostatic loading by the thousands of metres of ice on the continent, sediment starvation and periodic erosion by advancing ice sheets. Modern sediment supply to the Antarctic shelf is dominated by ice rafting, pelagic production and deposition and redistribution of material reworked from relict deposits on the seafloor. These processes involve vertical and/or horizontal transport of sediments through the shelf water column. An important role of sediments here is to provide a potential proxy record of shelf water column conditions. Textural and compositional data can be used to derive bottom current intensity and direction, as well as information about biological productivity in surface waters.

The continent of Antarctica is fringed by ice shelves, the floating portion of the Antarctic ice sheet. The stability of floating ice shelves is an important indicator of ocean circulation and ice shelf mass balance, and therefore, they are sensitive indicators of climate change (Mercer, 1978). The present day sedimentation processes beneath floating ice shelves must be intitially understood before any estimation of past sub-ice-shelf conditions can be made. Most Antarctic shelf studies have considered only the region north of the calving fronts of the ice shelves, but the ocean circulation and related processes beneath the shelf ice play a significant role in glaciomarine sedimentation, and are important information for understanding the impact of global warming on present day ice shelves, and the subsequent effect on global ocean circulation and climate. However, very few hard data are available

on the subject. Up until this study, the only comprehensive sediment observations taken beneath a large ice shelf are those from site J-9 on the Ross Ice Shelf (Clough and Hansen, 1979) where only sparse biological activity was observed and no measurable thickness of modern sediment was present (Webb et al., 1979; Harwood et al., 1989). Alley et al. (1989) highlighted the need for an ambitious project to drill through ice shelves for new observations of sub-ice-shelf sedimentation.

Water circulation under a floating ice shelf involves landward flow at depth, bringing warmer water into contact with the base of the glacier. This water is mixed with fresh meltwater which forms a bouyant mixture that flows toward the surface in a seaward direction along the base of the floating ice mass (Jacobs et al., 1992). Hydrodynamic models of the sub-ice-shelf circulation show a lateral separation of these landward and seaward flows by the coriolis force which can be described by a two-dimensional horizontal inflow/outflow circulation (Williams et al., 1998b, 2001). Several facies models have been proposed for the deposition of sediments beneath ice shelves, with very few observations. Of these, only limited reference has been given to the effects of sub-ice-shelf circulation and its lateral separation (Harris, 2000b).

The primary aim of this part of the thesis is to examine the sedimentological signatures that might be generated by water and sediment circulation patterns underneath, and directly in front of, the floating Amery Ice Shelf, and determine which processes dominate the mobilisation and transport of sediments in the ice shelf cavity.

Chapter 7 details the collection of sediments from beneath the Amery Ice Shelf, and from immediately adjacent to the calving ice shelf front. The interpretation of the surface sediment physical composition and distribution, along with diatom assemblages, reflects the modern day sedimentation patterns. When correlated to known oceanographic conditions, these may be used as a basis for a model to interpret down-core changes in the physical sedimentology and diatom assemblages as a response to palaeoclimate; in this case the glacial history of the Amery Ice Shelf.

However, the observation of processes in the cavity beneath the ice shelf is physically difficult and therefore datasets are sparse and do not provide an adequate spatial representation of these processes. As a result of these restrictions, numerical ocean modelling is an essential tool for the study of water and sediment circulation in the sub-ice-shelf cavity, allowing for the identification of dominant processes acting on the transportation of sediments. Sub-Ice-Shelf circulation is controlled by the thermodynamic conditions, however, Hambrey (1994) suggests tidal currents are likely to affect the composition of sediments where the

water depth is sufficiently shallow to allow significant tidal streams to develop.

Chapters 8 and 9 are aimed at using barotropic and baroclinic numerical ocean models to study the influence of tides on the sub-ice-shelf circulation, induced vertical mixing, basal melting of the Amery Ice Shelf, and its resultant effect on the circulation of sediments in the sub-ice-shelf environment. These chapters allow the dominant oceanographic processes operating in the cavity to be idenitified.

Chapter 9 draws together the results of this part of the thesis, and presents some main conclusions. The remainder of this chapter provides some background material for the following chapters.

6.2 Location and Setting

6.2.1 Prydz Bay

Prydz Bay lies at the oceanward end of the graben occupied by the Lambert Glacier and Amery Ice Shelf, situated between Mac-Robertson Land to the south-west, and Princess Elizabeth Land to the south-east in East Antarctica, between longitudes $68-80°E$ (Fig. 6.1).

The Lambert Glacier/ Amery Ice Shelf system is the major glacial influence on Prydz Bay. Prydz Bay, although smaller than the Ross and Weddell Seas is the largest shelf sea located around the East Antarctic Margin, and is probably the best known high latitude continental margin (Hambrey, 1994) after a combination of drilling and seismic surveys (Quilty, 1985; Stagg, 1985; O'Brien, 1994; O'Brien and Harris, 1996; O'Brien et al., 1999).

Prydz Bay is occupied by a broad topographic basin, the Amery Depression, which deepens toward the continent. Depressions of up to 1000 m are found in the southwestern corner of the Bay, on the western side of the Amery Ice Shelf front (the Lambert and Nanok deeps). Svenner channel is an elongated trough up to 1000m deep which runs parallel to the Ingrid Christensen Coast. The Prydz Channel, another elongated deep channel, extends to the continental shelf edge along the western edge of the Amery Depression. Prydz Channel resembles shelf-crossing valleys of the Ross Sea. Offshore from the Amery Depression, the shelf shallows to less than 200 m deep along the shelf edge, forming Fram Bank on the western side of Prydz Channel, and Four Ladies Bank on the eastern side. The area close to the Amery Ice Shelf front features broad valleys separated by narrow ridges trending parallel to ice flows (O'Brien, 1994).

The continental slope adjacent to Prydz Bay consists of a large, trough mouth fan offshore from the Prydz Channel, extending 90 km seawards of the shelf break, and 66 km

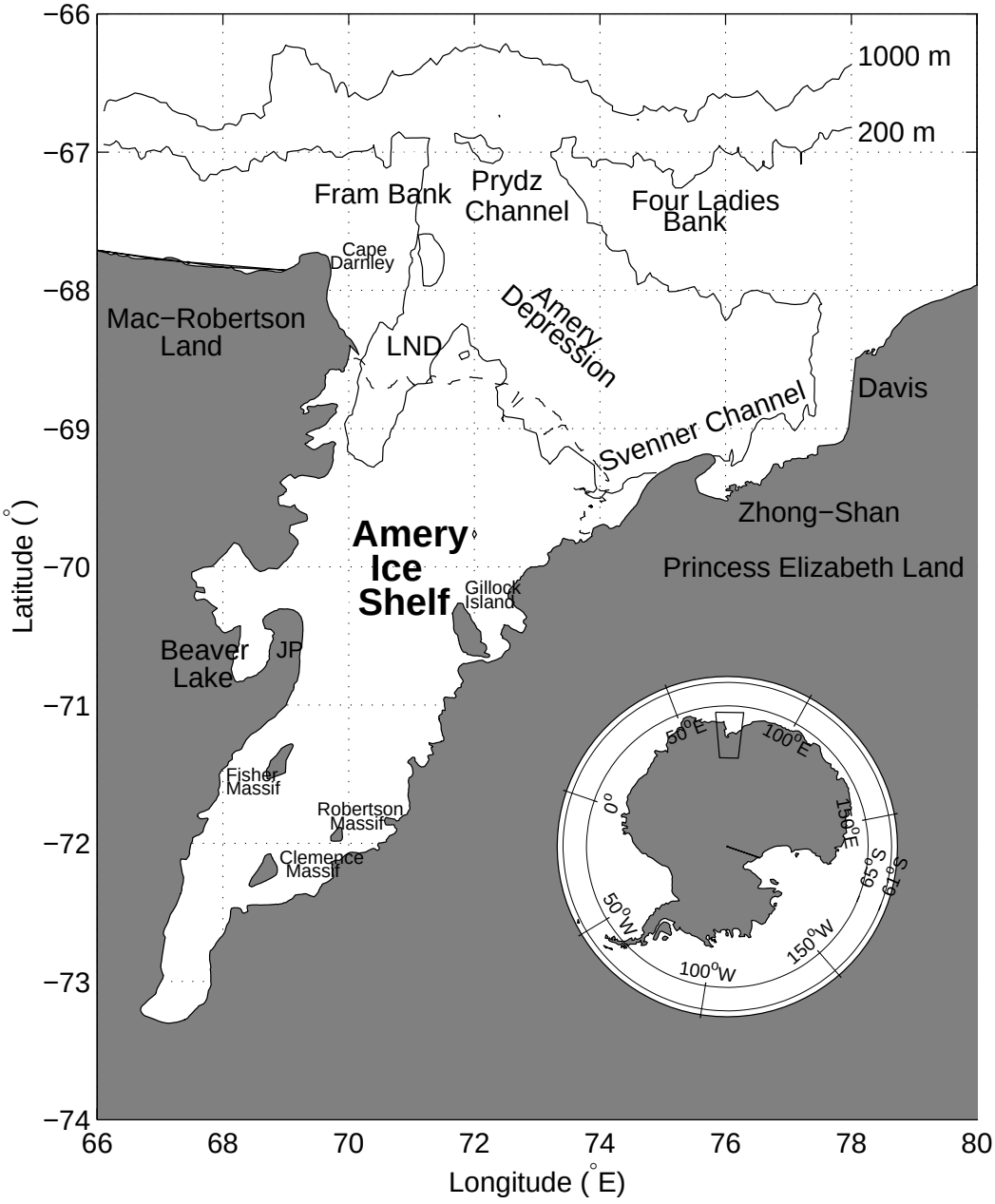

Figure 6.1: The location of Prydz Bay and Amery Ice Shelf in East Antarctica, key features are displayed along with the 1000 and 200 m depth contours. LND is the Lambert and Nanok Deeps, JP is Jetty Peninsula.

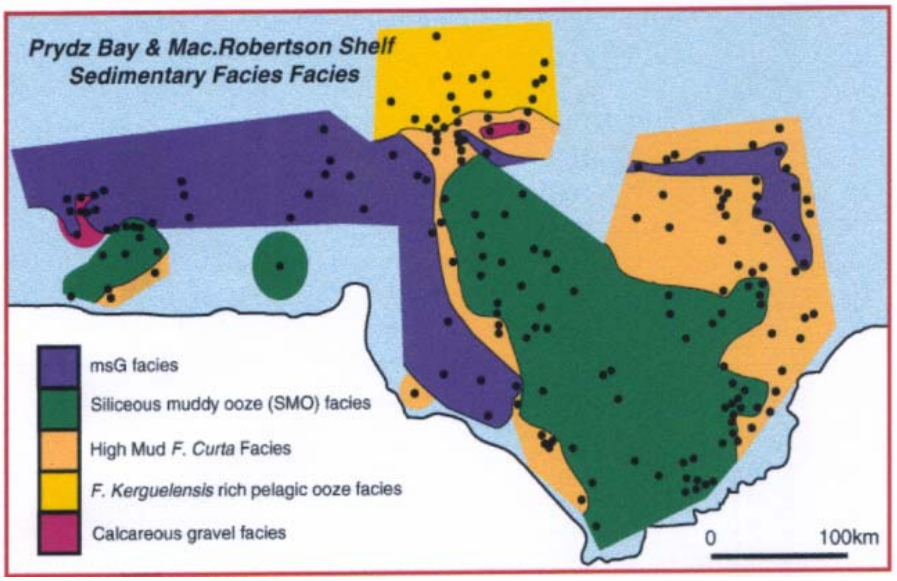

Figure 6.2: Prydz Bay Lithofacies. From Harris et al. (1999)

across. It lacks submarine canyons, where sediments deposited along the axis of the Lambert Glacier/ Amery Ice Shelf have prograded offshore (O'Brien, 1994).

Past glacial processes operating on the Prydz Bay seafloor have produced morainal banks and drumlin (streamlined hillocks, elongated to former ice flow directions, composed of glacial debris) features, flutes and large scale crag and tail features. Extensive megaflutes of inner Prydz Bay are up to 10 m high, 2 km across and up to tens of km long (O'Brien, 1994). Sediments are thin, or absent, over much of the inner shelf, particularly in south-east Prydz Bay (Stagg, 1985). O'Brien and Harris (1996) indicated erosional features on the inner section of Prydz Bay suggesting a zone of net erosion.

Surface sediments recovered on the inner shelf of Prydz Bay are composed mainly of fine grained mud and biosiliceous ooze. The thicker sediments of the outer shelf are characterised by coarse terrigenous and biogenic sediments.

Iceberg plough marks are common on the outer shelf, particularly over Fram and Four Ladies Banks (O'Brien, 1994; OBrien et al., 1997; Harris and O'Brien, 1996). Large scale dunes, attributed to strong bottom currents, are observed on the western Fram Bank.

Harris et al. (1999) identified five surface sediment lithofacies in Prydz Bay, based on biogenic silica, calcium carbonate, grain-size analysis, and the relative abundance of diatom taxa *Fragilariopsis curta* and *Fragilariopsis kerguelensis* (Fig. 6.2). These are: (1) Slightly gravelly sandy mud, (g)sM; (2) Siliceous Mud and Ooze, SMO; (3) *Fragilariopsis kerguelensis* pelagic ooze; (4) *Fragilariopsis curta* gravelly sandy mud, mgS; and (5) Calcareous gravel.

The (g)sM lithofacies is distributed on the shallower areas of the shelf, including Four

Ladies Bank and western Prydz Bay. It contains coarse, poorly-sorted sediment which has been reworked by iceberg ploughing. The SMO is the most extensive lithofacies in Prydz Bay. It is observed in the deepest areas of the continental shelf, such as the Amery Depression and Nielsen Basin, where it is protected from iceberg and ocean current reworking, and forms thicknesses greater than 5 m. The *F. kerguelensis* pelagic ooze is similar to the gsM lithofacies, but is characterised by a high abundance of *F. kerguelensis* frustules in the sediment, and is distributed offshore from the continental shelf break. The *F. curta* mgS forms a transitional belt between the gsM and the SMO, and is correlated to the iceberg ploughed zone on Four Ladies Bank. Calcareous gravel is the rarest lithofacies, observed in a small area at the apex of the Prydz Bay trough mouth fan, and also on Storegg Bank on MacRobertson shelf to the west.

O'Brien and Harris (1996) concluded that the morphology and stratigraphy of Prydz Bay results from the advance of the Lambert Glacier and ice from the eastern side of the Bay to the shelf edge, with a fast flowing ice stream occupying the Prydz Channel. Domack et al. (1998) suggest that the Last Glacial Maximum (LGM) was not a shelf wide glaciation, and that the Prydz Channel remained free of grounded ice during the LGM. O'Brien et al. (1999) indicate the Lambert Glacier occupied a series of grounding zones in the Amery Depression during the last glacial cycle, and constructed a number of sediment wedges in Prydz Bay. The LGM is recognised globally as the peak lowstand of eustatic sea-level and peak in glacial ice advance, and occurred $\sim$ 18 ka BP (Adamson and Pickard, 1986).

6.2.2 Amery Ice Shelf Cavity

The Amery Ice Shelf, in the Indian sector of the Southern Ocean (Fig. 6.1), is the largest of the East Antarctic Ice Shelves with an area of $\sim 60 \times 10^3 km^2$ (calculated from the most recent grounding line; Fricker et al., 2002). It is small compared to the two largest ice shelves, the Filchner-Ronne Ice Shelf (FRIS) and the Ross Ice Shelf (RIS), each $\sim 500 \times 10^3 km^2$ (Makinson and Nicholls, 1999; MacAyeal, 1984b). The Amery Ice Shelf receives drainage from $1.3 \times 10^6 km^2$, or 14%, of the East Antarctic ice sheet (Allison, 1979), of which 70% comprises the Lambert Glacier and its catchment basin. The Lambert Glacier is the largest glacier of the East Antarctic, and arguably the world's largest glacier system (Allison, 1979). Basal melting of the Amery Ice Shelf is thought to be a significant source of ice loss from the Lambert Glacier system (Williams et al., 1998b) with basal melting of ice shelves considered to account for approximately 20% of the ablation of the Antarctic ice sheet (Jacobs et al., 1992). The behaviour of the Lambert Glacier should reflect the overall state of the East

Antarctic Ice Sheet better than any other glacier because it drains such a large portion of East Antarctica (Allison, 1979).

Only recently has a combination of satellite and in-situ data provided the precise location of the grounding line of the Amery Ice Shelf (Fricker et al., 2002), altering the previous position by approximately 200 km, indicating a southern extent of the grounding line south of $73°S$. The ice shelf draft is thought to be quite well known (Ruddell, 2001), however efforts to map the seafloor beneath the ice shelf (BEDMAP; (Lythe et al., 2000)) have had difficulties due to sparse datasets. An additional aim of this part of the thesis is to use available tidal observations to further define the water column thickness (WCT; defined as the difference between the seabed depth and the ice shelf draft) beneath the Amery Ice Shelf through the use of a two-dimensional barotropic, hydrodynamic model (Chapter 8).

The current knowledge of the surface sediment distribution and modern day deposition processes beneath the Amery Ice Shelf have not been directly observed, and like sedimentation beneath all floating ice shelves, it can only be inferred from sediment cores taken from the open marine environment and theoretical studies (Orheim and Elverhoi, 1981; Drewry and Cooper, 1981; Barrett et al., 1987; Kellogg and Kellogg, 1988; Alley et al., 1989; Kennedy and Anderson, 1989; Anderson et al., 1991b; Domack et al., 1995; Domack and Harris, 1998). A discussion of these glacial-marine sedimentation processes is given in the next section.

6.3 Glacial-Marine Sedimentation

Many researchers have reviewed the processes of glacial-marine sedimentation. e.g., (Carey and Ahmed, 1961; Anderson et al., 1980; Drewry and Cooper, 1981; Molnia, 1983; Andrews and Matsch, 1983; Eyles et al., 1985; Kellogg and Kellogg, 1988; Anderson and Molnia, 1989; Hambrey, 1994; Anderson, 1999). The following discussion will initially introduce the primary processes of sediment supply, and then the secondary processes which redistribute, re-work or alter the structure of the sediment.

6.3.1 Sediment Delivery

The focus of this part of the thesis is on the sedimentation processes acting in the sub-ice-shelf zone of the glacial marine environment (Fig. 6.3). The model of sub-ice-shelf deposition as introduced by Domack and Harris (1998) is given here.

Deposition beneath large polar ice shelves is largely restricted to a zone (probably

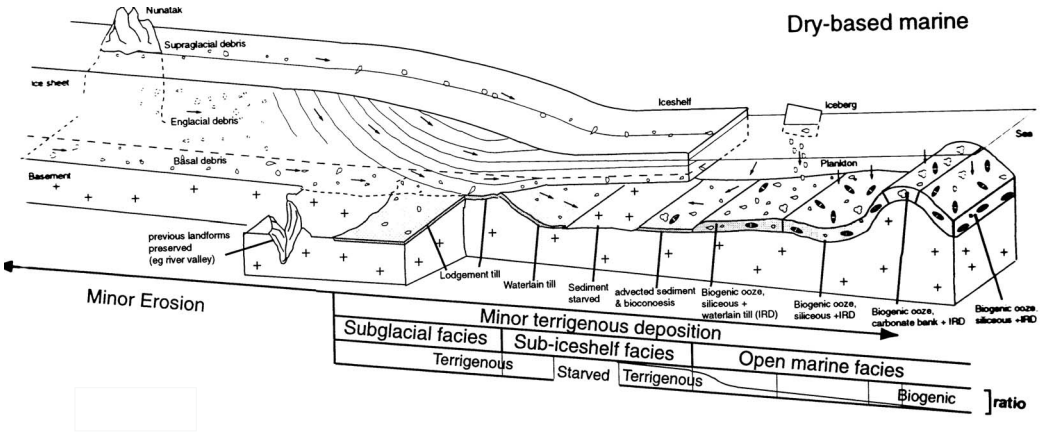

Figure 6.3: Glaciomarine sedimentation. From Whitehead (2000)

$< 100km$ width) near the grounding line. Landward of this zone is the 'lodgment till', identical to terrestrial lodgement deposits (Kellogg and Kellogg, 1988). It is generally a structureless diamicton, deposited by plastering on of glacial debris from the sliding base of a moving glacier by pressure melting and/or other mechanical processes. The lodgement till may be described as a non-stratified muddy sandstone or sandy mudstone with matrix supported clasts ($1 - 20\%$ of rock) with a reduction of water content of about 10% (Haase, 1986).

At the grounding line, where the ice shelf begins to float, seawater intrudes beneath the ice shelf to form a thin layer of water that expands in a seaward direction. In this zone, a number of processes control the deposition of the broadly termed 'waterlain till', including:

- A continuous rainout of basal debris from the floating ice shelf as a result of increased melt rates close to the grounding line;
- Presence, or absence, of subglacial outflow. Alley et al. (1989) suggest a supply of basal debris to the marine environment from beneath the Antarctic Ice Sheet. The fast flowing ice streams move over a water-saturated bed of till, thus deforming it and transporting it seawards. Transport ends when the ice stream merges with the floating ice shelf at the grounding line. Gravity flows and slump processes create a prograding complex of glacially derived, terrigenous rich, sediment, defined as a 'diamict apron';
- Currents, driven by tidal forcing and/or recirculation in the water column beneath the ice sheet basal debris zone, give rise to lateral advection of fine sediment grain sizes, winnowing out mud and fine sand to leave behind a coarse, granulated diamict facies with diffuse or whispy stratification. Domack and Harris (1998) suggest that cross bedding in a Ross Sea gravity core reflects the action of tidal currents at or near the

grounding line;

- Short term grounding line movements;
- Sea floor topography and water column thickness; and
- Sediment supply.

Deposition of ice shelf rafted debris is limited elsewhere beneath the ice shelf as a result of two major processes: the high melt rate at the grounding line; and, high surface accumulation rates which cause downward particle paths for ice and debris, i.e., any fallen rock debris or sands being blown on to the glacier surface upstream, and overlain by accumulated snow, is an additional source of ice rafted debris.

The facies characteristic of this 'grounding line' zone is a coarse, granulated diamict facies with possible diffuse or whispy stratification due to sorting as particles fall through the water column. Secondary processes, such as slumping and flow tills, may also have an influence resulting in a convoluted sedimentary structure (Hambrey, 1994).

Basal melting of ice shelves promotes sedimentation. Freezing of seawater at the base of the shelf may further isolate sediments from deposition. Any basal debris that has not been removed after melting near the grounding line is frozen in by bottom accumulation of saline ice and is therefore probably transported to the edge of the ice shelf and beyond. However, an absence of rock debris at the boundary between glacier and oceanic ice is observed in ice cores from the Amery Ice Shelf (Morgan, 1972), supporting the idea that the bulk of debris is lost in the melting zone at the grounding line of the ice shelf (Drewry and Cooper, 1981).

The granulated diamict reaches its greatest thickness at the grounding line and thins and becomes finer grained seawards, as the basal debris zone loses its load. Seawards of the zone influenced by raining basal debris, coarse material is rare, although some well sorted very fine sand may occur. Facies characteristic of this zone of sorted glacial marine muds is termed 'proximal glaciomarine sediment' by Domack and Harris (1998), and were described as laminated, to massively bedded mud. Occasional dropstones are also possibly observed in this facies.

With increasing distance seawards from the grounding line, and if the ice shelf is wide (greater than 5-10km), a 'null zone' of sedimentation occurs where only the finest particles are deposited, as the ice shelf is devoid of basal debris at this distance from the grounding line. Fine grained hemipelagic sediments are deposited after being advected landwards under the ice shelf by circulating currents, and this marine influence increases in seaward

direction. Marine sediment transported beneath the ice shelf contains diatoms and other phytoplankton along with fine grained iceberg-rafted debris deposited in the open marine environment. Biotic activity beneath ice shelves declines rapidly, in diversity and abundance, between the calving margin and the grounding line. The 'null zone' is represented by a well sorted, fine grained, massively bedded facies.

Seawards of the calving margin, deposition rates are much greater than beneath the ice shelf (Kellogg and Kellogg, 1988). Domack and Harris (1998) suggest that the calving line of the ice shelf is characterised by a concentration of coarse iceberg-rafted detritus having been deposited. Given that iceberg residence time is greater at an ice shelf barrier under favourable winds, than in the open marine setting, Domack and Harris (1998) suggest a high concentration of debris is expected to be deposited in this zone. This debris quite often has a different origin to the basal debris deposited near the grounding line (Anderson et al., 1991a).

Seawards of the ice shelf calving front, the influence of the open marine setting dominates, and the shelf is primarily composed of a siliceous mud and ooze (SMO), made up of diatom fragments with a minor ice-rafted terrigenous component, and is one of the most abundant surface sediment types of the Antarctic continental shelf (Anderson et al., 1984). SMO usually accumulates as a massively bedded unit of variable thickness, thickest ($\sim 5m$) in the troughs, and thinnest ($\sim 1m$) on the banks. The distribution of siliceous biogenic material on the inner continental shelf is strongly influenced by marine currents. Further north on the shallower outer banks of the shelf, calcareous sediments, comprising coccoliths and foraminifera, are found. These organisms settle directly to the bottom as part of the marine snow, or are predated and settle as faecal pellets. Carbonate biota, being composed of skeletal tests, is mostly confined to the coarse sand and gravel fractions. The gravel fraction consists of mainly bivalves, echinoderms and serpulid worms, while the sand fraction contains foraminifera, bryozoa and minor bivalves (Franklin, 1997). A brief introduction of diatoms, which account for a significant proportion of the Prydz Bay sediments (Taylor et al., 1997), is given here.

Diatoms

Diatoms (Division: Bacillariophyceae) are unicellular golden brown algae that inhabit the euphotic zone (generally $< 100m$) of almost all aquatic environments. They are characterised by an external box-like skeleton (frustule), and range in size from $1 - 1000\mu m$ (Barron, 1985). The frustule is comprised of hydrated amorphous silica which is deposited in a

regular pattern to create an ornamental cell surface made up of extensions, pores and striae. Taxonomy is based on the frustule structure and its ornamentation. Two diatom orders are recognised (Fig. 6.4; Medlin and Priddle, 1990): Centrales (radial symmetry) and Pennales (bilateral symmetry).

In the Antarctic marine environment, diatoms occur in high abundance and are the main primary producers, forming up to 90% of the suspended silica in surface water (Barron, 1985). Diatoms bloom in surface waters of polar seas in summer after being released from melting sea-ice. The diatoms then either settle through the water column, or become trapped within the ice when new ice forms. A variety of environmental variables including light, temperature, salinity, silica, sea-ice and water column stability, influence their distribution and abundance in the water column. Leventer and Harwood (1993) state that the understanding of how these variables control the distribution of specific species and species assemblages is a valuable tool for the reconstruction of past oceanographic and climatic conditions from the study of fossil diatoms.

Recycling, during sedimentation, and silica dissolution, prior to burial at the sediment-water interface, result in only a small proportion of the living diatom assemblage becoming preserved as part of the fossil assemblage.

Siliceous material in suspension tends to settle at a rate equivalent to that of $1-5\mu m$ quartz spheres (Lisitzin, 1971). The heaviest and coarsest diatom frustules take from 30-100 days to settle $5000m$ through the water column. The finest frustules may take tens of years. Over this period there is some lateral transport of the frustules by ocean currents which is generally ignored when interpreting downcore changes in the diatom assemblage to past oceanic conditions. Assuming there is no lateral transport of the diatoms is generally applicable, as the overlying living diatom assemblage does not differ from that of the underlying sediment (Taylor, 1999; Kozlova, 1966; Kozlova and Mukhina, 1967; Leventer and Dunbar, 1986, 1987, 1988). However, in a study of sub-ice-shelf sediments, where diatoms are not productive, lateral transport from productive open water is the only source of such material. Smayda (1970) commented on the settling rate of differing species of diatoms based on shape, size and other morphological attributes. In an environment where overlying diatom production does not exist, diatom settling rates may affect the distance over which a species is advected before deposition, thus altering the surface sediment diatom assemblage.

Only a small proportion of diatom frustules survive the sinking process as individuals (Gersonde and Wefer, 1987). Grazing by zooplankton incorporates the diatoms into faecal pellets which tends to both increase settling rate, and inhibit dissolution by enclosing them

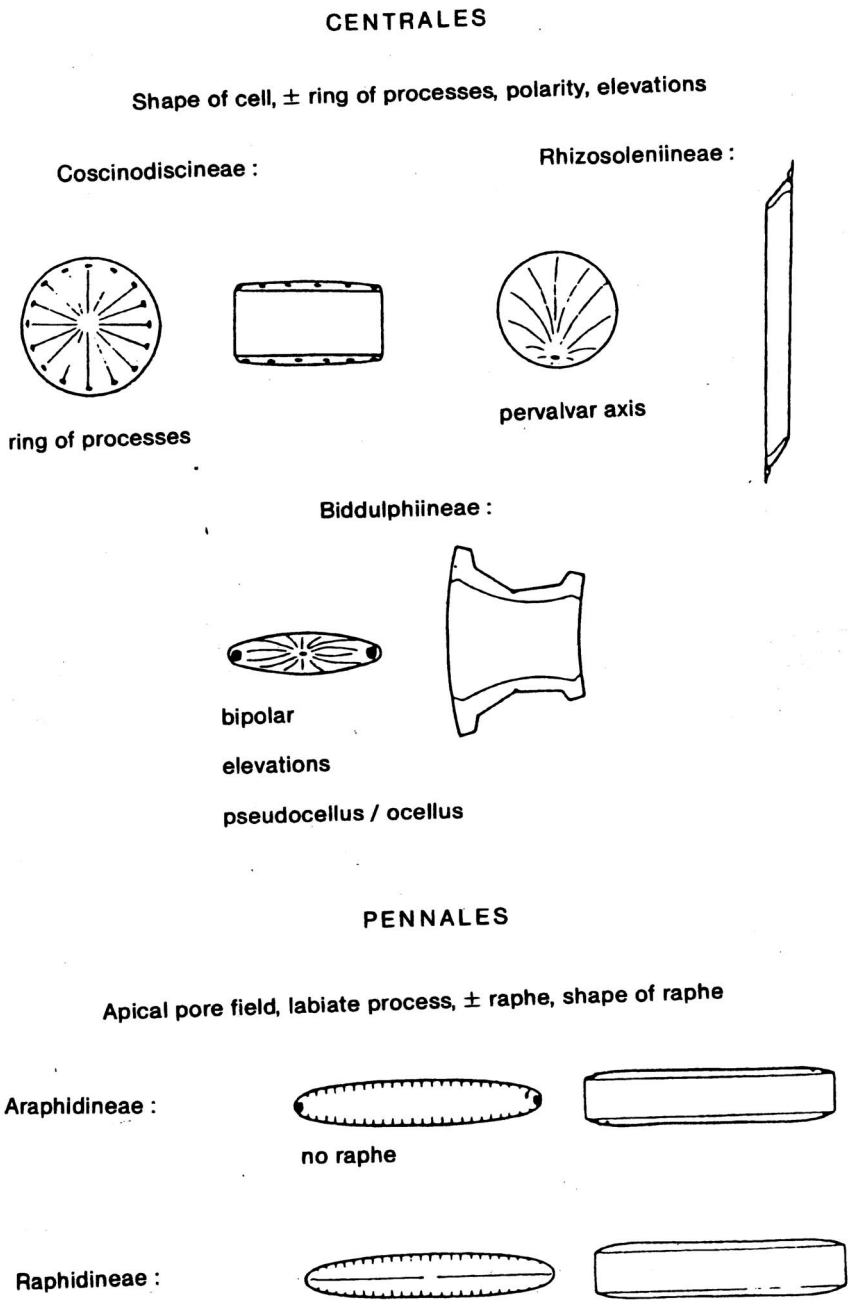

Figure 6.4: Diatom taxonomy. From Medlin and Priddle (1990)

in a protective membrane (Schrader, 1971). Faecal pellets act to rapidly transport silica from the active zone of dissolution in the surface layer, to a relatively passive zone at depth (Hurd, 1972). Grazing by zooplankton does not necessarily have a beneficial effect on frustule preservation. Mechanical breakage of the frustule by mastication, increasing the surface area, and chemical breakdown by digestion both increase the rate of frustule dissolution (Hurd, 1972). Frustule aggregation, formed during increased mucous secretion by diatoms (Smetacek, 1985), can also result in increased settling rates.

In Antarctic waters, dissolution of biogenic silica is exceptionally slow due to the low temperatures that prevail throughout the entire water column (Treguer et al., 1989). Stockwell et al. (1991) compared diatom assemblages in the water column with Holocene sediment assemblages from Prydz Bay, and concluded that diatom diversity is not greatly affected by dissolution. Past studies have demonstrated that fossil diatoms in Antarctic marine sediment can be used for proxies for past oceanographic and climatic conditions, including sea-surface temperature, water mass distribution and sea-ice distribution (Burckle, 1972; Kellogg and Truesdale, 1979; Leventer and Dunbar, 1988; Leventer, 1992; Leventer et al., 1993, 1996; Cunningham et al., 1999).

Taylor et al. (1997) assessed the surface diatoms assemblages of Prydz Bay from 97 surficial sediment samples, and employed a statistical cluster analysis to identify four diatom assemblages:

- a coastal assemblage, located mainly in the south-eastern section of Prydz Bay and characterised by sea-ice diatoms, notably *Fragilariopsis curta*;
- a continental shelf assemblage located over the inner and middle Prydz Bay and Mac-Robertson shelves, and characterised by sea-ice and ice edge diatoms;
- an oceanic assemblage located over Four Ladies Bank and the outer shelf to upper slope, characterised by open water diatoms, notably *Fragilariopsis kurguelensis*, and ;
- a Cape Darnley assemblage located over Fram Bank and characterised by heavily silicified sea-ice and open water diatoms.

The distribution of the assemblages is attributed to sea-ice conditions (coastal, shelf and oceanic assemblages) and ocean currents which have winnowed the surficial sediments on Fram Bank of fine-grained sizes, leaving a coarse lag deposit (Cape Darnley assemblage; Taylor et al., 1997).

Previous studies where sub-ice-shelf sediments have been collected from beneath a major embayed ice shelf (Clough and Hansen, 1979) returned no evidence of present day

diatom deposition. Some scientific discussion in the literature (Webb et al., 1979; Kellogg and Kellogg, 1981; Brady, 1983; Kellogg and Kellogg, 1983; Raiswell and Tan, 1985; Kellogg and Kellogg, 1986; Harwood et al., 1989) resulted with Kellogg and Kellogg (1986) believing diatoms were from the Miocene, as well as the Pliocene-Pleistocene, however, Harwood et al. (1989) concluded that all diatoms were of Miocene origin. Both interpretations implied that there is little or no modern landward transport of marine sediment beneath the ice shelf.

6.3.2 Oceanic Influence on Glacial-Marine Sedimentation

Ocean processes are important for the mobilisation and redistribution of sediments in the glaciomarine environment. The oceanic circulation on the Antarctic continental shelf is marked by seasonal melt and freeze of sea ice, prevailing winds off the ice sheet, and currents dominated by a westward drift and diurnal tides (Dunbar et al., 1985).

The depth of the Antarctic continental shelf and the presence of sea-ice over much of the year restricts the effects of swell and waves in reworking shelf sediments, implying there is no wave dominated coastal zone as found on continental shelves elsewhere. Thus, ocean currents and mass flow processes are the dominant energy type responsible for the physical reworking of sediments along the Antarctic Margin.

Bottom currents reach speeds of up to $1.96ms^{-1}$ (Hodgkinson et al., 1988) on the MacRobertson shelf, west of Prydz Bay. Within inner Prydz Bay, maximum bottom currents of $0.27ms^{-1}$ have been recorded (Hodgkinson et al., 1991a). Mean currents in each area have a magnitude of $0.49ms^{-1}$ and $0.05ms^{-1}$ respectively. These currents are comparable in terms of peak and mean velocities to those reported by Foldvik et al. (1985b) from the Weddell Sea of mean $0.06 - 0.07ms^{-1}$, and Pillsbury and Jacobs (1985) from near the Ross Ice Shelf of mean $0.05 - 0.09ms^{-1}$. Such currents of maximum magnitude reported above can scour sediments leaving a residual coarse-gravel lag deposit (Anderson et al., 1983). They are capable of resuspending, remobilising, or redistributing the finer fraction of the glacial marine sediment, especially if made less cohesive by bioturbation. Wind driven currents may redistribute sea ice and help maintain polynas, giving rise to regional variability in biological productivity. Currents are then able to transport the residue of that production. Ocean currents may also transport biogenic material into zones incapable of supporting life on their own, such as beneath the innermost parts of floating ice shelves (Hambrey, 1994).

The intensity of bottom currents is correlated with changes in grain size distribution, with regions of high activity being reflected in the winnowing of fine-grained lighter fractions (Huang and Watkins, 1977). Pudsey (1992) used the downcore grain size variation to infer

changes in bottom currents with time. Anderson and Kurtz (1985) suggest that this may be a gross simplification of the processes acting on the continental shelf. For example, fine particles ($< 30\ \mu m$) are maintained in suspension by very slow moving bottom currents ($< 4\ cms^{-1}$). Thus, deposition of fine silt and clay is generally assumed to occur via some physiochemical or biological aggregation (e.g., faecal pellets), and that size variations in deep-sea sediments are due to compositional differences, and not depositional processes (Anderson and Kurtz, 1985).

Tides have been proposed to be an important process beneath the floating ice masses; tidal mixing facilitates melting at the grounding line, which is capable of altering the mean sub-ice-shelf circulation (MacAyeal, 1984b). Tidal pumping at the grounding line are also thought to flush out suspended sediment, thus affecting the composition of sediment (Hambrey, 1994). Tidal currents may be strong enough to rework the seafloor, winnowing out the fine grained particles (Hambrey, 1994). Numerical tide simulations of the Ross Sea, and under the Ross Ice Shelf (MacAyeal, 1984a) and the Weddell Sea, and under the Filchner-Ronne Ice Shelves (Makinson and Nicholls, 1999; Robertson et al., 1998) show that periodic tidal currents of the order $30\ cms^{-1}$, drive steady residual barotropic circulation of the order of $10\ cms^{-1}$, capable of transporting marine sediments.

Sea ice formation is accompanied by a brine rejection which forms dense, salty shelf waters that accumulate in shelf depressions. As these depressions fill with this dense water, it may spill over the shelf edge flowing downslope as a strong gravity flow winnowing and/or eroding sediments from the shelf and slope - these waters may form Antarctic Bottom Water as they leave the shelf. Temporal and spatial variability in bottom water formation has been traced from down-core changes in East Antarctic sediments (Harris, 2000a; Harris et al., 2001a). The presence of sea ice also minimises the effects of wind on the water column, inhibiting mixing through the water column.

6.3.3 Sediment Reworking Processes

Other processes may significantly alter the structure and physical characteristics of the sediment.

Living organisms such as molluscs, crustaceans, worms and foraminifera (Franklin, 1997), which are sparsely spread through the sediment, play an important role in the mixing of that sediment. Bioturbation, or the reworking of sediments by benthic organisms, can destroy any sediment structure, and has the effect of making sediments less cohesive. This is common in glaciomarine sediments, and is recognised by mottling, or burrows, in the

sediment core.

The steep rugged Antarctic shelves suggest that subaquatic mass movement processes such as slipping, slumping, debris and turbidity flows are important. Ice rafted debris, which is unsorted, may become sorted by these processes.

When grounded ice advances across the sea floor, the sediment becomes overconsolidated, decreasing its water content. Prydz Bay is a thick glacial sequence where several overconsolidated horizons of diamictite are underlain by uncomformities (Hambrey et al., 1991).

6.4 Prydz Bay Oceanography

There have been numerous studies of the oceanography of Prydz Bay (Smith et al., 1984; Middleton and Humphries, 1989; Smith and Treguer, 1994; Wong, 1994; Nunez Vaz and Lennon, 1996; Wong et al., 1998). Oceanographic data collected as part of the Australian Biological Investigation of Marine Antarctic Systems and Stocks (BIOMASS) project, supplemented with data sets from French and Soviet cruises to the area, formed the basis of most of these studies. These were oppurtune data-sets, collected as part of the biological program, and hence not optimal for determining the physical oceanography of the region. The BIOMASS data lacked horizontal resolution in regions of oceanographic interest, such as the ice shelf front and over the continental slope (Wong, 1994). As a result, a more systematic oceanographic survey was carried out in Prydz Bay as part of the Fisheries and Oceanographic (FISHOG) voyage carried out by the Australian Antarctic Division in February 1992. From these data, Wong (1994) analysed the structure and dynamics of water masses and circulation. This work prompted interest in the interaction between the Amery Ice Shelf and the open ocean and the formation of the AMery Ice Shelf - Ocean interaction Research (AMISOR) program resulted. The AMISOR progam consists of a glaciological field component, a marine science field component, and modelling efforts at the Antarctic CRC in Hobart. At the time of this thesis (Dec, 2002), much of these data are still being processed by colleagues at the Antarctic CRC, and at present are unpublished. Some reference to unpublished work by personal communication will be given within the following chapters. A summary of the current knowledge of Prydz Bay oceanography, as presented by Wong et al. (1998), is given here.

On the continental shelf, the coldest waters ($< 2.0°C$) are found at an average depth of $\sim 200m$ proximal to the Amery Ice Shelf front. Warmer, saltier water is found at interme-

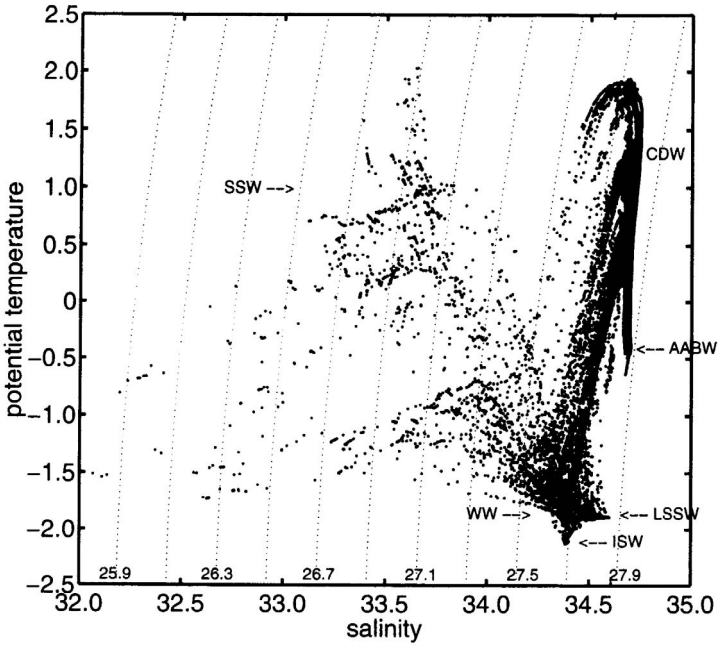

Figure 6.5: Prydz Bay FISHOG Potential Temperature-Salinity diagram. From Wong et al.(1998)

diate depths with shelf waters being generally saltier and warmer in the east than the west. Waters on the shelf are generally fresher and colder than waters beyond the shelf break. Sharp salinity gradients were observed near the coast in the FISHOG dataset (Wong, 1994).

6.4.1 Water Masses

By definition, relative to potential temperature and salinity, Wong et al. (1998) identified seven water masses in the vicinity of Prydz Bay (Fig. 6.5). The seven water masses are:

1. Summer Surface Water (SSW) is a distinct but highly variable layer whose temperature and salinity are dependent on the distribution and thickness of the sea-ice (Wong, 1994). The range in potential temperature in the FISHOG data is -1.8 to $+2.1°C$, and the salinity range is 30.6-34.2 psu (Wong, 1994). Within the shelf zone, SSW typically forms to a depth of 10-60 m.

2. Below the SSW layer, there is a layer of Winter Water (WW). This is a remnant of the winter mixed layer. The thickness of the WW layer varies from a maximum of 300 m over the continental shelf, to a minimum of $\sim 30m$ in the oceanic domain (Wong, 1994). Potential temperature ranges from $-1.9°C$ to $-1.5°C$, and the salinity range is $34.2 - 34.5$ psu.

3. Circumpolar Deep Water (CDW) is the most abundant water mass in the Antarctic

Oceanic domain. It is restricted to the oceanic part of the domain, its most southern extent associated with the deep upwelling which occurs at the Antarctic Divergence, at depths between 300 m and 3000 m. Potential temperature is in the range $0.0 - 2.0°C$ and salinity ranges from 34.67 to 34.75 psu.

4. Ice Shelf Water (ISW) is a saline, super-cooled, water mass with a potential temperature beneath the surface freezing point ($< 2.0°C$). The salinity range is $34.3 - 34.5$ psu in the FISHOG data (Wong, 1994). ISW was found in only a small region just to the north of the western side of the Amery Ice Shelf front. ISW is also observed immediately adjacent to the centre of ice shelf front (between longitudes 72 and $72.5°S$; Bindoff (2002)). This indicates interaction between Prydz Bay waters, and the ocean cavity beneath the ice shelf. ISW is formed by heat loss and freshening beneath the Amery Ice Shelf, and thus regions where ISW is observed would suggest regions of outflow from beneath the ice shelf. Evidence of ice crystals at depth (Penrose et al., 1994) are believed to have formed in a plume of supercooled water coming from beneath the ice shelf.

5. Modified Circumpolar Deep Water (MCDW), formed from the mixture of CDW and shelf waters, is found over most of the shelf. It is cooler and fresher than CDW with a potential temperature range of -1.5 to $-1.0°C$ and salinity range of 34.2 to 34.67 psu.

6. Low Salinity Shelf Water (LSSW) is referred to as High Salinity Shelf Water (HSSW) by Wong (1994). Both water masses are formed via the same mechanism; brine rejection during winter time sea-ice formation, however the saline shelf water found in Prydz Bay is not as saline as similar waters found in the Ross and Weddell Seas (Jacobs et al., 1970), and therefore, the distinction is made. LSSW has a potential temperature range of -2.0 to $-1.5°C$ and a salinity range of 34.5 - 34.6 psu, fully covering the saline shelf waters found in the deepest parts of the shelf in Prydz Bay.

7. Antarctic Bottom Water (AABW) is the deepest water mass close to the Antarctic continent and is characterised by potential temperatures less than $0°C$ and salinity ranging from 34.66 to 34.71 psu (Wong et al., 1998). AABW in the Prydz Bay region is classified into two types (Wong et al., 1998). A low salinity type ($S < 34.68$) and a high salinity type ($S > 34.68$). The low salinity type was generally observed to the east of Prydz Bay, and was believed to be formed due to the advection of Weddell Sea Bottom Water or Adelie Land Bottom Water. The high salinity AABW, generally observed in the western part of Prydz Bay, has anomalous water properties which cannot be explained by advection of bottom waters formed elsewhere (Wong et al., 1998). Wong et al. (1998) proposed that the high salinity AABW was formed locally. The local formation of AABW would require shelf

waters to reach a salinity range of 34.67 - 34.72 psu. If this water mass was sufficiently cold, it would be HSSW, but could only form if there was sufficient local brine rejection. Moorings deployed within Prydz Bay during the 2001 winter as part of the AMISOR program, showed no evidence of any water mass reaching these high salinities (Bindoff, 2002), suggesting local formation of AABW does not occur in Prydz Bay. Harris and O'Brien (1998) reported salinities of 34.65 from the deep basin off Mac Robertson land, suggesting a possible source of dense water.

6.4.2 Horizontal Circulation

Wong et al. (1998) calculated the geostrophic circulation from the FISHOG CTD data. Consistent with previous work (Nunez Vaz and Lennon, 1996; Smith et al., 1984), the geostrophic circulation in the Prydz Bay region was characterised by four main features.

1. An eastward zonal flow between $63 - 66°S$. This is characterised by waters from the broad, deep Antarctic Circumpolar Current (ACC), driven by prevailing westerly winds, transporting surface waters eastwards.

2. A narrow westward flowing slope current between $66 - 67°S$ associated with the east wind drift, which dominates south of the Antarctic Divergence (Wong, 1994). This current was estimated to have a transport of $\sim 0.2Sv$.

3. A strong ($\sim 8cms^{-1}$ (Wong, 1994)) westward flowing coastal current, driven by the mean easterly winds from the Antarctic plateau. This current is the principal source of inflow to Prydz Bay in the upper water column ($< 200m$).

4. A cyclonic gyre system, fed by a broad inflow of water from the northeast. The gyre is confined to the western half of Prydz Bay, centred at $(68.5°S, 73°E)$(Wong, 1994). The gyre has an average velocity of $\sim 1.5cms^{-1}$ (Wong, 1994). The gyre is recognised in contours of effective geopotential anomaly forming a dynamic low.

The gyre suggests the westward flowing coastal current could flow beneath the Amery Ice Shelf with a transport of $\sim 0.2 - 1.0$ Sv (Wong, 1994). This would introduce LSSW, or HSSW if it forms during winter, to the base of the Amery Ice Shelf at the eastern end of the ice front.

6.4.3 Tidal Motions

Prydz Bay Tidal Elevations

Prydz Bay experiences mixed diurnal-semidiurnal tides with a range of approximately 1-2 m. Tide gauges are situated at Davis and Zhong-Shan in south-east Prydz Bay, and Mawson

on the MacRobertson shelf to the west of the bay. King (2002) found that the Antarctic tide models CATS and CADA (Padman et al., 2002; section 6.5.1) are currently the best models available for modelling tides in the region, in comparison to other global tidal models which include the sub-ice-shelf cavity. e.g., FES99 (Lefevre et al., 2000).

Prydz Bay Tidal Currents

Hodgkinson et al. (1988, 1991a,b) gave detailed data reports of processed data from current meters moored in Prydz Bay. A tidal analysis of the currents was carried out and the periodic motions were summarised by Nunez Vaz and Lennon (1996). Moorings deployed at the front of the Amery Ice Shelf during the winter of 2001 as part of the AMISOR program were analysed for tidal constituents by Leffanue (2002). A brief overview of the tidal currents in Prydz Bay is given here. Details of the location of the current meters is left to Chapter 8 where they are presented for model comparison.

Tidal components of motion decrease from the shelf break towards the inner part of the bay. Close to the continental shelf break, strong tidal motions, predominantly of diurnal periods, with typical velocities of $0.25ms^{-1}$ were observed by Hodgkinson et al. (1988, 1991a,b). The major axis of the tidal ellipsoids were generally aligned north-south. As expected with strong tidal currents, O_1, K_1, M_2 and S_2 are the most significant tidal constituents. The semidiurnal constituents are greater at the top of the water column than the bottom. The opposite is true of the diurnal constituents. On the continental shelf edge, spring-neap variations are large, due to the similar magnitudes of the dominant diurnal constituents, O_1 and K_1.

In south-east Prydz Bay, north of Zhong-Shan, moorings reveal diurnal and semidiurnal current velocities $< 0.01ms^{-1}$ (Hodgkinson et al., 1988, 1991a,b). In the middle of the bay, non-tidal currents of order $0.1ms^{-1}$ were observed to dominate the tidal currents of order $0.05ms^{-1}$.

Moorings deployed during 2001 suggest similar characteristics. Tidal currents across the front of the Amery Ice Shelf front are typically of order $5cms^{-1}$. Maximum tidal currents of $\sim 12cms^{-1}$ are experienced on the far western ice shelf front mooring during periods of spring tides. The major axis of the tidal ellipsoids are generally alligned north-south, and O_1, K_1, M_2 and S_2 were the most significant tidal constituents. Tidal ellipsoids are relatively uniform with depth, except at the western most mooring, AM7-01, which showed significant tidal shear through the water column. The uppermost current meter (470 m) has a major axis aligned north west - south east for the major tidal constituents, with large

anticlockwise rotation. Further down the water column, the major axis of the tidal ellipsoids are alligned south west - north east with only small rotation for each constituent.

Current meter results are used for tidal model comparison in section 8.2.

Amery Ice Shelf Tidal Motion

Previous studies of the tides of the Amery Ice Shelf have been to determine tidal elevations, so that this "noise" can be removed from satellite altimeter data collected over the ice shelf for mass balance studies (King, 2002; Padman et al., 2002; Fricker and Padman, 2002). Thus, emphasis has been on determining the tidal elevations, rather than tidal currents.

Tidal motion is the source of the largest short-term vertical motion of an ice shelf, and therefore can be expected to have a significant impact on the ice shelf, particularly at the ice shelf front, the grounding zone, and in the shear margins. Holdsworth (1977) states that the tidal range at the hinge zone is a determining influence on whether glacier ice will become afloat without becoming detached from the continental ice. Tidal motions at the grounding line are responsible for some dynamic processes; Bending stresses in the floating ice (Holdsworth, 1977), and the pumping of water and sediments in the ocean cavity, although this effect is minimised by the presence of bottom crevasses in the ice, accommodating for flexure of the ice (Powell et al., 1996).

Tides also have a significant impact on the sub-ice-shelf cavities where they contribute to the melt and accumulation of basal ice, and hence mass balance calculations. Mixing in the sub-ice-shelf cavity alters the properties of water in contact with the base of the ice shelf and hence altered melt and freeze rates may occur.

King (2002) reviewed available tidal data for the Amery Ice Shelf, and presented additional GPS tidal elevation data from the Ice Shelf. It is convenient to present these data in section 8.2 for comparison to the barotropic model.

Further details of the current knowledge of the Amery Ice Shelf tides is presented in section 6.5.1; a discussion of existing barotropic tide models of the Amery Ice Shelf. All current knowledge of sub Amery Ice Shelf tidal currents is derived from the existing CATS/CADA models (Padman et al., 2002).

6.5 Numerical models of sub-ice-shelf circulation

Observations of the ocean cavity are physically difficult because of the ice shelf thickness, ranging from $\sim 2500m$ near the grounding line of the Amery Ice Shelf (Lythe et al., 2000)

to $\sim 200m$ near the ice shelf front. Some observations have been made in the ocean cavities, however they are sparse and of short time spans, e.g., Clough and Hansen (1979); Jacobs et al. (1979); Nicholls et al. (1991, 1997); Craven et al. (2001) and Craven et al. (2002). Due to these restrictions, the application of numerical models to the problem of sub-ice-shelf circulation has continued as an essential tool for understanding this environment.

Williams et al. (1998a) reviewed the mathematical models used to model sub-ice-shelf circulation. These include models driven by both tidal forcing alone (barotropic models), and thermohaline forcing alone (baroclinic models), including plume, two-dimensional and three-dimensional approaches.

This section reviews sub-ice-shelf circulation models which have been developed since the comprehensive Williams et al. (1998a) review.

6.5.1 Tidal Models

Further recent attempts have been made at large scale hydrodynamic tidal models which include ice shelf cavities within their domains. The most ambitious of these is the CATS and CADA models, presented by Padman et al. (2002).

CATS and CADA models

Padman et al. (2002) treat tides as noise that must be removed from satellite data collected over ice shelves, so their focus is the prediction of tidal height rather than tidal currents. They offer no discussion on the effects of tidal motion on circulation and mixing in the ice shelf cavities.

The Circum-Antarctic Tidal Simulation (CATS) model (Padman and Kottmeier, 2000) and the Circum-Antarctic Data Assimilation (CADA) model cover the entire southern ocean south of $\sim 56°S$ and attempt to predict the tidal constituents of elevation and velocity components both beneath the ice shelves, and in the open water surrounding the Antarctic continent.

As for each of the previous models of tides in the Southern Ocean including ice shelf cavities (Global tide models, FES95.2, (Le Provost et al., 1995), and FES98 (Lefevre et al., 2000); Ross Sea, (MacAyeal, 1984a); Weddell Sea, (Robertson et al., 1998; Makinson and Nicholls, 1999), CATS is a two-dimensional barotropic model application, where the ice shelf cavity is defined by a water column depth equivalent to the water column thickness (the difference between the ice draft and the seabed), and bottom friction in the cavity is doubled to represent drag both at the seabed, and at the base of the ice shelf. Errors in

these models are attributed to two sources: Simplifications in the model physics and errors in the water depth grid. Errors in the water depth are large beneath ice shelves, where inaccessibility means that the water column thickness in the sub-ice-shelf cavity is difficult to measure. Simplifications in model physics which are possible sources of error include parameterisations of bottom friction and lateral mixing. In the sub-ice-shelf cavity, the ice shelf is treated as a passive element floating freely on a perturbed, 'free' ocean surface. This ignores effects of flexural rigidity of the ice shelf, and may also contribute to model error. However this effect is thought to be important only within approximately 10 km of the grounding line (MacAyeal, 1984b).

To counteract for the effect of limitations in the knowledge of the water column thickness and the model simplifications, Padman et al. (2002) adopt a data assimilation approach. This model, CADA, uses tidal constituents determined from measurements to 'nudge' the dynamic CATS model towards satisfactory agreement with the data. The 'prior' solution is the CATS model, which models four diurnal (O_1, K_1, P_1 and Q_1), four semidiurnal (M_2, S_2, K_2 and N_2), and two long period (Mm and Mf) constituents on a domain south of $58°S$ on a grid with node spacing of $1/4°$ longitude by $1/12°$ latitude. The CATS model is driven by the global TPX05.1 tidal model at the boundary, and the tide generating force within the domain. Twenty five sea level records, consisting of tide gauges and bottom pressure recorders, were used for data assimilation within the domain. An additional 270 representers from the Topex/Poseidon data domain north of $\sim 66.2°S$ were also chosen for assimilation into the model.

A nominal requirement for tidal prediction accuracy was set at 10 cm (Padman et al., 2002). This requirement is generally met, however some regions of sparse assimilated data (The Ross Ice Shelf) have a standard deviation of the error of up to 22 cm. The East Antarctic coastline lies within relatively close proximity to the coverage of the Topex/Poseidon altimetry domain, except for the Amery Ice Shelf, and therefore tidal height predictions are quite good (Padman et al., 2002). Comparisons between short GPS records and CATS indicate an increase in error with increased distance south on the Amery Ice Shelf (King, 2002).

The CADA model indicates that tides in the Amery Ice Shelf cavity are mixed diurnal/semidiurnal. Tidal range is of the order 1-2 m. Tidal currents are typically less than $0.05 ms^{-1}$. An increase in phase from east to west for the major constituents (M_2, S_2, K_1 and O_1) is observed (Fig. 6.6). The M_2 tide has a node situated to the west of Mawson which significantly affects the M_2 tide in the Prydz Bay/ Amery Ice Shelf region. Ampli-

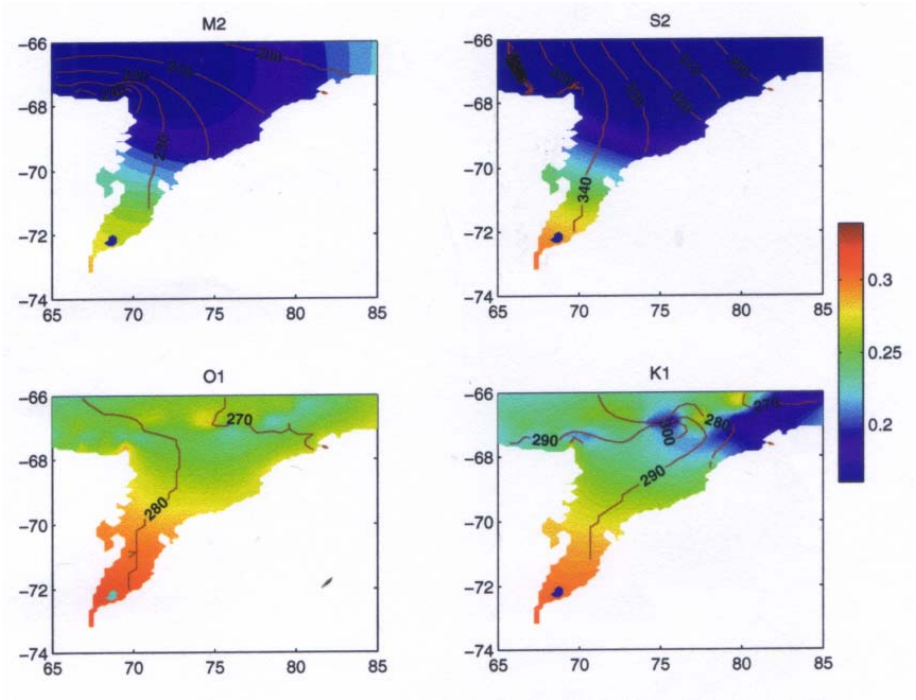

Figure 6.6: Amery Ice Shelf CADA predicted tides. From King (2001)

tudes along the Amery Ice Shelf show an increase from north to south of $\sim 150mm$ for the semidiurnal, and $50 - 100mm$ for the diurnal constituents.

Results of the CATS and CADA models are used for comparison to the barotropic model presented in Chapter 8.

6.5.2 Thermohaline models

The application of three-dimensional ocean circulation models has continued for the determination of the thermohaline circulation in the unique sub-ice-shelf cavity environment. Processes at the upper boundary dominate models of the baroclinic sub ice shelf circulation. Holland and Jenkins (1999) present a heirarchy of formulations to describe the thermodynamic interaction at the ice-ocean interface. A review of this process is presented here.

At equilibrium, a mixture of ice and water will always be at the freezing point. An input of heat will result in ice melt, and the water to remain at the freezing point. A withdrawal of heat to the surroundings will result in freezing.

The fundamental assumption of all models of the ice-ocean interface is that phase changes occur in thermodynamic equilibrium, so that temperature and salinity at the ice-ocean interface are always related by an expression for the freezing point at the appropriate depth (Holland and Jenkins, 1999). Away from the interface, the ice temperature decreases, resulting in a heat flux into the ice shelf. The ocean temperature may be higher (or lower)

than the freezing point, driving heat toward (or away from) the interface. Phase changes at the boundary also result in a fresh water flux, and thus alter salinity. This affects the freezing point and hence the temperature gradients in both the ice, and in the water.

Holland and Jenkins (1999) present three fundamental equations describing this interaction, which must be solved simultaneously.

A linearised version of the equation relating temperature, T and salinity, S at the ice-ocean interface:

$$T_b = aS_b + b + cp_b \tag{6.1}$$

where p_b is the pressure at the interface, and a, b, c are empirical constants with values of $-5.73 \times 10^{-2} {}^{\circ}Cpsu^{-1}, 9.39 \times 10^{-2} {}^{\circ}C$ and $-7.53 \times 10^{-8} {}^{\circ}CPa^{-1}$ respectively.

An equation balancing the divergence of the heat flux with the sink (source) of latent heat caused by melt (freeze):

$$Q_i^T - Q_M^T = Q_{latent}^T \tag{6.2}$$

where subscripts M and i indicate mixed layer and ice properties respectively, and the latent heat term is given by

$$Q_{latent}^T = \rho_M \Phi L_f \tag{6.3}$$

where $\rho_M \Phi$ represents the mass of ice that has frozen ($\Phi > 0$) or melted ($\Phi < 0$) per unit time, and L_f is the latent heat of fusion.

An equation describing the salt flux required to maintain the boundary salinity at S_b in the presence of a freshwater flux induced by the freeze/melt of ice with salinity S_i, balanced by the salt flux divergence at the interface:

$$Q_{brine}^S = -\rho_M \Phi \left(S_i - S_b\right) = Q_i^S - Q_M^S \tag{6.4}$$

Q_i^S represents the diffusive flux of salt into the ice shelf which is always zero. Following results of Oerter et al. (1992) and Eicken et al. (1994), measuring very low salinities in samples of marine ice found at the base of ice shelves, it is assumed that no salt is trapped within the ice during freezing and S_i is always zero.

The simplest approach used assumes the upper mixed layer of the ocean to relax instantaneously to the freezing point, thus there is no difference between the interface and mixed layer properties, and the ice-ocean interaction is described by equation 6.1 alone. Although simple, this approach determines the melt rate at the base of the ice shelf from the change in temperature of the ocean mixed layer. Therefore, it becomes a function of

model time step and mixed layer thickness. This is not ideal, and given that one of the main objectives of modelling ice-ocean interaction is to determine melt-rates at the ice-ocean interface, this approach is not used (Holland and Jenkins, 1999).

Recognising that the rate at which the mixed layer temperature relaxes toward the freezing temperature is a result of the diffusion of heat through the oceanic boundary layer. Estimates of each of the heat fluxes on the left hand side are made from equation 6.2.

$$Q_i^T = -\rho_i c_{pi} \kappa_i^T \frac{\partial T_i}{\partial z} |_b \tag{6.5}$$

$$Q_M^T = -\rho_M c_{pM} \kappa_M^T \frac{\partial T_M}{\partial z} |_b \tag{6.6}$$

where κ are thermal diffusivities adjacent to the ice-ocean interface, ρ are densities and c_p are specific heat capacities.

Equation 6.5 is a problem of estimating the temperature gradient at the ice shelf base, as all other terms are considered constant.

To solve equation 6.6, the boundary layer is assumed to be laminar, and thus T varies linearly between the interface and the mixed layer temperature. Thus, equation 6.6 becomes:

$$Q_M^T = -\rho_M c_{pM} \kappa_M^T \frac{(T_b - T_M)}{h}$$

where h is the boundary layer thickness.

Turbulence in the boundary layer results in a non-linear temperature profile. Thus:

$$Q_M^T = -\rho_M c_{pM} \gamma_T (T_b - T_M) \tag{6.7}$$

where γ_T is a thermal exchange velocity, which parameterises the effects of turbulence with the introduction of a Nusselt number, $Nu >> 1$, such that (Holland and Jenkins, 1999):

$$\gamma_T = \frac{Nu \kappa_M^T}{h}$$

.

Sub ice shelf models (Hellmer and Olbers, 1991; Determann and Gerdes, 1994; Grosfeld et al., 1997; Williams et al., 1998b; Williams, 1999) use this approach with a constant thermal exchange velocity of $1 \times 10^{-4}\ ms^{-1}$. Given that γ_T is a function of turbulence in the mixed layer, a more realistic approach is to treat it as a function of friction velocity at the ice-ocean interface, $u*$ (Holland and Jenkins, 1999; Jenkins and Holland, 2002; Williams

et al., 2002). An approximation is used in this study, taken from Figure 4: Holland and Jenkins (1999) where $\gamma_T = 0.01u*$.

This two equation formulation offers advantages in that it includes a diagnosis of the freeze rate. Thus, associated heat and freshwater fluxes may be applied to the model as per any other surface flux. Limitations of this formulation, however, are that to solve equation 6.1, the interface and mixed layer salinities must be assumed identical. This implies infinite salt diffusivity, whereas in reality, salt would be expected to diffuse at the same rate as, or slower than, heat. The errors associated with this assumption are expected to be small (Holland and Jenkins, 1999).

Holland and Jenkins (1999) present a three equation formulation which makes no prior assumptions about conditions at the interface. Analagous to equation 6.7, the remaining term on the right hand side of equation 6.4 is expressed:

$$Q_M^S = -\rho_M \gamma_S \left(S_b - S_M\right) \tag{6.8}$$

where γ_S is the salinity exchange velocity, which can be assumed constant, or as a function of friction velocity.

In each of these formulations, the pressure term in equation 6.1 is fundamental. At atmospheric pressure, the surface freezing point of seawater is about $-1.9°C$. The base of an ice shelf approaches depths of 2000m where the freezing point is as low as $-3.4°C$ (Millero, 1978). Even if seawater has been cooled to the surface freezing point by interaction with the atmosphere in open waters, it still has the potential to melt ice at depth. Melting at depth may potentially "supercool" the ocean to temperatures below the surface freezing point, generating "Ice Shelf Water" (ISW). If this "potentially supercooled" water is raised to the surface, in-situ supercooling would result, and frazil ice may form (Foldvik and Kvinge, 1974). The effect of supercooling in a sub ice-shelf environment was discussed by Doake (1976) and Robin (1979). Supposing a layer of water adjacent to the ice shelf base is maintained at the freezing point by phase changes, and currents and the slope of the ice shelf base drive the layer to greater depth, melting will result. Currents ascending an upward sloping base would cause freezing.

For the near freezing waters close to the Antarctic continent, density is determined almost entirely by salinity (Greisman, 1979). Therefore, the dilution caused by melting leads to upwelling, whereas the associated cooling has little impact on the water density, and acts more as a passive tracer of melting (Greisman, 1979). Positive buoyancy induced by melting

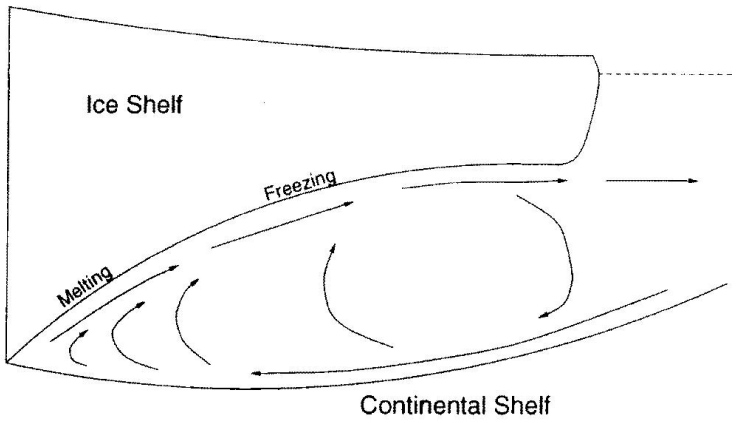

Figure 6.7: Overturning sub ice-shelf 'ice-pump' circulation. From Robin (1979)

is the driving force behind the overturning described by Robin (1979) (Fig. 6.7). This drives the circulation, where dense, cold, salty ocean water (LSSW or HSSW) flows beneath an ice shelf after having been formed in open waters through sea-ice freezing and brine rejection. Beneath the ice shelf, this water comes into contact with the shelf ice where it is warmer than the local freezing point, and hence causes melt. The melt freshens the seawater so that it rises again along the sloping underside of the ice shelf. It eventually reaches a point at which it is below the local freezing point again, and new ice crystals are formed and may adhere to the underside of the ice shelf in a layer known as 'marine ice'. This process was later referred to as an "ice pump" (Lewis and Perkin, 1986).

Three-dimensional circulation models have reproduced descending currents adjacent to the ice shelf, as a result of the dominant barotropic circulation, in contrast to the plume and two-dimensional models (Hellmer and Olbers, 1989; Hellmer and Jacobs, 1992, 1995) which generate currents ascending the ice shelf draft. These descending currents are capable of melting the ice, which allows for the formation of circulation systems which can melt ice off one side of a gyre and freeze ice onto the other side of the gyre, in effect forming a horizontal "ice pump" (Williams, 1999). The distribution of marine ice beneath the Amery Ice Shelf, obtained from the difference between a satellite altimeter derived ice thickness map which assumes hydrostatic equilibrium, and a second ice thickness map derived from airborne radio-echo sounding (RES) measurements which does not penetrate the marine ice, reflects the sub ice-shelf circulation (Fricker et al., 2001). Marine ice is thickest (up to 190 m) on the western side of the cavity, and thinnest (or non-existent) on the eastern side of the cavity (Fig. 6.8), consistent with accretion zones obtained from modelling the 3-D ocean circulation beneath the Amery Ice Shelf (see Chapter 9 or Williams et al., 2001).

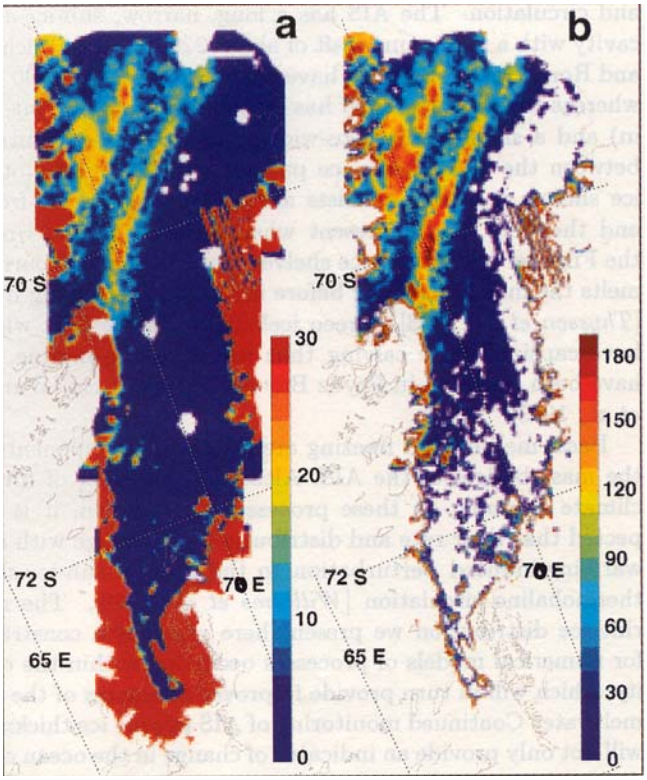

Figure 6.8: Distribution of a) hydrostatic height anomaly ($\delta h'$) and b) thickness of marine ice computed for the Amery Ice Shelf. Grey lines are a base map of the region. From Fricker et al. (2001)

Previous models

The Determann and Gerdes (1994) three-dimensional primitive-equation model, based on the work of Bryan (1969) and Cox (1984), adapted to σ-coordinates, has been applied to the realistic topography of the Filchner-Ronne Ice Shelf to derive typical sub-ice-shelf circulation patterns (Gerdes et al., 1999). Grosfeld and Gerdes (1998) included an open ocean coupled to the ice shelf cavity, allowing for free interaction between the open ocean and the ocean in the ice-shelf cavity, and assessed the effects of increased ocean temperatures and reduced sea-ice formation rates on the mass balance of the Filchner Ice Shelf.

Williams (1999) and Williams et al. (1998b, 2001, 2002) present applications of the same model to the Amery Ice Shelf cavity. The model domain generally covered only the cavity beneath the ice shelf, although some attempt at modelling the fluxes between the Amery Ice Shelf and Prydz Bay by the inclusion of Prydz Bay into the domain was made by Williams (1999). The model requires that the ice shelf calving front must run along a model parallel, which required a rotation of the model grid to best fit the ice front with a straight line. The model domain had a southern most extent of the grounding line of approximately $72.2°S$, and a maximum seabed depth of approximately 1200 m. More recent calculations

of the location of the grounding line (Fricker et al., 2002), and seismic work determining the ice shelf draft and seabed depth (Ruddell, 2001), indicate a southern most extent of the grounding line south of $73°S$, and large differences between ice shelf drafts and seabed depths in the model grid.

Current knowledge of the present day thermohaline driven circulation beneath the Amery Ice Shelf is taken from Williams et al. (2001). This built upon the knowledge obtained from the two-dimensional thermohaline model in the vertical plane beneath the Amery Ice Shelf (Hellmer and Jacobs, 1992). Simulations of the circulation show a predominant horizontal circulation that approximately follows contours of water column thickness. This is driven by the density gradient in the cavity which is strongly influenced by the heat and salt fluxes from melting and freezing processes occurring at the the ice-ocean interface, and by horizontal exchange of heat and salt occurring at the ice shelf front (Fig. 6.9). The dominant feature is a strong ($\sim 1-3Sv$) clockwise circulation called the Main Gyre (centred at $\sim 70.0°S, 71°E$) which accounts for most of the the meridional transport in the model (Fig. 6.9). It is positioned where the water column thickness is at a maximum in the model grid (Williams et al., 2001). Inflow into the cavity occurs across a broad region between approximately 72.5 and $74°E$. Most of this flow heads south into the Main Gyre (MG), turns west and north to flow along the western boundary out of the domain at $\sim 71°E$. Two weak topographically trapped gyres are observed in the north eastern portion of the ice shelf domain (NEG). South of the Main Gyre, an anticyclonic 'Southern Gyre' (SG) has flow heading south along the western boundary, before turning north at $\sim 71.8°S$, forming a broad flow along the eastern boundary. The overturning circulation is weak, and the vertical current shear is weak. Melting and freezing at the ice shelf base create a pressure torque that drives the rotational flow. In the top ocean layer, a 'plume' like behaviour occurs. Meltwater formed through melting near the grounding line rises along the base of the ice shelf. In the south, barotropic currents are small ($1-2cms^{-1}$), however currents in the top 'plume' layer can be much stronger ($6-10cms^{-1}$).

Williams et al. (1998b) assessed the impact of possible ocean climate change to the north of the Amery Ice Shelf. They found that when adjacent seas were assumed to warm by $1°C$, the net loss from the Amery Ice Shelf from excess basal melting over freezing increased from approximately $7.8Gta^{-1}$ under present day conditions to $31.6Gta^{-1}$, from which they conclude that the ice shelf geometry would be expected to be altered substantially. Williams et al. (2002) improved model physics to include boundary conditions at the ice-ocean interface as derived from the three equation formulation of Holland and Jenkins

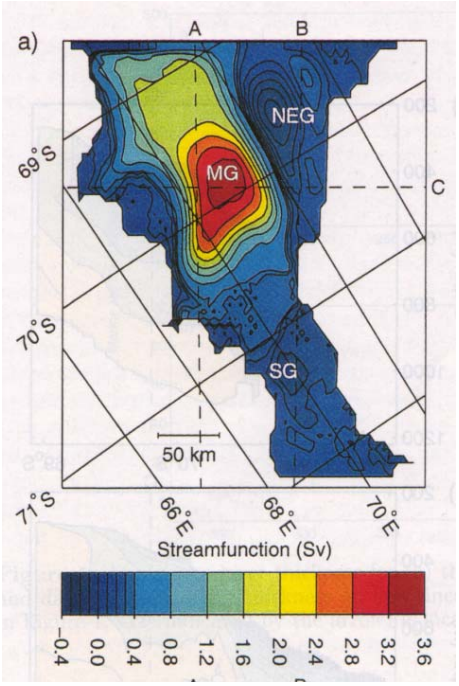

Figure 6.9: Horizontal sub Amery Ice-Shelf circulation stream function (Sv). Clockwise circulation about positive features. MG is the Main Gyre, NEG is the North-Eastern Gyre, and SG is the Southern Gyre. From Williams et al (2002)

(1999). This alteration significantly changed results, with present day net melting from the ice shelf calculated as $14.2Gta^{-1}$ (which more closely matches the oceanographic observational estimates of $14.7Gta^{-1}$; Wong et al., 1998), increasing to $\sim 39Gta^{-1}$ for a $1°C$ rise in ocean temperature, and increased to $96.1Gta^{-1}$ for a $3°C$ rise in ocean temperature.

Holland and Jenkins (2001) modified an isopycnic coordinate ocean general circulation model, the Miami Isopycnic Coordinate Ocean Model (MICOM; Bleck et al. (1992)), to incorporate a floating ice shelf as an upper boundary to the model domain. The modified model allows the introduction of an arbitrary surface pressure field, and includes entrainment into, and detrainment from, a surface mixed layer. Holland and Jenkins (2001) applied their model to an idealised ice shelf-ocean geometry similar to the tests of Grosfeld et al. (1997). A similar cyclonic circulation to Grosfeld et al. (1997) beneath the ice shelf, with high melt in the deep south eastern corner of the ice shelf covered region, and freeze in the shallower north western corner of the ice shelf covered region. Contrary to the results of Grosfeld et al. (1997), Holland and Jenkins (2001) found the abrupt change in water column thickness at the ice shelf front does not form a barrier to bouyancy driven circulation across the ice front, allowing exchange between the cavity in the south and the open ocean to the north.

An important difference between the models of Holland and Jenkins (2001) and Grosfeld et al. (1997) is the parameterisation of vertical heat transfer. Holland and Jenkins (2001)

use the three equation formulation (Holland and Jenkins, 1999) discussed previously, which Williams et al. (2002) indicate gives much more realistic estimates compared to oceanographic observations of net mass loss due to melting, whereas Grosfeld et al. (1997) use the vertical heat transfer parameterisation introduced by Hellmer and Olbers (1989). Grosfeld et al. (1997) however, also consider the transfer of salt, which was not considered previously by Hellmer and Olbers (1989).

The choice of isopycnic coordinates is advantageous for the study of density driven flows such as found beneath an ice shelf. It avoids problems of estimating pressure gradients as in the σ-coordinate system used by Determann and Gerdes (1994); Grosfeld et al. (1997); Williams et al. (1998b); Williams (1999); Williams et al. (2001, 2002) and this study. However the surface mixed layer is not well represented and requires the addition of a non-isopycnic layer at the top of the water column which can allow for bouyancy forcing (Holland and Jenkins, 2001). This makes the model quite complex, given the surface topography imposed by an ice shelf.

Jenkins and Holland (2002) applied the isopycnic coordinate model to a study of the ocean circulation beneath the Filchner-Ronne Ice Shelf, with the aim of investigating the bouyancy forced circulation on the continental shelf. A general anticyclonic circulation develops beneath the ice shelf in the model so that shelf waters entering the cavity in the west emerge colder and fresher in the east. This outflow contributes to a dense current that spills off the continental shelf and descends the continental slope, consistent with oceanographic observations which describe the overflow as a major source of Weddell Sea Bottom Water (Foldvik et al., 1985a; Nicholls and Makinson, 1998; Foldvik et al., 2001; Nicholls et al., 2001).

Chapter 7

Sedimentological Signature of Sub-Ice-Shelf Circulation

7.1 Introduction

Very few hard data are available on the sedimentation beneath floating ice shelves. The only previously collected sediments taken from beneath existing Antarctic ice shelves are those from just two sites: site J-9 as part of the Ross Ice Shelf Project (RISP; Clough and Hansen (1979), and one site from beneath the Novolazarevskiy Ice Shelf (Kolobov and Savatyugin, 1983). The age and origin of the RISP sediments remain unresolved (Webb et al., 1979; Kellogg and Kellogg, 1986; Harwood et al., 1989), and no evidence of Holocene age sediments was found. The sub Novolazarevskiy Ice Shelf sediments indicate contemporary, stagnant sedimentation conditions (Kolobov and Savatyugin, 1983).

The aims of this chapter are to qualitatively assess the relationship between the observed sediment distribution beneath the Amery Ice Shelf, and the sub-ice-shelf circulation. To carry out these aims, the spatial variability of sediment properties is required. This chapter details the collection, analysis methods, results and discussion of newly collected sub-ice-shelf sediments, and surface sediments collected adjacent to the ice shelf front. An interpretation of downcore changes in physical sedimentology and diatom assemblages as a response to the glacial history of the Amery Ice Shelf is also presented.

7.2 Sediment Collection

A new sub-ice-shelf sediment core was collected during the Austral summer of 2000/2001, from site AM02 ($69°42.8'S, 72°38.4'E$; (Craven et al., 2001)) beneath the Amery Ice Shelf, East Antarctica. This site is located approximtely 80 km southwards of the floating ice shelf edge. Based on numerical model results (Williams et al., 1998b), the AM02 site is thought to be a region of oceanic water inflow and basal melt (Fricker et al., 2001). At the site, the seafloor is 843 m below the ice shelf surface and the ice shelf is 373 m thick. A surface sediment sample from the AM01 hot water drill site ($69°26.5'S, 71°25.0'E$; (Craven et al., 2002)), occupied during the 2001/2002 summer, was also collected. AM01 lies approximately 50 km to the west of AM02, approximately 100 km from the open water of Prydz Bay, in a region of Ice Shelf Water (ISW) outflow and basal freeze. At AM01, the ice shelf is 479 m thick, of which the lower ~ 200 m is marine ice (Fricker et al., 2001), and the seafloor is 840 m below the ice shelf surface. The location of AM01 and AM02 are shown in Figure 7.1.

At both sites AM01 and AM02, an access hole was drilled through the ice shelf using a hot water drill as part of the Australian National Antarctic Research Expeditions (ANARE) Amery Ice Shelf Oceanographic Research (AMISOR) program. A gravity corer 10 cm in diameter and 150 cm long was lowered to the seafloor by winch. A 144 cm core was collected at site AM02. Attempts to retrieve a gravity core from the seafloor at site AM01 failed, however a surface sediment grab sample was obtained.

In addition to the sub-ice-shelf sediments, 23 Shipek surface sediment grabs were collected from immediately adjacent to the calving ice front of the Amery Ice Shelf. Eleven of these were collected from the RSV Aurora Australis during the 2000/2001 AMISOR voyage 6 (au0106) oceanographic program, and the remaining 12 grabs were collected during the 2001/2002 AMISOR voyage 7 (au0207). During both voyages, Acoustic Doppler Current Profiler (ADCP) measurements were taken concurrently along the ice shelf front, and CTD profiles were collected across the ice shelf front (Rosenberg et al., 2002). The location of the two sub-ice-shelf collection sites, and the 23 ice front grab locations are shown in Figure 7.1. Details of the collected sediments are contained in Table 7.1.

7.3 Methods

On return to Australia, the AM02 core was X-radiographed to examine any sedimentary structures present, and Ice Rafted Debris (IRD) granules ($2 - 4$ mm) and pebbles ($4 - 64$ mm) were counted for each 5 cm interval downcore. The AM02 core was then split,

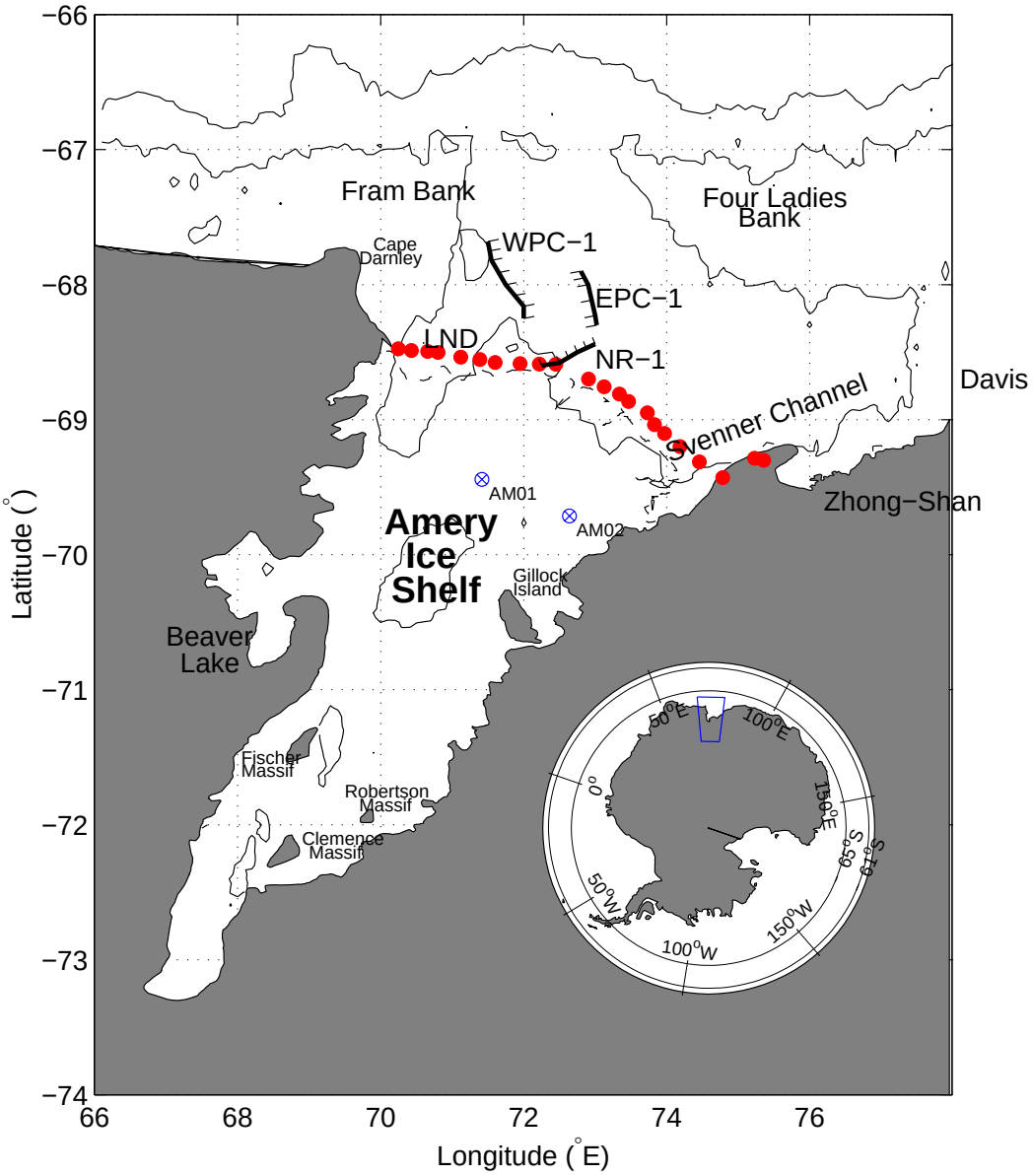

Figure 7.1: The location of the sub-ice-shelf core sites AM01 and AM02 (open circles with x), and the location of the 23 surface grabs from adjacent to the ice shelf front (solid circles). Major grounding line positions as determined by seismic reflection (Domack et al., 1998) are indicated. Grounding line "moraines" are named geographically and are the Eastern Prydz Channel 1 (EPC-1), Nella Rim 1 (NR-1) and Western Prydz Channel 1 (WPC-1). Hachures mark the steep, seaward slope of the grounding line "moraines".

Table 7.1: Details of sediment samples collected from beneath, and adjacent to the front of, the Amery Ice Shelf

Voyage	Sample No.	Latitude	Longitude	Water Depth (m)	Description
AM02	AM02	$69°42.8'S$	$72°38.4'E$	843	144 cm core. Description in text.
AM01	AM01	$69°26.5'S$	$71°25.0'E$	840	Fine dark olive grey mud.
au0106	GR01	$69°9.1'S$	$73°58.1'E$	713	Olive grey SMO & sparse black gravel
	GR02	$69°12.0'S$	$74°11.2'E$	674	Olive grey sandy mud
	GR03	$68°57.0'S$	$73°44.0'E$	724	Olive grey SMO
	GR04	$68°45.4'S$	$73°7.5'E$	783	Olive grey SMO
	GR05	$68°38.6'S$	$72°42.4'E$	508	1 cm diam. rock, trace sand.
	GR06	$68°35.1'S$	$71°57.0'E$	439	Sandy Gravel
	GR07	$68°32.3'S$	$71°7.2'E$	593	Olive grey SMO
	GR08	$68°29.3'S$	$70°25.8'E$	1111	Muddy sand
	GR09	$68°28.5'S$	$70°14.8'E$	332	Muddy sandy gravel. Contains Byrozoan & seaweed.
	GR10	$69°18.8'S$	$74°27.5'E$	775	Olive grey SMO
	GR11	$69°25.7'S$	$74°47.1'E$	292	Coarse gravelly sand.
au0107	GR01	$68°29.7'S$	$70°39.4'E$	874	Fine dark olive grey mud
	GR02	$68°30.1'S$	$70°48.1'E$	760	Fine dark olive grey mud.
	GR03	$68°33.2'S$	$71°23.2'E$	508	Coarse gravelly sand.
	GR04	$68°34.6'S$	$71°36.0'E$	486	Coarse sandy gravel. seaweed
	GR05	$68°35.3'S$	$72°13.2'E$	494	Coarse sandy mud with gravel.
	GR06	$68°35.3'S$	$72°27.0'E$	498	Coarse sandy mud with gravel.
	GR07	$68°42.0'S$	$72°54.2'E$	705	Coarse sandy mud with gravel & seaweed.
	GR08	$68°48.6'S$	$73°20.3'E$	784	Light Olive grey sandy mud.
	GR09	$68°51.9'S$	$73°28.1'E$	771	Olive grey SMO.
	GR10	$69°2.5'S$	$73°49.7'E$	697	Olive grey SMO.
	GR11	$69°17.2'S$	$75°13.7'E$	744	Olive grey SMO.
	GR12	$69°18.0'S$	$75°21.3'E$	608	Olive grey SMO.

visual descriptions prepared, and digital photographs of the core archive were taken. Core photographs and x-radiograph images are contained in Appendix E. The split core was then passed through a GEOTEK MS-2 multi-sensor core logger, logging at 1 cm intervals. The GEOTEK logs for Magnetic Susceptibility (MS) using a Bartington loop sensor, wet bulk density by measuring the gamma ray attenuation of the sediment from a Cs-137 source, and p-wave velocity by measuring the travel time of a 500kHz ultrasonic compressional pulse across the core. Fractional porosity, FP, may be determined directly from the wet bulk density, WBD, using the equation:

$$FP = \frac{\rho_{MG} - WBD}{\rho_{MG} - \rho}$$

where ρ_{MG} is the mineral grain density, defined as 2650 kgm^{-3} for high silica Antarctic shelf sediments, and ρ is the water density, defined as 1028 kgm^{-3}. This calculation assumes that the sediment is fully saturated. Dry bulk density, DBD, is determined using the equation:

$$DBD = WBD - \rho FP$$

Four Accelerator Mass Spectrometry (AMS) ^{14}C dates were obtained on bulk organic carbon (with dilute HCl pre-treatment) by the Institute of Geological and Nuclear Sciences,

Lower Hutt, New Zealand, from samples at 0-1 cm, 12 ± 0.5 cm, 37 ± 0.5 cm, and 51-52 cm of the AM02 core. An AMS ^{14}C date was also obtained for the AM01 surface sediment grab.

Samples of approximately 10 g taken from each of the surface sediment grabs, AM01 and grabs from the calving ice front, and every 5 cm from core AM02, were analysed for biogenic opal using the method outlined by Mortlock and Froelich (1989), and grain-size distribution using a Malvern Mastersizer 2000 laser particle sizer. Water content was determined from wet weight to dry weight comparison. Total Organic Carbon (TOC) was determined for the surface grabs collected during voyage au0106, and the upper 60 cm of core AM02, sampled at 5 cm intervals.

The diatom assemblages of the upper 55 cm of the AM02 core, sampled at 1 or 5 cm intervals, and of surface samples from AM01, and au0106 grab 1, au0106 grab 3, and au0207 grab1 from the calving ice front, were determined. Permanent slides were made using a variant of the method of Armand (1997), after initial oxidisation of the organic material, and the removal of any carbonates.

Diatoms were identified and counted using a Zeiss microscope at 1000x magnification, with an oil immersion objective lens. Each slide was traversed horizontally until 500 valves had been counted. Only valves in which more than half of the valve was intact were counted to avoid counting the same specimen twice. For elongate species such as *Trichotoxin* and *Thalassiothrix*, only end pieces were counted as these valves are rarely preserved intact. Diatom abundances were expressed as a percentage of the total number of cells. Absolute diatom abundance was computed using the method of Sancetta and Calvert (1988), which relates the number of valves counted on a slide to the proportion of the area on the slide that was counted, taking into account dilution factors and the weight of sediment processed.

$$ADA = \frac{N_{diatoms} \times A_{petri}(mm^2)}{(A_{FOV}(mm^2) \times N_{FOV}) \times (N_{drops} \times 0.15ml)} \times \frac{50ml}{dryweight(g)} \qquad (7.1)$$

where the A_{petri} is the area of the petri dish, used as the settling chamber is 1964 mm^2 (5 cm in diameter) and the area of the field of view (A_{FOV}) at 100X magnification is 0.031 mm^2 (200 μm diameter). $N_{diatoms}$ is the total count of diatoms, and N_{FOV} is the number of fields of view counted. The slide contains N_{drops} 0.15 ml drops of a 50 ml dilution of sediment mix.

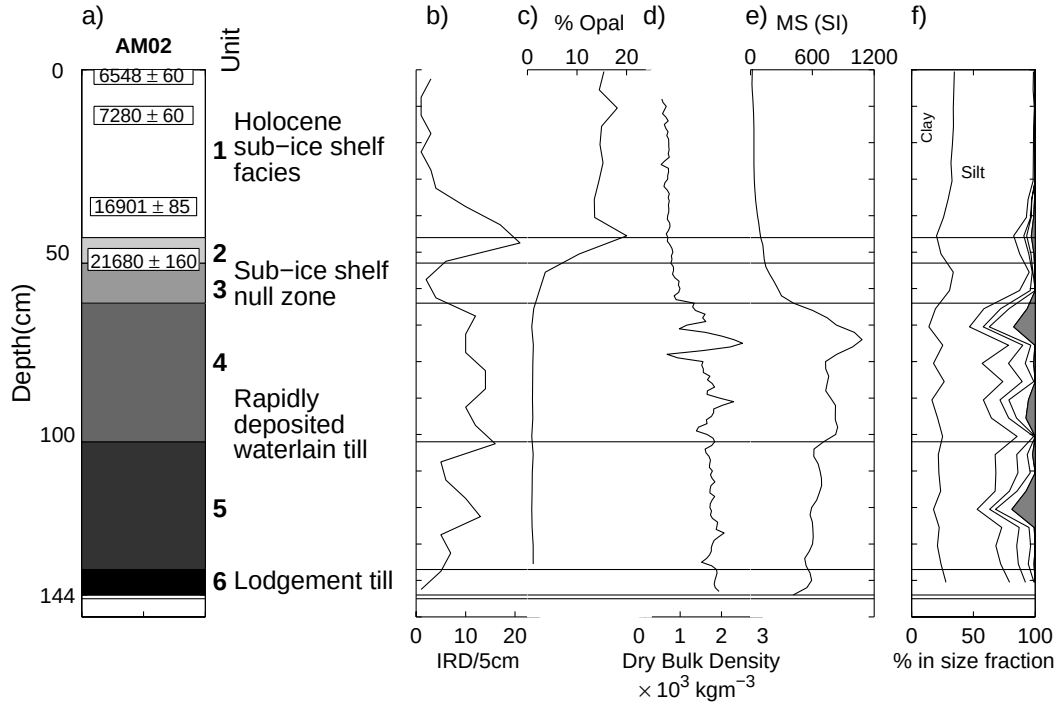

Figure 7.2: Visual AM02 corelog and down core profiles. (a) Visual core log showing facies succession. Numbers shown are uncorrected radiocarbon dates (with error limits). The laboratory reference numbers from the New Zealand Institute of Geological and Nuclear Sciences, Rafter Radiocarbon Laboratory, Lower Hutt (NZA) are NZA 13747 (0-1 cm), NZA 15924 (12 cm), NZA 15925 (37 cm) and NZA 13748 (51-52 cm). (b) Ice-rafted (gravel) debris (IRD) count per 5 cm. (c) Percentage biogenic opal per dry weight sediment. (d) Dry Bulk Density (kgm^{-3}). (e) Magnetic Susceptibility (MS), and (f) Grain-size distibution of the mud and sand fraction (up to 2 mm diameter). Contours are at 3.9, 62.5, 125, 250 and 500 μm. The component larger than 500μm is shaded. The core contains six units as indicated, the uppermost being siliceous mud and ooze of Holocene age.

7.4 Results

7.4.1 The AM02 core

Core Log Description

The AM02 core comprises six distinct lithological units (Figure 7.2):

Unit 6, at the base of the core from 138-144 cm, is an olive black, de-watered compacted muddy sand. The unit is too dense to observe IRD in the X-radiographs. Biogenic opal content is low (< 2%). An upwards increase in MS from 550 SI at the base to 600 SI, is accompanied by an upwards increase in fractional porosity (0.3 - 0.35) and upwards decrease in dry bulk density (2000 - 1700 kgm^{-3}).

Unit 5, from 103-137 cm, is an olive black, moderately-sorted sandy mud. Visual inspection of the core show slight laminations or bioturbation with olive grey laminations, however the density contrast in this material is too low for these features to be resolved

by the X-radiographs. IRD and MS increase upwards from the base of the unit. The IRD count shows large variation between 5 - 12 /5 cm interval. Biogenic opal content remains low (< 2%). Fractional porosity and dry bulk density are variable, as a result of the high IRD count, about a mean of ~ 0.45 and 1800 kgm^{-3} respectively. Water content remains relatively constant at $\sim 20\%$.

Unit 4, from 65-102 cm, is an olive grey, poorly sorted, massively bedded diamicton containing numerous gravel to pebble size clasts. IRD count is high (10-15 /5 cm interval) throughout the unit. Biogenic content remains low. MS reaches a peak of 1080 SI at 80 cm (associated with a cobble), and is in excess of 600 SI throughout the unit. Fractional porosity and dry bulk density indicate large variability associated with the high IRD counts, although a general increase (0.4 - 0.5) and decrease (1800 - 1500 kgm^{-3}) respectively is observed upwards through the unit.

Unit 3, from 54-64 cm, is an olive grey, well-sorted, massively-bedded, very fine grained silt. IRD is minimal in the unit and biogenic opal content increases from background levels (< 3%) to greater than 6% at 54 cm. MS decreases rapidly between unit 4 below, and unit 2 above, decreasing from ~ 600 SI to ~ 100 SI. Fractional porosity and water content indicate a large upwards increase of (0.5 - 0.8) and (20 - 45%) respectively, and dry bulk density shows a sharp upwards decrease ($\sim 1500 - 1200\ kgm^{-3}$).

Unit 2, from 46-53 cm, contains a light olive grey siliceous mud and diatom ooze with reddish brown laminae and olive grey mottles. Some cross laminations are observed in the X-radiographs of the unit (Appendix E). A high count of 1-2 mm sized granules (20 /5 cm interval) are observed in the X-radiographs, which appear to be associated with the reddish brown laminae. Biogenic opal content increases upwards through the unit from 6 to 20 %. MS is low (< 100 SI). Fractional porosity (~ 0.8), a relatively low dry bulk density (~ 800 kgm^{-3}), and water content (50%) each remain uniform.

Unit 1, from 0-45 cm is a light olive grey, massively bedded, siliceous mud and diatom ooze. A single burrow is observed between 30-40 cm. Gravel content is insignificant above 35 cm, decreasing rapidly from unit 2 below, and biogenic opal levels remain high (13-20 %). Maxima of biogenic opal content are observed at 10-11 cm (18.12 %), and 45-46 cm (20.05 %). MS is low throughout the unit, Fractional porosity and dry bulk density are uniform with values of 0.85 and 700 kgm^{-3} respectively. The top 6 cm is disturbed, having separated from the rest of the core.

Radiocarbon dates

AM02 downcore AMS ^{14}C dates, and the surface AM01 age, are listed in Table 7.2.

Table 7.2: AMS ^{14}C ages for bulk organic carbon samples from the sub-Amery Ice Shelf sediments.

Core No.	Depth (cm)	Age yr BP	± yrs BP	Corrected age[a]	Lab Ref. No.[b]
AM01[c]	0-1	11722	60	0	NZA 15923
AM02[d]	0-1	6548	60	0	NZA 13747
	12	7280	60	732	NZA 15924
	37	16901	85	10353	NZA 15925
	51-52	21680	160	15132	NZA 13748

[a]Corrected ages were determined by subtracting the surface age from all ages in the core.
[b]The laboratory reference numbers are from the New Zealand Institute of Geological and Nuclear Sciences Rafter Radiocarbon Laboratory, Lower Hutt.
[c]From $69°26.5'S, 71°25.0'E$
[d]From $69°42.8'S, 72°38.4'E$

When dating deep Antarctic marine sediments, a lack of calcium carbonate or large marine fossils requires dating bulk organic carbon, and using a standard reservoir correction value does not always result in bringing sediment core tops to modern age. AMS ^{14}C ages determined from the bulk organic matter contained in surface (0-1 cm) sediments were measured at 6548 ± 60 ^{14}C yr BP for core AM02, and 11722 ^{14}C yr BP for the AM01 surface sample. These surface ages are much older than the accepted ocean reservoir correction for Antarctica (1300 yrs; Berkman and Forman (1996)) but are within the range of bulk organic carbon samples from the Antarctic shelf (Andrews et al., 1999) and those of Prydz Bay (up to 9000 ^{14}C yrs; Harris (2002)). The greater reservoir effect in Antarctic waters is believed to arise from the depletion of ^{14}C in oceanic surface water around Antarctica, and relates to the antiquity of the carbon pool in the Southern Ocean (Berkman et al., 1998). The depletion of ^{14}C results in modern radiocarbon ages for Antarctic marine samples that appear too old. It is likely that factors including bioturbation and deposition of allocthonous recycled organic matter which dilutes the ^{14}C content of the TOC and affects the AMS ^{14}C age (Harris et al., 1996a) have affected the apparent surface ages. Andrews et al. (1999) present an inverse relationship between surface age and sediment accumulation rate on the Antarctic shelf. Therefore, in the sub-ice-shelf environment of very low accumulation rates (mean 0.03 mma^1), the surface age could be expected to be large.

In order to derive a chronology for the AM02 core, the AM02 surface age was subtracted from the ages lower down the core, as is consistent with other shelf workers (Andrews et al., 1999; Cunningham et al., 1999; Pudsey and Evans, 2001). This method assumes that contamination is constant with time, and assumes an age offset due to the reservoir effect. The progressively increasing ages downcore help to justify this assumption.

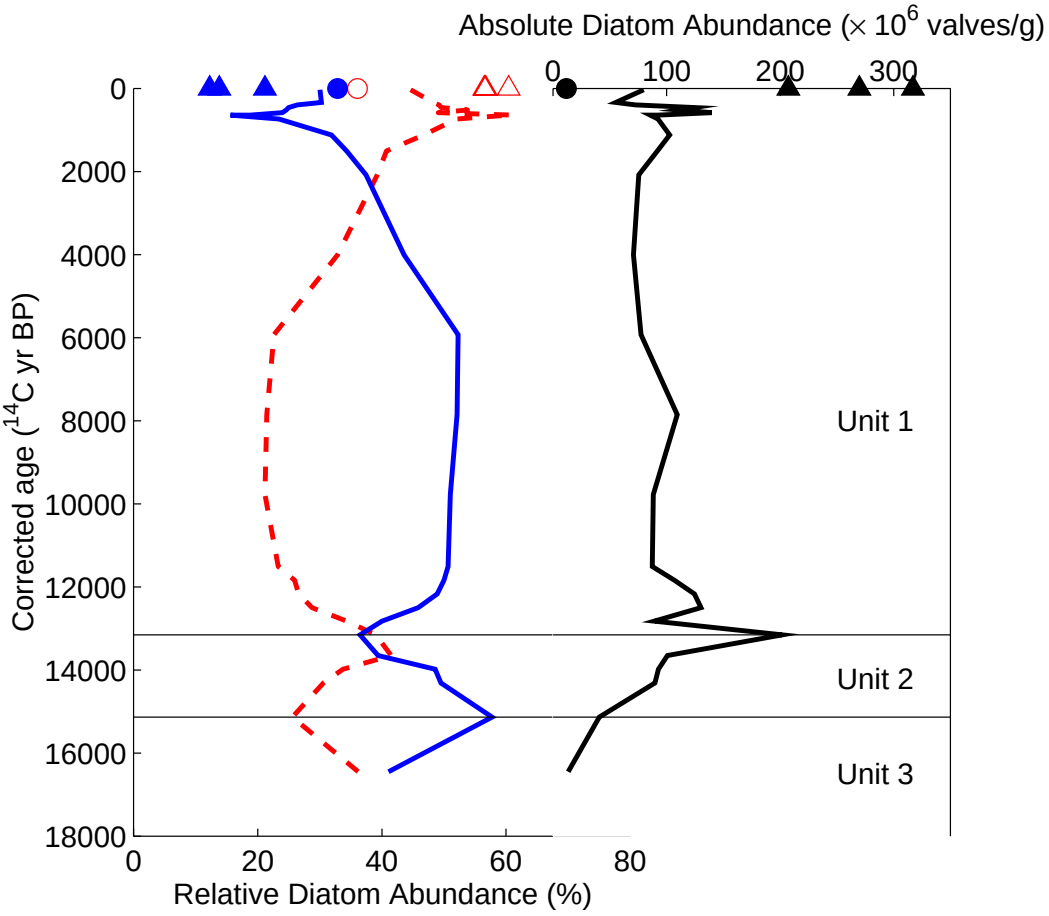

Figure 7.3: Left side x-axis: Distribution of *Fragilariopsis curta* (dashed red line) and *Thalassiosira antarctica* (solid blue line) relative abundance throughout Units 1 and 2 of the AM02 core. AM01 values are marked by circles, and ice shelf front values are marked by triangles. Solid markers represent *T. antarctica*, Unfilled markers represent *F.curta*. Right side x-axis: Solid black line; Distribution of Absolute Diatom Abundance (in valves per gram of dry weight sediment). AM01 values are marked by circles, and ice shelf front values are marked by triangles. The y-axis is corrected age in ^{14}C yr BP. The boundary between Units 1, 2 and 3 are shown.

Downcore Diatom Assemblages

Diatom species observed in the sub-ice-shelf sediments are outlined in Table 7.3. Diatoms are abundant and well preserved between 0 and 55 cm. Beneath this level, frustules are rare to absent. Two species co-dominate the diatom assemblage at the surface of the core, *Fragilariopsis curta* (44.6 %) and *Thalassiosira antarctica* resting spores (30 %), with an absolute diatom abundance (ADA) of 79.8×10^6 valves /g dry weight sediment, and biogenic opal content of 15.4 % (Figure 7.3). The relative abundance of *F. curta* increases downwards to 10-11 cm to a maximum of $\sim$ 60%, and the relative abundance of *T. antarctica* reaches a minimum of 18%. This is accompanied by a peak in ADA of 140×10^6 valves /g dry weight sediment, and biogenic opal of 18.12 %.

Table 7.3: Presence of diatom species in sub-ice-shelf sediments. F: indicates species was observed in sediments collected adjacent to the ice shelf front. I: indicates species was observed in surface sediments collected at the sub-ice-shelf inflow site, AM02. O: indicates species was observed in surface sediments collected at the sub-ice-shelf outflow site, AM01. D: indicates species was observed in sediments down AM02 core. Bold text indicates species relative abundance was greater than 2 %.

Species	Presence
Actinocyclus actinochilus (Ehr.) Sim.	D
Achnanthes charcotii M. Peragallo	D
Asteromphalus spp. (Ehr.)	FIOD
Azpeitia tabularis (Grun.) Fryxell et Sims	D
Chaetoceros (Ehr.) resting spores	**FIOD**
Cocconeis costata (Ehr.) Krebs	F
Coscinodiscus spp. (Ehr.)	D
Dactyliosolen antarcticus Castr.	ID
*Distephanus speculum** (Ehr.) Haeckel	I**D**
Eucampia antarctica (Castr.) Mang.	F**IOD**
Fragilariopsis curta (V. Heur.) Heiden	**FIOD**
F. cylindrus (Grun.) Krieger	**FIOD**
F. kerguelensis (OMea.) Hust.	F**IOD**
F. lineata (Castr.) Frenguelli	FOD
F. obliquecostata (V. Heur.) Heiden	FD
F. rhombica (OMea.) Hust	**FIOD**
F. separanda Hust.	FIOD
F. sublineata (V. Heur.) Heiden	**FIOD**
F. vanheurckii Hasle	F**OD**
Navicula directa (Smith) Ralfs	FD
*Pentalamina corona** Marchant	D
Pleurosigma directum (Grun.)	I
Porosira glacialis (Grun.) Jorg.	F**IOD**
P. pseudodenticulata (Hust.) Jouse	D
Rhizosolenia spp. (Brightwell)	FD
Stellarima microtrias (Ehr.) Hasle et Sims	FIOD
S. stellaris (Roper) Hasle et Sims	FD
Thalassiosira antarctica Comber resting spores	**FIOD**
T. gracilis (Karst.) Hust.	FID
T. lentiginosa (Jan.) Fryxell	FIOD
T. tumida (Jan.) Hasle	FIOD
Thalassiothrix antarctica Schimp. ex Karst.	FD
Trichotoxin reinboldii (V. Heur.) Reid et Round	ID
Other centrics	IOD

* denotes Chrysophyte species.

Between 11 and 25 cm, the relative abundance of *F. curta* decreases to $\sim 20\%$, and *T. antarctica* increases to $\sim 50\%$. Between 25 and 40 cm, *T. antarctica* dominates the assemblage, forming $\sim 50\%$ of the frustules observed. The relative abundance of *F. curta*, the ADA, and the biogenic opal content remain relatively uniform through this layer with values of $\sim 20\%$, 90×10^6 valves /g dry weight sediment, and $\sim 15\%$ respectively. A second peak in the relative abundance of *F. curta* ($\sim 39\%$), with an associated decrease in the relative abundance of *T. antarctica* ($\sim 36\%$), is observed at 45-46 cm. A peak in ADA (up to 190×10^6 valves /g dry weight sediment) and biogenic opal content (20 %) is observed at this level also. Below this peak, *F. curta* abundances decrease, *T. antarctica* abundances increase, and ADA and biogenic opal decrease. Full diatom abundance data are given in Appendix D. There is no visible reaction to HCl throughout unit 1 and 2 of AM02, indicating that calcareous shells, such as Foraminifera, are absent. No other fossils or fossilised structures were observed.

7.4.2 Surface Sediment Distribution

Figure 7.4 shows the surface distribution of grain size, biogenic opal and TOC obtained from the surface grabs collected adjacent to the calving ice front. Part (d) displays the horizontal transport (in Sv) perpendicular to the ice front, determined from the CTD data collected during voyage au0106 along the ice shelf front.

On the eastern side of the cavity, a large inflow to the east of longitude $74°E$ exists, and a return outflow between longitudes $72.8°E$ and $74°E$. On the western side of the ice front, a broader inflow of smaller magnitude between $71°E$ and $72.8°E$, and a larger outflow to the west of $71°E$ are observed. Sediment properties also display two peaks in biogenic fines. The peak on the eastern side of the ice shelf front is centred at $73.5°E$, and the peak on the western side is at $71°E$. It appears that associated with the inflow, the sediments with decreased mean grain size, and an increase in TOC and biogenic opal (up to 29%[1]) are found. Associated with the outflow are regions of coarser sediments, with reduced TOC and biogenic opal content. The eastern and western peaks show similar variation of sediment properties with the mass transport across the front, although the biogenic opal increase and grain size decrease in the west are not of the same magnitude as observed in the east. The circulation as measured by the CTD shows high variability between voyages au0106 and au0107 (Rosenberg et al., 2002), which may provide an explanation of the mismatch in peak locations.

[1] au0106 grab 10 indicates 50% biogenic opal, however grab 10 was taken further from the ice front, on the eastern side, than other grabs

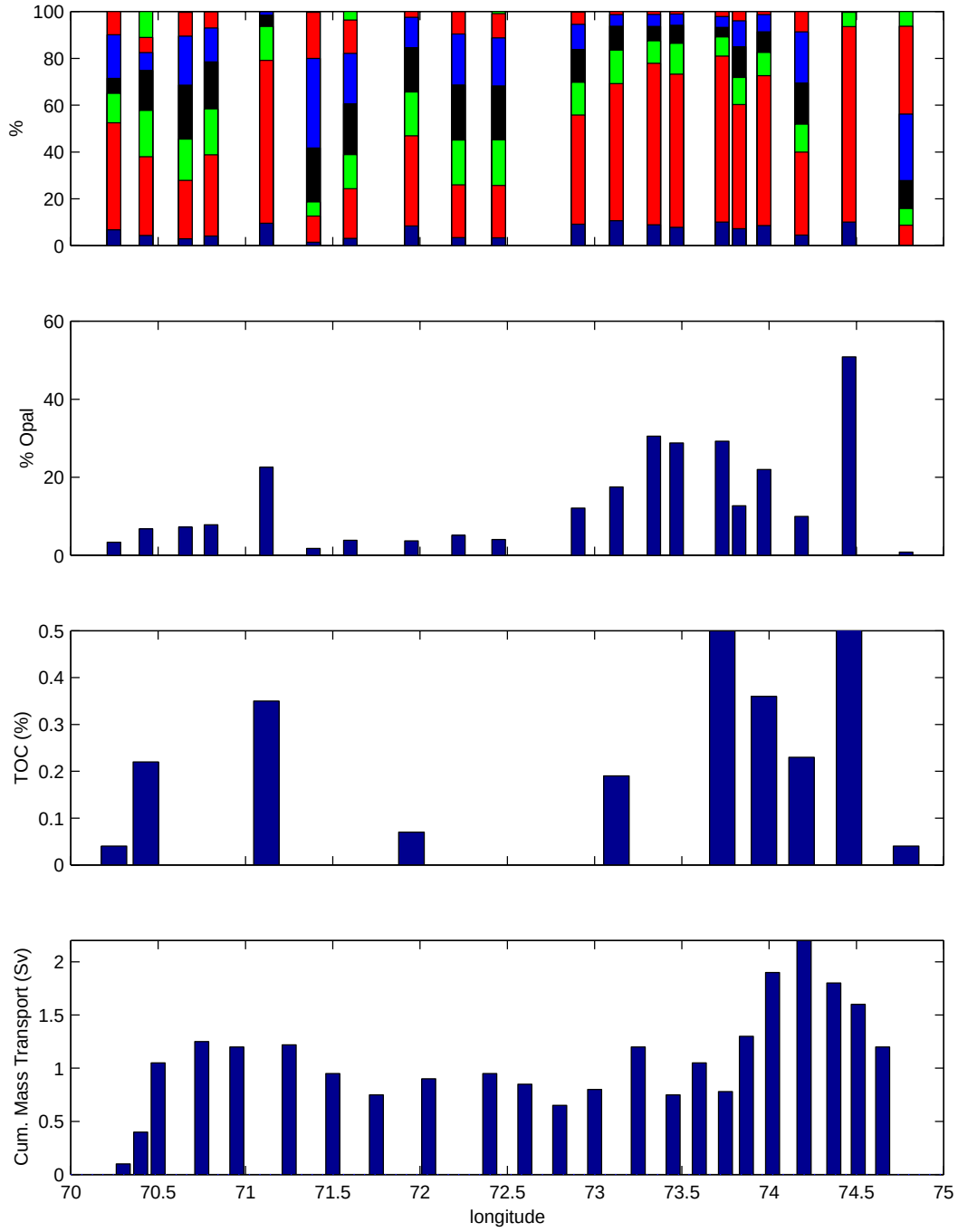

Figure 7.4: Sediment properties across the Amery Ice Shelf calving front as a function of longitude. (a) Grain-size distibution of the mud and sand component (up to 2 mm). Dark blue at the bottom is the fraction finer that $20\mu m$. The bottom red is the $20-63\mu m$ fraction, green is the $63-125\mu m$, black is the $125-250\mu m$ fraction, bright blue is the $250-500\mu m$ fraction, the upper red represents the $500\mu m-1mm$ fraction, and the upper green represents the $1-2mm$ fraction. (b) The percent biogenic opal per dry weight sediment. (c) The percent Total Organic Carbon per dry weight sediment, and (d) The cumulative mass transport, in Sv, out of the cavity. An eastwards increase relates to outflow, an eastwards decrease relates to inflow.

Sediments collected from the eastern side of the ice front (east of $73°E$) were generally olive grey siliceous mud and diatom ooze. Between longitudes $71.3°E$ and $73°E$, a zone of coarse sandy gravelly sediment is observed. A second small zone of siliceous mud and diatom ooze is observed between longitudes $70.5°E$ and $71.3°E$. West of $70.5°E$, sandy gravel sediments were collected. The western most surface grab, au0106 grab9, retrieved a sponge and bryozoan amongst coarse sandy gravel.

The diatom assemblage of sediments from au0106 grab1, au0106 grab 3, and au0207 grab 1 match the Prydz Bay sea-ice diatom assemblage described by Taylor et al. (1997), dominated by *F. curta* (50-60%) and sub-dominant *F. cylindrus* ($\sim 20\%$), and low abundances of *T. antarctica* ($< 5\%$). Absolute diatom abundance at each of the grabs is greater than 200×10^6 valves /g dry weight sediment. Biogenic opal content across the ice shelf front has been considered an adequate proxy for the distribution of marine sediments in this study. Further study of the diatom assemblages in the ice front sediment grabs is reccommended to assess whether the assemblage is altered as a result of the sub-ice-shelf circulation, or whether the nearby production destroys any ice shelf influence.

The sub-ice-shelf surficial sediments collected from AM01 and AM02 indicate spatial differences. At the site of the warm water inflow, AM02, surface sediments have high biogenic opal content (15.4 %), high ADA ($\sim 200 \times 10^6$ valves /g dry weight sediment), and a diatom assemblage with *F. curta* (44.4 %) and *T. antarctica* (30 %) co-dominant. At the site of ISW outflow, AM01, the surface sediment grab has a decreased biogenic opal content (3.6 %), a decreased ADA of $\sim 15 \times 10^6$ valves /g dry weight sediment, and a similar diatom assemblage with a decreased abundance of *F. curta* (36 %) and a slightly increased abundance of *Th. antarctica* (32 %). Surface diatom assemblage data are given in Appendix D.

7.5 Discussion

7.5.1 The Influence of Circulation on the Sub-Ice-Shelf Surface Sediment Distribution

The sediments collected from sites AM01 and AM02 beneath the Amery Ice Shelf are the first sediments collected from beneath a major-embayed ice shelf which show evidence of present day deposition. The AM02 core contains a Holocene age siliceous mud and diatom ooze surface layer of marine origin. Phytoplankton communities are not viable beneath ice shelves because of insufficient light for photosynthesis. Therefore, unless core site AM02 has been exposed to the open marine environment for a large period of the Holocene (which

recent observations would discount), any biogenic material deposited there must have been advected in with shelf water from Prydz Bay beneath the ice shelf. It is therefore proof that the landward transport of hemipelagic sediments occurs beneath floating ice shelves over distances of at least 80 km.

At the calving ice front, ADCP measured currents indicate the circulation is not a simple landward flow on the eastern side of the cavity, and seaward flow on the western side, as predicted by numerical models (Williams et al., 1998b; Williams, 1999; Williams et al., 2001, 2002), but a more complex circulation encompassing two inflow/outflow systems across the front of the ice shelf. These circulation patterns are observed in the depth-integrated transport perpendicular to the ice front (Figure 7.4), with a strong outflow observed on the western side of the shelf, corresponding to observations of ISW confined to the western side of Prydz Bay (Wong et al., 1998).

High clay/silt content, correlated with increased levels of biogenic opal, is associated with regions of inflow. Low clay/silt content, correlated with decreased levels of biogenic opal, is associated with regions of outflow. Greater amounts of biogenic fines are deposited amongst the terrigenous sediments, of increased grain size, in the regions of inflow. In the regions of outflow, the biogenic fines have been deposited beneath the ice shelf prior to arrival, so that the seaward flow is devoid of any marine sediments. The resulting surface sediment therefore has decreased marine influence (lower biogenic opal content), and the sediments have a greater component of the larger terrigenous sediments (IRD and suspended fines). Thus, the modern day surface deposition across the calving ice front appears to reflect the circulation pattern there.

The upper unit of the AM02 core is observed to have a volume weighted mean grain size of less than $10\mu m$. Volume weighted mean grain size of surface grab samples taken at the front of the ice shelf are of the order $50 - 100\mu m$, suggesting that the landward flow beneath the ice shelf is capable of transporting only the fines from Prydz Bay to the AM02 site, and the coarser particles settle before arrival at the site.

From the zone of productivity at the ice shelf front, to the sub-ice-shelf site located on the inflow (AM02), a large decrease in ADA and percent biogenic opal is observed. Similarly, a further decrease is observed between the site of inflow, AM02, and the sub-ice-shelf site located on the outflow, AM01. This is accompanied by a decrease in the dominance of *F. curta*, and an increase in the relative abundance of *T. antarctica* with progression between the three regions.

The sub-ice-shelf diatom assemblage found in surface sediments collected at sites

AM01 and AM02, co-dominated by *T. antarctica* resting spores and *F. curta* is distinct from the five diatom assemblages found in Prydz Bay (Taylor et al., 1997). Abundant *T. antarctica*, comparable to that found beneath the ice shelf do not occur in the surface sediments of Prydz Bay or the Mac-Robertson shelf. The specific ecology of *T. antarctica* is not well known (Cunningham and Leventer, 1998). Zielinski and Gersonde (1997) state that *T. antarctica* is an open water species, occupying habitats in near-shore regions where sea surface temperatures range from -2 to $1°C$. Taylor et al. (1997) present it as an indicator of the shelf diatom assemblage, supportive of other authors (Hasle and Heimdal, 1968; Fryxell, 1977; Villareal and Fryxell, 1983; Pichon et al., 1992) who have observed *T. antarctica* in ice edge regions. *Thalassiosira antarctica* has also been observed in sea ice samples (Horner, 1985; Krebs et al., 1987) and in the platelet ice found beneath coastal pack and fast ice (Villareal and Fryxell, 1983; Horner, 1985; Krebs et al., 1987; Smetacek et al., 1992; Leventer and Dunbar, 1996). Krebs et al. (1987) considered the resting spores to be truly cryophilic, however Taylor and McMinn (2002) treat this interpretation with caution as only a few samples were collected.

Layers of loosely consolidated platelet ice form when supercooled ISW streams out from beneath an ice shelf at depth, rise and accumulate as a dense slush layer under near shore pack and fast ice. The platelets may be transported over long distances and as they rise may accumulate planktonic organisms (Dieckmann et al., 1986). This platelet ice supports a unique diatom assemblage dominated by centric species (e.g. *T. antarctica*, *T. tumida*, *Porosira glacialis*, *Stellarima micrtrias*) (El-Sayed, 1971; Horner, 1985; Smetacek et al., 1992; Gleitz et al., 1996).

Cunningham and Leventer (1998) observed a high abundance of *T. antarctica* in surface sediments from the western Ross Sea, south of Drygalski Ice Tongue. They suggest that the high amount is possibly due to the importance of an autumn diatom bloom, initiated by scavenging of *T. antarctica* on loose ice crystals rising from beneath the Ross Ice Shelf.

Although *T. antarctica* resting spores have been extensively documented in sediments of the Ross Sea, no blooms of the species have been observed in the upper water column (Cunningham and Leventer, 1998). Leventer and Dunbar (1996) noted an increase in *T. antarctica* in sediment traps in the lower water column suggesting some localised lateral advection.

Cremer (1999) identified high abundance of *T. antarctica* in the surface sediments of the Laptev Sea, Arctic Ocean. The resting spores of *T. antarctica* are strongly silicified (McMinn, 1995; Cremer, 1999), however Cremer (1999) observed distinct traces of

dissolution in the *T. antarctica* assemblage. Cremer (1999) concluded that the assemblage indicated selective accumulation of strongly silicified diatom taxa, as a result of lateral transport processes which occur as sediment transport by the ocean currents in the region. Sancetta (1989) found that lateral transport processes strongly affect the composition of sediment communities in relationship to the circulation patterns, velocities and bed topography. Smayda (1970) also indicates the centric *Thalassiosira* genus remains in suspension preferentially over the pennate *Fragilariopsis* genus.

The greater relative abundance of *T. antarctica* in the sub-ice-shelf sediments appears to reflect a surface diatom assemblage that has undergone significant transport of diatoms beneath the ice shelf. The heavily silicified *T. antarctica*, which has been associated with sub-ice-shelf platelet ice in past studies, appears to have been preferentially transported and preserved, in comparison to the *F. curta* and *F. cylindrus* species which dominate the assemblage at the ice front. Similarly, Table 7.3 indicates that diatom species which are more heavily silicified (e.g., *Eucampia antarctica, F. kerguelensis*) show an increased abundance at the sub-ice-shelf sites, in comparison to the sediments taken from adjacent to the ice shelf front. This observation suggests that an increase in the abundance of *T. antarctica* in the sediments represents an increase in transport distance beneath the ice shelf.

Taylor and McMinn (2002) observed a diatom assemblage with co-dominant *T. antarctica* and *F. curta* downcore in core GC29, taken from Prydz Bay, between 11650 and 2600 ^{14}C yr BP, which they interpreted to represent a more open marine setting relative to that which occurs in inner Prydz Bay today. Cunningham et al. (1999) postulate that an increase in *T. antarctica* resting spores, and decrease in *F. curta*, in the Ross Sea between 6000 and 3000 ^{14}C yr BP indicates (i) a decrease in the significance of spring and summer ice blooms (after Cunningham and Leventer (1998)), and (ii) an increase in the temporal occurence or amount of loose pack ice during autumn. The high abundance of *T. antarctica* found in the sub-ice-shelf sediments presented herein have potential importance for such interpretations.

The AM01 surface age, measured at 11722 ± 60 yr BP (Table 7.2) is significantly older than the AM02 surface age of 6548 ± 60 yr BP. This is consisent with the findings of Harris (2000b) for two cores taken from either side of the ice shelf front of the Vanderford Glacier in Vincennes Bay, East Antarctica. Here the surface ^{14}C age at the outflow site (9393 ± 74 yr BP) was more than twice the age at the inflow site (4114 ± 77 yr BP). This was attributed to the export of recycled organic matter from the Vanderford Glacier (Harris, 2000b). If the ancient material responsible for the increased surface ages is derived from the glacial terrigenous source, an older age could be expected at the outflow AM01 site. The

old surface age however, may simply reflect sediment starvation during the Holocene at the outflow AM01 site.

The surface sediment distribution in the sub-ice-shelf cavity shows spatial variation of properties which supports models of lateral separation of the flow in the cavity. Increased marine influence is observed at the eastern AM02 site, agreeing with observed basal melt (Craven et al., 2001; Fricker et al., 2001) and predicted inflow circulation (Williams et al., 2001), which is not apparent at the AM01 site, where basal freeze and outflow are suggested (Craven et al., 2002). The lateral separation of flow therefore appears to have a strong influence on the sedimentation patterns and processes within the ice shelf cavity.

7.5.2 AM02 Core Interpretation: The Amery Ice Shelf since the Last Glacial Maximum

The AM02 core is interpreted as having been deposited during the retreat of the Amery Ice Shelf under post-glacial sea level rise, and may be used to clarify existing depositional models for sedimentation beneath floating ice shelves.

Unit 6, at the base of the core, displays a dense ($> 2000\ kgm^{-3}$) overcompacted unit which is interpreted as a lodgement till, deposited by plastering on of glacial debris of the grounded glacier by pressure melting and/or other mechanical processes. However, a gravity corer would not penetrate far into such a lodgement till, and thus only ~ 5 cm is found at the base of the core. Therefore, detailed geotechnical characteristics typical of a lodgment till (massively bedded diamict) can not be interpreted from the layer.

Unit 5, which exhibits sediment of a similar texture to the granulated facies described by Domack et al. (1998), is interpreted as a waterlain till, rapidly deposited in close proximity to the grounding line. The slight laminations observed suggests settling through the water column, and high counts of IRD are indicative of an ice shelf having just become afloat: increased melt rates close to the grounding line resulting in the continual rainout of basal debris from the floating ice shelf.

Unit 4 is also interpreted as a rapidly deposited waterlain till. The dissapearance of any laminations may reflect the deceleration of currents in the thicker cavity away from the grounding line.

Unit 3, which indicates deposition of a very fine grained silt, is interpreted as being equivalent to the "null zone" described by Domack and Harris (1998). Such a zone represents very slow rates of sedimentation of the finest terrigenous sediments distal to the grounding line, and becoming increasingly dominated upwards by biogenic sediment influx.

Harris (2000b) comments on the effect of the lateral separation of the sub-ice-shelf circulation on the"'null zone" of sedimentation. Such a lateral separation model would tend to suggest that the "null zone" would trend obliquely across the ice shelf. Its orientation may vary temporally, as a function of meltwater discharge and/or oceanographic factors associated with the density driven, sub-ice-shelf circulation. High levels of biogenic silica in the SMO unit of the AM02 core would suggest that the AM02 site lies seawards of the present day "null zone", and has done so for the majority of the Holocene (since 15132 ± 220 yr BP). Low levels of biogenic silica in the AM01 surface sample suggest that the AM01 site may lie within the "null zone" of sedimentation, reflecting the oblique tendency of sedimentation discussed by Harris (2000b).

Unit 2 indicates the initial onset of the marine influence of sedimentation in the sub-ice-shelf cavity. The reddish brown laminae, and peak in fine gravel, suggests current winnowing, perhaps coinciding with increased sub-ice-shelf currents capable of producing extensive dune fields (O'Brien et al., 1999). The reddish brown sediment originates from the Lambert Deep on the western side of the cavity (Domack et al., 1998). Given that these sediments are being observed on the eastern side of the cavity, this would suggest that the clockwise sub-ice-shelf gyre is south of the site at this time, so that eastward currents transport the reddish brown sediments to the AM02 site.

Unit 1, the massively bedded siliceous mud and diatom ooze unit, is interpreted as proof that fine grained marine sediment including diatoms and other phytoplankton is advected landwards beneath a major embayed floating ice shelf, carried in suspension by the sub-ice-shelf circulating currents, and has been for a large period of time that the ice shelf has been afloat (since $\sim 15132\ ^{14}C$ yr BP).

The corrected basal age of unit 2 (51-52 cm) is $15132 \pm 220\ ^{14}C$ yr BP (Table 7.2), suggesting that unit 1 and 2 represent deposition during the latest Pleistocene and throughout the Holocene. The lower three radiocarbon ages from units 1 and 2 imply an average sedimentation rate of 0.03 mma^{-1}. The two radiocarbon ages taken from the upper 12 cm imply an increased sedimentation rate of 0.157 mma^{-1} during the late Holocence. By comparison, accumulation rates in Prydz Bay are between 0.08 and 0.16 mma^{-1} (Franklin, 1997). Average sediment accumulation rates in the sub-ice-shelf cavity are therefore less than half those in open waters, as expected with decreasing marine influence with distance from the calving ice front for most of the Holocene.

The average sedimentation rate in units 1-2 (0.03 mma^{-1}) appears to be much less, however, than the waterlain till deposited in units 4-5. The Lambert Glacier is believed

to have begun its retreat from the Last Glacial Maximum grounding lines at EPC-1 (as indicated on Figure 7.1) in Prydz Bay (O'Brien, 1994) approximately 18000 yr BP ($\sim$ 16000 ^{14}C yr BP; Domack et al., 1998). Therefore the lower 90 cm of core AM02, from the base of unit 5 to the top of unit 3, must have been deposited extremely rapidly, prior to the deposition of units 1-2 at 15132 ^{14}C yr BP, with an accumulation rate orders of magnitude larger than the biogenic sedimentation rate of units 1 and 2.

Similarly, the Lambert Glacier's grounding line retreated $\sim$ 190 km from EPC-1 ($68°S$) to site AM02 ($69°42.8'S$) within this same time frame. A rapid rate of retreat of the grounding line as the ice shelf becomes afloat is thus implied. It may be expected that the rate of retreat over the entire length of the Amery Ice Shelf to the present grounding line location at $73°25'S$ (Fricker et al., 2002) was likewise rapid.

Domack et al. (1991) reported a corrected AMS ^{14}C date of 10600 yr BP for the onset of open water sedimentation at ODP site 740A in Prydz Bay using a reservoir correction of 1750 years. O'Brien and Harris (1996) indicate a corrected date of 11930 ^{14}C yr BP for the same period from core GC24 collected in the Amery Depression. Both sites lie to the east of the eastern most grounding feature in Prydz Bay, EPC-1. Their interpretation of open water sedimentation corresponds to the interface between silty clay and the biogenic unit; the same as the transition from units 2-3 in the AM02 core. Result herein suggest that this reflects sub-ice-shelf conditions, rather than open water.

Grounding line retreat appears to have been most rapid along the deep axis of the Prydz Channel, because the onset of marine sedimentation at AM02 $\sim$ 15000 ^{14}C yr BP predates the onset of similar sedimentation at sites flanking the Prydz Channel (e.g., sites east of EPC-1; O'Brien and Harris (1996)).

However, the surrounding bed elevation at the AM02 core site is unknown. The best data available at the time of writing (Ruddell, 2001), presented in Chapter 8, suggests the site lies in close proximity to a depression. The GC24 and ODP site 740A cores are taken from sites situated on the edge of shallower banks in Prydz Bay. It is possible that the sub-Amery depression was open to marine influence before the Prydz Bay sites as a result of the relative bed elevation.

Throughout the Holocene, the deposition of the upper bio-siliceous units 1 and 2 of the AM02 core shows variation in the diatom assemblage downcore. The relative position of the ice shelf front compared to the core site may be inferred from downcore variations in the relative abundance of *T. antarctica* and *F. curta*, and how this relates to the surface assemblages presented in the previous section. Two significant peaks in biogenic opal and

ADA are observed through these units; one (P = 0.052) centred at 45-46 cm, corresponding to $\sim$ 13500 ^{14}C yr BP, and the other (P = 0.025) centred at 10-11 cm, corresponding to $\sim$ 1000 ^{14}C yr BP. Peaks in biogenic opal and ADA are aligned with an increase in the relative abundance of *F. curta* (Figure 7.3), the latter of which has a strong negative correlation with the relative abundance of *T. antarctica* (R^2 = 0.94). From the surface assemblages presented in the previous section, peaks in biogenic opal, ADA and *F. curta* abundance are associated with increased proximity to the sea-ice-zone;an area of primary production. Thus the two peaks may represent periods where the ice shelf front was not as far advanced as its present day state.

The peak at $\sim$ 13500 ^{14}C yr BP may be attributed to the retreat of ice after the LGM, where the ice front retreated beyond the AM02 site, and later returned seaward of the site as it reached a point of equilibrium closer to its present location.

The relative abundance of *F. curta* (*T. antarctica*) beins to increase (decrease) at $\sim$ 5700 ^{14}C yr BP (25 cm) towards the peak in *F. curta* abundance and ADA observed c.a. 750 ^{14}C yr BP. This may be attributed to a gradual retreat of the ice front, thus bringing the productive sea-ice zone waters closer to the AM02 site over the period from $\sim$ 5700 ^{14}C yr BP to 750 ^{14}C yr BP. Many authors (review in Ingolfsson et al. (1998)) describe a mid-Holocene climatic optimum period, followed by late Holocene glacial advance in East Antarctica. Results here suggest that, in association with this mid-Holocene warm phase, a retreat of the Amery Ice Shelf resulted in the increased deposition of sea-ice associated diatoms at the AM02 site, which is currently more than 80 km from such a productive zone.

Modelling work (see Chapter 9, and Williams et al. (2002)) indicates an increased melt rate at the ice-ocean interface beneath the Amery Ice Shelf under the effects of a warming climate. Pudsey and Evans (2001) present evidence for the retreat of the recently collapsed Larsen Ice Shelf, Antarctic Peninsula, during the mid-Holocene. Given the Amery Ice Shelf appears to have shown some evidence of a similar mid-Holocene retreat, the future mass balance of the Amery Ice Shelf under present warming conditions may require close monitoring.

Chapter 8

Numerical modelling of the tides beneath the Amery Ice Shelf

Recent studies (Robertson et al., 1998; Makinson and Nicholls, 1999; MacAyeal, 1984b,a) have examined the influence of tides on the circulation, induced vertical mixing and basal melting of the Filchner-Ronne and Ross Ice Shelves respectively. The aim of this section of the thesis is to carry out a similar study to investigate tidally induced mixing beneath the Amery Ice Shelf, not to be concerned with the precise prediction of the tides for the region, but to estimate the likely effects of tidal processes on the oceanography of the ice shelf environs and the associated influence on sub-ice-shelf sedimentation patterns. The hypothesis is that the oceanographic conditions in some areas of the sub-ice-shelf cavity are likely to be driven by tidal, rather than purely thermohaline, processes.

Three components of the tidally-driven sub-ice-shelf circulation are of interest, and are outlined here.

1. Tidally Induced Vertical Mixing and Basal Melting

Morgan (1972) presented evidence from an Amery Ice Shelf ice core that up to 40% loss of ice mass is by basal melting close to the grounding zone. MacAyeal (1984b) suggests tidal stirring as a mechanism for basal melting beneath the Ross Ice Shelf.

Warm Low Salinity Shelf Water (LSSW) beneath the Amery Ice Shelf resides near the seabed because of its greater salinity. The ice shelf base is isolated from this relatively warm water by an intervening layer of cold water typical of glacial meltwater. Vertical heat transport through the water column, necessary for basal melting, requires mechanical energy to lift the warm but dense water into contact with the ice. A likely source of this mechanical energy beneath the ice shelf is small scale turbulence generated at the seabed

and ice shelf base by tidal currents. Ocean tides propagate freely beneath the Amery Ice Shelf with ranges of approximately 2m (King, 2001). Given the thick ice cover, turbulence generation by alternative means requiring air-sea contact is impossible. Tidal currents are identified as the most energetic process throughout the sub-ice-shelf cavity of the Ross Ice Shelf (MacAyeal, 1984b), and the same may be expected of the Amery Ice Shelf.

LSSW of the Prydz Bay region is less dense than the High Salinity Shelf Water (HSSW) of the Ross Sea region, and thus the stratification beneath the Ross Ice Shelf is greater than that beneath the Amery Ice Shelf. The question arises: 'Beneath the Amery Ice Shelf, what component of the mixing is driven by tidal currents, sufficient to stir the water column to destroy stratification and promote contact between the ice shelf and the warm water near the seabed?' And, 'does meltwater production in the region of strong tidally induced vertical mixing drive a thermohaline circulation which ventilates the deeper reaches of the sub-ice-shelf cavity?'

2. Residual Current Generation at the ice front.

Tidal oscillations over topographic features drive steady barotropic circulations, or residual currents, which contribute to the large scale transport of heat, salt, and other tracers. One of the most significant topographic features affecting the water column in the Prydz Bay region is the ice front of the Amery Ice Shelf. Makinson and Nicholls (1999) indicate residual currents of over $5cms^{-1}$ along the front of the Filchner-Ronne Ice Shelf, efficient in ventilating the front 150 km of the sub-ice-shelf cavity. Across some portions of the Amery Ice Shelf front, a step change of more than 40% is observed in the water column thickness. Therefore, another question arises: Are strong residual currents found at the Amery Ice Shelf front, analagous with the work of Makinson and Nicholls (1999)?

3. Sub-Ice Shelf Tidal Fronts

A tidal front is the hydrographic transition between a vertically well-mixed and a stratified region. A given water column has less gravitational potential energy when it is stratified than when it is vertically homogeneous. Therefore, tidal front positions may be predicted by comparing the local rate of tidal energy dissipation to the local rate at which gravitational potential energy is removed from the water column by buoyancy fluxes (MacAyeal, 1984a). The method of MacAyeal (1984a) is used to infer tidal front locations beneath the Amery Ice Shelf.

These three process are capable of altering the transport of heat and salt in the sub-ice-shelf cavity, and thus alter the mean thermohaline circulation and the consequent marine influence on sediment distribution.

8.1 Barotropic model

To investigate the contribution of tidal processes on the oceanographic regime in the vicinity of the ice shelf, a high resolution, non-linear, barotropic tidal model (MECO in 2-D) is applied to the Prydz Bay, Amery Ice Shelf cavity region. The domain covers the continental shelf, including the ice shelf covered region. The aim is to estimate likely effects of tidal processes on the oceanography of the ice shelf environs.

The depth averaged tidal model is compared to available tidal elevations and currents, and existing tidal models of the region (CADA and CATS; Padman et al., 2001). A description of the tidal environment, with average tidal currents and mixing energies, and the associated influence on tidally induced basal melting beneath the Amery Ice Shelf is given.

8.1.1 Model Topography

Perhaps the largest source of error in numerical models, particularly beneath floating ice shelves, are errors in the prescribed water depths. Under ice shelves, inaccessability means that the water column thickness (WCT) in the sub-ice-shelf cavity is hard to measure. Despite progress towards the precise location of the grounding line of the Amery Ice Shelf (Fricker et al., 2002), the water column thickness in the deepest parts of the cavity is still largely unknown.

The model grid used for the sub-Amery Ice Shelf cavity by Williams et al. (1998b, 2001, 2002) has some problems. Available data at the time were insufficient to create any better estimate of the ice shelf draft, bed elevation, or coastline. New data has been collected (Ruddell, 2001), and as a result, new, and quite different, model grids have been constructed for this study.

The model grids used in this part of the thesis were chosen to include all of the Amery Ice Shelf cavity and, to investigate the interaction between the ice shelf cavity and the open ocean, a large area of Prydz Bay out to the continental shelf slope. The model domain used for the two-dimensional barotropic model extends from $73°20'S$ to $66°S$ in latitude, and from $66°E$ to $78°E$ in longitude. The grid spacing is $1/10°$ in longitude, and $1/30°$ in latitude, resulting in a 120×219 array (Fig. 8.1). Computational speed is such that 50 model days takes approximately 24 hours on a 500 MHz desktop computer.

The world vector shoreline (National Geophysical Data Center, 2001) provided a coastline for the non-ice covered areas. The grounding line of the Amery Ice Shelf (Fricker

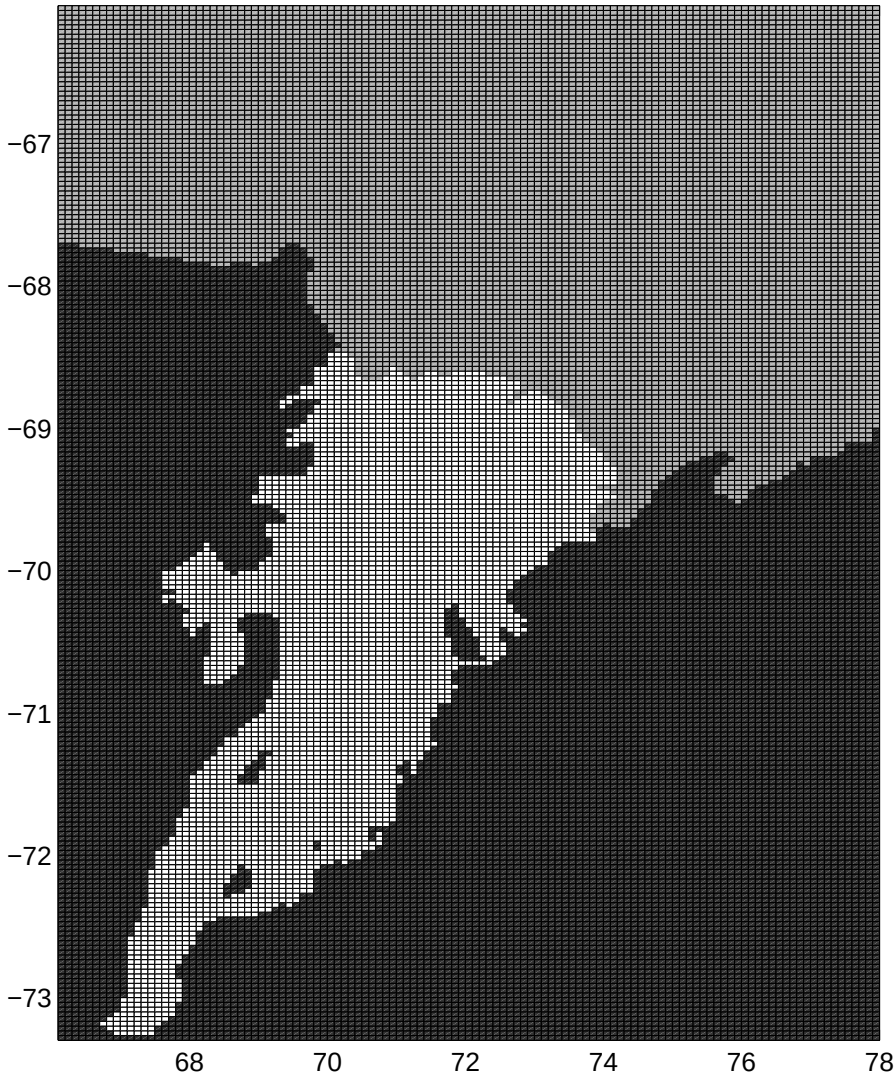

Figure 8.1: The model grid, coastline and grounding line. The white area indicates the ice shelf covered region where water depth is represented by the water column thickness, the light grey area indicates the region of open water, and the dark grey region indicates land.

et al., 2002) represents the coastline for the region covered by the floating ice shelf, and was also taken as a converging point of the water column thickness - the difference between the ice shelf draft, and bed elevation. Although the ice front advances at $\sim 1300\ ma^{-1}$ (Fricker et al., 2002), the position of the 1998 calving ice front (Fricker et al., 2002) was considered adequate for the application here.

Bathymetry in Prydz Bay, to the north of the ice front is calculated from ship track data in the region (O'Brien, 2001). These data were interpolated onto the model grid using the same inverse distance method as used in part I of this thesis (Equation 3.17). A minimum water depth of 50 m was specified.

Beneath the Amery Ice Shelf, measurements of the ice shelf draft and bed elevation are

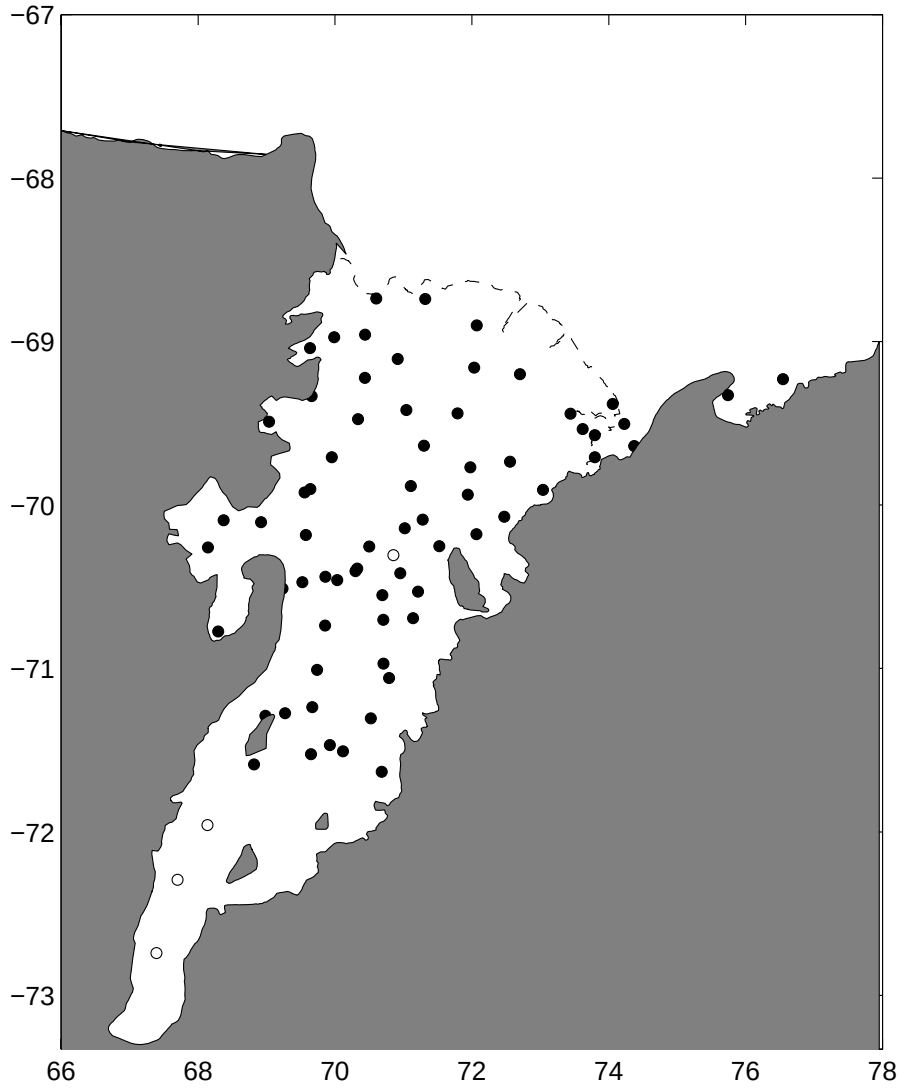

Figure 8.2: Avaliable bed elevation and ice draft measurement locations on the Amery Ice Shelf. Filled circles represent locations where both bed elevation and ice draft measurements are available, open circles represent points where only ice draft measurements are available. From Ruddell (2001)

restricted to approximately 70 sparse locations spread over the ice shelf (Fig. 8.2; Ruddell, 2001). Two sets of ice shelf draft measurements have been made at some of these points, with differences of up to 200 m observed (Ruddell, 2001). These 'available data points' are predominantly north of $71.6°S$. Only 3 points south of this latitude provide measurements of ice shelf draft and none of these provide estimates of bed elevation. Therefore, nothing is known of the cavity shape south of $71.6°S$. BEDMAP ice thickness data (Lythe et al., 2000) indicates the southern most extent of the Amery Ice Shelf grounding line is arguably one of the deepest points of bed elevation on the Antarctic continent.

Available ice shelf draft data have been interpolated onto the model grid using the

same interpolation method used elsewhere in this thesis. The ice draft at the calving ice front was specified as 200 m for interpolation purposes. Available bed elevation data were added to the Prydz Bay bathymetry data and were interpolated onto the model grid to provide a smooth map of bed elevation over the entire model domain. A number of model grids were created with varying bed elevation, all matching the available data to approximately the same degree of accuracy (within $rms(wct_{model} - wct_{data}) < 80m$). Ice shelf draft was held constant, as it is thought to be better known than the bed elevation (Ruddell, 2001). Bed elevation was adjusted south of $71.6°S$ so that mean water column thickness over this region was between 50 to 600 m. North of $71.6°S$, some variation of bed elevation was allowed in regions of sparse data, or at locations of points with large error. A water column thickness grid was then determined from the depth difference between the ice draft and the bed elevation. Three model grids are presented in this thesis: A - the shallow grid (mean WCT within the cavity of 185 m.); B - the mid-depth grid (mean WCT of 350 m.); and, C - the deep grid (mean WCT of 412 m). The model grid used within the CATS00.10 and CADA00.10 series of models (section 6.5.1), which has interpolated the Williams et al. (1998b) cavity geometry onto a model grid with the grounding line supplied by Fricker et al. (2002), was interpolated onto the model grid described above, to compare tidal results using the 'CADA grid' to those using the new model grids. A minimum WCT beneath the ice shelf of 50 m was specified for each of the model grids, except grid A for which 20 m is specified. Figure 8.3 displays a cross-section of the zonally averaged, from coastline to coastline, bed elevation and ice draft for each of the four model grids. Figure 8.4 displays a map of the water cavity thickness for grid B.

Interpolation of the sparse data from beneath the Amery Ice Shelf is likely to lead to a smoother model topography than exists in reality. Large differences between the model and real topography may occur, particularly in the southern portion of the model domain where no bed elevation data are available.

8.1.2 Numerical Modelling Approach

2-D model

The MECO model (presented in section 3) was used in a two-dimensional barotropic mode to simulate tides in the Amery Ice Shelf cavity and Prydz Bay. The model grid has been descibed in section 8.1.1. Consistent with previous barotropic Antarctic sub-ice shelf tidal models (MacAyeal, 1984b; Le Provost et al., 1995; Robertson et al., 1998; Makinson and Nicholls, 1999; Lefevre et al., 2000; Padman et al., 2002), the water depth term, $H(x, y)$ in

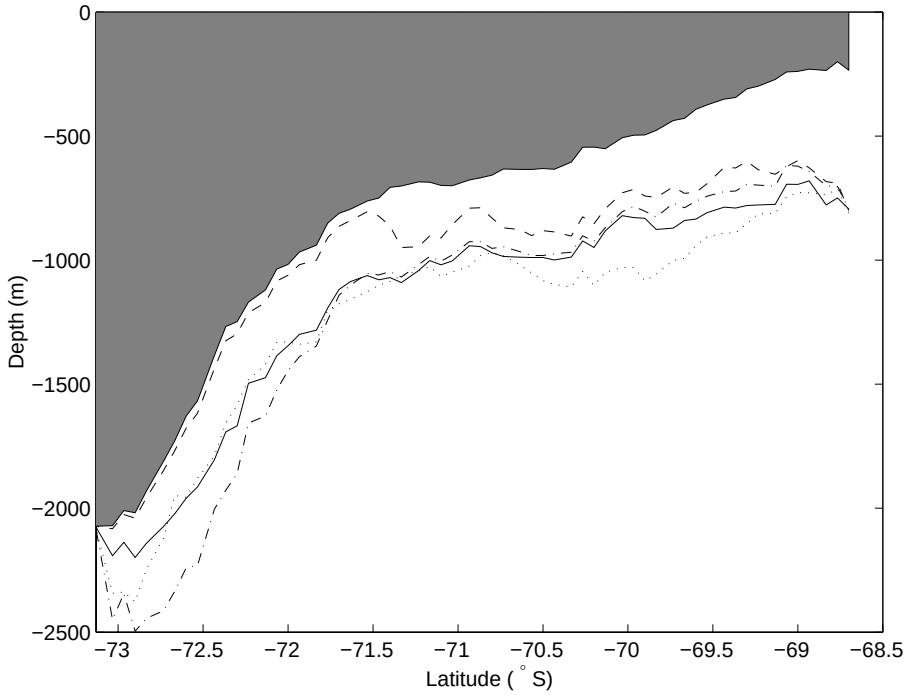

Figure 8.3: Zonal mean bed elevation for the sub-ice-shelf portion of the four model grids discussed in this section of the thesis. Dashed line (- - -) - Grid A; solid line - Grid B; dash-dot line (_._._) - Grid C; dotted line - Grid CADA. Filled section represents the zonal mean ice shelf thickness

the model equations (section 3) represents water depth in the open ocean, and water column thickness in the ice shelf covered region.

The seabed stress within the model is related to the depth mean current using a quadratic friction law using a coefficient of bottom friction set at 0.003. This value is in line with that used by other models (MacAyeal, 1984b; Robertson et al., 1998; Makinson and Nicholls, 1999; Padman et al., 2002). Sensitivity studies varying C_D between 0.0020 - 0.0035 indicate only minor variation in tidal height and currents. Beneath the ice shelf area, the value was doubled to account for the additional drag at the ice-ocean interface. Apart from providing a second frictional surface and reducing the water column thickness, the ice shelf has no influence on the tides in this model. Smithson et al. (1996) noted that model-observation comparisons were best when C_d was increased by a factor of 50 beneath the Filchner-Ronne Ice Shelf, and suggested that the increase represents the dissipation of energy associated with ice shelf flexure at the grounding line.

A horizontal viscosity coefficient, A_H, of $100 m^2 s^{-1}$ is specified. The same value was used by (MacAyeal, 1984b) in the Ross Sea, and by Makinson and Nicholls (1999) in the Weddell Sea, and is an order of magnitude smaller than that used by Robertson et al. (1998) in the Weddell Sea.

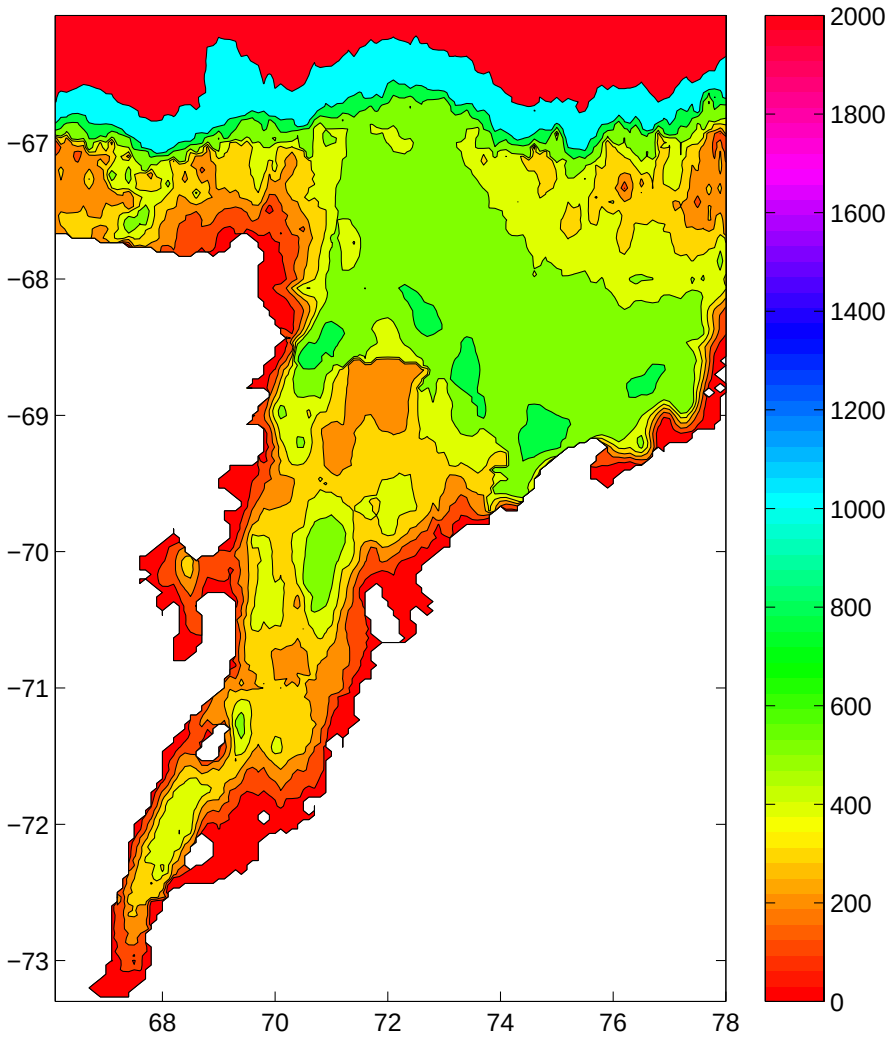

Figure 8.4: Map showing the water column thickness (m) for grid B. Contours are at 0, 100, 200, 300, 400, 500, 750, 1000, 2000 (m).

Along the open boundary, time series of sea surface heights for each node are used to force the model. Tide height coefficients obtained from the CADA00.10 model (Padman et al., 2002) were interpolated onto the boundary nodes. The amplitude and phase of 6 tidal constituents ($Q_1, O_1, K_1, N_2, M_2, S_2$) were used. King (2002) recognised CADA00.10 as the most accurate tidal model in the Amery Ice Shelf region of available tidal models. Within the model domain, the model was forced by the astronomical tide-generating force.

An 8s time step was chosen to satisfy the Courant-Friedrichs-Lewy (CFL) condition $dt < ds/\sqrt{2gH}$ where ds is the grid spacing, g is the gravitational acceleration and H is the water column thickness. Equations of continuity and motion are solved using an explicit finite difference method.

Initial model conditions consisted of no currents and an undisturbed sea surface. The model was run for 50 days with the elevations and currents being recorded hourly over the

final 30 days. The recorded time series were used for the harmonic analysis of elevations and currents to obtain amplitude and phase of the six tidal constituents that drive the model. Amplitude and phase of the eastward and northward components of each tidal current constituent were used to construct tidal ellipses.

Dominant sources of error in the model are uncertanties in bathymetry, boundary conditions and use of a depth-averaged model. Boundary conditions are dependent on the accuracy of CADA00.10. In the region of Prydz Bay waters, the accuracy of CADA is believed to be quite good due to assimilation of Davis and Mawson tide gauge data (Padman et al., 2002). Parameterisations of bottom stress and lateral viscosity are potential sources of error. There is no consideration of sea ice, and thus stress at the sea-ice/ocean interface. Baroclinicity and ice shelf flexure are all additional sources of error. The topography beneath the Amery Ice Shelf is poorly known. Model grids A, B, C, and CADA were used to assess this major source of error in the model, to obtain a best estimate of the topography in the domain for the baroclinic model runs presented in Chapter 9.

8.2 Available Data

8.2.1 Elevation Measurements

Two types of elevation measurements, tide gauges and GPS sites, were available for model validation. Crossover points from the TOPEX/Poseidon data have a southern limit of $66°S$, so are of little use for validation of this model. A preliminary study using ERS satellite radar altimeter data to retrieve tidal harmonics over the Filchner-Ronne Ice Shelf was carried out by Fricker and Padman (2002) obtaining an accuracy of $\sim 2-8$ cm, and may provide a useful dataset for model validation in the future.

Eight sites, shown in Figure 8.5, with available elevation data long enough for tidal analysis were found in the model domain, and are summarised in Table 8.1.

Available tide gauge[1] data within the model domain consist of elevation time series at 3 locations on the Antarctic continent.

- Davis ($68°35'S$, $77°58'E$) lies on the eastern model boundary. As Davis lies on the boundary, it is not a useful time series for model validation.
- Zhong-Shan ($69°23'S$, $76°22'E$) lies on the Antarctic coast in Nella Fjord within Prydz Bay, 56 nautical miles SW of Davis; and

[1] Data for each of these sites was supplied by the National Tidal Facility (National Tidal Facility, 2000).

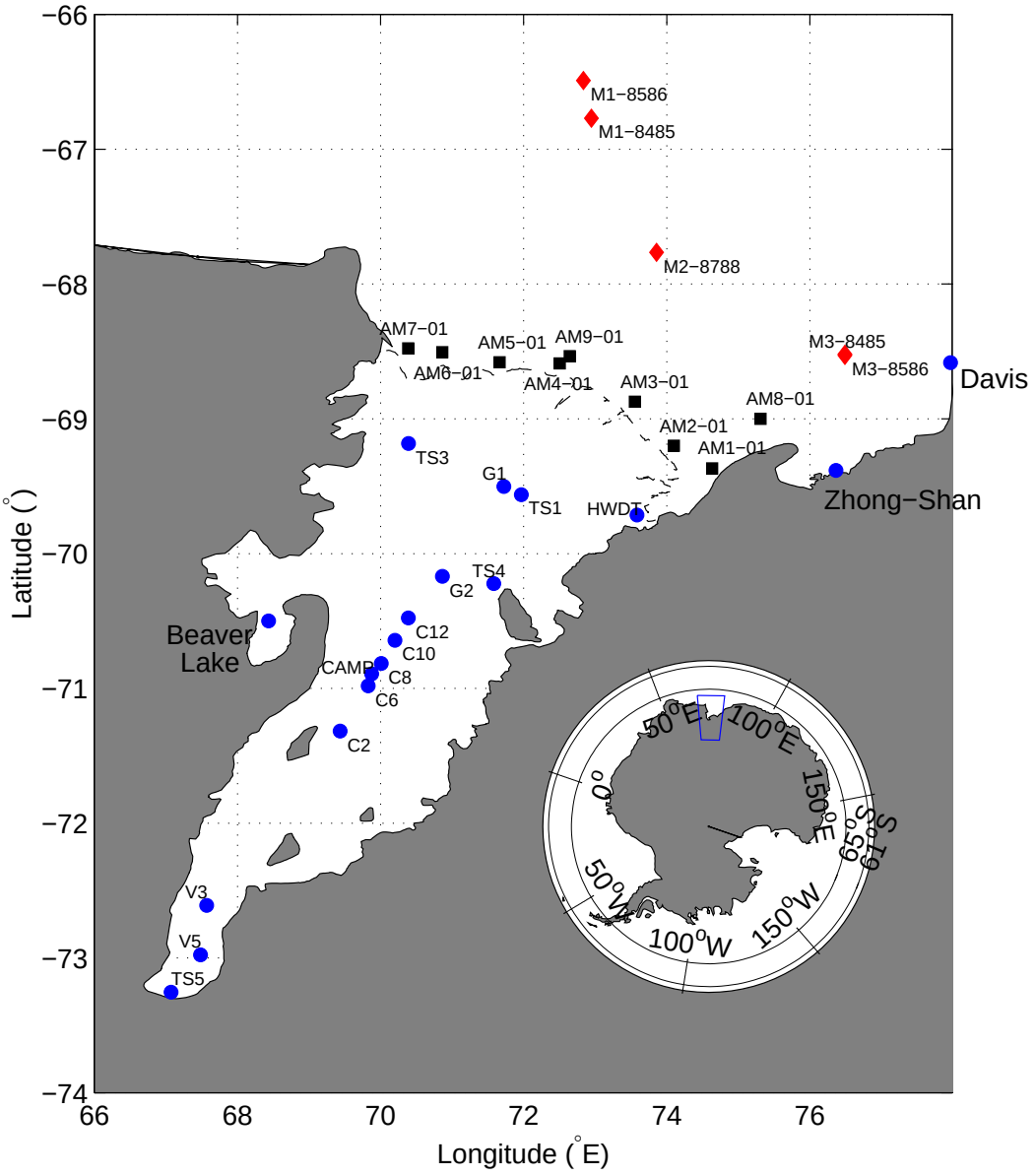

Figure 8.5: Location of data measurement points, available for tidal comparison. Blue dots represent positions of tidal elevation comparison, red diamonds represent positions of Prydz Bay Current Meters, and Black squares represent positions of 2001 Amery Ice Shelf front Current Meter Moorings.

Table 8.1: Tidal sea-surface elevation observation sites for the Amery Ice Shelf, Prydz Bay Region.

Site	Latitude	Longitude	Record Length (days)	Instrument
Davis	$68°35'S$	$77°58'E$	365+	Tide Gauge
Zhong-Shan	$69°23'S$	$76°22'E$	365+	Tide Gauge
Beaver Lake[a]	$70°48.5'S$	$68°9.5'E$	39	Tide Gauge
HWDT	$69°43'S$	$73°35'E$	26	GPS
TS1	$69°34'S$	$71°58'E$	48.4	GPS
TS3	$69°11'S$	$70°23.5'E$	67.8	GPS
TS4	$70°13'S$	$71°35'E$	64.6	GPS
TS5[b]	$73°15'S$	$67°4'E$	82.9	GPS
G1	$69°30'S$	$71°43'E$	0.83	GPS
G2	$70°10'S$	$70°52'E$	1.83	GPS
C12	$70°29'S$	$70°23'E$	1.125	GPS
C10	$70°39'S$	$70°12'E$	1.2	GPS
C8	$70°49'S$	$70°1'E$	0.96	GPS
CAMP	$70°53.5'S$	$69°52'E$	10.5	GPS
C6	$70°59'S$	$69°50'E$	1	GPS
C2	$71°19'S$	$69°26'E$	1.125	GPS
V3	$72°37'S$	$67°34'E$	3.5	GPS
V5	$72°59'S$	$67°29'E$	3.8	GPS

[a] The longer 1997/1998 Beaver Lake Tidal Gauge data are used for comparison.
[b] TS5 is not included in the general tidal analysis as it lies within the flexure zone near to the southern grounding line: see text.

- Beaver Lake ($70°48.5'S$, $68°9.5'E$) located in the Amery Ice Shelf region in the Prince Charles Mountains. Two sets of observations (from 1991 and 1998) have been obtained from Beaver Lake from two different locations separated by less than 1km. No attempt has been made to relate the two sets to the same height datum, so a bias exists between them. For comparisons in this study, only relative differences are required and so the constituents from the longer (39 days) 1998 series are used only.

In general, ice shelves are freely floating more than 9km from their grounding zone, and a Global Positioning System (GPS) station situated outside this area will act as a tide gauge. GPS is currently the most convenient and most precise method available for the measurement of sub-ice-shelf tidal signals on a point by point basis (King, 2002). King (2002) details the processing of GPS data on fast moving, floating ice shelves. GPS sites of sufficient period to resolve the main tidal constituents include five sites from on the Amery Ice Shelf.

- At the AMISOR hot water drill pilot borehole site occupied during the 1999/2000 Austral summer ($69°42.8'S$, $73°35'E$), a GPS was deployed for 31 days (King, 2002). This sea level record is referred to as HWDT.

- At site TS1 ($69°33.72'S$, $71°58.08'E$), GPS tidal elevation data were obtained for 48.4

days during the 2000/2001 Austral summer.

- At site TS3 ($69°10.98'S$, $70°23.46'E$), GPS tidal elevation data were obtained for 67.8 days during the 2000/2001 Austral summer.

- At site TS4 ($70°13.38'S$, $71°34.80'E$), GPS tidal elevation data were obtained for 64.6 days during the 2000/2001 Austral summer.

- At site TS5 ($73°15.20'S$, $67°4.23'E$), GPS tidal elevation data were obtained for 82.9 days during the 2000/2001 Austral summer. TS5 was deployed within approximately 4-5 km of the southern extent of the grounding line. During the first $\sim 20-25$ days of the TS5 sea-level record, a gradual decline is observed in the mean value about which the sea-level oscillates. Photos of the GPS receiver indicate that the GPS had melted into the snow surface. Thus, the first ~ 25 days of record, assumed to be the period over which the receiver was melting into the snow, was removed before the tidal analysis was carried out on a 50 day record beginning at 0030 31st Jan 2001 UT.

King (2002) details a number of additional locations where GPS tidal measurements have been made. However the collected time series have been short (generally < 5 days), and hence significant errors in the obtained constituents, by inference from the Beaver Lake tide gauge data, is probable. At least 15 days of hourly data are required to resolve M_2 from S_2, and O_1 from K_1, and errors in specific constituents will become much larger as record lengths become shorter than this. King (2002) states that estimates of the amplitude of inferred diurnal constituents are too high, and for semi-diurnal contituents too low. These sites are also listed in Table 8.1. Site C4 has been omitted since the GPS derived constituents are believed to be of poor quality (King, 2002).

Another GPS, TS6, was deployed south of the southern grounding line at $73°24.08'S$, $66°40.59'E$ during the 2000/2001 Austral summer (King, 2002). This site is grounded and excluded from analysis.

Estimates of errors in instruments are needed before these measurements can be used to evaluate model performance. Typical measurement precisions of the vertical motion of an ice shelf induced by tides for bottom mounted tide gauges and GPS are 5-10 mm, and 10-50 mm respectively (King, 2002).

8.2.2 Velocity Measurements

Hodgkinson et al. (1988, 1991a,b) deployed current meter moorings in Prydz Bay. A total of 5 current measurement sites that lie within the model domain are used for model comparisons.

Table 8.2: Tidal velocity observation sites for the Amery Ice Shelf and Prydz Bay Region. *-Minimum record length from available current meters at each mooring.

Mooring	Latitude	Longitude	Record Length* (days)	Depth Obs (m)	Depth Model (m)	Category
M1_8485	$66°46'S$	$72°57'E$	181	540	601	Shelf Break
M3_8485	$68°31'S$	$76°29'E$	111	640	642	SE Prydz
M1_8586	$66°29'S$	$72°50'E$	95	566	1417	Shelf Break
M3_8586	$68°32'S$	$76°29'E$	145	640	642	SE Prydz
M2_8788	$67°46'S$	$73°51'E$	283	565	540	Mid Bay
AM1_01	$69°22'S$	$74°38'E$	186	750	740	AIS Front
AM2_01	$68°12'S$	$74°05'E$	216	672	664	AIS Front
AM3_01	$68°52'S$	$73°33'E$	369	768	783	AIS Front
AM4_01	$68°35'S$	$72°30'E$	222	538	536	AIS Front
AM5_01	$68°34'S$	$71°39'E$	358	472	465	AIS Front
AM6_01	$68°30'S$	$70°51'E$	196	786	855	AIS Front
AM7_01	$68°28'S$	$70°23'E$	313	1135	1108	AIS Front
AM8_01	$69°0'S$	$75°19'E$	358	717	699	AIS Front
AM9_01	$68°32'S$	$72°39'E$	363	629	613	AIS Front

The current meter sites, shown in Figure 8.5, fall into three groups, and are summarised in Table 8.2.

- Two continental shelf edge sites at ($\sim 66°30'S$, $72°50'E$).
- Two sites in the south east corner of Prydz Bay at ($\sim 66°45'S$, $76°30'E$), where the bottom slopes to the south. Water currents at these sites are influenced by bathymetry (Hodgkinson et al., 1991a); and
- One site in the central portion of the shelf in Prydz Bay ($\sim 67°46'S$, $73°51'E$). The seabed is relatively flat in this area.

Each of these moorings consisted of 4 current meters, of which only some data were recoverable. The accuracy of derived tidal ellipses is dependent upon the length of the time series. Observations were not used for those current meters which were in the bottom boundary layer, defined as within 50 m of the seabed: currents in the boundary layer may not be representative of the mean water column velocity, which is being simulated by the barotropic model.

In addition to the current meter moorings deployed by Hodgkinson et al., nine current meter moorings, with up to five current meters per mooring, were deployed across the Amery Ice Shelf front during the 2001 Austral winter. Leffanue (2002) carried out a tidal analysis on each current meter record, which were available for model comparison. Details of these current meter mooring locations are also given in Table 8.2.

No available current meter data from beneath the Amery Ice Shelf currently exists.

8.3 Water Column Thickness Sensitivity

Model runs were carried out using each of the four model grids, A, B, C, and CADA, discussed in section 8.1.1. Model time series, and the tidal constituents derived from a harmonic analysis of model time series, from each model run were compared to the available tidal elevation data.

The regions where the bed elevation is adjusted to create each model grid, lay too large a distance from Prydz Bay to significantly alter the model results in Prydz Bay. Comparisons between model and observed current velocities at the current meter mooring sites are therefore left until the next section (Section 8.4). In this section, the sensitivity of sea-level predictions to changes in the model water column thickness is presented.

8.3.1 Tidal constituent comparisons

Tidal amplitude and phase of the four main tidal constituents (M_2, S_2, K_1 and O_1) for each model run using WCT grids A, B, C, and CADA were compared to the tidal constituents derived from each sea-level record. Tidal constituents for the eight short GPS records, taken directly from King (2002), were also included for comparison.

Table 8.3 shows the simulated tidal amplitude and phase for each sea-level record site, from the model run using WCT grid B. The respective observed values are shown for comparison. The standard deviation of the difference between the simulated and observed tidal amplitudes and phases for each constituent, from all sites, are listed also. Tables F.1 and F.2 in Appendix F show the comparison between observed and predicted tidal harmonic constituents at each sea-level record site, for each model run using WCT grids A, B, C, and CADA. Summarising the results shown in Appendix F, to assess the sensitivity of the model to changes in the water column thickness, Table 8.4 compares the standard deviation of the difference between the modelled and observed constituents for each model run using WCT grids A, B, C, and CADA.

The TS5 site lies within 10 km of the southern extent of the grounding line. Tidal flexure is thought to be important in this zone (MacAyeal, 1984b). Consequently, analysis of the TS5 sea-level record has been treated separately, and are not included in the results presented in Tables 8.3 and 8.4. The results of the harmonic analysis of the TS5 sea-level record are shown in Table 8.5, along with predicted values from the MECO model using

Table 8.3: Comparison of the simulated (S) and observed (O) tidal amplitude and phase at 13 sites in the model domain, as shown in Figure 8.5, from the MECO model using WCT grid B. *-Tidal phase is in degrees relative to GMT.

Amplitude (cm)								
	M2		S2		K1		O1	
Location	S	O	S	O	S	O	S	O
Zhong-Shan	18	20	17	18	25	27	29	28
Beaver Lake	25	24	24	25	27	28	31	30
HWDT	19	19	19	20	25	26	30	28
TS1	20	21	20	20	25	32	30	28
TS3	20	21	19	16	25	29	30	25
TS4	23	26	23	22	26	32	31	31
G1	20	18	20	16	25	27	30	28
G2	23	24	23	21	26	34	31	35
C12	25	29	25	25	27	31	31	32
C10	25	28	25	24	27	28	32	29
C8	26	27	26	23	27	29	32	30
CAMP	27	26	27	22	27	32	32	33
C6	27	29	27	25	27	39	32	41
C2	29	28	29	25	27	23	32	24
V3	32	23	32	20	28	33	33	34
V5	32	25	33	22	28	34	33	35
SDev. of diff.	2.3		3.2		4.3		2.8	
RMS (%)	14		22		16		12	
Phase*								
	M2		S2		K1		O1	
Location	S	O	S	O	S	O	S	O
Zhong-Shan	207	212	318	311	281	287	278	259
Beaver Lake	219	253	332	357	286	296	284	288
HWDT	208	215	319	319	282	281	279	272
TS1	213	222	325	323	284	294	281	266
TS3	220	228	333	330	287	296	284	262
TS4	211	211	323	316	283	298	280	259
G1	214	217	327	316	284	305	282	298
G2	214	233	326	332	284	278	282	271
C12	215	228	327	327	285	283	282	276
C10	215	227	328	327	285	289	282	282
C8	216	239	328	339	285	294	282	287
CAMP	216	220	329	320	285	285	283	278
C6	216	230	329	330	285	276	283	269
C2	216	221	329	320	285	275	283	268
V3	216	247	329	347	285	282	283	274
V5	216	238	329	338	285	281	283	274
SDev. of diff.	13		7		7		11	

Table 8.4: Comparing MECO results using the different water column thickness model grids. Standard deviation of the difference in amplitude (SD_A in (cm)) and phase (SD_ϕ (°)) of the main four tidal constituents between the observed and predicted constituents from the 13 sea-level measurement sites presented in Table 8.1. Model grids are described in the text.

WCT Grid	M_2		S_2		K_1		O_1	
	SD_A	SD_ϕ	SD_A	SD_ϕ	SD_A	SD_ϕ	SD_A	SD_ϕ
A	20.9	11	28.0	31	3.6	8	3.2	13
B	2.3	13	3.2	7	4.3	7	2.8	11
C	2.4	13	4.1	7	4.2	7	2.8	11
CADA	3.5	12	2.6	8	3.9	7	2.7	12

Table 8.5: The results of harmonic analysis of the TS5 sea-level record. Comparison of the simulated (S) and observed (O) tidal amplitude and phase, from the MECO(grid B) and CADA models. *-Tidal phase is in degrees relative to GMT.

Amplitude, $10^{-2}m$								
	M2		S2		K1		O1	
Location	S	O	S	O	S	O	S	O
MECO	33	10	33	11	28	11	33	10
CADA00.10	29		30		31		32	
Phase*								
	M2		S2		K1		O1	
Location	S	O	S	O	S	O	S	O
MECO	216	290	329	306	285	239	283	301
CADA00.10	233		341		290		280	

WCT grid B. The predicted constituents from the CADA model are also shown, and are discussed in the section 8.4. Observed constituents at site TS5 indicate strongly reduced amplitudes and large shifts in phase in comparison to respective values at site V5, for each of the four main constituents, e.g., The observed M_2 constituent shows a change in amplitude from 25 cm at V5 (latitude $72.97°S$) to 10 cm at TS5 (latitude $73.05°S$), and respective phase change from 238° to 290°. The large changes in tidal constituents are likely to be a result of the effects of ice flexure (Vaughan, 1995). The tidal model does not include the effects of ice flexure. Consequently, the model does not predict these large changes in phase and amplitude at the TS5 site.

Diurnal tidal constituents are observed to be the most robust to changes in model bathymetry, a result of the longer wavelength of the diurnal tide. They show a slight amplification from $\sim 28cm$ at the ice front to $\sim 31cm$ at the grounding line for each model run. The standard deviation of the difference between simulated and observed tidal amplitudes for the diurnal tides is approximately 3-4 cm for all 4 cavity shapes. The phase shift from ice front to grounding line is of the order of 4 degrees for the diurnal tides, and the stan-

dard deviation of the difference between simulated and observed tidal phase from all sites (excluding TS5) is approximately the same for all four cavity shapes ($7-8°$ for K_1, $11-13°$ for O_1).

The most shallow model run, A, has a mean water column thickness beneath the ice shelf of $\sim$ 185 m. Model results indicate large amplification of the semi-diurnal tidal constituents from $\sim 20cm$ in open water, to $\sim 115cm$ at the southern extent of the cavity. In an open basin, the natural period of oscillation is given by (Pond and Pickard, 2000):

$$T_n = \frac{4L}{\sqrt{gh}}$$

where L is the length of the ice shelf cavity (510 km) and h is the mean water column thickness of the cavity. This calculation ignores effects of rotation and spatial variation of the water column thickness, and therefore may have significant error. A flat bottom basin of uniform 185 m depth has a natural period of oscillation of ~ 13.2 hours, which suggests resonance of the semi-diurnal tides in the prescribed ice shelf cavity is a possibility. The observed tidal amplitudes do not show amplification towards the south of the cavity to the same extent as the predicted values. Some amplification is observed ($\sim$ 20 cm in open water tp ~ 25 cm in the south of the cavity) as a result of the "funnelling effect" caused by narrowing of the ice shelf cavity, and possibly shoaling of the water column thickness away from the ocean. The standard deviation of the difference between simulated and observed values of amplitude are therefore large, 21 and 28 cm for the M_2 and S_2 tides respectively, when using WCT grid A. A large phase shift ($\sim 60°$) for each constituent from the ice front to the grounding line, is much greater than the data suggests ($\sim 25°$). The large standard deviation of the differences in tidal phase of $11°$ and $31°$ for the M_2 and S_2 constituents respectively, suggest that the long tidal waves are travelling slower in the model cavity than the real cavity, as a result of the water column thickness being too shallow in the south of the domain. The slower tidal wave results in the predicted resonance which is not observed by the GPS tidal elevation measurements. Consequently, the large amplitude errors are observed in the model when WCT grid A is used.

Grid B has a mean depth of approximately 350 m. Therefore, the cavity has a slightly shorter natural period and resonance does not occur in the model cavity. The predicted amplification in amplitude from $\sim 20cm$ in open water, to $\sim 32cm$ towards the grounding line more closely matches the observed amplitudes (20 to $25cm$) with a standard deviation of the differences in tidal amplitude of less than 5 cm (less than the instrumental error) for both

the M_2 and S_2 tides (2.3 and 3.2 cm respectively). The standard deviation of the differences in phase for the M_2 and S_2 tides are 13° and 7° respectively. Of those observations with a reasonable analysis record length, amplitude and phase errors lie well within the standard errors for each constituent.

Grid C, that with the deepest cavity, has a mean depth of $\sim$ 400. Amplification towards the grounding line is similar to that shown using grid B (20 to 33cm), although the difference between predicted and observed amplitudes has started to diverge from a best fit value. This suggests that the natural period of the cavity is too fast; i.e., the depth of the basin is overestimated in the model. However, comparisons are still much better than for model grid A, given the standard deviation of the difference in amplitude is less than 4.2 cm, and phase differences are equivalent to grid B, for each of the 4 constituents.

Grid CADA shows agreement as good as, or better than, grid B. The standard deviation of the differences in tidal amplitude is less than 4 cm for each of the four constituents, and the standard deviation of the phase differences is approximately the same as those using grid B. Grid CADA shows best agreement in amplitude towards the grounding line (20 to 27cm), with both the M_2 and S_2 amplitude errors within the instrument precision at the V3 and V5 GPS sites.

8.3.2 Time-series comparison and regression analysis

A regression analysis of modelled and observed time-series has been carried out, in addition to time-series comparisons at 8 of the sites for which time series data were available. Figures 8.6 and 8.7 display a scatter plot comparison of model, using grid B, and observed data. The regression statistics, R^2 and slope, m, for each model run are displayed in Table 8.6. Values of m greater than 1 indicate that the model underestimates the observed sea-level, values of m less than 1 indicates that the model overestimates the observed sea-levels. Figures 8.8 and 8.9 overlay model (using grid B) and observed time series at each of the sites. Table 8.6 lists the standard deviation between model and observed elevation values at each site, for each model run. The short GPS data records from V3 and V5 have been included in this analysis as they are useful indicators of the accuracy of the model toward the southern extent of the domain. Site TS5, as mentioned previously, lies within the flexure zone. Time-series comparisons and results of the regression analysis indicate little correlation between the observed and predicted sea-levels. Using model grid B, values of the standard deviation between sea-levels, R^2, and the slope, m, are 0.282 m, 0.237, and 0.126 respectively.

Time series comparisons at GPS sites HWDT, TS1, TS3, and TS4, and tide gauges

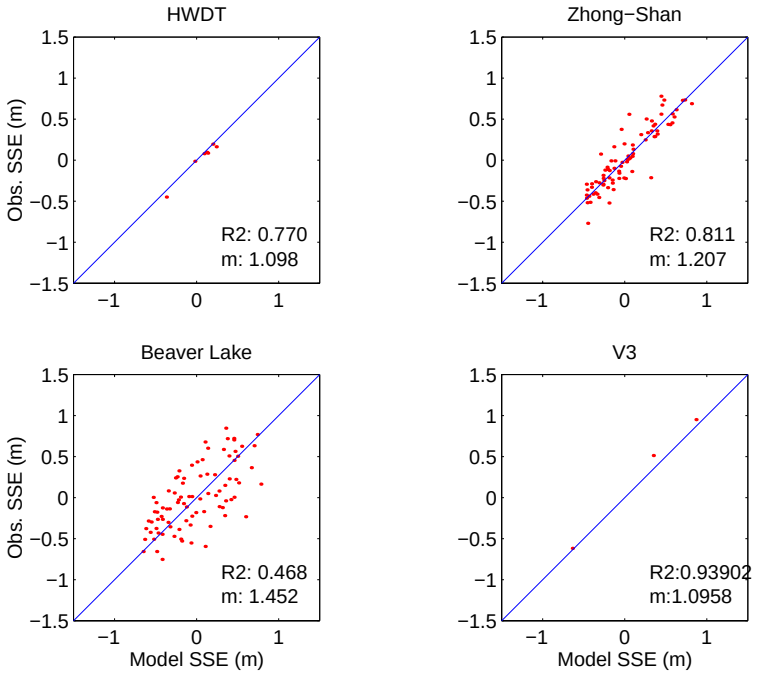

Figure 8.6: Scatter plot comparisons of predicted (using MECO with WCT grid B) and observed tidal elevation at the labelled locations in the Amery domain. Regression statistics are also shown.

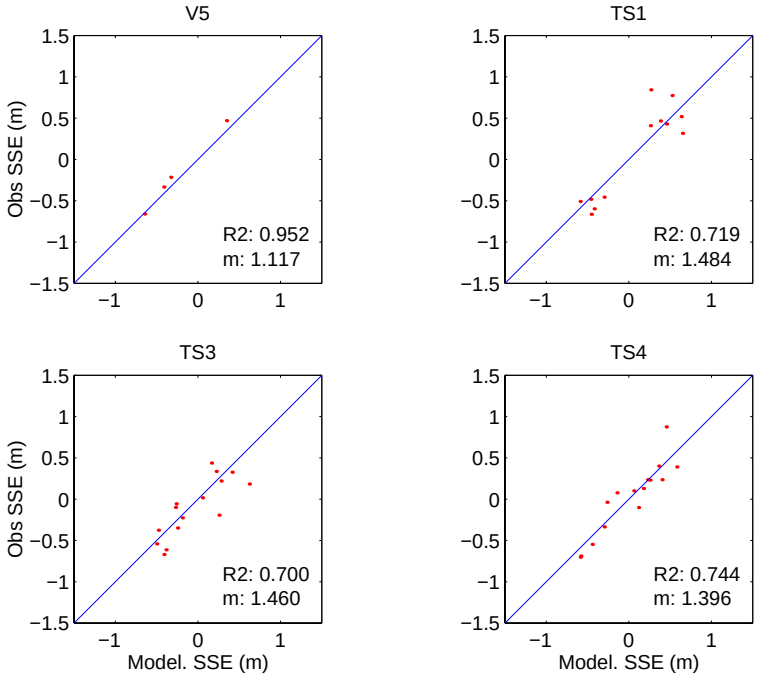

Figure 8.7: Scatter plot comparisons of predicted (using MECO with WCT grid B) and observed tidal elevation at the labelled locations in the Amery domain. Regression statistics are also shown.

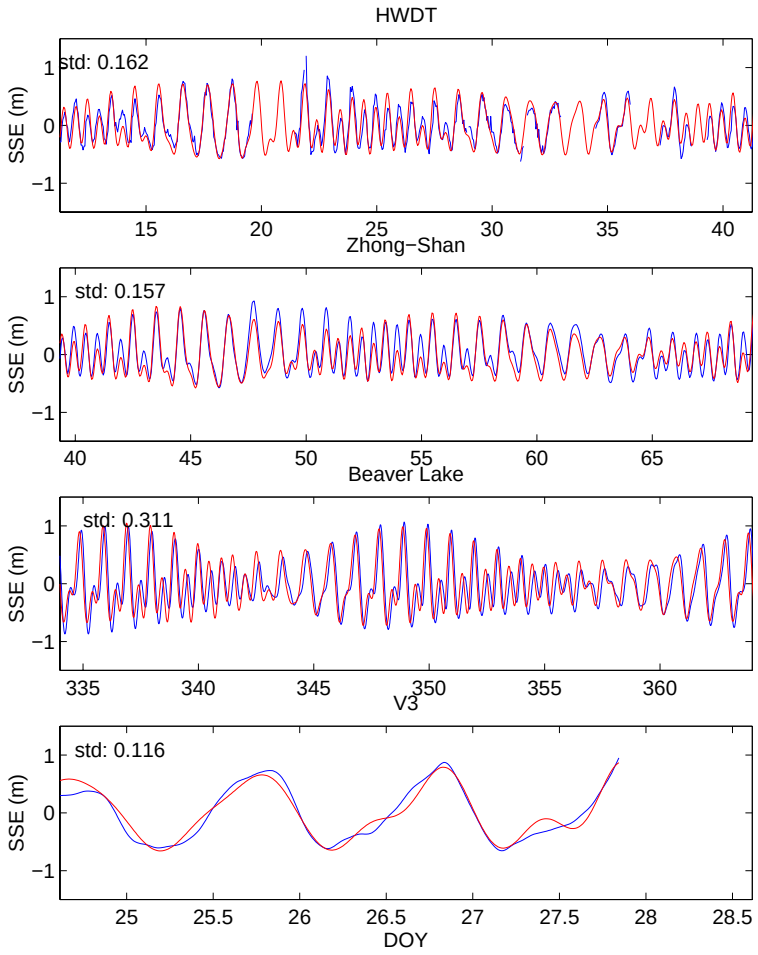

Figure 8.8: Time series comparisons of predicted (using MECO with WCT grid B) and observed tidal elevation at the labelled locations in the Amery domain. Model time series in red, observed time series in blue. SSE on the y-axis is sea-surface elevation. Standard deviation values are quoted in metres.

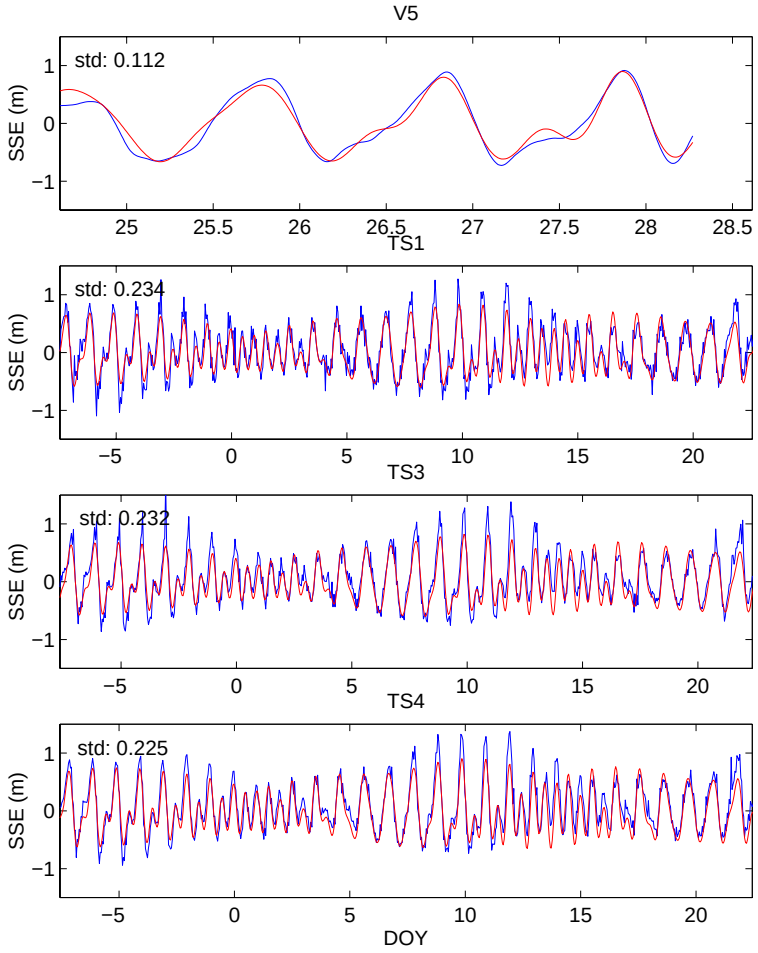

Figure 8.9: Time series comparisons of predicted (using MECO with WCT grid B) and observed tidal elevation at the labelled locations in the Amery domain. Model time series in red, observed time series in blue. SSE on the y-axis is sea-surface elevation. Standard deviation values are quoted in metres.

Table 8.6: Results of regression analysis and sea-level time series comparisons at sea-level record points in the Amery domain, for each model run with varying Water Column Thickness (WCT) grids. SD is standard deviation in m.

Station	WCT Grid	SD	R^2	m
HWDT	A	0.171	0.783	0.989
	B	0.162	0.770	1.098
	C	0.164	0.768	1.083
	CADA	0.166	0.748	1.167
Zhong-Shan	A	0.156	0.817	1.163
	B	0.157	0.811	1.207
	C	0.157	0.811	1.203
	CADA	0.166	0.789	1.279
Beaver Lake	A	0.277	0.855	0.709
	B	0.311	0.468	1.452
	C	0.315	0.480	1.368
	CADA	0.292	0.485	1.572
V3	A	0.522	0.405	1.075
	B	0.116	0.939	1.096
	C	0.112	0.943	1.093
	CADA	0.168	0.874	1.230
V5	A	0.734	0.361	0.897
	B	0.112	0.952	1.117
	C	0.106	0.958	1.111
	CADA	0.159	0.909	1.242
TS1	A	0.245	0.689	1.377
	B	0.234	0.719	1.484
	C	0.234	0.718	1.464
	CADA	0.250	0.679	1.608
TS3	A	0.243	0.670	1.429
	B	0.232	0.700	1.460
	C	0.232	0.699	1.441
	CADA	0.242	0.673	1.560
TS4	A	0.258	0.695	1.179
	B	0.225	0.744	1.396
	C	0.225	0.743	1.362
	CADA	0.237	0.721	1.515

Zhong-Shan, and Beaver Lake, differ only marginally for each model run. Model topography has not been changed significantly in these regions, and it therefore appears that variation of water column thickness in the southern portion of the grid has very little influence on the sea surface elevations in the northern half of the Amery Ice Shelf cavity, or Prydz Bay. Large variation in sea surface elevation is observed between model runs at GPS sites V3 and V5. Grid A displays reduced R^2, and increased standard deviation values at these points. Analagous to the comparisons of tidal constituents, very little difference is observed between the three remaining grids, B, C, and CADA.

A phase lag is observed at Beaver Lake for all runs. This lag is greatest for grids B and C. Local effects not resolved in the model topography are expected to account for this difference.

Largest amplitude errors are observed towards the southern grounding line of the Amery Ice Shelf, where the model predicts a greater amplification of semi-diurnal tides towards the south, and a lesser amplification of the diurnal tides to the south, in comparison to the observations. In reality, however, model comparisons may be slightly better given that King (2002) recognises that the inferred constituents from the short GPS records suggest amplitudes are too low for the semi-diurnal tides, and too high for the diurnal tides.

Another possible explanation for increased amplitudes in the model output in the southern portion of the floating ice shelf is the physics of the grounding line. The southern portion of the Amery Ice Shelf has a mean width of approximately 60km. Given that on each side of the shelf, a 9-10km grounding line hinge zone will exist, this leaves a narrow 40km wide shelf which is expected to behave as a free surface. The model, in its present state, does not include ice flexure dynamics. It is possible over such a narrow channel that the ice flexure effects are more important beneath the southern portion of the Amery Ice Shelf than they are thought to be on the larger Filchner-Ronne Ice Shelf and Ross Ice Shelf. The large differences observed at site TS5 suggest ice flexure points may be important.

There are a variety of reasons for the observed differences between the model output, and the available data. The two sources of error which are considered to dominate are errors in the model bathymetry, and constituent errors due to the short data records on the ice shelf.

Comparison of tidal constituents, and sea surface elevation time series, between the modelled and observed values show best results are obtained when the CADA model grid is implemented. However, the CADA model grid does not agree with available bed elevation measurements (Fig. 8.3; Ruddell, 2001). The CADA grid has a greater WCT than the

observed values in the northern portion of the Amery Ice Shelf, where many observations have been made. The CADA grid is a non-physical estimate of the basin topography. The 'best-estimate' model grid which is physically consistent with available data is grid B. Grid C results in model to observation agreement of similar resolution to that using grid B. However, the deep basin in the south of the domain is expected to be an overestimate, given that it reaches depths 500m greater than the grounding line depths which are already some of the deepest points on the Antarctic continent. All reference to the MECO Amery Ice Shelf tide model from this point will refer to the use of model grid B.

8.4 Comparison with other models

The effect of the new bathymetry and the increased resolution is evaluated by comparing the results of the model presented in this section of the thesis, to the forward stepping Circum-Antarctic Tidal Simulation (CATS) model, and the Circum-Antarctic Data Assimilation (CADA) tides model, as presented in section 6.5.1. The results of the *OzPOM* tide simulation, presented in Chapter 9, are also presented here for comparison.

8.4.1 Elevations

As with the comparisons between different MECO model runs, differences between each of the tide models are presented by comparison of the tidal amplitude and phase from the four main constituents from each model to the observed values, and through comparison of the results of regression analyses and time-series comparisons. Tables F.3 and F.4 presented in Appendix F show comparison of tidal constituents at each sea-level record site, for each of the MECO, CADA00.10, CATS00.10 and *OzPOM* models. Summarising the results from these tables, Table 8.7 shows the standard deviation of the difference between the predicted and observed tidal constituents, for each of the four tide models. Table 8.8 displays the standard deviation between predicted and observed elevation values, and the regression statistics, R^2 and slope, m, at each site, for each of the four tide models.

Comparing tidal constituents (Table 8.7), the MECO model (grid B) presented in this thesis reproduces tidal elevations better than the CATS forward stepping model, particularly the semi-diurnal constituents. The standard deviation of the difference in amplitudes for MECO is 2.3 and 3.2 cm for the M_2 and S_2 tides respectively. Corresponding values for CATS are 3.6 and 8.0 cm. Tidal phase over all constituents is best predicted, of all of the models, by *OzPOM*. However, differences in phase between all models are small,

Table 8.7: Comparing different tide models. Standard deviation of the difference in amplitude (SD_A in (cm)) and phase (SD_ϕ (°)) of the main four tidal constituents between the observed and predicted constituents from the 13 sea-level measurement sites presented in Table 8.1. MECO and *OzPOM* are presented in this thesis, CADA and CATS are tide models presented by Padman et al. (2002).

Model	M_2		S_2		K_1		O_1	
	SD_A	SD_ϕ	SD_A	SD_ϕ	SD_A	SD_ϕ	SD_A	SD_ϕ
MECO:B	2.3	13	3.2	7	4.3	7	2.8	11
OzPOM	3.5	8	6.0	7	6.5	7	2.9	9
CADA00.10	2.6	9	2.4	13	3.0	7	2.5	10
CATS00.10	3.6	8	8.0	8	3.0	7	3.6	10

each displaying a standard deviation of the phase differences of approximately 10° for all constituents.

The agreement in amplitude is slightly less accurate for MECO than for the CADA model, where real data are assimilated into the tidal solution. The amplification of the semi-diurnal tides towards the south of the domain is better reproduced by CADA than any of the other models, although amplitudes are still overestimated by $4-10$ cm. The standard deviation of phase differences is slightly better in CADA (9°) than MECO (13°) for the M_2 constituent, however the S_2 phase is better predicted by MECO (7°) than CADA (13°). Phase differences for the diurnal constituents are similar between the two models.

The *OzPOM* model shows the smallest standard deviation of the differences between predicted and observed phase ($< 9°$) over all constituents, of all the models. However, the standard deviation of the differences between predicted and observed tidal amplitude of the S_2 (6.0 cm) and K_1 (6.5 cm) constituents, are slightly increased in comparison to the barotropic models. The S_2 amplitude error is smaller than that from the CATS model. The semi-diurnal constituents are reproduced within the error bounds set by the other models. Tidal forcing of the *OzPOM* model is from sea surface elevations on the open boundary only. No astronomical tide-generating force is specified within the domain, which may result in the slightly increased amplitude error. However, MECO model runs which were carried out without the tide-generating force included, show only slight differences to model runs carried out with the force included, indicating that the influence of the tide-generating force over the scale of the model domain is small.

The predicted amplitude and phase of each constituent at site TS5, from the CADA and MECO models, are listed separately in Table 8.5. The rapid changes in amplitude and phase observed at site TS5 are not predicted by any of the models; none of which include tidal flexure of the ice shelf within the dynamics.

Table 8.8: Results of regression analysis and sea-level time series comparisons at tidal elevation points in the Amery domain, comparing the four models. SD is standard deviation in m.

Station	Model	SD	R^2	m
HWDT	MECO:B	0.162	0.770	1.098
	OzPOM	0.142	0.806	1.160
	CADA00.10	0.113	0.895	0.969
	CATS00.10	0.137	0.898	1.160
Zhong-Shan	MECO:B	0.157	0.811	1.207
	OzPOM	0.152	0.827	1.294
	CADA00.10	0.123	0.885	1.120
	CATS00.10	0.138	0.877	0.980
Beaver Lake	MECO:B	0.311	0.468	1.452
	OzPOM	0.190	0.775	1.143
	CADA00.10	0.117	0.920	0.989
	CATS00.10	0.173	0.872	0.895
V3	MECO:B	0.116	0.939	1.096
	OzPOM	0.212	0.793	1.211
	CADA00.10	0.144	0.914	1.116
	CATS00.10	0.156	0.934	1.229
V5	MECO:B	0.112	0.952	1.117
	OzPOM	0.193	0.849	1.163
	CADA00.10	0.158	0.904	1.092
	CATS00.10	0.154	0.939	1.202
TS1	MECO:B	0.234	0.719	1.484
	OzPOM	0.242	0.699	1.553
	CADA00.10	0.196	0.800	1.284
	CATS00.10	0.192	0.914	1.244
TS3	MECO:B	0.232	0.700	1.460
	OzPOM	0.231	0.703	1.511
	CADA00.10	0.182	0.820	1.247
	CATS00.10	0.188	0.926	1.241
TS4	MECO:B	0.225	0.744	1.396
	OzPOM	0.223	0.749	1.395
	CADA00.10	0.189	0.812	1.304
	CATS00.10	0.175	0.838	1.139

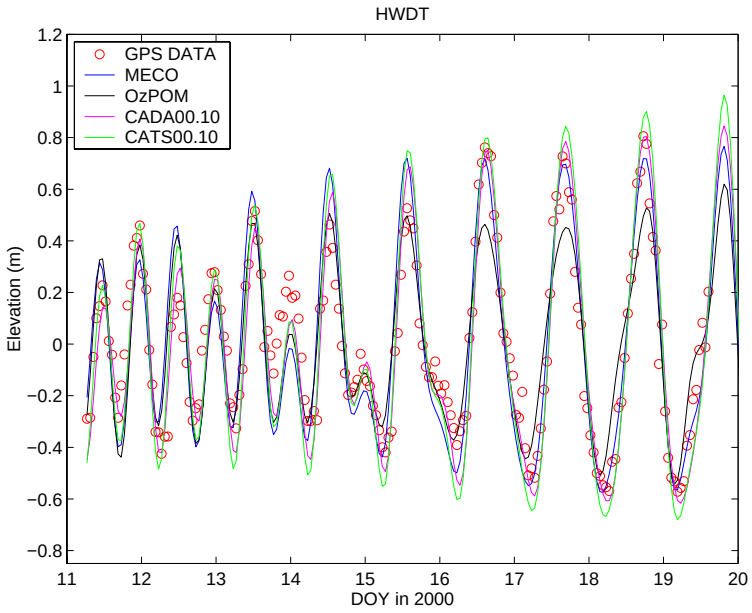

Figure 8.10: HWDT time series comparisons of predicted and observed tidal elevation using the MECO, *OzPOM*, CADA and CATS models.

Results of the time series comparisons and the regression analyses (Table 8.8) indicate that the best model agreement occurs with the data-assimilated CADA model. The CATS model shows good agreement at sites TS1, TS3, and TS4. Contrary to the results of the tidal constituent comparisons, MECO indicates better correlation to the observed GPS sea-level records at the southern sites V3 and V5 than the CADA model. As noted from the tide constituent comparisons, *OzPOM* does not predict tidal elevations as accurately as the barotropic models. However, tides are not included in the *OzPOM* model to provide accurate estimates of sea-level, but to determine the effects of increased mixing caused by tides on the sub-ice-shelf thermohaline circulation (Chapter 9). For this application, the tidal comparisons from the *OzPOM* model are considered acceptable, and no tuning of model parameters to improve the tidal solution was carried out. The similarity between each of the models is easily observed in Figure 8.10, where predicted sea-levels from the HWDT site from each of the four models, overlay the observed GPS data. These similarities are observed for the other GPS sites also.

Both of the models presented in this thesis, MECO and *OzPOM*, give comparable agreement in amplitude and phase to the CATS and CADA models. MECO indicates a slight improvement over the forward stepping CATS model, and very comparable to the assimilated CADA model. This can be attributed to the increased resolution, and the improved bathymetry beneath the ice shelf.

Given that almost all of the observation sites are ice shelf locations, the observed

model error is considered small by way of comparison. The tidal model of the Weddell Sea and the Filchner-Ronne Ice Shelf presented by Robertson et al. (1998) present a percent error of the difference in amplitude of up to 51% (S_2), and the standard deviation of the difference in phase of 70° (K_1) in comparison to tide gauges beneath the ice shelf.

In conclusion, model to observed sea-level comparisons are best for the MECO model when using WCT grid B. In comparison to other models, sea-levels predicted by MECO display improvement over previous forward-stepping barotropic sub-Amery Ice Shelf tide models, and results analagous with the data-assimilated CADA model. Although the *OzPOM* model does not predict sea-level to the same accuracy as the barotropic models, errors are still small, and for all but the K_1 constituent are within the error bounds set by the CATS model. Consequently, the model is deemed acceptable for its purpose, presented in detail in Chapter 9. Although improvements in the WCT grid are required to improve the accuracy of the models, the general effects of the tides in the sub-ice-shelf cavity are expected to be well represented by the present models.

8.4.2 Velocities

Model velocities were compared with velocity measurements from seven of the moorings deployed across the Amery Ice Shelf front, and to the five Prydz Bay Moorings, described in section 6.4.3. Tidal constituents were obtained after vertical integration of the tidal currents through the profile of current meters available. Model velocities were then compared at each mooring site, for each of the four models, MECO, *OzPOM*, CATS and CADA. Given the low velocities, only the semi-major axis is considered reliable for comparison. Each of the other tidal ellipse descriptors (semi-minor axis, inclination, and phase) are ignored as they have significant variation. Therefore, only the modelled and observed major axes of the tidal ellipsoids are compared. This approach was also taken by Robertson et al. (1998).

At each mooring location, the model velocities were scaled by the ratio of the model water depth to the reported depth at the mooring site; i.e., the depth-integrated barotropic transports were compared. The two Prydz Bay mooring sites on the continental shelf edge have considerable differences in depth, the model bathymetry indicating the sites were on the continental slope, the mooring site depths suggesting the two sites are on the shelf.

A regression analysis was carried out comparing model semi-major axes for each of the four main constituents to those observed for each set of moorings separately, for each of the four models. Table 8.9 and 8.10 display the regression statistics, R^2 and slope, m, obtained from the analysis for the Prydz Bay moorings and the Amery Ice Shelf front

Table 8.9: Correlation statistics of modelled vs observed tidal semi major axes for current-meter data from the Hodgkinson Prydz Bay Moorings. Comparisons of results from the MECO, *OzPOM*, CADA00.10 and CATS00.10 models. Slope values, $m > 1$ indicate that the model underestimates velocities.

Semi-major axis, cms^{-1}								
	M2		S2		K1		O1	
Model	R^2	m	R^2	m	R^2	m	R^2	m
MECO	0.853	0.995	0.962	0.940	0.708	1.432	0.639	2.093
OzPOM	0.230	1.250	0.244	1.390	0.984	1.259	0.990	7.418
CADA00.10	0.651	1.568	0.973	2.068	0.340	1.207	0.181	3.209
CATS00.10	0.459	1.543	0.971	1.712	0.766	10.45	0.388	1.664

Table 8.10: Correlation statistics of modelled vs observed tidal semi major axes for current-meter data from 2001 Amery Ice Shelf front Moorings. Comparisons of results from the MECO, *OzPOM*, CADA00.10 and CATS00.10 models. Slope values, $m > 1$ indicate that the model underestimates velocities.

Semi-major axis, cms^{-1}								
	M2		S2		K1		O1	
Model	R^2	m	R^2	m	R^2	m	R^2	m
MECO	0.395	1.113	0.458	1.068	0.367	1.468	0.401	1.472
OzPOM	0.730	0.656	0.335	0.632	0.530	1.250	0.930	1.020
CADA00.10	0.668	0.879	0.545	0.840	0.846	2.135	0.637	1.025
CATS00.10	0.762	0.756	0.695	0.669	0.847	2.143	0.386	0.854

moorings respectively. A slope, m, value less than 1 indicates that the model underestimates the observed semi-major axis of the tidal ellipse.

At the locations of the Amery Ice Shelf front moorings (Table 8.10) typical semi-major axis magnitudes are approximately 1.5 cms^{-1} for the semi-diurnal constituents, and 1.2 cms^{-1} for the diurnal constituents, for each of the nine moorings. Velocities are slightly decreased at Mooring 1 on the eastern side of the ice front ($\sim 0.9 cms^{-1}$ and $0.5 cms^{-1}$) respectively). MECO provides the poorest comparison ($R^2 \sim 0.4$) to observed semi-major axes over all constituents. MECO consistently underestimates the observed velocities. *OzPOM* provides the best estimate, although semi-diurnal constituents are overestimated ($m \sim 0.65$), and the S_2 tide correlation is low. CADA and CATS show similar characteristics, with CATS displaying slightly less accuracy. The K_1 semi-major axes are underestimated in both the CATS and CADA models. Otherwise, CADA and *OzPOM* compare equally well to the observed currents.

At each of the Prydz Bay Moorings, Table 8.9, comparisons for each model are quite poor. MECO provides the best estimates of the semi-major axes of all of the models.

However, MECO considerably underestimates the diurnal constituent velocities. CADA and CATS prove quite poor over all constituents for velocity comparisons at each of the Prydz Bay moorings. *OzPOM* is capable of reproducing the K_1 constituent major axis, but the semi-diurnal constituents show very low R^2 values ($R^2 < 0.25$) and the O_1 tide is significantly underestimated ($m = 7.418$).

For individual moorings: the south-east bay current meter mooring sites (M3-8485 and M3-8586), MECO does significantly better at reproducing the tidal currents, both diurnal and semi-diurnal, than both the CADA and CATS models. At the shelf break sites (M1-8485 and M1-8586), CADA and CATS both outperform MECO, however the CADA/CATS bathymetry recognises these points as on the shelf, and not on the shelf slope as in the new bathymetry. The mid bay mooring (M2-8788) shows best comparisons for the diurnal tides using the MECO model. Semi-diurnal tides are reproduced more accurately by CADA. The MECO model reproduces the measured tides as well as the assimilated model, and improves on that of the forward stepping model. Note that no current velocity measurements are assimilated into the CADA model.

Increased accuracy of tidal velocities in *OzPOM* at the Amery Ice Shelf front over the other three models is a likely result of the baroclinicity, and better resolution of drag processes in the cavity, being accounted for in the *OzPOM* model, which are not resolved in the other 2-D barotropic models. The simplistic temperature and salinity field in Prydz Bay used in the *OzPOM* model may result in a poor estimate of the baroclinicity in Prydz Bay. This may explain the poor tidal current comparisons of *OzPOM* to the Prydz Bay current meter observations. However, *OzPOM* is comparable to the CATS and CADA models in reproducing tidal velocities at these sites.

Very few observations of the tidal currents within the model domain have been collected. Each of the four tide models which have been compared here, appear to produce tidal currents representative of the current limited knowledge of the tides in the region. Again, model bathymetry and measurement errors are expected to be the largest sources of error.

8.5 Model Results

8.5.1 Tidal Elevations

Tidal observations indicate that the Amery Ice Shelf is a region of mixed semi-diurnal and diurnal tides, with a range of 1-2m. Figures 8.11 to 8.14 display elevation amplitude and phase for the M_2, S_2, K_1, and O_1 constituents respectively. Noisy boundary effects must

be discounted from the analysis. These figures are comparable to similar figures from the CADA model (Fig. 6.6). In the open waters of Prydz Bay, the magnitudes of the diurnal tides (0.25 m) are generally observed to be slightly larger than those of the semi-diurnal tides (0.15 m). In the ice shelf cavity, amplitudes of the semi-diurnal constituents is amplified so that at the southern most extent of the grounding line, the amplitude of the semi-diurnal constituents (0.35 m) is larger than the amplitude of the diurnal constituents (0.30 m).

At the southern end of the Amery Ice Shelf, the model predicts the M_2 constituent (Fig. 8.11) to have a tidal amplitude of 0.33m and phase of 218° with respect to Greenwich. In Prydz Bay at Zhong-Shan, the model predicts an M_2 tidal amplitude of 0.17 m, and phase of 210°. Phase generally propagates from east to west along the Antarctic continent. The phase changes very little beneath the Amery Ice Shelf. The S_2 constituent (Fig. 8.12) is structurally similar to the M_2 tide, with similar amplitudes and phase variation beneath the shelf. No amphidromic points occur in the model domain for the semidiurnal constituents, however, one is believed to exist just to the west of the model domain on the Mac-Robertson shelf for the M_2 tide (Padman et al., 2002), and strongly influences tides in the region. The model predicts a co-oscillating tidal environment, consistent of a narrow channel, with an increase in amplitude and only small variation of phase and amplitude beneath the ice shelf.

The tidal amplitude for the diurnal constituent, K_1, (Fig. 8.13) displays only a slight increase southwards beneath the Amery Ice Shelf. Phase changes are small for the diurnal constituent over the entire model domain, but shows slight propagation from east to west. At the southern end of the Amery Ice Shelf, the model predicts the K_1 constituent to have a tidal amplitude of 0.3 m and phase of 281°. At Zhong-Shan, Prydz Bay, the model predicts a K_1 tidal amplitude of 0.26 m, and phase of 283° with respect to Greenwich. The structure of the O_1 constituent (Fig. 8.14) is very similar to K_1, with similar amplitudes and phase differences beneath the shelf. Four Ladies Bank appears to be a region of complex localised tides. The K_1 constituent decreases in amplitude over the bank, and the O_1 increases in amplitude. A local minima in phase of the K_1 constituent over the bank suggests eastward propagation of the K_1 constituent tidal energy towards the bank. Shallow water off Cape Darnley reduces the amplitude, and alters the phase, of the diurnal constituents. The amplitude of the K_1 constituent reduces to 0.18 m in this region.

The propagation of tides beneath the Amery Ice Shelf differs markedly from beneath the other major embayed ice shelves around the Antarctic continent, namely the Filchner-Ronne and Ross Ice Shelves. The Amery Ice Shelf is significantly narrower ($\sim 200km$) than the other two ice shelves ($\sim 700km$). This results in the co-oscillation of the tides

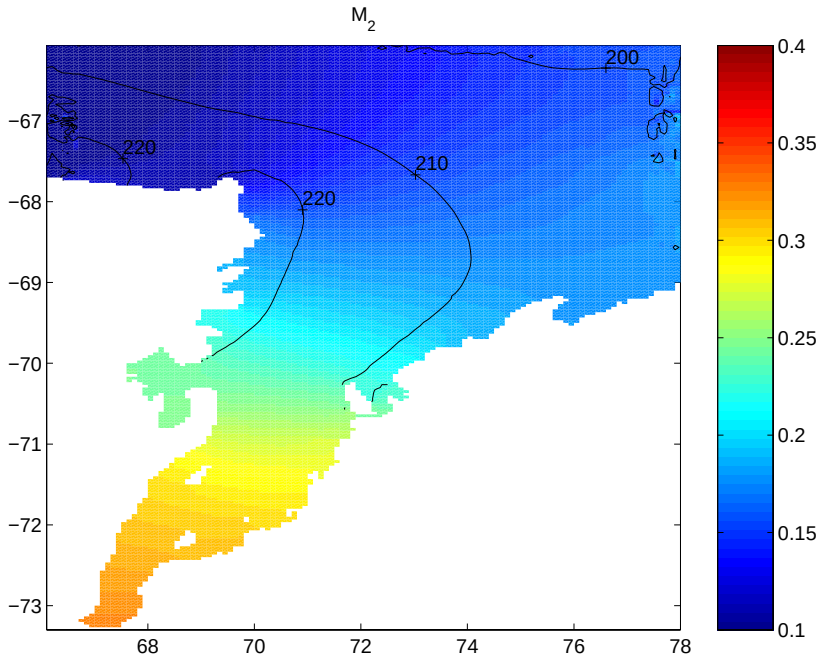

Figure 8.11: The predicted elevation (m) and phase (°) for the M_2 constituent, with the amplitude given by the colour scale and the phase by the contour lines. The contour interval is 10° in phase

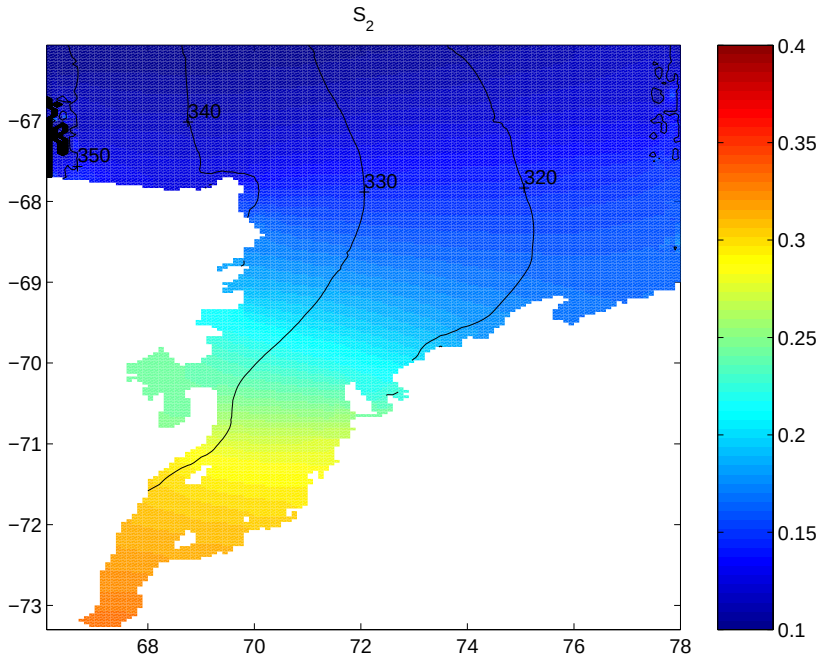

Figure 8.12: The predicted elevation (m) and phase (°) for the S_2 constituent, with the amplitude given by the colour scale and the phase by the contour lines. The contour interval is 10° in phase

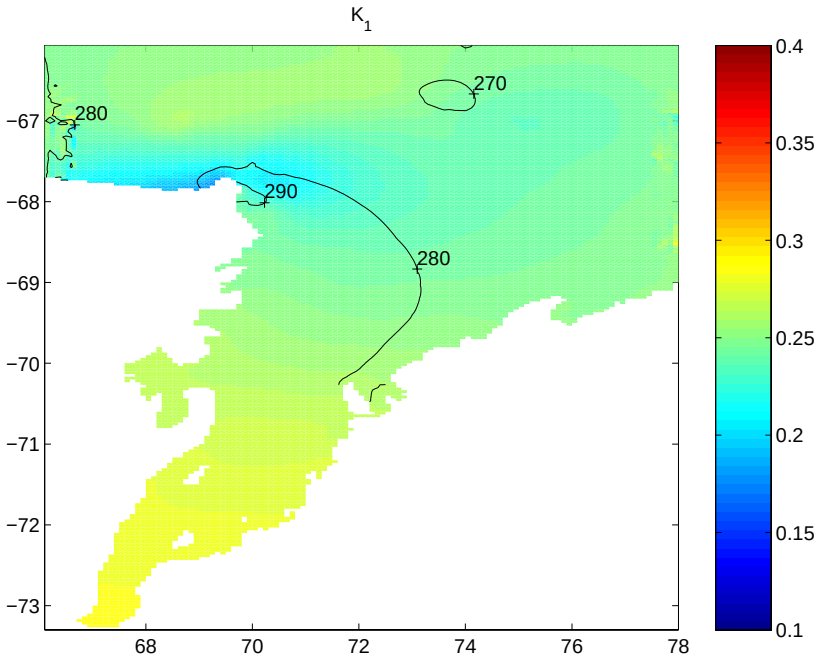

Figure 8.13: The predicted elevation (m) and phase (°) for the K_1 constituent, with the amplitude given by the colour scale and the phase by the contour lines. The contour interval is 10° in phase

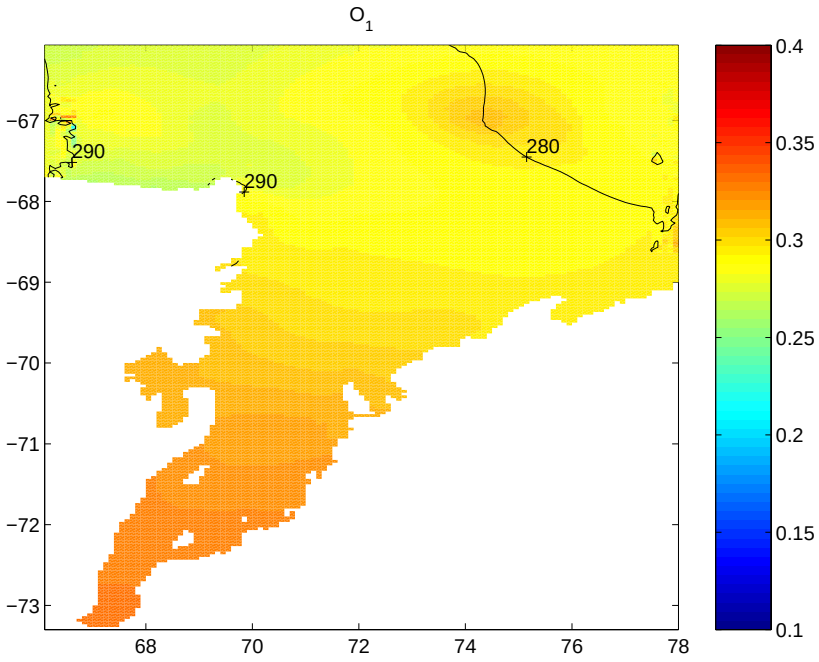

Figure 8.14: The predicted elevation (m) and phase (°) for the O_1 constituent, with the amplitude given by the colour scale and the phase by the contour lines. The contour interval is 10° in phase

beneath the Amery Ice Shelf, in contrast to the more complex propagation observed beneath the larger ice shelves, which suggest a Kelvin wave propagating anticlockwise (westwards) around the embayment (MacAyeal, 1984b; Makinson and Nicholls, 1999). Robertson et al. (1998) indicate amphidromes of the semidiurnal constituents observed beneath the Filchner-Ronne Ice Shelf. The amplitude of the semi-diurnal constituents beneath the FRIS exceed 1 m in the far southern reaches. Diurnal amplitudes are approximately 0.4 m. This leads to a tidal range much greater than that observed beneath the Amery Ice Shelf.

8.5.2 Tidal Velocities

The tidal ellipsoids for each of the four main constituents have been calculated over the whole model domain. Figures 8.15 to 8.18 display the tidal ellipsoids over the grid, for every fifth point in the $i-$direction (east), and every ninth point in the $j-$direction, for the M_2, S_2, K_1, and O_1 constituents respectively.

The magnitude of the major axis, u_{maj} of the semi-diurnal ellipsoids are generally less than $5cms^{-1}$ beneath the Amery Ice Shelf. One region, to the south-west of Gillock Island, predicts u_{maj} values in excess of $5cms^{-1}$ for both the M_2 (Fig. 8.15) and S_2 (Fig. 8.16) constituents. Beneath the northern portion of the Amery Ice Shelf, u_{maj} has a mean value of approximately $3cms^{-1}$ for both semi-diurnal constituents. Towards the southern grounding lines, the semi-diurnal major axes decrease to less than $2cms^{-1}$. In the open waters of Prydz Bay, the largest values of u_{maj} are predicted off the point of Cape Darnley, on Fram bank and on Four Ladies Bank of up to $6cms^{-1}$. Decreased values of u_{maj} are observed in regions of deep water, such as Svenner Channel, and the Amery Depression. Alignment of the tidal ellipsoids is north-south throughout the model domain for all constituents. An increase in magnitude of the semi-diurnal tidal currents is predicted at the ice front, becoming stronger in the reduced depths of the sub-ice-shelf cavity.

For the diurnal constituents, K_1 (Fig. 8.17) and O_1 (Fig. 8.18), values of u_{maj} are predicted to be less than that from the semi-diurnal constituents beneath the ice shelf, with values less than approximately $2cms^{-1}$ under the entire ice shelf. However, diurnal tidal currents appear to be larger than the semi-diurnal within Prydz Bay, with values of u_{maj} in excess of $10cms^{-1}$ on Fram Bank, off the point of Cape Darnley, and as large as $7cms^{-1}$ on Four Ladies Bank. Low speed diurnal currents ($< 2cms^{-1}$) are predicted in Svenner Channel, and the Amery Depression. Very little amplification of diurnal tidal currents is predicted at the step in water column thickness at the ice front. The diurnal ellipsoids suggest more anticlockwise rotation than observed in the semi-diurnal constituents, with a

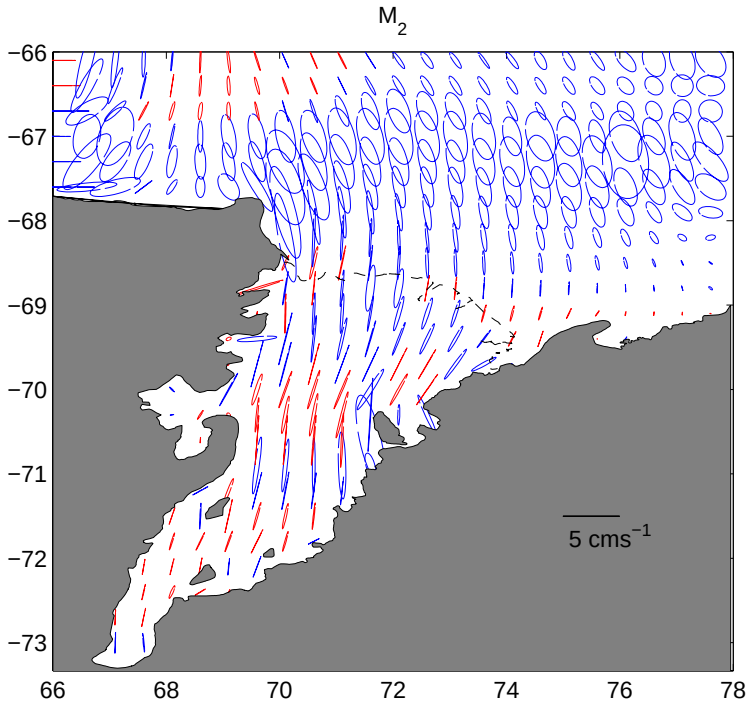

Figure 8.15: Modelled tidal current ellipses plotted at every 5th point in the the $i-$direction (east), and every 9th point in the $j-$direction (north), for the M_2 constituent. Blue ellipses indicate anti-clockwise rotation, red ellipses indicate clockwise rotation.

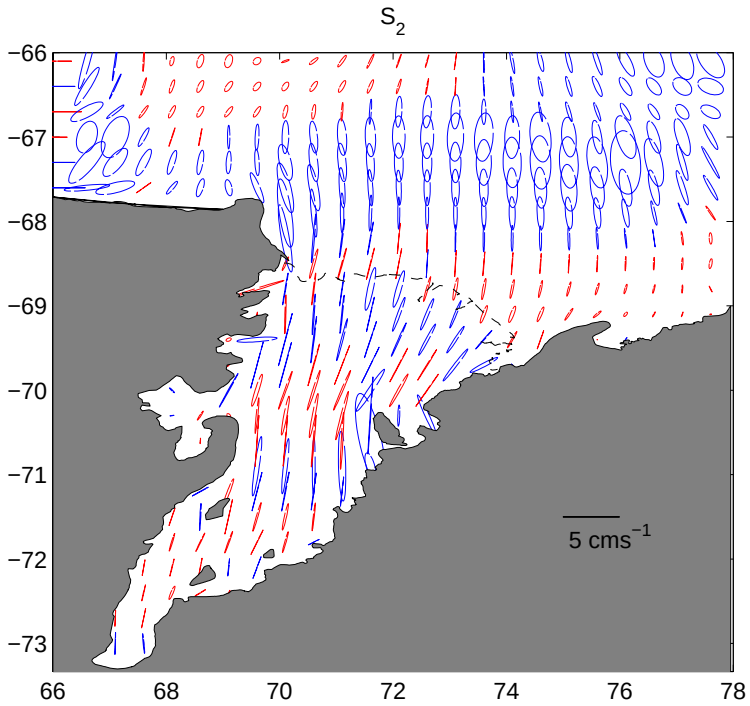

Figure 8.16: Modelled tidal current ellipses plotted at every 5th point in the the $i-$direction (east), and every 9th point in the $j-$direction (north), for the S_2 constituent. Blue ellipses indicate anti-clockwise rotation, red ellipses indicate clockwise rotation.

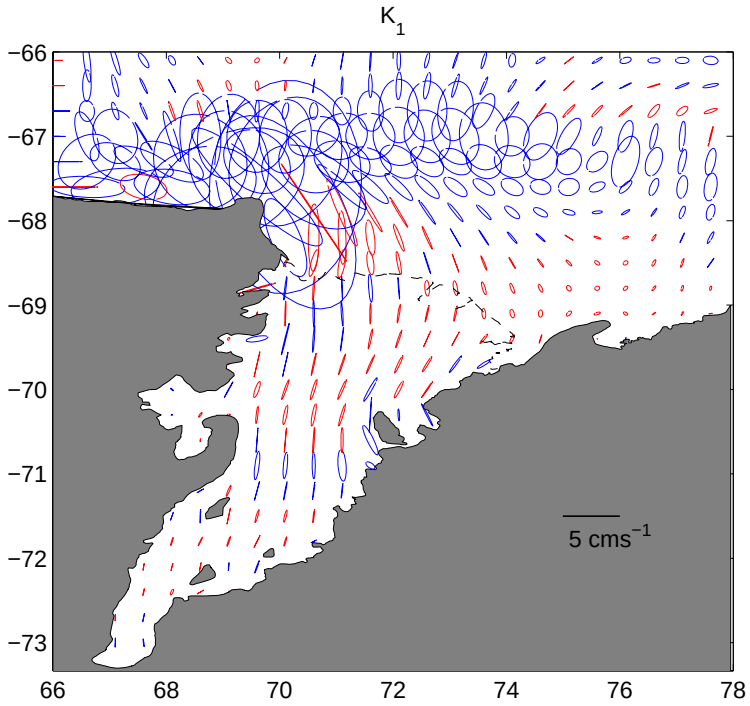

Figure 8.17: Modelled tidal current ellipses plotted at every 5th point in the the $i-$direction (east), and every 9th point in the $j-$direction (north), for the K_1 constituent. Blue ellipses indicate anti-clockwise rotation, red ellipses indicate clockwise rotation.

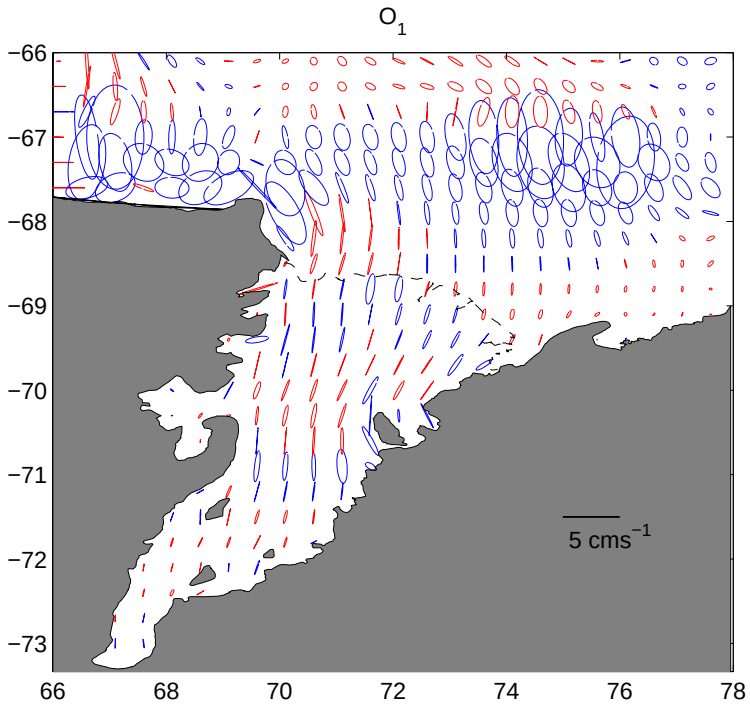

Figure 8.18: Modelled tidal current ellipses plotted at every 5th point in the the $i-$direction (east), and every 9th point in the $j-$direction (north), for the O_1 constituent. Blue ellipses indicate anti-clockwise rotation, red ellipses indicate clockwise rotation.

much greater east-west flow component.

A useful measure of typical tidal current magnitude is given by (Robertson et al., 1998):

$$u_{typ} = \left[\sum_{i=1}^{4}(u_i^2 + v_i^2)\right]^{\frac{1}{2}}$$

where u_i and v_i are the amplitudes of the east and north components of velocity for tidal constituent i, representing the four main tidal constituents (Fig. 8.19). u_{typ} is physically the maximum current available as a result of the four considered tidal constituents. Values of u_{typ} are typically of the order $5-10\ cms^{-1}$ beneath the northern portion of the Amery Ice Shelf, decreasing to $2-3\ cms^{-1}$ towards the southern extent of the grounding line. The small region to the south-west of Gillock Island, and a region on the western side of the Amery Ice Shelf, both suggest larger tidal currents of the order $7-10\ cms^{-1}$. Only a slight amplification of tidal currents is predicted at the rapid change in bathymetry at the ice front. Svenner Channel shows low tidal currents, as also found in Prydz Channel, and the Amery Depression, all predicting u_{typ} currents of less than $5\ cms^{-1}$. Currents on Fram and Four Ladies Banks are the strongest in the model domain, with u_{typ} values of up to $25\ cms^{-1}$. u_{typ} values reach up to $45\ cms^{-1}$ off Cape Darnley.

The observed decrease in tidal currents from the shelf break to the Svenner Channel compares well to the observations of Nunez Vaz and Lennon (1996) where such a decrease was observed in the current meter data collected (section 6.4.3; Hodgkinson et al., 1988, 1991a,b). u_{typ} values of $25\ cms^{-1}$ on the shelf break compare well to observed tidal currents observed on the shelf break of order $25cms^{-1}$.

In conclusion, the maximum tidal currents beneath the Amery Ice Shelf are generally weak, with maximum values of u_{typ} of $10-15\ cms^{-1}$, and typical values of u_{typ} of $5-10\ cms^{-1}$ predicted. The outer shelf in Prydz Bay suggest larger tidal currents of up to $25\ cms^{-1}$. Bed shear stress values associated with such small maximum current speeds are of the order of $0.1Nm^{-2}$, which are large enough to mobilise only the finest (up to $\sim 100\mu m$) non-cohesive sediments. Grain size analysis of surface sediments taken from the ice shelf front, presented in chapter 7, indicate typical mean grain sizes ranging from $20\mu m$ to $600\mu m$, however, the silicous mud and ooze facies common to the Prydz Bay continental shelf, and found in the sub-ice shelf sediment samples (Chapter 7), are highly cohesive. Therefore, tidal currents are predicted not to be of sufficient magnitude to mobilise sediments beneath the Amery Ice Shelf, however, currents on the shallow banks on the continental shelf edge

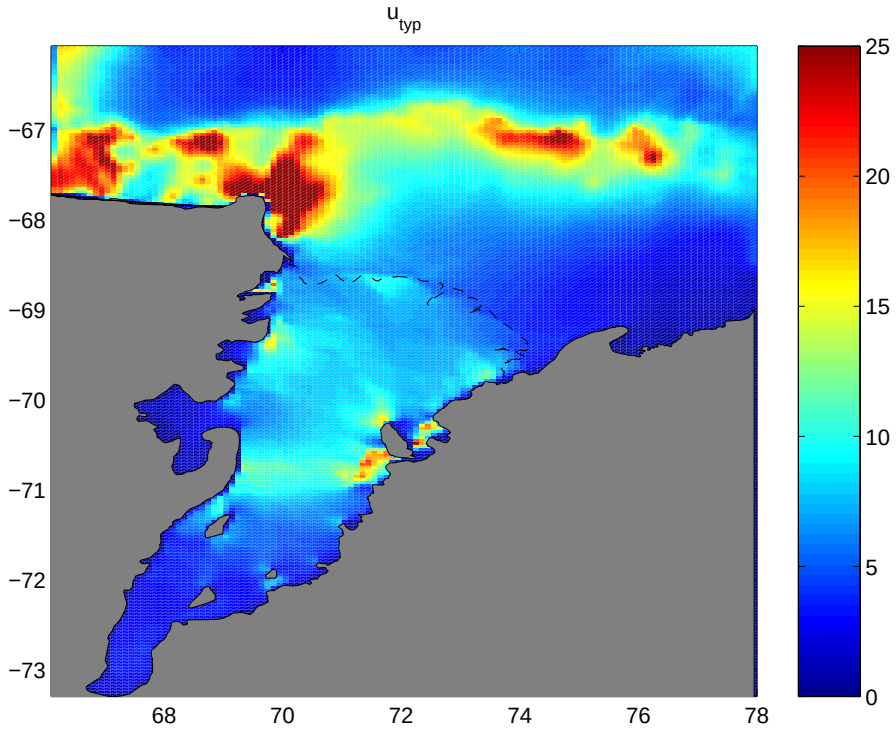

Figure 8.19: The combined typical current speed, u_{typ}, (cms^{-1}) for the four principal tidal constituents for the entire model domain.

in Prydz Bay may be large enough to do so during periods of spring tide.

The tidal currents beneath the Amery Ice Shelf are significantly smaller than those predicted beneath the FRIS and RIS. To the west of the Berkner Island near the calving ice front of the FRIS, u_{typ} values in excess of 100 cms^{-1} are predicted in the sub ice shelf cavity (Robertson et al., 1998), which drive residual currents of approximately 6 cms^{-1}, westwards along the ice shelf front (Makinson and Nicholls, 1999); i.e., the residual tidal currents at the FRIS ice shelf front are approximately the same magnitude as the maximum tidal currents beneath the Amery Ice Shelf. Maximum residual currents across the Amery Ice Shelf front, computed from the MECO model, are less than 1 cms^{-1} westwards. The semi-major axis of the K_1 constituent alone reaches ~ 50 cms^{-1} in the sub-Ross Ice Shelf cavity (MacAyeal, 1984b). Residual currents at the Ross Ice Shelf front, north-west of Roosevelt island, are also predicted to be ~ 6 cms^{-1}. The small residual tidal currents at the Amery Ice Shelf front have little impact on the flux of heat and salt beneath the ice shelf.

8.6 Tidal Energy and Vertical Mixing beneath the Ice Shelf

The tidal energy flux, $\vec{E}$, vectors were computed over the model domain using (Makinson and Nicholls, 1999).

$$\vec{E} = \vec{u}(g\rho H\eta + \rho H\frac{1}{2}|\vec{u}|^2)$$

where $\vec{u}$ is the depth averaged tidal velocity, H is the water column thickness, η is the displacement of the sea surface from equilibrium level, g is the gravitational acceleration, and ρ is seawater density (1028 kgm^{-3}). The first term, which dominates, represents work being done against gravity, and the second term represents the kinetic energy. Figure 8.20 is a map of the average energy flux vectors over the model domain.

The energy flux is predominantly westward along the Princess Elizabeth Land coast, turning southward under the Amery Ice Shelf via the depression on the eastern side of the ice front. A small amount of energy turns to the left and exits as part of a small anticlockwise feature in the north-eastern extent of the ice shelf cavity, however the majority of the tidal energy propagates clockwise beneath the northern portion of the ice shelf before emerging on the western side of the ice shelf front in the Lambert and Nanok deeps. A small amount of energy returns to the east beneath the northern extent of the Ice Shelf. The energy leaving the cavity propagates in a northward jet along the coast past Cape Darnley, where it turns to join the strong eastward return energy propagation along the continental slope.

Within the cavity, the energy drops markedly at $\sim 70°S$, where a constriction in model cavity thickness is observed between Jetty Peninsula and Gillock Island, at the southern limit of the clockwise propagating energy flux. Energy passes to the south of the domain via a broad southward flow on the western side of the cavity to join a second clockwise propagating 'eddy' in the south of the domain. This southern feature has a broad southward band of propagation past both Robertson and Clemence Massif, before turning northwards at $\sim 71.3°S$ and propagating in a narrow northward jet along the west coast between Jetty Peninsula and Fisher Massif. South of 71.3°, the energy flux is small and variable, suggesting very little tidal energy reaches the southern extent of the domain, having dissipated through friction in the cavity. In reality, ice shelf flexure may also contribute to further energy dissipation, although this is not represented in the model.

Along the Antarctic coast, the westward propagation along the Princess Elizabeth

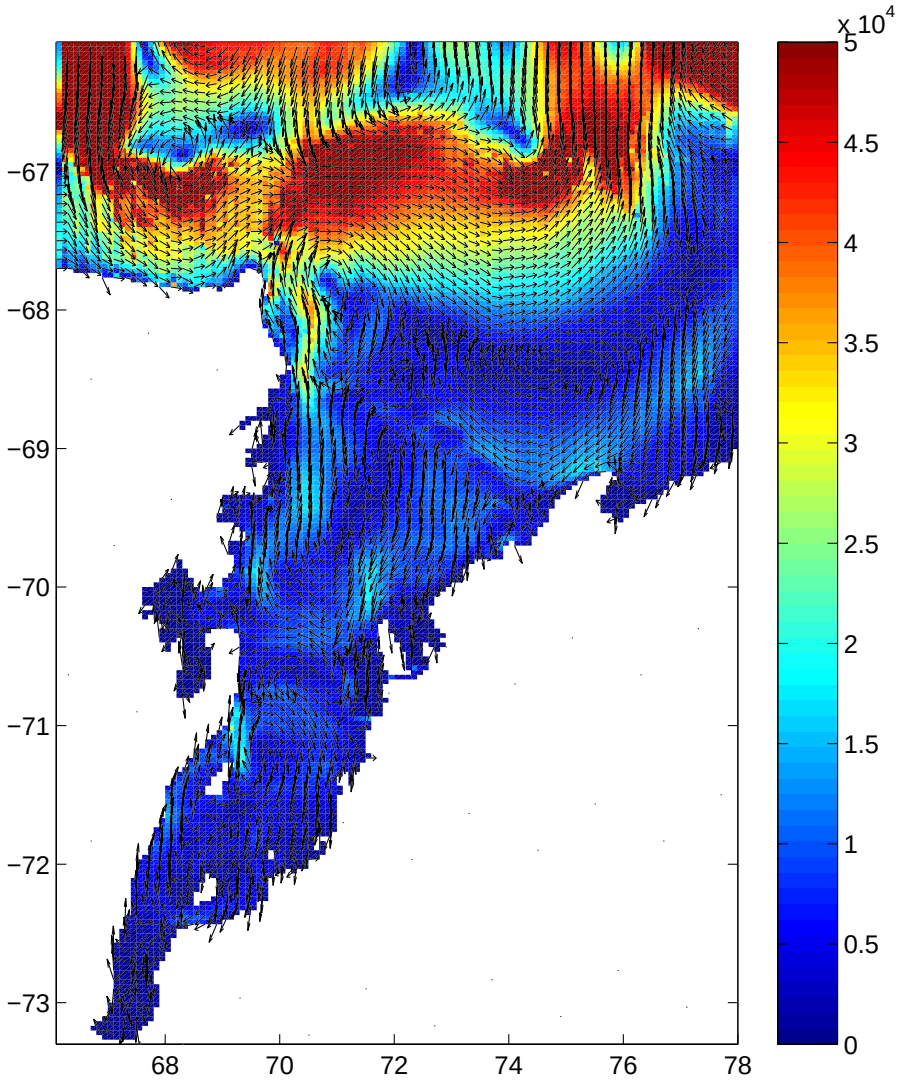

Figure 8.20: Average tidal energy flux vectors are plotted for every second grid point on the model domain. Shading indicates flux magnitude ($Jm^{-1}s^{-1}$) according to the colour scale, arrows are unit vectors indicating direction.

Land coast disappears to the western side of the Amery Ice Shelf. A strong eastward flux is observed along the continental slope. The likely cause is the amphidromic point in the M_2 tide constituent to the west of the model domain, significantly altering the propagation of tidal energy in the region. This serves to shift the east-west propagation of M_2 tidal energy to a north-south direction. This combined with the eastward propagation of the K_1 constituent results in the strong observed flux.

The sub-ice-shelf tidal energy flux shows similar features to the depth-integrated thermohaline circulation predicted by Williams et al. (2002) in the Ice Shelf cavity, with a main northern clockwise gyre, and a second smaller gyre in the south of the domain. This may suggest that the thermohaline circulation, and the propagation of tidal energy in the cavity is strongly dependent on the water cavity thickness.

Within the sub-ice shelf cavity, isolation from atmospheric forcing suggests that tidal currents are likely to be a principal source of energy for mixing (MacAyeal, 1984a; Makinson and Nicholls, 1999). Frictional drag from the seafloor and the base of the ice shelf produce vertical shear; the resulting turbulence causing vertical mixing throughout the water column. Under a quadratic drag law assumption, the time averaged rate of energy dissipation per unit area by surface friction, D_B, is given by:

$$D_B = \rho C_D \left\langle |\vec{u}|^3 \right\rangle$$

where the angle brackets denote time averaging over the tidal analysis period of the model run. As in the model runs, the frictional drag coefficient, C_D, is doubled for grid points covered by the ice shelf to account for the second frictional interface at the ice shelf base. The mean dissipation rate per unit area due to surface friction at the Ice Shelf base and the seabed, for the region covered by the Amery Ice Shelf, is calculated as $0.1 \times 10^{-3} W m^{-2}$. Over the $\sim 60000\ km^2$ area of the cavity, $\sim 6MW$ of energy is dissipated through surface drag in the cavity. Regions of high energy dissipation rate are obviously correlated with regions of high velocities, as a result of the cube relation of water speed. The largest of these being in the small area to the south-west of Gillock Island. In comparison to the other major embayed ice shelves, Robertson et al. (1998) predict $\sim 27GW$ is dissipated due to friction in the Filchner-Ronne Ice Shelf cavity, at a mean rate of $67 \times 10^{-3} W m^{-2}$. MacAyeal (1984b) calculates $\sim 3.5GW$ of tidal energy is dissipated due to friction in the Ross Ice Shelf cavity, at a mean rate of $6 \times 10^{-3} W m^{-2}$. Dissipation rates beneath the Amery Ice Shelf are therefore an order of magnitude smaller than those beneath the Ross Ice Shelf, and two

orders of magnitude less than those beneath the Filchner-Ronne Ice Shelf, indicating that the Amery Ice Shelf cavity is a very small sink of tidal energy around the Antarctic coastline.

Doake (1978) proposed that the interaction of tides with the glacial ice shelves surrounding Antarctica may be a major sink of the total global tidal energy. The mechanism suggested, flexing of the glacial ice by spatial gradients in the tidal elevation, is not included in this model. Barotropic models predicting tides beneath the Filchner-Ronne Ice Shelf (Robertson et al., 1998; Makinson and Nicholls, 1999), argue that their good fit of modelled elevations and currents with observations without the inclusion of this mechanism indicates that tidal flexure at the ice shelf margins does not dissipate much energy. Similarly, Ray and Egbert (1997) found the flux of energy across $60°S$ toward the Antarctic coastline, using ocean-tide models derived from Topex/Poseidon satellite altimeter measurements, to be small, and therefore concluded that Antarctica is an insignificant sink in the global tidal energy budget, ruling out the suggestion made by Doake (1978). However, Smithson et al. (1996) suggested that tidal flexure may be important as a tidal energy sink in their tidal model, as they found that a factor of 50 increase in the friction coefficient beneath the Filchner-Ronne Ice Shelf resulted in better model to observation comparison. They suggested that the increase in energy dissipation, caused by the increase in friction coefficients, represent the energy loss in the hinge zone at the grounding line. Following the work of Smithson et al. (1996), model runs were carried out in this study with the friction coefficient, C_D, increased by a factor of 5, 10, 20 and 50, beneath the ice shelf compared to that in open water to represent both frictional interfaces and the increased dissipation as a result of ice shelf flexure at the grounding line. A 50 times increase of the friction coefficient decreased tidal elevations at the southern extent of the Amery Ice Shelf cavity by just 2 cm; i.e., the tidal elevation was still overestimated by ~ 8 cm, and provided little improvement of model results.

The Amery Ice Shelf has proportionally a much greater length grounding line than other major embayed ice shelves, relative to the size of the ice shelf. The approach of Smithson et al. (1996) of increasing the friction coefficient in the cavity is likely a poor estimate of the energy dissipation due to ice flexure at the grounding line. A possible improvement for an approximation of the dissipation of energy as a result of this effect in future models could be a radiation boundary condition, allowing energy to propagate into the ice shelf grounding line, without reflection of the tidal energy back into the cavity.

MacAyeal (1984a) and Makinson and Nicholls (1999) have all taken the same approach to estimate the minimum basal melt rate required to maintain stratification in the water

column. The same approach will be used here. It is estimated that $1-2\%$ of the tidal energy dissipated at frictional surfaces is available for vertical mixing of the water column (Fearnhead, 1975; Schumacher et al., 1979). The power required to mix freshwater, melted from the ice shelf base, through the water column is dependent on the rate of freeze, Φ (or melt, $\Phi < 0$). The power required to entrain surface meltwater into an otherwise well mixed but salty water column of depth H is given by MacAyeal (1984a):

$$-2\Phi\rho\beta gSH$$

where $\beta = \frac{1}{\rho}\left(\frac{\partial\rho}{\partial S}\right) = 0.8\times10^{-3}$, and S is the salinity in the lower half of the water column. In the Amery Ice Shelf cavity, water in this layer is LSSW ($S \sim 34.6$). For the applications beneath the Ross and Filchner-Ronne Ice Shelves, HSSW ($S \sim 34.75$) is found in this layer (MacAyeal, 1984a; Makinson and Nicholls, 1999). The power available from tidal dissipation is:

$$\alpha\rho C_D \left\langle|\vec{u}|^3\right\rangle$$

where $\alpha(0.015)$ is the fraction of total energy estimated to be available for vertical mixing. Therefore, for a water column to be well mixed, the rate of negative freeze (melt) must be less than Φ_M, where Φ_M is given by (MacAyeal, 1984a).

$$\Phi_M = \frac{\alpha\rho C_D \left\langle|\vec{u}|^3\right\rangle}{\frac{1}{2}\rho\beta gSH}$$

In areas where the rate of negative freeze (melt) is greater than Φ_M, stratification will prevail. The spatial distribution of Φ_M beneath the Amery Ice Shelf indicates no value in excess of $1\times10^{-3}ma^{-1}$; the largest value being in the zone of stronger currents to the south-west of Gillock Island. Low tidal current speeds result in very little tidal mixing in the sub-Amery Ice Shelf cavity to overcome the stratification. Makinson and Nicholls (1999) suggest that in regions of basal freeze, where frazil ice crystals form in the water column, stratification is enhanced as a result of the additional bouyancy provided by the ice crystals (Bombosch and Jenkins, 1995). This serves to reduce the deposition of these frazil ice crystals on the ice shelf base, and the mixing of warmer water up through the water column.

Throughout most of the Amery Ice Shelf cavity, Φ_M is significantly less than estimated melt rates in the cavity (Fricker et al., 2001; Williams et al., 2002; and Chapter 9). This predicts a well stratified environment, and a consequently small vertical transfer of heat

through the water column, shutting down the high melt rates. It seems therefore, that other mechanisms may be important in mixing the sub-ice-shelf water column. The high vertical heat fluxes required to maintain the predicted basal melt pattern may be induced by the shear between the deeper, warmer water and the plumes of Ice Shelf Water rapidly ascending the steep basal slope (MacAyeal, 1984a; Jenkins, 1991; Makinson and Nicholls, 1999). Such ISW plumes may be initiated near the grounding line, where the water column pinches out, and tidal mixing will be locally high - unresolved by the current model resolution. Once this circulation is generated, the associated mixing continues to drive basal melting to a level of equilibrium.

The effects of tides beneath the Amery Ice Shelf appear much less important for processes of mixing, than the tides beneath the other major embayed ice shelves. Vertical mixing in the cavity appears more a property of the thermohaline circulation, than that of the tides, and therefore the tidal motion has only a small influence on the thermohaline circulation in the Amery Ice Shelf cavity. The influence of tides on sediment motion within the ice shelf cavity appears restricted to the dynamic pumping processes occurring at the grounding line, and the distribution of any suspended particles is likely a property of the thermohaline circulation only.

Chapter 9

Baroclinic modelling of the sub-Amery Ice Shelf circulation of water and sediments

9.1 Introduction

In the previous chapter, it was shown that tidal currents provide little direct influence on the transport or mobilisation of sediments in the sub-ice-shelf cavity. In this chapter, the influence of tides on the thermohaline circulation within the cavity is examined.

The thermohaline 'ice-pump' circulation in the sub-ice-shelf ocean cavity provides the mean circulation responsible for the transport of suspended sediments in the cavity. The circulation is unique, given the ice shelf insulates the ocean from the effects of atmospheric interaction, and the increasing ice draft to the south of the ice shelf provide a temperature gradient along the cavity through the pressure dependence of the freezing temperature. This causes melting in the deeper regions of the cavity. The resultant input of low salinity buoyant meltwater drives an overturning circulation beneath the ice shelf. Some freezing in the shallower regions may result as the rising plume is supercooled.

The aims of the baroclinic modelling of the sub-Amery Ice Shelf cavity are to determine the thermohaline circulation patterns beneath the Ice Shelf, and how these vary with the inclusion of tidal mixing dynamics in the model. Passive tracers are added to the model, with settling velocities representative of diatoms in the water column, so that the transport paths of diatoms, produced in the open waters of Prydz Bay, can be traced beneath the Ice Shelf. Some qualitative comparisons can then be made with the observed sub-ice-shelf sediments (Chapter 7). The sensitivity of the sub-ice-shelf circulation to changes in open ocean temperature is also investigated in order to examine the effects of a warming climate

on the sub-ice-shelf circulation, and the resultant sediment transport pathways.

The application of the model to the cavity beneath the Amery Ice Shelf follows the presentation of the model used.

9.2 The Baroclinic model

The MECO model (Section 3) is a z-layer model. A z-layer model has not been previously used to model the baroclinic ocean circulation within a sub-ice-shelf cavity, and therefore, some simple tests were initially carried out to determine whether a z-layer model could be applied to such a study. A simple model domain was constructed extending over 10° of longitude, and 5° latitude on a 125×10 model grid. Six z-layer interfaces were defined at 100, 70, 50, 30, 10 and 0 m. A sloping ice shelf was imposed, deepest in the west (90 m), and shallowest in the east (5 m) over a seabed of constant depth of 120 m. The depressed sea surface was prescribed by a large atmospheric pressure: the inverse barometer effect results in a surface depression, such that 1 m ice draft is approximately equivalent to an atmospheric pressure of 10 hPa. On each attempt, large gradients in the surface elevation where it crossed z-layer interfaces resulted in an instability in the vertical velocity, with large downward velocities of order 20 cms^{-1}, on the upward side of where the surface intersected the z-interface. Numerous attempts were made to counteract this numerical problem, with little improvement. Consequently, MECO was considered unsuitable for determining the baroclinic flow beneath an ice shelf, and an alternate model was chosen for this part of the thesis. A σ-layer model, as has been previously used in sub-ice-shelf cavity models, was chosen to determine the sub-ice-shelf baroclinic circulation. Such a model has other advantages in modelling the sub-ice-shelf circulation which are discussed later in the chapter.

The model used for the application of the three-dimensional circulation beneath the floating Amery Ice Shelf is presented here. A description of the continuous equations governing the adopted model is followed by a finite difference representation of the most important model equations. Boundary conditions applied to the model domain are then presented.

9.2.1 Model Background and Setup

OzPOM

The model used for application to the sub-ice-shelf circulation problem is *OzPOM* (unpublished: Hunter (2002)); A revised version of the Princeton Ocean Model (POM; (Blumberg and Mellor, 1987; Mellor, 2002)). Major changes to POM to create *OzPOM* are the inclu-

sion of atmospheric pressure (atmospheric pressure in the Amery Ice Shelf application is simulated by the ice shelf draft, pushing the sea surface down by hundreds of metres in a similar way to the inverse barometer effect), and a surface freshwater flux (Evaporation - Precipitation, or in the Amery Ice Shelf application, Freeze - Melt).

The principle attributes of POM are (Mellor, 2002):

- It contains an embedded second moment turbulence closure sub-model to provide vertical mixing coeeficients (Mellor and Yamada, 1982). The Level 2.5 scheme is used together with a prognostic equation for the turbulence macroscale.

- A sigma (σ) coordinate model is used such that the vertical coordinate is scaled on the water column thickness. The advantages of using a σ-coordinate scheme over a z-coordinate scheme, is that it allows for a convenient specification of the kinematic boundary conditions at the ice shelf-ocean interface and at the seafloor. This is a result of the two boundaries being represented by the top and bottom sigma layers respectively.

- The horizontal grid uses curvilinear orthogonal coordinates and an "Arakawa C" differencing scheme.

- Horizontal time differencing is explicit, whereas the vertical time differencing is implicit. The latter eliminates time constraints for the vertical coordinate and permits the use of fine vertical resolution in the surface and bottom boundary layers.

- The model has a free surface and a split time step. The external (barotropic) mode portion of the model is two dimensional and uses a short time step based on the Courant-Friedrich-Levy (CFL) condition and the external wave speed $\sqrt{gH}$. The internal (baroclinic) mode is three-dimensional and uses a long time step based on the CFL condition and the internal wave speed. This technique known as mode splitting allows the calculation of the free surface elevation with little sacrifice in computational time by solving the vertically-averaged velocity separately from the three-dimensional calculation of the velocity and thermodynamic properties. The external mode calculation results in updates for surface elevation, η, and the vertically averaged velocities, $(\bar{U}, \bar{V})$. The internal mode calculation results in updates for U, V, T, S and the turbulence quantities, q^2 and $q^2 l$.

- Complete thermodynamics are implemented.

The major difference between POM and MECO is the vertical coordinate system of each model. MECO implements the z coordinate system, where z represents the vertical distance from a resting ocean surface at $z = 0$ (z positive upwards) and $z = -H(x, y)$ is the topography. Advantages of z coordinates are (Griffies et al., 2000):

- allowing the simplest of numerical discretisation approaches;
- easy representation of the horizontal pressure gradient for a Boussinesq fluid;
- clean and accurate representation of the equation of state for seawater; and
- natural parameterisation of the surface mixed layer using a z-coordinate.

Disadvantages are:

- cumbersome representation of tracer advection and diffusion along inclined density surfaces in the ocean interior;
- unnatural representation and parameterization of the bottom boundary layer; and
- difficult representation of bottom topography. MECO has an improvement on the standard z coordinate system in the form of a variable bottom layer thickness to better resolve complex bathymetry.

POM implements the terrain following or σ coordinate system, originally introduced in atmospheric modelling (Phillips, 1957) and is defined as: $\sigma = (z-\eta)/(H+\eta)$ where $\eta(x, y, t)$ is the displacement of the ocean surface from its resting position $z = 0$ and $z = -H(x, y)$ is the ocean bottom. Convention is that $\sigma = 0$ is the ocean surface, and $\sigma = -1$ is the ocean bottom. The advantages of this coordinate scheme are (Griffies et al., 2000):

- a smooth representation of the ocean bottom topography with isolines concentrated where bottom boundary layer processes are most important; and
- good representation of the thermodynamic effects associated with the equation of state.

Disadvantages include

- variable representation of the surface mixed layer, i.e. more surface layers in shallow than in deeper water;
- cumbersome representation of advection and diffusion along inclined density surfaces in the ocean interior, and
- difficulty in accurately representing the horizontal pressure gradient, which is the difference of two relatively large numbers.

Basic Equations

The basic equations of *OzPOM* have been cast in a bottom following, sigma coordinate system. The derivation of the sigma coordinate equations are based on the transformations (Phillips, 1957; Blumberg and Mellor, 1987):

$$x* = x, y* = y, \sigma = \frac{z-\eta}{H+\eta}, t* = t. \tag{9.1}$$

where x, y, z are conventional cartesian coordinates, and t is time.

If $D = H + \eta$ where $H(x, y)$ is the bottom topography, and $\eta(x, y, t)$ is the surface elevation, then the following relationships linking derivatives in the z-coordinate system, as used in section 3 for MECO, to those in the σ coordinate system are obtained (Mellor, 2002):

$$\frac{\partial G}{\partial x} = \frac{\partial G}{\partial x*} - \frac{\partial G}{\partial \sigma}\left(\frac{\sigma}{D}\frac{\partial D}{\partial x*} + \frac{1}{D}\frac{\partial \eta}{\partial x*}\right)$$

$$\frac{\partial G}{\partial y} = \frac{\partial G}{\partial y*} - \frac{\partial G}{\partial \sigma}\left(\frac{\sigma}{D}\frac{\partial D}{\partial y*} + \frac{1}{D}\frac{\partial \eta}{\partial y*}\right)$$

$$\frac{\partial G}{\partial z} = \frac{1}{D}\frac{\partial G}{\partial \sigma}$$

$$\frac{\partial G}{\partial t} = \frac{\partial G}{\partial t*} - \frac{\partial G}{\partial \sigma}\left(\frac{\sigma}{D}\frac{\partial D}{\partial t*} + \frac{1}{D}\frac{\partial \eta}{\partial t*}\right)$$

where G is an arbitrary field variable, and σ ranges from $\sigma = 0$ at $z = \eta$ to $\sigma = -1$ at $z = -H$.

Thus the equations of motion, as expressed in section 3.1, with the inclusion of $p_{atm}(\zeta = -\frac{p_{atm}}{g\rho_o})$ and the freeze rate, Φ, $(= (E - P))$ transform to:

$$\frac{\partial \eta}{\partial t} + \frac{\partial UD}{\partial x} + \frac{\partial VD}{\partial y} + \frac{\partial \omega}{\partial \sigma} = -\Phi \tag{9.2}$$

$$\frac{\partial UD}{\partial t} + \frac{\partial U^2 D}{\partial x} + \frac{\partial UVD}{\partial y} + \frac{\partial U\omega}{\partial \sigma} - fVD \quad + \quad gD\frac{\partial(\eta-\zeta)}{\partial x} + \frac{gD^2}{\rho_0}\int_\sigma^0 \left[\frac{\partial \rho'}{\partial x} - \frac{\sigma'}{D}\frac{\partial D}{\partial x}\frac{\partial \rho'}{\partial \sigma'}\right] d\sigma'$$
$$= \frac{\partial}{\partial \sigma}\left[\frac{K_M}{D}\frac{\partial U}{\partial \sigma}\right] + F_x \tag{9.3}$$

$$\frac{\partial VD}{\partial t} + \frac{\partial UVD}{\partial x} + \frac{\partial V^2 D}{\partial y} + \frac{\partial V\omega}{\partial \sigma} + fUD \quad + \quad gD\frac{\partial(\eta-\zeta)}{\partial y} + \frac{gD^2}{\rho_0}\int_\sigma^0 \left[\frac{\partial \rho'}{\partial y} - \frac{\sigma'}{D}\frac{\partial D}{\partial y}\frac{\partial \rho'}{\partial \sigma'}\right] d\sigma'$$

$$= \frac{\partial}{\partial \sigma}\left[\frac{K_M}{D}\frac{\partial U}{\partial \sigma}\right] + F_y \tag{9.4}$$

$$\frac{\partial TD}{\partial t} + \frac{\partial TUD}{\partial x} + \frac{\partial TVD}{\partial y} + \frac{\partial T\omega}{\partial \sigma} = \frac{\partial}{\partial \sigma}\left[\frac{K_H}{D}\frac{\partial T}{\partial \sigma}\right] + F_T \tag{9.5}$$

$$\frac{\partial SD}{\partial t} + \frac{\partial SUD}{\partial x} + \frac{\partial SVD}{\partial y} + \frac{\partial S\omega}{\partial \sigma} = \frac{\partial}{\partial \sigma}\left[\frac{K_H}{D}\frac{\partial S}{\partial \sigma}\right] + F_S \tag{9.6}$$

$$\begin{aligned}\frac{\partial q^2 D}{\partial t} \quad + \quad & \frac{\partial U q^2 D}{\partial x} + \frac{\partial V q^2 D}{\partial y} + \frac{\partial \omega q^2}{\partial \sigma} = \frac{\partial}{\partial \sigma}\left[\frac{K_q}{D}\frac{\partial q^2}{\partial \sigma}\right] \\ & + \frac{2K_M}{D}\left[\left(\frac{\partial U}{\partial \sigma}\right)^2 + \left(\frac{\partial V}{\partial \sigma}\right)^2\right] + \frac{2g}{\rho_o}K_H\frac{\partial \tilde{\rho}}{\partial \sigma} - \frac{2Dq^3}{B_1 l} + F_q\end{aligned} \tag{9.7}$$

$$\begin{aligned}\frac{\partial q^2 l D}{\partial t} \quad + \quad & \frac{\partial U q^2 l D}{\partial x} + \frac{\partial V q^2 l D}{\partial y} + \frac{\partial \omega q^2 l}{\partial \sigma} = \frac{\partial}{\partial \sigma}\left[\frac{K_q}{D}\frac{\partial q^2 l}{\partial \sigma}\right] \\ & + E_1 l\left(\frac{K_M}{D}\left[\left(\frac{\partial U}{\partial \sigma}\right)^2 + \left(\frac{\partial V}{\partial \sigma}\right)^2\right] + E_3\frac{g}{\rho_o}K_H\frac{\partial \tilde{\rho}}{\partial \sigma}\right)\tilde{W} - \frac{Dq^3}{B_1} + F_l\end{aligned} \tag{9.8}$$

where definitions of the variables are contained in Appendix G. ω is the transformed vertical velocity, transformed to the cartesian coordinate using:

$$W = \omega + U\left(\sigma\frac{\partial D}{\partial x} + \frac{\partial \eta}{\partial x}\right) + V\left(\sigma\frac{\partial D}{\partial y} + \frac{\partial \eta}{\partial y}\right) + \sigma\frac{\partial D}{\partial t} + \frac{\partial \eta}{\partial t}$$

The local vertical dependence on pressure is given by the hydrostatic relation:

$$\frac{\partial p}{\partial \sigma} = -g\rho D \tag{9.9}$$

The density depends on pressure, p, potential temperature, T, and salinity, S in the model:

$$\rho = \rho\left(T, S, p\right) \tag{9.10}$$

It is represented by an adaptation of the UNESCO equation of state (Mellor, 1991).

Horizontal viscosity and diffusion terms are defined:

$$F_x = \frac{\partial}{\partial x}\left(D\tau_{xx}\right) + \frac{\partial}{\partial y}\left(D\tau_{xy}\right) \tag{9.11}$$

$$F_y = \frac{\partial}{\partial x}\left(D\tau_{xy}\right) + \frac{\partial}{\partial y}\left(D\tau_{yy}\right) \tag{9.12}$$

where:

$$\tau_{xx} = 2A_M\frac{\partial U}{\partial x}, \tau_{xy} = \tau_{yx} = A_M\left(\frac{\partial U}{\partial y} + \frac{\partial V}{\partial x}\right), \tau_{yy} = 2A_M\frac{\partial V}{\partial y} \tag{9.13}$$

and,

$$F_\phi = \frac{\partial}{\partial x}\left(Dq_x\right) + \frac{\partial}{\partial y}\left(Dq_y\right) \tag{9.14}$$

where:

$$q_x = A_H\frac{\partial \phi}{\partial x}, q_y = A_H\frac{\partial \phi}{\partial y} \tag{9.15}$$

and where ϕ represents T, S, q^2 or q^2l. A_M is the along σ-level momentum mixing coefficient defined using the Smagorinsky diffusivity (Mellor, 2002):

$$A_M = C\Delta x\Delta y\left[\left(\frac{\partial u}{\partial x}\right)^2 + \frac{1}{2}\left(\frac{\partial v}{\partial x} + \frac{\partial u}{\partial y}\right)^2 + \left(\frac{\partial v}{\partial y}\right)^2\right]^{\frac{1}{2}}$$

Values of C (the HORCON parameter) are in the range 0.10 to 0.20 (Mellor, 2002). A_H is the along σ-level tracer mixing coefficient defined using:

$$A_H = TPRNI \times A_M$$

Chosen values for $TPRNI$ are 0.1667 so that A_M is 6 times larger than A_H. This is consistent with Grosfeld et al. (1997) for sub-ice-shelf modelling when the open ocean domain is included.

Vertical turbulent mixing is modelled through the use of the eddy viscosity and diffusion coefficients, K_M and K_H. A second-order turbulence closure scheme (Mellor and Yamada, 1974, 1982) is applied to compute these coefficients. This scheme provides weak diapycnal mixing within the ocean interior, strong mixing associated with the surface boundary layer, and enhanced mixing near the ocean bottom (Mellor and Yamada, 1982). The effects of this scheme were assessed by also defining constant values of K_M and K_H of $1 \times 10^{-3}m^2s^{-1}$ and $5 \times 10^{-5}m^2s^{-1}$, respectively, in early ideal ice-shelf domain runs.

For computer economy, the external mode (vertically integrated equations) is separated from the internal mode (vertical structure equations) using the mode-splitting technique.

The external mode, volume transport, equations are obtained by integrating the internal mode equations 9.2 to 9.4 over the depth. Integrating equation 9.2 from $\sigma = -1$ to

$\sigma = 0$ and using the boundary conditions:

$$\omega(0) = \Phi, \omega(-1) = 0 \tag{9.16}$$

an equation for the surface elevation can be written:

$$\frac{\partial \eta}{\partial t} + \frac{\partial \overline{U} D}{\partial x} + \frac{\partial \overline{V} D}{\partial y} = -\Phi \tag{9.17}$$

After integration, the momentum equations, 9.3 and 9.4, become:

$$\begin{aligned} \frac{\partial \overline{U} D}{\partial t} + \frac{\partial \overline{U}^2 D}{\partial x} + \frac{\partial \overline{UV} D}{\partial y} \quad - \quad & \tilde{F}_x - f\overline{V}D + gD\frac{\partial(\eta - \zeta)}{\partial x} = - < wu(0) > + < wu(-1) > \\ & G_x - \frac{gD}{\rho_o}\int_{-1}^{0}\int_{\sigma}^{0}\left[D\frac{\partial \rho'}{\partial x} - \frac{\partial D}{\partial x}\sigma'\frac{\partial \rho'}{\partial \sigma}\right] d\sigma' d\sigma \end{aligned} \tag{9.18}$$

$$\begin{aligned} \frac{\partial \overline{V} D}{\partial t} + \frac{\partial \overline{UV} D}{\partial x} + \frac{\partial \overline{V}^2 D}{\partial y} \quad - \quad & \tilde{F}_y + f\overline{U}D + gD\frac{\partial(\eta - \zeta)}{\partial y} = - < wv(0) > + < wv(-1) > \\ & G_y - \frac{gD}{\rho_o}\int_{-1}^{0}\int_{\sigma}^{0}\left[D\frac{\partial \rho'}{\partial y} - \frac{\partial D}{\partial y}\sigma'\frac{\partial \rho'}{\partial \sigma}\right] d\sigma' d\sigma \end{aligned} \tag{9.19}$$

The overbars denote vertically integrated velocities, such that:

$$(\overline{U}, \overline{V}) = \int_{-1}^{0} (U, V)\, d\sigma \tag{9.20}$$

The surface stress components are $- < wu(0) >$ and $- < wv(0) >$, and the bottom stress components are $- < wu(-1) >$ and $- < wv(-1) >$. The quantities $\tilde{F}_x$ and $\tilde{F}_y$ are vertical integrals of the horizontal momentum diffusion, and G_x and G_y are the dispersion terms, representing vertical averages of the cross-products of the velocity departures from the vertically integrated velocity (Mellor and Blumberg, 1985; Blumberg and Mellor, 1987).

The external mode equations have not been subtracted from the original equations to form the more conventional internal mode set as used in Bryan (1969). To avoid the divergence of the external mode velocities from the vertical integral of the internal mode due to truncation errors, the vertical mean of the internal velocity is replaced by the external mode velocity at every time step (Mellor, 2002).

Finite Difference Formulation

The equations in the previous section may be solved numerically using finite difference techniques.

The formulation of the finite difference equations used in solving the model equations is grid dependent. *OzPOM* uses the "Arakawa C" grid on the constant σ-surfaces to distribute surface elevation, velocity and tracer points. The vertical grid points are also staggered, with horizontal velocities and tracers defined at the centres of vertical boxes, and ω, q^2, q^2l, K_M and K_H defined at the interfaces between boxes. The arrangement of grid points, for both horizontal and vertical sections is equivalent to the MECO model, shown in Figure 3.1, except that z must be replaced by σ, and the turbulence quantities q^2 and q^2l are defined at the same location as ω.

To simplify the representation of the finite difference equations, the following sum and difference operations are defined:

$$\overline{F(x,y,\sigma,t)}^{x} = \frac{F(x+\frac{\Delta x}{2},y,\sigma,t)+F(x-\frac{\Delta x}{2},y,\sigma,t)}{2} \tag{9.21}$$

$$\delta_x F(x,y,\sigma,t) = \frac{F(x+\frac{\Delta x}{2},y,\sigma,t)-F(x-\frac{\Delta x}{2},y,\sigma,t)}{\Delta x} \tag{9.22}$$

$$\delta_x \overline{F(x,y,\sigma,t)}^{x} = \frac{F(x+\Delta x,y,\sigma,t)-F(x-\Delta x,y,\sigma,t)}{2\Delta x} \tag{9.23}$$

and

$$\overline{F(x,y,\sigma,t)}^{xy} = \overline{\overline{F(x,y,\sigma,t)}^{x}}^{y} = \overline{\overline{F(x,y,\sigma,t)}^{y}}^{x} \tag{9.24}$$

A variable $F(x,y,\sigma,t)$ can now be written $F^n_{i,j,k}$, where i,j,k are used to indicate the grid points of interest and apply to the coordinates x,y,σ respectively, at some time level n.

The finite difference equations governing the baroclinic modes, 9.2, 9.3 and 9.4 are:

$$\delta_t\eta + \delta_x\left(\overline{D}^{x}U\right) + \delta_y\left(\overline{D}^{y}V\right) + \delta_\sigma\left(\omega\right) = -\Phi \tag{9.25}$$

$$\begin{aligned}\delta_t\overline{\left(\overline{D}^{x}U\right)}^{t} \quad &+\delta_x\left(\overline{\overline{D}^{x}U}^{x}\overline{U}^{x}\right)+\delta_y\left(\overline{\overline{D}^{y}V}^{x}\overline{U}^{y}\right)-\overline{f\overline{V}^{y}D}^{x}+\delta_\sigma\left(\overline{\omega}^{x}\overline{U}^{\sigma}\right)+g\overline{D}^{x}\delta_x(\eta-\zeta)\\ &=\delta_\sigma\left[\frac{\overline{K_M}^{x}}{\overline{D}^{x}}\delta_\sigma\left(U\right)^{n+1}\right]-\frac{g\left(\overline{D}^{x}\right)^2}{\rho_o}\delta_x\left[\sum_{m=1}^{k}\overline{\rho_{m-\frac{1}{2}}}^{\sigma}\overline{\Delta\sigma_{m-\frac{1}{2}}}^{\sigma}\right]+F_x^{n-1}\end{aligned} \tag{9.26}$$

$$\begin{aligned}\delta_t\overline{\left(\overline{D}^{y}V\right)}^{t} \quad &+\delta_x\left(\overline{\overline{D}^{x}U}^{x}\overline{V}^{x}\right)+\delta_y\left(\overline{\overline{D}^{y}V}^{y}\overline{V}^{y}\right)+\overline{f\overline{U}^{x}D}^{y}+\delta_\sigma\left(\overline{\omega}^{y}\overline{V}^{\sigma}\right)+g\overline{D}^{y}\delta_y(\eta-\zeta)\\ &=\delta_\sigma\left[\frac{\overline{K_M}^{y}}{\overline{D}^{y}}\delta_\sigma\left(V\right)^{n+1}\right]-\frac{g\left(\overline{D}^{y}\right)^2}{\rho_o}\delta_y\left[\sum_{m=1}^{k}\overline{\rho_{m-\frac{1}{2}}}^{\sigma}\overline{\Delta\sigma_{m-\frac{1}{2}}}^{\sigma}\right]+F_y^{n-1}\end{aligned} \tag{9.27}$$

k in each of the above is the number of vertical grid points over which the summation is carried out, and $\Delta\sigma$ is the spacing of the vertical layers. Superscripts $n+1$ and $n-1$ are

used to indicate the appropriate time level. All other terms are understood to be at time step n.

The conservation equation for a scalar, θ_i (e.g., S, T, and the turbulent kinetic energy terms q^2 and $q^2 l$) as in equations 9.5 and 9.6 is differenced as:

$$\delta_t \left(\overline{\theta_i D}\right)^t + \Gamma_{\theta_i}(\theta_i) = \delta_\sigma \left(\frac{K_H}{D}\delta_\sigma \theta_i\right)^{n+1} + F_{\theta_i}^{n-1} \tag{9.28}$$

The advective operator for the scalar properties, S, T and the turbulent kinetic energy terms q^2 and $q^2 l$, $\Gamma_{\theta_i}(\theta_i)$ is the iterative, second order accurate "Smolarkiewicz" advection scheme (Smolarkiewicz, 1984).

The external mode equations 9.17 through 9.19 are entirely explicit. The continuity equation is given:

$$\delta_t \overline{\eta}^t + \delta_x \left(\overline{D}^x \overline{U}\right) + \delta_y \left(\overline{D}^y \overline{V}\right) = -\Phi \tag{9.29}$$

and for the momentum equations:

$$\delta_t \overline{\left(\overline{D}^x \overline{U}\right)}^t + \delta_x \left(\overline{\overline{D}^x \overline{U}}^x \overline{\overline{U}}^x\right) + \delta_y \left(\overline{\overline{D}^y \overline{V}}^x \overline{\overline{U}}^y\right) - \overline{f\overline{\overline{V}}^y D}^x + g\overline{D}^x \delta_x(\eta - \zeta) - \overline{F}_x^{n-1} = \phi_x \tag{9.30}$$

$$\delta_t \overline{\left(\overline{D}^y \overline{V}\right)}^t + \delta_x \left(\overline{\overline{D}^x \overline{U}}^y \overline{\overline{V}}^x\right) + \delta_y \left(\overline{\overline{D}^y \overline{V}}^y \overline{\overline{V}}^y\right) + \overline{f\overline{\overline{U}}^x D}^y + g\overline{D}^y \delta_y(\eta - \zeta) - \overline{F}_y^{n-1} = \phi_y \tag{9.31}$$

ϕ_x and ϕ_y are composed of quantities in 9.18 and 9.19 provided by the internal mode, and are computed by the vertical integration of the corresponding terms in the internal mode equation.

Boundary Conditions

The Amery Ice Shelf cavity/Prydz Bay model domain has four different types of boundary: the sea bed, the ice shelf-ocean interface, the open ocean boundaries, and the coast or grounding line. The coast or grounding line, the sea bed boundary, and the open ocean boundary conditions are similar to those used in other ocean models. The ice shelf-ocean interface boundary is more complex.

Grounding line or coast boundaries Along the coast, or grounding line, which lies on elevation grid points, the boundary conditions ensure conservation of mass and tracers by ensuring no flow across the boundary wall. A half slip condition is imposed on the tangential velocities. A no-slip boundary condition was imposed for sensitivity studies.

The half slip boundary conditions imply:

$$U_{\eta_{ij}} = \frac{U_{ij}}{2}$$

The no slip boundary conditions imply:

$$U_{\eta_{ij}} = 0$$

where $U_{\eta_{ij}}$ represents the tangential velocity on the closed boundary (elevation, η) point, and n denotes the local normal derivative.

The zero flux condition was also defined at the closed boundaries. i.e.,

$$\frac{\partial T}{\partial n} = 0$$

Vertical boundary conditions The vertical boundary conditions for the continuity equation 9.2 are:

$$\omega\left(0\right) = \Phi$$

and

$$\omega\left(-1\right) = 0$$

This indicates the vertical velocity at the sea surface is given by the freeze rate, Φ, and the sea bed is a model coordinate surface so there is no flow through it.

The boundary conditions for the momentum equations 9.3 and 9.4 are:

$$\frac{K_M}{D}\left(\frac{\partial U}{\partial \sigma}, \frac{\partial V}{\partial \sigma}\right) = -\left(< wu(0) >, < wv(0) >\right), \sigma \to 0 \tag{9.32}$$

where the right-hand-side of 9.32 is the input value of the surface turbulent momentum flux. This is discussed further in the section below.

At the sea bed, the boundary condition is given by:

$$\frac{K_M}{D}\left(\frac{\partial U}{\partial \sigma}, \frac{\partial V}{\partial \sigma}\right) = \left(\frac{\tau_{Bx}}{\rho}, \frac{\tau_{By}}{\rho}\right) = C_Z\left[U^2 + V^2\right]^{1/2}\left(U, V\right), \sigma \to -1 \tag{9.33}$$

where

$$C_Z = MIN\left(MAX\left[\frac{k^2}{\left[ln((1+\sigma_{kb-1})D/z_o)\right]^2}, 0.0025\right], 1.0\right) \tag{9.34}$$

k is the von Karman constant and z_o is the roughness parameter, and D_o is the initial water column thickness. i.e., the difference between the inital ice draft and bed topopgraphy (Hunter, 2002; Mellor, 2002).

The boundary conditions on the scalar conservation equations 9.5 and 9.6 are:

$$\frac{K_H}{D}\left(\frac{\partial T}{\partial \sigma}, \frac{\partial S}{\partial \sigma}\right) = -(< w\theta(0) >), \sigma \to 0 \tag{9.35}$$

$$\frac{K_H}{D}\left(\frac{\partial T}{\partial \sigma}, \frac{\partial S}{\partial \sigma}\right) = 0, \sigma \to -1 \tag{9.36}$$

indicating that no heat or salt flux is permitted across the seabed, and at the surface, the heat and salt flux are related to the freeze rate, discussed below.

The boundary conditions for the turbulence kinetic energy, and turbulence macroscale equations 9.7 and 9.8 are:

$$\left(q^2(0), q^2 l(0)\right) = \left(B_1^{2/3} u_*^2(0), 0\right) \tag{9.37}$$

and

$$\left(q^2(-1), q^2 l(-1)\right) = \left(B_1^{2/3} u_*^2(-1), 0\right) \tag{9.38}$$

where B_1 is one of the turbulence closure constants and u_* is the friction velocity at the top or bottom as denoted.

Ice shelf base boundary conditions The ice shelf is a solid boundary exerting a drag on the motion of the water, much like the effect of the sea bed. Here we specify a drag law parameterisation at the ice-ocean boundary, much like at the sea bed (equation 9.33). Other models (Determann and Gerdes, 1994; Grosfeld et al., 1997; Williams et al., 1998b; Williams, 1999) have specified a free-slip boundary condition at this interface.

The thermodynamic interaction at the ice shelf - ocean interface is given by the two equation formulation as described by (Holland and Jenkins, 1999), presented in Section 6.5.2. Initially, a linear relationship between the thermal exchange velocity and the friction velocity, estimated from Figure 4 in Holland and Jenkins (1999), i.e.,:

$$\gamma_T = 0.01 \times u_* \tag{9.39}$$

was assumed, and presented as the more realistic formulation. However, to determine the effects of this parameterisation in comparison to previous sub-ice-shelf circulation models

(Determann and Gerdes, 1994; Jenkins and Bombosch, 1995; Grosfeld et al., 1997; Williams et al., 1998b), a constant thermal exchange velocity of $1 \times 10^{-4}\ ms^{-1}$, corresponding to a friction velocity of $\sim 0.01\ ms^{-1}$, was defined for a second set of runs.

It is assumed that the ice shelf is a perfect insulator, with no diffusion into the ice shelf ($Q_I^T = 0$). This assumption has been used by Determann and Gerdes (1994); Jenkins and Bombosch (1995); Grosfeld et al. (1997); Williams et al. (1998b), and is justified provided that the conducted heat flux into the ice shelf is always small compared to the latent heat term.

In regions of freeze (melt), freshwater at a reference freezing temperature is removed from (added to) the system at the freeze rate, altering the volume of water in the model. The reference freezing temperature T_{fREF}, taken as the freezing temperature at 400 decibars and salinity of 34.57 psu (i.e., -2.1988 °C) is used instead of an in-situ freezing temperature so that both the calculated freeze rate, Φ, and the cavity temperature can reach steady state. This implies that the heat flux at the ice-ocean interface is given by the combination of the surface diffusive temperature flux, and the advective heat gain (loss) to (from) the surface mixed layer associated with freeze (melt). i.e.,

$$w\theta(0) = \rho C_p \left(\gamma_T (T - T_f) + \Phi T_{fREF}\right) \tag{9.40}$$

where T_f is the in-situ freezing temperature, or the temperature of the base of the ice shelf, and T is the temperature of the surface layer of the ocean beneath the ice shelf. To conserve heat at the ice shelf base, and assuming no diffusion into the ice shelf, the freeze rate Φ is given by:

$$\Phi = -\frac{C_p}{L}\gamma_T (T - T_f) \tag{9.41}$$

The assumption of no diffusive salt flux into the ice shelf base indicates that the advective salt flux associated with the removal (addition) of freshwater as a result of freezing (melting) is the only salt flux at the ice-ocean interface.

This formulation differs to that used in the model used by Determann and Gerdes (1994), Grosfeld et al. (1997), and Williams et al. (1998b, 2001), which prescribes no removal (addition) of water, or mass, to the model under freezing (melting) conditions, but instead inputs (removes) salt from the model when freezing (melting) occurs.

The ice shelf is assumed to have no flexural rigidity in free surface models, thus the ice shelf distorts freely with the tides. MacAyeal (1984b) considered this assumption to be a poor approximation only within about 10km of the grounding line.

Open ocean tracer boundary conditions Open ocean tracer boundary conditions are treated differently depending on whether tides are implemented or not.

When tides are implemented, so that variable elevations are defined on the open boundary, the values of the tracer quantities are clamped at the same values as the initial values.

When tides are not implemented, open lateral boundary conditions for tracers are implemented differently depending on whether the boundary point is located on an inflow, or an outflow. On an inflow boundary, tracer values are dependent on values prescribed immediately outside of the model domain. At outflowing boundaries, the internal tracer values are important. The tracer values on all open boundaries are given by the upstream formulation:

$$\frac{\partial}{\partial t}(T,S) + U_n \frac{\partial}{\partial n}(T,S) + \omega \frac{\partial}{\partial \sigma}(T,S) = 0 \tag{9.42}$$

where the subscript n is the coordinate normal to the boundary.

The distinction between inflow and outflow regions is made since if the velocity on the open boundary is directed out of the domain, then the values of the tracers on the open ocean boundary will have been determined by processes inside the domain. Similarly, in an inflow region, it would be expected that processes outside the domain would be most important and boundary forcing values should influence the model.

The advective term in the finite difference formulation of equation 9.42 is in a non-conservative form using upstream differencing. This allows the advective term to be retained without including unknown terms from outside the domain.

The open boundary scheme for the turbulent quantities (q^2 and q^2l) is similar to that for the other scalar quantities, T and S. However, the turbulent quantities (q^2 and q^2l) are prescribed zero values on the open boundaries, and the vertical velocity term is absent.

The prescribed salinity and potential temperature fields used in the model are discussed later in the chapter.

Open ocean velocity and surface elevation boundary conditions In model applications where tides are implemented, *OzPOM* requires the prescription of the elevation as a function of time and space on the open boundary. The depth-averaged velocity is defined in the direction normal to the boundary only, set equal to the value from one grid cell within the model domain, and there is no tangential velocity.

If tides are not implemented, the normal barotropic velocities are defined by the

simple radiation condition (Mellor, 2002):

$$H\overline{U} \pm c_e \eta = 0$$

where c_e is the local shallow water wave speed $\sqrt{gD}$ (D is the water column thickness), and the tangential velocity is set equal to zero.

The internal velocities are defined by a simple radiation condition regardless of whether tides are implemented or not. The form of this condition is (Mellor, 2002):

$$\frac{\partial U_n}{\partial t} \pm c_i \frac{\partial U_n}{\partial n} = 0$$

where c_i is an approximation to the internal wave speed, and n is the coordinate normal to the boundary.

Non-linear terms in the momentum equations are neglected at the open boundary, as they are generally small compared with other terms in the equation. Hence unknown values outside the model domain are not required.

9.3 The Amery Ice Shelf Application

The *OzPOM* model has been applied to the sub-Amery Ice Shelf cavity. The baroclinic model domain differs slightly to that used for the barotropic model domain (Chapter 8), covering a slightly larger area of Prydz Bay, extending from $73°20'S$ to $66°45'S$ in latitude, and from $66°E$ to $80°E$ in longitude.

As with the barotropic modelling (Section 8), the dominant source of error expected in the baroclinic model is the given topography. To assess the sensitivity of the baroclinic model to changes in cavity shape, model grids of bed topography and ice shelf draft from grids A, B, C, and CADA (Section 8.1.1) were used, with additional Prydz Bay bathymetry data interpolated onto the extra area in the east of the model grid. The water column thickness model grids A, B, and C used in the barotropic model were obtained directly from the respective grids of bed topography and ice shelf draft, which are used for the baroclinic model. The CADA grid was interpolated directly from the CADA (Padman et al., 2002) water column thickness grid. The CADA bed elevation grid was obtained by the addition of the ice shelf draft (which was assumed constant for all model runs) and the CADA water column thickness grid. Some manual smoothing was applied across the resulting discontinuity at the ice shelf front. Bed elevation for model grid B and the ice shelf draft

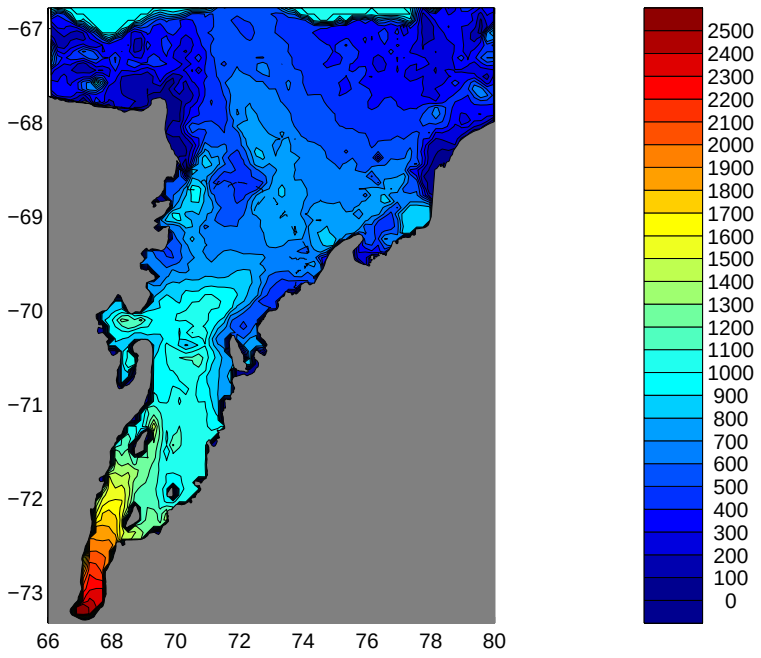

Figure 9.1: The sub-Amery Ice Shelf and Prydz Bay bed elevation: model grid B. The dotted line marks the ice shelf front. Depths are in metres.

Table 9.1: Vertical layer thicknesses as a percentage of the water column thickness, numbered from top to bottom

layer	1	2	3	4	5	6	7	8	9	10
%	4.17	4.17	8.33	16.67	16.67	16.67	16.67	8.33	4.17	4.17

used for each model run are displayed in Figures 9.1 and 9.2 respectively.

Model runs were typically carried out with a horizontal resolution one half of that of the barotropic model. A horizontal grid spacing of $1/5^\circ$ in longitude, and $1/15^\circ$ in latitude is defined. One model run (BFR) was carried out using model grid B, at the finer resolution used in the barotropic model. i.e., a horizontal grid spacing of $1/10^\circ$ in longitude and $1/30^\circ$ in latitude. For all model runs, 11 $\sigma-$interfaces are defined. The percentage thicknesses of the $\sigma-$ layers are given in Table 9.1. An external time step of 24 s was chosen to satisfy the CFL criterion with an internal time step of 720 s. For model run BFR, the respective time steps were halved.

The model grid is typically defined by a $70 \times 99 \times 11$ model array. Baroclinic model runs were carried out on an SGI Origin 3400 supercomputer, compiled with 02 optimisation, automatic parallelisation, double precision, and runs carried out using 2 or 4 cpu's. The resulting model run time was approximately 74 (125) hours per 10000 model days using 4 (2) cpu's. The model grid for run BFR is defined by a $140 \times 198 \times 11$ array. Resulting model

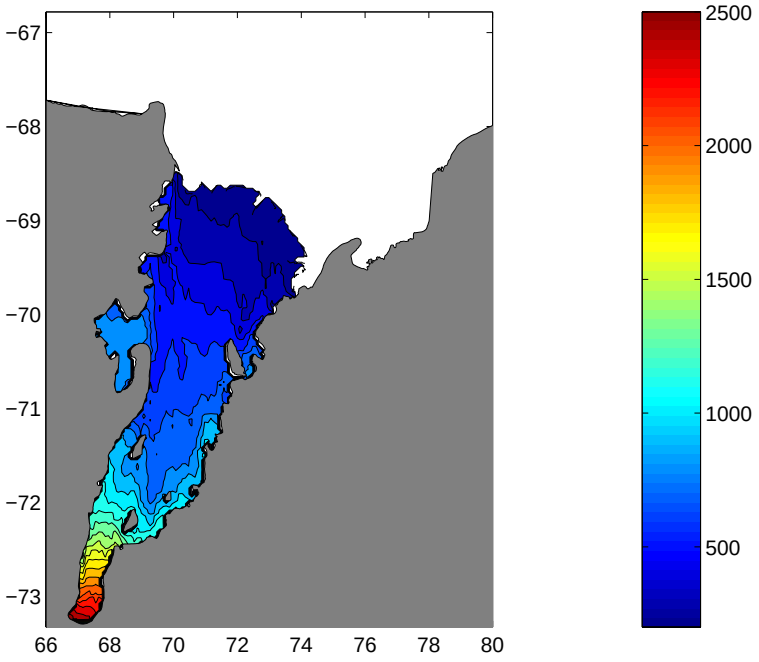

Figure 9.2: The Amery Ice Shelf ice draft as used for each model run. Contours are at 100 m. intervals.

run time is approximately 660 (1300) hours per 10000 model days using 4 (2) cpu's.

The model domain is initialised with an ocean at rest, a homogeneous salinity field, set equal to 34.57 psu, and a potential temperature field set equal to the the surface freezing temperature (-1.8976°C). These values were chosen as they are typical of water formed due to sea-ice freezing in the open waters on the continental shelf in Prydz Bay during the winter months. This initialisation field is similar to the 'cool' run defined by Williams et al. (2002). Other homogeneous initialisation salinity fields, varying salinity between 34.5 and 34.6 psu, were trialled, and they showed little variation between steady state solutions.

There is no formulation for sea-ice and wind forcing in the open ocean included in the model. A drag friction law is defined at the seabed and at the ice-shelf-ocean interface. At each interface, a roughness, z_0 of 0.01 m, and a minimum and maximum friction coefficient of 0.0025 and 1.0 respectively are defined. There are three open boundaries to the model domain; an eastern, northern, and western boundary. Each open boundary is treated the same, as described in Section 9.2.1.

The thermohaline effects of heat and freshwater fluxes at the ice shelf base, as described in Section 6.5.2, provide the only forcing for the model within the domain. As previously stated, two sets of model runs were carried out. Five model runs were carried out with the thermal exchange velocity, γ_T, assumed to be a linear function of the friction veloc-

ity, $u*$, at the ice-shelf-ocean interface (Eqn. 9.39). Nine further runs removed the influence of a variable thermal exchange velocity by prescribing a constant value of $1 \times 10^{-4}\ ms^{-1}$ as used in previous sub-ice-shelf models, to examine various other effects, and to determine the effects of a constant γ_T parameterisation. Table 9.2 details the forcing characteristics of each of the fourteen Amery Ice Shelf model runs.

From the results of the barotropic tide modelling (Section 8), model grid B was found to be the best estimate of the cavity shape beneath the Amery Ice Shelf. Therefore, the standard set of runs which define the thermal exhange velocity as a function of the friction velocity (NT, T, T+0.2°C, NT+1°C, and NT+1°C) are executed using model grid B.

Model run NT had no tidal forcing at the open boundary, and provide a direct comparison to the circulation presented by Williams et al. (2001) given the new model, and ice draft and bed elevation data.

Model run T was carried out with tidal forcing at the open boundaries for comparison against model run NT. The run aims to determine the influence of tidal mixing on the sub-ice-shelf circulation and the consequent melt-rates. Tidal elevations on the open boundaries are determined from the four major constituents (M_2, S_2, K_1, and O_1) taken from the CADA model (Section 6.5.1; Padman et al. (2002)), interpolated onto each of the open boundary elevation points.

Model runs NT and T are initialised with temperatures cooler than found in Prydz Bay under present climatic conditions. Model run T+0.2°C is carried out as an estimate of present day conditions, providing temperatures adjacent to the ice shelf front similar to those found during the AMISOR CTD transects from voyages au0106 and au0207 in the region ($\sim -1.82°C$). The run has potential temperature initialised, and defined at the open boundaries, 0.2°C warmer than the standard runs NT and T. Model run T+0.2°C provides an estimate of the mass balance of the Amery Ice Shelf under present conditions for comparison to oceanographic observational estimates.

The two final $\gamma_T(u*)$ model runs, NT+1°C and T+1°C, are carried out analagous to runs NT and T, but the potential temperature is initialised, and defined at the open boundaries, 1°C warmer than the surface freezing temperature as used in the previous runs, i.e., $-0.8976°C$. The aim of these two runs was to determine the effects of a warmer climate on the thermohaline circulation within the sub-ice-shelf cavity, with and without tidal mixing included in the model dynamics. These runs also allow an estimate of the change in the mass balance of the Amery Ice Shelf under such conditions, and comparison to the warming climate scenario results of Williams et al. (2002).

Table 9.2: Overview of Amery Ice Shelf baroclinic model experiments. x indicates tidal elevation forcing is applied at the open boundary. γ_T is the thermal exchange velocity, $u*$ is the friction velocity at the ice-ocean interface.

Model Run	Bed Elevation Grid	Resolution (lon×lat)	Tides	γ_T
NT	B	$1/5° \times 1/15°$		$0.01u*$
T	B	$1/5° \times 1/15°$	x	$0.01u*$
T+0.2°C	B	$1/5° \times 1/15°$	x	$0.01u*$
NT+1°C	B	$1/5° \times 1/15°$		$0.01u*$
T+1°C	B	$1/5° \times 1/15°$	x	$0.01u*$
A	A	$1/5° \times 1/15°$		$1 \times 10^{-4}\ ms^{-1}$
B	B	$1/5° \times 1/15°$		$1 \times 10^{-4}\ ms^{-1}$
C	C	$1/5° \times 1/15°$		$1 \times 10^{-4}\ ms^{-1}$
CADA	CADA	$1/5° \times 1/15°$		$1 \times 10^{-4}\ ms^{-1}$
B-T	B	$1/5° \times 1/15°$	x	$1 \times 10^{-4}\ ms^{-1}$
CADA-T	CADA	$1/5° \times 1/15°$	x	$1 \times 10^{-4}\ ms^{-1}$
BFR	BFR	$1/10° \times 1/30°$		$1 \times 10^{-4}\ ms^{-1}$
B+1°C	B	$1/5° \times 1/15°$		$1 \times 10^{-4}\ ms^{-1}$
B-T+1°C	B	$1/5° \times 1/15°$	x	$1 \times 10^{-4}\ ms^{-1}$

The remaining nine model runs prescribe a constant thermal exchange velocity, γ_T. Runs A, B, C, and CADA, carried out with the previously discussed varying topographies, are aimed at determining the influence that a poorly known cavity shape may have on the modelled sub-ice-shelf circulation. These runs had no tidal forcing at the open boundaries, and run B provides a direct comparison to the circulation presented by model run NT, to determine the effects of the differing γ_T paramterisations.

Runs B-T and CADA-T were carried out with tidal forcing at the open boundaries for comparison to runs B and CADA respectively. These runs are aimed at determining the influence of tidal mixing on the sub-ice-shelf thermohaline circulation if a constant γ_T value is assumed. i.e., the effect of tides is an increase in vertical mixing only, and has no influence on the friction velocity at the ice-ocean interface, and hence melt-rates. Model grids B and CADA were chosen, as these provide the best comparisons to tidal elevation and current data using the MECO model (Chapter 8).

Run BFR was carried out with the fine resolution version of model grid B, without tidal forcing. This run aims to provide a fine resolution view of the model results in comparison to run B, however model run time is 8 times longer.

Finally, model runs B+1°C and B-T+1°C were carried out analagous to runs NT+1°C and T+1°C, but with constant γ_T. These runs determine the influence of assuming a constant γ_T on estimates of mass balance of the Amery Ice Shelf under the effects of a warmer climate.

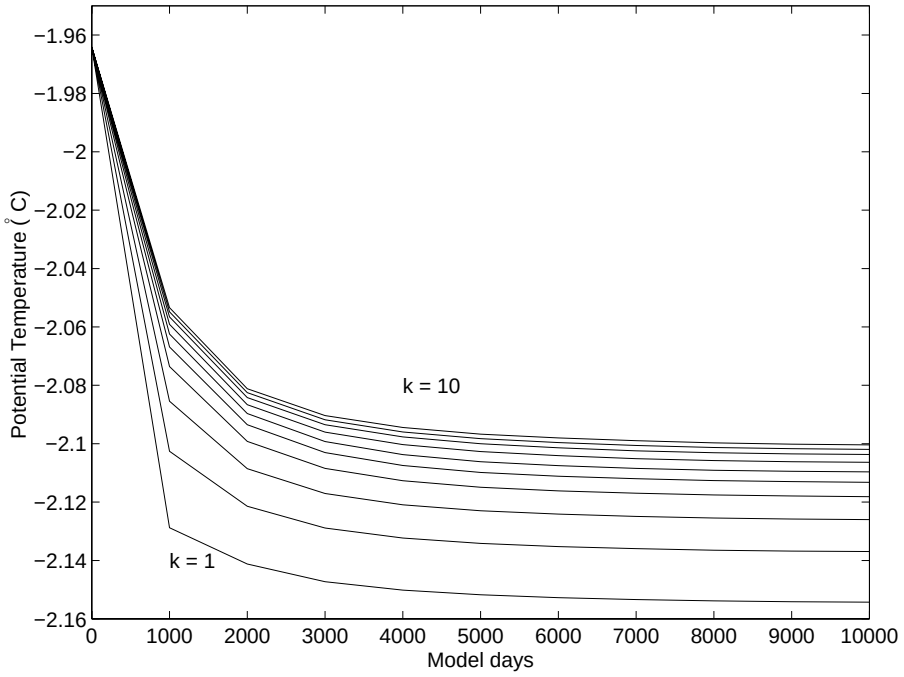

Figure 9.3: Amery domain baroclinic model spin up time for model run NT. Level averaged temperatures are plotted against integration time. The uppermost layer is indicated by k = 1, and the bottom layer is indicated by k = 10.

9.3.1 Results and Discussion

Sub-Ice-Shelf circulation

The results of model run NT is given here first as the 'standard' estimate of the sub-Amery Ice Shelf circulation. The model was run for 10000 model days for run NT. Figure 9.3 plots level averaged temperatures against model integration time, and shows that the model has reached approximately steady state conditions by 6000 days. All following runs were consequently run for 6000 days only. Results from run NT, presented below, are taken from 6000 days for consistency with following model run results.

The main circulation features for each of the experiments below are presented by means of approximate vertically and zonally integrated mass transport streamfunctions. The horizontal streamfunction, ψ, is defined by:

$$M_x = -\frac{\partial \psi}{\partial y}, M_y = \frac{\partial \psi}{\partial x}$$

where M_x and M_y are the horizontal depth-integrated mass transports in the x (east) and y (north) directions respectively. The vertical streamfunction, ψ_v, is defined by:

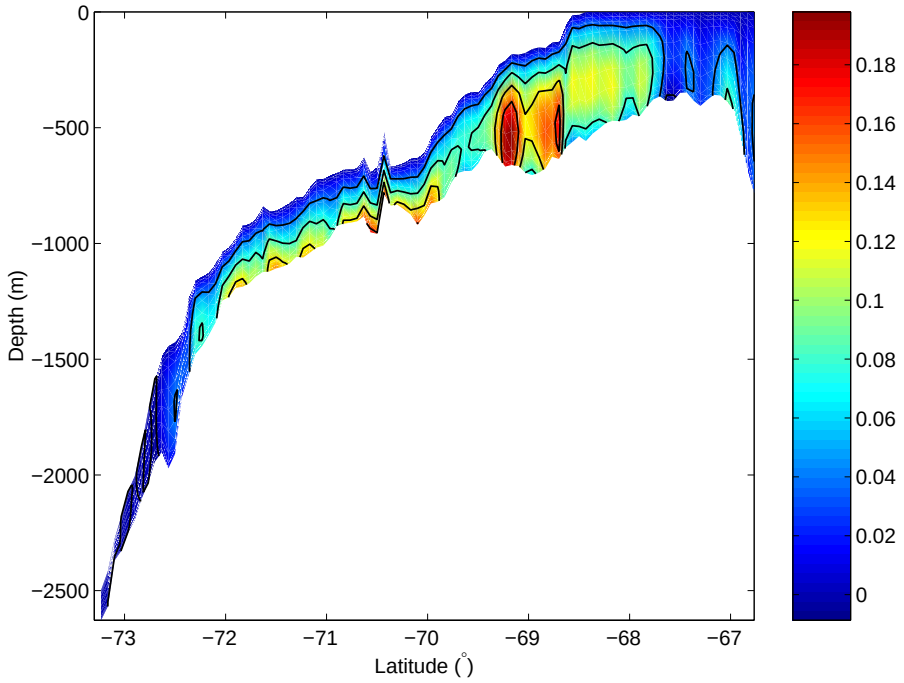

Figure 9.4: The zonally-integrated streamfunction (Sv) for model run NT. Circulation is clockwise about positive features. Contours are displayed at 0.04 Sv intervals.

$$M_{vy} = -\frac{\partial \psi_v}{\partial z}, M_z = \frac{\partial \psi_v}{\partial y}$$

where M_{vy} is the the zonally-integrated northward mass transport, and M_z is the zonally integrated vertical mass transport. The streamfunctions are only approximate, as the input/removal of freshwater at the ice-ocean interface has not been taken into account. These input fluxes are small, and therefore the effects can be assumed to be small for the calculation of both the horizontal and vertical streamfunction.

The results of previous sub-ice-shelf models (Determann and Gerdes, 1994; Grosfeld et al., 1997; Gerdes et al., 1999; Williams et al., 2001), which have each used the same model, indicate a velocity field which is nearly entirely barotropic, and hence well described by the vertically-integrated streamfunction. Other studies (Jenkins and Holland, 2002) have also interpreted results based on the horizontal circulation. Model results here suggest an overturning circulation with transports, determined from the zonally-integrated streamfunction (Fig. 9.4), in the northern portion of the Ice Shelf cavity with magnitudes (~ 0.2 Sv) of the same order as the horizontal transports, determined from the depth-integrated streamfunction (Fig. 9.5).

The sub-ice-shelf "ice pump" circulation, with northward transport of the cold, fresh

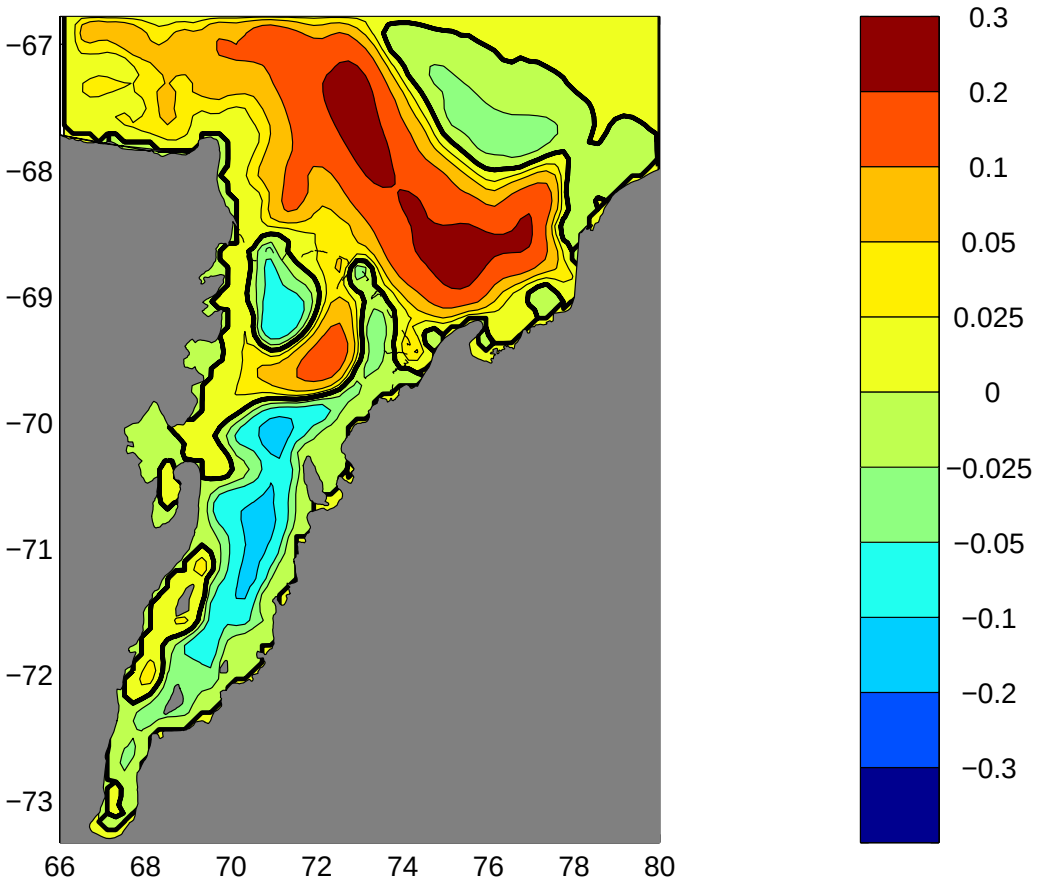

Figure 9.5: The vertically-integrated streamfunction (Sv) for model run NT. Circulation is clockwise about positive features.

buoyant meltwaters in the surface layers, and southward transport of the dense warmer, salty waters from the open water in the bottom layers is well represented by the zonally-integrated overturning streamfunction (Fig. 9.4). The relative magnitude of the overturning streamfunction is greater in the north of the ice shelf cavity, than in the south of the domain. However, this is not reflective of the relative strength of the overturning circulation in each region, but reflects the decrease in zonal width of the cavity with progression southwards, and hence the observed decreased transport of mass. The southern region is characterised by steep ice shelf draft and bed topography. The deep ice shelf draft results in large temperature gradients between the base of the ice shelf, which is at the in-situ freezing temperature, and the underlying ocean. The large temperature gradients lead to the occurrence of strong melting, and therefore large volumes of cold, fresh, buoyant meltwater which ascend the ice shelf base. In the south of the domain, where ice draft rapidly decreases with progression northwards, this ascent is rapid. Similarly, the dense salty inflowing waters rapidly descend

the steep gradients in bed topography towards the south of the domain in the bottom layers of the model.

In regions of basal freeze, the rejection of salt leads to downwelling in the model. The mass balance of the ice shelf defines a net loss (melt) in the ice shelf cavity. Buoyant meltwater flowing along the ice shelf base dominates the zonal-integration of the overturning circulation, thus tending to obscure the effects of downwelling, driven by freezing, in Figure 9.4.

The depth-integrated horizontal streamfunction is of the same order of magnitude in size as the overturning streamfunction ($\sim$ 0.2 Sv). Although the magnitudes of the barotropic circulation is approximately an order of magnitude smaller than the circulation described by Williams et al., (2001; henceforth WEA01), similarities between the circulation pattern of that of model run NT and that of WEA01 are evident. Differences in the magnitude of the barotropic circulation is a property of the model used. The results of the model presented in this study indicate greater overturning beneath the ice shelf than the WEA01 results, and therefore the depth-integrated horizontal transports reduce in magnitude.

The dominant feature of the WEA01 circulation is the clockwise circulating gyre filling a large portion of the northern half of the cavity (centred at $70°S$, $71°E$), called the Main Gyre (Williams et al., 2001). It is this feature which is responsible for most of the meridional transport of salt and heat in their model. The results of model run NT, presented here, show a similar central clockwise gyre (centred at $69.5°S$, $72°E$) situated where the water column thickness is greatest. The relative magnitude of this gyre (0.16 Sv) is the largest of the sub-ice-shelf gyres, however its spatial extent is relatively quite small. For parallel comparisons to the WEA01 results, the term 'Main Gyre' is maintained here. WEA01 noted a decrease in the magnitude of the Main Gyre when the barotropic exchange across the ice shelf front was eliminated. Results of Grosfeld et al. (1997) suggest the large step in water column thickness at the ice shelf front may form a barrier to barotropic flow across the ice shelf front. The depth-integrated streamfunction (Fig. 9.5) would also suggest only a small barotropic exchange is present at the ice shelf front for model run NT.

However, the WEA01 Main Gyre fills the entire north-western portion of the cavity, defining an outflow along the western boundary from as far south as $70.5°S$. This is where the two models differ. Figure 9.5 indicates the presence of an anticlockwise gyre in the north-west of the cavity which is termed the North-Western (NW) Gyre (centred at $69°S$, $71°E$) here, and has a magnitude of 0.09 Sv. The NW gyre defines a region of inflow near to the western side of the cavity, between longitudes $70°E$ and $71°E$, which is collected in

the gyre and follows the outflow, which is jointly associated with the Main Gyre, to exit the cavity between longitudes $71.5°E$ and $72°E$.

Williams (1999) trialled the definition of a zero streamfunction along the open boundary of the ice shelf cavity. The effect this had on the circulation presented by WEA01, was to separate the Main Gyre into a pair of gyres (Williams, 1999, page 86). The clockwise 'Central Gyre' was pushed southwards, making way for the slightly smaller magnitude anticlockwise 'Northern Gyre'. The 'Northern Gyre' defined an inflow near the western side of the cavity, similar to that observed in Figure 9.5.

Water is removed on the western side of the cavity via two paths. A weak outflow of water along the western coast of the cavity is collected from the northern tip of Jetty Peninsula at $70.5°S$ and is traced northward along the western boundary of the cavity to join the stronger northwards current observed in the open water which travels past Cape Darnley. The volume of this flow is small and therefore it is an ineffective transport mechanism. The second outflow is associated with the Main Gyre. However, this has a southern extent to only $69.9°S$, and therefore does not contribute greatly to the ventilation of the southern reaches of the cavity.

Other features of the horizontal circulation in the northern portion of the cavity described by WEA01, are gyres described to be topographically trapped in the north-east of the cavity. The more prominent anticlockwise gyre east of $72°E$ is named the North-Eastern (NE) Gyre, and is adjacent to the Main Gyre. The second un-named gyre is a small clockwise gyre east of $73°E$. The results of model run NT display similar circulation features. In the far north-east of the cavity, centred in open water at $69.3°S$, $74.5°E$, a small clockwise circulating feature is observed which does not contribute any significant exchange of heat or salt into or out from beneath the cavity. This feature is similar to the un-named gyre of WEA01. The anticlockwise feature equivalent to the North-Eastern Gyre contributes to the largest meridional transport beneath the cavity, as it joins the anticlockwise circulating gyres in the south of the cavity. It collects the northward outflow, which dominates the sub-ice-shelf circulation, that travels along the entire length of the eastern side of the cavity. The NE gyre does not contribute to the any depth-integrated cavity-ocean exchange. A continuous streamline from the east coast of the ice shelf at $\sim 75°E, 69.6°S$ passes north, then west, and then south-west to join with the west coast of the cavity at $\sim 69°E, 70.5°S$. Therefore, the only exit for the depth-integrated flow is therefore the narrow western coastal current, and consequently, the overturning circulation appears to contribute the dominant portion of the cavity-ocean exchange.

In model run NT, the main inflow beneath the ice shelf is that associated with the North-Eastern and Main Gyres between longitudes $72°E$ and $72.5°E$. It travels southwards along the $72.5°$ meridian to $\sim 69.9°S$, before turning westwards. A small portion of this flow recirculates with the Main Gyre, most of it continuing southwards in a meandering flow near the western side of the cavity. A weak northward western boundary current is observed between latitudes $72.2°S$ and $71°S$ which defines a weak (0.03 Sv) clockwise circulating gyre around Fisher Massif. The southward flow continues to the southern extent of the grounding line, before returning along the eastern side of the cavity as a broad, relatively strong, northward flow which travels the entire length of the cavity, collected on the eastern flank of the North-Eastern Gyre east of $73°E$. This extensive gyre, called the 'Southern Gyre', is large in spatial extent and has a magnitude of 0.14 Sv, with maximum surface currents of $\sim 6\ cms^{-1}$ northwards. It is responsible for the transport of heat and salt to the southern reaches of the cavity, and defines the outflow path of meltwater derived from the melting in the deep cavity. The WEA01 circulation displays an anticlockwise circulation in the south of the domain, however the magnitude of the WEA01 'Southern Gyre' is less than one tenth the magnitude of the WEA01 Main Gyre in the north of the domain.

There are two mechanisms for the northward current along the eastern side of the cavity. Some component of the flow may be contributed to by a vorticity balance in the overturning circulation. Within the ocean cavity beneath the ice shelf, the buoyancy of meltwater results in the surface flow travelling northwards along the ice shelf base. This flow entrains water from below, resulting in an upwelling and flow divergence in the layers immediately beneath the ice shelf. This upwelling and flow divergence results in the relative vorticity to increase in an anticlockwise sense (in the southern hemisphere), tending to induce an anticlockwise circulation in the upper layers beneath the ice shelf. The northward surface flow adjusts by moving to the eastern boundary to dissipate the anticlockwise vorticity, via drag at the lateral boundary inducing some clockwise relative vorticity. Consequently, the northward flow may shift to the eastern side of the cavity. The variations in water density beneath the ice shelf set up by such a circulation may then induce a barotropic circulation presented in Figure 9.5. However, the other factor which may be more important in developing the northward flow along the eastern side of the cavity is the ice shelf draft used in the model studies (Fig. 9.2). Fresh buoyant meltwaters formed as a result of melting near the southern extent of the grounding line ascend the ice shelf base. The shallower side of the ice shelf is on the eastern side of the cavity. As a result, a preferential tendency for the northward buoyant meltwater plume to flow towards the eastern side of the cavity may

exist.

In the open waters of Prydz Bay, a large clockwise gyre resembling the Prydz Bay Gyre is observed. The flow along the ice shelf front is westwards with a transport of $\sim 0.28Sv$ and depth-averaged current speeds of $0.02ms^{-1}$. The speed of the current is small compared to the observed $0.08ms^{-1}$ currents (Wong et al., 1998), however, this can be expected with no wind forcing in the open ocean portion of the model domain. Despite this, Smith et al. (1984) obtained westward geostrophic currents in the flow along the ice shelf front of $0.03ms^{-1}$. Other estimates of up to $0.1ms^{-1}$ have been made (Nunez Vaz and Lennon, 1996). At longitude $72.5°E$, approximately one half of the transport along the ice shelf front turns southwards beneath the ice shelf, circulates about the Main Gyre, and returns to the westward ice front flow. At the western coast, the flow again diverges. Half of the flow turns southwards beneath the ice shelf, and the remaining half turns northwards to travel along the coast past Cape Darnley, of which some turns westwards to follow the Mac-Robertson coast, and some recirculates back into Prydz Bay.

The sub-ice-shelf circulation is closely coupled to the forcing provided by the ice shelf. The ice shelf forcing is well represented by the rates of freeze and melt at the ice-ocean interface. At locations of melt, the top of the water column is cooled and freshened, increasing the buoyancy of the water. Locations of freeze result in salt rejection and heat effectively being added to the system.

The rates of melt and freeze at the ice-ocean interface after 6000 days for model run NT show that strongest melting occurs near the southern extent of the grounding line where the ice shelf is thickest (Fig. 9.6). The relatively warm, salty waters from the open waters of Prydz Bay, together with cool, salty waters formed beneath the ice shelf by freezing, descend southwards along the seabed beneath the ice shelf and reach the deep, southern extent of the cavity. The large temperature difference between this water (temp. $\sim -2°C$) and the base of the ice shelf, which is at the in-situ freezing point ($\sim -3.4°C$ at pressure 2000 db and salinity 34.57 psu), results in strong melting in this deep southern zone. Maximum predicted melt rates are $2.78ma^{-1}$ for run NT, and occur in this region (Table 9.3).

Melting occurs near the ice shelf front as water, advected horizontally from open water into the cavity, comes into contact with the base of the ice shelf. The same mechanism is responsible for melting in other areas of the cavity. In regions where the surface currents (Fig. 9.7) drive water down-slope along the base of the ice shelf, the temperature difference between the water and the ice shelf will increase, leading to the occurrence of melt at the ice-ocean interface. The most notable of the regions where this mechanism is evident beneath

Table 9.3: Maximum melt and freeze rates at the base of the Amery Ice Shelf for each model run

Model Run (AIS)	Maximum Melt Rate (ma^{-1})	Maximum Freeze Rate (ma^{-1})
NT	2.78	0.33
T	1.35	0.69
T+0.2°C	1.39	0.39
NT+1°C	5.99	0.044
T+1°C	6.70	0.00
B	7.10	2.56
B-T	3.5	1.83
CADA	13.3	2.48
CADA-T	12.0	2.27
A	4.68	1.54
C	10.7	2.11
BFR	6.40	2.89
B+1°C	15.9	0.75
B-T+1°C	14.9	0.31

the ice shelf is the large area of melt in the northern portion of the ice shelf cavity centred at 69.7°S, 72°E. Water is advected south-westwards, downslope along the ice shelf base, on the south-eastern flank of the clockwise circulating 'Main Gyre' (Fig. 9.7). Similarly, the southward flow on the western side of the cavity, south of 70.5°S (Fig. 9.7), also has a zone of associated melt ($\sim$ 71°S, 70°E).

The maximum rate of freeze in the model domain is 0.33 ma^{-1} (Table 9.3). The regions where freezing occurs at the ice-ocean interface are similarly closely linked with the underlying ocean circulation. Steep ice shelf gradients allow the rapid ascent of water which has been cooled and freshened by melting at depth. During its ascent, this water becomes supercooled, beneath the in-situ freezing point, resulting in freezing. Such coupling between the regions of melt and freeze is observed in Figure 9.6. Each zone of freeze lies in an area where a steady supply of fresh meltwater from a melt zone is ascending the ice shelf base. This process is most easily observed in the regions of large areas of freeze. In the northern portion of the ice shelf cavity, the clockwise circulating main gyre has a zone of freeze occurring as part of the outflow observed on the north-western flank of the gyre (centred at 69.2°S, 71°E; Fig. 9.6). The melt-zone, discussed above, on the south-eastern flank of the gyre provides a plume of ascending cold, fresh, buoyant, meltwater along the ice shelf base (Fig. 9.7) which most easily reaches the cold temperatures required for freezing.

The second large area of freeze is observed in the south of the domain. High melt-rates at the southern extent of the cavity provide an abundant source of meltwater, which ascend the ice shelf base, supercool, and freeze. In the southern domain, the ascending flow tends to the eastern side of the cavity (Fig. 9.7) and freezing occurs. The resulting region of freeze is centred at 71.5°S, 70°E, and can be traced along almost the entire length of the eastern

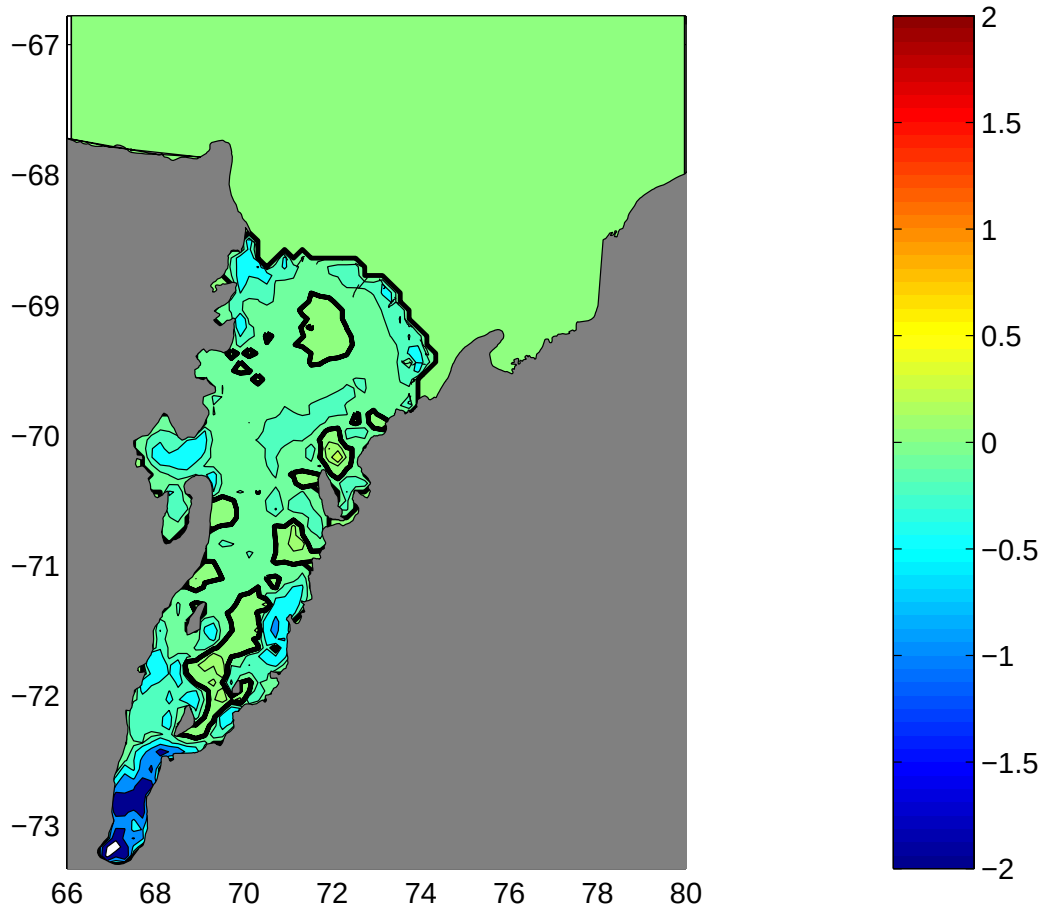

Figure 9.6: Freeze rates (ma^{-1}) for model run NT. Positive regions represent freezing, negative regions represent melting. The bold contour denotes the boundary between melting and freezing. Contours are at -2, -1, -0.5, -0.2, -0.1, 0.0, 0.1, 0.2, 0.5, 1 and 2 ma^{-1}. The white area in the south of the domain displays the region where melt rates are greater than 2 ma^{-1}, i.e., outside the contour range.

side of the sub-ice-shelf cavity. A thin line of melt is observed at the eastern-most extent of the cavity at $71.5°S$ as a result of the sharp increase in ice draft near to the grounding line there.

The melt/freeze pattern is supported by observations at the two hot water drill sites, AM01 and AM02. An ice core taken from site AM01 ($69°26.5'S$, $71°25.0'E$) indicates the presence of marine ice, and therefore the site appears to be a region of basal freeze (Craven et al., 2002). The AM01 site lies in the centre of the freeze zone in the northern portion of the ice shelf, and has a predicted freeze rate of 0.012 ma^{-1}. No evidence of the presence of marine ice at site AM02 ($69°42.8'S$, $72°38.4'E$) was obtained, and therefore the site is assumed to lie within a region of basal melt (Craven et al., 2001). Site AM02 lies to the east of AM01 on the eastern inflowing flank of the main clockwise gyre. A melt rate of 0.088

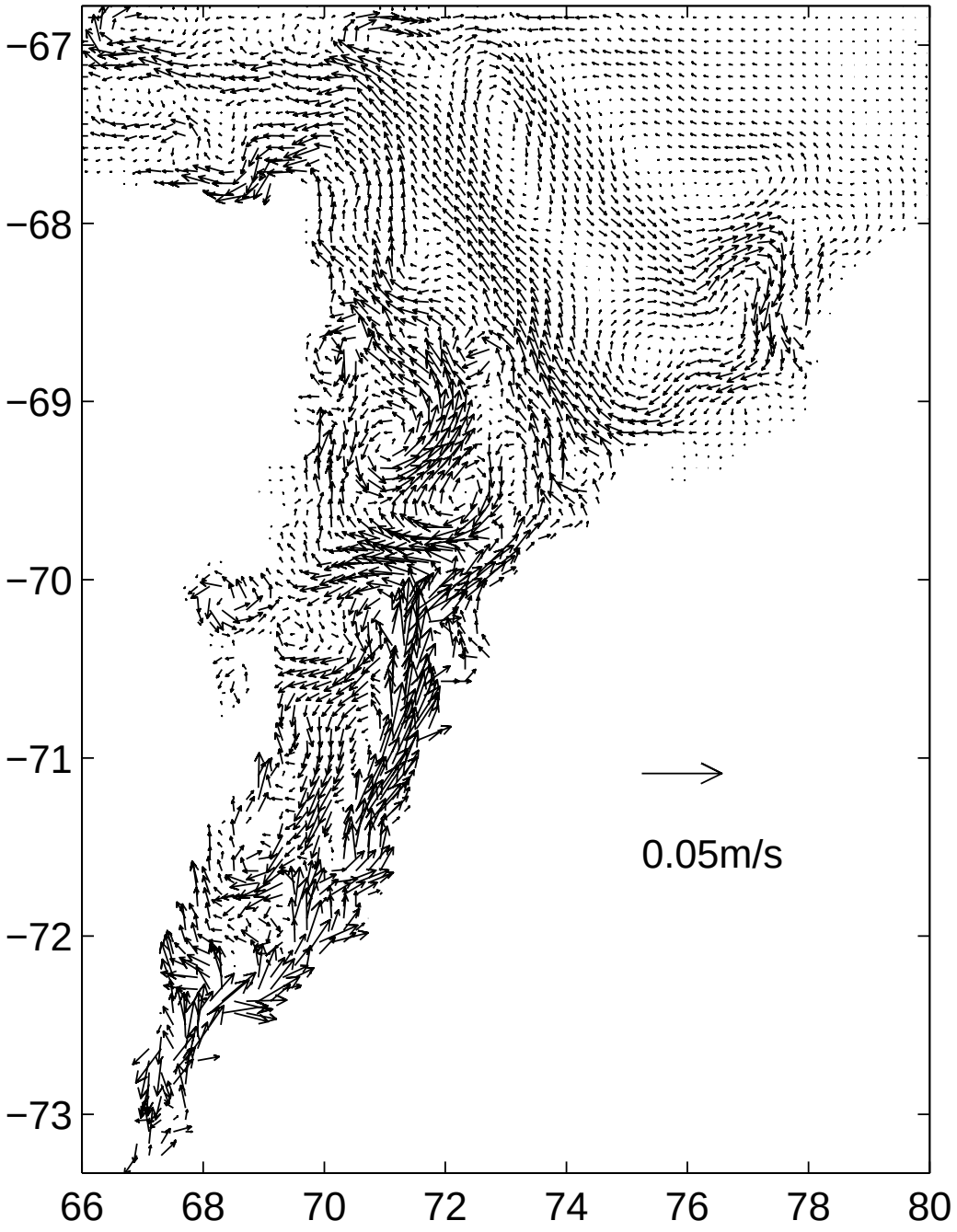

Figure 9.7: Horizontal currents (ms^{-1}) in the surface (k=1) layer for model run NT.

Table 9.4: Estimates of the mass balance rates at the base of the Amery Ice Shelf, with varying topographies and a varied ocean temperature. The rates in the first three columns are the area-averaged rates for regions where freezing or melting occur, and for the total ice shelf area. The percentage area of the ice shelf where melting is occuring is included in column 5. The last three columns show the mass gain from freezing, the mass loss from melting, and the net mass loss from the ice shelf. The total area of the ice shelf given the new grounding line is $5.82 \times 10^4\ km^2$.

Model Run	Mean Rates for			Area of	Mass Change Rates		
(AIS)	Freezing (ma^{-1})	Melting (ma^{-1})	Whole (Loss) (ma^{-1})	Melt %	Freezing (Gta^{-1})	Melting (Gta^{-1})	Net Loss (Gta^{-1})
NT	0.05	0.16	0.13	83.8	0.45	7.61	7.2
T	0.07	0.18	0.14	84.0	0.69	8.65	8.0
T+0.2°C	0.06	0.27	0.25	94.5	0.18	15.0	14.8
NT+1°C	0.04	0.82	0.82	99.8	0.003	49.3	49.3
T+1°C	0.00	0.87	0.87	99.9	0.0	52.5	52.5
B	0.29	0.38	0.15	64.6	5.7	14.2	8.5
B-T	0.18	0.27	0.15	73.7	2.8	11.4	8.7
CADA	0.34	0.51	0.17	60.3	7.9	17.7	9.8
CADA-T	0.24	0.40	0.17	78.6	5.5	15.4	9.9
A	0.18	0.45	0.25	68.5	3.2	18.1	14.9
C	0.33	0.64	0.29	63.1	6.5	22.5	16.0
BFR	0.30	0.38	0.14	64.5	6.3	14.4	8.1
B+1°C	0.17	1.19	1.08	90.7	0.7	66.0	65.2
B-T+1°C	0.09	1.06	1.04	98.3	0.09	62.8	62.7

ma^{-1} is predicted at site AM02 by model run NT.

Integrating the rates of melting and freezing at the ice-ocean interface allows the mass balance of the base of the ice shelf to be determined (Table 9.4). For model run NT, the net mass loss from the ice shelf is 7.2 Gta^{-1}. The initial conditions used for the model in this study are similar to conditions prescribed for the AIS_{cold} and AIS_{cool} model runs presented by Williams et al. (2002) (henceforth WEA02). The AIS_{cold} run is initialised with water temperatures set equal to the in-situ freezing temperatures corresponding to the minimum ice shelf draft at the Amery ice front (235 m.). The AIS_{cool} run is initialised with water temperatures set equal to the surface freezing temperature, except where the water is already cooler. WEA02 predict a net mass loss of 5.4 Gta^{-1} from the ice shelf for model run AIS_{cold}, 11.9 Gta^{-1} for run AIS_{cool}, and 14.2 Gta^{-1} for model run AIS_{pres}, forced with present day salinity and temperature values (taken from the FISHOG data set) at their open boundary at the ice shelf front. The 7.2 Gta^{-1} net loss figure presented here agrees well with the values given by the WEA02 model when forced with lower temperatures. i.e., AIS_{cold} and AIS_{cool}. Some variation in the net mass loss from the ice shelf between the two models could be expected, given the slightly different ice shelf area (the WEA02 ice shelf area is $5.6 \times 10^4\ km^2$) and the deeper ice draft in the south of the new model grids.

The density distribution describes the movement of water masses in the model domain. Figures 9.9 - 9.11 display the cross-sections of potential density from three transects in the model domain for model run NT. The positions of the three transects are shown in Figure 9.8.

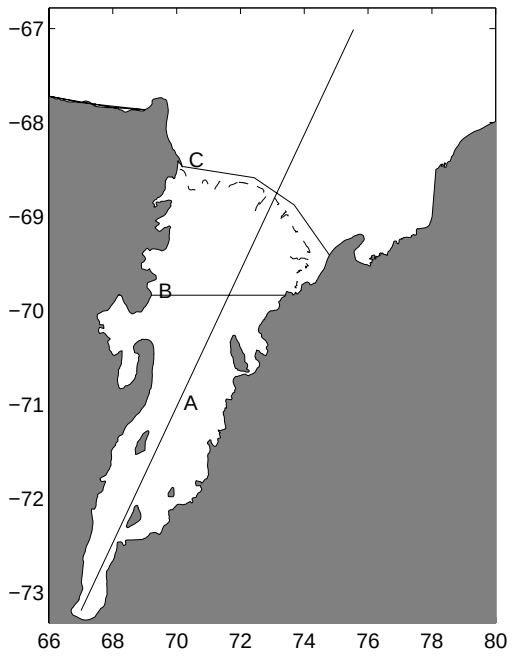

Figure 9.8: Positions of the three transects for which potential density cross-sections are presented.

Transect A is a transect along the longitudinal axis of the ice shelf, transect B is an east-west transect taken across the ice shelf at latitude $69.83°S$, and transect C is in open water along the ice shelf front, and closely follows the path taken by the *RSV Aurora Australis* AMISOR oceanographic research cruise au0106, undertaken during January 2001.

In areas of melt, a cold, fresh, meltwater layer forms at the top of the water-column. Regions of high melt are generally in the areas where the ice shelf draft is greatest, and therefore, the meltwater ascends the ice shelf base. This divergence allows upwelling of the warm, salty water from below, which continues to drive the predicted melt. In areas of high melt, steep vertical gradients in density are observed.

The effect of freezing on the water column is quite different. Freezing results in a slight warming of the surface water, but more dramatically, the rejection of salt into the top of the watercolumn through the removal of cold fresh water at the surface. The input of salt increases the water density, driving strong overturning of the watercolumn. Consequently, in regions of freeze, the watercolumn will appear well mixed, with small vertical density gradients.

The density cross-section taken from transect A (Fig. 9.9) reflects many of these processes. In the south of the domain, south of $72°S$, strong density gradients are observed, both with longitude (across shelf) and vertically within the watercolumn. These strong

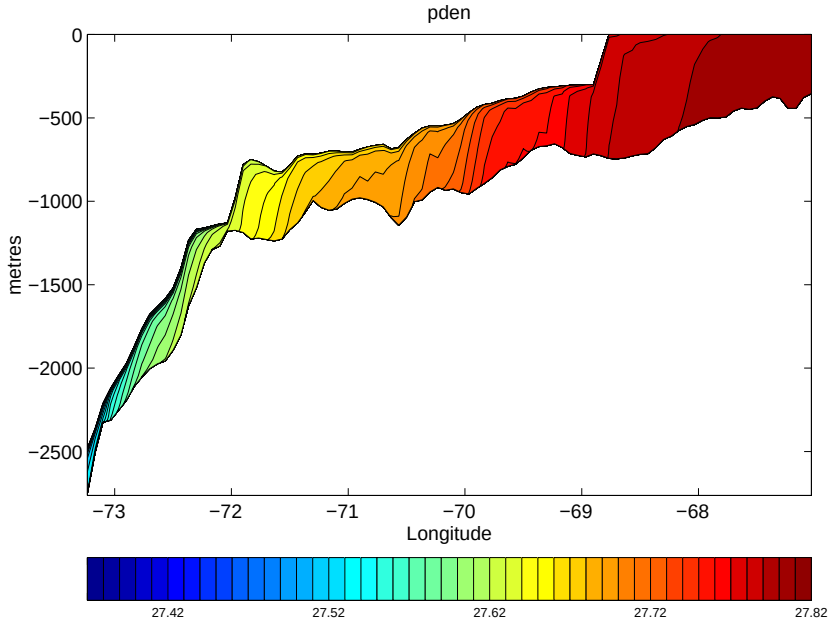

Figure 9.9: Density (σ_θ) cross-section for model run NT along transect A.

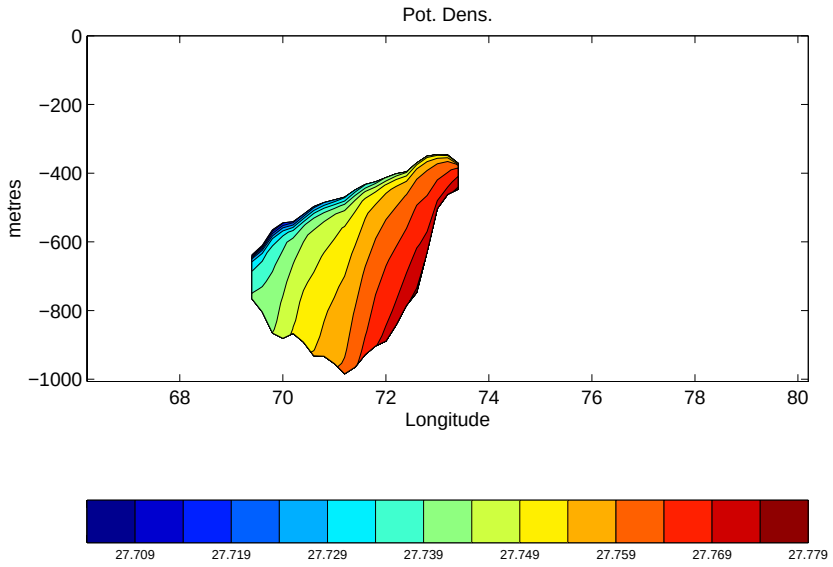

Figure 9.10: Density (σ_θ) cross-section for model run NT along transect B.

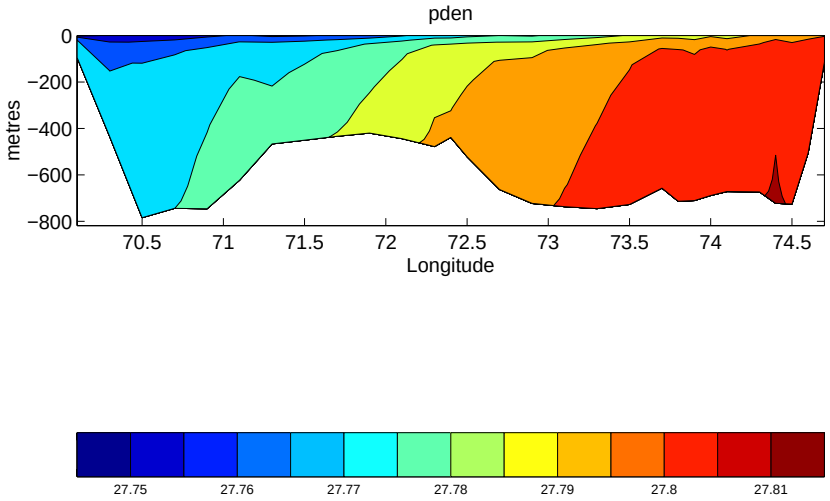

Figure 9.11: Density (σ_θ) cross-section for model run NT along transect C.

gradients result from the high melt rates predicted in the south of the domain, which forms the cold, fresh, meltwater layer near the surface. This layer of melt becomes thinner towards $72°S$, where it is reduced as a result of freezing at the surface. North of $71.8°S$, melting again leads to the formation of a thin surface meltwater layer. Section A does not pass through any other strong freezing zones, however near to the small area of freeze just south of $70°S$, the water column is more vertically mixed. The effects of freezing are easily destroyed in the density cross-sections through the continual replacement of the watercolumn by horizontal advection. In the open water portion of the model domain, the plume of meltwater can be observed to extend out to the surface layers of the open ocean, setting up a stratified water body, with the low density meltwaters overlying the dense shelf waters (LSSW).

The model results presented here show much stronger horizontal density gradients beneath the ice shelf than predicted by WEA02. WEA02 show a temperature range beneath the ice shelf of $\sim 0.6°C$. Melting of ice into a mixed layer causes the T/S properties to evolve along a straight line, the gradient of which $\frac{\partial T}{\partial S}$ is approximately 2.5 $°Cpsu^{-1}$ (Nost and Foldvik, 1994). Therefore, in combination with the equation of state, a change in temperature may be used as a proxy for the change in density, according to:

$$\frac{d\rho}{dT} = 0.266$$

, and thus, a $0.6°C$ temperature change corresponds to a change in density of 0.16 kgm^{-3}. Figure 9.9 indicates a change in density of $\sim$ 0.4 kgm^{-3} beneath the ice shelf in model run NT. The difference in density gradients beneath the ice shelf of the two models reflects the deep ice drafts in the "new" geometry. Large areas of melt towards the deep southern

grounding lines input larger volumes of fresh water, setting up these large gradients.

Section B displays the zonal variation of density in the northern portion of the cavity. Advection of meltwater formed on the western side of the cavity, and southwards of the section, follows the base of the ice shelf towards the shallower eastern side of the cavity. The zone of freeze north Gillock Island removes some of this meltwater from the surface on the eastern side of the cavity. The section runs quite oblique to the centre line of the ice shelf. This accounts for a large component of the predicted sloping isopycnals.

Although there are no major outflows on the western side of the cavity from beneath the ice shelf, the density cross-section taken from transect C from along the ice shelf front displays a large west to east gradient, with less dense water on the western side of the section. Cold, fresh, low density meltwaters leave the cavity at $\sim 72°E$ longitude. The westward current which is observed along the ice shelf front, which is a well known feature in Prydz Bay, appears to move this meltwater directly to the western side of the ice shelf front soon after its exit from the cavity in the model. Wong et al. (1998) suggested the outflow of ISW from beneath the Amery Ice Shelf was confined to the western end of the ice shelf front, given that ISW was only observed in CTD stations in the immediate vicinity north of the western front of the ice shelf. It would appear from the model results that only a small outflow occurs on the western side of the ice front, but the presence of ISW remains confined to the western side of the ice front as a result of the open water currents. CTD sections taken across the ice shelf front during voyage au0106 indicate the largest presence of cold ($< 2°C$) water indicative of ISW at $\sim 72°$ longitude (Rosenberg et al., 2002), suggesting the presence of an outflow in the region, consistent with the results of model run NT.

Many previous sub-ice-shelf ocean circulation models have assumed a constant thermal exchange velocity, γ_T, of $1 \times 10^{-4}\ ms^{-1}$ (Hellmer and Olbers, 1989). Model run B is identical to run NT, except γ_T is not a function of the friction velocity, $u*$, but is held constant at the pre-defined value. Friction velocities at the ice-ocean interface in model run NT are typically of order $1 \times 10^{-3}\ ms^{-1}$, indicating that the thermal exhange velocity in run NT is an order of magnitude smaller than the value assumed by Hellmer and Olbers (1989). The parameterisation used here differs to that of Hellmer and Olbers (1989) in that the two-equation formulation for heat transfer at the ice-ocean interface (Holland and Jenkins, 1999) is used here, ignoring the contribution of heat from the transfer of salt. Hellmer and Olbers (1989) include a constant salt transfer coefficient in their parameterisation of the ice-ocean interface.

The constant γ_T parameterisation prescribed for model run B does not significantly

alter the sub-ice-shelf circulation. Table 9.5 displays the magnitude of each of the main circulation features within the model domain. Differences between model runs NT and B are observed to be small, indicating the circulation predicted by model run B is very similar to that for run NT, shown in Figure 9.5. However, the melt and freeze rates and distribution predicted by model run B (Fig. 9.12) differ to those predicted by run NT. The increased γ_T leads to greater rates of melting in the cavity. Maximum melt rates of 7.10 ma^{-1} for run B are approximately three times larger than those predicted for run NT (2.78 ma^{-1}; Table 9.3). Increased melting at the ice-ocean interface leads to a larger volume of buoyant meltwater in the cavity which, during its ascent along the ice shelf base, more readily supercools, and hence cause greater rates of freezing. Maximum freeze rates for run B of 2.56 ma^{-1} are much greater than those for run NT (0.33 ma^{-1}). Marine ice layer thicknesses have not been computed along the ice shelf flow-lines, however the dominant area of freeze predicted by model run B in the north-west of the cavity, when accumulated along flow-lines of the ice shelf, are more likely to lead to a more consistent marine ice distribution beneath the ice shelf to those estimated using combined in-situ and satellite methods (Fig. 6.8, Fricker et al., 2001), than from freeze rates predicted by run NT. This might suggest that melt and freeze rates beneath the ice shelf are underestimated in model run NT. A change in melt/freeze distribution and rates influences the estimated mass balance of the Amery Ice Shelf (Table 9.4). Although the percentage area of melt for model run B (64.6%) is much less than for run NT (83.8%), the greater melt rates result in a much larger rate of mass loss by melting from run B than run NT (14.2 and 7.7 Gta^{-1} respectively). The mass gain from freezing however, is similarly altered, so that the mass gain for run B is greater than for run NT (5.7 and 0.45 Gta^{-1} respectively). Consequently, the net mass loss from the ice shelf is largely unchanged between model run B (8.5 Gta^{-1}) and run NT (7.2 Gta^{-1}), both being consistent with previous estimates forced under similar conditions (Williams et al., 2002). WEA02 parameterise the thermal exchange velocity, γ_T, as a function of the friction velocity, similar to model run NT. However, WEA02 assume a free-slip condition at the ice-ocean interface, and therefore friction velocities at the interface are likely to be overestimated. This may be important to the WEA02 predicted rates and distribution of melt and freeze beneath the Amery Ice Shelf.

Model run BFR was carried out analagous to run B, but the spatial resolution was doubled. Very little is gained by running the model at high resolution. The pattern of circulation predicted using model grid BFR is well described by the circulation using model grid B, as above. Similarly, the distribution of melt and freeze is unchanged, and this is

Table 9.5: Transport in the main features of the thermohaline circulation. Positive values indicate clockwise transport.

Model Run	Overturning circulation (Sv)	Main gyre (Sv)	Northeastern gyre (Sv)	Northwestern gyre (Sv)	Southern gyre (Sv)	Prydz Bay gyre (Sv)
NT	0.2	0.16	-0.04	-0.09	-0.14	0.27
T	0.19	0.16	-0.04	-0.09	-0.13	0.29
T+0.2°C	0.25	0.19	-0.06	-0.12	-0.16	0.39
NT+1°C	0.46	0.27	-0.12	-0.25	-0.26	0.70
T+1°C	0.46	0.26	-0.12	-0.21	-0.23	0.65
B	0.2	0.16	-0.04	-0.1	-0.14	0.28
B-T	0.19	0.16	-0.04	-0.09	-0.13	0.28
B+1°C	0.48	0.28	-0.13	-0.28	-0.27	0.75
B-T+1°C	0.46	0.29	-0.13	-0.22	-0.24	0.76

shown in Table 9.4 by the percent area of melt showing a 0.1 % decrease when the higher resolution model grid BFR is used in comparison to run B. Similarly, the estimated net mass loss from the ice shelf as a result of melting at the ice shelf base shows less than 5 % decrease from 8.5 Gta^{-1} (Run B) to 8.1 Gta^{-1} (Run BFR) when the finer resolution model grid is used.

The influence of tidal mixing

Model run T was executed for 6030 days. Results of the residual circulation of model run T, presented in this section, are determined by averaging the hourly output from the final 30 days of the model run. This was carried out to assure the removal of the oscillating component associated with each forcing tidal constituent. Run T has a thermal exchange velocity dependent on the friction velocity at the ice shelf base.

One effect of tides on the sub-ice-shelf oceanography in the model is to increase the vertical mixing in the cavity. This serves to more readily mix the warm salty waters, which flow southwards downslope along the seabed beneath the ice shelf from open waters, upwards to come into contact with the cold ice shelf base. The temperature difference between the ice shelf base and the warm salt waters which are mixed up from below drives melting at the ice-ocean interface. An increase in the volume of warm waters at the ice shelf base through tidal mixing will result in increased rates of melting in the cavity. The effects of increased mixing from tides is expected to be greatest in regions of small water column thickness, where tidal currents are largest. Similarly, friction velocities at the ice-ocean interface will be greater in these regions, and hence the diffusion of heat into the ice shelf increases as a result of the relationship between the thermal exchange velocity and the friction velocity (Holland and Jenkins, 1999).

However, a negative feedback mechanism exists. Stronger melt rates within the cavity lead to a meltwater layer of greater thickness at the surface. The greater the thickness of

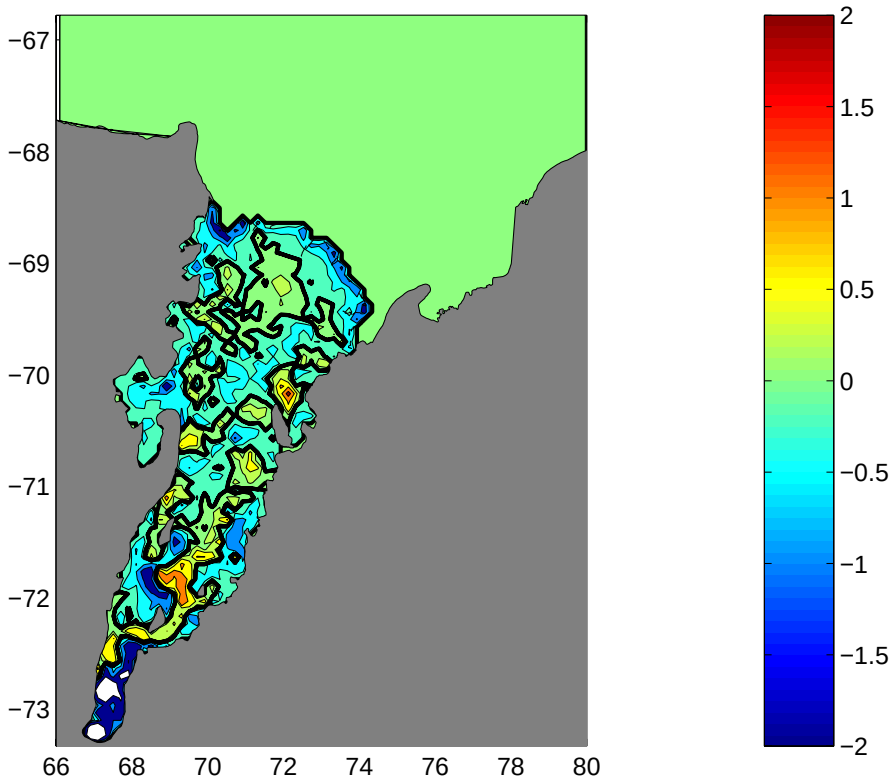

Figure 9.12: Freeze rates (ma^{-1}) for model run B. Positive regions represent freezing, negative regions represent melting. The bold contour denotes the boundary between melting and freezing. Contours are at -2, -1, -0.5, -0.2, 0.0, 0.2, 0.5, 1 and 2 ma^{-1}. The white area in the south of the domain displays the region where melt rates are greater than 2 ma^{-1}, i.e., outside the contour range.

this meltlayer, the more mixing that is required to destroy the stratification and allow the warmer waters from below to come into contact with the ice shelf base and drive further melting.

In Chapter 8, it was predicted that the energy available for vertical mixing, through tidal dissipation at frictional interfaces, was too small to overcome the stratification induced by melting.

Differences between the results of model run T, including tides, and model run NT, which does not, beneath the Amery Ice Shelf are small. Some small changes are observed in the distribution and rates of freeze at the ice-ocean interface. Figure 9.13 displays the melt/freeze distribution for model run T. Although the maximum melt rates at the base of the ice shelf are smaller for model run T (1.35 ma^{-1}) than for run NT (2.78 ma^{-1}; Table 9.3), the mean rate of melt shows an increase for run T (0.18 ma^{-1}) in comparison to run NT (0.16 ma^{-1}; Table 9.4). The percentage area of melt increases only very slightly

from 83.8% to 84.0% with tides included in the model. Therefore, the increased mean melt rates result in a slightly increased volume of meltwater in the ice shelf cavity for model run T than run NT. The ascent of the meltwater plume along the ice shelf base results in the water to become supercooled, and freezing to occur. Mean, and maximum, freeze rates beneath the ice shelf are consequently greater for run T than model run NT (Tables 9.3 and 9.4). The increase in mass loss from melting brought about via increased mixing of warmer water up to the ice shelf base in run T, is counteracted by a related increase in the mass gain from freezing. As a result, the net mass loss from the ice shelf shows only a relatively small shift from 7.2 Gta^{-1} for model run NT, to 8.0 Gta^{-1} for run T which includes the effects of tides.

Potential temperature adjacent to the ice shelf front (transect C) in model runs NT and T are approximately $-2°C$. Observations from the FISHOG data, and the au0106 and au0207 CTD transects, suggest that the mean potential temperature near to the ice front is closer to $-1.85°C$. Therefore, the temperatures beneath the ice shelf in the model are probably much less than actually occur, and predicted melt-rates are too low. As a result, model run T+0.2$°C$ was carried out to estimate the sub-ice-shelf circulation, and the ice shelf mass balance, under present day conditions. The mean potential temperature along transect C for run T+0.2$°C$ is $-1.82°C$, similar to the observed temperatures. The sub-ice-shelf circulation strength increases slightly for model run T+0.2$°C$ (Table 9.5), however the circulation pattern remains the same as for runs NT and T. The mass balance of the Amery Ice Shelf for model run T+0.2$°C$, as an estimate of present day conditions, suggests a net mass loss from the ice shelf of 14.8 Gta^{-1} (Table 9.4). This value agrees well with the predicted net mass loss value from WEA02 of 14.2 Gta^{-1}, and the oceanographic observational estimates which indicate a mass loss ranging between 10.7 and 21.9 Gta^{-1}, with a preferred mean of 14.7 Gta^{-1} (Wong et al., 1998). Similarly, CTD data collected in a section across the ice shelf front during the au0106 AMISOR voyage provides an estimate of the freshwater transport out from beneath the ice shelf of 18.3 Gta^{-1} (Shanahan, 2002).

The small influence which tides have on the oceanography of the cavity beneath the Amery Ice Shelf is reflected in the distribution of density in the cavity. Figures 9.14 - 9.16 display density cross-sections taken from the same transects A, B, and C, as presented in the previous section, for model run T. In the sub-ice-shelf sections, A and B, the density distribution is largely unchanged from those presented for run NT.

In the open water portion of the model domain, the influence of tidal mixing on the water properties is more easily recognised. In the open water portion of transect A (Fig. 9.14), the water column is observed to be well mixed in comparison to the non-tidal

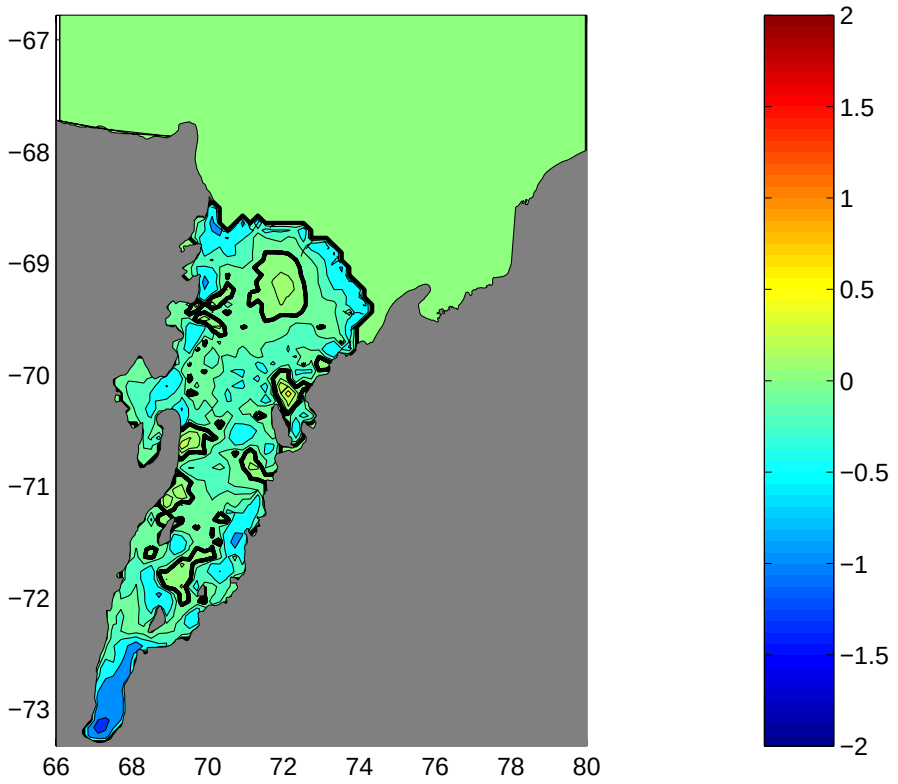

Figure 9.13: Freeze rates (ma^{-1}) for model run T. Positive regions represent freezing, negative regions represent melting. The bold contour denotes the boundary between melting and freezing. Contours are at -2, -1, -0.5, -0.2, -0.1, 0.0, 0.1, 0.2, 0.5, 1 and 2 ma^{-1}. The white area in the south of the domain displays the region where melt rates are greater than 2 ma^{-1}, i.e., outside the contour range.

conditions in run NT. Along transect C (Fig. 9.16), the water column is also relatively well-mixed but the east-west gradients have increased across the ice shelf front in comparison to those observed in run NT.

As with other features of the sub-ice-shelf oceanography, the mean circulation within the ocean cavity beneath the ice shelf for model run T is also largely unchanged to that from run NT with the inclusion of tides to the model. Table 9.5 compares the strength of the major sub-ice-shelf circulation features between model runs which include tidal forcing, and those which do not. Figure 9.17 displays the tidally-averaged, zonally-integrated, overturning streamfunction for model run T, and Figure 9.18 displays the respective, tidally-averaged, depth-integrated streamfunction. The strength and pattern of circulation in the cavity shows very little variation with the inclusion of tides. The small northward current along the western boundary of the northern portion of the cavity has dissapeared, and the interchange between the North-eastern gyre and the Southern gyre has reduced.

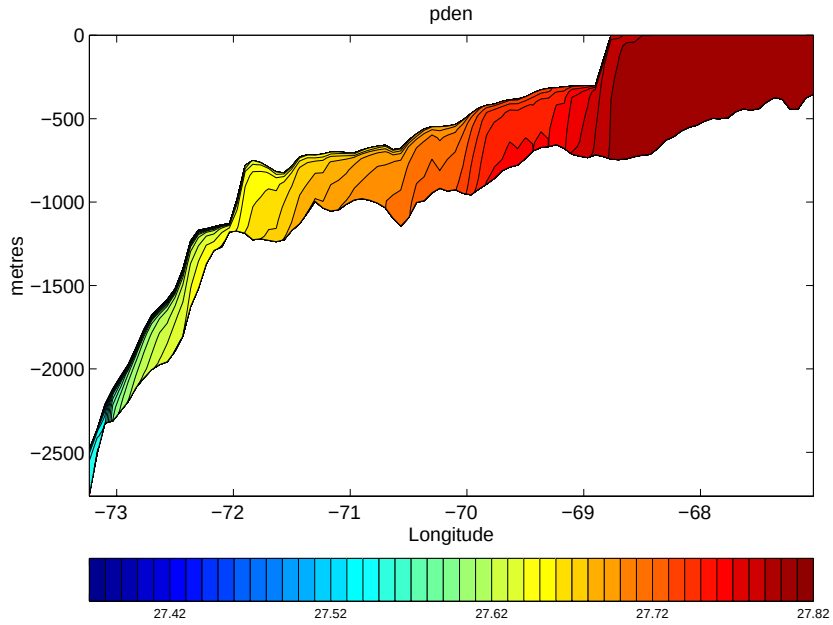

Figure 9.14: Density (σ_θ) cross-section for model run T along transect A.

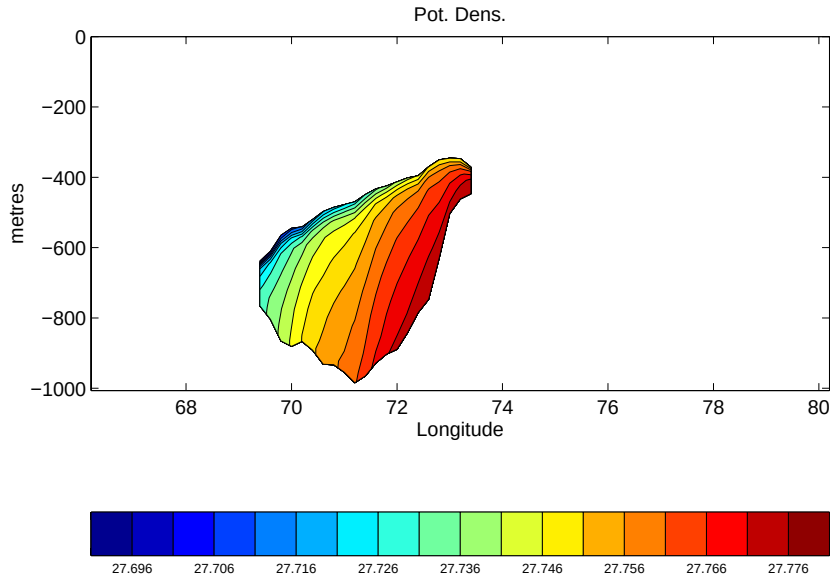

Figure 9.15: Density (σ_θ) cross-section for model run T along transect B.

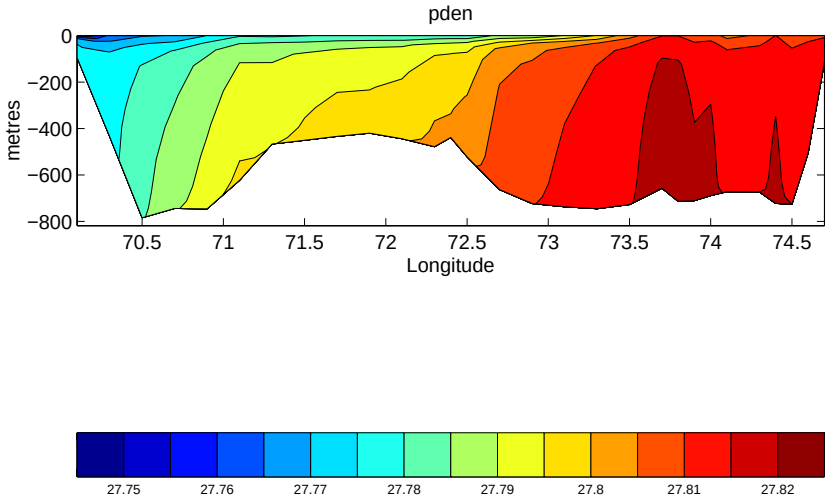

Figure 9.16: Density (σ_θ) cross-section for model run T along transect C.

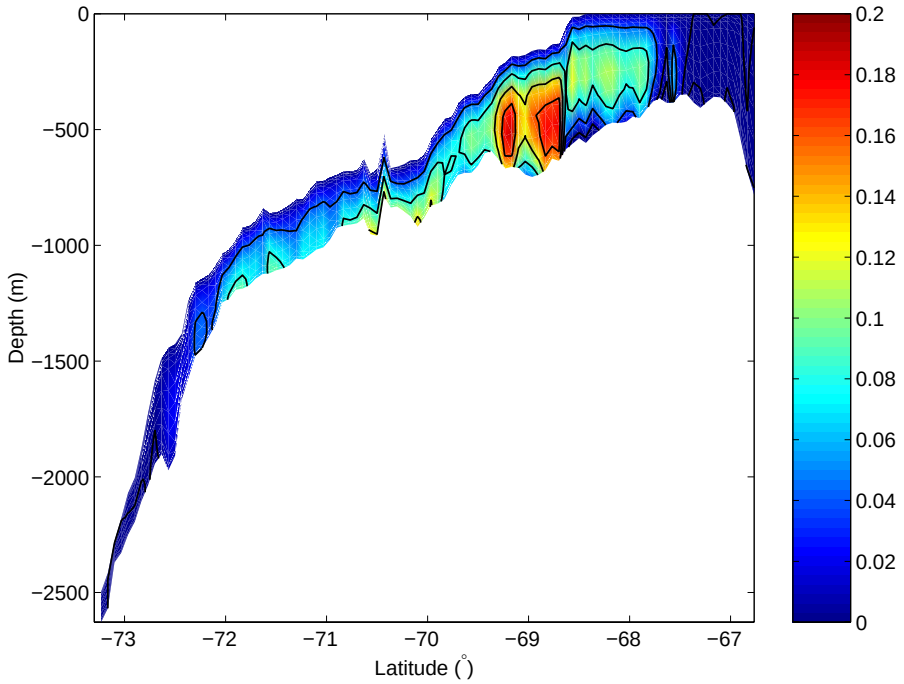

Figure 9.17: The zonally-integrated streamfunction (Sv) for model run T. Circulation is clockwise about positive features. Contours are displayed at 0.04 Sv intervals.

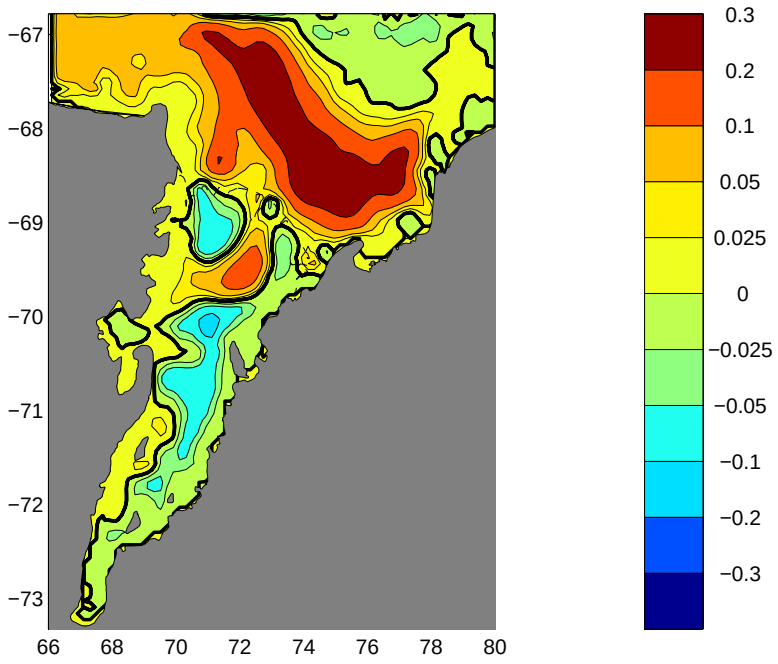

Figure 9.18: The vertically-integrated streamfunction (Sv) for model run T. Circulation is clockwise about positive features.

As observed with the modelled tidal currents presented in Chapter 8, maximum combined tidal and thermohaline current speeds at the seabed are too weak to initiate sediment motion in the sub-ice-shelf cavity. Maximum bottom current speeds of 16 cms^{-1} are predicted during periods of spring tide, which are too weak to mobilise the cohesive sub-ice-shelf sediments which would require currents in excess of ~ 25 cms^{-1} to initiate motion (Dyer, 1986).

Model run B-T was carried out analagous to run T, but with a constant thermal exchange velocity, γ_T, of 1×10^{-4} ms^{-1} prescribed. Even with tidal currents included, the maximum friction velocities predicted at the ice shelf base in run T result in γ_T values less than half the magnitude of the defined Hellmer and Olbers (1989) value. As with the comparison between model runs NT and B, the greater γ_T value results in an alteration of the mass balance estimates of the Amery Ice Shelf between runs T and B-T (Table 9.4). The increase in net mass loss from the ice shelf from 8.0 Gta^{-1} (run T) to 8.7 Gta^{-1} (run B-T) is again small.

The inclusion of tides in model run B-T, in comparison to run B, indicates a contrary response in melt and freeze rates to that observed between model runs T and NT. Greater mixing in run B-T has the effect of reducing both melt and freeze rates at the ice-ocean interface in comparison to those predicted by model run B. However, the percentage area

of melt increases in run B-T, and therefore, a slight increase in the net mass loss from the ice shelf is still predicted with the inclusion of tides (Table 9.4). Decreased rates of melt and freeze beneath the ice shelf with increased mixing suggests a second negative feedback mechanism may exist beneath the ice shelf. Tides, via increased vertical transfer of heat, can mix warmer salty waters into the ascending meltwater plume, reducing the buoyancy of the plume, and consequently the rate of ascent of the plume. The supercooling process of the ascending meltwater will then slow, reducing the rates and distribution of freeze in the cavity. A reduction in freezing results in less salt rejection, and hence vertical overturning, in the watercolumn, counteracting the effects of increased mixing from tides. These feedback mechanisms are likely to reduce the impact of tides in the cavity, particularly beneath the Amery Ice Shelf where tidal velocities are small.

Previous models of the sub-ice shelf circulation in sub-ice-shelf cavities (Determann and Gerdes, 1994; Grosfeld et al., 1997; Gerdes et al., 1999; Williams et al., 2001, 2002) have not included the influence of the sub-ice-shelf tides. Beneath the Amery Ice Shelf, the effects of tides on the mean circulation and the overall mass balance of the ice shelf have been shown to be small. However, tidal currents beneath the other major embayed ice shelves, i.e., the Ross and Filchner-Ronne Ice Shelves, are much greater than beneath the Amery Ice Shelf. The energy available to vertical mixing through the dissipation of tidal currents at frictional interfaces has been shown to be much larger beneath the other ice shelves (MacAyeal, 1984b; Makinson and Nicholls, 1999) than beneath the Amery, and therefore inclusion of tides into the baroclinic models of the ocean cavity beneath these other ice shelves is expected to have greater influence on the respective estimates of the ice shelf mass balance. A widely used application of sub-ice-shelf circulation models is to assess the mass balance of ice shelves under the effects of changing ocean temperatures (Jenkins, 1991; Hellmer and Jacobs, 1995; Grosfeld and Gerdes, 1998; Williams et al., 1998b, 2002). Processes of tidal mixing within the ice shelf cavity may be important to such studies in more dynamic environments than found beneath the Amery Ice Shelf.

The effects of an altered topography

The model was run using each of the four bed elevation grids A, B, C, and CADA with a constant thermal exchange velocity (γ_T), and no tidal forcing. The results using model grid B, assumed to be the best estimate of the sub-ice-shelf topography, have been presented in section 9.3.1. Changes in bed elevation however, are observed to significantly alter the barotropic circulation pattern, and the consequent melt/freeze patterns, in the cavity.

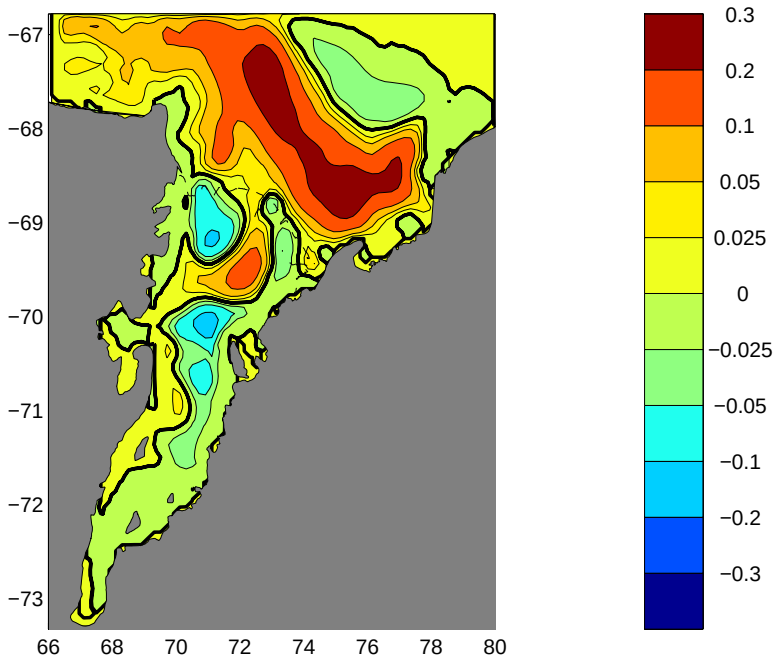

Figure 9.19: The vertically-integrated streamfunction (Sv) for model run A. Circulation is clockwise about positive features.

The overturning circulation for each of the model runs A, B, C, and CADA, does not differ substantially to that presented in the previous sections. Similarly, cross-sections of density reflect the same processes discussed previously. Consequently, these are not raised again in this section. Changes between model runs are most easily identified in the depth-integrated horizontal streamfunction, and these are discussed here along with changes to the estimated mass balance of the ice shelf.

Model run A uses the model grid with the smallest mean water column thickness. Differences between the barotropic circulation predicted using grid A (Fig. 9.19) to that using grid B (Fig. 9.5) are small, and limited to the south of the domain where significant differences in the bed elevation exist. Therefore, it appears that the watercolumn thickness in the south of the domain does not significantly alter the circulation in the northern portion of the domain. Reduction of the water column thickness south of $71°S$ is observed to reduce the transport in the southern portion of the cavity. Circulation remains anti-clockwise.

In the southern part of the cavity, the reduction in water column thickness reduces the exchange of warm salty shelf waters and the cold fresh meltwaters. This has the result of reducing maximum melt rates in the south of the domain to 4.68 ma^{-1} for model run A, in comparison to the analagous constant γ_T run using grid B (model run B) which has a maximum melt rate of 7.10 ma^{-1} (Table 9.3).

Reduced maximum melt rates in the south of the cavity lead to a decrease in the volume of meltwater ascending the base of the ice shelf, and thus, less supercooled water in the cavity. Consequently, the amount of freezing which occurs in the cavity reduces. Therefore, despite the reduced maximum melt rates as a result of the decreased exchange of water beneath the southern portion of the ice shelf, the mean melt rates increase and the net mass loss from the ice shelf base increases to 14.9 Gta^{-1}, through the reduction in area over which ice accretion takes place (melt area increases to 68.5 %; Table 9.4).

Model run C also shows an increase in the net mass loss from the ice shelf base. Model run C displays a net loss of 16.0 Gta^{-1} from the ice shelf (Table 9.4), however the mechanism for this increase differs to that for model run A. Bed elevation grid C is that with the greatest water column thickness in the southern portion of the ice shelf cavity. This allows for a greater exchange of the warm, salty shelf waters and the cold, fresh meltwaters in the southern portion of the domain. The greater influx of warm, salty water to the south of the cavity drives increased melt rates of up to 10.7 ma^{-1} (Table 9.3). The area over which melting occurs in the cavity (63.1%) decreases, as the increased volume of meltwater ascending the ice shelf base provides more supercooled waters in the cavity which more readily freeze at the ice-ocean interface. Therefore, the mass change rates due to both melting and freezing increase (Table 9.4). However, the high melt rates in the southern cavity, a result of the increased water exchange, result in an increase in the net mass loss from beneath the ice shelf for model run C.

The horizontal circulation predicted using model grid C (Fig. 9.20) may be compared with that predicted using model grid B (Run B; Table 9.5), which is very similar to that presented for Model run NT (Fig. 9.5). Increased water exchange in the southern cavity serves to increase the magnitude of the southern gyre from 0.14 Sv (Run B) to 0.23 Sv (Run C). The increase in the magnitude of the southern gyre increases the exchange between the southern gyre and the north-eastern gyre, while the magnitude of the main gyre is reduced from 0.16 Sv (Run B) to 0.09 Sv (Run C). Model run C displays reduced transport across the ice shelf front. Two circulation cells exist across the ice front, the northwestern gyre fills the western side of the cavity, and the extended northeastern gyre defines in and out flows on the eastern side of the cavity (Fig. 9.20).

The CADA bed elevation grid was constructed as an attempt to replicate the WEA01 topography with the new coastline. However, given that the ice draft used in the WEA01 model differs to that used for model runs presented in this thesis, the estimate of the bed elevation from the CADA water column thickness grid will be poor. Therefore, the circula-

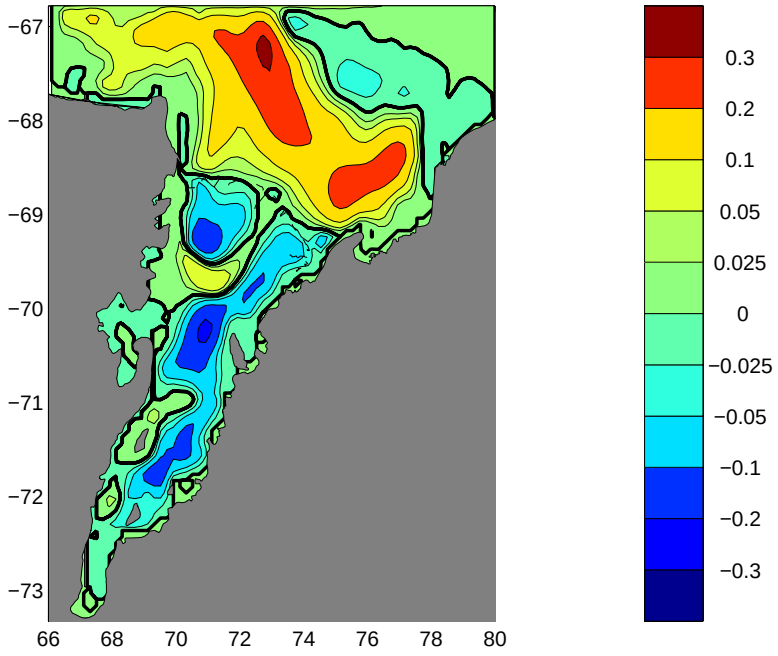

Figure 9.20: The vertically-integrated streamfunction (Sv) for model run C. Circulation is clockwise about positive features.

tion derived from the CADA grid is not particularly useful as a comparison to the WEA01 circulation. The sub-ice-shelf circulation predicted using the CADA grid differs substantially to that using other model grids (Fig. 9.21). Each of the main circulation features are unrecognisable in the CADA circulation. The clockwise gyre has shifted to the western side of the cavity (centred at $69.7°S$, $70.5°E$) and defines a northward current along the western boundary. The three main anticlockwise gyres, the northeastern, the northwestern, and the southern gyres, have joined to create a large anticlockwise gyre filling a large part of the cavity. South of $71°S$, the clockwise gyre circulating around Fisher Massif has increased in magnitude and spatial extent, extending over the full width of the cavity, so that southward flow exists on the eastern side of the cavity in the south of the domain.

Despite these large changes in the sub-ice-shelf circulation, integrated values of the melt and freeze rates at the ice-ocean interface estimating the mass balance of the ice shelf provide values comparable to the other runs (Table 9.4). However, the CADA model run results appear to be a poor estimate of the circulation as it drives a melt/freeze pattern (Fig. 9.22) inconsistent with those interpreted from satellite altimetry estimates (Fricker et al., 2001), and the ground truth positions, AM01 and AM02. At site AM01, a known area of accretion at the ice shelf base, model run CADA predicts a melt rate of 0.28 ma^{-1}. At site AM02, a known site of basal melt, model run CADA predicts a freeze on rate of 0.12

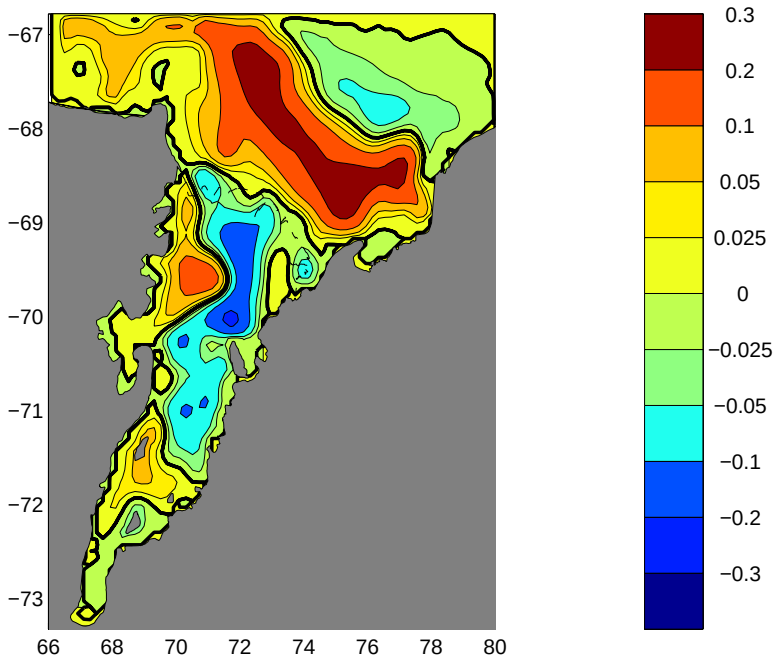

Figure 9.21: The vertically-integrated streamfunction (Sv) for model run CADA. Circulation is clockwise about positive features.

ma^{-1}.

Model run CADA-T uses the CADA model grid, with tidal forcing included at the open boundaries. As with model runs B and B-T, and runs NT and T, the effects of tidal forcing on the mean circulation is minimal. Model run CADA-T predicts a mean horizontal circulation similar to run CADA, and drives a melt/freeze pattern which is inconsistent with the observations. Similarly, integration of the melt/freeze rates over the ice shelf cavity provide an estimate of the mass balance of the ice shelf which predicts only a small variation in the net mass loss from the ice shelf under the influence of tidal mixing in the model (Table 9.4).

It has been shown that variations in the bed elevation cause variation in the sub-ice-shelf circulation. The sub-ice-shelf circulation appears to be dominated by the general cavity shape. Large changes in the cavity shape lead to significant changes to the pattern of circulation. Such changes are important given the scarcity of both ice draft and bed elevation data in the cavity. Changes in the bed elevation in the southern portion of the ice shelf cavity, for which no data are available, can lead to a doubling in the predicted net mass loss as a result of melt and freeze at the ice shelf base. The model is also sensitive to the water column thickness of the southern cavity, a larger water column thickness leading to increased flushing by warm water, and hence increased melting. Decreased volumes

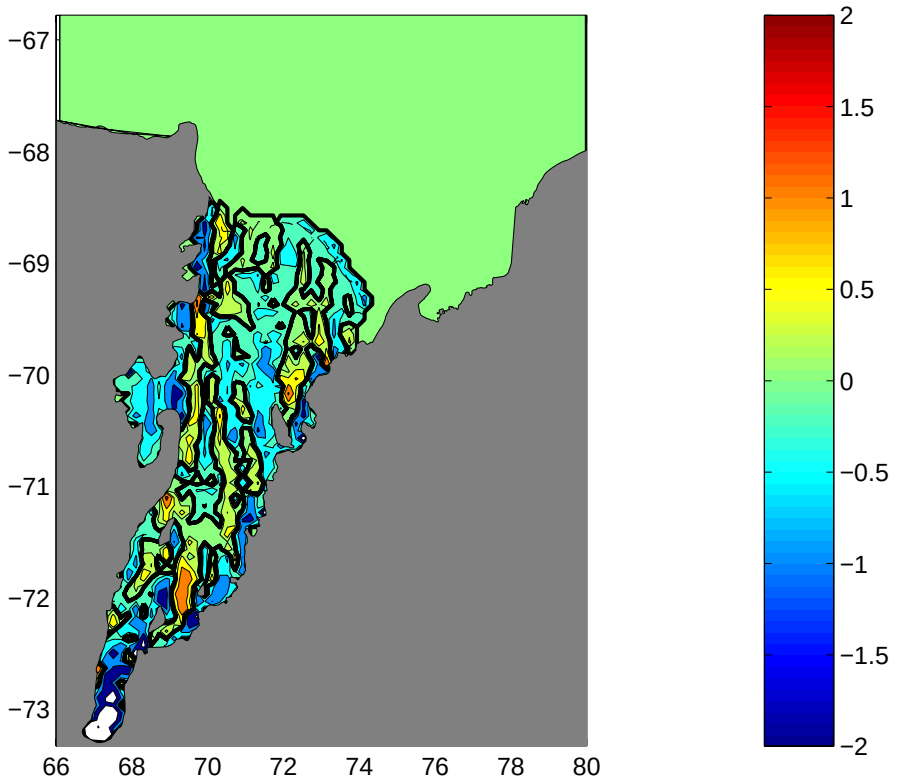

Figure 9.22: Freeze rates (ma^{-1}) for model run CADA. Positive regions represent freezing, negative regions represent melting. The bold contour denotes the boundary between melting and freezing. Contours are at -2, -1, -0.5, -0.2, 0.0, 0.2, 0.5, 1 and 2 ma^{-1}. The white area in the south of the domain displays the region where melt rates are greater than 2 ma^{-1}, i.e., outside the contour range.

of buoyant meltwater reduce the volume of water which is supercooled in the cavity, and therefore the amount of freezing. Therefore, with a too-narrow cavity, not enough mass is gained at the ice shelf base through freeze and the net loss is too high.

A warming climate scenario

A selection of model runs were carried out with the potential temperature in Prydz Bay prescribed $1°C$ warmer than for the standard set of 'cool' runs. No change in salinity was prescribed. These $+1°C$ model runs were carried out to achieve two key aims:

- To investigate the effects of a global warming scenario on the ocean circulation and basal melting predicted by the model. Coupled ocean-atmospheric general circulation models suggest oceanic temperature changes along the Antarctic coast on the order of $3.0°C$ may occur over the next century in waters immediately to the north of the Amery Ice Shelf (Williams et al., 2002). Temperature increases of up to $1°C$ could be

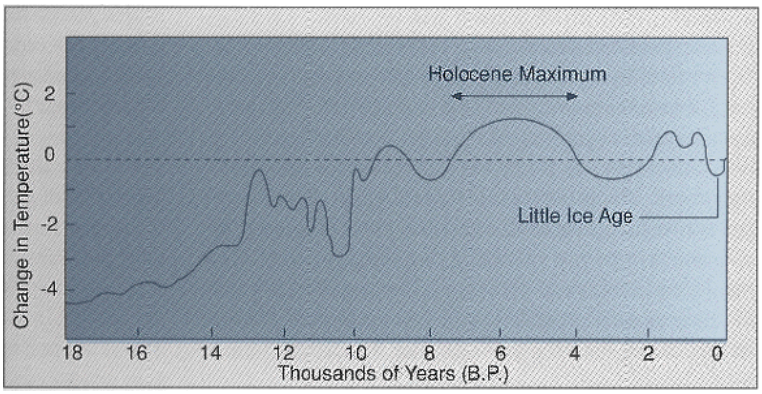

Figure 9.23: Variations in global averaged surface temperatures for the last 18000 years, estimated from a variety of sources. From Crowley (1996)

expected without any associated change in salinity (Williams et al., 2002). Temperature increases greater than $1°C$ adjacent to the ice shelf front may be accompanied by increases in salinity as reductions in the rate of sea-ice formation and reduced deep convection in the southern ocean allow warmer and more saline water with characteristics closer to CDW to encroach onto the continental shelf in Prydz Bay (Williams et al., 2002), and;

- To simulate the change in sub-ice-shelf circulation and the resultant patterns of sedimentation which may have occurred during the mid-Holocene climatic optimum. Figure 9.23 displays the variation in global average surface temperatures for the last 18000 years, as compiled from various sources based on the IPCC report (IPCC, 1990; Crowley, 1996). The Holocene maximum, recorded between 7000 and 4000 yr BP displays temperatures $\sim 1°C$ warmer than present day conditions. Results in Chapter 7 indicate changes in the sub-ice-shelf sedimentation occurred during the period of the mid-Holocene climatic optimum, perhaps as a response to increases in ocean temperature. The $1°C$ temperature rise is likely to be an overestimate of ocean temperature changes which occurred along the Antarctic continental shelf during the mid-Holocene, however the aim is to provide useful insight on the changes which may occur beneath the ice shelf under the effects of a warmer climate, future or past.

Model run NT+$1°C$, with no tidal forcing and a thermal exchange velocity dependent on friction velocity, is presented first.

The increase in potential temperature in the ice shelf cavity is observed to strengthen the sub-ice-shelf circulation. Increases in ocean temperature can be expected to drive larger, and stronger, regions of melting. The zonally integrated streamfunction (Fig. 9.24) displays a large increase in the magnitude of the overturning circulation. The peak value of the

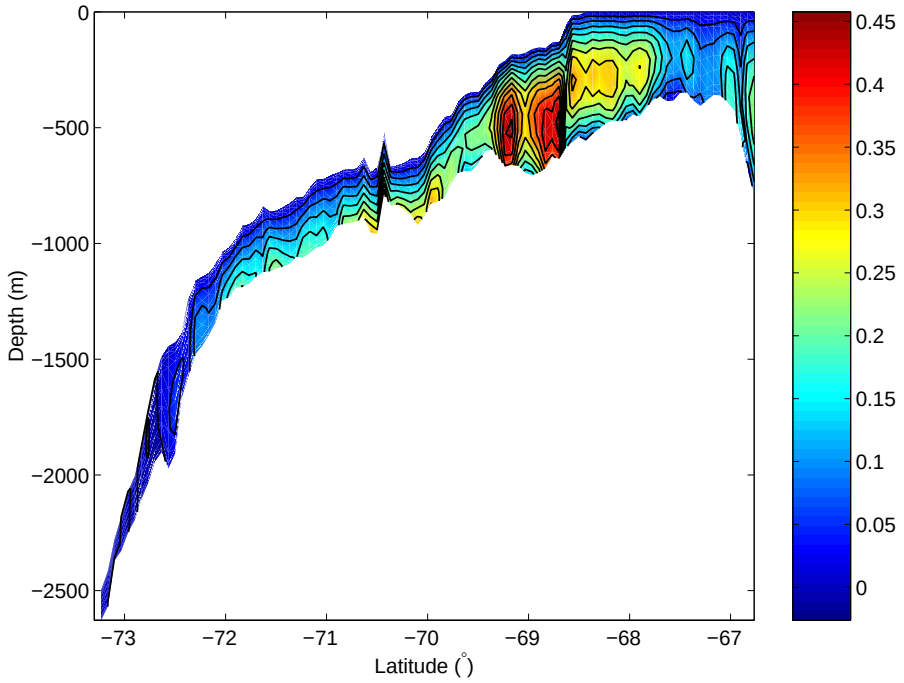

Figure 9.24: The zonally-integrated streamfunction (Sv) for model run NT+1°C. Circulation is clockwise about positive features. Contours are displayed at 0.04 Sv intervals.

overturning transport increases by more than a factor of 2, increasing from 0.20 Sv in run NT to 0.48 Sv in run NT+1°C (Table 9.5).

The strengthening of the sub-ice-shelf circulation is similarly observed in the barotropic circulation (Fig. 9.25), however the pattern of circulation for run NT+1°C remains similar to that simulated for run NT (Fig. 9.5). Table 9.5 compares the transport of each of the main circulation features in the model for model runs NT, T, NT+1°C, and T+1°C, B, B-T, B+1°C, and B-T+1°C. A factor 2-3 increase in the transport of each gyre with a 1°C increase in temperature is observed regardless of the parameterisation of the thermal exchange velocity. WEA02 found a similar 2-3 times strengthening in the magnitude of sub-ice-shelf gyres with a 1°C temperature increase, although WEA02 predict a 7 times increase in the magnitude of the southern gyre with such a temperature rise.

At the ice-ocean interface, an increase in the mass lost from the ice shelf base with an increase in ocean temperature is observed. Figure 9.26 shows the freeze rate predicted at the base of the ice shelf for model run NT+1°C. Comparing Figure 9.26 with that from run NT (Fig. 9.6), a general increase in the rates of melting can be observed over the entire ice shelf portion of the domain. Melt rates are greatest in the southern region as per previous model runs, but also at the ice front, and in a tongue of melt which lies along the southwestward inflow on the southeastern flank of the main gyre.

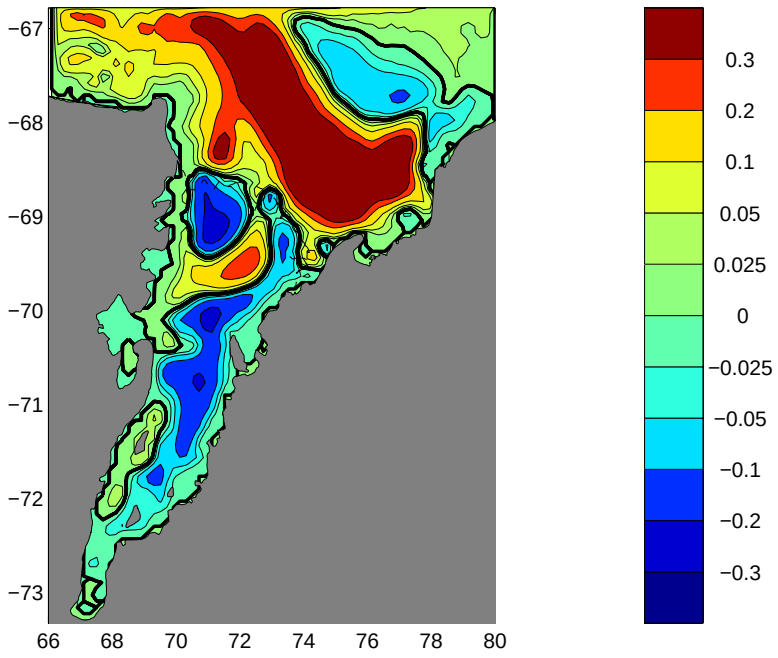

Figure 9.25: The vertically-integrated streamfunction (Sv) for model run NT+1°C. Circulation is clockwise about positive features.

Increase in the melt rates are predicted to occur with the increase in ocean temperature (Fig. 9.27). The influence of warming is to increase the net amount of melting. Some small regions of predicted freeze remain for run NT+1°C, however large areas of freeze predicted in model run NT (Fig. 9.6) have dissapeared as a response to the increased ocean temperatures. The area over which melting occurs increases from 83.8% in run NT to 99.8% in run NT+1°C. The mean rates of melting increase from 0.16 to 0.82 ma^{-1} respectively. Similarly, the mean rates of freezing have decreased from 0.05 to 0.04 ma^{-1}. This contradicts the results of WEA02 who predict an increase in the amount of ice accreted in warming scenario runs. Consequently, the net mass loss for run NT+1°C shows a factor of 7 increase from 7.2 to 49.3 Gta^{-1} compared with a factor 3 increase (14.2 to 39.4 Gta^{-1}) for WEA02.

Williams et al. (2002) estimate the present ice input to the Amery Ice Shelf to be approximately 46 Gta^{-1}, for the grounding line used in their model. The grounding line used in this study includes a larger area of the ice shelf to the south, and therefore the estimated ice input is likely to be also larger. Although snow accumulation over the ice shelf would be expected to increase with global warming in the coastal location of the Amery Ice Shelf (of the order of about 10% per 1°C (Smith et al., 1998)), the large increase in mass loss for model run NT+1°C predicts an eventual removal of the ice shelf. The prescribed ice draft used for the model studies equates to a mass of the ice shelf of $\sim 3.9 \times 10^4$ Gt.

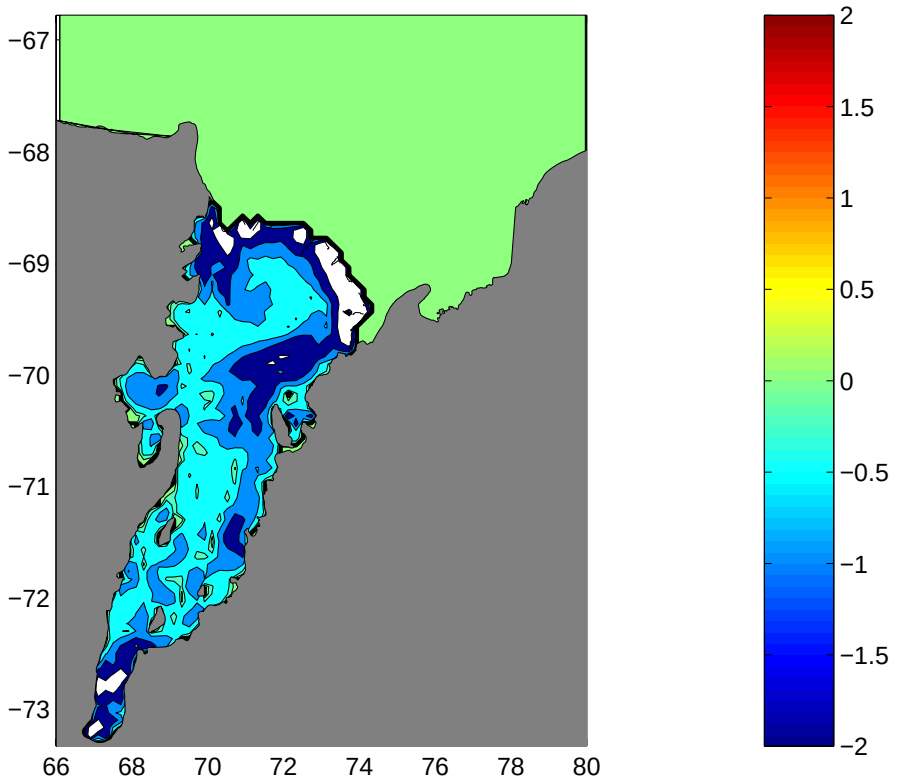

Figure 9.26: Freeze rates (ma^{-1}) for model run NT+1°C. Positive regions represent freezing, negative regions represent melting. The bold contour denotes the boundary between melting and freezing. Contours are at -2, -1, -0.5, -0.2, -0.1, 0.0, 0.1, 0.2, 0.5, 1 and 2 ma^{-1}. The white areas display regions where melt rates are greater than 2 ma^{-1}, i.e., outside the contour range.

Therefore, an increase in the net mass loss from the base of the ice shelf of $\sim$ 42 Gta^{-1} (7.2 to 49.3 Gta^{-1} for run NT and NT+1°C respectively), suggests that increased melting as a result of a 1°C temperature increase would remove the entire Amery Ice Shelf after approximately 900 years. The WEA02 model suggests slightly less dramatic changes to the ice shelf geometry and dynamics with a 1°C temperature rise.

Changes in the ice shelf geometry or dynamics may be expected to occur mainly at the ice front, or at the grounding lines. The regions of strong melt near the ice front, in excess of 2 ma^{-1}, may be responsible for a retreat of the Amery Ice Shelf under a warming climate scenario, beginning at the calving ice front. Any changes which occur in grounding line positions, or ice shelf thickness, may impact on the flow of the glaciers into the ice shelf. A reduction in the restrictions from the ice shelf may potentially increase the rate of glacial flow. An increase in the rate of glacial flow has implications for the sub-ice-shelf sedimentation. Ice rafted debris will be transported a greater distance within the ice shelf

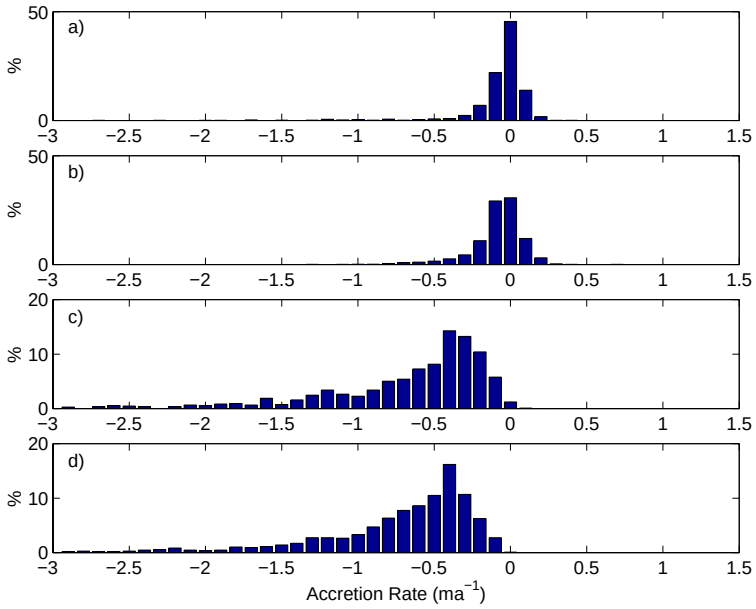

Figure 9.27: Frequency distribution of melting (-) and freezing rates (+) for model runs a) NT, b) T, c) NT+1°C, and d) T+1°C. The y-axis is percentage area of the ice shelf. Note different y-scales between subplots. Bin size is 0.1 ma^{-1}. The frequency distributions are cropped at melt rates of 3 ma^{-1}. The percentage area with melt rates greater than 3 ma^{-1} is shown in the most negative bin.

assuming a greater rate of advance, but constant melt rates. Therefore, glacially derived terrigenous sediments will be deposited a greater distance seaward of the grounding line, than under present day conditions. However, increased melt-rates are likely to counteract this effect, tending to deposit ice-rafted-debris nearer to the grounding line than presently occurs, with greater load.

The influence of tides on the warming scenario model run has been investigated with model run T+1°C. The pattern of the residual barotropic circulation (Fig. 9.29), the overturning circulation (Fig. 9.28), and the overall mass balance at the ice-ocean interface (Table. 9.4) for model run T+1°C, all show little variation to those predicted in model run NT+1°C. Therefore, as concluded from the cool model runs, the influence of tides on the sub-ice-shelf oceanography is small, however a slight increase in net mass loss from the ice shelf is predicted. As with run T, the residual circulation is determined from the 30 day average of hourly model output from between 6000 and 6030 days.

Analagous to the cold runs, increased mixing in the water column as a result of tides warms the ascending meltwater plume, decreasing freezing in the cavity thereby slightly altering the distribution of melt and freeze in the cavity (Fig. 9.30). Model run T+1°C predicts no freezing to occure beneath the ice shelf. The area over which melting occurs increases to 99.9 % (Table 9.4). The change in mass balance under the influence of warmer

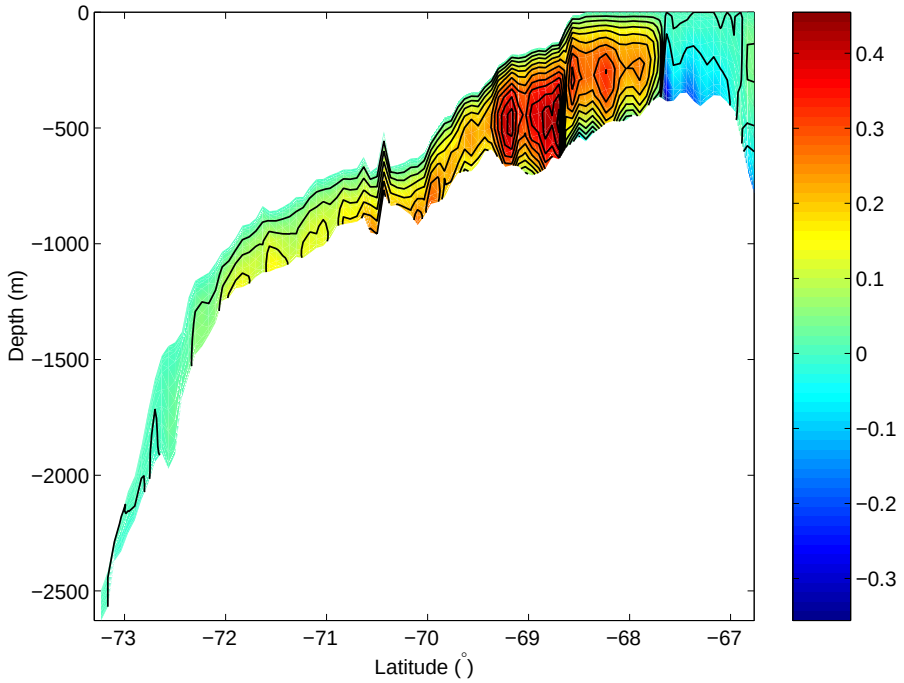

Figure 9.28: The zonally-integrated streamfunction (Sv) for model run T+1°C. Circulation is clockwise about positive features. Contours are displayed at 0.04 Sv intervals.

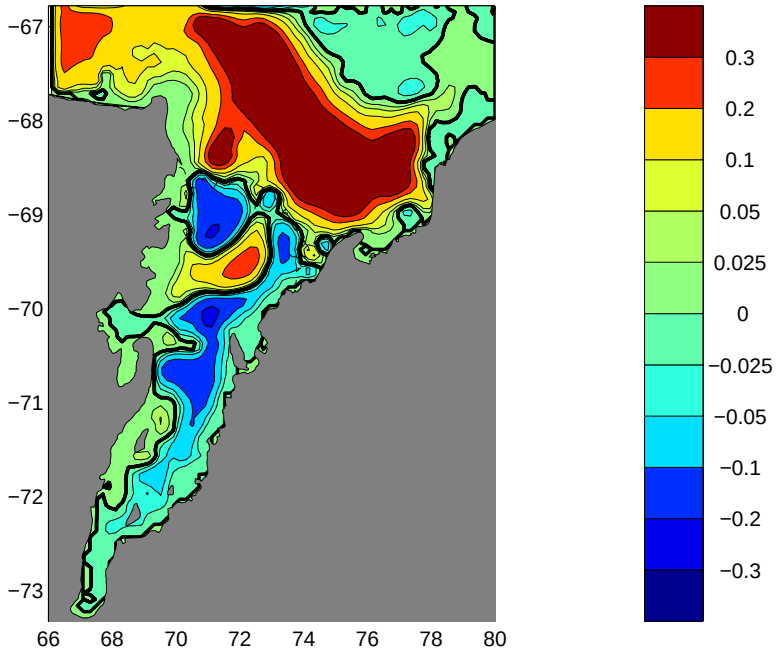

Figure 9.29: The vertically-integrated streamfunction (Sv) for model run T+1°C. Circulation is clockwise about positive features.

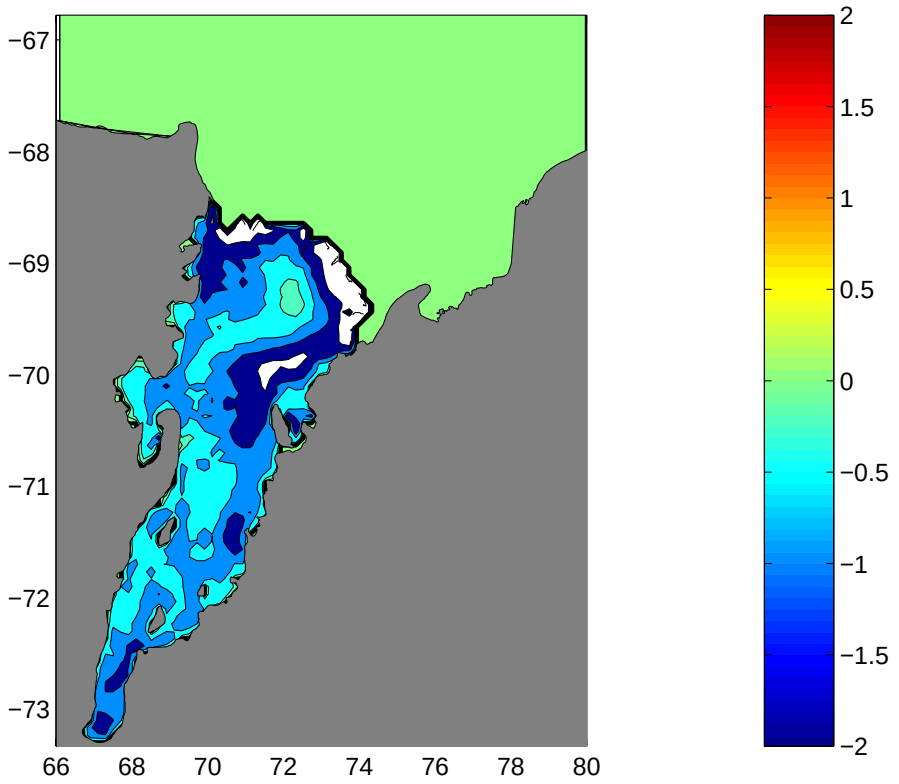

Figure 9.30: Freeze rates (ma^{-1}) for model run T+1°C. Positive regions represent freezing, negative regions represent melting. The bold contour denotes the boundary between melting and freezing. Contours are at -2, -1, -0.5, -0.2, -0.1, 0.0, 0.1, 0.2, 0.5, 1 and 2 ma^{-1}. The white areas display regions where melt rates are greater than 2 ma^{-1}, i.e., outside the contour range.

ocean temperatures and the influence of tides is very similar to that of the cool runs. Tides increase the predicted net mass loss from basal melting from 49.3 Gta^{-1} in run NT+1°C to 52.5 Gta^{-1} in run T+1°C (Table 9.4). However, these effects are small, and as concluded from the cool model runs, the influence of tides on the sub-Amery Ice Shelf circulation, and ice shelf mass balance, is insignificant in comparison to other factors affecting the oceanography in the cavity, e.g., the water column thickness and ocean temperature.

Mass change rates estimated from model runs T, T+0.2°C, and T+1°C suggest that the relationship between the net mass loss from the ice shelf and the forcing temperature defined in Prydz Bay is roughly linear (Fig. 9.31).

Model runs B+1°C and B-T+1°C, with a prescribed constant thermal exchange velocity of 1×10^{-4} ms^{-1}, display a similar strengthening of the circulation, and factor 7-8 increase in the net mass loss from the ice shelf, with the 1°C temperature rise, in comparison to model runs B and B-T.

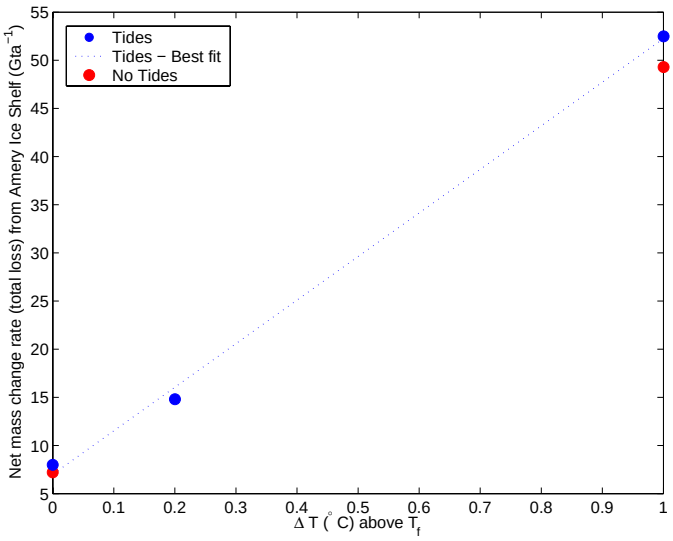

Figure 9.31: Rate of net mass loss from the ice shelf vs temperature increase, from the surface freezing temperature, used to force the model in the open waters of Prydz Bay. The net mass loss from model runs T, T+0.2°C, and T+1°C are shown in blue, and from runs NT, NT+1°C in red. The relationship is roughly linear.

The effects of increases in temperature on the ocean cavity beneath the Amery Ice Shelf are twofold; Firstly, rates of melting at the ice-ocean interface increase suggesting that substantial modification of the Amery Ice Shelf may occur in a warmer climate, and secondly, the strength of the sub-ice-shelf circulation increases.

9.3.2 The sub-ice-shelf transport of suspended material from Prydz Bay

After a steady state had been reached in model runs NT, T, NT+1°C, and T+1°C, passive tracers representing diatoms in suspension were introduced to the model. The "diatoms" were defined to have a settling velocity of 0.3 $mday^{-1}$, representing the *Thalassiosira* genus, after Smayda (1970). A second set of tracers (diatoms) were introduced with a settling velocity of 0.5 $mday^{-1}$, representing the *Fragilariopsis* genus. The "diatoms" were introduced in the upper 5 model layers of the open waters of Prydz Bay, north of the ice shelf front at a concentration of 0.1 mg/l. The initial distribution of the diatoms is shown in Figure 9.32. The diatom distribution is initially concentrated to the eastern side of the Prydz Bay Gyre, after the results presented in Chapter 7 of this thesis, Harris et al. (1999) and Taylor et al. (1997), which all indicate a siliceous mud and ooze facies and greater diatom abundance on the eastern side of Prydz Bay, suggesting greater diatom production in this area than on the western side of the Bay. Massom et al. (1998) indicate the presence of a coastal polynya in south-eastern Prydz Bay near the front of the Amery Ice Shelf, which may be conducive to

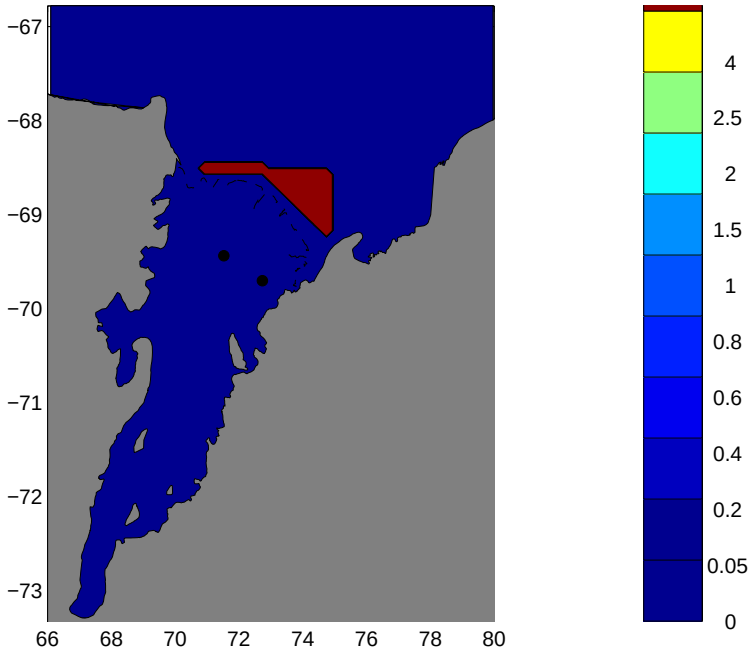

Figure 9.32: The initial distribution of tracers in Prydz Bay. Tracers were placed in the upper 5 $\sigma-$layers of the water column at a concentration of 0.1 mg/l.

the production of diatoms in the area. Care was taken to not place the tracers too close to the ice shelf front, so that the transport of the tracers beneath the ice shelf was independent of their placement. Therefore, the tracers were introduced on the northern side of an east to west streamline, north of the Ice Shelf front, within the Prydz Bay gyre. No tracer flux was prescribed anywhere in the model, i.e., no diatom production is included. However, any tracer that leaves the model domain at an open boundary is not returned to the domain. The tracer field is included in *OzPOM* in the same manner as the other passive tracers, salinity and potential temperature. The model is run for a further 6 months to determine the pathways of suspended material beneath the Amery Ice Shelf.

Only a small difference in sub-ice-shelf transport pathways between the two diatom species is observed. As expected, the slower settling speed results in the *Thalassiosira* genus being advected slightly further beneath the ice shelf than the *Fragilariopsis* genus, although the difference is too small to be conclusive. The results presented below are for the *Thalassiosira* genus only. The small difference in transport distance beneath the ice shelf between the two species suggests that reduced diatom dissolution may be the dominant mechanism for the observed preferential settling of *Thalassiosira antarctica* beneath the ice shelf, rather than the effects of a slower settling speed.

Figure 9.34 shows the depth-integrated concentration distribution of the *Thalasiosira*

genus tracer, as a percentage of the initial Prydz Bay concentration, six months after being introduced into Prydz Bay for model run NT. The location of the two hot water drill sites, AM01 and AM02, from which the sediments presented in Chapter 7 have been collected, are also shown. It is observed that the eastern site, AM02, lies in the inflow region on the eastern flank of the Main Gyre. Surface sediments at the AM02 site consist of siliceous mud and diatom ooze, made up of diatom frustules which have been carried in from the open waters of Prydz Bay. Model run NT predicts greater concentrations of diatoms to be deposited at the inflow site AM02, consistent with the observations. The central AM01 site lies in the region of outflow on the western flank of the Main Gyre. Surface sediments at the AM01 site displayed a reduced absolute diatom abundance and decreased biogenic silica content. Consistent with the observations, concentrations of the diatom tracers are reduced at the AM01 site in the model, suggesting a reduced influence of marine sedimentation would be expected there. The concentration distribution displayed in Figure 9.34 is qualitatively consistent with the sub-ice-shelf surface sediment distribution presented in Chapter 7.

Without the inclusion of diatom production in the model, the distribution of sediments across the ice shelf front can not be expected to be reproduced. However, the modelled circulation is qualitatively consistent with the pattern of sedimentation across the ice shelf front. Figure 9.33 shows a zoomed view of the depth-integrated streamfunction, for model run NT, in the region of the ice shelf front. Overlaying the streamfunction, bullet points have been added representing the biogenic silica content of sediments collected from adjacent to the ice shelf front, as presented in Chapter 7. A correlation exists between regions of inflow and outflow, and the opal content (a proxy for the influence of marine sedimentation) at the grab site. The silica content of the sediments is greatest in regions where the modelled flow is parallel with the ice shelf front. Silica content is clearly decreased in the regions where outflow is perpendicular to the ice shelf front, as observed between longitudes $71.5°E$ and $72.5°E$, and west of $70.5°E$. It appears therefore, that sedimentation across the ice shelf front is generally unchanged to what would be expected in productive open waters, except in regions of outflow where water, depleted of biogenic suspended sediments, flows out from beneath the ice shelf and reduces the marine influence of sedimentation.

The inclusion of tides into the model dynamics was shown in the previous sections to cause only minor changes to the mean barotropic circulation. The influence of tidal mixing on the sub-ice-shelf transport of Prydz Bay derived diatoms is shown in Figure 9.35, which displays the concentration distribution of the tracer 6 months after introduction for model run T. The effects of the tides is small, and the concentration distribution remains

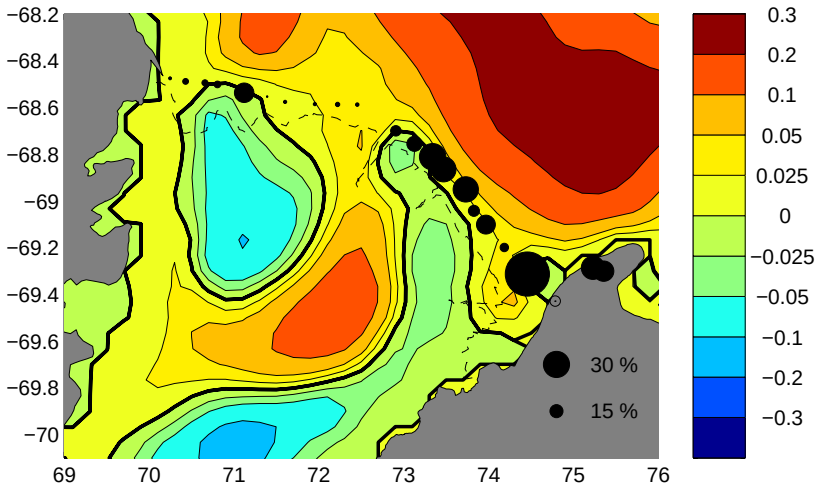

Figure 9.33: A zoomed in view of the depth-integrated streamfunction near the ice shelf front from the results of model run NT. Circulation is clockwise about positive features. Bullets representing the biogenic silica content of surface sediments collected from adjacent to the ice shelf front, as presented in Chapter 7, overlay the streamfunction. Bullet locations represents the location from which the surface grab was taken, bullet size represents the biogenic silica content of the sediment according to the scale shown in the bottom right. The ice shelf front is represented by the dashed line.

qualitativeley consistent with the observed sub-ice-shelf sediments. The effects of tides appears to more clearly define the inflow and outflow paths of the tracer beneath the cavity, so that a larger concentration gradient is observed between sites AM01 and AM02. This has the effect of increasing the relative influence of marine sedimentation at site AM02, and decreasing the relative marine influence of sedimentation at site AM01. However, the figure is generally supportive of the previous section which suggests little change in the barotropic residual circulation is experienced with tides included in the model.

Run NT+1°C and T+1°C simulate the sub-ice-shelf circulation under the effects of a warmer climate. Tracers were introduced to the model under the same conditions as described above. Figures 9.36 and 9.37 show the depth-integrated tracer concentration as a percentage of the initial concentration in Prydz Bay for model runs NT+1°C and T+1°C respectively, 6 months after being introduced. The strengthened sub-ice-shelf circulation, described in the previous section, significantly alters the transport pathways of Prydz Bay derived diatoms beneath the ice shelf. Although the pathways are less well defined under the effects of a warmer climate, it is observed that the transport distance of diatoms beneath the ice shelf has increased, reaching distances of greater than 300 km into the cavity.

In Chapter 7, evidence for the sub-ice-shelf transport of diatoms over distances of at least 80 km under present climatic conditions was presented. Down-core changes in the diatom assemblages lead to the conclusion that greater diatom deposition occurred during

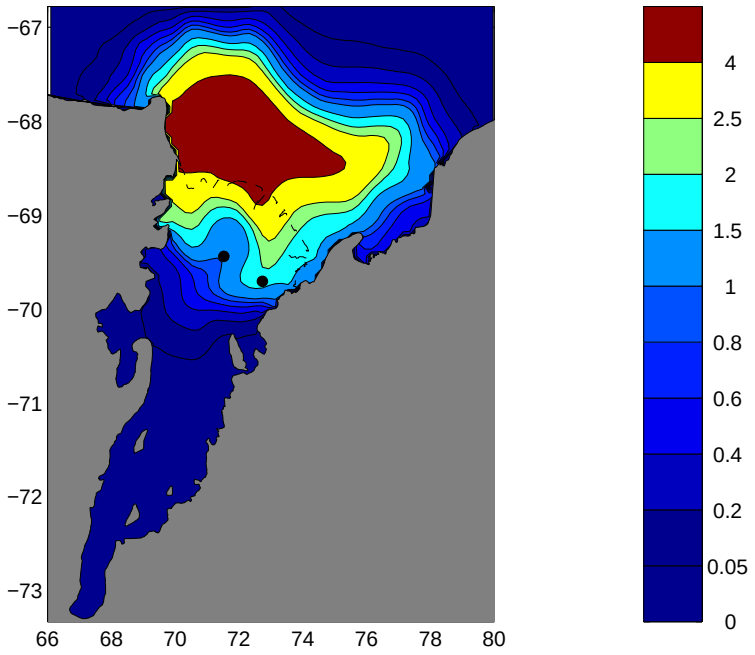

Figure 9.34: The depth-integrated concentration distribution of the *Thalasiosira* genus tracer, as a percentage of the initial Prydz Bay concentration, six months after being introduced into Prydz Bay for model run NT. The position of the two hot water drill sites, AM01 and AM02, are shown.

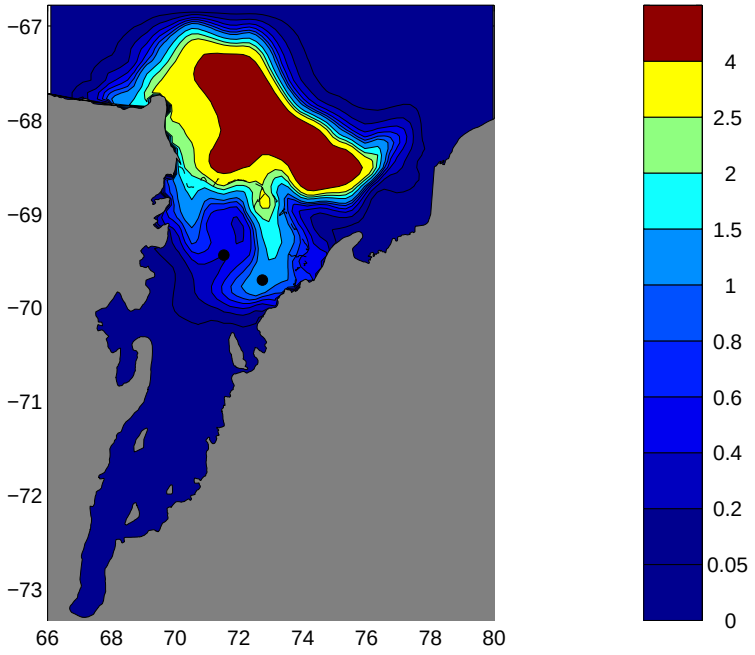

Figure 9.35: The depth-integrated concentration distribution of the *Thalasiosira* genus tracer, as a percentage of the initial Prydz Bay concentration, six months after being introduced into Prydz Bay for model run T. The position of the two hot water drill sites, AM01 and AM02, are shown.

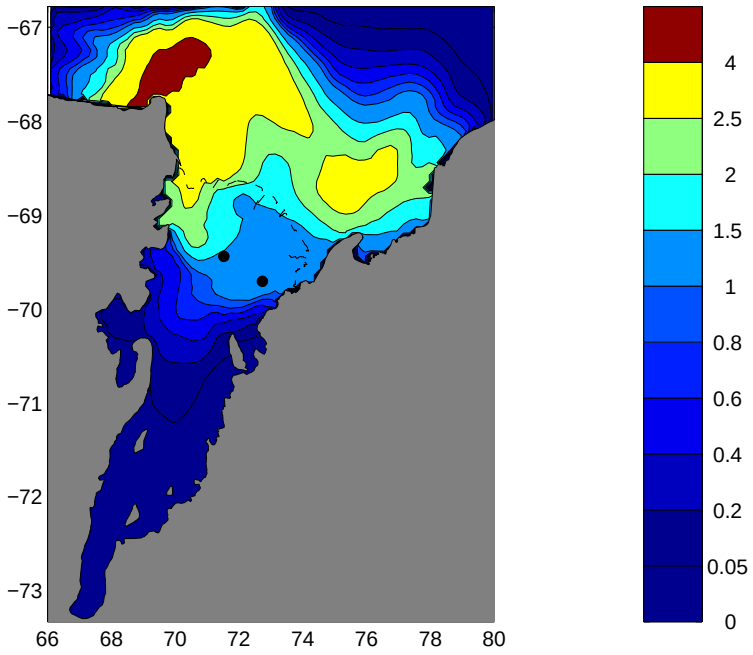

Figure 9.36: The depth-integrated concentration distribution of the *Thalasiosira* genus tracer, as a percentage of the initial Prydz Bay concentration, six months after being introduced into Prydz Bay for model run NT+1°C. The position of the two hot water drill sites, AM01 and AM02, are shown.

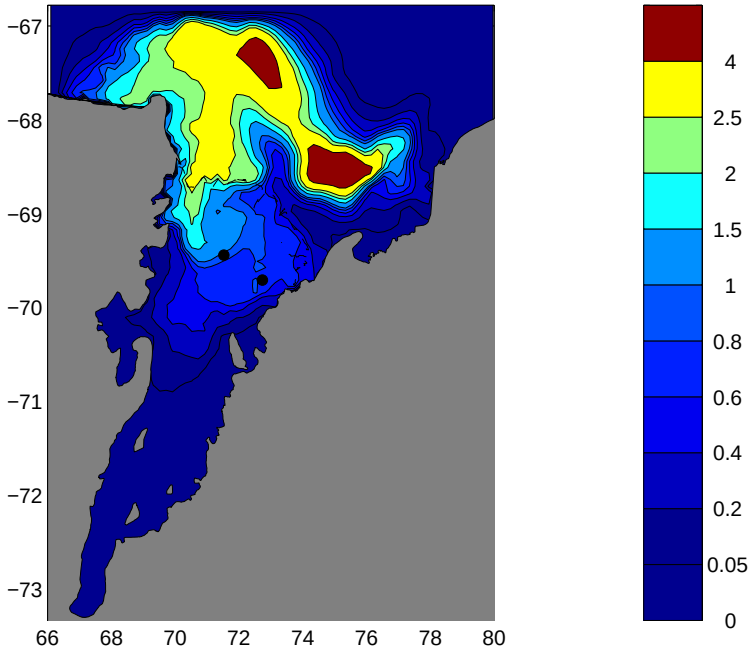

Figure 9.37: The depth-integrated concentration distribution of the *Thalasiosira* genus tracer, as a percentage of the initial Prydz Bay concentration, six months after being introduced into Prydz Bay for model run T+1°C. The position of the two hot water drill sites, AM01 and AM02, are shown.

the mid-Holocene climatic optimum period. This change in sedimentation was attributed to the possible retreat of the Amery Ice Shelf front, bringing the productive open waters of Prydz Bay closer to the sub-ice-shelf core site. Model results presented here would suggest a strengthening of the sub-ice-shelf circulation to occur under the effects of a warmer climate, capable of transporting diatoms greater distances beneath the ice shelf than observed under present conditions.

It is concluded therefore, that a combination of these two processes; ice shelf retreat, and strengthening of the sub-ice-shelf circulation, would lead to the increased deposition of sea-ice associated diatoms at the AM02 site during a period of warmer climate, as may have occurred along the Antarctic continental shelf during the mid-Holocene climatic optimum.

Chapter 10

Summary, Discussion and Outlook

The aim of the research presented in this part of the thesis was to determine the main dispersal pathways of sediments, derived from biological production in the open waters of Prydz Bay, beneath the Amery Ice Shelf, and to determine the main physical processes responsible for the sediment distribution in the ice shelf cavity. These aims, and some background material to this part of the thesis, were introduced in Chapter 6.

Three methods of approach were carried out to achieve these aims, and divided into three chapters. Chapter 7 details the collection of sediments from beneath, and directly in front of, the Amery Ice Shelf, and describes the surface sediment distribution observed in the sub-ice-shelf environment. These results allowed a basis for interpretation of down-core changes of the sedimentology as a response of changing conditions in the ice shelf cavity to the palaeoclimate.

Chapters 8 and 9 take a numerical modelling approach to determine those oceanic processes responsible for the distribution of sediments in the cavity beneath the Amery Ice Shelf. Chapter 8 presents a two-dimensional barotropic model of the tides in the ice shelf cavity to determine whether tidal currents are of sufficient magnitude to mobilise the cohesive sub-ice-shelf sediments. In Chapter 9, a three-dimensional baroclinic model of the sub-ice-shelf thermohaline circulation is presented. The relative influence of tidal mixing on the residual circulation, and the resultant transport of sediments, is assessed. The impact of a warming climate on the sub-ice-shelf circulation, and the mass balance of the Amery Ice Shelf, is described. This application allowed estimation of the changes which may take place to the sedimentation processes under the effects of future climate change, or comparison to mid-Holocene events suggested from the sub-ice-shelf sediment record, presented in Chapter 7.

A simplistic approach was taken to model the thermohaline circulation in the sub-ice-shelf cavity. The only source of saline waters, available to flow beneath the ice shelf, is from the open boundaries, where potential temperature and salinity are defined as being equivalent to Low Salinity Shelf Water (LSSW; $T = -1.8976°C$, $S = 34.57$ psu; Wong et al., 1998) through the entire water column. This is specified to represent the influence of sea-ice freezing at the water surface. Sea-ice freezing leads to salt rejection, and consequently strong overturning and a well-mixed water column. No parameterisation of sea-ice, nor any surface momentum flux, is included in the open water portion of the model domain. Forcing within the model domain is limited to the surface salt and temperature fluxes which occur as a result of melting and/or freezing at the ice-ocean interface within the cavity.

Despite this simple approach, model tracers, introduced in regions of high primary biological production in the the open ocean portion of the model domain, show dispersal pathways qualitatively consistent with the distribution of marine sediments collected from beneath, and adjacent to the calving front of, the Amery Ice Shelf. The surface sediment distribution exhibits areas of greater marine influence in regions of inflow (e.g., the AM02 core site). Marine sediments are deposited beneath the ice shelf. Therefore, in regions of outflow (e.g., the AM01 site), the marine influence of sedimentation is reduced, as indicated by the decrease in absolute diatom abundance and biogenic opal content in surface sediments between sites AM02 and AM01. Similarly, surface sediments collected at the ice shelf front display properties which appear to be correlated with ocean circulation in the region. Productivity in the surface waters of Prydz Bay dominates sediment accumulation adjacent to the ice shelf front. However, in regions of predicted model outflow, sediments display reduced biogenic opal content, and an increase in mean grain size. This suggests that the deposition of marine sediments beneath the ice shelf results in outflow of glacial meltwater devoid of biogenic fines, thus reducing the influence of marine sedimentation in regions of outflow. In Chapter 7 it was shown that the diatom assemblage changes with transport distance beneath the Amery Ice Shelf. Given that variation of biogenic opal content and mean grain size across the ice shelf front appear to reflect patterns of inflow and outflow from beneath the Amery Ice Shelf, it is hypothesised that changes in the diatom assemblage may be observed in sediments collected adjacent to the ice shelf front, which are similarly correlated to the ocean circulation. It is recommended for future research that the diatom assemblage in surface samples collected from adjacent to the ice shelf front be studied to answer this question. However, the signal may be obscured by biological production in the overlying water column.

In addition to providing tracer dispersal pathways qualitatively consistent with the sub-ice-shelf sediment distribution, the modelled thermohaline circulation predicts areas of melt and freeze qualitatively consistent with the marine ice distribution predicted by satellite altimetry measurements (Fricker et al., 2002). Quantitatively, integration of the melt and freeze rates over the ice shelf portion of the model domain provide net mass loss estimates from the base of the Amery Ice Shelf under cool conditions, where potential temperature on the open boundaries are prescribed equal to the surface freezing temperature, of 7.2 - 8.0 Gta^{-1}. With the prescribed potential temperature increased by $0.2°C$, so that the mean potential temperatures adjacent to the ice shelf front are analogous to observed potential temperatures, the estimated rate of net mass loss from the ice shelf is 14.8 Gta^{-1}, when tides are included in the model dynamics. These values are consistent with oceanographic observational estimates (10.7 - 21.9 Gta^{-1}, with a preferred mean of 14.7 Gta^{-1} (Wong et al., 1998), and 18.3 Gta^{-1} (Shanahan, 2002)) and previous models of the Amery Ice Shelf cavity (5.4 (cold) - 14.2 (present) Gta^{-1} (Williams et al., 2002)).

Although model comparisons show good qualitative agreement with available data, several improvements to the baroclinic model can be made.

At the ice front, near surface sigma levels slope steeply from open water to beneath the ice shelf. Steep topography in sigma-coordinate models can lead to large errors in the pressure gradient term in the model, leading to spurious results (Haney, 1991). Having run the model prognostically for over 10 years, the larger component of the error in the pressure gradient term (SEFK; Mellor et al., 1998) is expected to be small (Mellor et al., 1998). However, some error (SESK; Mellor et al., 1998) remains. Model runs which were carried out with no forcing applied with the given topography suggest this error is small. In the region of the steep 'sloping' ice front, the maximum currents were of order $10^{-4} ms^{-1}$, approximately 1% of the magnitude of the predicted physical currents in the region. A future improvement planned for the model is to terminate sigma levels at the ice-shelf front, so that there are a greater number of sigma-layers in open water than beneath the ice shelf, thus reducing the need for steep sloping sigma levels at this unique topographic feature.

Robin (1979) suggested that the deposition of frazil ice crystals (which grow in the supercooled water column) on the ice shelf base contribute most of the basal accumulation beneath ice shelves. This has been supported by observations of the marine ice layer from beneath the base of ice shelves, which indicate an unconsolidated mixture of ice crystals and water (Engelhardt and Determann, 1987; Nicholls et al., 1997). Jenkins and Bombosch (1995) include the dynamics of frazil ice into a sub-ice-shelf plume model. The ascending

plume of Ice Shelf Water (ISW) was defined so as to contain a suspended load of frazil ice, which evolved in response to the supercooling of the water, and the inverted sedimentation of crystals on to the ice shelf base. Jenkins and Bombosch (1995) found that the inclusion of frazil ice had two dominant effects on the model. Thermodynamically, the inclusion of suspended frazil ice crystals provided a much greater surface area on which freezing could take place, and therefore, supercooled water was more readily converted to ice. Consequently, lower levels of supercooling resulted, reducing the influence of direct freezing to the ice shelf base. Dynamically, the suspended ice crystals increase the buoyancy of the ISW plume. Hence, when the concentration of frazil ice increased, the momentum of the plume increased, reducing the deposition of crystals on the ice shelf base. Similarly, once precipitation commenced, the loss of buoyancy caused the plume to decelerate, increasing the rate of deposition. Density inversions were also predicted in the water column as a result of the increased buoyancy provided by the suspended ice crystals. The inclusion of frazil ice dynamics in the baroclinic model of the circulation in the sub-ice-shelf cavity is expected to alter the flow dynamics in the cavity, and is a recommended step for future model improvements.

Exchange between the ice shelf cavity and the open ocean is predicted to be small in the baroclinic model. However, the model includes no forcing in the open ocean portion of the model domain. Wind stress fields along the Antarctic coast are characterised by a band of easterly winds, blowing from off the Antarctic plateau. North of the Antarctic divergence, and seawards of the continental shelf slope, the prevailing winds are westerly. The inclusion of such a wind stress field into the model, forcing the open ocean, may have two effects. First, Ekman transport and therefore vertical velocities are introduced at the ice shelf edge, and second, a cyclonic circulation in Prydz Bay is forced to more accurately represent the Prydz Bay Gyre. Such effects may influence the exchange between the ice shelf and open ocean and are suggested for future model runs, However, Grosfeld et al. (1997) state that the inclusion of such a wind stress field on the open ocean portion of idealised ice shelf domains gave essentially the same results as when the wind stress fields were not included.

The effect of sea-ice in Prydz Bay is not considered in the model. Supply of saline waters, such as LSSW, is from the open ocean boundaries only. The parameterisation of sea-ice in the model would allow for the formation of saline water masses through freezing at the open ocean surface. The formation of such water masses drives deep convection, transporting cold and saline water to the seabed, which then flows beneath the ice shelf. Williams (1999) attempted to model the exchange between the ocean cavity beneath the ice shelf and the

open ocean, assimilating present day ocean conditions into the open ocean portion of the domain. Under these conditions, warm shelf water entered the ice shelf cavity, driving increased melt rates. The simple model parameterisation used in this thesis, assuming cool conditions throughout the water column, is similar to the $EXDOM_{cool}$ model run carried out by Williams (1999), where he found that the colder conditions provided better melt estimates beneath the ice shelf. Williams (1999) trialled the inclusion of a simple sea-ice model with present day open ocean conditions, and found that the cold and saline waters could only be produced via sea-ice freezing if the circulation of warm water within the water column was artificially restricted. Future model runs may include temperature and salinity data assimilated into the open ocean portion of the model domain. Such a temperature distribution in the model may have the effect, as observed by Williams (1999), of warm water entering the ice shelf cavity and consequently increased melt rates in the cavity. The influence of sea-ice freezing may require consideration in such model runs.

The boundary conditions at the ice-ocean interface in the baroclinic model are derived from the two-equation formulation described by Holland and Jenkins (1999), and assumes no diffusion of heat into the ice shelf. The two-equation formulation assumes that the salinity at the ice-ocean interface, and in the ocean mixed-layer, are identical. A similar approach, but with a constant thermal exchange velocity which corresponds to a mixed layer velocity of $\sim 0.2\ ms^{-1}$, has been used in previous ocean cavity models (Determann and Gerdes, 1994; Grosfeld et al., 1997; Williams et al., 1998b). The three-equation formulation described by Holland and Jenkins (1999) makes no prior assumptions about conditions at the ice-ocean interface. Williams et al. (2002) updated the model presented by Williams et al. (1998b) to include the three-equation formulation at the ice-ocean interface, resulting in the predicted net mass loss from the ice shelf to increase from 7.8 Gta^{-1} (Williams et al., 1998b) to 14.2 Gta^{-1} (Williams et al., 2002). The three-equation formulation significantly improved model-observation comparisons. Incorporation of the three-equation formulation may provide some improvement to the three-dimensional baroclinic model in the future.

The *OzPOM* model used in this thesis to simulate the sub-ice-shelf density driven circulation undertakes a different modelling approach to previous sub-ice-shelf cavity models. Although there are many consistencies, there is also some variation between the predicted circulation beneath the Amery Ice Shelf presented in Chapter 9, using a free surface model, and that presented by Williams et al. (2001), using a rigid-lid model. New ice shelf geometry (ice draft, bed elevation, and grounding line) are likely to account for a large portion of the observed variability between the two sets of simulations, however the modelling approach

may also be important. In sub-ice-shelf simulations using the rigid-lid approach, the velocity field is nearly barotropic and is well described by the vertically integrated streamfunction (Determann and Gerdes, 1994; Grosfeld et al., 1997; Gerdes et al., 1999; Williams et al., 2001, 2002). The velocity field predicted using the free surface approach used in this thesis shows an overturning circulation of the same order of magnitude as the horizontal circulation. The work presented in this thesis has initiated a collaborative model intercomparison study, to compare the results predicted by each of the sub-ice-shelf ocean cavity models within ideal ice shelf cavity domains, similar to those presented by Grosfeld et al. (1997). Details of this work are available from the Antarctic Co-operative Research Centre in Hobart.

In Chapter 8, tidal results predicted by the MECO and *OzPOM* models were shown to both be comparable to sea-level and current meter observations. Tidal phase is better predicted using *OzPOM* than MECO, and also improves on the predictions from previous tide models, CADA and CATS. Simulations of tidal amplitude by *OzPOM* are also comparable to those from the other three models. Previous rigid-lid, sub-ice-shelf, three-dimensional, baroclinic models have not had the opportunity for comparison of results against more readily available tidal data. The good model to observation comparison of the tides beneath the Amery Ice Shelf provide extra confidence in the use of *OzPOM* to simulate the sub-ice-shelf thermohaline circulation.

Future model runs will benefit from the growing data-sets available from the AMISOR project. At the time of writing in November 2002, large amounts of data are being processed to improve the understanding of oceanographic processes which occur beneath the Amery Ice Shelf. These data include the salinity and temperature data collected from transects across the Amery Ice Shelf front during research voyages during the summers of 2001 and 2002, current meter mooring data from an array deployed across the Amery Ice Shelf front for twelve months in 2001, salinity and temperature data from sub-ice-shelf moorings at the AM01 and AM02 hot water drill sites, and some short current meter records from the drill sites. Initial qualitative assessment of the model results against the observed density distribution at the ice shelf front suggests that overturning in the model may be overestimated. Such differences may be overcome in the future through the tuning of model parameters. However, the model appeared insensitive to variations of mixing schemes and lateral, seabed and ice-ocean interface friction parameters, in initial model studies. The observational temperature and salinity data may also be useful if a data assimilation approach is taken in future model runs.

The *OzPOM* model used for the baroclinic model is a free surface model. Such a

model, as also used for the barotropic modelling of the tides, ignores the effects of ice shelf flexure. This assumption has little influence on the changes in sea-level associated with the density-driven circulation, however the influence of tides may be sensitive to the inclusion of flexure at the ice shelf grounding lines. Tide model sea-surface elevations and GPS measured elevations at a site within $\sim 5\ km$ of the southern grounding line show poor comparison, with sea-levels being significantly overestimated by the model. Dissipation in the hinge zone, as a result of ice flexure near the grounding line, leads to a large reduction in observed sea-levels near to the grounding line, which are not predicted by the models. Addition of ice flexure to the model dynamics increases its complexity, and has not been attempted in this study. It is suggested that the effects of ice flexure may be more important beneath the Amery Ice Shelf than the other large ice shelves (i.e., the Ross and Filchner-Ronne Ice Shelves) as a result of the increased length of the grounding line relative to the area of the ice shelf. To investigate the relative importance of ice flexure on the Amery Ice Shelf, its inclusion into future tidal models of the Amery Ice Shelf is recommended.

Although each of the model improvements discussed above may lead to better model-observation comparisons, the largest source of error present in both the barotropic and baroclinic models are errors in the water column thickness. Tides beneath the Amery Ice Shelf were found to be particularly sensitive to variation in the water column thickness. Comparisons between predicted and observed tidal elevations allowed a 'best-estimate' of the water column thickness to be determined, particularly in the southern portion of the cavity where no water column thickness data are available. Similarly, the thermohaline circulation shows some sensitivity to variation of the water column thickness. Only changes in the bed elevation were considered in Chapter 9, however the density driven circulation is likely to be more sensitive to changes to the ice draft. Variation of the mean circulation influences the transport of heat and salt in the cavity, and consequently the distribution of melt and freeze at the ice-ocean interface. Errors in the water column thickness in the model are likely to be large, given that interpolation of ice draft and bed elevation between sparse observation points leads to a cumulative error in the water column thickness. Observation errors of ice draft and bed elevation are also large, with differences between ice draft values from the same location of up to 200 m (Ruddell, 2001). These large errors are attributed to radio-echo sounding returns finding the interface between meteoric and marine ice, rather than the marine ice-ocean interface. Therefore, the deepest value was chosen on each occasion. A greater number of observations of both ice thickness and bed elevation are required, particularly at the southern end of the cavity, before estimates of the sub-ice-shelf

circulation and tides using a numerical modelling approach will provide good quantitative comparisons to the observations.

The relative magnitudes of tidal and density-driven currents in the ocean cavity beneath the Amery Ice Shelf has been investigated to determine the processes which dominate the mobilisation of sediments. Away from the grounding line, maximum currents occur at the seabed during periods of spring tides. The magnitude of the maximum tidal currents is approximately 10-15 cms^{-1} (Chapter 8), approximately three times the magnitude of the maximum density driven currents at the seabed (4-5 cms^{-1}; Chapter 9). The combined maximum bottom currents are concluded to be too small to mobilise the highly cohesive sub-ice-shelf sediments. Sediments from beneath the Amery Ice Shelf at sites AM01 and AM02 exhibit a mean grain size of approximately 100 μm (Chapter 7), and of a cohesive mud and ooze lithology. These sediments require a bed shear stress of approximately 1.25 Nm^{-2}, or current speeds of $\sim$ 25 cms^{-1}, to be remobilised from the seabed (Mitchener and Torfs, 1996). Currents of this magnitude are not predicted in the ocean cavity beneath the Amery Ice Shelf. However, bottom current speeds on Fram and Four Ladies Banks, in Prydz Bay, reach magnitudes capable of resuspending sediments (up to 25 cms^{-1}) during periods of spring tide. A sub-ice-shelf process, which is not resolved by the models, is tidal flushing at the grounding zone. Ebb and flow of the tides are likely to result in large currents in the restricted cavity near the grounding line, capable of localised resuspension. Away from this 'coastal zone', currents are small, and any suspended sediments are unlikely to be transported large distances before resettling to the seabed. Hence, the net transport of sediments resuspended in the grounding zone is predicted to be small.

The tidal range, and resulting tidal current magnitudes, beneath the Amery Ice Shelf, are significantly smaller than those predicted beneath the other major embayed ice shelves in Antarctica, i.e., Ross and Filchner-Ronne Ice Shelves. Whereas tidal currents are too small to mobilise sediments beneath the Amery Ice Shelf, this does not hold for the other ice shelves. Makinson and Nicholls (1999; Fig. 3) show predicted average root mean square (RMS) tidal water speeds beneath the Filchner-Ronne Ice Shelf greater than 20 cms^{-1} in areas of relatively shallow water ($<$ 200 m). Makinson and Nicholls (1999) state that RMS spring tide speeds are typically double the average RMS speeds. Haase (1986) collected sediments from adjacent to the Ronne Ice Shelf front, which indicated a broad diversity of properties. Very well sorted sands were collected from Berkner Shelf, and were concluded to originate from quartzitic sediments transported by the strong tidal currents which flow beneath the ice shelf at velocities in excess of 20 cms^{-1}, as predicted by the Makinson and Nicholls (1999)

tidal model. Further to the north-west, in the area of intermediate water depth (400-500 m), sediments consisted of muddy to sandy muds consistent with sediments deposited in a very calm environment (0-2 cms^{-1}). The sediments collected in this region are similar to those collected from adjacent to the Amery Ice Shelf front, reflecting similar low energy conditions. Haase (1986) describes fine sand sediments displaying current ripples collected from the ridge near to the north-western end of the Ronne Ice front. RMS tidal current speeds, predicted by Makinson and Nicholls (1999), over the ridge are 18-20 cms^{-1}. Currents of this magnitude are capable of mobilising the fine non-cohesive sandy sediments and create the observed ripples. In the Ronne Depression, and close to the Antarctic Peninsula, Haase (1986) describes pebbly to gravelly muds of glacial origin, deposited in a quiet current regime.

Coarse sandy gravelly sediment is observed between longitudes $71.3°E$ and $73°E$ adjacent to the Amery Ice Shelf front, over a ridge in the bathymetry. From the results of Haase (1986), increased tidal currents may be predicted here, reducing the deposition of fines. However, tidal modelling, carried out in Chapter 8, predicts that maximum bottom current speeds are too small to influence sediment properties. The observed changes across the ice shelf front are attributed to differing sediment sources in relation to the mean current direction flowing into, or out of, the cavity beneath the ice shelf.

It was shown in Chapter 9 that the mean circulation within the cavity is not sensitive to the inclusion of tidal mixing in the model dynamics. Similarly, in Chapter 8, residual tidal circulation was shown to be small. It is concluded, therefore, that the dispersal of marine sediments, made up of decaying diatoms which were produced in the open waters of Prydz Bay, beneath the Amery Ice Shelf is almost entirely a result of the mean, thermohaline circulation. The density-driven circulation is capable of transporting sediments in suspension a large distance ($\sim$ 150 km) beneath the ice shelf. The influence of tides on sub-Amery Ice Shelf sedimentation is concluded to be insignificant.

In Chapter 8, the tidal energy available for vertical mixing, as a result of dissipation at frictional interfaces, was shown to be too small to overcome the stratification set up by melting at the ice-ocean interface throughout most of the ice shelf cavity. This was confirmed by studies in Chapter 9, where the estimated net mass loss from the ice shelf as a result of melting of 7.2 Gta^{-1}, with no tides, increased only slightly to 8.0 Gta^{-1} when tides were included in the baroclinic model. The small increase in predicted mass loss from the ice shelf is attributed to increased mixing, and consequently greater vertical transport of heat in the water column, which occurs in the narrower regions of the cavity. The greater friction velocity as a result of tides, leads to an increased thermal exchange velocity at the ice shelf

base (Holland and Jenkins, 1999), and therefore may also contribute to the slightly increased melting. However, it is concluded that the model-based estimates of net mass loss from the Amery Ice Shelf as a result of basal melting, like the mean circulation, are largely insensitive to the inclusion of tides in the model dynamics. Further study of the influence of tides on sub-ice-shelf environments is recommended. Artificial amplification of the tides beneath the Amery Ice Shelf in the model, to determine the current magnitudes required to influence the ice shelf mass balance, would be an interesting exercise in the future. Similarly, assessing the sensitivity of frictional parameters on model runs used to study the influence of tidal mixing on the sub-ice-shelf oceanography is recommended.

The energy available for vertical mixing from tidal dissipation at frictional interfaces is much greater beneath the Ross and Filchner-Ronne Ice Shelves (MacAyeal, 1984b; Makinson and Nicholls, 1999). This has possible ramifications for the mass balance estimates of these ice shelves which have been determined using rigid-lid sub-ice-shelf cavity models, which do not include the effects of tides (Grosfeld and Gerdes, 1998). Previous sub-ice-shelf, ocean cavity models have not included the effects of tides in the dynamics. However, large constant vertical mixing coefficients may artificially introduce the effects of increased mixing in the cavity. Studies examining the sensitivity of the Mellor-Yamada mixing schemes to alternative mixing schemes in the model, with and without tides, may be a useful exercise in the future, as more data becomes available allowing more quantitative comparisons.

Although not a key aim of the thesis, the baroclinic model of sub-ice-shelf circulation presented in Chapter 9 allows for comment on the mass balance of the Amery Ice Shelf. Williams et al. (2002) estimated the mass flux into the ice shelf is 46 Gta^{-1} for the ice shelf defined for their model. This consists of 23 Gta^{-1} from the Lambert Glacier (Allison, 1979), 14 Gta^{-1} from glaciers feeding the sides of the ice shelf (Budd et al., 1967), and 9 Gta^{-1} from snow accumulation on the ice shelf (Budd et al., 1967). The new grounding line presented by Fricker et al. (2002) covers a larger area, and consequently, the mass flux into the ice shelf is likely to be greater than the above mentioned value. Two components of mass loss from the ice shelf exist; iceberg calving and basal melting. An estimate of the net mass loss as a result of basal melt has been made in Chapter 9 of 14.8 Gta^{-1} under conditions estimated to be representative of a present day climate. As stated previously, this value is consistent with basal mass loss estimates from oceanographic observations (Wong et al., 1998; Shanahan, 2002), and previous model estimates (Williams et al., 2002). Therefore, to remain in mass balance, the amount of ice discharged in the form of icebergs from the front of the Amery Ice Shelf is estimated to be greater than 31 Gta^{-1}.

Maximum melt rates at the southern extent of the cavity are predicted to be of the order of $\sim 2\ ma^{-1}$ under the cool conditions. Melt rates of this magnitude are significantly less than those estimated from satellite radar interferometry by Rignot and Jacobs (2002) of $\sim 31\ ma^{-1}$ immediately seaward of the Lambert/Amery grounding line. Maximum melt rates are sensitive to the parameterisation of the thermal exchange velocity, γ_T, at the ice-ocean interface. Assuming a constant value of $\gamma_T = 1 \times 10^{-4}\ ms^{-1}$, the maximum melt rate increased to $\sim 7\ ma^{-1}$ in the cool model runs. A linear relationship exists between γ_T and the friction velocity, $u*$. An increase in the drag coefficient at the ice shelf base does not significantly alter current speeds in the cavity, but does increase the friction velocity. Therefore, tuning of the friction parameters at the ice shelf base, and therefore γ_T, may result in more realistic melt-rates in future model runs. Maximum melt rates are also sensitive to the choice of water column thickness in the southern extent of the cavity. Assuming a constant value of γ_T, widening the cavity thickness (baroclinic model run C; Chapter 9) increases the maximum melt-rates in the south of the domain to over $10\ ma^{-1}$. Therefore, any large errors in the water column thickness in the south of the domain will also contribute significantly to the differences between observed and predicted melt-rates.

The effects of increasing the ocean temperature by $1°C$ on the dominant mean thermohaline circulation, and the ice shelf mass balance, were investigated in Chapter 9. A $1°C$ temperature rise altered the rates of melt and freeze at the ice shelf base substantially. Baroclinic model runs show an increase in the net basal mass loss as a result of melting from ~ 7.2 to $49.3\ Gta^{-1}$ with the given temperature increase. This 8-fold increase in mass loss is much larger than the factor of 3-4 increase predicted by Williams et al. (2002) for an ocean warmed by $1°C$. The greater depths in the south of the new predicted cavity topography lead to larger temperature differences between the warmer inflowing shelf water, and the basal ice shelf temperature, thus driving greater melting.

A limitation of the model, particularly under the effects of a warmer climate, is the fixed nature of the ice shelf front. Current estimates of the rate at which the ice shelf front advances is $\sim 1300\ ma^{-1}$ (Fricker et al., 2002; Young and Hyland, 2002), and major calving events are estimated to occur at intervals of 60-70 years[1] (Budd, 1966). The estimated mass loss due to basal melting under the effects of a $1°C$ temperature rise ($\sim 50\ Gta^{-1}$) exceeds the present estimated flux of ice into the ice shelf ($46\ Gta^{-1}$; Williams et al., 2002). This is likely to cause large changes to the ice shelf geometry, particularly at the ice shelf front, and at the grounding line. The influence of changes in the ice shelf geometry to variation

[1]The last major calving event of the Amery Ice Shelf took place in 1963, and reduced the ice shelf extent by approximately one-fifth (Budd, 1966).

of the sub-ice-shelf circulation is not represented by the model. Future studies may include altered ice shelf front positions to determine the influence of such changes on the circulation within the cavity.

Similarly, during periods of glacial advance, the circulation within the sub-ice-shelf cavity will be altered significantly. An increase of the flux into the ice shelf may have the effect of reducing the water column thickness beneath the ice shelf. Decreases in the water column thickness are likely to increase the relative influence of tides on the sub-ice-shelf sedimentation processes, i.e., a narrow cavity may lead to tidal currents of sufficient magnitude to resuspend sediments from the seabed. The AM02 sediment core shows evidence of cross-laminations soon after marine sedimentation commenced at the site ($\sim 15132\ ^{14}C$ yr BP; Chapter 7), during the period of sea-level rise. It is suggested that during this period, the water column thickness was sufficiently narrow as to result in tidal currents capable of remobilisation of some of the finer portion of the coarse, glacial, ice-rafted debris, and the fine diatomaceous marine sediments. Tidal model runs with the ice shelf in a state of advance, reducing the water column thickness, would provide interesting insights into the changing influence of tides within the cavity.

Ultimately, a fully coupled baroclinic ocean cavity - ice shelf model would remove the need for specifying the draft and extent of the ice shelf, and allow the impact of changes in climate on the ice shelf, the sub-ice-shelf circulation, and the resultant sedimentation patterns, to be determined with changing ice front positions.

The mean, thermohaline circulation is predicted to strengthen beneath the Amery Ice Shelf with a $1^{\circ}C$ temperature increase (Chapter 9). Although the pattern of circulation in the ocean cavity was insensitive to the temperature change, the strength of the circulation, both the depth-integrated and overturning components, doubled, increasing the transport distance of marine sediments beneath the ice shelf. Down-core AM02 changes in the diatom assemblage indicate a period $\sim 5 - 2$ ka BP, coinciding with a previously described mid-Holocene climatic optimum (Ingolfsson et al., 1998), with an increase in the deposition of diatoms representative of those found at the present day ice front. It is suggested that the increased deposition of sea-ice associated diatoms during this period is a combined result of a retreat of the ice shelf front, bringing productive waters closer to the core site, and a strengthening of the sub-ice-shelf circulation transporting suspended diatoms greater distances beneath the ice shelf. An increase in ocean temperatures during the mid-Holocene climatic optimum could lead to the above mentioned signal. A similar ice shelf response may occur under the influence of future global warming.

The two key diatom species in the surface, late Pleistocene-Holocene, units 1 and 2 of the AM02 core are *Fragilariopsis curta* and *Thalassiosira antarctica*. Sub-ice-shelf sediments show an increase in the relative abundance of *T. antarctica*, and a correlated decrease in the relative abundance of *F. curta* and absolute diatom abundance, in comparison to sediments collected in the open waters of Prydz Bay, adjacent to the Amery Ice Shelf front. The change in diatom assemblage with transport distance beneath the ice shelf was attributed to *T. antarctica* being more heavily silicified that *F. curta*. Supporting this suggestion, the relative abundance of other heavily silicified diatom species, such as *F. kerguelensis* and *Eucampia antarctica*, also show an increase beneath the ice shelf, despite *F. kerguelensis* being one of the most valuable indicators of open water deposition (Krebs et al., 1987; Leventer, 1992; Zielinski and Gersonde, 1997). The slower settling speed of the centric *T. antarctica*, in comparison to the pennate *F. curta*, was also suggested as a possible mechanism for the change in diatom assemblage beneath the ice shelf. However, the small differences in settling speed between the two species were shown to have an insignificant impact on the transport, and hence concentration, of diatom tracers at the sub-ice-shelf core site (Chapter 9).

Taylor and McMinn (2002) identified a downcore diatom assemblage "CL3" in core GC29, collected from inner Prydz Bay approximately 50 km from the Vestfold Hills (or Davis Station), analagous to the sub-ice-shelf diatom assemblage. The CL3 diatom assemblage displays co-dominant *T. antarctica* and *F. curta* and a small increase in relative abundance of *F. kerguelensis*. Taylor and McMinn (2002) interpreted the increase in relative abundance of *T. antarctica* and *F. kerguelensis* as indicative of a more open marine setting to that which occurs in Prydz Bay today. The sub-ice-shelf samples provide a modern analog to the CL3 diatom assemblage, suggesting sub-ice-shelf conditions. Taylor and McMinn (2002) present data from qualitative diatom slides. The production of quantitative diatom slides from core GC29 is recommended to determine the absolute diatom abundance (ADA), to observe whether diatom assemblage CL3 shows a decrease in ADA, as observed in the sub-ice-shelf assemblage. Similar conclusions could be drawn from measurements of the biogenic opal content taken from down the GC29 core. A decrease in ADA, or biogenic opal content, correlated with diatom assemblage CL3 would predict the presence of an ice shelf over the GC29 site between 11650-2600 ^{14}C yr BP. Taylor and McMinn (2002) suggest rare and fragmented diatom frustules downcore of the CL3 assemblage represent grounded ice over the site during the Last Glacial Maximum (LGM). The suggested presence of an ice shelf over the GC29 site after 11650 ^{14}C yr BP is supportive of the transition from glaciomarine

clays to diatom ooze at 10700 ^{14}C yr BP at the nearby ODP site 740A (Domack et al., 1991). A similar transition in the lithology is observed between unit 3 and unit 2 in the AM02 core, and has been interpreted as the transition from the 'null-zone' of sedimentation beneath the ice shelf, and the onset of the marine influence of sedimentation in the sub-ice-shelf cavity. Thus, predicting the presence of a floating ice shelf over ODP site 740A 10700 ^{14}C yr BP. Domack et al. (1991) indicate a transition from diatom ooze back to silty clay between 7400 and 3300 ^{14}C yr BP at ODP site 740A and suggested this indicated a shift from open water to sub-ice-shelf conditions, i.e., a readvance of the ice shelf front over the core site. The AM02 core results support the suggestion of readvance of the floating ice shelf over ODP site 740A, however they suggest the observed transition is from the zone of sub-ice-shelf marine sedimentation back to the 'null-zone' and that the site was sub-ice-shelf for the entire period. This is consistent with the GC29 core which shows no evidence of the readvance of floating glacial ice during this period (Taylor and McMinn, 2002). The transition from the zone of sub-ice-shelf marine sedimentation to open shelf conditions is not well represented by changes in the sediment lithology. However, changes in the diatom assemblage with transport distance beneath the ice shelf appears to be a useful proxy. At the GC29 site, the diatom assemblage shifts from the CL3 assemblage to a modern day shelf assemblage at 2600 ^{14}C yr BP, indicated by an increase in the relative abundance of *F. curta*, and decrease in the relative abundance of *T. antarctica*, suggesting the ice shelf front retreated past the site at this time.

During the mid-Holocene climatic optimum, a retreat of the Amery Ice Shelf front may have occurred, and possibly an increased sub-ice-shelf circulation transporting larger quantities of diatoms to the AM02 core site, as a result of increased ocean temperatures. However, an advance of floating ice over ODP site 740A is suggested during the same period, possibly from the expansion of coastal glacial drainage systems in Princess Elizabeth Land over eastern Prydz Bay (Domack et al., 1991). Therefore, the response of the Amery Ice Shelf/Lambert Glacier system during the mid-Holocene climatic optimum differs from the ice advance which occurs over eastern Prydz Bay. Differing drainage times of the two glacial systems may explain variation in the response of the ice flow. The two systems also exhibit differing responses at the end of the LGM. The first appearance of marine sedimentation at the AM02 core site after the LGM occurred 15132 ^{14}C yr BP. The corresponding event occurred at the eastern Prydz Bay core site approximately 11000 ^{14}C yr BP (Domack et al., 1991; O'Brien and Harris, 1996; Taylor and McMinn, 2002). It is concluded the Lambert Glacier grounding line retreated more rapidly along the main axis of the Amery

Ice Shelf, than the retreat of ice from the coastal drainage systems in eastern Prydz Bay. The nature of the glacial system catchment must also be considered. During periods of warmer climate, a larger increase in precipitation is predicted near the Antarctic coast than in the Antarctic interior (Smith et al., 1998). Increased coastal precipitation may increase the ice discharged by coastal glaciers draining Princess Elizabeth Land. The Lambert/Amery catchment however, fills a large portion of the East Antarctic interior (Allison, 1979), and may not be subject to large increases in precipitation during warmer periods, thus decreasing the relative ice flux of the Lambert/Amery system.

Additional hot water drill sites on the Amery Ice Shelf are proposed for coming seasons (2003-2004 and 2004-2005). The continued collection of sub-ice-shelf sediment cores is recommended to both improve our understanding of sub-ice-shelf circulation and sedimentation processes, and to confirm the ice shelf response to changes in climate, observed in the AM02 core, which may have occurred during the Holocene.

Many questions have been raised from the study, and hence, several proposals for future study have been outlined. Continued investigation of the oceanography, glaciology, and sedimentology of this unique, sub-ice-shelf environment can only improve our understanding of how the Amery Ice Shelf is likely to respond to future changes in climate.

Summary of Part II of the thesis Results from this study provide insight into the sedimentation processes which occur in the ocean cavity beneath the Amery Ice Shelf. This has been achieved via sampling of sub-ice-shelf sediments, allowing the first glimpse of the spatial distribution, and temporal variability, of sediments beneath an existing, major-embayed ice shelf, and provided proof of the landward transport of hemipelagic sediments beneath floating ice shelves. Application of both barotropic and baroclinic numerical ocean models, despite their limitations, allowed the identification of the processes responsible for the present day sediment distribution, showing that density driven circulation dominates tidal driven circulation in the ice-shelf cavity, and helped to explain how these density driven currents may strengthen under the effects of a warmer climate.

Such changes in the sedimentation patterns in the ice shelf cavity have important implications for the interpretation of sediment cores as indicators of past climate. Results presented in Part II of the thesis suggest the mid-Holocene climatic optimum lead to a change in the distribution of marine sediments in the ice shelf cavity, either via increased current magnitudes, or the ice shelf calving. Such observations are valuable tools for predicting the response of the Antarctic Ice Sheet to future changes in climate.

Part III

GENERAL DISCUSSION AND CONCLUSIONS

And so castles made of sand melt into the sea eventually

Jimmy Hendrix, 1969

Chapter 11

General Discussion and Conclusions

The influence of ocean processes on the sedimentation in two contrasting continental shelf environments has been investigated with the aim of identifying the differences between the dominant processes. In Part I of the thesis, the three-dimensional hydrodynamic numerical ocean model, MECO, was applied to determine the tidal, meteorologically (wind and atmospheric pressure), and density - driven circulation in the Torres Strait/Gulf of Papua region, and how this varied on a seasonal scale. The modelled ocean circulation, and available wave data, were used to present the energetic ocean processes responsible for the distribution of sediments in Torres Strait and the Gulf of Papua. In Part II, a depth-averaged version of the MECO model, and the three-dimensional, hydrodynamic *OzPOM* model, were applied to investigate the less dynamic tide and density-driven currents in the ocean cavity beneath the Amery Ice Shelf, to determine their influence on the sedimentology of the sub-ice-shelf environment. Here, results from the two parts of the study are compared and contrasted.

11.1 Modelling Approach

The ocean models used for each application were different. For the Torres Strait/Gulf of Papua application, the z-layer MECO model was used to determine the three-dimensional circulation in the region. The z-layer model was ultimately chosen for this application as it was considered that the rapid changes in depth associated with the coral reefs and steep shelf slopes in the model domain may lead to large numerical errors in the pressure gradient calculation in a $\sigma-$layer model (Haney, 1991; Mellor et al., 1994). Validation of the three-dimensional MECO model with available sea-surface elevation and current meter data, and with new current meter data collected for this study, indicates that the model performs well

enough to resolve the seasonal variation of oceanic processes which influence sedimentation on the continental shelf.

Tides beneath the Amery Ice Shelf were modelled using MECO as a two-dimensional, depth-averaged, model (Chapter 8), with the ice shelf portion of the domain having a water depth defined as being equal to the water column thickness (i.e., the difference between the ice draft and bed elevation), and friction parameters doubled to represent the two frictional interfaces at the sea-bed and at the base of the ice shelf. This approach is similar to that taken by previous researchers in other ice shelf environments (Ross Ice Shelf, MacAyeal, 1984b; Filchner-Ronne Ice Shelf, Robertson et al., 1998, Makinson and Nicholls, 1999). In Chapter 8, it was shown that the MECO tide model provides sea-surface elevation predictions to good accuracy in comparison to available GPS derived sea-level measurements. Tidal harmonic amplitude errors of the four main constituents (M_2, S_2, K_1, and O_1) are less than 5 cm, and respective phase errors are $\sim 10°$. These model results suggest the accuracy of sea-level predictions are as good as, or better than, previous models of the Amery Ice Shelf tidal environment.

However, when a large surface pressure, representing the effects of a floating ice shelf, was imposed in the three-dimensional z-layer MECO model, instabilities in the results occurred, and these were unable to be resolved. Consequently, a change in modelling approach was required, and a terrain-following $\sigma-$layer model (*OzPOM*; a version of the Princeton Ocean Model, Hunter, 2002) was chosen to simulate the sub-ice-shelf thermohaline circulation (Chapter 9). Aside from the different formulations for the vertical grid, and the slightly more sophisticated vertical mixing and advection schemes implemented in *OzPOM*, the two models, MECO and *OzPOM*, are similar. *OzPOM*, like MECO, is a free surface model. The use of a free surface, $\sigma-$layer model to predict the three-dimensional circulation in the ocean cavity beneath a floating ice shelf differs from previous modelling efforts which have used rigid-lid, $\sigma-$layer (Determann and Gerdes, 1994; Grosfeld et al., 1997; Gerdes et al., 1999; Williams, 1999; Williams et al., 1998b, 2001, 2002) and isopycnic models (Holland and Jenkins, 2001; Jenkins and Holland, 2002). The predicted sub-Amery Ice Shelf circulation presented in this study suggests some variation to that described by Williams et al. (2001), using a rigid-lid model, which is not explained by the changes in ice shelf geometry. Consequently, this study has prompted a model intercomparison study to be carried out using ideal ice shelf domains.

The free surface *OzPOM* model allowed the effect of tides on the sub-Amery Ice Shelf thermohaline circulation to be investigated (Chapter 9), and consequently, the tidal

environment beneath the ice shelf to be determined. The tidal solution provided by the baroclinic *OzPOM* model was therefore available for direct comparison to the solution predicted by the depth-averaged MECO model. The comparison between the tides predicted by each model were presented in Chapter 8, and indicate very little difference between the two models. *OzPOM* displays slightly improved estimates of tidal phase in comparison to observed values, and MECO provides slightly improved estimates of tidal amplitude. The good model-model comparisons impart further confidence in the solution given by each model, for each application presented in the thesis.

11.2 Sediment Supply

As outlined in the Introduction, the two regions chosen for study in the thesis display some similarities associated with sediment supply.

11.2.1 Terrigenous Sediment

High rainfall in the Papua New Guinea highlands result in a freshwater discharge from the Fly River into the Gulf of Papua of $\sim 238\ km^3a^{-1}$, or $\sim 7500\ m^3s^{-1}$ (Alongi et al., 1992). Despite the low precipitation rates over the Antarctic continent, the large catchment area of the Lambert Glacier results in a present estimate of ice input into the Amery Ice Shelf of $\sim 46\ Gta^{-1}$ (Williams et al., 2002), which equates to $\sim 46\ km^3a^{-1}$, or $\sim 1500\ m^3s^{-1}$. Therefore, although the outflow of the Amery Ice Shelf, which is contributed to by both basal melting and iceberg calving, is approximately one fifth of the outflow of the Fly River, each shelf region has a significant freshwater inflow which is capable of transporting large quantities of terrigenous sediment from off the continent to the continental shelf.

The distribution of terrigenous sediments across the Torres Strait and Gulf of Papua shelf is a direct function of the dispersal pathways of the Fly River plume, and the rate at which sediments settle out from it. These sediment dispersal pathways were investigated with the model, and how these varied at differing time scales is discussed in section 11.3 below.

The transport of terrigenous sediment across the Antarctic continental shelf is dominated by a very different process. Sediments derived from the Antarctic land-mass are transported to the continental shelf generally held within glacial ice. When the glacier reaches the coast and flows into the ocean to form a floating ice shelf, or ice tongue, the warmer ocean waters cause basal melting of the floating ice. Beneath the Amery Ice Shelf,

melt rates are greater in the deep southern reaches of the ice shelf cavity (Chapter 9), which results in the rapid deposition of basal debris near to the southern grounding line. Surface sediments collected from site AM02 beneath the Amery Ice Shelf, $\sim$ 80 km landward of the present day calving ice front, display high biogenic opal content (Chapter 7), and therefore, deposition of terrigenous sediment at that site appears to be small, with the majority of any land-derived material having been deposited close to the grounding line. Some ice rafted debris (IRD) is likely to remain in the ice, as basal accretion of marine ice will further isolate the IRD from the ocean, and therefore the likelihood of deposition. Iceberg calving at the front of the ice shelf allows the sediment held within the ice to be transported in the iceberg, possibly thousands of kilometres from the feeding glacier, before melting of the berg results in deposition of the sediments contained therein. Sedimentation of terrigenous material on the Antarctic continental shelf is therefore a function of the mean ocean currents transporting icebergs, and the melt-rates at the base of the floating ice.

11.2.2 Marine Sediments

Each of the continental shelf environments chosen for study in this thesis contain sediment deposits derived of material produced by marine organisms. In the Torres Strait/Gulf of Papua region, the marine deposits have a high carbonate content, derived from benthic foraminifers, and other calcareous organisms. The distribution of marine deposits across the continental shelf is dependent on the wave and current energy which is available to both initially break up the organisms, and also lift the material into suspension. Once in suspension, the residual circulation is responsible for the sediment dispresal. On the Antarctic continental shelf, marine deposits are derived mostly from diatoms which live in the photic surface layer of the open ocean. Diatoms, unless trapped within sea-ice as new ice forms, settle to the sea-bed after death. They either settle individually to the sea-bed at very slow speeds, or fall rapidly as part of a faecal pellet after having been grazed upon by zooplankton. As the diatoms settle, the residual circulation leads to lateral transport, and thus influences the spatial variability of the siliceous surface sediment distribution. A fundamental difference therefore exists between the dominant marine sediment supply in each region. The calcareous sediments of the Northern Great Barrier Reef and Torres Strait require energetic reworking by waves and strong tidal currents before they are able to be resuspended and then transported by the mean flows, whereas the siliceous sediments on the Antarctic continetal shelf are supplied at the water surface. Therefore, the currents on the Antarctic continental shelf need not be as energetic as those in Torres Strait to disperse

marine sediments from the site of production across the shelf.

Predicted currents in the Torres Strait/Gulf of Papua region identify an area of maximum current-induced bed shear stress along the Northern Great Barrier Reef (Chapter 4). Bed stress magnitudes of up to 3 Nm^{-2} suggest that currents are large enough to rework, breakdown, and consequently resuspend, the clastic carbonates in the region. Resuspension mechanisms are not parameterised into the model, however, tracers were introduced near the sea-bed at the site of greatest bed stress, and the dispersal pathways of the suspended calcareous muds across the continental shelf were determined. As with the distribution of terrigenous sediments, the dispersal of resuspended marine sediments is a function of the transport by the residual circulation. The oceanic processes which dominate the dispersion of marine-derived sediments are also discussed below.

Similarly, in the region of Prydz Bay and beneath the Amery Ice Shelf, the dispersal of marine diatomaceous sediments beneath the ice shelf is a function of the mean, residual circulation. Tracers, representing diatoms in suspension, were introduced into the surface layers of Prydz Bay in the baroclinic model to determine the spatial distribution of marine sediments across the shelf. The ocean processes influencing the circulation, and consequent sedimentation of marine-derived sediments, on the Antarctic shelf at different time-scales are discussed in the following section.

11.3 Ocean influences on sedimentation as a function of time-scale

An aim of the thesis has been to identify the time scale of the oceanic processes which dominate sedimentation in each of the two chosen continental shelf environments. The discussion below separates the processes depending on their time scale, and begins at the shorter time scales of oceanic turbulence, and continues through with discussion of processes at the surface gravity wave, tide, synoptic, seasonal, thermohaline current, and sea-level change, time periods.

11.3.1 Oceanic turbulence

At short time scales, turbulent mixing is an important process in both the Torres Strait, and the sub-Amery Ice Shelf, regions.

A newly constructed benthic data collection frame, the Benthic Research for Underwater sediment ConcEntrations probe (BRUCE) was deployed in Torres Strait during the

summer of 2002. The probe contained a suite of instruments for investigating the transport and resuspension of sediments in continental shelf environments of up to 300m depth. It was found that maximum turbulent shear stresses were experienced at the sea-bed during periods of increased winds. Thus, it was concluded that the turbulent transfer of momentum through the water column from the surface momentum flux is greater than the turbulence created from the drag of tidal currents at the sea-bed (Chapter 3). Model predicted current-induced bed shear-stresses at the BRUCE site were too small to initiate mobilisation. This implies that storm events are likely to be an important influence on localised sediment mobility.

Beneath the Amery Ice Shelf, turbulence is responsible for mixing warm salty waters from near the seafloor upwards to the base of the ice shelf, and thus affect melting and the consequent overturning thermohaline 'ice-pump' circulation. Away from the influence of air-sea interactions, turbulence beneath the ice shelf is likely to be generated at the sea-bed and ice shelf base by tidal currents. Beneath the ice shelf, vertical mixing competes with the stratifying influence of basal melting. The inclusion of tides into the baroclinic model resulted in only a slight variation of the melt and freeze distribution beneath the Amery Ice Shelf (Chapter 9). The tidal energy beneath the Ice Shelf is concluded to be too small to overcome the stratification induced by melting. MacAyeal (1984b) suggested that in areas beneath the Ross Ice Shelf where this occurred, the vertical heat fluxes necessary to maintain the basal melting were probably induced by the shear between the deeper, warmer water masses and plumes of low density Ice Shelf Water (ISW) rapidly ascending the steep basal slope. The ISW plumes are likely to be initiated very near to the grounding line where the ice shelf cavity pinches out and the water column is well mixed.

11.3.2 Surface Gravity Waves

The primary characteristic of the Antarctic continental shelf is its great depth, which occurs as a result of isostatic depression by the grounded ice sheet and glacial erosion. The 500 m average depth is beneath the wave base of surface gravity waves, and therefore the influences of wave processes on the Antarctic continental shelf is almost nil. Beneath the ice shelf, there is no direct influence of ocean processes driven by air-sea interaction. Consequently, no consideration of surface gravity waves were taken into account in Part II of the thesis, which focussed on the oceanic processes in the region of Prydz Bay and beneath the Amery Ice Shelf on the Antarctic continental shelf.

However, in the Torres Strait and Gulf of Papua region, waves are an important oceanic influence on sedimentation on the continental shelf, particularly during the Trade

season when swell generated in the Coral Sea is continually impinging on the south coast of Papua New Guinea. Currents alone, without wave motions considered, are capable of mobilising sediment over large areas of the shelf for short periods of time. However, currents mobilise sediments over only a small area of the shelf for lengthy periods of time. Waves provide a much more energetic environment. Although waves alone do not mobilise large areas of the shelf at some point of time, they mobilise larger areas of the shelf for longer periods of time, than currents do. Consideration of the non-linear interactions between the waves and currents further influences how much sediment is mobilised at the sea-bed - outlining the importance of waves on the shelf. Considering only the 0.5 mm diameter, cohesionless sediment on the shelf ($\tau_{cr} = 0.27\ Nm^{-2}$) during the Trade season, currents on their own would mobilise less than 2% of the shelf area for 80% of the time, and waves alone would mobilise $\sim 15\%$ of the shelf area. The combined wave-current motions mobilise more than 40% of the shelf area for 80% of the time during the Trade season. During the monsoon, the influence of waves is not quite as great, however they do influence sediment mobility on the shelf. The area over which the seasonal differences are most notable is along the south coast of Papua New Guinea in the Gulf of Papua, where Coral Sea generated swell moves onto the coast during the Trade season. Classification of which processes dominate mobilisation on the shelf within the Torres Strait and Gulf of Papua model domain indicate that in Torres Strait, wave action and tidal currents are equally responsible for sediment mobilisation from the sea-bed, whereas the continental shelf in the Gulf of Papua is generally a wave dominated environment.

11.3.3 Tides

In the introduction to the thesis, it was hypothesised that tides were equally important to features of the surface sediment characteristics in each of the Torres Strait/Gulf of Papua, and sub-Amery Ice Shelf, environments focussed on for the study.

Tidal currents in Torres Strait and the Gulf of Papua were found to account for greater than 75% of the predicted current magnitudes at the sites of previous current meter moorings. Maximum current-induced bed shear stress vectors differ only slightly between the Trade and Monsoon seasons. Current induced threshold exceedances also show little variation with the seasons. The similarities observed, despite the strongly variable meteorological conditions of each season, suggest that tidal currents, along with the previously discussed wave energy, dominate over the wind and density driven currents in mobilising sediments on the Torres Strait and Gulf of Papua sea-bed.

Beneath the Amery Ice Shelf, it was proposed that the constriction of the water column thickness due to the imposing ice shelf accelerates tidal currents to a point where they could alter the characteristics of surface sediments through sorting and/or mobilisation processes, as observed adjacent to the Filchner-Ronne Ice Shelf front (Haase, 1986). Modelling of the tides in Chapter 8 indicate that maximum tidal current magnitudes in the ice shelf cavity are $\sim 15\ cms^{-1}$, which coincide with bed stress magnitudes of $\sim 0.1\ Nm^{-2}$ - too small to mobilise the cohesive siliceous mud and ooze sediments observed beneath the ice shelf. Predicted maximum tidal currents do, however, reach speeds of up to 45 cms^{-1} on the shallow banks in the open waters of Prydz Bay. Mobilisation by tidal currents may influence the sedimentary characteristics in these regions. Beneath the ice shelf, maximum tidal currents are approximately twice the speed of the ISW plume which ascends the steep basal slope of the ice shelf towards the open ocean. However, residual tidal currents are minimal ($< 2\ cms^{-1}$), and do not contribute significantly to the mean sub-ice-shelf circulation responsible for the dispersal of suspended sediment. The tidal currents in the restricted cavity near the grounding line, where the water column thickness is less than 20 m, are not resolved by the models presented in Chapters 8 and 9. This zone can be likened to the coastal zone found in Torres Strait and the Gulf of Papua, where significantly different processes are acting to those in deeper continental shelf waters. Wave breaking and coastal currents (e.g., longshore drift) are likely to be important in the Torres Strait/Gulf of Papua coastal zone. In the grounding line zone beneath the ice shelf, tidal flushing processes may be an important influence on the sedimentary characteristics. However, away from this area the influence of tides on sedimentation beneath the Amery Ice Shelf is minimal.

11.3.4 Synoptic scale influences

The effects of synoptic scale meteorological events on ocean processes have not been considered in detail in this study. In the Torres Strait and Gulf of Papua region, tropical cyclones occur at an average frequency of approximately one every two years (Bureau of Meteorology, 2002). The influence of tropical cyclones which occur more frequently in the Coral Sea will, however, be felt along the southern Papua New Guinea coast. Wave motion has been shown to be a dominant oceanic influence for mobilising sediments on the continental shelf in the Torres Strait/Gulf of Papua domain. Surface sediment characteristics are likely to be altered as a result of resuspension and erosion of sediment caused by the increased wave energy associated with storm, or cyclone, events in the region. Wind-driven currents, which become stronger with increased wind speeds, transport sediments in suspension, and there-

fore storm events are likely to lead to altered distribution of sediments across the continental shelf. Transmissometer, salinity, temperature, and current meter measurements taken using the BRUCE instrument mooring indicate that a period of increased north-westerly winds experienced during Monsoon conditions resulted in extended advection of the fresh, turbid, Fly River plume past the mooring site, displaying a sensitivity to synoptic scale events.

Beneath the Amery Ice Shelf, the influence of ocean processes requiring air-sea interaction is small, and therefore, synoptic scale events beneath the ice shelf are expected to be negligible. Storm events in the open waters of Prydz Bay may lead to increased sea-ice formation and consequent formation of dense bottom waters which flow beneath the ice shelf. Therefore, a delayed response to meteorological systems beneath the ice shelf may be experienced, however this is likely to be very small. Synoptic scale meteorological forcing could be easily implemented in future applications of the sub-ice-shelf ocean model, however, an accurate sea-ice model must be included within the model dynamics before any realistic synoptic signal could be detected.

11.3.5 Seasonal influences

Both the Torres Strait/Gulf of Papua, and the Prydz Bay/Amery Ice Shelf settings display strong seasonal climate differences. Seasonal wind variability in the tropical setting of Torres Strait and the Gulf of Papua is well described. Steady south-easterly Trade winds experienced for two thirds of the year (Apr-Nov), provide a continual supply of energy for generating waves and currents in the area, and give way to the relatively calm north-west Monsoon during the southern hemisphere summer (Dec-Mar). In the Antarctic, the increase in sea-ice cover across the continental shelf waters, associated with the dissapearance of the sun, during the winter months are similarly well known.

In Chapter 4, the effects of seasonal wind changes on the ocean circulation and the consequent dispersal of terrigenous sediments suspended in the Fly River Plume, and resuspended calcareous muds from the Northern Great Barrier Reef, across the continental shelf, were investigated. The predicted budget of the Fly River terrigenous sediments across the shelf displays a strong seasonal dependence which is not resolved by previous field data derived estimates of the budget. Approximately 50% of the 85×10^6 tonnes of sediment discharged from the Fly River annually is deposited in the River Delta (Harris et al., 1993). Of the sediments which remain in suspension, the largest component is transported by wind and density driven currents north-eastwards in the Gulf of Papua along the south coast of Papua New Guinea. During the monsoon, 34% of the total Fly River sediment load is pre-

dicted by the model to be transported north-eastwards. The field derived budget suggests 40% of the total load is transported in this direction (Harris et al., 1993). The remaining suspended terrigenous sediment follows various paths across the continental shelf. During the monsoon, $\sim 10\%$ of the total load is predicted to move southwards to the east of Cape York, inside the Northern Great Barrier Reef, $\sim 3\%$ heads westward through Torres Strait, and the remaining 3% is transported directly offshore to be deposited in the Coral Sea. During the Trade season, increased sediment load (11%) is predicted to be transported westwards towards Torres Strait. 24% of the total sediment load moves north-eastwards along the south coast of Papua New Guinea, and 13% is transported directly offshore to the Coral Sea. Just 2% travels southwards past the eastern coast of Cape York. The strong seasonal dependence on the predicted transport of suspended terrigenous sediment across the continental shelf from the Fly River displays the dominance of wind-generated currents on the residual circulation in the Torres Strait/Gulf of Papua region. Similarly, the dispersal of the marine-derived calcareous muds from the Northern Great Barrier Reef is influenced strongly by the seasonal varying, wind-driven, residual circulation. During both Trade and Monsoon seasons, a large amount of the resuspended marine sediments move onshore towards the Fly Delta. During the monsoon, larger volumes move north-eastwards along the Papua New Guinea coast, and during the Trades, a greater component was transported westwards into Torres Strait.

Other seasonal influences in Torres Strait and the Gulf of Papua are apparent in the model predictions. Despite tidal currents dominating the maximum current-induced bed-shear stress vectors, some small areas including the Adolphus Channel and the shallow waters to the west of Cape York, display seasonal changes in maximum bed stress direction. These regions correspond with areas where seasonally reversing bedform assymetry have been observed (Harris, 1989). Therefore, seasonal changes of the wind-driven currents are concluded to have a large influence on the surface sediment characteristics in the Torres Strait model domain.

The seasonal variability of waves in the Torres Strait and Gulf of Papua have been mentioned above. Sediments on the continental shelf along the south coast of Papua New Guinea in the Gulf of Papua are more readily mobilised during the Trade season. This is qualitatively consistent with sediment cores collected previously from the Fly River delta front (Harris et al., 1993). The core lithology suggests that during the low energy Monsoon period, a mud drape was deposited, while during the Trade season, the increased wave energy reworks the mud and sand to winnow out the fines, resulting in seasonal sand-mud

interbeds (varves) in the sediment record. However, within Torres Strait, the seasonal influence of waves is altered. During the Trade season, the north-westwards propagating Coral Sea generated swell is sheltered from Torres Strait by the Northern Great Barrier Reef. Therefore, despite the lower wind speeds, the greater fetch, which results from the north-westerly winds, leads to an increase in wave-induced sediment mobility in Torres Strait during the monsoon, in comparison to the Trade season.

Without an accurate sea-ice model implemented into the baroclinic model presented in Chapter 9, the influence of seasonal climate variations on the circulation beneath the Amery Ice Shelf can not be predicted. During the winter months, the lack of solar radiation and increased winds from off the Antarctic continent lead to an increase in sea-ice formation in the open waters around the Antarctic coastline, e.g., Prydz Bay. Salt rejection follows, resulting in the formation of a dense water mass which sinks to the seafloor, despite its relatively warmer temperature (which is approximately equal to the surface freezing temperature). The density of this water mass means that it will flow downslope in a landwards direction beneath the Amery Ice Shelf, and consequently slightly increase water temperatures in the sub-ice-shelf cavity during winter. An increase in temperature of $\sim 0.1°C$ is observed beneath the Filchner-Ronne Ice Shelf during the winter months (Nicholls, 1996). A similar signal is observed in the year-long temperature time series collected from beneath the Amery Ice Shelf at the AM02 hot water drill site (Craven et al., 2002). With an increase in temperature beneath the ice shelf, an increase in area over which melting occurs may result, resulting in a slightly stronger sub-ice-shelf circulation and increased advection of marine sediments into the cavity. However, the seasonal variation of temperature is quite small, and consequently is likely to have little influence on these processes.

Increased sea-ice cover during winter results in a seasonal decrease of diatom production in Prydz Bay waters. Any increase in circulation which may occur during winter therefore has a decreased marine-derived sediment load to advect beneath the ice shelf, thus reducing any possible seasonal signal preserved in the sediment record. Regardless, present day accumulation rates at the sub-ice-shelf AM02 sediment core site are $\sim 0.157\ mma^{-1}$, and therefore any seasonal variability of diatom production rates in Prydz Bay will not be resolved by sampling the core at 1-5 cm intervals.

11.3.6 The long period thermohaline circulation

Spatial density variations in each environment drive distinctly different very long period, mean thermohaline circulations.

Tidal and meteorologically driven currents contribute to $\sim 94\%$ of the current speeds in Torres Strait and the Gulf of Papua. The remaining $\sim 6\%$ of the current is provided by the density-driven currents. Alone, these thermohaline flows are unlikely to mobilise sediments on the continental shelf. Despite the large density variations associated with the input of freshwater from the large Papua New Guinea rivers, the only predicted effect of the density driven flow in the model domain was the north-eastwards transport of suspended sediment along the southern coast of Papua New Guinea, which was shown to be strongly diverted by prevailing wind-driven currents. Consequently, it was concluded that the influence of the density driven circulation on the distribution of sediments on the continental shelf in Torres Strait and the Gulf of Papua is small.

Beneath the Amery Ice Shelf, the pressure dependence of the freezing point of seawater and the landward deepening ice draft provide a large temperature gradient along the ocean cavity. At the deep southern grounding lines, the large temperature difference between the ice shelf base, which is at the in-situ freezing temperature, and the inflowing dense water which is formed in the open waters of Prydz Bay, drives strong melting at the ice-ocean interface, and consequently forms a fresh, cold, bouyant water mass (Ice Shelf Water; ISW). Given its increased buoyancy, ISW rapidly ascends the steep basal slope of the ice shelf, thus defining the sub-ice-shelf overturning 'ice-pump' thermohaline circulation. As the ISW ascends the ice shelf base, it becomes supercooled, such that it becomes cooler than the in-situ freezing temperature, and some freezing may occur leading to the accretion of marine ice onto the base of the ice shelf. The baroclinic model of the circulation beneath the Amery Ice Shelf, presented in Chapter 9, indicates that the overturning circulation displays some lateral separation, dependent on the cavity geometry.

Sediments collected from beneath, and adjacent to the calving ice front, of the Ice Shelf display characteristics which reflect the lateral separation of the density-driven inflow and outflow circulation (Chapter 7). In regions of inflow (AM02), surface sediments display increased levels of biogenic silica in comparison with regions of outflow (AM01). The dispersal pathways of marine diatoms predicted by the baroclinic model are consistent with the observed surface sediment characteristics. The flow mechanism which dominates the distribution of the marine derived sediments is the sub-ice-shelf thermohaline circulation (Chapter 9). Jacobs (1989) suggested that tidal currents were an important component of the larger scale circulation beneath floating ice shelves. However, although maximum tidal currents are approximately twice the magnitude of the density-driven currents, the mean circulation beneath the ice shelf, responsible for the dispersal of sediments in suspension, is

primarily a function of the density-driven currents. The effects of tides, via tidal residual currents or increased mixing, altering melt-rates and therefore the density driven currents, on the sediment distribution beneath the Amery Ice Shelf were shown to be insignificant in comparison to the mean thermohaline circulation (Chapters 8 and 9). Given that neither tidal or density driven flows are strong enough to mobilise sediments from the sea-bed, the dominant oceanographic influence on the sedimentation in the sub-ice-shelf cavity is the locally generated thermohaline currents transporting suspended sediments.

The thermohaline circulation is similarly an important influence on the distribution of melt and freeze at the ice shelf base. Melting at the base of Antarctic ice shelves is a major source of ice loss from the Antarctic ice sheet. Model estimates of the net mass loss as a result of melting at the ice shelf base, under cool climate conditions (where the open ocean temperature throughout the water column is equal to the surface feezing temperature) are $\sim 8.0\ Gta^{-1}$. Under present-day temperature conditions ($0.2°C$ warmer than the cool runs), the estimated net mass loss predicted by the model is $14.8\ Gta^{-1}$, consistent with present day oceanographic observations and previous model estimates of $\sim 15\ Gta^{-1}$ (Wong et al., 1998; Shanahan, 2002; Williams et al., 2002). These estimates are sensitive to the sub-ice-shelf geometry, and the ocean temperature. An increase in open ocean temperature of $1°C$ above the cool runs results in an increase of the estimated net mass loss as a result of melting from $8.0\ Gta^{-1}$ to $\sim 52\ Gta^{-1}$. This increase is predicted to strengthen the sub-ice-shelf circulation, and may be important for interpretation of the sub-ice-shelf sediment record during periods of a warmer climate, sea-level rise, and ice shelf retreat.

11.3.7 Over periods of sea-level rise: The Transgression

On longer time scales, the oceanographic processes which dominate sedimentation on the continental shelf have possibly changed with rising sea-levels since the Last Glacial Maximum (LGM).

During the LGM at $\sim 20,000$ yr BP, the eustatic sea-level fell to approximately 120 m below its present position (Thom and Roy, 1983; Chappel et al., 1983; Pillans, 1987). During this period, Torres Strait formed a land bridge between Australia and Papua New Guinea, and the Fly River, draining the Papua New Guinea highlands, incised valleys into marine, coastal, and fluvial deposits in the area that is the present day Gulf of Papua continental shelf (Harris et al., 1996b).

Harris et al. (2002) mapped some of these submarine valleys across the Gulf of Papua shelf. The floors of the channels are mostly $<$ 100 m water depth, and therefore above

sea-level during the last glaciation. However, Harris et al. (2002) also found some over-deepened channels in the south which exhibit surface sediments of well-sorted, carbonate gravelly sand, suggesting that they may have formed by tidal scour. The model presented in Chapter 3 suggests currents in the region of these scoured channels are relatively weak, and therefore unable to form such features under present conditions.

Sea-level rise began about 19,000 yr BP, and reached a maximum rate of ~ 20 m/1000 yr about 11,000-12,000 yr BP (Chappel et al., 1983). A relative sea-level highstand of 1-2 m above present occurred during the mid-Holocene at 5,000-6,000 yr BP along the north-eastern Australian shoreline (Nakada and Lambeck, 1989). During the period of sea-level rise, the Fly River retreated landward, the continental shelf broadened, and coral reefs became locally re-established (Harris et al., 1996b). Harris et al. (2002) presented a fixed bathymetry depth-averaged tidal model and applied 8 different sea-levels at 10 m increments below present sea-level. They found that tidal currents reached a maximum value over the site of the observed deepest shelf valleys when sea-level was approximately 40 m below its present position. Harris et al. (2002) therefore concluded that the over deepened shelf valleys observed on the shelf are relict features formed during periods when sea-level was $\sim 40-50$ m below its present level - not necessarily in the period since the LGM. Therefore, the relative importance of tides on the shelf has varied with changing sea-levels on the Torres Strait/Gulf of Papua continental shelf.

During the Holocene post-glacial transgression, only limited deposition of the huge sediment loads carried down the Fly River have been deposited on the shelf in the Gulf of Papua (Harris et al., 1996b). Harris et al. (1996b) propose that during this period, the Coral Sea Coastal Current (CSCC) transported sediment north-eastwards to a narrow section of the shelf, where gravity currents moved it downslope, particularly prior to 11,000 yr BP. This suggests that the importance of the CSCC on the transport of sediment across the continental shelf to the deep ocean may have been greater during periods when sea-level was lower than present. Results presented in this study suggest that, under present conditions, the influence of the CSCC on the distribution of sediments on the shelf is small in comparison to those from tidal and meteorologically driven currents.

On the Antarctic continental shelf, advance of the grounded ice sheet during the LGM results in dramatic changes to the sedimentation processes occuring on the shelf. During the LGM, the Amery Ice Shelf is thought to have been grounded in central Prydz Bay (Domack et al., 1998). The AM02 sediment core collected from beneath the present day ice shelf provides a full sediment record of the processes associated with the retreat of the ice shelf

during the transgression. As the grounding line retreated landward of the sub-ice-shelf core site, strong melting resulted in the rapid deposition of a waterlain till over the lodgement till. During this period, the primary influence of the ocean on sedimentation is its ability to melt the IRD out from the glacial ice. However, the water column thickness is much narrower at this time than occurs presently. Tidal currents accelerate in the narrow cavity, winnowing out some of the fine sediments. Faint laminations in the sediment record suggest the influence of increased currents on the sub-ice-shelf sediments occurred through the AM02 core, to the period when the ice shelf front is sufficiently close to the core site so as to allow biogenic marine sediments to be deposited there. Eventually, the cavity widens, and the sub-ice-shelf tidal currents decelerate to the slow speeds predicted under present ice shelf conditions. Therefore, although tides are unimportant today in distributing sub-ice-shelf sediments, they may have been a dominant oceanographic influence on the sedimentation beneath the Amery Ice Shelf during some period of the transgression.

Since $\sim 15,132\ ^{14}C$ yr BP, biogenic marine sediments have been deposited at the sub-ice-shelf AM02 core site at an average accumulation rate of $\sim 0.03\ mma^{-1}$. Circulation transports particulate material in suspension from the open waters of Prydz Bay beneath the ice shelf. The accumulation of diatoms at the AM02 site has not been constant during the Holocene, with rates ranging from $0.027\ mma^{-1}$ to $0.157\ mma^{-1}$. Consequently, the absolute diatom abundance, and the diatom assemblage, display variability during the Holocene sediment record. The present day sub-ice-shelf diatom assemblage differs to that found in the productive open waters of Prydz Bay. Heavily silicified diatom species with slow settling speeds are preferentially preserved beneath the ice shelf, and the absolute diatom abundance consequently decreases with transport distance beneath the ice shelf. During the mid-Holocene, an increase in deposition of sea-ice associated diatoms beneath the ice shelf results in a diatom assemblage similar to that found in the open waters of Prydz Bay today. In Chapter 9, a $1°C$ increase of the ocean temperatures in Prydz Bay was trialled in the baroclinic model. It was found that during periods of warmer ocean temperature, particulate material, that derives from the productive open water region of Prydz Bay, is advected beneath the ice shelf further and more rapidly as a result of the increased strength of the sub-ice-shelf circulation. Similarly, an increase in ocean temperature leads to larger melt rates beneath the ice shelf, which are likely to alter the ice shelf geometry. It was suggested that during the mid-Holocene, the combined effects of a retreat of the ice shelf bringing productive waters closer to the core site, and the strengthened sub-ice-shelf circulation more readily transporting diatoms beneath the ice shelf, resulted in the observed increase in sea-

ice associated diatoms being deposited at the AM02 core site, as a response of the Amery Ice Shelf to a mid-Holocene climatic optimum period as described by previous researchers (Ingolfsson et al., 1998). Therefore, changes in the density-driven ocean circulation on the time scale of thousands of years may be important to sedimentation beneath the Amery Ice Shelf.

11.4 Conclusions and Outlook

At the beginning of the thesis, the classification scheme for continental shelves presented by Swift and Niedoroda (1985) was outlined. They proposed that a continental shelf could be classified by the oceanic processes which dominate sediment reworking and transport, and defined three continental shelf environments; those dominated by tidal processes, storm events, and intruding ocean currents.

In this study, it has been shown that a somewhat typical continental shelf environment, such as that found in Torres Strait and the Gulf of Papua where the oceanographic influence on sedimentation is dominated by tidal and meteorologically driven processes, may be classified by such a scheme. Sediment mobilisation processes on the continental shelf in the Gulf of Papua have been shown to be dominated by waves, and dispersal by wind-generated currents. Such an environment is well classified as a storm-dominated shelf. The continental shelf in Torres Strait has been shown to be a region where tidal currents and surface gravity waves interact to influence the mobility of sediments equally. Additional research assessing the effects of synoptic scale storm-events on the sedimentation processes in Torres Strait is required to define the continental shelf environment, as it could be classified as either a tide or storm dominated shelf setting. Nevertheless, Torres Strait is not dissimilar to 97% of the worlds continental shelves, which are also dominated by tides and/or storms (Swift and Niedoroda, 1985). However, the main aim of the thesis was to display the unique properties of the continental shelf environment found beneath, and adjacent to the front of, the Amery Ice Shelf (which is possibly typical of an Antarctic continental shelf) in comparison to a more common temperate shelf environment. The uniqueness of the sub-Amery Ice Shelf continental shelf setting is clearly demonstrated by the Swift and Niedoroda (1985) classification scheme.

The oceanographic influence on sedimentation on the outer Prydz Bay shelf is probably dominated by the circumpolar current moving onto the shelf edge, and therefore may be classified in the small (3%) portion of the worlds continental shelves where sedimentation

on the continental shelf is dominated by intruding ocean currents. However, on the inner continental shelf, and beneath the floating Amery Ice Shelf, locally-generated density-driven currents dominate in the transport of particulate material and its consequent deposition. Such an environment has no 'bin' into which it can be placed under the Swift and Niedoroda (1985) classification scheme, thus demonstrating the uniqueness of the region.

Ocean processes on the continental shelf are important factors in many environmental issues, some of which have been touched upon in this thesis. As with all research, the increase in knowledge of continental shelf ocean processes obtained from this study is far outweighed by the number of questions it has raised. Many suggestions for future research have been given for each of the Torres Strait and Amery Ice Shelf regions in the respective 'Summary, Discussion, and Outlook' chapters, 5 and 10. For the Torres Strait region, many model predictions, essential to key environmental questions, such as the fate of the large Fly River sediment load, and regions of scour important to the fate of a proposed gas pipeline, are not resolved by available data. The study called for additional data to be collected in the region to validate some of the model predictions. Beneath the Amery Ice Shelf, this study provided significant advance in the knowledge of sub-ice-shelf sedimentation. However, additional sediment cores need to be collected from beneath ice shelves to further understand the distribution of sub-ice-shelf sediment properties. As more data become available for model comparisons, the suggested additions to the model dynamics may be implemented to improve model predictions. It is anticipated that the increased knowledge of sub-ice-shelf sedimentation will allow more accurate identification of sub-ice-shelf conditions from the sediment record on the Antarctic continental shelf, allowing better representation of the response of the Antarctic ice sheet to the changing paleoclimate, and therefore, further understand what response is expected under the effects of future changes in climate.

The thesis has identified one, or two, oceanic processes as being of fundamental importance for sediment transport in each of the two chosen regions. Although the distinction of individual processes is beneficial for obtaining fundamental knowledge and insights, the ocean environment is not quite so simplistic. Quite often, shelves, Torres Strait being a good example, are strongly influenced by two or more processes which may interact non-linearly. The non-linear interactions between different tidal constituents and the combined effects of surface gravity waves and steady currents are well documented examples. Future studies of the oceanic processes influencing sedimentation should address these more complex interactions, in shelf regions which display a variety of influencing oceanic processes, but also consider the influence of differing biological and geological characteristics.

References

Adamson, D. A. and Pickard, J. (1986). Cainozoic history of the Vestfold Hills. In Pickard, J., editor, *Antarctic Oasis. Terrestrial environments and hiistory of the Vestfold Hills*, pages 63–93. Academic Press, Sydney.

Alley, R. B., Blankenship, D. D., Rooney, S. T., and Bentley, C. R. (1989). Sedimentation beneath ice shelves - the view from ice stream B. *Marine Geology*, 85:101–120.

Allison, I. (1979). The mass budget of the Lambert Glacier drainage basin, Antarctica. *Journal of Glaciology*, 22:223–235.

Alongi, D. M., Christoffersen, P., Tirendi, F., and Robertson, A. I. (1992). The influence of freshwater and material export on sedimentary facies and benthic processes within the Fly Delta and adjacent Gulf of Papua (Papua New Guinea). *Cont. Shelf Res.*, 12(2):287–326.

Amin, M. (1978). A statistical analysis of storm surges in Torres Strait. *Australian Journal of Marine and Freshwater Research*, 29:479–496.

Anderson, J. B. (1999). *Antarctic Marine Geology*. Cambridge University Press, 289 pp.

Anderson, J. B., Bartek, L. R., and Thomas, M. A. (1991a). Seismic and sedimentological record of glacial events on the Antarctic Peninsula shelf. In Thomson, M. R. A., Crame, J. A., and Thomson, J. W., editors, *Geological evolution of Antarctica*, pages 687–691. Cambridge University Press, Cambridge.

Anderson, J. B., Brake, C., Domack, E. W., Myers, N., and Sing (1984). Sedimentary dynamics on the continental shelf. In Oliver, R., James, P., and Jago, J., editors, *Antarctic Earth Science*.

Anderson, J. B., Brake, C., Domack, E. W., Myers, N., and Wright, R. (1983). Development of a polar, glacial-marine sedimentation model from Antarctic Quaternary deposits and

glaciological information. In Molnia, B. F., editor, *Glacial-marine sedimentation*, pages 233–264. Plenum, New York.

Anderson, J. B., Kennedy, D. S., and Smith, M. (1991b). Sedimentary facies associated with Antarctica's floating ice masses. In Anderson, J. and Ashley, G., editors, *Glacial Marine sedimentation; paleoclimatic significance*, pages 1–25. Geological Society of America, Boulder CO. GSA Special Paper 261.

Anderson, J. B. and Kurtz, D. (1985). The use of silt grain size parameters as a paleovelocity gauge: A critical review and case study. *Geo-Marine Letters*, 5:55–59.

Anderson, J. B., Kurtz, D., Domack, E. W., and Balshaw, K. M. (1980). Glacial and glacial marine sediment on the Antarctic continental shelf. *Journal of Glaciology*, 88:399–414.

Anderson, J. B. and Molnia, B. F. (1989). Glacial marine sedimentation. Short course in geology 9, Washington D.C., American Geophysical Union.

Andrewartha, J. R. and Walker, S. J. (1997). Boags rocks environmental impact assessment program task 6.4: Hydrodynamic modeling study, preliminary report. Technical report No. OMR-96/107, CSIRO Division of Marine Research.

Andrewartha, J. R. and Walker, S. J. (1999). North west shelf modelling project preliminary report. Technical report No. OMR-123/122, CSIRO Marine Research.

Andrews, J. C. and Clegg, S. (1989). Coral Sea circulation and transport deduced from modal information models. *Deep-Sea Research*, 36:957–974.

Andrews, J. T., Domack, E. W., Cunningham, W. L., Leventer, A., Licht, K. J., Jull, A. J. T., DeMaster, D., and Jennings, A. E. (1999). Problems and possible solution concerning radiocrabon dating of surface marine sediments, Ross Sea, Antarctica. *Quaternary Research*, 52:206–216.

Andrews, J. T. and Matsch, C. L. (1983). *Glacial marine sediments and sedimentation, and anotated bibliography.* Geo Abstracts, Norwich, 227 pp.

Armand, L. K. (1997). *The use of diatom transfer functions in estimating sea-surface temperature and sea-ice in cores from the southeast Indian Ocean.* PhD thesis, Australian National University, Canberra.

Australian Hydrographic Office (1999). *Australian National Tide Tables.* Australian Government Publishing Service, Canberra, 394 pp.

Bagnold, R. A. (1966). An approach of sediment transport model from general physics. *USGS Prof. Paper*, 422(1).

Barrett, P. J., Elston, D. P., Harwood, D. M., McKelvey, B. C., and Webb, P. N. (1987). Mid-Cenozoic record of glaciation and sea level change on the margin of the Victoria Land Basin, Antarctica. *Geology*, 15(7):634–637.

Barron, J. (1985). Miocene to Holocene plankton diatoms. In Bolli, H., Saunders, J., and Perch-Nielsen, K., editors, *Plankton Stratigraphy*, pages 763–809. Cambridge University Press, Cambridge.

Beckmann, A. and Haidvogel, D. (1993). Numerical simulation of flow around a tall isolated seamount. *J. Phys. Oceanogr.*, 23:1736–1753.

Berkman, P. A., Andrews, J. T., Bjorck, S., Colhoun, E., Emslie, S. D., Goodwin, I. D., Hall, B. L., Hart, C. P., Hirakawa, K., Igarashi, A., Ingolfsson, O., Lopez-Martinez, J., Lyons, W. B., Mabin, M. C. G., Quilty, P. G., Taviani, M., and Yoshida, Y. (1998). Circum-Antarctic coastal environmental shifts during the Late Quaternary reflected by emerged marine deposits. *Antarctic Science*, 10(3):345–362.

Berkman, P. A. and Forman, S. L. (1996). Pre-bomb radiocarbon and the resevoir correction for calcareous marine species in the Southern Ocean. *Geophysical Research Letters*, 23(4):363–366.

Bindoff, N. (2002). Unpublished Data. Antarctic Co-operative Research Centre, Hobart.

Bleck, R., Rooth, C., Hu, D., and Smith, L. (1992). Salinity driven thermocline transients in a wind-forced and thermohaline forced isopycnic coordinate model. *J. Phys. Oceanogr.*, 22:1486–1505.

Blumberg, A. F. and Herring, J. (1987). Circulation modelling using orthogonal curvilinear coordinates. In Nihoul and Jamart, editors, *Three-dimensional models of marine and estuarine dynamics*. Elsevier.

Blumberg, A. F. and Mellor, G. L. (1987). A description of a three-dimensional coastal ocean circulation model. In Heaps, N., editor, *Three-dimensional Coastal Ocean Models*, pages 1–16. American Geophysical Union, Washinton, D.C.

Bode, L. and Mason, L. B. (1994). Tidal modelling in Torres Strait and the Gulf of Papua. In Choat, J. H., Bellwood, O., and Saxena, N., editors, *Recent Advances in in*

Marine Science and Technology, 95. Proceedings of the PACON Symposium (July 1994). Townsville, Australia., pages 55–65.

Bombosch, A. and Jenkins, A. (1995). Modelling the formation and deposition of frazil ice beneath Filchner-Ronne Ice Shelf. *J. Geophys. Res.*, 100:6983–6992.

Bowden, F. K. and Hamilton, P. (1975). Some experiments with a numerical model of circulation and mixing in a tidal estuary. *Estuarine and Coastal Marine Science*, 3:281–301.

Brady, H. T. (1983). Interpretation of sediment cores from the Ross Ice Shelf site J-9, Antarctica. *Nature*, 303:510–512.

Bryan, K. (1969). A numerical method for the study of the circulation of the world ocean. *Journal of Computational Physics*, 4:347–376.

Budd, W. F. (1966). The dynamics of the Amery Ice Shelf. *J. Glac.*, 6(45):335–358.

Budd, W. F., Landon-Smith, I., and Wishart, E. (1967). The Amery Ice Shelf. In *Physics of snow and ice: International conference on low temperature science, 1966. Proceedings 1 (2)*, pages 447–467. Sapporo, Hokkaido University. Institute of Low Temperature Science.

Burckle, L. (1972). Diatom evidence bearing on the Holocene in the South Atlantic. *Quaternary Research*, 2:323–326.

Bureau of Meteorology (2002). Bureau of Meteorology WWW page. *http://www.bom.gov.au*.

Carey, S. W. and Ahmed, N. (1961). Glacial marine sedimentation. In *Proceedings of the first International symposium on Arctic Geology*, volume 2, pages 865–894. University of Toronto Press, Toronto, Ont.

Chapman, D. C. (1985). Numerical treatment of cross-shelf open boundaries in a barotropic coastal ocean model. *J. Phys. Oceanogr.*, 15:1060–1075.

Chappel, J., Chivas, A. amd Wallensky, E., Poloch, H. A., and Aharon, P. (1983). Holocene paleo-environmental changes, central to north Great Barrier Reef inner zone. *Journal of Australian Geology and Geophysics*, 8:223–236.

Christofferson, J. B. and Jonsson, I. G. (1985). Bed friction and dissipation in a combined current and wave motion. *Ocean Engineering*, 12(5):387–423.

Church, J. A. and Forbes, A. M. G. (1981). Non-linear model of the tides in the Gulf of Carpentaria. *Australian Journal of Marine and Freshwater Research*, 32:685–697.

Clough, J. W. and Hansen, B. L. (1979). The Ross Ice Shelf Project. *Science*, 203:433–434.

Cox, M. D. (1984). A primitive equation, 3-dimensional model of the ocean. GFDL ocean group technical report 1, Princeton University, Princeton, New Jersey.

Craven, M., Brand, R., Elchiekh, A., Jones, A., Thost, D., and Donoghue, S. (2002). AMISOR-3 2001-02 Hot water drill - Second scientifically instrumented borehole. Technical report, Antarctic CRC. Hobart, Tasmania, 55 pp.

Craven, M., Brand, R., Elchiekh, A., Jones, N., Baldwin, R., and Hemer, M. (2001). AMISOR-2 2000-01 Hot water drill - First scientifically instrumented borehole. Technical report, Antarctic CRC. Hobart, Tasmania, 62 pp.

Cremer, H. (1999). Distribution patterns of diatom surface sediment assemblages in the Laptev Sea (Arctic Ocean). *Marine Micropaleontology*, 38:39–67.

Crowley, T. J. (1996). Remembrance of things past: Greenhouse lessons from the geologic record. *Consequences*, 2(1):1–13.

Csanady, G. T. (1982). *Circulation in the Coastal Ocean*. D. Reidel Publishing company, 277 pp.

Cunningham, W. L. and Leventer, A. (1998). Diatom assemblages in surface sediments of the Ross Sea: Relationship to present oceanographic conditions. *Antarctic Science*, 10(2):134–146.

Cunningham, W. L., Leventer, A., Andrews, J. T., Jennings, A. E., and Lickt, K. (1999). Late Pleistocene-Holocene marine conditions in the Ross Sea, Antarctica: Evidence from the diatom record. *The Holocene*, 9:129–139.

Davies, A. G. (1985). Field observations of the threshold of sediment motion by wave action. *Sedimentology*, 32:685–704.

Determann, J. and Gerdes, R. (1994). Melting and freezing beneath ice shelves: implications from a three-dimensional ocean-circulation model. *Annals of Glaciology*, 20:413–419.

Dieckmann, G., Rohardt, G., Hellmer, H., and Kipfstuhl, J. (1986). The occurence of ice platelets at 250 m depth near the Filchner Ice Shelf and its significance for sea ice biology. *Deep. Sea Res.*, 33:141–148.

Doake, C. S. M. (1976). Thermodynamics of the interaction between ice shelves and the sea. *Polar Rec*, 18:37–41.

Doake, C. S. M. (1978). Dissipation of tidal energy by Antarctic ice shelves. *Nature*, 275:304–305.

Domack, E., Jull, A., and Donahue, D. (1991). Holocene chronology for the unconsolidated sediments at hole 740a: Prydz Bay, East Antarctica. *Proceedings of the Ocean Drilling Program, Scientific Results*, 119:727–750.

Domack, E., O'Brien, P., Harris, P., Taylor, F., Quilty, P. G., De Santis, L., and Raker, B. (1998). Late Quaternary sediment facies in Prydz Bay, East Antarctica and their relationship to glacial advance onto the continental shelf. *Antarctic Science*, 10(3):236–246.

Domack, E. W. and Harris, P. T. (1998). A new depositional model for ice shelves, based upon sediment cores from the Ross Sea and the Mac. Roberson shelf, Antarctica. *Annals of Glaciology*, 27:281–284.

Domack, E. W., Ishman, S. E., Stein, A. B., McClennen, C. E., and Jull, A. J. T. (1995). Late Holocene advance of the Muller Ice Shelf, Antarctic Peninsula: sedimentological, geochemical and palaeontological evidence. *Antarctic Science*, 7(2):159–170.

Drewry, D. J. and Cooper, A. P. R. (1981). Processes and models of Antarctic glaciomarine sedimentation. *Annals of Glaciology*, 2:117–122.

Dunbar, R. B., Anderson, J. B., Domack, E. W., and Jacobs, S. S. (1985). Oceanographic influences on the sedimentation along the Antarctic continental shelf. In Jacobs, S., editor, *Oceanology of the Antarctic Continental Shelf*, volume 11, pages 78–91. AGU.

Dyer, K. R. (1986). *Coastal and Estuarine Sediment Dynamics*. John Wiley and Sons, 342 pp.

Dyer, K. R. (1989). Sediment processes in estuaries: future research requirements. *J. Geophys. Res.*, 94:14327–14339.

Eicken, H., Oerter, H., Miller, H., Graf, W., and Kipfstuhl, J. (1994). Textural characteristics and impurity content of meteoric and marine ice in the Ronne Ice Shelf. *J. Glaciol.*, 40:386–398.

El-Sayed, S. Z. (1971). Observations on phytoplankton bloom in the Weddell Sea. *Antarctic Research Series*, 17:301–312.

Emery, W. J. and Thomson, R. E. (1998). *Data Analysis Methods in Physical Oceanography.* Pergamon Press, 634 pp.

Engelhardt, H. and Determann, J. (1987). Borehole evidence for a thick layer of basal ice in the central Ronne Ice Shelf. *Nature*, 327:318–319.

Eyles, C. H., Eyles, N., and Miall, A. D. (1985). Models of glaciomarine sedimentation and their application to the interpretation of ancient glacial sequences. *Palaeogeography, Palaeoclimatology and Palaeoecology*, 51:15–84.

Fearnhead, P. G. (1975). On the formation of fronts by tidal mixing around the British Isles. *Deep. Sea Res.*, 22:311–321.

Fenton, J. D. (1990). Nonlinear wave theories. In Le Mehaute, B. and Hanes, D., editors, *The Sea*, volume 9 of *The Sea*, pages 3–26. Wiley-Interscience, New York.

Flater, D. (1999). Harmonic tide clock and tide calculator. *http://www.flaterco.com/xtide/.*

Fofonff, P. and Millard, R. J. (1983). UNESCO 1983. algorithms for computation of fundamental properties of seawater. *UNESCO Technical Paper of Marine Science*, 44:1–53.

Foldvik, A., Gammelsrod, E., Nygaard, E., and Osterhus, S. (2001). Current measurements near Ronne Ice Shelf: Implications for circulation and melting. *J. Geophys. Res.*, 106:4463–4477.

Foldvik, A., Gammelsrod, T., and Torresen, T. (1985a). Circulation and Water Masses on the southern Weddell Sea shelf. In Jacobs, S., editor, *Oceanology of the Antarctic Continental Shelf*, volume 11, pages 5–20. AGU.

Foldvik, A. and Kvinge, T. (1974). Conditional instability of sea water at the freezing point. *Deep Sea Research*, 21:169–174.

Foldvik, A., Kvinge, T., and Torresen, T. (1985b). Bottom currents near the continental shelf break in the Weddell Sea. In Jacobs, S., editor, *Oceanology of the Antarctic Continental Shelf*, volume 11, pages 21–34. AGU.

Franklin, D. (1997). *The sedimentology of Holocene Prydz Bay: Sedimentary patterns and processes.* PhD thesis, University of Tasmania.

Fricker, H. A., Allison, I., Craven, M., Hyland, G., Ruddell, A., Young, N. W., Coleman, R., King, M., Krebs, K., and Popov, S. (2002). Redefinition of the grounding zone of the Amery Ice Shelf, East Antarctica. *J. Geophys. Res.*, 107(B5):10.1029/2001JB000383.

Fricker, H. A. and Padman, L. (2002). Tides on Filchner-Ronne Ice Shelf from ERS radar altimetry. *Geophysical Research Letters*, 29(12):501–504.

Fricker, H. A., Popov, S., Allison, I., and Young, N. (2001). Distribution of marine ice beneath the Amery Ice Shelf. *Geophysical Research Letters*, 28(11):2241–2244.

Fryxell, G. (1977). *Thalassiosira australis* peragallo and *T. lentiginosa* (janish) g. fryxell, comb. nov: two Antarctic diatoms (bacillariophyceae). *Phycologia*, 16:95–104.

Gerdes, R., Determann, R., and Grosfeld, K. (1999). Ocean circulation beneath Filchner-Ronne Ice Shelf from three-dimensional model results. *J. Geophys. Res.*, 104:15827–15842.

Gersonde, R. and Wefer, G. (1987). Sedimentation of biogenic siliceous particles in Antarctic waters from the Atlantic sector. *Marine Micropaleontology*, 11:311–332.

Gill, A. E. (1982). *Atmosphere-Ocean Dynamics*. Academic Press.

Gleitz, M., Grossman, S., Scharek, R., and Smetacek, V. (1996). Ecology of diatom and bacterial assemblages in water associated with melting summer sea ice in the Weddell Sea, Antarctica. *Antarctic Science*, 8:135–146.

Grant, W. D. and Madsen, O. S. (1979). Combined wave and current interaction with a rough bottom. *J. Geophys. Res.*, 84(4):1797–1808.

Grant, W. D. and Madsen, O. S. (1986). The continental shelf bottom boundary layer. *Ann. Rev. Fluid Mech.*, 18:265–305.

Greenslade, D. (2001). Unpublished Data. Bureau of Meteorology, Melbourne.

Greisman, P. (1979). On upwelling driven by melt of ice shelves and tidewater glaciers. *Deep Sea Research., Part A*, 26:1051–1065.

Griffies, S. M., Boning, C., Bryan, F. O., Chassignet, E. P., Gerdes.R., Hasumi, H., Hirst, A., Treguier, A.-M., and Webb, D. (2000). Developments in ocean climate modelling. *Ocean Modelling*, 2:123–192.

Grosfeld, K. and Gerdes, R. (1998). Circulation beneath the Filchner Ice Shelf, Antarctica, and its sensitivity to changes in the oceanic environment: a case study. *Annals Glac.*, 27:99–104.

Grosfeld, K., Gerdes, R., and Determann, J. (1997). Thermohaline circulation and interaction between ice shelf cavities and adjacent open ocean. *J. Geophys. Res.*, 102:15595–15610.

Haase, G. M. (1986). Glaciomarine sediments along the Filchner/Ronne Ice Shelf, Southern Weddell Sea - First results of the 1983/84 Antarktis-ii/4 expedition. *Mar. Geol.*, 72:241–258.

Hambrey, M. J. (1994). *Glacial Environments*. UCL Press, London, 271 pp.

Hambrey, M. J., Ehrmann, W. U., and Larsen, B. (1991). Cenozoic glacial record of the Prydz Bay continental shelf, East Antarctica. *Proceedings of the Ocean Drilling Program, Scientific Results*, 119:77–132.

Haney, R. L. (1991). On the pressure gradient force over steep topography in sigma coordinate ocean models. *J. Phys. Oceanogr.*, 21:610–619.

Hardisty, J. (1983). An assessment and calibration of formulations for Bagnolds bedload equation. *Journal of Sedimentary Petrology*, 53(3):1007–1010.

Harris, P. T. (1988). Sediments, bedforms and bedload transport pathways on the continental shelf adjacent to Torres Strait, Australia-Papua New Guinea. *Cont. Shelf Res.*, 8(8):979–1003.

Harris, P. T. (1989). Sandwave movement under tidal and wind-driven currents in a shallow marine environment: Adolphus Channel, northeastern Australia. *Cont. Shelf Res.*, 9:981–1002.

Harris, P. T. (1991). Reversal of subtidal dune asymmetries caused by seasonally reversing wind-driven currents in Torres Strait, northeastern Australia. *Cont. Shelf Res.*, 11(7):655–662.

Harris, P. T. (1993). Near-bed current measurements from Torres Strait obtained during January-March 1993 aboard RV Southern Surveyor. Technical Report 29, Ocean Sciences Institute, University of Sydney, 68 pp.

Harris, P. T. (1994a). Comparison of tropical, carbonate and temperate, siliclastic tidally dominated sedimentary deposits: Examples from the Australian continental shelf. *Aust. J. Earth Sc.*, 41:241–254.

Harris, P. T. (1994b). Muddy Waters: The Physical Sedimentology of Torres Strait. In Choat, J. H., Bellwood, O., and Saxena, N., editors, *Recent Advances in Marine Science and Technology, 95. Proceedings of the PACON Symposium (July 1994). Townsville, Australia.*, pages 149–160.

Harris, P. T. (1995). Marine geology and sedimentology of the Australian continental shelf. In Zann, L. P. and Kailola, P., editors, *The state of the marine environment report for Australia. Technical annex: 1*, pages 11–23. Department of the Envionment, Sport and Territories, Canberra.

Harris, P. T. (1999). Environmental management of Torres Strait: A marine geologist's perspective. In Gostin, V. A., editor, *Gondwana to Greenhouse: environmental geoscience - an Australia perspective*.

Harris, P. T. (2000a). Ripple cross-laminated sediments on the East Antarctic shelf: evidence for episodic bottom water production during the Holocene? *Marine Geology*, 170(3-4):317–330.

Harris, P. T. (2000b). Sedimentological signatures of sub-ice-shelf circulation: An example from Vincennes Bay, East Antarctica. *Proc. Royal Society of Tasmania*, 133(3):57–62.

Harris, P. T. (2002). Unpublished Data. Antarctic CRC and Geoscience Australia, Hobart.

Harris, P. T. and Baker, E. K. (1991). The nature of sediments forming the Torres Strait turbidity maximum. *Australian Journal of Earth Sciences*, 38:65–78.

Harris, P. T., Baker, E. K., Cole, A. R., and Short, S. A. (1993). A preliminary study of sedimentation in the tidally dominated Fly River Delta, Gulf of Papua. *Cont. Shelf Res.*, 13(4):441–472.

Harris, P. T., Brancolini, G., Armand, L., Busetti, M., Beaman, R. J., Giorgetti, G., Presti, M., and Trincardi, F. (2001a). Continental shelf drift deposit indicates non-steady state Antarctic Bottom Water production in the Holocene. *Marine Geology*, 179(1-2):134–138.

Harris, P. T., Heap, A., Passlow, V., Hughes, M., Porter-Smith, R., Beaman, R., Hemer, M., Daniell, J., Buchanan, C., Collins, D., Bleakley, N., and Anderson, O. (2002). Cross-shelf sediment transport in the Torres Strait-Gulf of Papua region. RV Franklin Cruise 01/02, Jan-Feb 2002. Geoscience Australia cruise 234. Technical report, Geoscience Australia, 108 pp.

Harris, P. T. and O'Brien, P. E. (1996). Geomorphology and sedimentology of the continental shelf adjacent to Mac. Robertson Land, East Antarctica: A scalped shelf. *Geo-Marine Letters*, 16:287–296.

Harris, P. T. and O'Brien, P. E. (1998). Bottom currents, sedimentation and ice-sheet retreat facies successions on the Mac Robertson Shelf, East Antarctica. *Marine Geology*, 151:47–72.

Harris, P. T., O'Brien, P. E., Sedwick, P., and Truswell, E. M. (1996a). Late Quaternary history of sedimentation on the Mac-Robertson Shelf, East Antarctica: problems with ^{14}C dating of marine sediments. *Papers and Proceedings of the Royal Society of Tasmania*, 130:47–53.

Harris, P. T., Pattiaratchi, C. B., Keene, J. B., Dalrymple, R. W., Gardner, J. V., Baker, E. K., Cole, A. R., Mitchell, D., Gibbs, P., and Schroeder, W. W. (1996b). Late Quaternary deltaic and carbonate sedimentation in the Gulf of Papua foreland basin: Response to sea-level change. *Journal of Sedimentary Research*, 66(4):801–819.

Harris, P. T., Porter-Smith, R., Anderson, O., Coleman, R., and Greenslade, D. (2001b). GEOMAT -Modelling of continental shelf sediment mobility in support of Australia's regional marine planning process. AGSO Record Number 2000/41, Australia Geological Survey Organisation, 37 pp.

Harris, P. T., Taylor, F., Pushina, Z., Leitchenkov, G., O'Brien, P. E., and Smirnov, V. (1999). Lithofacies distribution in relation to the geomorphic provinces of Prydz Bay. East Antarctica. *Antarctic Science*, 10(3):227–235.

Harwood, D. M., Scherer, R. P., and Webb, P. N. (1989). Multiple Miocene marine productivity events in West Antarctica as recorded in upper Miocene sediments beneath the Ross Ice Shelf (site J-9). *Marine Micropalaeontology*, 15:91–115.

Hasle, G. and Heimdal, B. (1968). Morphology and distribution of the marine centric diatom *Thalassiosira antarctica* comber. *Journal of the Royal Microscopy Society*, 88(3):357–369.

Hellmer, H. H. and Jacobs, S. S. (1992). Ocean interactions with the base of the Amery Ice Shelf, Antarctica. *J. Geophys. Res.*, 97:20305–20317.

Hellmer, H. H. and Jacobs, S. S. (1995). Seasonal circulation under the eastern Ross Ice Shelf, Antarctica. *J. Geophys. Res.*, 100:10873–10885.

Hellmer, H. H. and Olbers, D. J. (1989). A two-dimensional model for the thermohaline circulation under an ice shelf. *Antarctic Science*, 1:325–336.

Hellmer, H. H. and Olbers, D. J. (1991). On the thermohaline circulation beneath the Filchner-Ronne Ice Shelves. *Antarctic Science*, 3(4):433–442.

Hemer, M. A. and Harris, P. T. (2003). Sediment core from beneath the Amery Ice Shelf, East Antarctica, suggests mid-Holocene ice-shelf retreat. *Geology*.

Hemer, M. A., Harris, P. T., Coleman, R., and Hunter, J. (2003). Sediment mobility due to currents and waves in the Torres Strait - Gulf of Papua region. *Cont. Shelf Res.*

Hodgkinson, R. P., Colman, R. S., Kerry, K. R., and Robb, M. S. (1988). Water currents in Prydz Bay, Antarctica, during 1985. Australian National Antarctic Research Expedition notes 59, Australian Antarctic Division, Kingston Tasmania, Australia.

Hodgkinson, R. P., Colman, R. S., Robb, M. S., and Williams, R. (1991a). Current meter moorings in the region of Prydz Bay, Antarctica, 1986. Australian National Antarctic Research Expedition notes 81, Australian Antarctic Division, Kingston Tasmania, Australia.

Hodgkinson, R. P., Colman, R. S., Robb, M. S., and Williams, R. (1991b). Current meter moorings in the region of Prydz Bay, Antarctica, 1987. Australian National Antarctic Research Expedition notes 82, Australian Antarctic Division, Kingston Tasmania, Australia.

Hogan, P. J. and Hurlburt, H. E. (2002). Sensitivity of simulated circulation to surface wind forcing in the Japan/East Sea. *Deep. Sea Res.*

Holdsworth, G. (1977). Tidal interaction with ice shelves. *Annals Glac.*, 33(1):133–146.

Holland, D. and Jenkins, A. (1999). Modeling thermodynamic ice-ocean interactions at the base of an ice shelf. *J. Phys. Oceanogr.*, 29:1787–1800.

Holland, D. and Jenkins, A. (2001). Adaptation of an isopycnic coordinate ocean model for the study of circulation beneath ice shelves. *Monthly Weather Review*, 129:1905–1927.

Horner, R. A. (1985). Ecology of sea ice microalgae. In Horner, R., editor, *Sea-Ice Biota*, pages 83–103. CRC Press, Boca-Raton.

Huang, T. C. and Watkins, N. D. (1977). Contrasts between the Brunhes and Matuyama sedimentary records of bottom water activity in the South Pacific. *Marine Geology*, 23:113–132.

Hunter, J. (2002). *OzPOM*: A version of the princeton ocean model. *http://www.antcrc.utas.edu.au/ johunter/ozpom.html*.

Hurd, D. (1972). Factors affecting solution rate of biogenic opal in seawater. *Earth and Planetary Science Letters*, 15:411–417.

Ingolfsson, O., Hjort, C., Berkman, P. A., Bjorck, S., Colhoun, E. A., Goodwin, I. D., Hall, B. L., Hirakawa, K., Melles, M., Moller, P., and Prentice, M. L. (1998). Antarctic glacial history since the Last Glacial Maximum: an overview of the record on land. *Antarctic Science*, 10(3):326–344.

IPCC (1990). *Climate Change: The IPCC Scientific Assessment.* Cambridge University Press, Cambridge, U.K. Houghton, J., Jenkins, G. and Ephraums, J. (eds.), 364 pp.

Jacobs, S. S. (1989). Marine controls on modern sedimentation on the Antarctic continental shelf. *Marine Geology*, 85:121–153.

Jacobs, S. S., Amos, A. F., and Bruchhausen, P. M. (1970). Ross Sea oceanography and Antarctic Bottom Water formation. *Deep. Sea Res.*, 17:935–962.

Jacobs, S. S., Gordon, A. F., and Ardai, J. L. (1979). Circulation and melting beneath the Ross Ice Shelf. *Science*, 203:439–443.

Jacobs, S. S., Hellmer, H. H., Doake, C. S. M., Jenkins, A., and Frolich, R. M. (1992). Melting of ice shelves and the mass balance of Antarctica. *Journal of Glaciology*, 38:375–387.

Jenkins, A. (1991). A one dimensional model of ice shelf-ocean interaction. *J. Geophys. Res.*, 96:20671–20677.

Jenkins, A. and Bombosch, A. (1995). Modelling the effects of frazil ice crystals on the dynamics and thermodynamics of ice shelf water plumes. *J. Geophys. Res.*, 100:6967–6981.

Jenkins, A. and Holland, D. (2002). A model study of ocean circulation beneath Filchner-Ronne Ice Shelf, Antarctica: Implications for bottom water formation. *Geophysical Research Letters*, 29(8):341–344.

Johnson, M. A., Kenyon, N. H., Belderson, R. H., and Stride, A. H. (1982). Sand Transport. In Stride, A. H., editor, *Offshore tidal sands: process and product*, pages 58–94. Chapman and Hall, London.

Jonsson, I. G. (1966). Wave boundary layers and friction factors. In *Proceedings of the 10th Conference on Coastal Engineering, ASCE, Tokyo*, volume 1, pages 127–148.

Kalnay, E., Kanamitsu, M., Kistler, R., Collins, W., Deaven, D., Gandin, L., Iredell, M., Saha, S., White, G., Woollen, J., Zhu, Y., Chelliah, M., Ebisuzaki, W., Higgins, W., Janowiak, J., Mo, K. C., Ropelewski, C., Wang, J., Leetmaa, A., Reynolds, R., Jenne, R., and Joseph, D. (1996). The NCEP/NCAR 40-Year Reanalysis Project. *Bulletin of the American Meteorological Society*, 77(3):437–471.

Kellogg, T. and Truesdale, R. (1979). Late Quaternary paleoecology and paleoclimatology of the Ross Sea: the diatom record. *Marine Micropaleontology*, 4:137–158.

Kellogg, T. B. and Kellogg, D. E. (1981). Pleistocene sediments beneath the Ross Ice Shelf. *Nature*, 293:130–133.

Kellogg, T. B. and Kellogg, D. E. (1983). Interpretation of sediment cores from the Ross Ice Shelf site J-9, Antarctica - Reply. *Nature*, 303:511–513.

Kellogg, T. B. and Kellogg, D. E. (1986). Diatom biostratigraphy of sediment cores beneath the Ross Ice Shelf. *Micropalaeontology*, 32:74–79.

Kellogg, T. B. and Kellogg, D. E. (1988). Antarctic cryogenic sediments; biotic and inorganic facies of ice shelf and marine-based ice sheet environments. *Palaeogeography,Plaeoclimatology,Palaeoecology*, 67:51–74.

Kennedy, D. S. and Anderson, J. B. (1989). Quaternary glacial history of Marguerite Bay, Antarctic Peninsula. *Quaternary Research*, 31:375–387.

King, M. A. (2002). *The dynamics of the Amery Ice Shelf from a combination of terrestrial and space geodetic data*. PhD thesis, University of Tasmania.

Knight, R. J. and McLean, J. R. (1986). *Shelf Sands and Sandstones*. Canadian Society of Petroleum Geologists, Calgary, 347 pp.

Kolobov, D. D. and Savatyugin, L. M. (1983). Bottom sediments under the Novolazarevskiy Ice Shelf. *Polar Geography and Geology*, 6:267–271.

Kozlova, A. P. (1966). *Diatom algae of Indian and Pacific sectors of Antarctica*. Academy of Sciences of the USSR Institute of Oceanology, Moscow, 191 pp.

Kozlova, O. and Mukhina, V. (1967). Diatoms and silicoflagellates in suspension and floor sediments of the Pacific Ocean. *International Geology*, 9(10):1322–1342.

Krebs, K. J., Lipps, J., and Burckle, J. (1987). Ice diatom flora. Arthur Harbor, Antarctica. *Polar Biology*, 7:163–171.

Large, W. G. and Pond, S. (1981). Open ocean momentum flux measurements in moderate to strong winds. *J. Phys. Oceanogr.*, 11:324–336.

Le Provost, C., Genco, M., and Lyard, F. (1995). Modeling and predicting tides over the World Ocean. In *Quantitative skill assessment for coastal ocean models*, pages 175–201. American Geophysical Union.

LeBlond, P. H. and Mysak, L. A. (1978). *Waves in the Ocean.* Elsevier, 602 pp.

Lefevre, F., Lyard, F. H., and Le Provost, C. (2000). FES98: A new global tide finite element solution independent of altimetry. *Geophysical Research Letters*, 27(17):2717–2721.

Leffanue, H. (2002). Unpublished Data. Flinders University of South Australia, Adelaide.

Leventer, A. (1992). Modern distributions of diatoms in sediments from the George V Coast, Antarctica. *Marine Micropaleontology*, 19:315–332.

Leventer, A., Domack, E. W., Ishman, S. E., Brachfeld, S., McClennen, C. E., and Manley, P. (1996). Productivity cycles of 200-300 years in the Antarctic Peninsula region: understanding linkages among the sun, atmosphere, oceans, sea-ice and biota. *GSA Bulletin*, 108(12):1626–1644.

Leventer, A. and Dunbar, R. (1986). Dissolution and transport of particulate silica, McMurdo Sound, Antarctica. *Antarctic Journal of the United States*, 21:134–137.

Leventer, A. and Dunbar, R. (1987). Surface sediment diatom assemblages, McMurdo Sound, Antarctica. *Antarctic Journal of the United States*, 22:194–196.

Leventer, A. and Dunbar, R. (1988). Recent diatom record of McMurdo Sound, Antarctica: implications for history of sea-ice extent. *Paleoceanography*, 3(3):259–274.

Leventer, A. and Dunbar, R. (1996). Factors influencing the distribution of diatoms and other algae in the Ross Sea. *J. Geophys. Res.*, 101(C8):18489–18500.

Leventer, A., Dunbar, R., and DeMaster, D. J. (1993). Diatom evidence for Late Holocene climatic events in Granite Harbor, Antarctica. *Palaeoceanography*, 8(3):373–386.

Leventer, A. and Harwood, D. (1993). The geological use of polar marine diatoms. *Workshop on Antarctic Glacial Marine and Biogenic Sedimentation. Notes for a Short Course. Part 2. Biogenic Sedimentation.*, pages 134–253.

Lewis, E. L. and Perkin, R. G. (1986). Ice pumps and their rates. *J. Geophys. Res.*, 91:11756–11762.

Lisitzin, A. (1971). Distribution of siliceous microfossils in suspension and in bottom sediments. In Funnell, B. and Riedel, W., editors, *The Micropalaeontology of Oceans*. Cambridge University Press, Cambridge.

Long, B., Skewes, T., Taranto, T., Thomas, M., Isdale, P., Pitcher, R., and Poiner, I. (1997). Seagrass dieback in north-western Torres Strait. Technical Report No. MR-GIS-97/6, CSIRO Division of Marine Research.

Lou, J. and Ridd, P. V. (1996). Modelling of suspended sediment transport in coastal areas under waves and currents. *Estuarine Coastal and Shelf Science*, 45:1–16.

Lythe, M. B., Vaughan, D. G., and the BEDMAP Consortium (2000). BEDMAP - bed topography of the Antarctic. 1:10,000,000 scale map. British Antarctic Survey (misc) 9. *http://www.antarctica.ac.uk/aedc/bedmap/*.

MacAyeal, D. R. (1984a). Numerical simulations of the Ross Sea Tides. *J. Geophys. Res.*, 89:607–615.

MacAyeal, D. R. (1984b). Thermohaline circulation below the Ross Ice Shelf: A consequence of tidally induced vertical mixing and basal melting. *J. Geophys. Res.*, 89:597–606.

Madsen, O. S. (1994). Spectral wave-current bottom boundary layer flows. In *Proceedings of the 24th International Conference on Coastal Engineering, ASCE, Kobe.*, pages 384–398.

Madsen, O. S. and Grant, W. D. (1976). Quantitative description of sediment transport by waves. In *Proceedings of the 15th International Conference on Coastal Engineering, ASCE*, volume 2, pages 1093–1112.

Makinson, K. and Nicholls, K. W. (1999). Modeling tidal currents beneath Filchner-Ronne Ice Shelf and on the adjacent continental shelf: their effect on mixing and transport. *J. Geophys. Res.*, 104:13449–13465.

Massom, R. A., Harris, P. T., Michael, K. J., and Potter, M. J. (1998). The distribution and formative processes of latent-heat polynyas in East Antarctica. *Annals Glac.*, 27:420–426.

Mathisen, P. P. and Madsen, O. S. (1993). Waves and currents over a fixed rippled bed 1. bottom roughness experienced in the presence and absence of currents. *J. Geophys. Res.*, 101(7):16533–16542.

McMinn, A. (1995). Comparison of diatom preservation between oxic and anoxic basins in Ellis Fjord, Antarctica. *Diatom Research*, 10:145–151.

Medlin, L. and Priddle, J. (1990). *Polar Marine Diatoms*. British Antarctic Survey, 214 pp.

Mellor, G. L. (1991). An equation of state for numerical models of oceans and estuaries. *Atmos. Oceanic Tech.*, 8:609–611.

Mellor, G. L. (2002). Users guide for a three-dimensional, primitive equation, numerical ocean model. Technical report, Program in Atmospheric and Oceanic Sciences, Princeton University.

Mellor, G. L. and Blumberg, A. F. (1985). Modelling vertical and horizontal diffusivities and the sigma-coordinate system. *Monthly Weather Review*, 113:1379–1383.

Mellor, G. L., Ezer, T., and Oey, L.-Y. (1994). The pressure gradient conundrum of sigma coordinate ocean models. *Journal of Atmospheric and Ocean Technology*, 11(2):1126–1134.

Mellor, G. L., Oey, L.-Y., and Ezer, T. (1998). Sigma coordinate pressure gradient errors and the seamount problem. *Journal of Atmospheric and Ocean Technology*, 15:1122–1131.

Mellor, G. L. and Yamada, T. (1974). A heirarchy of turbulence closure models for planetary boundary layers. *Journal of Atmospheric Science*, 31:1791–1896.

Mellor, G. L. and Yamada, T. (1982). Development of a turbulence closure model for geophysical fluid problems. *Reviews of Geophysics and Space Physics*, 20(4):851–875.

Melville, W. K. and Buchwald, V. T. (1976). Oscillations of the Gulf of Carpentaria. *J. Phys. Oceanogr.*, 4:83–90.

Mercer, J. H. (1978). West Antarctic CO_2 greenhouse effect; a threat of disaster. *Nature*, 271:321–325.

Middleton, J. and Humphries, S. (1989). Thermohaline structure and mixing in the region of Prydz Bay, Antarctica. *Deep. Sea Res.*, 38(8):1255–1266.

Millero, F. J. (1978). Annex 6: Freezing point of seawater. eighth report of the joint panel of oceanographic tables and standards. *UNESCO Technical Paper of Marine Science*, 28:29–31.

Mitchener, H. and Torfs, H. (1996). Erosion of mud/sand mixtures. *Coastal Engineering*, 29:1–25.

Molnia, B. F. (1983). *Glacial-Marine sedimentation*. Plenum Press, New York, 234 pp.

Morgan, V. T. (1972). Oxygen isotope evidence for bottom freezing on the Amery Ice Shelf. *Nature*, 238:393–394.

Mortlock, R. A. and Froelich, P. N. (1989). A simple method for the rapid determination of biogenic opal in pelagic marine sediments. *Deep Sea Res.*, 36:1415–1426.

Nakada, M. and Lambeck, K. (1989). Late Pleistocene and Holocene sea-level change in the Australian region and mantle rheology. *Geophysical Journal*, 96:497–517.

National Geophysical Data Center (1988). Data announcement 88-MGG-02, Digital relief of the Surface of the Earth. noaa, National Geophysical Data Center, Boulder, Colorado. *http://www.ngdc.noaa.gov/mgg/global/etopo5.HTML*.

National Geophysical Data Center (2001). NOAA, National Geophysical Data Center,Boulder. World Vector Shoreline. *http://rimmer.ngdc.noaa.gov/coast/*.

National Tidal Facility (2000). National Tidal Facility, Flinders University of South Australia. *http://www.ntf.flinders.edu.au*.

Nicholls, K. W. (1996). Temperature variability beneath Ronne Ice Shelf, Antarctica, from thermistor cables. *J. Geophys. Res.*, 101:1199–1210.

Nicholls, K. W. and Makinson, K. (1998). Ocean circulation beneath the western Ronne Ice Shelf, as derived from in situ measurements of water currents and properties. In Jacobs, S. and Weiss, R., editors, *Ocean, Ice and Atmosphere: Interactions at the Antarctic Continental Margin*, volume 75 of *Antarct. Res. Ser.*, pages 301–318. AGU, Washington, D.C.

Nicholls, K. W., Makinson, K., and Johnson, M. R. (1997). New oceanographic data from beneath the Ronne Ice Shelf. *Geophysical Research Letters*, 24:167–170.

Nicholls, K. W., Makinson, K., and Robinson, A. V. (1991). Ocean circulation beneath the Ronne Ice Shelf. *Science*, 203:439–443.

Nicholls, K. W., Osterhus, S., Makinson, K., and Johnson, M. R. (2001). Oceanographic conditions south of Berkner Island, beneath Filchner-Ronne Ice Shelf, Antarctica. *J. Geophys. Res.*, 106:11481–11492.

Nittrouer, C. A. and Wright, L. D. (1994). Transport of particles across continental shelves. *Reviews of Geophysics*, 32(1):85–113.

Nost, O. A. and Foldvik, A. (1994). A model of ice shelf ocean interaction with application to the Filchner-Ronne Ice Shelf and Ross Ice Shelves. *J. Geophys. Res.*, 99:14243–14254.

Nunez Vaz, R. A. and Lennon, G. W. (1996). Physical oceanography of the Prydz Bay region of Antarctic waters. *Deep. Sea Res.*, 43(5):603–641.

O'Brien, P. (1994). Morphology and late glacial history of Prydz Bay, Antarctica based on echo sounder data. *Terra Antarctica*, 1(2):403–405.

O'Brien, P. (2001). Unpublished Data. Geoscience Australia, Canberra.

O'Brien, P. and Harris, P. T. (1996). Patterns of glacial erosion and deposition in Prydz Bay and the past behaviour of the Lambert Glacier. *Papers and Proceedings of the Royal Society of Tasmania*, 130(2):79–85.

O'Brien, P. E., De Santis, L., Harris, P. T., Domack, E., and Quilty, P. G. (1999). Ice shelf grounding zone features of the Western Prydz Bay, Antarctica: Sedimentary processes from seismic and sidescan images. *Antarctic Science*, 11(1):78–91.

OBrien, P. E., Leitchenkov, G., and Harris, P. T. (1997). Iceberg plough marks, subglacial bedforms and grounding zone moraines in Prydz Bay, Antarctica. In Davies, T., Bell, T., Cooper, A., Josenhans, H., Polyak, L., Solheim, A., Stoker, M., and Stravers, J., editors, *Glaciated continental margins: an atlas of acoustic images*, pages 228–231. London, Chapman and Hall.

Oerter, H. J., Kipfstuhl, J., Determann, J., Miller, H., Wagenbach, D., Minikin, A., and Graf, W. (1992). Evidence for basal marine ice in the Filchner-Ronne Ice Shelf. *Nature*, 358:399–401.

Orheim, O. and Elverhoi, A. (1981). Model for submarine glacial deposition. *Annals Glac.*, 2:123–128.

Padman, L., Fricker, H. A., Coleman, R., Howard, S., and Erofeeva, L. (2002). A new tide model for the Antarctic Ice Shelves and Seas. *Annals Glac.*, 34:247–254.

Padman, L. and Kottmeier, C. (2000). High-frequency ice motion and divergence in the Weddell Sea. *J. Geophys. Res.*, 105:3379–3400.

Penrose, J. D., Conde, M., and Pauly, T. J. (1994). Acoustic detection of ice crystals in Antarctic waters. *J. Geophys. Res.*, 99:12573–12580.

Philips, O. M. (1977). *The dynamics of the Upper Ocean.* Cambridge University Press, 336 pp.

Phillips, N. A. (1957). A coordinate system having some special advantages for numerical forecasting. *Journal of Meteorology*, 14:184–185.

Pichon, J. J., Labeyrie, L., Baraeille, G., Labracherie, M., Duprat, J., and Jouzel, J. (1992). Surface water temperature changes in the high latitudes of the Southern Hemisphere over the last glacial-intergalcial cycle. *Paleoceanography*, 7(3):289–318.

Pillans, B. J. (1987). Quaternary sea-level changes: southern hemisphere data. In Devoy, R. J. N., editor, *Sea surface studies: A global view*, pages 264–293. Croom Helm, Kent, UK.

Pillsbury, R. D. and Jacobs, S. S. (1985). Preliminary observations from long term current meter mooring near the Ross Ice Shelf, Antarctica. In Jacobs, S., editor, *Oceanology of the Antarctic Continental Shelf*, volume 11, pages 87–107. AGU.

Pond, S. and Pickard, G. L. (2000). *Introductory Dynamical Oceanography.* Butterworth Heinemann, Oxford, 329 pp.

Porter-Smith, R. (2000). Unpublished Data. Geoscience Australia, Hobart.

Powell, R. D., Dawber, M., McInnes, J. N., and Pyne, A. R. (1996). Observations of the grounding-line area at a floating glacier terminus. *Annals Glac.*, 22:217–223.

Prandtl, L. (1945). Ueber ein neues formelsystem fuer die ausgebildete turbulenz. *Nachr. Akad. Wiss. Goettingen.*

Pudsey, C. J. (1992). Late quarternary changes in Antarctic bottom water velocity inferred from sediment grain size in the northern Weddell Sea. *Marine Geology*, 107:9–33.

Pudsey, C. J. and Evans, J. (2001). First survey of Antarctic sub-ice-shelf sediments reveals mid-Holocene ice shelf retreat. *Geology*, 29:79–91.

Quilty, P. G. (1985). Distributions of foraminiferids in sediments of Prydz Bay, Antarctica. *Special Publication: South Australian Department of Mines and Energy*, 5:329–340.

Raiswell, R. and Tan, M. (1985). Diagnesis of sediments from beneath the Ross Ice Shelf and their sedimentary history. *Nature*, 315:483–485.

Ray, R. D. and Egbert, G. D. (1997). The flux of tidal energy across latitude $60°s$. *Geophysical Research Letters*, 24(5):543–546.

Ridgway, K. R., Dunn, J. R., and Wilkin, J. D. (2001). Climatology of the waters around Australasia by 4-dimensional weighted least-squares fitting. *Subm. to J. Atmos. Ocean. Tech.*

Rignot, E. and Jacobs, S. S. (2002). Rapid bottom melting widespread near Antarctic Ice Sheet grounding lines. *Science*, 296:2020–2023.

Roache, P. J. (1976). *Computational Fluid Dynamics*. Hermosa Publisher, Alburquerque, N.M., 446 pp.

Robertson, R. A. L., Padman, L., and Egbert, G. D. (1998). Tides in the Weddell Sea. In Jacobs, S. and Weiss, R., editors, *Ocean, Ice and Atmosphere: Interactions at the Antarctic Continental Margin*, volume 75 of *Antarct. Res. Ser.*, pages 341–369. AGU, Washington, D.C.

Robin, G. d. Q. (1979). Formation, flow, and disintegration of ice shelves. *J. Glaciol*, 24:259–271.

Rosenberg, M., Bindoff, N. B., Curran, C., Helmond, I., Miller, K., McLaughlan, D., Church, J., Richman, J., and Leffanue, H. (2002). Amery ice shelf (AMISOR) marine science cruises au0106 and au0207 - oceanographic field measurements and analysis. Technical report, Antarctic CRC. Hobart, Tasmania, 34 pp.

Ruddell, A. (2001). Unpublished Data. Antarctic Co-operative Research Centre, Hobart.

Sancetta, C. (1989). Processes controlling the accumulation of diatoms in sediments: a model derived from British Columbian fjords. *Paleoceanography*, 4:235–251.

Sancetta, C. and Calvert, S. E. (1988). The annual cycle of sedimentation in Saanich Inlet, British Columbia: Implications for the interpretation of diatom fossil assemblages. *Deep. Sea Res.*, 35:71–90.

Schrader, H. (1971). Faecal pellets: role in sedimentation of pelagic diatoms. *Science*, 174:55–57.

Schumacher, J. D., Kinder, T. H., Pashinski, D. J., and Charnell, R. L. (1979). A structural front over the continental shelf of the eastern Bering Sea. *J. Phys. Oceanogr.*, 9:79–87.

Shanahan, M. (2002). Ocean circulation and ocean-ice shelf interaction at the front of the Amery Ice Shelf. Honours Thesis, IASOS, University of Tasmania, Hobart.

Smayda, T. J. (1970). The suspension and sinking of phytoplankton in the sea. *Oceanography and Marine Biology Annual Review*, 8:353–414.

Smetacek, V. (1985). Role of sinking in diatom life-history cycles: ecological, evolutionary and geological significance. *Marine Biology*, 84:239–251.

Smetacek, V., Scharek, R., Gordon, L. I., Eicken, H., Fahrback, E., Rohardt, G., and Moore, S. (1992). Early spring phytoplankton blooms in ice platelet layers of the southern Weddell Sea. *Deep. Sea Res.*, 39:153–168.

Smith, I. N., Budd, W. F., and Reid, P. (1998). Model estimates of Antarctic accumulation rates and their relationship to temperature changes. *Annals of Glaciology*, 27:246–250.

Smith, J. D. (1977). Modeling of sediment transport on continental shelves. In Goldberg, E. D., McCare, I. N., Obrien, J. J., and Steele, J. H., editors, *The Sea*, volume 6 of *The Sea*, pages 539–577. Wiley-Interscience, New York.

Smith, N. and Treguer, P. (1994). *Physical and Chemical Oceanography in the vicinity of Prydz Bay, Antarctica. Southern Ocean ecology: The BIOMASS perspective.* Cambridge University Press, Cambridge.

Smith, N. R., Zhaoqian, D., and Wright, S. (1984). Water masses and circulation in the region of Prydz Bay, Antarctica. *Deep. Sea Res.*, 31(9):1121–1147.

Smithson, M. J., Robinson, A. V., and Flather, R. A. (1996). Ocean tides under the Filchner-Ronne Ice Shelf, Antarctica. *Annals Glac.*, 23:217–225.

Smolarkiewicz, P. K. (1984). A fully multidimensional positive definite advection transport algorithm with small implicit diffusion. *Journal of Computational Physics*, 54:325–362.

Stagg, H. (1985). The structure and origin of Prydz Bay and Mac-Robertson Shelf, East Antarctica. *Tectonophysics*, 114:315–340.

Stockwell, D., Kang, S., and Fryxell, G. (1991). Comparisons of diatom biocoenoses with Holocene sediments in Prydz Bay, Antarctica. *Proceedings of the Ocean Drilling Program, Scientific Results*, 119:667–673.

Stride, A. H. (1982). *Offshore tidal sands: process and product.* Chapman and Hall, London, 276 pp.

Swift, D. J. P., Han, G., and Vincent, C. E. (1986). Fluid processes and sea-floor response on a modern storm-dominated shelf: middle Atlantic shelf of North America. Part 1:

The storm-current regime. In Knight, R. J. and McLean, J. R., editors, *Shelf Sands and Sandstones*, pages 99–119. Canadian Society of Petroleum Geologists, Calgary.

Swift, D. J. P. and Niedoroda, A. (1985). Fluid and sediment dynamics on continental shelves: Short course 13. In Tillman, R. W., Swift, D. J. P., and Walker, R. G., editors, *Shelf Sands and Sandstone resevoirs*, pages 47–133. Society of Economic Palaeontologists and Mineralogists.

Swift, D. J. P., Stanley, D. J., and Curray, J. R. (1971). Relict sediments on continental shelves: A reconsideration. *Jounal of Geology*, 79:322–346.

Taylor, F. (1999). *Sedimentary Diatom Assemblages of Prydz Bay*. PhD thesis, University of Tasmania, Hobart.

Taylor, F. and McMinn, A. (2002). Late Quaternary diatom assemblages from Prydz Bay, Eastern Antarctica. *Quaternary Research*, 57:151–161.

Taylor, F., McMinn, A., and Franklin, D. (1997). Distribution of diatoms in surface sediments of Prydz Bay, Antarctica. *Marine Micropalaeontology*, 32:209–229.

Thom, B. G. and Roy, P. S. (1983). Sea-level change in New South Wales over the past 15,000 years. In Hopley, D., editor, *Australian sea-levels in the past 15,000 years: A Review*, pages 64–84. James Cook University, Department of Geography, Townsville, Australia.

Treguer, P., Kamatani, A., Gueneley, S., and Queguiner, B. (1989). Kinetics of dissolution of Antarctic diatom frustules and the biogeochemical cycle of silicaon in the Southern Ocean. *Polar Biology*, 9:397–403.

Vanney, J. R. and Johnson, G. L. (1985). Gebco Bathymetric sheet 5.18 (Circum-Antarctic. In Jacobs, S., editor, *Oceanology of the Antarctic Continental Shelf*, volume 11 of *Antarct. Res. Ser.*, pages 291–312. AGU, Washington, D. C.

Vaughan, D. G. (1995). Tidal flexure at ice shelf margins. *J. Geophys. Res.*, 100:6213–6224.

Villareal, T. A. and Fryxell, G. A. (1983). Temperature effects on the valve structure of the bipolar diatoms *Thalassiosira antarctica* and *Porosira glacialis*. *Polar Biology*, 2:163–169.

Walker, S. J. (1996). Hydrodynamic models of Port Phillip Bay. Technical report 38, CSIRO Port Phillip Bay Environmental Study.

Walker, S. J. (1999). Coupled hydrodynamic and transport models of Port Phillip Bay, a semi-enclosed bay in south-eastern Australia. *Mar. Freshwater Res.*, 50:469–481.

Walker, S. J. and Fandry, C. B. (1993). Modelling effluent dispersion in Australian coastal waters - devonport 1991-1992, hydrodynamic modelling. Technical report No. OMR-59/40, CSIRO Division of Oceanography.

Walker, S. J. and Waring, J. R. (1998). MECO Model for Estuaries and Coastal Oceans. Internal report No. OMR-118/120, CSIRO Marine Research.

WAMDI Group (1988). The WAM model - a third generation ocean wave prediction model. *J. Phys. Oceanogr.*, 18:1775–1810.

Webb, P. N., Ronan Jnr, T. E., Lipps, J. H., and DeLaca, T. E. (1979). Miocene glaciomarine sediments from beneath the Southern Ross Shelf. *Science*, 203:435–437.

Wessel, P. and Smith, W. (1996). A global self-consistent, hierarchical, high-resolution shoreline database. *J. Geophys. Res.*, 101:8741–8743.

Whitehead, J. (2000). *Cenozoic Palaeoenvironment of the Southern Ocean and East Antarctica: Geological and Palaeontological Evidence from the Kerguelen Plateau, Vestfold Hills and Prince Charles Mountains.* PhD thesis, University of Tasmania.

Wiberg, P. L. and Smith, J. D. (1993). A comparison of field data and theoretical models for wave current interaction at the bed on the continental shelf. *Cont. Shelf Res.*, 2:147–162.

Williams, M., Jenkins, A., and Determann, J. (1998a). Physical controls on ocean circulation beneath ice shelves revealed by numerical models. In Jacobs, S. S. and Weiss, R. F., editors, *Ocean, Ice and Atmosphere. Interactions at the Antarctic Continental Margin*, volume 75 of *Antarct. Res. Ser.*, pages 285–299. AGU, Washington D.C.

Williams, M. J. M. (1999). *A numerical study of ocean circulation and ice-ocean interaction, beneath the Amery Ice Shelf, Antarctica.* PhD thesis, University of Tasmania.

Williams, M. J. M., Grosfeld, K., Warner, R. C., Gerdes, R., and Determann, J. (2001). Ocean circulation and ice-ocean interaction beneath the Amery Ice Shelf, Antarctica. *J. Geophys. Res.*, 106.

Williams, M. J. M., Warner, R. C., and Budd, W. F. (1998b). The effects of ocean warming on melting and ocean circulation under the Amery Ice Shelf, East Antarctica. *Annals Glac.*, 27:75–80.

Williams, M. J. M., Warner, R. C., and Budd, W. F. (2002). Sensitivity of the Amery Ice Shelf, Antarctica to changes in the climate of the Southern Ocean. *Journal of Climate*, 15:2740–2757.

Wolanski, E. (1986). The physical oceanography of Torres Strait. In Haines, A., Williams, G. C., and Coates, D., editors, *Torres Strait Fisheries Seminar*, pages 275–291. Australian Govt. Publ. Service, Canberra, Aust.

Wolanski, E. and Eagle, M. (1991). Oceanography and fine sediment transport, Fly River Estuary and Gulf of Papua. *"Coastal Engineering - Climate for Change" 10th Australasian Conference on Coastal and Ocean Engineering, Auckland, 2-6 Dec. 1991*, pages 453–457.

Wolanski, E., Pickard, G. L., and Jupp, D. L. B. (1984). River plumes, coral reefs and mixing in the Gulf of Papua and the northen Great Barrier Reef. *Estuarine, Coastal and Shelf Science*, 18:291–314.

Wolanski, E., Ridd, P., and Inoue, M. (1988). Currents through Torres Strait. *J. Phys. Oceanogr.*, 18:1535–1545.

Wolanski, E. and Ruddick, B. (1981). Water circulation and shelf waves in the Northern Great Barrier Reef lagoon. *Australian Journal of Marine and Freshwater Research*, 32:721–740.

Wolanski, E. and Thomson, R. E. (1984). Wind driven circulation on the Northern Great Barrier Reef continental shelf in summer. *Estuarine, Coastal and Shelf Science*, 18:271–289.

Wolanski, E., Trenorden, M., and King, B. (1990). Fly River estuary and Gulf of Papua oceanography and sediment dynamics data report: November 1990. Technical report, Ok Tedi Mining Ltd.

Wong, A. P. (1994). Structure and dynamics of Prydz Bay, Antarctica, as inferred from a summer hydrographic data set. Master's thesis, University of Tasmania, Hobart.

Wong, A. P. S., Bindoff, N. L., and Forbes, A. (1998). Ocean-ice shelf interaction and possible bottom water formation in Prydz Bay, Antarctica. In Jacobs, S. and Weiss, R., editors, *Ocean, Ice and Atmosphere: Interactions at the Antarctic Continental Margin*, volume 75 of *Antarct. Res. Ser.*, pages 173–187. AGU, Washington, D. C.

Woodruff, S. D., Lubker, S. J., Wolter, K., Worley, S. J., and Elms, J. D. (1993). Comprehensive ocean-atmosphere data set (COADS). Release 1a: 1980-92. *Earth System Monitor*, 4(1):1–8.

Wright, L. D. (1989). Dispersal and deposition of river sediments in coastal seas: Models from Asia and the tropics. *Netherlands Journal of Sea Research*, 23:493–500.

Wyrtki, K. (1960). Surface Circulation in the Coral and Tasman Seas. Technical Paper No. 8, CSIRO Division of Fisheries and Oceanography.

Young, N. W. and Hyland, G. (2002). Velocity and strain rates derived from InSAR analysis over the Amery Ice Shelf, East Antarctica. *Annals Glac.*, 34:228–234.

Zielinski, U. and Gersonde, R. (1997). Diatoms distribution in the Southern Ocean surface sediments (Atlantic Sector): Implications for paleoenvironmental reconstructions. *Palaeogeography, Palaeoclimatology, Palaeoecology*, 129:213–250.

Appendix A

Harmonic Analysis of Torres Strait Sea Surface Elevation: Model - ANTT constituent comparison

Table A.1: Observed and modelled tidal harmonic constituents for Torres Strait points. Amplitudes are in metres, phase in degrees relative to GMT.

Location	M_2		S_2		K_1		O_1	
	Ampl.	Phase	Ampl.	Phase	Ampl.	Phase	Ampl.	Phase
AI. obs	0.5954	8.06	0.5124	32.20	0.4657	151.69	0.2145	204.47
R1	0.6407	17.97	0.4856	22.07	0.3988	162.28	0.2128	221.54
R2	0.7391	18.10	0.5435	28.78	0.4026	159.28	0.2123	221.71
R3	0.5748	18.20	0.4222	24.28	0.3734	167.15	0.2052	226.61
R4	0.6424	17.80	0.4875	21.95	0.3992	162.17	0.2129	221.42
R5	0.6652	7.50	0.7356	9.77	0.4927	138.39	0.2395	194.97
R7	0.6436	17.93	0.4882	22.05	0.4000	162.13	0.2133	221.41
R8	0.6382	5.18	0.0011	-79.24	0.0002	96.70	0.0001	90.87
R10	0.6329	20.85	0.4812	22.87	0.4016	163.62	0.2164	223.08
R11	0.8367	43.48	0.1331	56.14	0.4587	126.52	0.2261	177.89
R12	0.7737	7.50	0.4641	30.50	0.2838	163.72	0.1409	230.69
BI. obs	0.7160	229.60	0.1410	98.20	0.6890	166.50	0.4260	228.80
R1	0.8972	169.51	0.1538	8.57	0.4850	167.70	0.2827	228.37
R2	0.9464	167.21	0.0607	-24.39	0.4699	170.71	0.2569	232.74
R3	0.8017	172.13	0.1618	11.21	0.4543	170.13	0.2667	230.46
R4	0.8976	169.38	0.1527	8.44	0.4853	167.68	0.2828	228.37
R5	1.0285	157.87	0.0232	276.13	0.5853	156.57	0.3436	221.43
R7	0.9007	169.38	0.1530	8.33	0.4861	167.63	0.2831	228.31
R8	0.9528	188.61	0.0014	133.30	0.0001	318.82	0.0001	297.43
R10	0.9340	170.22	0.1633	6.86	0.4795	168.05	0.2750	228.10
R11	0.9230	132.76	0.1735	-57.74	0.4955	145.69	0.2842	210.40
R12	0.2661	137.96	0.1589	210.06	0.0642	201.83	0.0347	282.14
CG. obs	0.6287	57.00	0.4733	102.13	0.2960	175.19	0.1590	204.87
R1	0.6472	40.15	0.4141	100.30	0.3363	182.58	0.1656	204.73
R2	0.6094	38.50	0.3740	99.96	0.3177	182.23	0.1658	205.37
R3	0.6287	42.40	0.3958	102.78	0.3308	184.10	0.1633	205.98
R4	0.6475	40.13	0.4144	100.28	0.3363	182.56	0.1656	204.71
R5	0.6498	36.67	0.4377	96.93	0.3363	180.36	0.1641	202.92
R7	0.6476	40.12	0.4145	100.28	0.3364	182.55	0.1656	204.71
R8	0.6512	37.43	0.0011	-19.87	0.0001	3.13	0.0000	88.32
R10	0.6423	40.77	0.4102	100.97	0.3362	182.96	0.1659	205.01
R11	0.5564	43.51	0.3545	98.41	0.3368	180.18	0.1640	201.80
R12	0.6542	40.52	0.4094	100.31	0.3338	182.68	0.1642	204.98
DI. obs	0.7112	80.98	0.4239	125.56	0.3677	190.24	0.1781	216.63
R1	0.7601	101.71	0.5027	169.22	0.3392	222.38	0.1710	235.28
R2	0.6954	110.23	0.4953	179.08	0.3439	223.07	0.1717	236.41
R3	0.7304	103.25	0.4694	169.94	0.3304	224.26	0.1691	237.52
R4	0.7628	101.40	0.5051	168.87	0.3399	222.16	0.1713	235.00
R5	0.7152	91.44	0.5964	169.00	0.3705	215.38	0.1797	227.03
R7	0.7604	101.63	0.5034	169.24	0.3394	222.35	0.1712	235.24
R8	0.8147	97.77	0.0016	38.94	0.0002	29.33	0.0000	154.57
R10	0.7761	101.13	0.5069	168.56	0.3393	221.85	0.1712	233.99
R11	1.0083	216.45	0.4451	251.13	0.5078	215.21	0.2612	218.71
R12	0.7773	105.80	0.4755	167.03	0.3210	220.59	0.1583	234.46
ES. obs	0.4714	345.49	0.5254	24.80	0.4949	149.72	0.2505	206.99
R1	0.6648	364.00	0.3901	20.65	0.4189	161.18	0.2286	225.13
R2	0.7549	357.43	0.4742	24.24	0.4248	156.85	0.2232	224.34
R3	0.5725	366.06	0.3236	22.92	0.3887	166.33	0.2182	229.61
R4	0.6661	363.79	0.3920	20.50	0.4194	161.06	0.2288	225.02
R5	0.6805	358.75	0.6224	7.66	0.5331	137.44	0.2715	202.59
R7	0.6680	363.94	0.3925	20.60	0.4205	161.00	0.2293	225.00
R8	0.5751	356.52	0.0010	-56.81	0.0002	99.02	0.0001	121.21
R10	0.6919	365.55	0.3988	22.58	0.4222	162.28	0.2299	225.70
R11	0.9574	364.73	0.1045	89.64	0.4871	119.15	0.2542	176.38
R12	0.7141	340.94	0.4281	35.08	0.2456	166.99	0.1241	240.72

Table A.2: Observed and modelled tidal harmonic constituents for Torres Strait points. Amplitudes are in metres, phase in degrees relative to GMT.

Location	M_2		S_2		K_1		O_1	
	Ampl.	Phase	Ampl.	Phase	Ampl.	Phase	Ampl.	Phase
GI. obs	0.5290	228.50	0.2030	59.40	0.6730	160.30	0.3970	223.10
R1	0.8314	165.36	0.0846	31.29	0.4727	166.12	0.2641	229.69
R2	0.8924	163.23	0.0998	85.37	0.4703	166.19	0.2495	230.97
R3	0.7323	168.27	0.0712	17.99	0.4373	169.91	0.2455	233.06
R4	0.8317	165.16	0.0849	32.39	0.4728	166.10	0.2642	229.71
R5	0.9323	151.88	0.2596	80.78	0.5809	152.05	0.3230	221.02
R7	0.8350	165.22	0.0851	31.94	0.4742	166.00	0.2648	229.59
R8	0.7776	183.12	0.0013	56.09	0.0000	293.76	0.0001	279.07
R10	0.8793	166.56	0.0817	22.22	0.4734	166.33	0.2597	229.60
R11	0.9750	131.60	0.1367	204.62	0.4960	136.19	0.2713	202.05
R12	0.4387	122.67	0.2630	119.63	0.1257	188.77	0.0650	271.01
IP. obs	0.3670	318.22	0.4190	21.14	0.5460	152.07	0.2730	211.20
R1	0.7272	322.07	0.3146	20.44	0.4243	165.10	0.2316	230.73
R2	0.7745	322.94	0.3306	17.68	0.4438	157.71	0.2312	222.89
R3	0.6225	325.41	0.2510	20.85	0.3944	169.38	0.2200	233.81
R4	0.7283	321.93	0.3159	20.24	0.4249	164.97	0.2320	230.59
R5	0.7954	318.14	0.5238	8.87	0.5533	141.79	0.2857	208.41
R7	0.7311	321.97	0.3169	20.45	0.4258	164.95	0.2323	230.64
R8	0.6191	321.67	0.0011	-51.63	0.0001	104.00	0.0000	172.18
R10	0.7609	322.68	0.3299	22.71	0.4257	166.24	0.2311	230.74
R11	0.9815	310.70	0.1120	105.28	0.4933	121.89	0.2627	181.68
R12	0.6727	295.47	0.4022	37.09	0.2229	175.86	0.1114	253.89
K. obs	0.5500	68.00	0.3300	102.00	0.2900	161.00	0.1400	205.00
R1	0.5997	52.60	0.3603	91.04	0.2872	153.57	0.1425	201.93
R2	0.5997	52.60	0.3603	91.04	2872	153.57	0.1425	201.93
R3	0.5953	52.50	0.3573	90.83	0.2866	153.60	0.1423	201.98
R4	0.6001	52.51	0.3607	90.94	0.2872	153.53	0.1425	201.89
R5	0.6029	51.39	0.3620	90.52	0.2877	152.97	0.1426	201.24
R7	0.5999	52.58	0.3604	91.02	0.2872	153.55	0.1425	201.92
R8	0.5974	50.78	0.0011	-29.21	0.0001	318.87	0.0000	75.63
R10	0.6010	52.65	0.3611	91.01	0.2874	153.44	0.1430	201.72
R11	0.9947	220.80	0.7156	215.75	0.5051	170.70	0.2667	214.05
R12	0.5987	52.74	0.3604	90.86	0.2870	153.49	0.1424	201.85
KTM. obs	0.7560	62.70	0.3950	89.00	0.3400	169.50	0.1400	204.50
R1	0.7877	49.28	0.4813	74.06	0.3093	172.41	0.1526	202.89
R2	0.7904	48.64	0.4874	74.18	0.3098	172.38	0.1528	202.89
R3	0.7714	49.41	0.4696	73.85	0.3080	172.60	0.1520	203.04
R4	0.7897	48.87	0.4830	73.58	0.3096	172.19	0.1526	202.66
R5	0.8266	47.52	0.5129	75.10	0.3160	171.51	0.1547	201.85
R7	0.7881	49.28	0.4815	74.08	0.3094	172.41	0.1526	202.89
R8	0.7960	47.29	0.0014	-50.31	0.0001	332.63	0.0000	107.18
R10	0.7891	49.10	0.4810	73.73	0.3087	172.18	0.1521	202.50
R11	1.4235	202.33	0.9283	188.88	0.5535	184.49	0.2866	208.39
R12	0.7843	49.86	0.4808	73.43	0.3084	172.08	0.1518	202.61
Me. obs	1.1300	312.01	0.4550	207.30	0.7960	199.58	0.5020	269.03
R1	1.1396	304.80	0.4512	199.85	0.7558	195.92	0.4801	265.69
R2	1.1401	304.79	0.4522	199.84	0.7545	195.90	0.4805	265.66
R3	1.1396	304.80	0.4512	199.85	0.7558	195.92	0.4801	265.69
R4	1.1396	304.80	0.4512	199.85	0.7558	195.92	0.4801	265.69
R5	1.1396	304.80	0.4512	199.85	0.7558	195.92	0.4801	265.69
R7	1.1396	304.80	0.4512	199.85	0.7558	195.92	0.4801	265.69
R8	1.1392	333.75	0.0020	338.84	0.0001	176.56	0.0001	316.26
R10	1.1396	304.80	0.4512	199.85	0.7558	195.92	0.4801	265.69
R11	1.1396	304.80	0.4512	199.85	0.7558	195.92	0.4801	265.69
R12	0.0000	192.91	0.0000	196.84	0.0000	219.69	0.0000	372.16

Table A.3: Observed and modelled tidal harmonic constituents for Torres Strait points. Amplitudes are in metres, phase in degrees relative to GMT.

Location	M_2		S_2		K_1		O_1	
	Ampl.	Phase	Ampl.	Phase	Ampl.	Phase	Ampl.	Phase
PR. obs	0.3960	233.60	0.1190	154.10	0.5020	161.40	0.3000	218.40
R1	0.3224	163.69	0.1667	104.45	0.3678	153.65	0.2671	213.44
R2	0.3224	163.69	0.1667	104.45	0.3678	153.65	0.2671	213.44
R3	0.3189	164.22	0.1668	105.27	0.3680	153.46	0.2660	213.16
R4	0.3223	163.55	0.1666	104.34	0.3677	153.64	0.2671	213.45
R5	0.3252	163.41	0.1606	101.84	0.3700	154.10	0.2698	214.12
R7	0.3224	163.70	0.1666	104.43	0.3679	153.66	0.2671	213.45
R8	0.4158	187.28	0.0008	239.42	0.0001	128.90	0.0000	293.95
R10	0.3250	163.91	0.1681	104.62	0.3681	153.70	0.2672	213.62
R11	0.3411	160.02	0.1567	97.82	0.3731	152.07	0.2662	211.21
R12	0.0099	153.65	0.0062	330.08	0.0015	208.37	0.0007	284.98
SI. obs	0.2145	329.62	0.7383	328.94	0.5453	114.85	0.3355	181.60
R1	0.5997	321.13	0.4499	265.59	0.4147	93.40	0.2271	178.31
R2	0.7067	315.32	0.5322	268.74	0.4200	88.22	0.2222	176.52
R3	0.5218	322.14	0.3800	268.06	0.3855	98.68	0.2178	183.17
R4	0.6012	320.90	0.4520	265.43	0.4151	93.27	0.2273	178.19
R5	0.5660	316.08	0.6949	251.83	0.5240	69.32	0.2649	155.12
R7	0.6025	321.08	0.4527	265.53	0.4162	93.22	0.2278	178.17
R8	0.5587	306.98	0.0009	178.98	0.0002	35.56	0.0001	46.31
R10	0.6190	323.27	0.4560	267.46	0.4179	94.53	0.2290	179.01
R11	0.9494	333.43	0.1224	313.65	0.4881	51.55	0.2516	129.38
R12	0.7327	303.64	0.4391	277.53	0.2607	94.86	0.1320	187.75
Su. obs	0.5454	348.52	0.5636	16.41	0.4994	147.56	0.2109	179.68
R1	0.5639	379.58	0.4112	11.89	0.4275	164.29	0.2350	177.42
R2	0.6643	367.90	0.4914	9.18	0.4341	155.94	0.2318	172.36
R3	0.4820	380.70	0.3437	13.99	0.3957	169.54	0.2240	181.97
R4	0.5649	379.32	0.4133	11.70	0.4280	164.15	0.2352	177.29
R5	0.5836	383.12	0.6797	-2.21	0.5645	137.72	0.2916	152.62
R7	0.5666	379.52	0.4141	11.81	0.4294	164.09	0.2359	177.26
R8	0.4834	365.82	0.0007	-65.13	0.0001	108.34	0.0001	89.90
R10	0.5919	381.25	0.4184	14.45	0.4292	165.72	0.2367	177.81
R11	1.0410	373.37	0.1332	62.48	0.5086	115.39	0.2672	122.93
R12	0.6877	355.79	0.4090	27.23	0.2398	166.06	0.1224	188.92
TH. obs	0.3350	262.84	0.2990	32.64	0.6290	155.19	0.3570	214.84
R1	0.8051	233.45	0.1103	-2.12	0.4685	157.87	0.2603	215.17
R2	0.8269	228.76	0.1678	28.17	0.4726	158.26	0.2517	218.36
R3	0.7043	235.86	0.0856	-4.44	0.4299	162.53	0.2399	219.69
R4	0.8051	233.15	0.1114	-0.81	0.4682	157.89	0.2600	215.24
R5	0.9021	220.63	0.3179	27.69	0.5831	142.90	0.3208	205.76
R7	0.8087	233.33	0.1114	-1.95	0.4703	157.71	0.2613	215.02
R8	0.7296	250.40	0.0012	3.37	0.0000	130.09	0.0001	251.61
R10	0.8542	234.95	0.1014	-7.17	0.4708	158.56	0.2573	215.95
R11	0.9841	200.07	0.1283	146.63	0.4978	126.39	0.2708	186.34
R12	0.4670	189.83	0.2794	64.96	0.1375	177.62	0.0724	252.77
TI. obs	0.5040	347.08	0.5030	22.03	0.5010	150.29	0.2340	205.42
R1	0.6708	370.61	0.3808	16.96	0.4211	162.79	0.2297	222.02
R2	0.7549	360.61	0.4742	18.75	0.4248	158.00	0.2232	221.18
R3	0.5765	372.82	0.3143	18.99	0.3906	167.83	0.2192	226.30
R4	0.6720	370.42	0.3826	16.80	0.4216	162.67	0.2300	221.90
R5	0.7016	365.90	0.6165	4.20	0.5380	138.73	0.2741	199.42
R7	0.6741	370.55	0.3832	16.91	0.4227	162.61	0.2305	221.89
R8	0.5751	363.91	0.0010	-58.69	0.0002	100.16	0.0001	128.32
R10	0.6977	372.23	0.3886	18.95	0.4246	163.96	0.2318	222.46
R11	0.9710	368.27	0.1062	88.46	0.4906	119.91	0.2574	172.64
R12	0.7080	346.59	0.4242	32.05	0.2413	169.08	0.1220	238.31

Table A.4: Observed and modelled tidal harmonic constituents for Torres Strait points. Amplitudes are in metres, phase in degrees relative to GMT.

Location	M_2		S_2		K_1		O_1	
	Ampl.	Phase	Ampl.	Phase	Ampl.	Phase	Ampl.	Phase
ThI. obs	0.3580	297.44	0.3501	24.84	0.5521	154.92	0.2875	215.75
R1	0.8314	303.17	0.0846	-37.23	0.4727	155.40	0.2641	214.97
R2	0.8924	301.11	0.0998	16.45	0.4703	155.43	0.2495	216.24
R3	0.7323	306.08	0.0712	-50.52	0.4373	159.19	0.2455	218.33
R4	0.8317	302.97	0.0849	-36.13	0.4728	155.38	0.2642	214.98
R5	0.9323	289.69	0.2596	12.27	0.5809	141.33	0.3230	206.30
R7	0.8350	303.02	0.0851	-36.57	0.4742	155.28	0.2648	214.86
R8	0.7776	320.93	0.0013	-12.43	0.0000	283.04	0.0001	264.35
R10	0.8793	304.37	0.0817	-46.29	0.4734	155.61	0.2597	214.87
R11	0.9750	269.41	0.1367	136.10	0.4960	125.47	0.2713	187.32
R12	0.4387	260.48	0.2630	51.11	0.1257	178.05	0.0650	256.28
UI. obs	0.9196	39.36	0.5713	59.61	0.3120	160.31	0.1490	200.88
R1	0.6926	17.86	0.4154	32.59	0.2757	164.73	0.1477	203.43
R2	0.7717	25.78	0.4697	43.97	0.2928	167.74	0.1489	207.83
R3	0.6941	18.21	0.4144	32.46	0.2795	164.80	0.1483	204.11
R4	0.6942	17.47	0.4168	32.14	0.2760	164.50	0.1478	203.15
R5	0.8426	14.31	0.5237	33.83	0.3158	159.20	0.1580	198.41
R7	0.6931	17.80	0.4156	32.57	0.2757	164.71	0.1477	203.40
R8	0.7308	14.94	0.0014	-93.99	0.0002	331.76	0.0001	155.71
R10	0.7369	16.00	0.4487	30.51	0.2810	163.90	0.1394	206.65
R11	1.4274	149.15	0.8559	127.37	0.5547	162.53	0.2844	196.57
R12	0.6898	19.16	0.4133	31.36	0.2740	163.97	0.1460	203.19
W. obs	0.3710	212.80	0.1120	150.20	0.4410	143.70	0.3010	201.60
R1	0.2073	161.63	0.1299	122.11	0.3332	136.68	0.2708	198.90
R2	0.1423	200.70	0.0971	152.36	0.2956	155.03	0.2562	217.33
R3	0.2091	161.48	0.1300	122.31	0.3339	136.18	0.2702	198.47
R4	0.2072	161.62	0.1299	122.09	0.3332	136.68	0.2708	198.91
R5	0.2073	158.14	0.1301	117.45	0.3309	135.65	0.2693	197.90
R7	0.2075	161.53	0.1300	121.98	0.3334	136.64	0.2709	198.85
R8	0.3022	170.51	0.0005	256.35	0.0000	127.05	0.0000	265.15
R10	0.2133	162.39	0.1315	123.27	0.3350	136.83	0.2723	198.93
R11	0.1872	154.24	0.1137	114.88	0.3227	133.86	0.2619	196.19
R12	0.0004	130.22	0.0002	-17.38	0.0001	212.16	0.0000	276.49

Appendix B

Torres Strait Model to Current Meter Comparisons

station 5, 1990 This station is located on the south coast of Daru Island, on the northern side of Missionary Passage at position $9°10.7'S$, $143°15.0'E$. The current meter was deployed from the 25-02-90 to the 24-04-90.

The mean measured and modelled currents over the entire period at this site are shown in Table 3.9. The mean current magnitude is overestimated by the model by approximately 40%, and a directional offset of about 45° anticlockwise relative to the measured currents is observed. This directional offset was also observed in the low-pass filtered currents.

There is moderate agreement between the model and measurements. Current speeds are well represented by the model in Figure B.1. Model and measurements appear to be out of phase in the higher frequencies.

The E-W component of current shows a better correlation ($R^2 = 0.64$) than the N-S component ($R^2 = 0.44$).

A major source of error at this station is likely to be bathymetry. The current meter was deployed in 31m of water which is likely to be in Missionary Passage. Model bathymetry at this position indicates that it is not part of the passage, with a depth of 7m.

station 6, 1990 This station is located at the southern end of the Warrior Reefs, on the eastern side of Torres Strait at position $10°17.5'S$, $142°51.2'E$. The current meter was deployed from the 24-02-90 to the 24-04-90.

The mean measured and modelled currents over the entire period at this site are shown in Table 3.9. The mean current is well represented by the model, apart from a slight

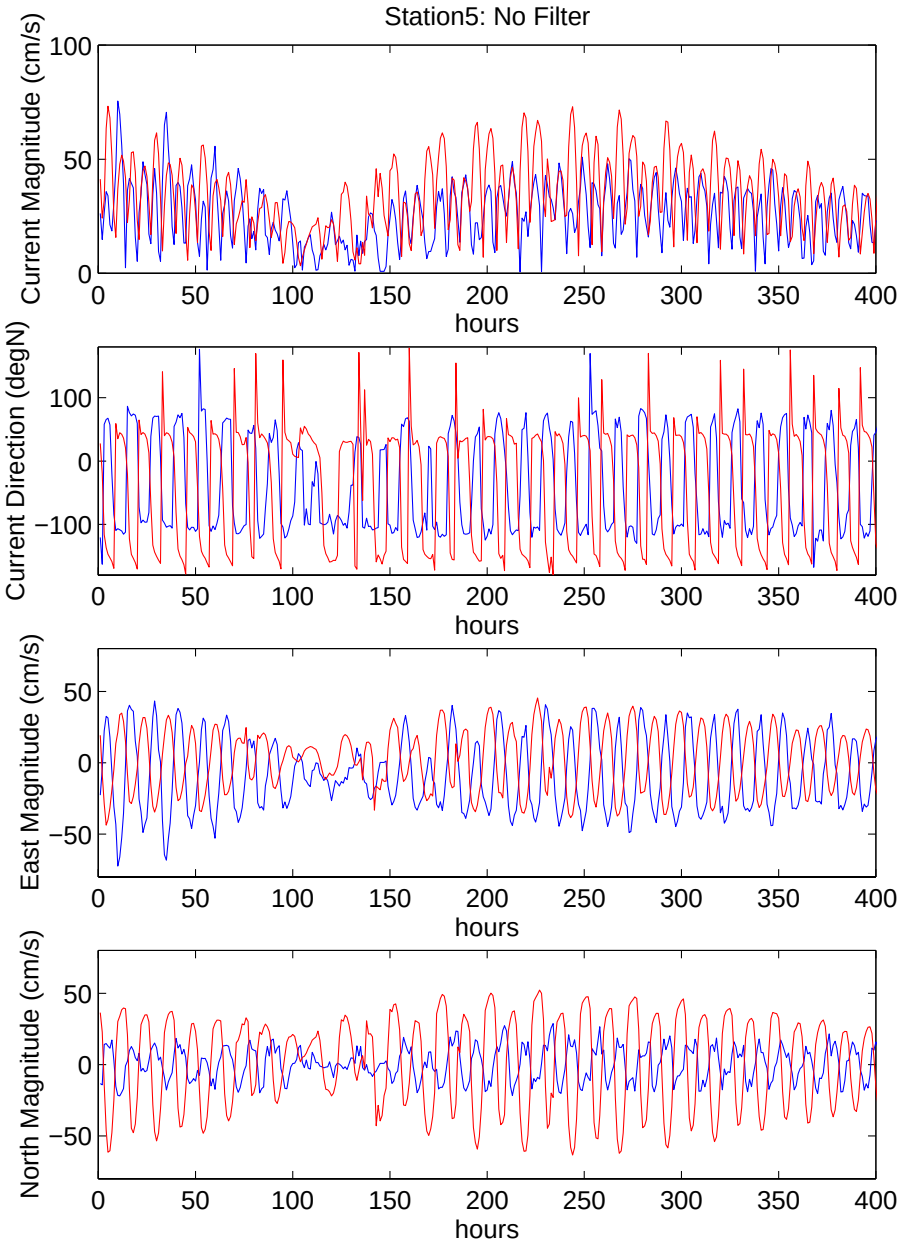

Figure B.1: Station 5: Time series comparison of measured (blue line) and modelled (red line) currents.

overestimation of current magnitude by the model of roughly 20%.

There is moderate agreement between the model and measurements. Current speeds are of similar order in Figure B.2, however a phase difference is observed in the comparisons with no filter applied. Although the mean direction is well represented, an observed phase difference is clearly apparent in Figure B.2.

The correlation of both the N-S component ($R^2 = 0.07$) and the E-W component ($R^2 = 0.09$) are low.

station 7, 1990 This station is located slightly north of station 6, along the inner western side of the Warrior Reefs at position $9°52.0'S$, $142°48.9'E$. The current meter was deployed from the 25-02-90 to the 26-04-90.

The mean measured and modelled currents over the entire period at this site are shown in Table 3.9. The mean current is well represented by the model at this station.

There is moderate agreement between the model and measurements. Current speeds are of the same order, however, a slight phase difference is observed. Current direction comparisons are quite good, although the slight phase difference is still observed (Fig. B.3). At the lower frequencies, the model does well with a good representation of speeds and directions.

The low correlation of the N-S component of current ($R^2 = 0.05$) and the E-W component ($R^2 = 0.17$) are likely to be a result of the observed phase lag.

station 12, 1993 This station is located on the outer shelf at the northern end of the Great Barrier Reef at position $11°25.1'S$, $143°40.2'E$. The current meter was deployed from the 16-01-93 to the 29-03-93.

The mean measured and modelled currents over the entire period at this site are shown in Table 3.9. The mean current is well represented by the model, apart from a directional offset of about 30° anticlockwise relative to the measured currents. This directional offset can also be seen in the low-pass filtered currents. Possible explanations in the direction offset include some systematic error or local bathymetry effect given that the Anderaa current meter was deployed at a depth of 21m in 28m of water.

There is moderate agreement between the model and measurements. The model generally overestimates current speeds by approximately 20%. The model represents times of strong and weak currents well despite the general overestimation. The low frequency fluctuations driven by the wind shows less variability in the model than the measured currents. Low current speeds result in current speeds of zero being recorded in the current meter

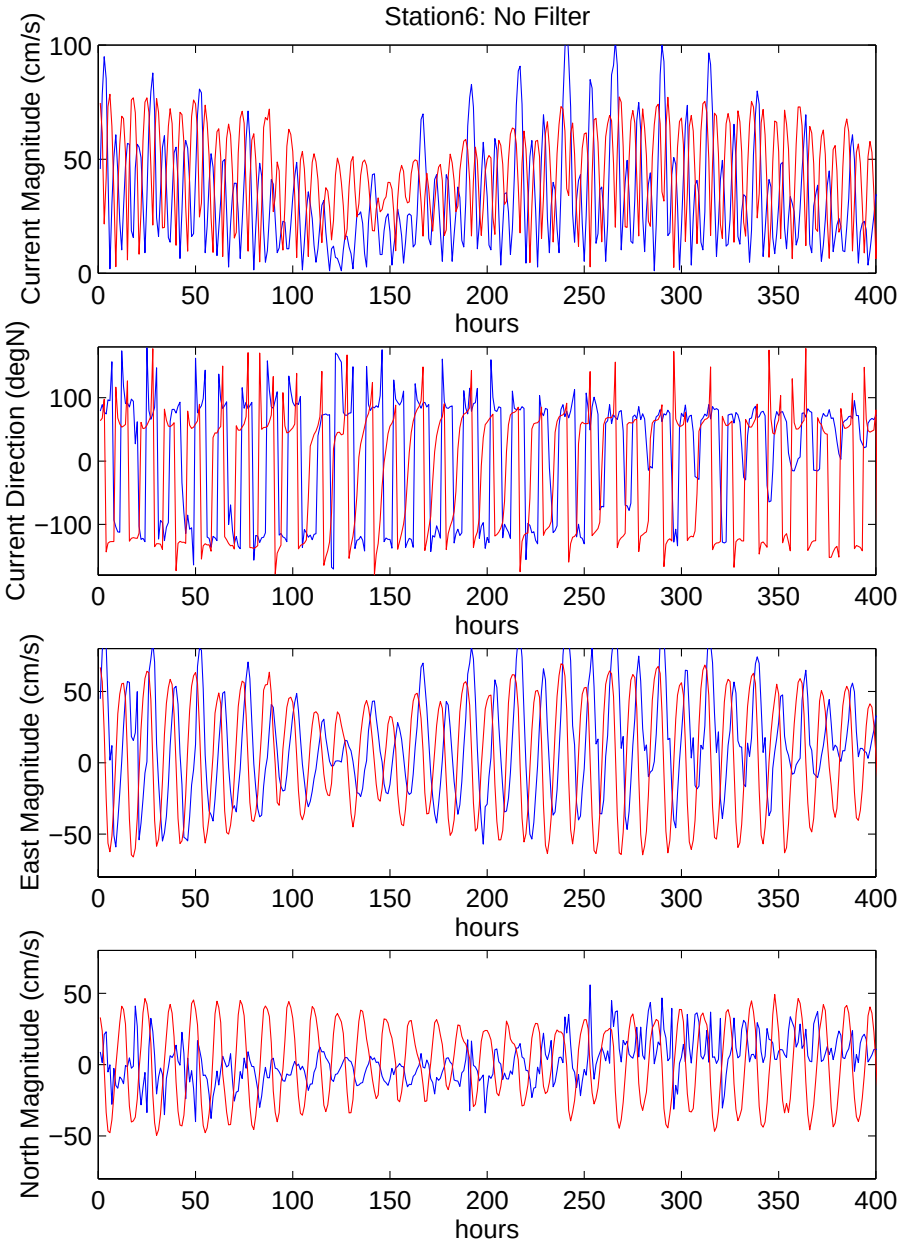

Figure B.2: Station 6: Time series comparison of measured (blue line) and modelled (red line) currents.

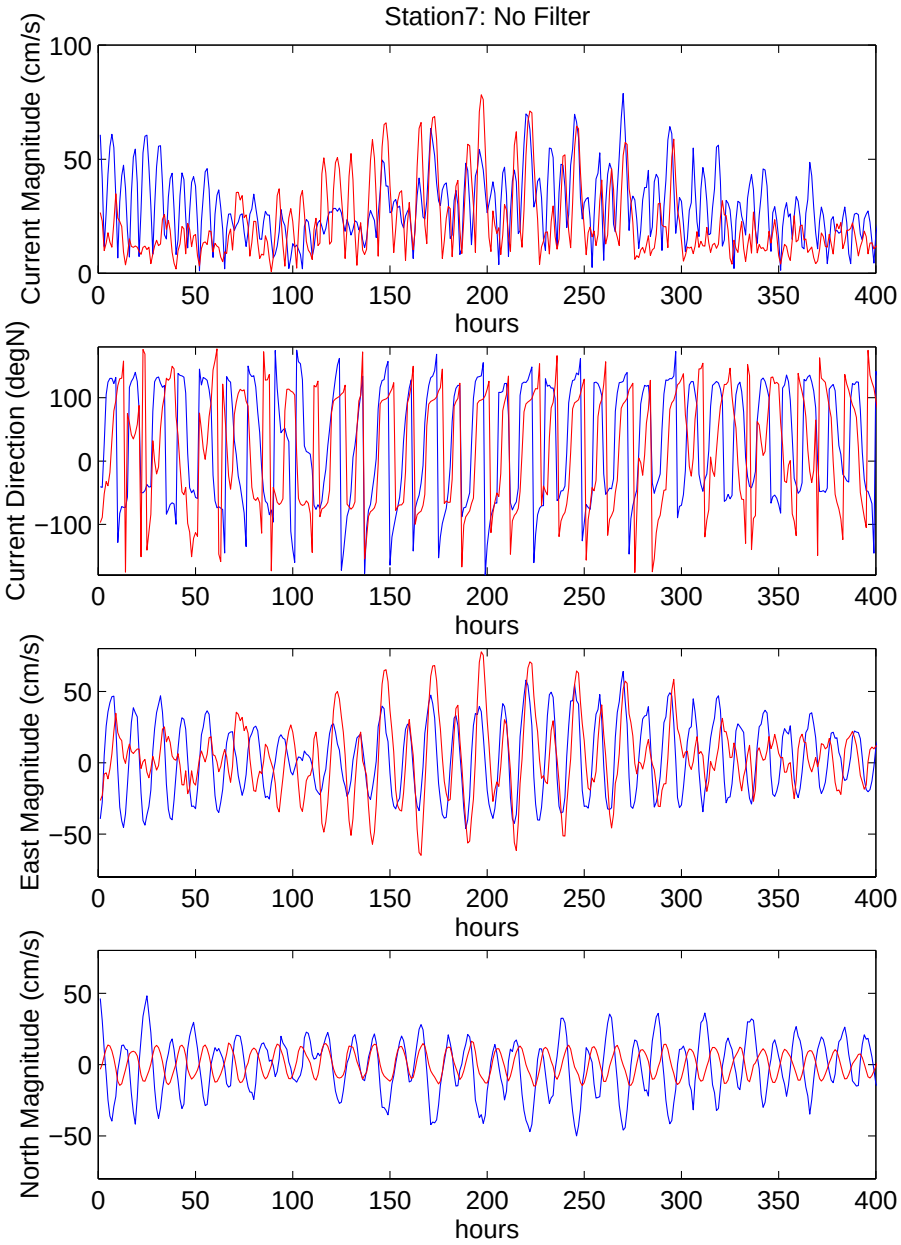

Figure B.3: Station 7: Time series comparison of measured (blue line) and modelled (red line) currents.

due to the static friction of the Anderaa current meter. The presence of dynamic friction would suggest that the current meter may underestimate current speeds so that the error between model and measurements may be less than is apparent. Current direction has good representation in the model as seen in Figure B.4.

The N-S component of current shows a better correlation ($R^2 = 0.48$) than the E-W component ($R^2 = 0.18$).

station 13, 1993 This station is located nearshore to the east of the northern tip of Cape York at position $10°59.6'S$, $143°40.2'E$. The current meter was deployed from the 15-01-93 to the 28-03-93.

The mean measured and modelled currents over the entire period at this site are shown in Table 3.9. The mean current is underestimated by approximately 30% by the model, and a directional offset of about 40° anticlockwise relative to the measured currents exists. This directional offset was also observed in the low-pass filtered currents. Model bathymetry indicates that the water depth at the site of station 13 is 23.5m deep. The recorded depth of the current meter was 22m.

Model to measured current comparisons are similar to station 12 with an acceptable agreement between the model and measurements. The model generally overestimates current speeds at the tidal frequencies, but underestimates at the lower frequencies. Periods of strong and weak currents are well represented at all frequencies despite the general discrepancies. Current direction has good representation in the model as seen in Figure B.5.

The E-W component of current shows a better correlation ($R^2 = 0.66$) than the N-S component ($R^2 = 0.24$).

station 14, 1993 Station 14 is situated on the shelf out from the Fly River Delta at position $9°00.2'S$, $143°47.5'E$. It is in this region that the seasonal sediment varves, as described in Harris et al. (1993), are found. The current meter was deployed from the 17-01-93 to the 28-03-93.

The mean measured and modelled currents over the entire period at this site are shown in Table 3.9. The mean current is underestimated by the model, and a directional offset of 90° clockwise relative to the measured currents is apparent in the low pass filtered results. This current meter was also placed one metre above the seafloor, and local features may have a significant effect on the measured currents.

There is moderate agreement between the model and measurements. The model overestimates current speeds at the tidal frequencies, and underestimates at lower frequencies.

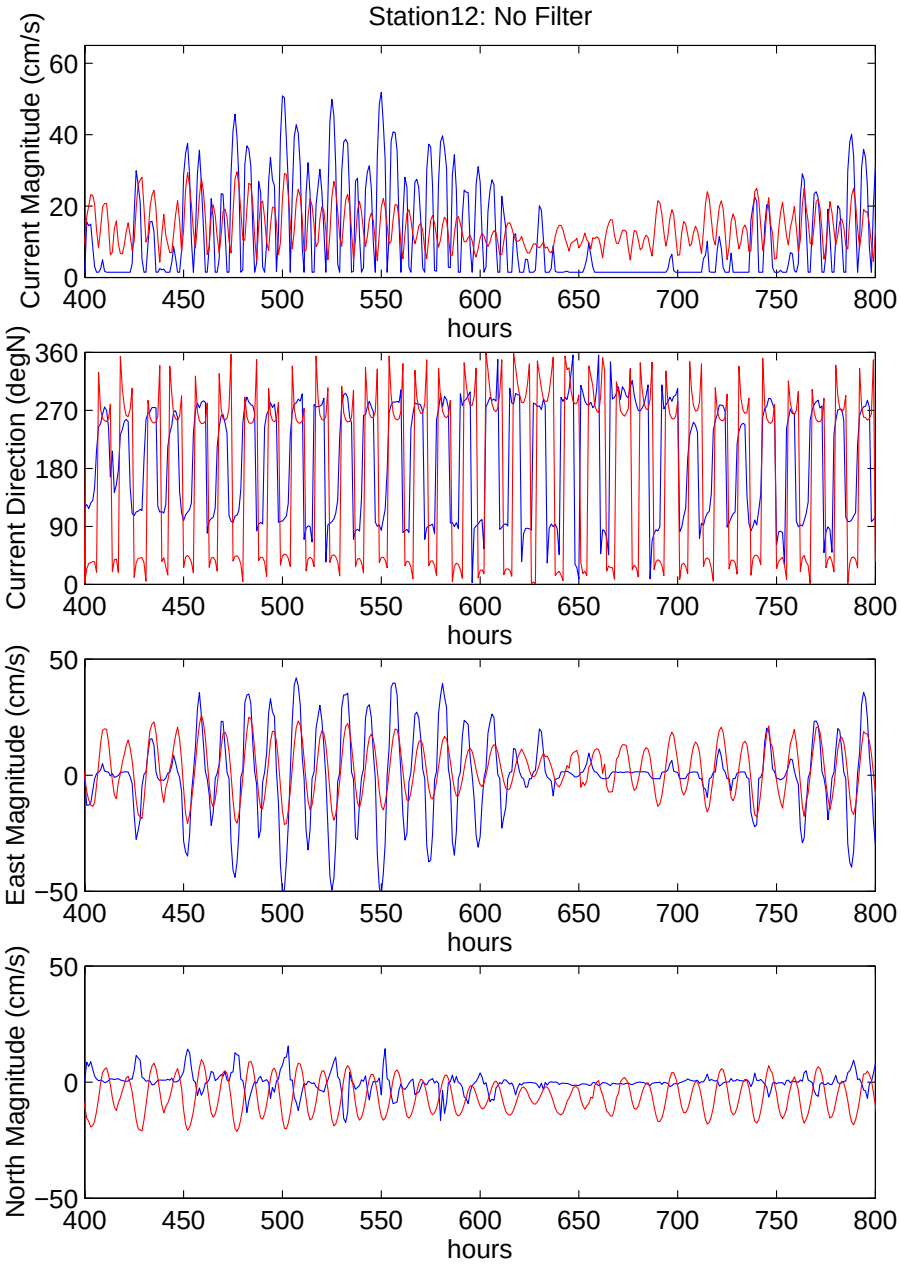

Figure B.4: Station 12: Time series comparison of measured (blue line) and modelled (red line) currents.

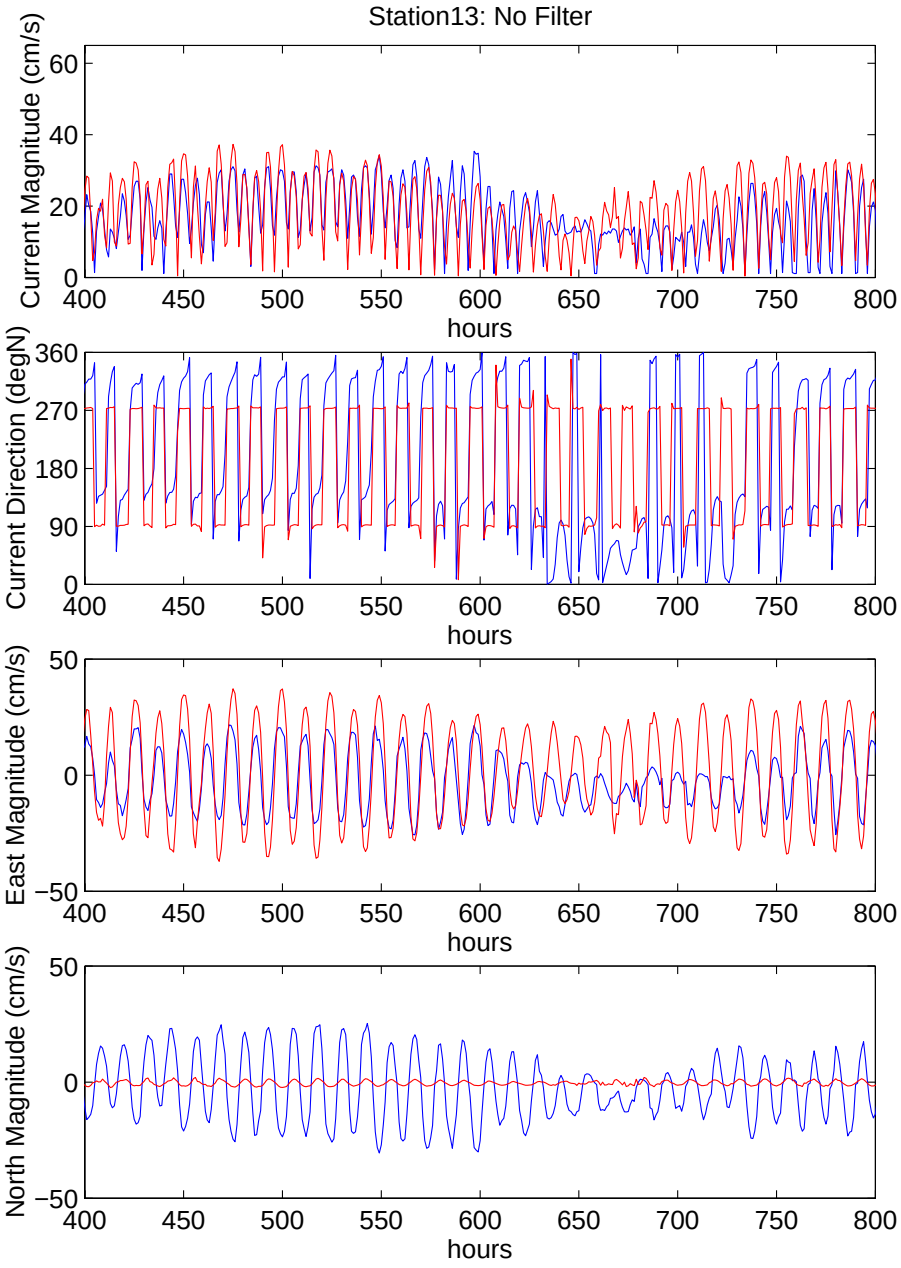

Figure B.5: Station 13: Time series comparison of measured (blue line) and modelled (red line) currents.

The model, once again, represents times of strong and weak currents. Early in the period however, the model significantly underestimated current speeds at low frequencies. At tidal frequencies, current direction is well represented in the model as seen in Figure B.6.

Figure B.6 shows a period of time 600 hours after the beginning of current measurements began, where a significant effect is predicted by the model which is not evident in the current measurements. This is possibly an error in the NCEP-NCAR wind and pressure forcing variables. Hogan and Hurlburt (2002) present the effects of seven differing wind climatologies on a simple hydrodynamic primitive equation model in the Japan/East Sea. They concluded that there was significant differences in the solutions purely as a result of the different surface momentum flux forcing. The NCEP dataset proved quite poor relative to other climatologies, in comparison to observations.

The N-S component of current shows a better correlation ($R^2 = 0.45$) than the E-W component ($R^2 = 0.44$). These correlations are likely to be offset by the incorrect prediction of the above mentioned significant event.

station 16, 1993 This station is positioned just to the east of the Warrior Reefs at the northern end of the Great Barrier Reef at position $9°49.2'S$, $143°15.1'E$. The current meter was deployed from the 16-01-93 to the 27-03-93.

The mean measured and modelled currents over the entire period at this site are shown in Table 3.9. The mean current is well represented by the model, apart from a directional offset of about 30° clockwise relative to the measured currents. This directional offset is also observed in the low-pass filtered currents.

There is moderate agreement between the model and measurements. Again, the model overestimates current speeds at tidal frequencies by approximately 20%. At the lower frequencies, the measured currents are well represented and indicate times of strong and weak currents well. Current direction has good representation in the model as seen in Figure B.7.

The N-S component of current shows a better correlation ($R^2 = 0.56$) than the E-W component ($R^2 = 0.49$).

Figure B.7 shows a period of an event predicted in the model which is unobserved in the measurements substantiating the idea that the wind and pressure data are erroneous over that period in the northern GBR area.

station 17, 1993 This station is located on the western side of Torres Strait at position $9°32.8'S$, $141°21.3'E$. The current meter was deployed from the 18-01-93 to the 27-03-93.

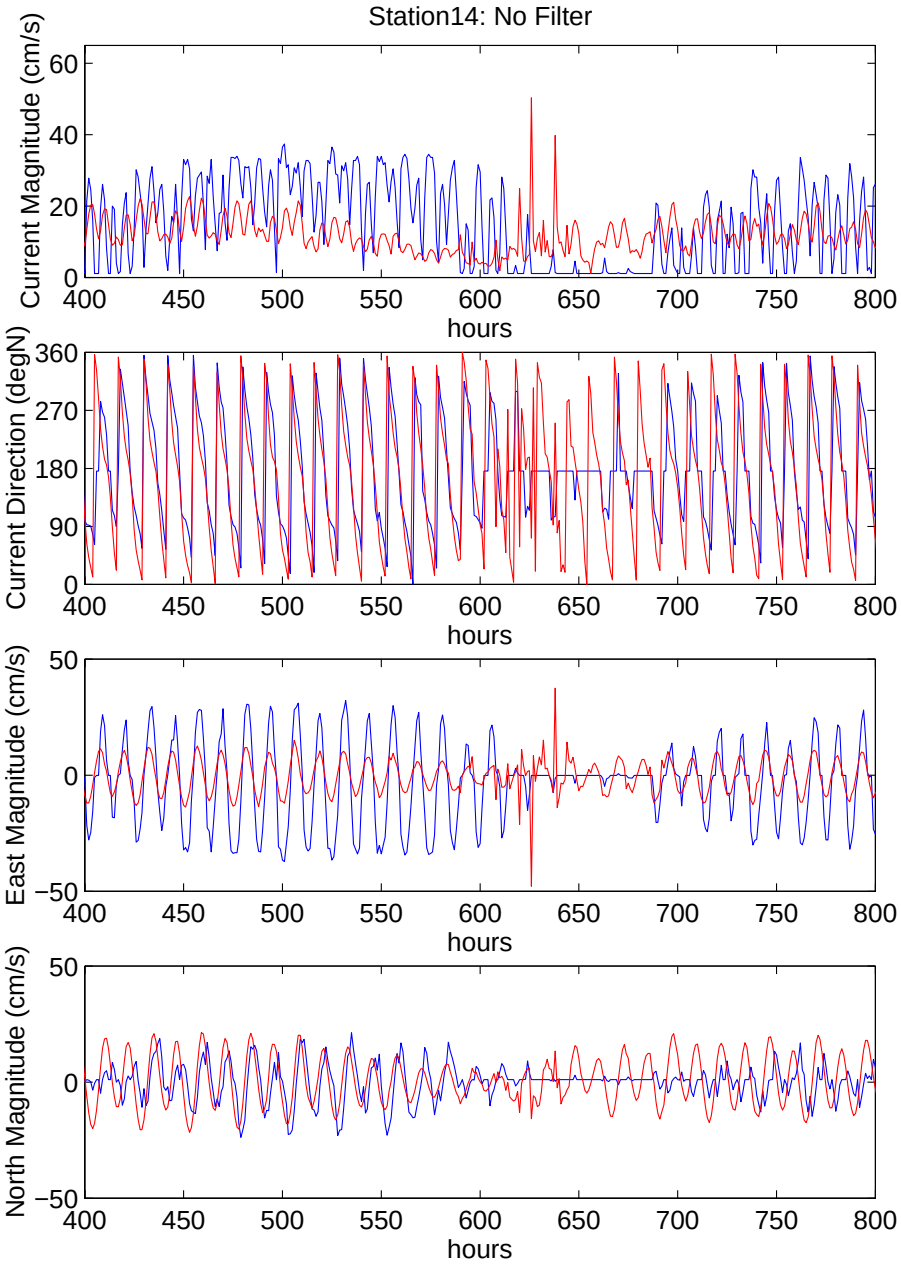

Figure B.6: Station 14: Time series comparison of measured (blue line) and modelled (red line) currents.

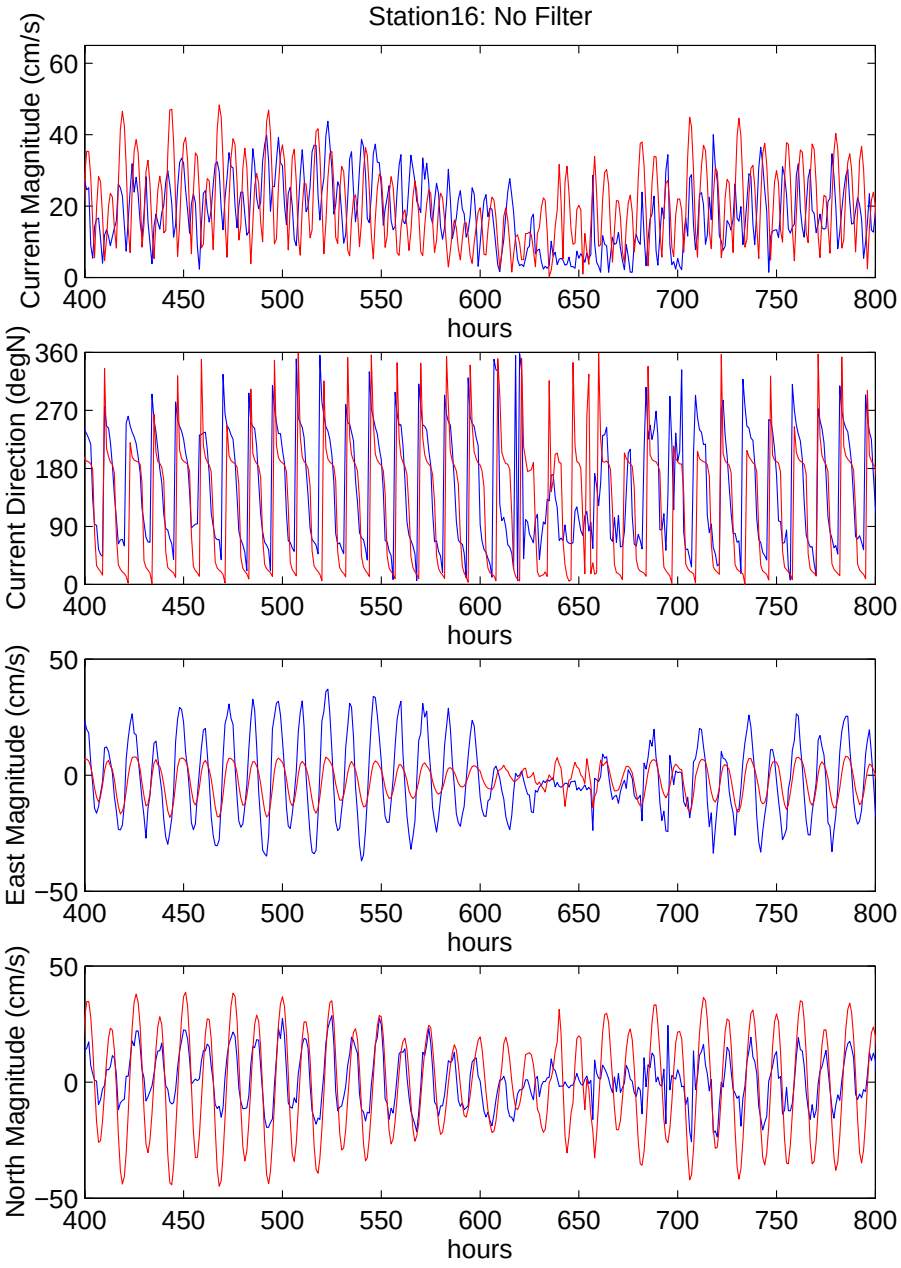

Figure B.7: Station 16: Time series comparison of measured (blue line) and modelled (red line) currents.

The mean measured and modelled currents over the entire period at this site are shown in Table 3.9. The model overestimates mean current magnitudes by 30% and a directional offset of about 20° anticlockwise relative to the measured currents is observed. This directional offset is also observed in the low-pass filtered currents.

The model at this station does poorly. Current speeds are generally of similar magnitudes, but are out of phase at all frequencies. The low frequency fluctuations driven by the wind are also poorly represented.

Both the N-S component of current correlation ($R^2 = 0.09$) and the E-W component ($R^2 = 0.012$) are poor.

station 19, 1993 This station is located in the south-west corner of Torres Strait at position $10°29.8'S$, $141°39.9'E$. The current meter was deployed from the 19-01-93 to the 28-03-93.

The mean measured and modelled currents over the entire period at this site are shown in Table 3.9. The mean model current is predicted to be twice as large as the mean measured current. Mean directions are approximately equal.

There is moderate agreement between the model and measurements. Current speeds are of similar magnitude at tidal frequencies (Fig. B.9), however they are commonly out of phase. The low frequency signal of the model is larger than the measured signal, particularly late in the record. Current direction is generally well represented in the model as seen in Figure B.9.

The correlations of the N-S component of current ($R^2 = 0.37$) and the E-W component ($R^2 = 0.50$) are significantly better than those of the other stations in the west of Torres Strait, station 17.

station 20, 1993 This station is located in Endeavour Strait at the northern tip of the Cape York, amongst the Torres Strait islands at position $10°51.8'S$, $142°10.0'E$. The current meter was deployed from the 18-01-93 to the 27-03-93.

The mean measured and modelled currents over the entire period at this site are shown in Table 3.9. The mean model current is, once again, twice the mean measured current. A directional offset of about 30° clockwise relative to the measured currents also exists. Local bathymetry is likely to affect the measured currents with the current meter at 11m depth in the shallow Endeavour Strait.

There is moderate agreement between the model and measurements. The model currents are of similar magnitudes, and only slightly out of phase. The maximum currents at

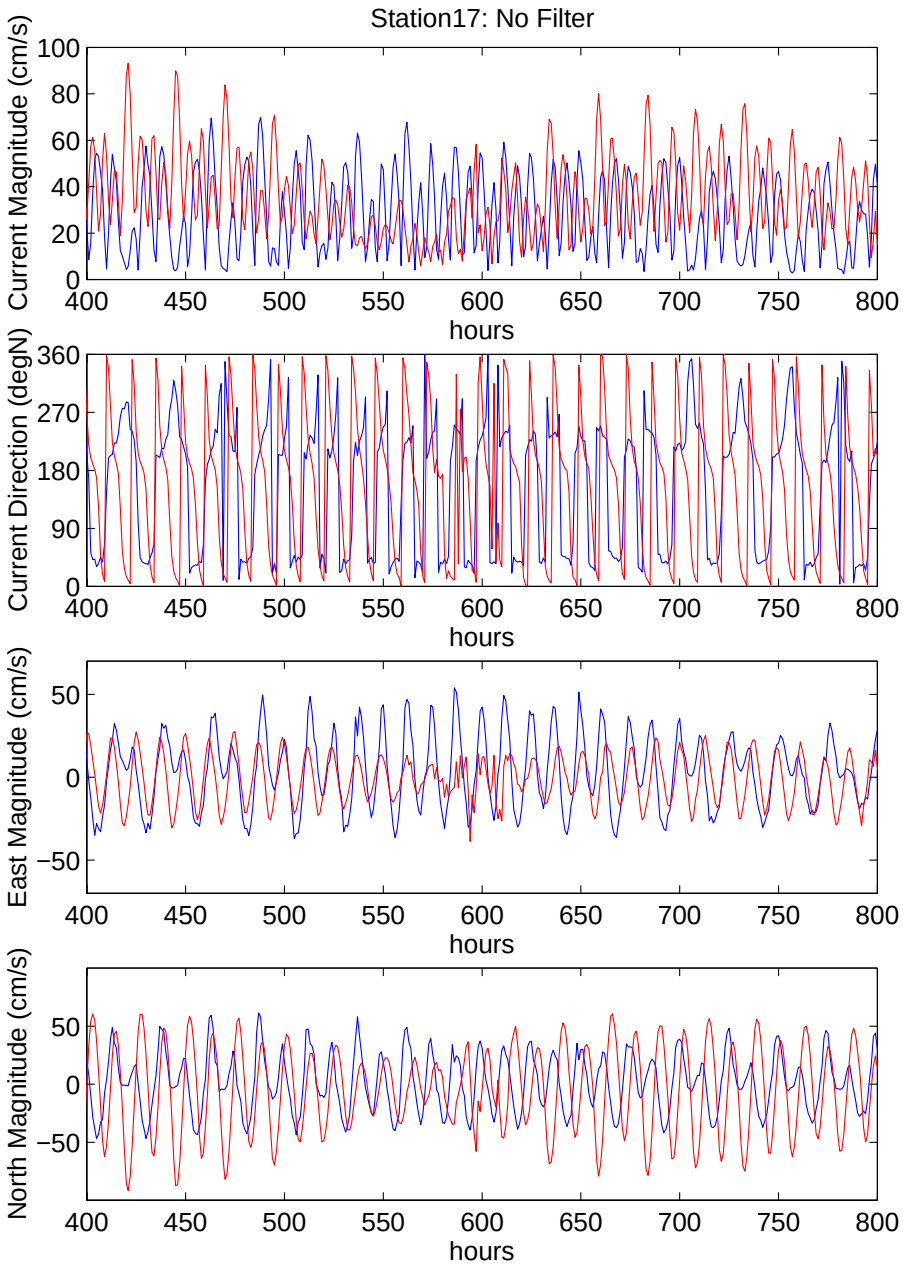

Figure B.8: Station 17: Time series comparison of measured (blue line) and modelled (red line) currents.

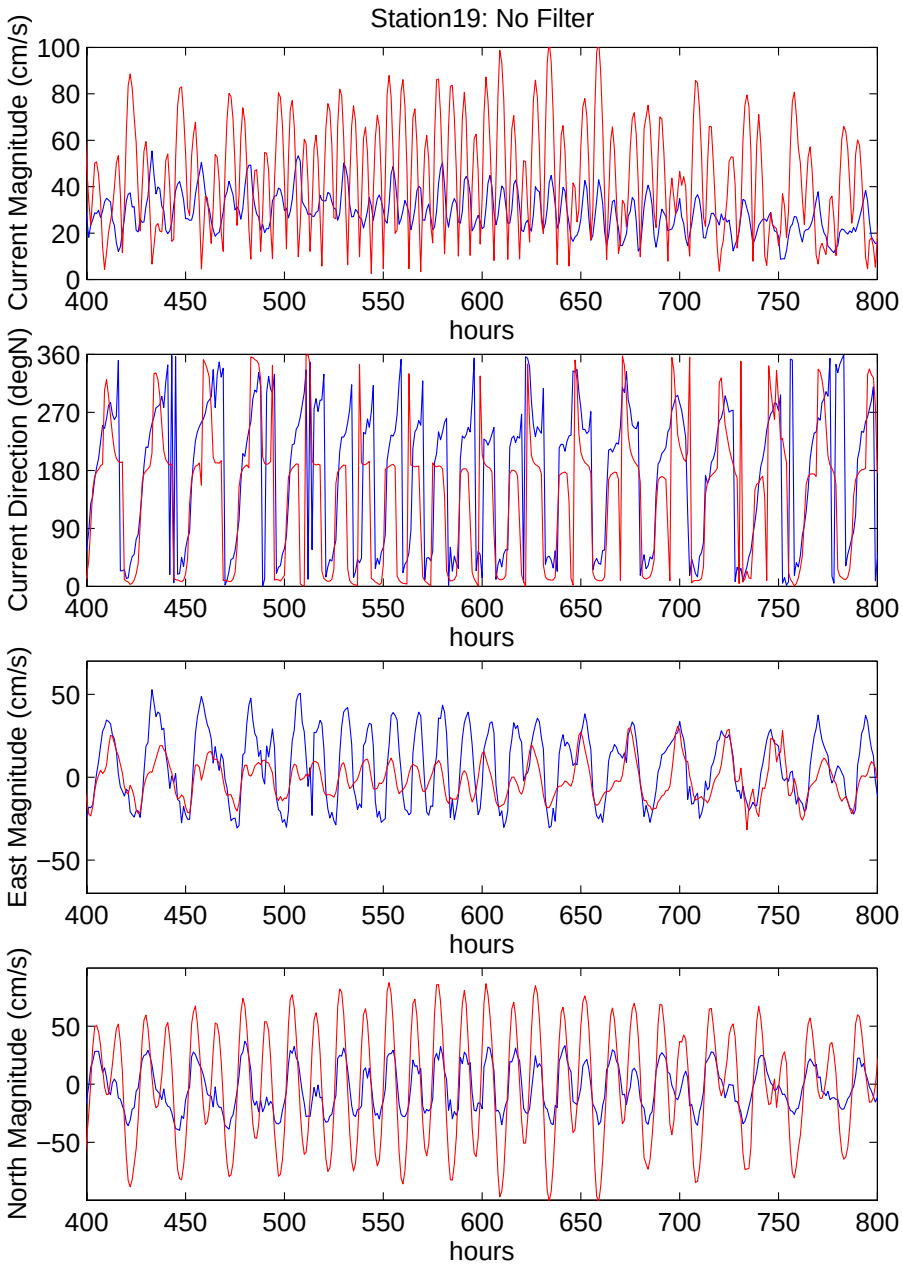

Figure B.9: Station 19: Time series comparison of measured (blue line) and modelled (red line) currents.

the tidal frequencies appear to be overestimated by the model (Fig. B.10). The low frequency signal shows only small fluctuations in magnitude in comparison to the measured currents. Current directions are generally well reproduced and are in phase with the measured directions.

The N-S component of current shows a better correlation ($R^2 = 0.66$) than the E-W component ($R^2 = 0.24$).

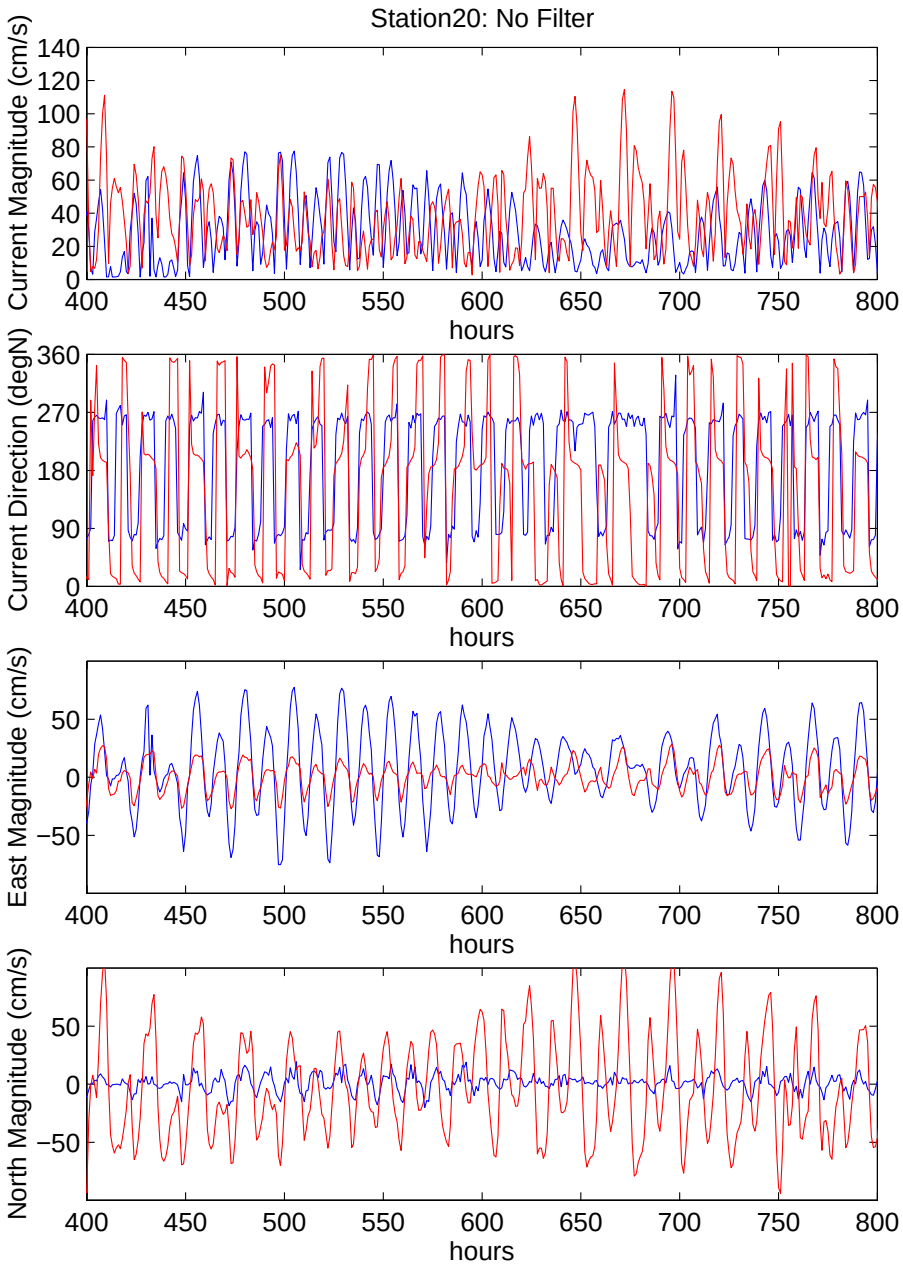

Figure B.10: Station 20: Time series comparison of measured (blue line) and modelled (red line) currents.

Appendix C

Threshold Exceedance Maps of Torres Strait and the Gulf of Papua.

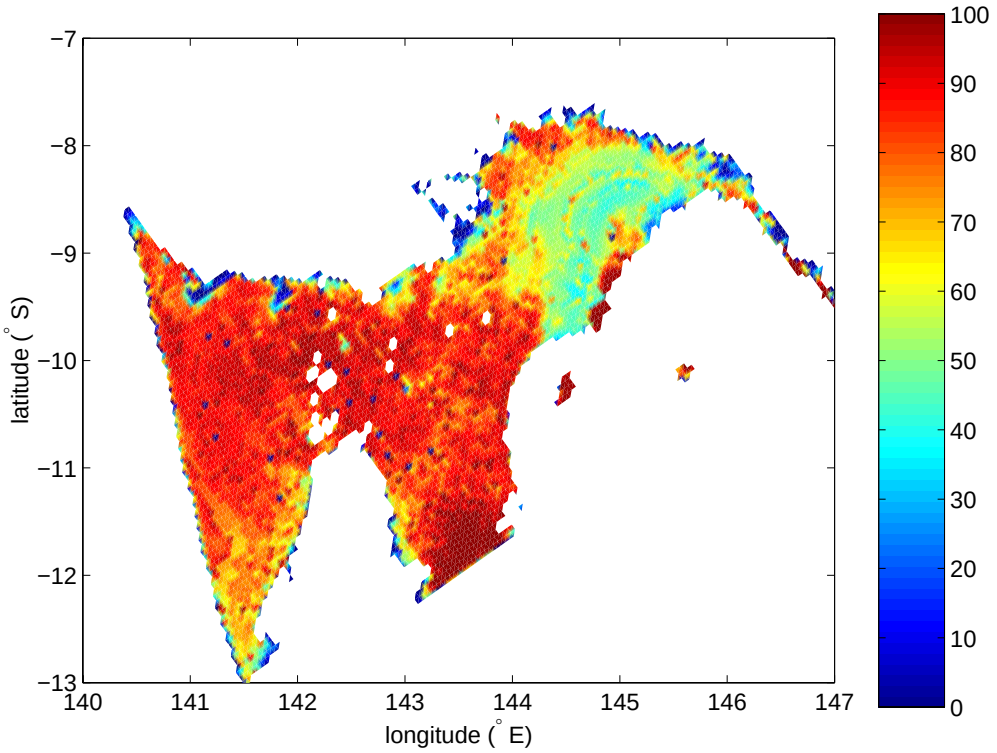

Figure C.1: Percentage time threshold exceedance due to currents during the NW Monsoon. $\tau_{cr} = 0.05 N m^{-2}$, i.e., 0.01 mm diameter cohesionless sediment

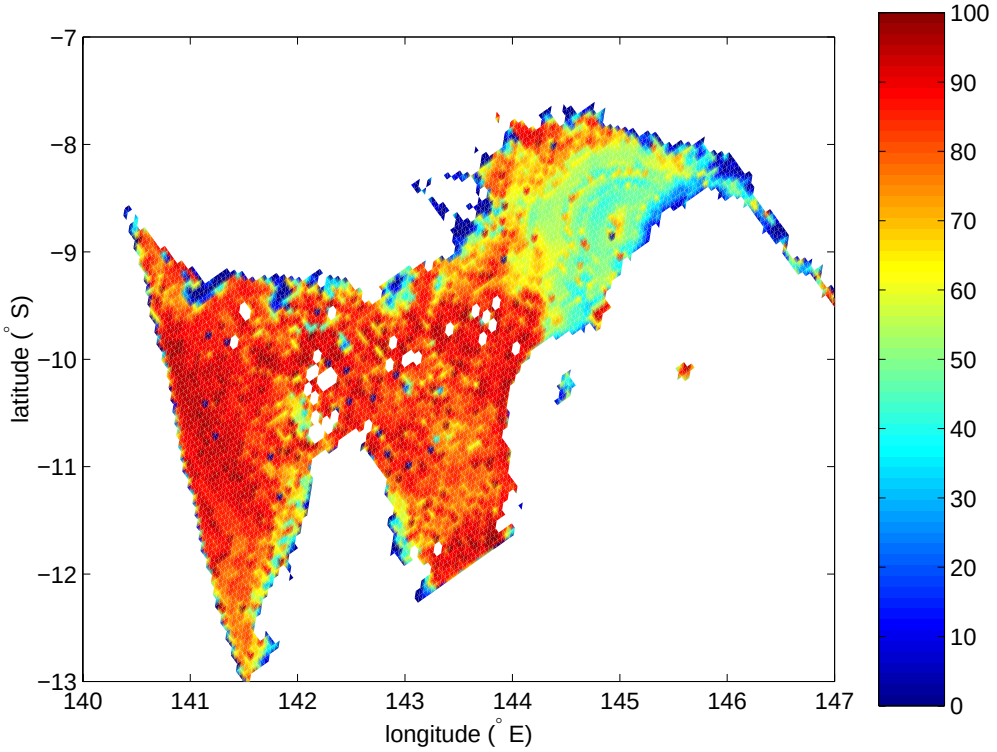

Figure C.2: Percentage time threshold exceedance due to currents during the SE Trades. $\tau_{cr} = 0.05 N m^{-2}$, i.e., 0.01 mm diameter cohesionless sediment

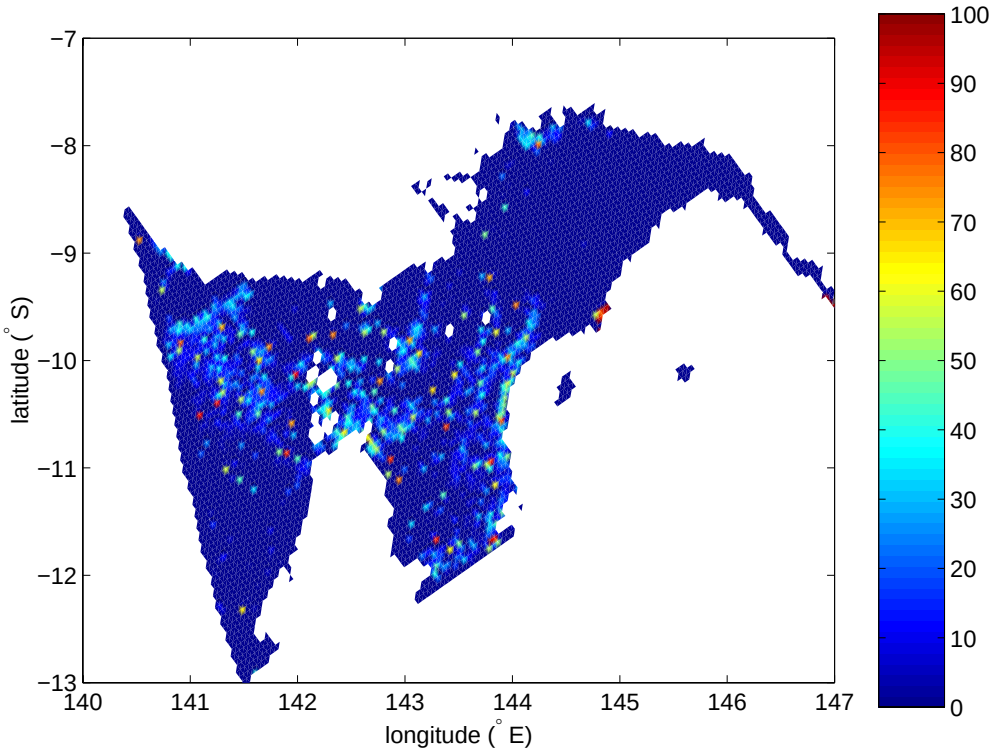

Figure C.3: Percentage time threshold exceedance due to currents during the NW Monsoon. $\tau_{cr} = 1.25 N m^{-2}$, i.e., 2 mm diameter cohesionless sediment

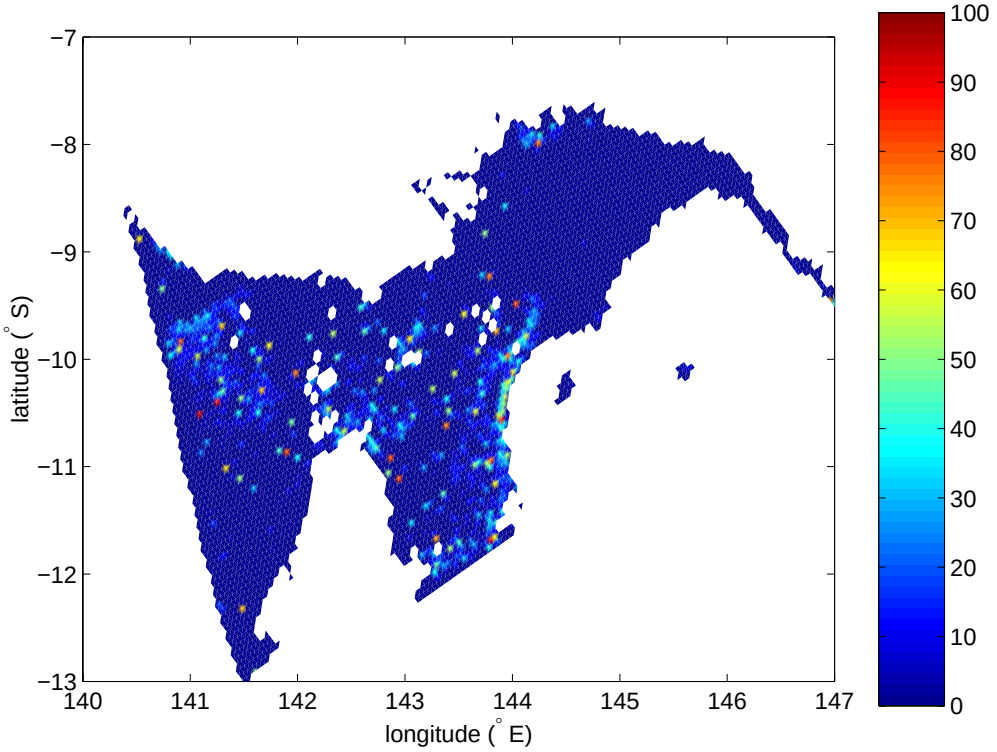

Figure C.4: Percentage time threshold exceedance due to currents during the SE Trades. $\tau_{cr} = 1.25 N m^{-2}$, i.e., 2 mm diameter cohesionless sediment

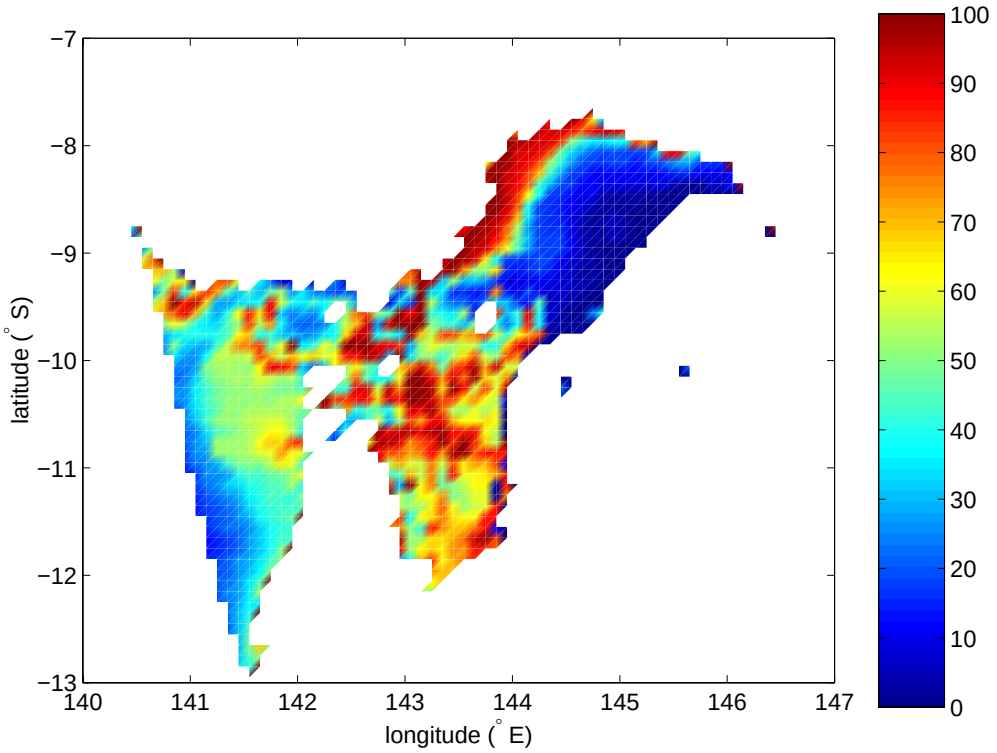

Figure C.5: Percentage time threshold exceedance due to waves during the NW Monsoon. $\tau_{cr} = 0.05 N m^{-2}$, i.e., 0.01 mm diameter cohesionless sediment

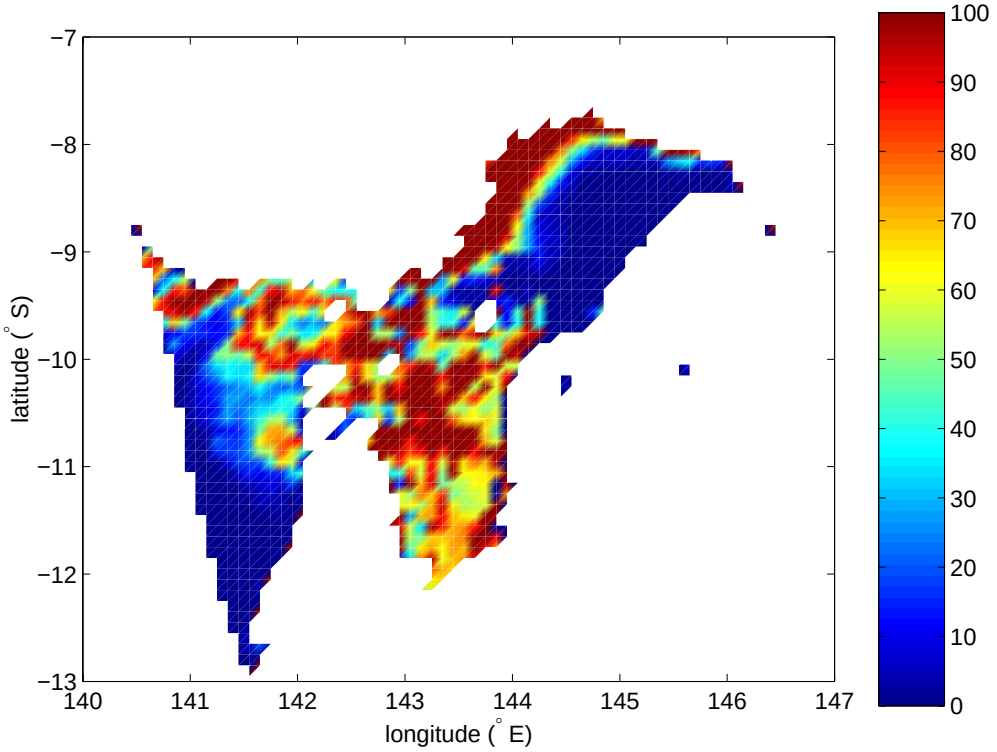

Figure C.6: Percentage time threshold exceedance due to waves during the SE Trades. $\tau_{cr} = 0.05 N m^{-2}$, i.e., 0.01 mm diameter cohesionless sediment

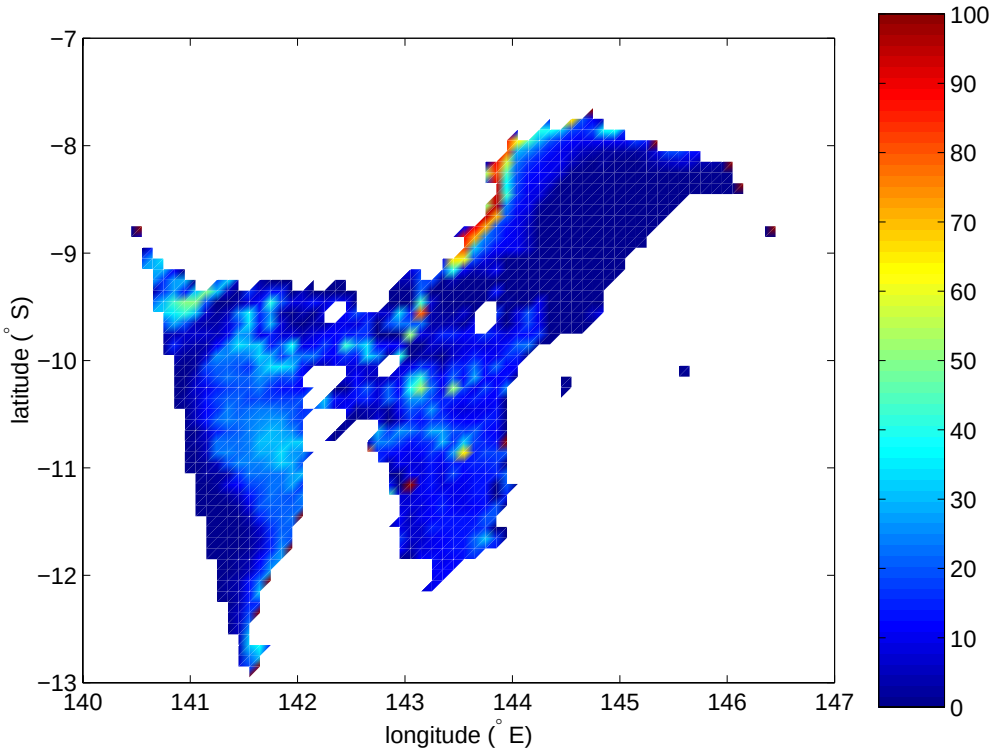

Figure C.7: Percentage time threshold exceedance due to waves during the NW Monsoon. $\tau_{cr} = 1.25 N m^{-2}$, i.e., 2 mm diameter cohesionless sediment

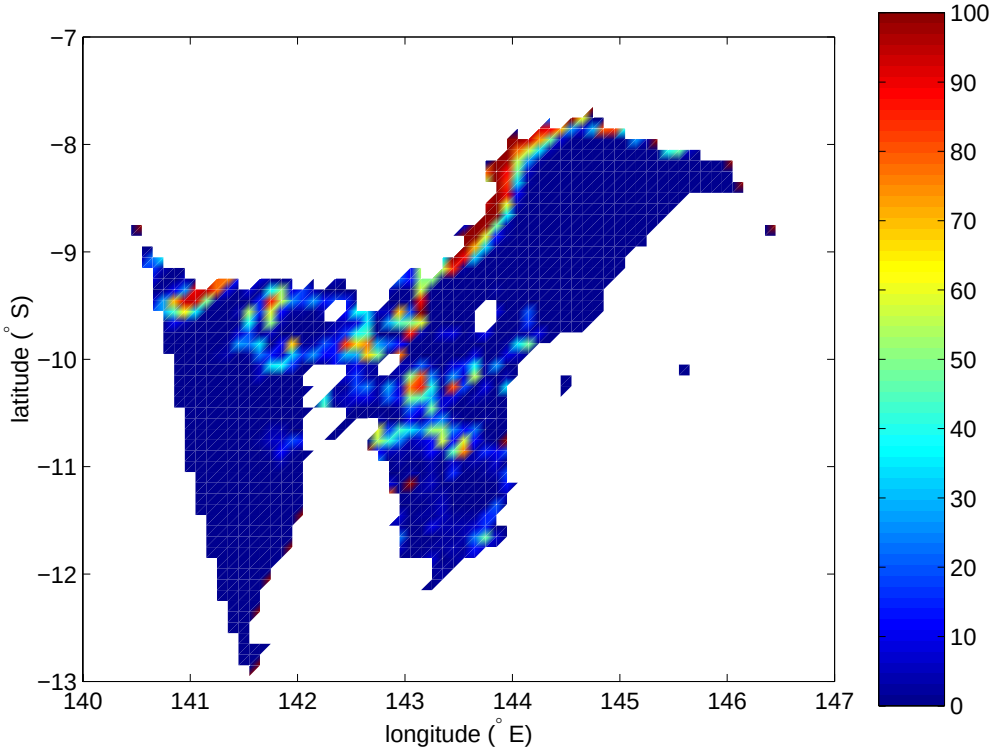

Figure C.8: Percentage time threshold exceedance due to waves during the SE Trades. $\tau_{cr} = 1.25 N m^{-2}$, i.e., 2 mm diameter cohesionless sediment

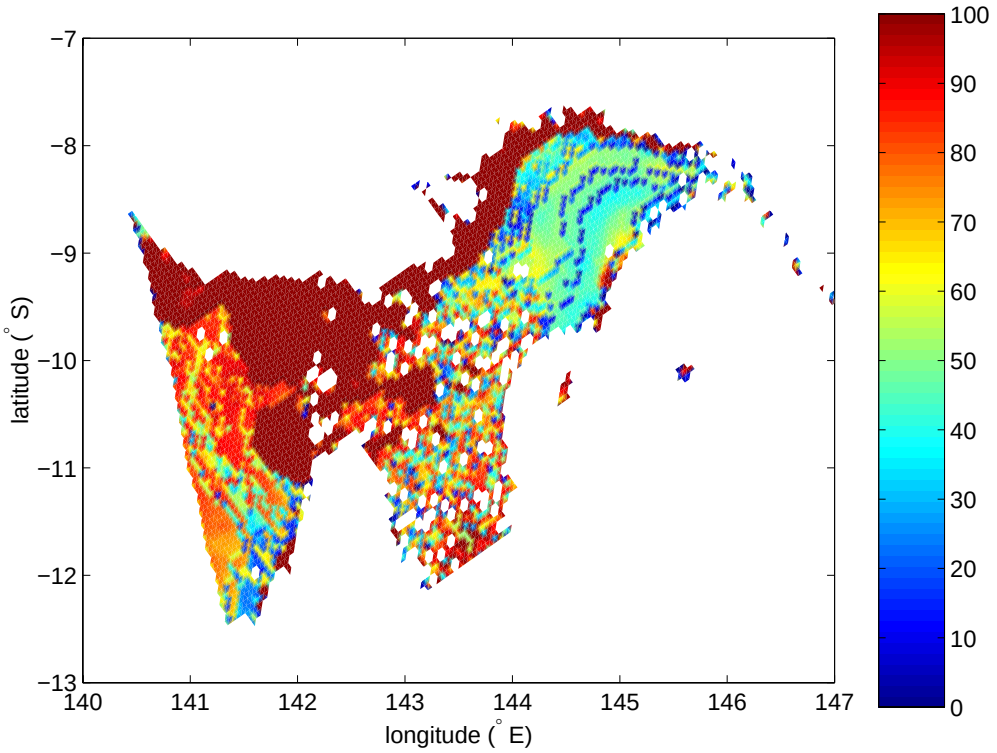

Figure C.9: Percentage time threshold exceedance due to wave-current flow during the NW Monsoon. $\tau_{cr} = 0.05 Nm^{-2}$, i.e., 0.01 mm diameter cohesionless sediment

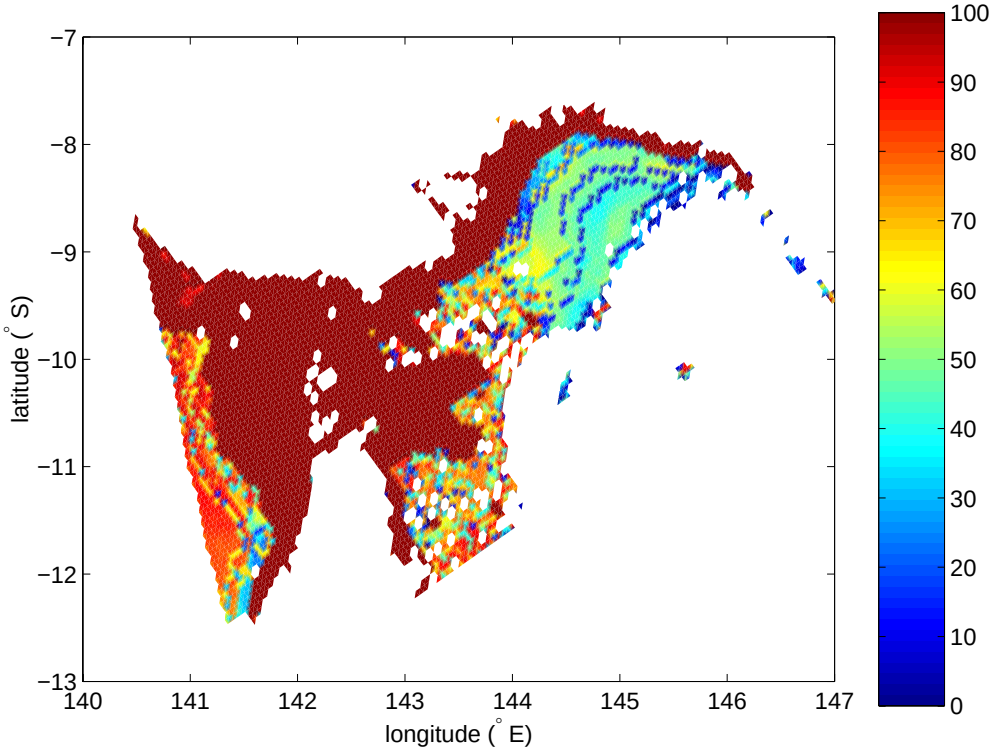

Figure C.10: Percentage time threshold exceedance due to wave-current flow during the SE Trades. $\tau_{cr} = 0.05 Nm^{-2}$, i.e., 0.01 mm diameter cohesionless sediment

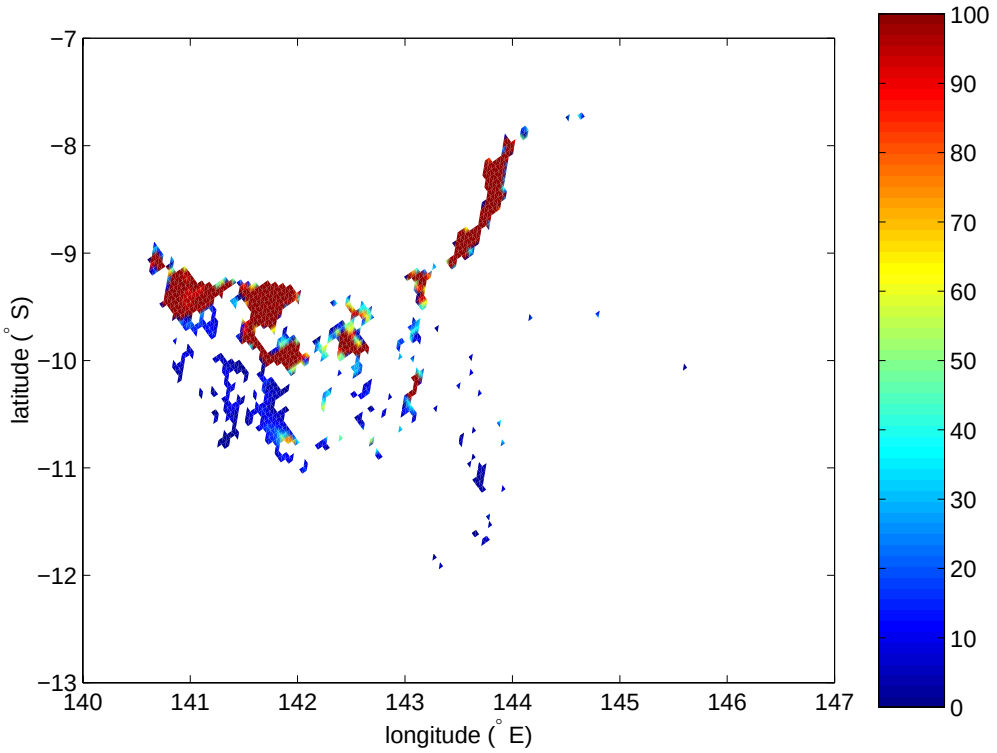

Figure C.11: Percentage time threshold exceedance due to wave-current flow during the NW Monsoon. $\tau_{cr} = 1.25 Nm^{-2}$, i.e., 2 mm diameter cohesionless sediment

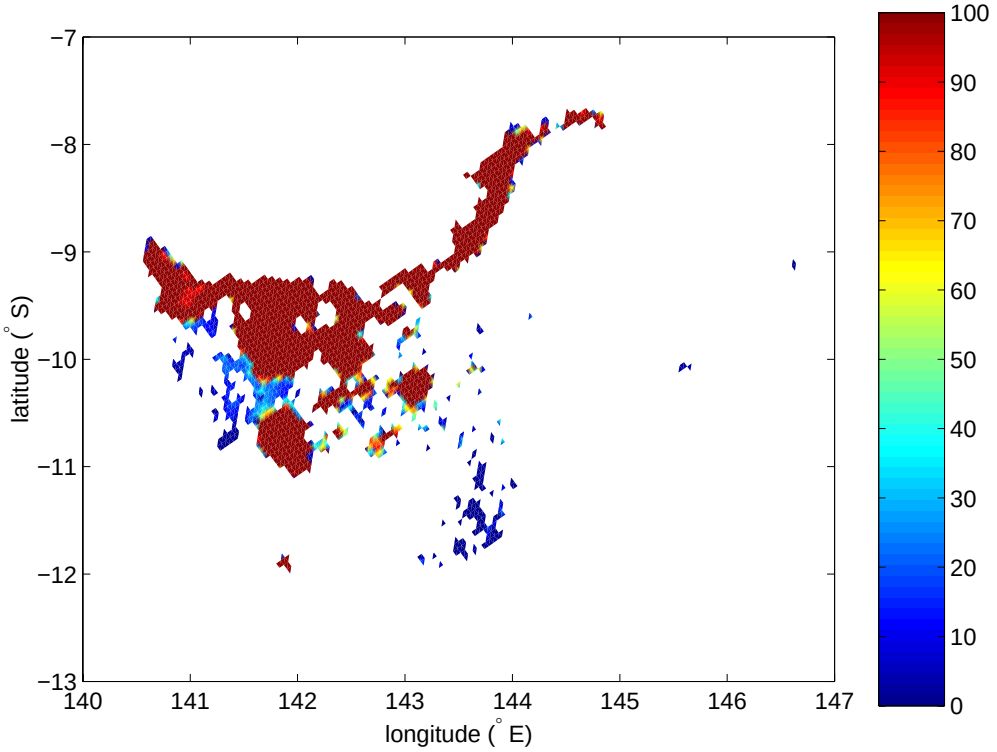

Figure C.12: Percentage time threshold exceedance due to wave-current flow during the SE Trades. $\tau_{cr} = 1.25 Nm^{-2}$, i.e., 2 mm diameter cohesionless sediment

Appendix D

Relative Diatom Abundances from surface samples collected adjacent to the Amery Ice Shelf front, and from down AM02 core

Table D.1: Relative Diatom Abundances (%). Surface Grab samples from adjacent to the Amery Ice Shelf front and at the AM01 site, and AM02 down-core samples (as labelled in cm from surface).

SAMPLE	au0106 Grab1	au0106 Grab3	au0207 Grab1	AM01	0-1cm	5-6cm	6-7cm
Actinocyclus actinochilus	0.00	0.00	0.00	0.00	0.00	0.23	0.45
Achnantes Charcotti	0.00	0.00	0.00	0.00	0.00	0.00	0.00
Asteromphalus spp.	0.23	0.23	0.00	0.23	0.22	0.23	0.22
Azp. Tabularis	0.00	0.00	0.00	0.00	0.00	0.00	0.00
Cocconeis costata	0.23	0.00	0.00	0.00	0.00	0.00	0.00
Cosconodiscus spp.	0.00	0.00	0.00	0.00	0.00	0.00	0.00
Dactyliosolen antarcticus	0.00	0.00	0.00	0.00	0.45	0.00	0.22
Distephanus speculum	0.00	0.00	0.00	0.00	2.47	2.77	1.34
Eucampia antarctica	0.47	0.93	0.96	4.34	1.57	1.39	0.67
Fragilariopsis curta	60.42	56.71	56.49	36.07	44.62	48.27	49.22
Fragilariopsis cylindrus	14.29	14.12	3.37	2.51	0.67	0.92	3.13
Fragilariopsis kerguelensis	0.47	0.93	0.24	2.74	2.02	3.93	1.57
Fragilariopsis lineata	0.00	0.00	0.24	0.68	0.00	0.46	0.00
Fragilariopsis obliquecostata	0.00	0.00	0.24	0.00	0.00	0.00	0.00
Fragilariopsis rhombica	1.64	2.31	4.09	6.62	5.38	5.31	4.47
Fragilariopsis separanda	0.00	1.39	0.00	1.14	0.22	0.46	0.22
Fragilariopsis sublineata	4.68	4.63	9.38	6.39	4.71	1.39	3.36
Fragilariopsis vanheurckii	0.94	0.93	0.96	2.05	0.00	1.15	1.34
Navicula directa	0.00	0.23	0.00	0.00	0.00	0.00	0.00
Pentalamina corona	0.00	0.00	0.00	0.00	0.00	0.00	0.00
Pleurosigma directum	0.00	0.00	0.00	0.00	0.22	0.00	0.00
Porosira glacialis	0.94	1.39	0.96	2.05	2.91	0.69	2.91
Porosira pseudodenticulara	0.00	0.00	0.00	0.00	0.00	0.00	0.00
Rhizosolenia spp.	0.00	0.23	0.00	0.00	0.00	0.00	0.22
Stellarima microtrias	0.23	0.46	0.96	0.91	0.22	0.23	0.67
Stellarima stellaris	0.70	0.46	0.00	0.00	0.00	0.00	0.00
Thalassiosira antarctica	13.82	12.27	21.15	32.88	30.04	30.25	26.40
Thalassiosira gracilis	0.47	1.85	0.72	0.00	2.47	0.92	0.89
Thalassiosira lentiginosa	0.23	0.23	0.24	0.46	0.45	0.69	1.34
Thalassiosira tumida	0.23	0.46	0.00	0.68	0.67	0.69	0.89
Thalassiothrix antarctica	0.00	0.23	0.00	0.00	0.00	0.00	0.00
Trichotoxin reinboldii	0.00	0.00	0.00	0.00	0.45	0.00	0.22
Other centrics	0.00	0.00	0.00	0.23	0.22	0.00	0.22
TOTAL	100.00	100.00	100.00	100.00	100.00	100.00	100.00
Chaetoceros cysts	6.09	3.47	2.40	9.82	4.48	4.62	10.07

Table D.2: Relative Diatom Abundances (%). AM02 down-core samples.

SAMPLE	7-8 cm	8-9 cm	9-10cm	10-11cm	10-11cm(2)	12+/-0.5cm	13+/-0.5cm	14+/-0.5cm
Actinocyclus actinochilus	0.45	0.23	0.00	0.00	0.23	0.45	0.47	0.23
Achnantes Charcotti	0.00	0.00	0.00	0.00	0.00	0.00	0.00	0.00
Asteromphalus spp.	0.45	0.23	0.68	0.00	0.00	0.23	0.23	0.46
Azp. Tabularis	0.00	0.00	0.00	0.00	0.00	0.00	0.00	0.00
Cocconeis costata	0.00	0.00	0.00	0.00	0.00	0.00	0.00	0.23
Cosconodiscus spp.	0.00	0.00	0.00	0.00	0.00	0.00	0.00	0.00
Dactyliosolen antarcticus	0.23	0.00	0.23	0.00	0.00	0.68	0.00	0.46
Distephanus speculum	1.82	1.61	0.91	0.48	0.70	1.14	0.47	1.14
Eucampia antarctica	0.91	0.92	1.60	0.48	0.70	3.41	1.16	2.52
Fragilariopsis curta	49.55	53.79	49.09	61.05	60.37	52.05	46.74	40.73
Fragilariopsis cylindrus	3.41	1.38	1.83	0.48	3.50	1.82	1.16	2.52
Fragilariopsis kerguelensis	2.05	2.30	0.68	4.75	1.40	2.05	1.63	2.29
Fragilariopsis lineata	0.00	0.00	0.23	0.00	0.00	0.23	0.00	0.00
Fragilariopsis obliquecostata	0.00	0.00	0.00	0.24	0.00	0.00	0.00	0.23
Fragilariopsis rhombica	3.86	4.83	6.16	6.65	5.13	3.41	3.72	3.66
Fragilariopsis separanda	0.00	0.00	0.23	0.00	1.40	0.23	0.47	0.69
Fragilariopsis sublineata	6.36	3.45	7.31	3.56	6.29	5.23	6.74	5.03
Fragilariopsis vanheurckii	2.50	2.30	1.37	0.48	0.70	0.00	0.93	0.69
Navicula directa	0.00	0.00	0.00	0.00	0.00	0.68	0.00	0.00
Pentalamina corona	0.00	0.00	0.00	0.00	0.00	0.00	0.00	0.00
Pleurosigma directum	0.00	0.00	0.00	0.00	0.00	0.00	0.00	0.00
Porosira glacialis	1.36	2.07	1.83	0.95	1.40	1.82	2.33	1.83
Porosira pseudodenticulara	0.00	0.00	0.00	0.00	0.00	0.00	0.00	0.23
Rhizosolenia spp.	0.00	0.00	0.00	0.00	0.23	0.00	0.23	0.00
Stellarima microtrias	0.00	0.00	0.46	0.00	0.00	0.91	0.23	1.14
Stellarima stellaris	0.00	0.00	0.00	0.00	0.93	0.00	0.00	0.00
Thalassiosira antarctica	25.00	24.60	23.97	18.76	15.62	23.41	31.86	34.32
Thalassiosira gracilis	0.45	0.69	0.91	1.19	0.23	0.91	0.23	0.92
Thalassiosira lentiginosa	1.14	0.69	0.23	0.24	0.00	0.91	0.70	0.46
Thalassiosira tumida	0.23	0.69	1.60	0.24	0.93	0.45	0.23	0.23
Thalassiothrix antarctica	0.00	0.00	0.23	0.00	0.00	0.00	0.00	0.00
Trichotoxin reinboldii	0.23	0.23	0.46	0.48	0.23	0.00	0.47	0.00
Other centrics	0.00	0.00	0.00	0.00	0.00	0.00	0.00	0.00
TOTAL	100.00	100.00	100.00	100.00	100.00	100.00	100.00	100.00
Chaetoceros cysts	7.73	8.97	3.88	2.85	7.93	7.95	10.70	8.47

Table D.3: Relative Diatom Abundances (%). AM02 down-core samples.

SAMPLE	15-16cm	20-21cm	25-26cm	30-31cm	35-36cm	40-41cm	41-42cm	42-43cm
Actinocyclus actinochilus	0.23	0.23	0.00	0.24	0.00	0.23	0.00	0.48
Achnantes Charcotti	0.00	0.00	0.00	0.00	0.00	0.00	0.00	0.00
Asteromphalus spp.	0.46	0.23	0.23	0.00	0.46	0.00	0.23	0.24
Azp. Tabularis	0.00	0.00	0.00	0.00	0.00	0.00	0.46	0.00
Cocconeis costata	0.00	0.00	0.00	0.00	0.00	0.00	0.00	0.00
Cosconodiscus spp.	0.00	0.00	0.00	0.00	0.00	0.00	0.00	0.00
Dactyliosolen antarcticus	0.23	0.47	0.23	0.47	0.00	0.00	0.46	0.48
Distephanus speculum	2.74	1.63	3.39	1.65	1.38	1.36	0.93	0.48
Eucampia antarctica	1.14	1.17	0.23	2.59	3.68	2.94	3.70	3.80
Fragilariopsis curta	39.27	32.87	22.62	21.46	21.15	23.30	25.93	26.60
Fragilariopsis cylindrus	2.74	2.80	0.90	2.59	1.61	1.58	2.31	3.09
Fragilariopsis kerguelensis	3.65	4.66	5.43	7.31	6.21	5.20	3.70	3.80
Fragilariopsis lineata	0.00	0.00	0.68	0.00	0.46	0.23	0.00	0.00
Fragilariopsis obliquecostata	0.00	0.23	0.00	0.00	0.23	0.23	0.46	0.00
Fragilariopsis rhombica	4.79	5.83	5.66	4.01	5.06	1.81	1.39	0.48
Fragilariopsis separanda	0.00	0.00	0.00	0.00	0.00	0.00	0.00	0.24
Fragilariopsis sublineata	1.83	1.86	1.36	2.12	2.76	4.52	5.56	6.89
Fragilariopsis vanheurckii	0.46	0.47	0.23	0.94	1.38	1.13	1.16	0.00
Navicula directa	0.23	0.00	0.00	0.00	0.00	0.00	0.23	0.48
Pentalamina corona	0.00	0.00	0.00	0.00	0.00	0.00	0.00	0.00
Pleurosigma directum	0.00	0.00	0.00	0.00	0.00	0.00	0.00	0.00
Porosira glacialis	1.83	0.93	1.36	1.65	0.69	0.45	0.23	0.48
Porosira pseudodenticulara	0.00	0.00	0.00	0.00	0.00	0.00	0.00	0.00
Rhizosolenia spp.	0.00	0.47	0.90	0.24	0.23	1.13	0.00	0.00
Stellarima microtrias	0.00	0.00	0.00	0.00	0.00	0.23	0.23	0.48
Stellarima stellaris	0.00	0.00	0.00	0.00	0.00	0.00	0.00	0.00
Thalassiosira antarctica	37.44	43.59	52.26	52.12	51.03	50.68	50.00	48.93
Thalassiosira gracilis	0.68	0.47	2.71	0.71	0.92	2.04	1.62	1.43
Thalassiosira lentiginosa	1.37	1.17	1.13	1.18	1.84	1.58	0.46	0.71
Thalassiosira tumida	0.00	0.70	0.68	0.71	0.69	0.23	0.93	0.95
Thalassiothrix antarctica	0.46	0.00	0.00	0.00	0.00	0.90	0.00	0.00
Trichotoxin reinboldii	0.46	0.23	0.00	0.00	0.23	0.00	0.00	0.00
Other centrics	0.00	0.00	0.00	0.00	0.00	0.23	0.00	0.00
TOTAL	100.00	100.00	100.00	100.00	100.00	100.00	100.00	100.00
Chaetoceros cysts	6.16	10.49	10.41	9.43	13.10	23.08	22.69	16.15

Table D.4: Relative Diatom Abundances (%). AM02 down-core samples.

SAMPLE	43-44cm	44-45cm	45-46cm	47+/-0.5cm	48+/-0.5cm	49+/-0.5cm	51-52cm	55-56cm
Actinocyclus actinochilus	0.24	0.24	0.23	0.24	0.24	0.00	0.00	0.23
Achnantes Charcotti	0.00	0.00	0.00	0.24	0.00	0.00	0.00	0.00
Asteromphalus spp.	0.00	0.47	0.23	0.00	0.24	0.24	0.47	0.00
Azp. Tabularis	0.00	0.00	0.00	0.00	0.00	0.00	0.00	0.00
Cocconeis costata	0.00	0.00	0.00	0.00	0.00	0.00	0.00	0.00
Cosconodiscus spp.	0.48	0.00	0.00	0.24	0.24	0.00	0.00	0.00
Dactyliosolen antarcticus	0.00	0.47	0.46	0.71	0.24	0.24	0.23	0.00
Distephanus speculum	1.19	0.71	0.46	0.47	1.65	0.24	1.41	0.93
Eucampia antarctica	1.19	3.53	3.00	2.12	1.18	2.91	1.17	2.32
Fragilariopsis curta	28.74	34.35	39.03	41.51	33.73	30.58	25.59	36.19
Fragilariopsis cylindrus	5.94	4.24	1.85	2.12	1.65	2.43	0.94	2.78
Fragilariopsis kerguelensis	3.33	3.29	3.93	2.59	1.89	3.16	6.34	3.94
Fragilariopsis lineata	0.00	0.00	0.46	0.00	0.00	0.00	0.00	0.23
Fragilariopsis obliquecostata	0.00	0.00	0.23	0.24	0.00	0.00	0.00	0.46
Fragilariopsis rhombica	0.95	1.41	1.15	0.47	0.94	0.97	0.70	0.46
Fragilariopsis separanda	0.00	0.00	0.00	0.24	0.00	0.00	0.00	0.46
Fragilariopsis sublineata	8.79	7.53	7.85	5.90	6.37	6.07	1.41	5.57
Fragilariopsis vanheurckii	0.00	0.47	1.39	1.18	0.71	0.73	0.94	1.39
Navicula directa	0.48	0.24	0.00	0.24	0.24	0.00	0.00	0.23
Pentalamina corona	0.00	0.00	0.00	0.00	0.00	0.00	0.00	0.23
Pleurosigma directum	0.00	0.00	0.00	0.00	0.00	0.00	0.00	0.00
Porosira glacialis	0.48	0.71	0.23	0.00	0.24	0.49	0.47	0.00
Porosira pseudodenticulara	0.00	0.00	0.00	0.00	0.00	0.00	0.00	0.00
Rhizosolenia spp.	0.00	0.47	0.23	0.24	0.00	0.24	0.47	0.00
Stellarima microtrias	0.00	0.00	0.23	0.24	0.24	0.00	0.00	0.23
Stellarima stellaris	0.00	0.00	0.00	0.00	0.00	0.00	0.00	0.00
Thalassiosira antarctica	45.84	40.00	36.49	39.39	48.58	49.51	57.75	41.07
Thalassiosira gracilis	0.24	0.47	0.92	0.47	0.71	1.70	0.23	0.46
Thalassiosira lentiginosa	0.95	0.71	0.23	0.71	0.71	0.00	0.94	0.93
Thalassiosira tumida	0.95	0.47	1.39	0.47	0.24	0.49	0.70	1.16
Thalassiothrix antarctica	0.00	0.00	0.00	0.00	0.00	0.00	0.00	0.00
Trichotoxin reinboldii	0.24	0.24	0.00	0.00	0.00	0.00	0.23	0.70
Other centrics	0.00	0.00	0.00	0.00	0.00	0.00	0.00	0.00
TOTAL	100.00	100.00	100.00	100.00	100.00	100.00	100.00	100.00
Chaetoceros cysts	21.38	17.41	16.17	13.44	20.52	18.20	6.57	19.95

Appendix E

The AM02 core

Next Page: Digital images of the AM02 core: Left Panel: 0 - 80 cm, Right Panel: 80 - 145 cm.

Following page: Scanned AM02 x-ray radiograph images: Left Panel: 0 - 60 cm, Right Panel: 60 - 145 cm.

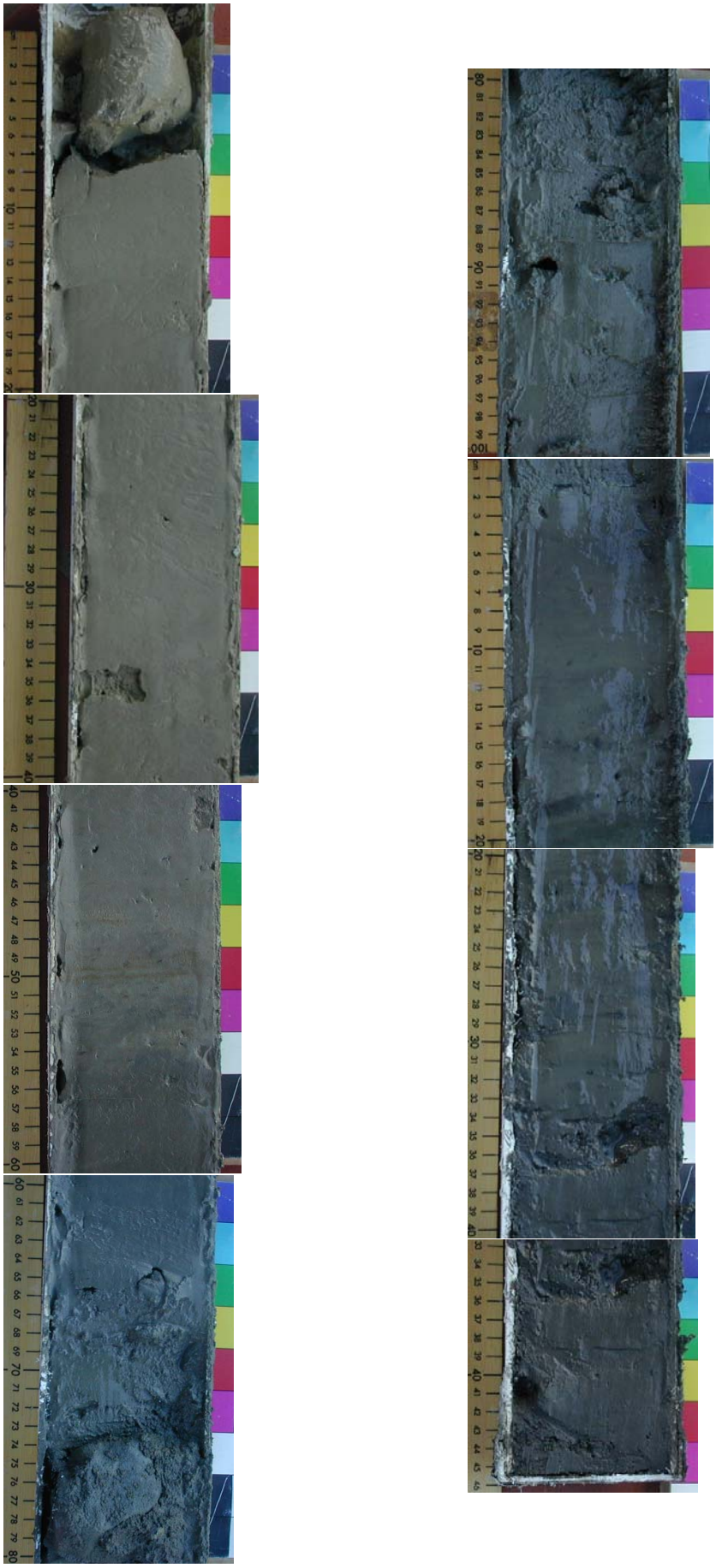

Appendix F

Harmonic Analysis of Amery Tide Models:

Model to Observed constituent Comparisons.

Table F.1: Observed and predicted tidal harmonic constituents for GPS and Tide Gauge sites in the Amery Ice Shelf/Prydz Bay model domain. A comparison MECO model runs with different WCT grids. Amplitude is in metres, Phase is in degrees relative to GMT. ZS represents Zhong-Shan, and BL represents Beaver Lake.

Location/	M_2		S_2		K_1		O_1	
WCT grid	Ampl.	Phase	Ampl.	Phase	Ampl.	Phase	Ampl.	Phase
ZS.obs	0.20	212	0.18	311	0.27	287	0.28	259
A	0.20	208	0.19	322	0.25	281	0.29	277
B	0.18	207	0.17	318	0.25	281	0.29	278
C	0.18	207	0.17	317	0.25	281	0.30	278
CADA	0.17	209	0.16	319	0.26	282	0.29	279
BL.obs	0.24	253	0.25	357	0.28	296	0.30	288
A	0.40	275	0.43	39	0.29	301	0.32	299
B	0.25	219	0.24	332	0.27	286	0.31	284
C	0.26	220	0.26	333	0.27	287	0.32	284
CADA	0.22	220	0.21	332	0.27	287	0.30	285
HWDT.obs	0.19	215	0.20	319	0.26	281	0.28	272
A	0.24	212	0.24	328	0.25	281	0.30	278
B	0.19	208	0.19	319	0.25	282	0.30	279
C	0.20	207	0.19	318	0.25	282	0.30	278
CADA	0.18	211	0.17	322	0.26	283	0.29	281
TS1.obs	0.21	222	0.20	323	0.32	294	0.28	266
A	0.25	224	0.25	344	0.25	284	0.30	281
B	0.20	213	0.20	325	0.25	284	0.30	281
C	0.21	213	0.20	325	0.25	284	0.30	281
CADA	0.19	215	0.18	327	0.26	285	0.29	283
TS3.obs	0.21	228	0.16	330	0.29	296	0.25	262
A	0.22	238	0.21	359	0.25	288	0.30	286
B	0.20	220	0.19	333	0.25	287	0.30	284
C	0.20	221	0.20	334	0.25	287	0.30	285
CADA	0.18	220	0.17	333	0.26	287	0.29	285
TS4.obs	0.26	211	0.22	316	0.32	298	0.31	259
A	0.33	224	0.35	345	0.26	284	0.31	281
B	0.23	211	0.23	323	0.26	283	0.31	280
C	0.24	210	0.24	322	0.26	283	0.31	280
CADA	0.21	214	0.20	325	0.27	285	0.30	282
TS5.obs	0.10	290	0.11	306	0.11	239	0.10	301
A	1.43	277	1.74	41	0.38	297	0.40	295
B	0.33	216	0.33	329	0.28	285	0.33	283
C	0.33	216	0.34	329	0.28	285	0.33	283
CADA	0.28	218	0.27	330	0.29	286	0.32	284
G1.obs	0.18	217	0.16	316	0.27	305	0.28	298
A	0.25	227	0.25	346	0.25	285	0.30	282
B	0.20	214	0.20	327	0.25	284	0.30	282
C	0.21	214	0.20	327	0.25	285	0.30	282
CADA	0.19	216	0.18	328	0.26	286	0.29	283
G2.obs	0.24	233	0.21	332	0.34	279	0.35	271
A	0.34	230	0.35	352	0.27	285	0.32	282
B	0.23	214	0.23	326	0.26	284	0.31	282
C	0.24	214	0.24	326	0.26	285	0.31	282
CADA	0.21	216	0.20	328	0.27	286	0.30	283

Table F.2: Observed and predicted tidal harmonic constituents for GPS and Tide Gauge sites in the Amery Ice Shelf/Prydz Bay model domain. A comparison MECO model runs with different WCT grids. Amplitude is in metres, Phase is in degrees relative to GMT. ZS represents Zhong-Shan, and BL represents Beaver Lake.

Location/	M_2		S_2		K_1		O_1	
WCT grid	Ampl.	Phase	Ampl.	Phase	Ampl.	Phase	Ampl.	Phase
C12.obs	0.29	228	0.25	327	0.31	283	0.32	276
A	0.38	235	0.40	358	0.27	286	0.32	283
B	0.25	215	0.25	327	0.27	285	0.31	282
C	0.26	215	0.26	327	0.27	285	0.31	282
CADA	0.22	217	0.21	329	0.27	286	0.30	284
C10.obs	0.28	227	0.25	327	0.28	289	0.29	282
A	0.40	237	0.43	0	0.28	286	0.32	283
B	0.25	215	0.25	328	0.27	285	0.32	282
C	0.27	215	0.27	328	0.27	285	0.32	282
CADA	0.22	217	0.21	329	0.27	286	0.30	284
C8.obs	0.27	239	0.23	339	0.29	294	0.30	287
A	0.43	240	0.46	3	0.28	286	0.33	284
B	0.26	216	0.26	328	0.27	285	0.32	282
C	0.28	216	0.28	328	0.27	285	0.32	283
CADA	0.23	217	0.22	329	0.27	286	0.30	284
CAMP.obs	0.26	220	0.22	320	0.32	285	0.33	278
A	0.44	241	0.48	4	0.28	287	0.33	284
B	0.27	216	0.27	329	0.27	285	0.32	283
C	0.28	216	0.28	328	0.27	285	0.32	283
CADA	0.23	217	0.22	329	0.27	286	0.30	284
C6.obs	0.29	230	0.25	330	0.39	276	0.41	269
A	0.46	241	0.49	5	0.28	287	0.33	284
B	0.27	216	0.27	329	0.27	285	0.32	283
C	0.29	216	0.29	329	0.27	285	0.32	283
CADA	0.23	217	0.23	329	0.27	286	0.30	284
C2.obs	0.28	221	0.25	321	0.23	275	0.24	268
A	0.51	243	0.56	7	0.29	287	0.34	284
B	0.29	216	0.29	329	0.27	285	0.32	283
C	0.30	216	0.30	329	0.28	285	0.32	283
CADA	0.24	217	0.24	329	0.28	286	0.31	284
V3.obs	0.23	247	0.20	347	0.33	282	0.34	274
A	1.09	261	1.29	26	0.34	291	0.38	289
B	0.32	216	0.32	329	0.28	285	0.33	283
C	0.33	216	0.33	328	0.28	285	0.33	283
CADA	0.27	217	0.26	329	0.28	286	0.31	284
V5.obs	0.25	238	0.22	338	0.34	281	0.35	274
A	1.28	267	1.55	32	0.36	293	0.39	291
B	0.32	216	0.33	329	0.28	285	0.33	283
C	0.33	216	0.34	328	0.28	285	0.33	283
CADA	0.27	217	0.27	329	0.29	286	0.31	284

Table F.3: Observed and predicted tidal harmonic constituents for GPS and Tide Gauge sites in the Amery Ice Shelf/Prydz Bay model domain. A comparison between available models. MECO and *OzPOM* are presented in this thesis, CADA, CATS and FES are tidal models from previous workers. Amplitude is in metres, Phase is in degrees relative to GMT. ZS represents Zhong-Shan, and BL represents Beaver Lake. ** indicates site is on land in the model grid.

Location/	M_2		S_2		K_1		O_1	
MODEL	Ampl.	Phase	Ampl.	Phase	Ampl.	Phase	Ampl.	Phase
ZS.obs	0.20	212	0.18	311	0.27	287	0.28	259
MECO	0.18	207	0.17	318	0.25	281	0.29	278
OzPOM	0.20	212	0.18	314	0.22	286	0.27	264
CADA00.10	0.19	216	0.18	324	0.26	286	0.28	276
CATS00.10	0.22	211	0.22	311	0.30	284	0.31	276
FES99	0.20	326	0.20	42	0.29	79	0.30	274
BL.obs	0.24	253	0.25	357	0.28	296	0.30	288
MECO	0.25	219	0.24	332	0.27	286	0.31	284
OzPOM	0.28	227	0.29	330	0.24	292	0.29	269
CADA00.10	0.24	235	0.24	343	0.29	291	0.30	281
CATS00.10	0.28	226	0.30	326	0.32	289	0.33	282
FES99	0.33	57	0.36	317	0.31	43	0.32	67
HWDT.obs	0.19	215	0.20	319	0.26	281	0.28	272
MECO	0.19	208	0.19	319	0.25	282	0.30	279
OzPOM	0.22	214	0.21	316	0.23	286	0.27	264
CADA00.10	0.20	222	0.19	331	0.27	288	0.28	277
CATS00.10	0.24	215	0.24	316	0.30	285	0.32	278
FES99	0.21	321	0.22	36	0.29	78	0.30	273
TS1.obs	0.21	222	0.20	323	0.32	294	0.28	266
MECO	0.20	213	0.20	325	0.25	284	0.30	281
OzPOM	0.23	220	0.22	323	0.23	289	0.27	267
CADA00.10	0.20	229	0.20	337	0.27	290	0.28	279
CATS00.10	0.24	221	0.25	322	0.30	287	0.31	280
FES99	0.21	314	0.21	29	0.30	77	0.31	272
TS3.obs	0.21	228	0.16	330	0.29	296	0.25	262
MECO	0.20	220	0.19	333	0.25	287	0.30	284
OzPOM	0.22	228	0.22	332	0.23	292	0.27	270
CADA00.10	0.20	235	0.20	343	0.27	293	0.28	282
CATS00.10	0.24	227	0.25	328	0.30	290	0.31	283
FES99	0.19	304	0.19	19	0.29	73	0.31	88
TS4.obs	0.26	211	0.22	316	0.32	298	0.31	259
MECO	0.23	211	0.23	323	0.26	283	0.31	280
OzPOM	0.26	218	0.26	321	0.24	288	0.28	266
CADA00.10	0.22	228	0.22	336	0.28	289	0.29	279
CATS00.10	0.26	220	0.28	320	0.31	287	0.33	280
FES99	0.26	291	0.31	10	0.30	69	0.31	87
TS5.obs	0.10	290	0.11	306	0.11	239	0.10	301
MECO	0.33	216	0.33	329	0.28	285	0.33	283
OzPOM	0.37	223	0.38	326	0.26	290	0.31	268
CADA00.10	0.29	233	0.30	341	0.31	290	0.32	280
CATS00.10	0.34	224	0.38	324	0.35	288	0.36	281
FES99	**	**	**	**	**	**	**	**
G1.obs	0.18	217	0.16	316	0.27	305	0.28	298
MECO	0.20	214	0.20	327	0.25	284	0.30	282
OzPOM	0.22	222	0.22	325	0.23	290	0.27	268
CADA00.10	0.20	230	0.20	338	0.27	291	0.28	280
CATS00.10	0.24	222	0.25	323	0.30	288	0.31	281
FES99	0.21	313	0.21	27	0.30	77	0.31	272
G2.obs	0.24	233	0.21	332	0.34	279	0.35	271
MECO	0.23	214	0.23	326	0.26	284	0.31	282
OzPOM	0.26	222	0.26	324	0.24	289	0.28	267
CADA00.10	0.22	231	0.22	339	0.28	290	0.29	279
CATS00.10	0.27	222	0.28	322	0.31	287	0.33	281
FES99	0.27	86	0.30	348	0.30	58	0.31	79

Table F.4: Observed and predicted tidal harmonic constituents for GPS and Tide Gauge sites in the Amery Ice Shelf/Prydz Bay model domain. A comparison between available models. MECO and *OzPOM* are presented in this thesis, CADA, CATS and FES are tidal models from previous workers. Amplitude is in metres, Phase is in degrees relative to GMT. ZS represents Zhong-Shan, and BL represents Beaver Lake. ** indicates site is on land in the model grid.

Location/	M_2		S_2		K_1		O_1	
MODEL	Ampl.	Phase	Ampl.	Phase	Ampl.	Phase	Ampl.	Phase
C12.obs	0.29	228	0.25	327	0.31	283	0.32	276
MECO	0.25	215	0.25	327	0.27	285	0.31	282
OzPOM	0.28	222	0.28	325	0.24	290	0.29	267
CADA00.10	0.23	232	0.24	340	0.28	290	0.29	280
CATS00.10	0.28	223	0.30	323	0.32	288	0.33	281
FES99	0.33	75	0.37	337	0.31	51	0.31	74
C10.obs	0.28	227	0.25	327	0.28	289	0.29	282
MECO	0.25	215	0.25	328	0.27	285	0.32	282
OzPOM	0.29	223	0.29	325	0.24	289	0.29	267
CADA00.10	0.24	232	0.24	340	0.29	290	0.30	280
CATS00.10	0.29	223	0.31	323	0.32	288	0.34	281
FES99	0.37	71	0.43	333	0.31	48	0.32	73
C8.obs	0.27	239	0.23	339	0.29	294	0.30	287
MECO	0.26	216	0.26	328	0.27	285	0.32	282
OzPOM	0.30	223	0.30	326	0.24	290	0.29	268
CADA00.10	0.24	232	0.25	340	0.29	290	0.30	280
CATS00.10	0.29	223	0.32	323	0.32	288	0.34	281
FES99	0.37	69	0.43	331	0.32	47	0.32	72
CAMP.obs	0.26	220	0.22	320	0.32	285	0.33	278
MECO	0.27	216	0.27	329	0.27	285	0.32	283
OzPOM	0.30	224	0.31	326	0.24	290	0.29	268
CADA00.10	0.25	233	0.25	341	0.29	291	0.30	280
CATS00.10	0.30	224	0.32	324	0.32	288	0.34	281
FES99	0.41	69	0.47	331	0.33	47	0.33	72
C6.obs	0.29	230	0.25	330	0.39	276	0.41	269
MECO	0.27	216	0.27	329	0.27	285	0.32	283
OzPOM	0.31	223	0.31	326	0.25	290	0.29	268
CADA00.10	0.25	233	0.26	341	0.29	290	0.30	280
CATS00.10	0.30	224	0.32	324	0.33	288	0.34	281
FES99	0.41	69	0.47	331	0.33	47	0.33	72
C2.obs	0.28	221	0.25	321	0.23	275	0.24	268
MECO	0.29	216	0.29	329	0.27	285	0.32	283
OzPOM	0.32	224	0.33	326	0.25	290	0.30	268
CADA00.10	0.26	233	0.27	341	0.29	290	0.30	280
CATS00.10	0.31	224	0.34	324	0.33	288	0.34	281
FES99	**	**	**	**	**	**	**	**
V3.obs	0.23	247	0.20	347	0.33	282	0.34	274
MECO	0.32	216	0.32	329	0.28	285	0.33	283
OzPOM	0.36	223	0.37	326	0.26	290	0.30	268
CADA00.10	0.28	233	0.30	341	0.31	290	0.31	280
CATS00.10	0.34	224	0.38	324	0.34	288	0.35	281
FES99	**	**	**	**	**	**	**	**
V5.obs	0.25	238	0.22	338	0.34	281	0.35	274
MECO	0.32	216	0.33	329	0.28	285	0.33	283
OzPOM	0.36	223	0.37	326	0.26	290	0.31	268
CADA00.10	0.29	233	0.30	341	0.31	290	0.32	280
CATS00.10	0.34	224	0.38	324	0.35	288	0.36	281
FES99	**	**	**	**	**	**	**	**

Appendix G

List of Symbols

Symbol	Description	Units
x, y, z	Cartesian coordinates	m
t	Time coordinate	s
U, V	Horizontal velocities	ms^{-1}
W	Vertical velocity	ms^{-1}
ω	σ-coordinate vertical velocity	ms^{-1}
H	Water Depth	m
η	Surface elevation	m
D	Water Column Thickness $(H + \eta)$	m
g	Gravitational acceleration	ms^{-2}
f	Coriolis parameter	s^{-1}
S	Salinity	psu
T	Temperature	$^{\circ}C$
T_F	Freezing Temperature	$^{\circ}C$
ρ	Water Density	kgm^{-3}
ρ_o	Reference Water Density	kgm^{-3}
p	Pressure	$decibar$
p_{atm}	Atmospheric pressure	$decibar$
K_H	Vertical heat diffusivity	m^2s^{-1}
K_M	Vertical eddy diffusivity	m^2s^{-1}
q^2	Turbulence kinetic energy	m^2s^{-2}
l	Turbulence length scale	m
B_1, E_1, E_3	Turbulence closure constants	[ ]
κ	Von Karman's constant	[ ]
τ_B	Bottom Stress	Nm^{-2}
C_Z	Drag Coefficient	[ ]
z_0	Roughness parameter	m
$u*$	Friction velocity	ms^{-1}
γ_T	Thermal exchange velocity	ms^{-1}
C_p	Specific Heat of seawater	$Jkg^{-1}K^{-1}$
Φ	Rate of Freeze	ms^{-1}
Ψ	Depth-integrated streamfunction	Sv
Ψ_V	Zonally-integrated streamfunction	Sv